PROCEEDINGS

Impact of Aircraft Emissions upon the Atmosphere

VOLUME II

International Colloquium
PARIS 15-18 October 1996

IMPACT OF AIRCRAFT UPON THE ATMOSPHERE

INTERNATIONAL COLLOQUIUM

PARIS-CLAMART - 15-18 OCTOBER 1996

COLLOQUIUM CHAIRMAN

Jean Carpentier, Comité Avion-Ozone

INTERNATIONAL SCIENTIFIC ADVISORY COMMITTEE

Georges Amanatidis, EU, Belgium
Reinhold Busen, DLR, Germany
Guy Brasseur, CNRS, France
Daniel Cadet, CNRS, France
Marie-Lise Chanin, CNRS, France
Rainer Dunker, EU, Belgium
Adolf Ebel, Univ. Köln, Germany
David Fahey, NOAA, USA
Randall Friedl, NASA Hdq, USA
Roger Gardner, Dep. of Transport, United Kingdom
André Girard, ONERA, France
Didier Guffond, ONERA, France
John Holton, Univ. Washington,USA
Paul Kuentzmann, ONERA, France
David Lister, DRA, United Kingdom
Nicole Louisnard, ONERA, France
Bruno Massé, Snecma, France
Gérard Mégie, CNRS, France
Philippe Mirabel, Univ. Strasbourg, France
Jean-Louis Parent, Aérospatiale, France
Jean-Claude Petit, CNRS, France
Richard Ramaroson, ONERA, France
A. Ravishankara, NOAA, USA
Adolf Schmitt, DLR, Germany
Ulrich Schumann, DLR, Germany
Adrian Tuck, NOAA, USA
Howard Wesoky, NASA, USA

SUPPORTING ORGANIZATIONS

European Union Brussels DGXII
Délégation Générale de l'Avation Civile
Office National d'Etudes et de Recherches Aérospatiales

ORGANIZED BY ONERA

OFFICE NATIONAL D'ETUDES ET DE RECHERCHES AEROSPATIALES
under the auspices of the Association of European Research Establishment in Aeronautics (AEREA)

CONTENTS

VOLUME I

SESSION 1 - PRESENT STATUS AND PERSPECTIVE

SESSION 2 - EMISSION AND TRAFFIC

SESSION 3 - PHYSICS AND CHEMISTRY IN THE AIRCRAFTWAKE

SESSION 4 - MESOSCALE: CORRIDORS - S/T EXCHANGE

SESSION 5 - NATURAL AND ANTHROPOGENIC EMISSIONS - SPECIFIC INSTRUMENTATION

SESSION 6 - GLOBAL SCALE - CHEMISTRY

SESSION 7 - GLOBAL SCALE - CLIMATE

VOLUME II

POSTERS PART I (ACCOMPANYING SESSIONS 1-2-3)

POSTERS PART II (ACCOMPANYING SESSIONS 4-5-6-7)

EU-project AEROJET:
Non-intrusive measurements of aircraft engine exhaust emissions

K. Schäfer[1], J. Heland[1], R. Burrows[2], M. Bernard[3], G. Bishop[4], E. Lindermeir[5], D. H. Lister[6], P. Wiesen[7], M. Hilton[8]

[1]FhG-IFU: Fraunhofer-Institut für Atmosphärische Umweltforschung, Kreuzeckbahnstraße 19, D-82467 Garmisch-Partenkirchen, F.R.G.
[2]RR: Rolls-Royce, Engine Support Laboratory, U.K.
[3]AUXITROL: Auxitrol, S.A., Aerospace Equipment Division, France
[4]BAe: British Aerospace, Sowerby Research Centre, U.K.
[5]DLR: Deutsche Forschungsanstalt für Luft- und Raumfahrt e.V., Institut für Optoelektronik, F.R.G.
[6]DRA: Defence and Research Agency, Propulsion and Development Department, U.K.
[7]BUGHW: Bergische Universität-Gesamthochschule Wuppertal, FB 9/Physikalische Chemie, F.R.G.
[8]U. Reading: University of Reading, Department of Physics, U.K.

1. Objectives

The environmental impact of air traffic and economical aspects require aircraft engines to be developed which have reduced trace gas emissions and, at the same time, increased efficiency. Each new engine developed must be shown to meet the environmental requirements laid down by regulatory bodies [1], and exhaust gas measurements which accompany all stages of engine development are an essential part of this development process. Non-intrusive measurements are the method of choice within the AEROJET project [2] promising to avoid the disadvantages of the gas sampling techniques which are currently used.

In addition to offering the capabilities of conventional gas species determination systems, the proposed optical techniques will demonstrate the following benefits

(a) lower operational costs, easier handling and versatility provide for early characterisation of engine emissions including design alerts,
(b) improve and expand the database of engine emissions,
(c) avoid the costly design and manufacture of extractive sampling rakes,
(d) exclude chemical changes which may occur within the probe extraction system before reaching the analytical equipment,
(e) avoid the need to demonstrate the representativeness of rake samples, and
(f) reduce the risks of engine damage during measurement.

Different ground based non-intrusive measurement methods ~~will be~~ are demonstrated during a final evaluation phase. Several non-intrusive techniques ~~will be~~ are compared with conventional gas sampling and analysis techniques.

The main goal of the AEROJET programme is to demonstrate the equivalence of remote measurement techniques to conventional extractive methods for both gaseous and particulate measurements. The different remote measurement techniques ~~will be~~ are compared and calibrated. A demonstrator measurement system for exhaust gases, temperature and particulates including data-analysis software ~~will be~~ is regarded as result of this project.

2. Experimental

The consortium of partners already has experience in determining compounds and temperature of exhaust gases by non-intrusive spectroscopic measurement techniques. New solutions shall be found for cost-effectiveness (narrow-band spectroscopy) and particulate measurements. Spectrally high resolved measurements by FTIR provide spectroscopic inputs for those tasks.
The impact of the severe acoustical load typical for the test rig environment on these optical methods has to be investigated and possibly to be reduced by measures at the test bed as well as within the measurement systems.
The effectiveness of each of the non-intrusive techniques developed would then be demonstrated experimentally and the results of measurements validated by comparing the results with those from conventional measurements carried out by DRA. For this purpose DRA will map the exhaust of a typical gas turbine engine for at least 2 power settings incl. the idle and a maximum continuous thrust level with respect to CO_2, CO, UHC, NO_x, and smoke.

2.1 FTIR Techniques

Both the FTIR emission and absorption technique will be used for jet engine test rig measurements and will be investigated with regard to their ability to quantify different species in the exhaust.
The engine exhaust gases have strong characteristic infrared active transition bands for which the FTIR technique has the ability to monitor remotely all the components simultaneously. The possibility of making measurements of CO_2, CO, H_2O, NO, NO_2, NO_y, SO_x, and UHC shall be investigated by DLR, BAe, U. Reading, and FhG-IFU with different FTIR spectrometers. The application of FTIR absorption spectroscopy includes the use of an open long-path absorption cell (multi path reflection) in order to increase the sensitivity for the detection of certain species such as NO and NO_2. A long-path White mirror system will be designed by BUGHW and installed in a ground level test rig at DRA.
Data calibration for each instrument with a known amount of gases in a heatable cell is performed during the measurement. The cell is being supplied by DLR with the necessary technical descriptions for the adaptation of each instrument. Each partner involved is responsible for the optical adaptation of their instrument to the cell. Help will be provided by BUGHW.
The partners involved use a variety of retrieval methods to obtain the results from the measured spectra. Within the project these retrieval techniques will be further developed to match the given application and later be evaluated by comparing the data with those obtained by conventional techniques.

2.2 High-Temperature Spectroscopic Data Base, Laboratory Work

The state-of-the-art knowledge of CO_2, H_2O, and CO at high temperatures is in the HITEMP line-by-line database which, after its final release to the public, will be an extension of the well-known molecular HITRAN database [3] for higher temperatures.
Two problems are associated with the spectra under the given conditions: firstly the high temperature causes a very high spectral line density and secondly the high air pressure causes the spectral structure to be smeared out and thus the spectral information to be reduced. Thus, line-by-line calculations often fail when applied to 1000 mbar total air pressure at high temperature. Very often spectroscopic parameters are obtained at much lower total pressures and thus have to be extrapolated. In order to obtain reliable emission indices from the observed spectra, it will be

necessary to carry out new laboratory measurements under the required conditions. In case where isolated lines cannot be observed under the given conditions, absorption cross sections as a function of temperature and gas pressure will be given.
The main objective of the laboratory work at DLR is to provide a molecular database for the species NO, NO_2, H_2O, CO, CO_2 in order to determine the concentrations from measured engine exhaust spectra with high accuracy. Absorption spectra of the individual gases will be recorded with a commercial high resolution Fourier-Transform-Spectrometer. An adequate number of spectra will be obtained to cover the temperature range 300-800 K. If mostly isolated lines are observed, the following line parameters will be evaluated: line position, line strength, pressure broadening parameters as a function of temperature. In case of broad band absorptions, absorption cross sections will be retrieved.

2.3 Narrow-Band Spectroscopy

The narrow-band spectroscopy is innovative in that it measures energies in pre-determined, narrow bands (of about 5-10 nm) and bases its measurement on relative variations of amplitude lines in specific wavelengths within these narrow bands. The use of a simple static scattering element and a suitable number of detectors, largely simplifies the measurement which makes it suitable for application on an industrial scale due to reduced cost and signal processing. The absence of moving parts makes the technique particularly attractive to future airborne applications. Furthermore, as in each narrow band ("band head") there are a number of amplitude lines, the method allows for the direct measurement of concentration (and temperature) in several sections along the optical line-of-sight. Most available optical techniques require several measurements followed by data analysis based on simplified theoretical models to deduce discrete concentrations.
The new product which will emanate from this research at AUXITROL is a proof-of-concept technology demonstrator of an optical gas analyser using narrow-band (or "band head") analysis. The demonstrator device will measure CO_2 concentration in a specific aero-engine exhaust gas configuration chosen for this programme. A process derived from this technique allows particle size determination thus opening the scope for other new products. The principle can also be applied to remote detection of temperature and super critical water vapour (icing conditions) which AUXITROL is exploring. The possibility also exists of measuring temperature using this technique, resulting in the possibility of a combined temperature/concentration technique.

2.4 Remote Particulate Measurements

Particulate size and number density measurement by light scattering measurements have been used for about 100 years. Smoke measurements using light obscuration instruments have been developed over the past 25 years and some correlation with filter stain measurements has been empirically determined. The application of optical techniques in high noise, high vibration environments with large temperature gradients and turbulent flows represents a considerable degree of innovation.
The broad band, highly spectral resolved FTIR measurements will be analysed for information about optical parameters of particulate matter.
The remote particulate measurement techniques will be studied at RR, a suitable technique will be selected, and the results compared with those from the stained filter reflectance technique currently specified for engine certification. Comparison may be made with size distributions of extracted samples, and it is hoped that a correlation can be developed between the different smoke parameters.

3. Working Plan

The project started in May 1996 and will be running for two years.
During an initial phase for planning the experiments and the fabrication of the mirror system the partners will start to adapt their instruments and software to the special measurements made in AEROJET. The systems will then be installed and tested together with the mirror arrangement. A check of the assembly will be carried out during test measurements. After some modifications the final demonstration measurements will be made in month 17 of the project. Parallel to the experimental work with the engines the measurements of high temperature spectral data and the development of the retrieval techniques will be carried out.
The experimental tests will take place on the Glen Test bed at DRA Pyestock, Farnborough, UK, which is a sea level test facility allowing excellent access to the engine exhaust for both intrusive and non-intrusive measurements.
After the measurements comparisons will be made between the raw and calibrated data gathered by all partners. These include the FTIR emission and absorption mode with the multi-path reflection compartment, the conventional passive emission mode, the narrow-band spectroscopic data and the particulate measurements. This will enable conclusions to be drawn concerning the performance of the instruments, the accuracy of calibration techniques, and the retrieval algorithms used. Finally the technique with the most potential can be selected.

References

[1] ICAO, International Civil Aviation Organization, "Environmental Protection", Annex 16, Vol. II, Aircraft Engine Emissions, Second Edition-1993, ICAO Document Sales Unit, 1000 Sherbrooke Street West, Suite 400, Montreal, Quebec, Canada H3A 2R2 (1993)

[2] Schäfer, K.; Burrows, R.; Bernard, M.; Bishop, G.; Lindermeir, E.; Lister, D. H.;Wiesen, P; Hilton M., "Non-intrusive measurements of aircraft engine exhaust emissions (AEROJET)", Brite/EuRam project BE95-1357, Project Programme, 8. Feb. 96 (1996)

[3] Rothman, L. S.; Gamache, R. R.; Tipping, R. H.; Rinsland, C. P.; Smith, M. A. H.; C. Benner, D.; Malathy Devi, V.; Flaud, J.-M.; Camy-Peyret, C.; Perrin, A.; Goldman, A.; Massie, S. T.; Brown, L. R.; Toth, R. A., "The HITRAN molecular database: editions of 1991 and 1992", J. Quant. Spectrosc. Radiat. Transfer, 48, 469-508 (1992)

AIRFORCE: AIRCRAFT EMISSIONS AND RADIATIVE FORCING FROM EMISSIONS

E.W. Meijer[1], J.P. Beck[2], H. Kelder[1], J. Lelieveld[3], B.A. Scheeren[3], G.J.M. Velders[2], P.F.J. van Velthoven[1], W.M.F. Wauben[1]

Abstract. The Dutch AIRFORCE project focuses on the effects of subsonic aircraft emissions on the chemical composition of the atmosphere and subsequent radiative forcing. It includes measurements in the tropopause region and the modelling of exhaust plumes and large-scale effects. An aircraft exhaust plume model has been developed to study plume processes. The results of the plume model are used in the global transport chemistry model CTMK to determine large-scale effects of plume processes. Due to the efficient conversion of NO_x into HNO_3 inside aircraft exhaust plumes, a decrease of about 25% of the O_3 perturbation was found in the NAFC at 200 hPa in July. Measurements of hydrocarbons revealed a dominant role of the anthropogenic continental emissions of light hydrocarbons in the tropopause region.

1. INTRODUCTION

The AERONOX project [1] predicted a contribution of aircraft emissions of 20% to 70%, depending on season, to the concentration of NOx in the North Atlantic Flight Corridor (NAFC), with a subsequent photochemically generated increase in ozone of 2-9%. The additional ozone in the tropopause region enhances the greenhouse effect. The climate sensitivity to changes in ozone are larger in the tropopause region compared to other regions [7] [8].

However, intercomparison of global transport chemistry models revealed large differences in background concentrations, due to the description of vertical transport. Stratosphere-troposphere exchange determines to a large extent the budgets of trace gases in the lower stratophere, deep convection influences strongly the perturbations in the flight corridors through vertical redistribution of the emissions.

Although, the AERONOX project included studies of the effects of aircraft exhaust plumes (SP2), the effects in the dispersion regime have not been studied. Moreover, the chemical conversion of NOx into other nitrogen oxides in the aircraft exhaust plumes affects the effective emissions of aircraft pollutants at large scales. The role of plume processes are not integrated in modelling efforts on a global scale, yet.

In the AIRFORCE project an effort is made to integrate measurements and modelling on both plume-scale and global scale. Three measuring campaings will be conducted in the period 1995-1997 in the North Atlantic Region. Our global chemistry transport models MOGUNTIA [20], with monthly-mean meteorological data, used for fast scenario calculations, and CTMK with 6-hourly meteorology data for detailed studies, will be validated with the results from the measuring campaigns and the data from the projects STREAM and POLINAT, to which we have access. Further, an aircraft exhaust plume model has been developed to study the plume processes in the dispersion regime.

In this paper we present the current state of the project, according to the following outline: In chapter 2 the plume model is described and some of the major results are presented. In the next chapter the results of the plume model are used in the global chemistry transport model CTMK, which is shortly described in the same chapter. The results are compared with

[1] KNMI, Royal Netherlands Meteorological Institute, De Bilt, The Netherlands
[2] RIVM, National Institute of Public Health and the Environment, Bilthoven, The Netherlands
[3] IMAU, Institute for Marine and Atmospheric Research Utrecht, Utrecht, The Netherlands

results with unmodified aircraft emissions. In chapter 4 some results of one of our measuring campaigns are presented, followed by the conclusions in chapter 5.

2. Modelling of an aircraft exhaust plume.

An aircraft exhaust plume has been developed to calculate the conversions of nitrogen oxides in the exhaust plumes of aircraft. The model focuses on the dispersion regime, since it has been shown that conversions of NO_x in the early jet and vortex phases are small [5][6][10]. The model consists of a plume cross-section, subdivided in 10 elliptical rings, with an initial gaussian concentration profile. Chemistry in each ring and exchange between neighbouring rings as well as entrainment of ambient air is implemented. The mathematical description of this modelling approach is decribed in detail by others [11][18]. The dispersion parameters are adopted from Dürbeck and Gerz [4], with a horizontal diffusion constant of D_h = 20 m^2/s and a vertical diffusion constant of D_v = 0.15 m^2/s. Initial dispersion coefficients are σ_h = 117 m and σ_v = 83 m at the start of the dispersion regime (t = 100 s). The chemistry mechanism is very similar to the EMEP-scheme and was adapted for the free troposphere by Strand and Hov [16]. Heterogeneous reactions of N_2O_5 on sulphate aerosol and ice particles have been added to the mechanism with crude estimations for the surface areas, which will not be discussed here. The effect of these heterogeneous reactions is small.

The main objective of our plume model is to translate NO_x aircraft emissions in modified emissions of several nitrogen compounds for usage in global chemistry transport models. For this reason, the results will be presented as fractions of nitrogen oxides. Figure 1 shows the time evolution of the fraction of the major nitrogen oxides in January and July, at a latitude of 50° N and an altitude of 10 km, which can regarded as a representative for the NAFC. The emissions took place at midday. In July, the conversion of NO_x into other nitrogen oxides is very efficient, whereas the the conversion ratio in January is much smaller. In July, the main contributor to NO_y is HNO_3, in January N_2O_5. Series of plume simulations have been performed by varying latitude, altitude and season. In figure 2 the fractions of NO_x, remaining after 48 hours are represented for all latitudes at altitudes from 5 to 12 km for July. The patterns reveal the dominant roles of temperature and photolytical activity.

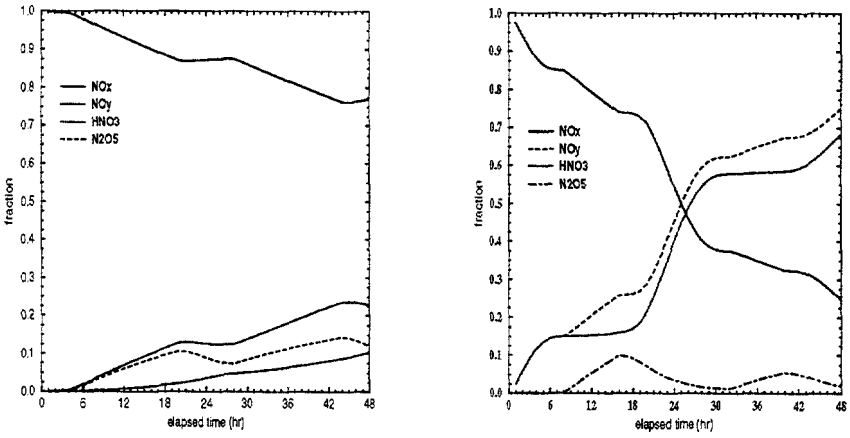

Figure 1. The time evolution of the fractions nitrogen oxides in an aircraft exhaust plume at 10 km altitude and 50° N in January (left) and July (right).

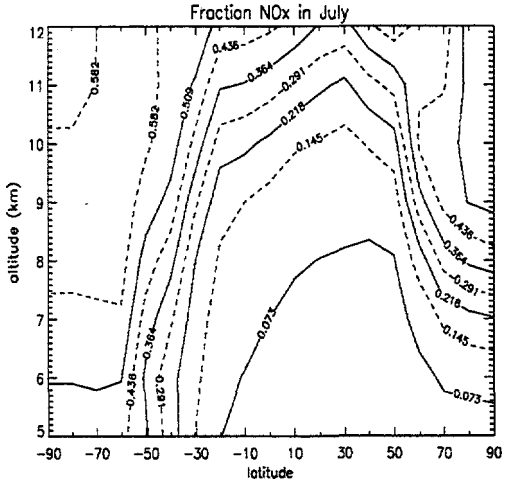

Figure 2. The fraction NO_x after 48 hours in an aircraft exhaust plume in July for altitudes 5-12 km and all latitudes.

3. Global modelling with modified aircraft emissions.

Neglecting plume-effects in global models will generally overestimate the ozone production due to aircraft emissions. To account for plume-effects in modelling for the global scale, the results of our plume model are used to modify the aircraft emission in global model calculations. The model used here, is the Chemistry Transport Model KNMI (CTMK) and is a three dimensional model [19]. CTMK calculates the horizontal and vertical transport of tracers on the basis of 6-hourly output from the European Centre for Medium-Range Weather Forecasts (ECMWF) model [17]. The chemistry scheme in CTMK contains the daytime chemistry of 13 trace gases with photolytical and anorganic reactions of NO_x, O_3, HO_x, CO and it contains methane oxidation. Nightime chemistry consists of an off-line parameterized heterogeneous reaction, which converts NO_2 and O_3 into HNO_3. This parametrization is based on the work of Dentener and Crutzen [3]. CTMK has 15 sigma-levels up to 10 hPa and has a horizontal resolution of 4° in longitude and 5° in latitude. However, the first preliminary runs have been performed with a lower resolution of 8° in longitude and 10° in latitude.

First, a reference run with the unmodified NO_x aircraft emissions from the ANCAT database has been made, followed by a run with modified emissions, based on the results of the plume calculations. Figure 3 shows O_3 perturbation due to modified aircraft emissions at 200 hPa for July. The ozone perturbations in the NAFC vary from 2 to 3 ppbv, the NO_x perturbations are 20-70 pptv. Figure 4 shows the plume-correction to the ozone-perturbation (the difference between the run with unmodified emissions and modified emissions) at 200 hPa for July. The concentration of ozone decreased 0.6-0.8 ppbv (25%), due to the incorporation of plume processes. The plume-corrections to the NO_x perturbations cause an decrease of around 20%, the HNO_3 concentrations increased about 10%.

4. Hydrocarbon measurements form AIRFORCE 1995

The AIRFORCE project also involves three measuring campaigns in the period 1995-1997 performed with a twinjet Citation aircraft. The flights are conducted from Amsterdam airport into the North Atlantic region. The main objective is to study the role of synoptic disturbances in the vertical redistribution of the natural en anthropogenic ozone and its chemical precursors, in particular in the tropopause region. As an example, the results of hydrocarbon measurements during the AIRFORCE 1995 campaign aircraft are presented.

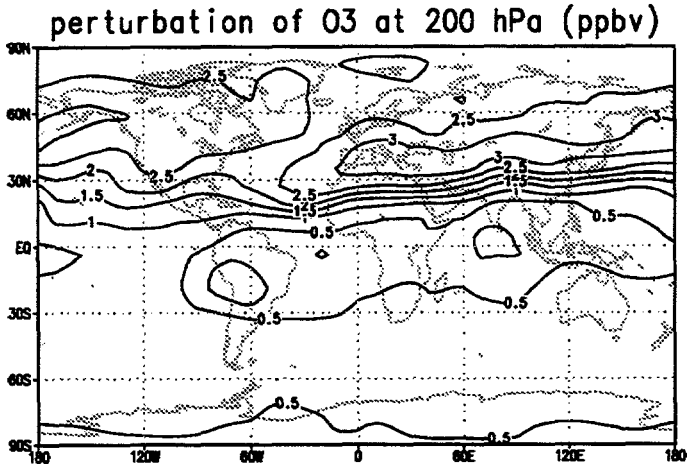

Figure 3. The ozone perturbation due to aircraft emissions at 200 hPa in July

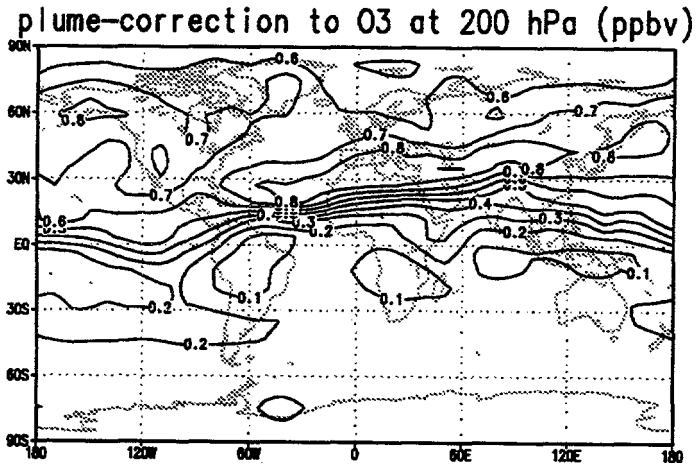

Figure 4. The plume-correction to the ozone perturbation at 200 hPa in July. The modified aircraft emissions cause a 25% less ozone perturbation.

In total 21 whole air samples have been collected in stainless steel canisters between 6 and 12.5 km altitude over the North sea area on board a Cessna Citation on November the 27th and December the 3th. Results are presented of ethane, acetylene, the sum of acetylene + propane + n-butane + i-butane + n-pentane +i -pentane (sum of C_2 - C_5) and tetrachloroetylene (C_2Cl_4) which all have strong anthropogenic sources in the continental boundary layer [2][9]. The results are discussed in more detail by Scheeren et al. [13]. Ethane is a major constituent among the light hydrocarbons species that can be measured in aircraft exhaust [15]. Tetrachloroetylene is recognized as a sensitive boundary layer tracer for urban/industrial pollution since its sources are only anthropogenic [14]. A good correlation between C_2Cl_4 and ethane and other light hydrocarbons suggests that they have similar anthropogenic sources [2][14]. A poor correlation with C_2Cl_4 indicates the influence of other sources like natural gas losses or emissions from soils and vegetation [12] or possibly subsonic aircraft exhaust at cruise altitudes. Our results show a high correlation of ethane with acetylene, the sum of C_2 - C_5 and the urban tracer C_2Cl_4.

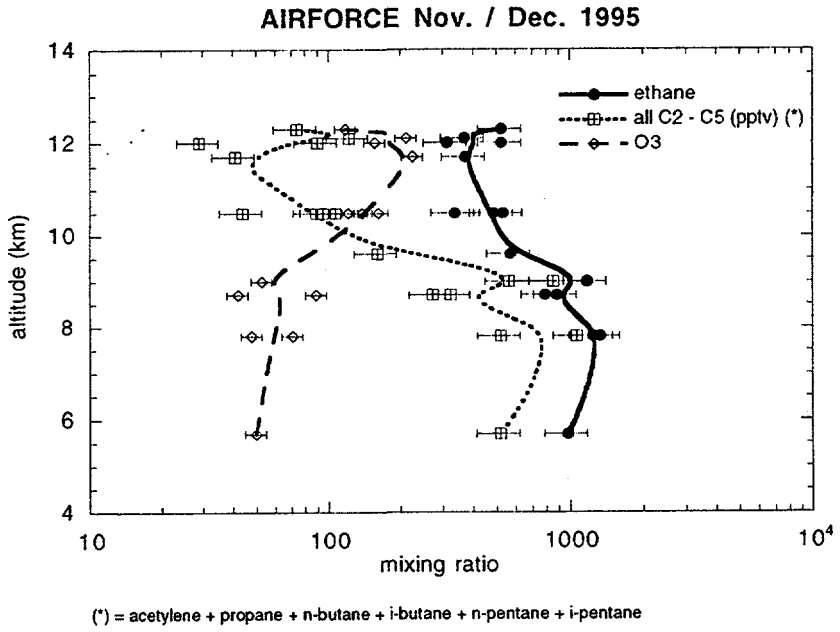

Figure 5. *The average vertical profiles of ozone (ppbv), ethane and the sum of measured light hydrocarbons (pptv). The light hydrocarbons show a significant anti-correlation with ozone. The increase of light hydrocarbons and subsequent decrease of ozone at the highest flight altitudes are caused by variations of the tropopause heights.*

5. Conclusions

The new developed plume model enables the modification of aircraft emissions for global models to account for plume effects. Preliminary calcultations with CTMK show O_3 perturbations of 2-3 ppbv at 200 hPa for July, which is about 25% less compared with the results of calculations with unmodified aricraft emissions. The perturbations of NO_x decreased about 20%, the perurbation of HNO_3 increased about 10%. The high conversion rates of NO_x to HNO_3 inside the emission plumes of aircraft in summer conditions cause a significant diminishment of the perturbations of aircraft pollutants and ozone at a global scale.

During the AIRFORCE 1995 campaign different light hydrocarbons were measured. Our results show a high correlation of ethane with acetylene, the sum of C_2 - C_5 and the urban tracer C_2Cl_4 which emphasizes the role of anthropogenic continental pollution as the major source of light hydrocarbons in the tropopause region at the conditions during AIRFORCE.

The uncertainty of the light hydrocarbons data is in the order of 20%. The C_2Cl_4 data have a precision in the order of 10% but the concentrations are not absolute and have to be considered as preliminary.

6. References

[1] AERONOX, The impact of NOx Emissions from Aircraft upon the Atmosphere at Flight Altitudes 8-15 km, U. Schumann (ed.), Final report to the CEC (1995).

[2] Blake, D.R., Smith, T.W., Jr., Chen, T.-Y, Whipple, W.J., and Rowland, F.S., 1994. Effects of biomass burning on summertime nonmethane hydrocarbon concentrations in the Canadian wetlands, J. of Geophys. Res., vol. 99, p. 1699-1719.

[6] Fahey, D.W., *et al.* In situ observations in aircraft exhaust plumes in the lower stratosphere at midlatitudes. Journal of Geophysical Research, Vol. 100, no. D2, pp. 3065-3074 (1995).

[7] Fortuin J.P.F., R. van Dorland, W.M.F. Wauben and H. Kelder, Greenhouse Effects of Aircraft Emissions as Calculated by a Radiative Transfer Model, Ann. Geoph. 13, 413-418 (1995).

[8] Lacis, A.A., D.J. Wuebbles and J.A. Logan, Radiative Forcing of Climate by Changes on the Vertical Distribution of Ozone, J. Geoph. Res., 96, pp.13003-13065 (1991).

[9] Lightman, P., Kallend, A.S., Marsh, A.R.W., Jones, B.M.R., Penkett, S.A., 1990. Seasonal variation of hydrocarbons in the free troposphere at mid-latitudes, Tellus, vol. 42 B, p. 408-422.

[10] Louisnard, N.,C.,*et al.* AERONOX Sub-Project 2: Physics and Chemistry in the Aircraft Wake. Aeronox report, editor U. Schumann (1995).

[11] Melo, O.T., M.A. Lusis, R.D.S. Stevens. Mathematical modelling of dispersion and chemical reactions in a plume - oxidation of NO to NO2 in the plume of a power plant. Atmospheric Environment, Vol. 12, pp. 1231-1234 (1978).

[12] Rudolph, J. The tropospheric distribution and budget of ethane, J. of Geophys. Res., vol. 100, p. 11369-11381 (1995).

[13] Scheeren et al.. paper in preparation (1996).

[14] Singh, H.B., O'Hara, D., Herlth, D., Blake, D.R., Bradshaw, J.D., Kanakidou, M., and Crutzen, P.J.. Acetone in the atmophereP: Distribution, sources, and sinks, J. of Geophys. Res., vol. 99, p. 1805-1819 (1994).

[15] Spicer, C.W., Holdren, M.W., Lyon, T.F., and Riggin, R.M.. Composition and Photochemical Reactivity of Turbine Engine Exhaust, RDVS-report no. ESL-TR-84-28, Tyndall (F), USA (1994).

[16] Strand, A and Hov, Ø. A two-dimensional global study of tropospheric ozone production. J. Geoph. Res., Vol. 99, No. D11, pp. 22877-22895 (1994).

[17] Velders, G.J.M., L.C. Heijboer and H. Kelder, The Simulation of Aircraft Emissions by a Three-Dimensional Global Model, Ann. Geoph. 12, pp. 385-393 (1994).

[18] Vilà-Guerau de Arellano, J. A.M. Talmon and P.J.H. Builtjes, A chemically Reactive Plume Model for the NO-NO2-O3 System, Atmos. Env. 24A, pp. 2237-2246 (1990).

[19] Wauben, W.M.F., P.F.J. van Velthoven and H. Kelder, A 3D chemistry transport model study of changes in atmospheric ozone due to aircraft NOx emissions, accepted by Atmos. Env., 1996.

[20] Zimmerman, P.H., MOGUNTIA: A handy Global Tracer model, In: H. van Dop (ed.), Air Pollution Modelling and its Applications VI, NATO/CCMS, Plenum, New York, pp. 593-608 (1988).

Optimal flight altitude and flight routes with respect to environmental and economical aspects

D. Nodorp[1], R. Sausen[1], C. Land[1] and F. Deidewig[2]

[1)] DLR, Institut für Physik der Atmosphäre, Oberpfaffenhofen, Germany
[2)] DLR, Institut für Antriebstechnik, Köln, Germany

Abstract

A flight routing method is presented. In additon to conventional minimisation of travel time and/or fuel consumption it also takes into account the environmental impact of the aircraft emissions on the climate system. In the process the ECHAM general circulation model is used to trace the pollutants after release, estimate their potential to cause damage and to weight this environmental relative to the economical aspect. Some case studies are presented for an Airbus A340 in the North Atlantic flight corridor.

1. Introduction

The total amount of emissions from aircraft engines is small compared to those from anthropogenic surface sources. But this fact only holds for CO_2 but not for other pollutants like NO_x and H_2O because the location of their release in the upper atmosphere is a region of complicated chemical and radiative equilibrium with only little background concentration and long residance times. Furtheron the predicted growth of air traffic in the near future makes the problem more urgent. Meanwhile there is a substantial knowledge about the different aspects of aircraft exhausts like NO_x (e. g. Schumann, 1995), ozone (e. g. Sausen et al., 1996) and contrails (e. g. Ponater et al., 1996). This paper is no further studie about the environmental consequences of airtraffic but it is our aim to put this knowledge to practical use.

First of all the best method to avoid environmental damage is to avoid unecessary airtraffic. Another way is to develope and use better aircraft engines with less fuel consumption and emission indices. The method we will present in this paper is to do a better flight routing. In addition to conventional minimisation of travel time and fuel consumption, it also takes into account the environmental sensibility of the flight area to aircraft pollutants which can be estimated by numerical climate models. Our method is of special practical interest for the future because the development of the free flight concept and a better navigational equipment of each aircraft makes it possible to apply it in routine flight managment.

2. Method

The method is based on the assumption that only emissions that are found in the stratosphere 10 days after their release are harmful to the climate system. This is an important extension to the common sinple demand that the aircraft has to stay below the tropopause. The starting point for a flight routing is the weather forecast of a numerical model, which will provide wind, temperature humidity and other meteorological quantities. For our method we give an additional quantity which measures the environmental sensitivity of a special area and which we call the environmental penalty function. This quantity is computed as follows.

At each point of the flight area a unit quantity of an emission is released. We use the climate model ECHAM to follow the emission as it is transtorted and distributed in the atmosphere

depending on the current weather situation. The numerical model ECHAM is the climate version of the forecast model of the European Centre for Medium Range Weather Forecasts. It has been adopted for climate studies by the Meteorological Institut of the Univertity of Hamburg and by the Max Planck Institute of Meteorology in Hamburg and has proven to be suitable especially for tracer studies because of a sophisticated parameterisation of transport by vertical and horizontal convektion and diffusion. A closer investigation of the tracer behavour is given by Land (1994).

To find the optimal flight route $\vec{S}$ we have to ninimize the integral

$$\int_{\vec{S}} \pi(\vec{s})\, d\vec{s}\,. \tag{1}$$

In this equation $\pi = \pi(\vec{s})$ is a penalty function. To weight economical (ec) and environmental (en) aspects the penalty function will be composed out of two components:

$$\pi = \alpha_{en}\pi_{en} + \alpha_{ec}\pi_{ec}\,, \tag{2}$$

α_{en} and α_{ec} represent political weight factors. The economical and the environmental parts are defined by

$$\pi_{ec} = f\,\frac{|\vec{v}_{TAS}|}{|\vec{v}_G|}\,, \tag{3}$$

$$\pi_{en} = f\,EI_{\mathrm{NOX}}\frac{|\vec{v}_{TAS}|}{|\vec{v}_G|}\,g\,. \tag{4}$$

f is fuel consumption per distance, $\vec{v}_{TAS}$ is true air speed and $\vec{v}_G$ is the speed relativ to ground. EI_{NOX} is the emission index. In the next section we will give an example for f and $f\,EI_{\mathrm{NOX}}$. g is the environmental weight function:

$$g(\vec{x}) = \frac{\int_{\text{globe}} c_{\mathrm{NOX}}(\vec{r})\omega(\vec{r})\,d\vec{r}}{\int_{\text{globe}} c_{\mathrm{NOX}}(\vec{r})\,d\vec{r}}\,, \tag{5}$$

where $\vec{x}$ is the place of release. $c_{\mathrm{NOX}}(\vec{r})$ is the pollutant concentration at place $\vec{r}$ 10 days after release at place $\vec{x}$. The integration in equation (5) covers the global atmosphere. The function ω implies our hypothesis, that only pollutants that are found in the stratosphere 10 days after release are harmful for the environment.

$$\omega(\vec{r}) = \begin{cases} 1 & , \text{ if } \vec{r} \text{ is above the tropopause;} \\ 0 & , \text{ elsewhere.} \end{cases} \tag{6}$$

We also tried some other dependencies for $\omega(\vec{r})$ but this seems to be most reasonable for a case stude. The tropopause is defined by the WMO thermal lapse rate criterion of a -0.002 K/m threshold.

An normalization between the economical and the environmental part is necessary. Each component is nomalised by the standard deviation along the great circle course. The great circle will be the first guess in the numerical iteration in order to make (1) a minimum:

$$\tilde{\pi}_{en} = \frac{\pi_{en}}{\sigma_{en}}\;;\;\; \tilde{\pi}_{ec} = \frac{\pi_{ec}}{\sigma_{ec}}\,. \tag{7}$$

$\tilde{\pi}_{en}$ and $\tilde{\pi}_{ec}$ will substitute π_{en} and π_{ec} in *Equation (2).*

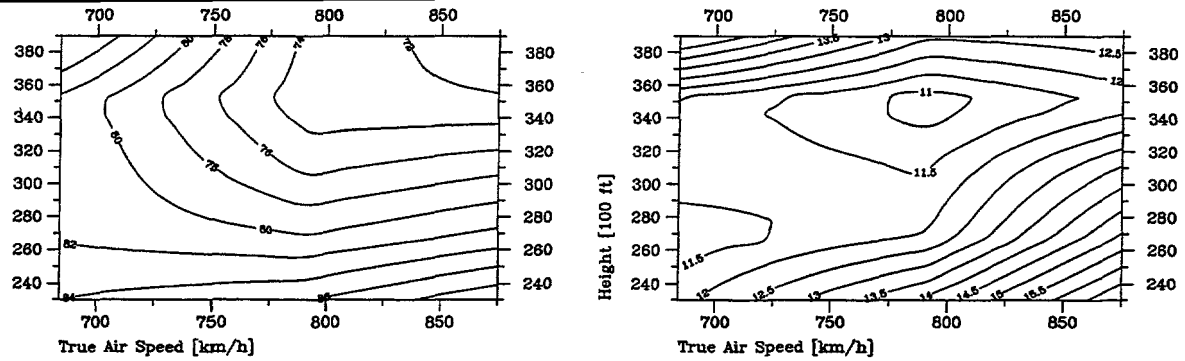

Fig. 1 - Fuel consumption [10^{-4} kg/m] (left) and NO_x–Emissions per unit distance [10^{-5} kg/m] (right) of Airbus A340–300 (4 engines CFM56–5C2) at cruise (TO-weight 220×10^3 kg).

3. Application

To demonstrate the outlined method a case study is performed. We choose a flight across the North Atlantic from Frankfurt (FRA) to New York (JFK) with an Airbus A340-300. The characteristics of the aircraft and of the weather situation are first shown. This leads to a penalty function. The optimal course as a result of our special weight factors are then calculated and the scores are compared.

3.1 Aircraft Characteritics

To determine the economical and the ecological part of the penalty function it is necessary to calculate fuel consumption and NO_x–emissions for the given aircraft/engine combination and for the specific flight situation. These informations come from a special computer model (Deidewig and Lecht, 1994). The engine emission correlation is based on a semi–empirical method, which combines measured values at sea level static tests with a thermodynamic engine performance model. The fuel consumption for an Airbus A340, that we chose for our study, is shown in *Figure 1 (left)*. The calculations are valid for a take–off weight of $220 \text{x} 10^3$ kg which is reasonable for the mission. The fuel characteristic recommends to go as high and as fast as possible. The aircraft is designed for cruise at konstant machnumber 0.83, but we will assume a cruise speed at 0.8, which seems to be realistic. From looking at fuel consumption and travel time only we can conclude that it is favourable to go high and fast. *Figure 1 (right)* gives the NO_x–emissions of the aircraft. We have a minimum at flight level 350 and an overall NO_x–structure, which makes it favorable to travel fast at hight altitudes and slow at low altitudes.

3.2 Weather Situation

For our case studie a special weather situation is choosen. *Figure 2* gives the seasurface pressure and the height of the tropopause for this situation. The main feature is a strong cyclone structure south of Greenland and an anticyclone over Europe. The tropopause reflects this conditions and is of special interest because it appears in *Equation (6)*. The cyclone and the tropopause low are shiftet in phase to each other. A flight from FRA to JFK will go across the cyclone. The weather situation was choosen because the penalty function will reflect the low tropopause and the up–wind area of the cyclone.

The weather situation is the starting point for the tracer studies with the ECHAM climate model and brings us to the ecological penalty function for the flight area.

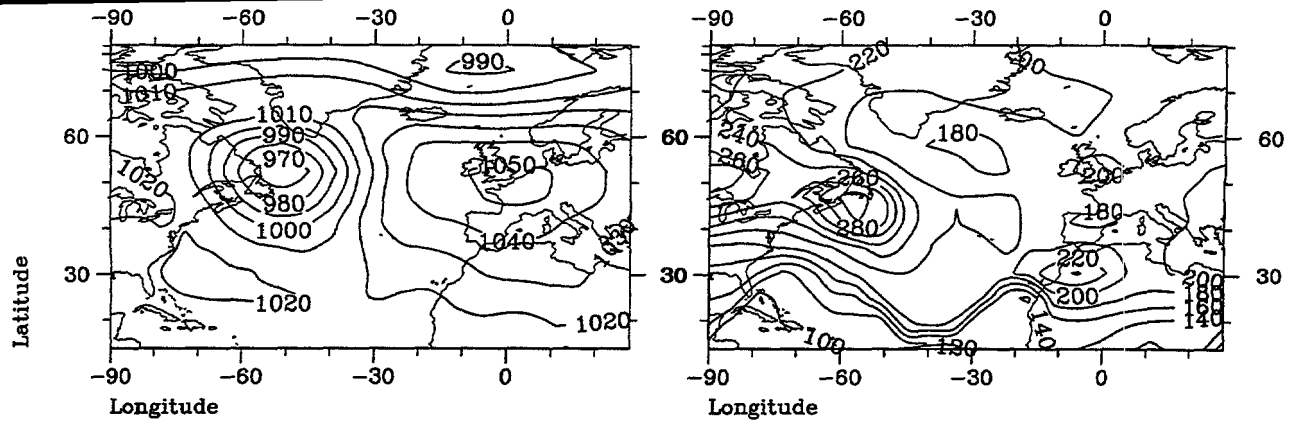

Fig. 2 - Surface pressure [hPa] (left) and tropopause height [hPa] (right) of the weather situation.

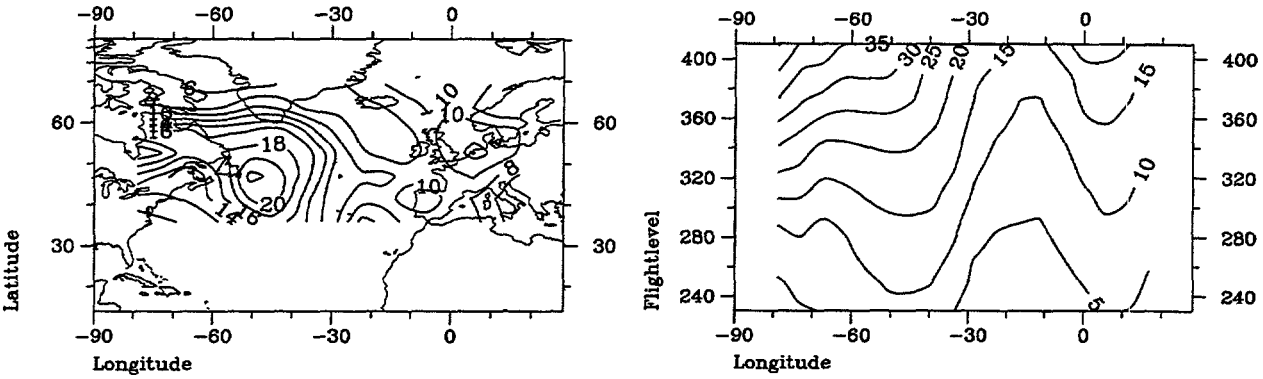

Fig. 3 - Penalty weight (x100) at flight level 330 [hPa] (left) and at latitude 52.6^0N (right).

3.3 Penalty Function

Figure 3 gives us the penalty function for flight level 330 and a vertical profile of the penalty function a latitude 52.6°N. We notice the high values in the area of the low tropopause. This is also due to the upwind area of the cyclone. When staying on the same flight level the penalty function varies by a factor of 2. This means that the flight distance can be twice as long in order to end up with the same environmental score. Furthermore the vertical profile (right) shows growing values when going west at konstant flight level. The maximum corresponds to the cyclone and the minimum to the height. When the optimization is done only with respect to this penalty function the result would be to go as low and as slow as possible. This is opposite to the conclusions from aircraft characteristic. The optimization process will bring both tendencies together according to the weightening factors.

3.4 Optimal Flight Routes

The optimization process is done only with respect to *Equation (1)*. We do not pay any attention to adminitrative constrains like flight routes, other aircrafts or restricted flight areas. *Figure 4 (left)* shows the resulting flight routes when keeping the flight level fix and doing the optimization only in the horizontal direction. The most northern course corressponds to flight level 330. This course tries to circumvent the area of high penalty values which belong to the upwind area of the cyclone. The optimal flight distance at flight level 330 is 6758 km compared to 6189 km of the great circle distance. But the integral

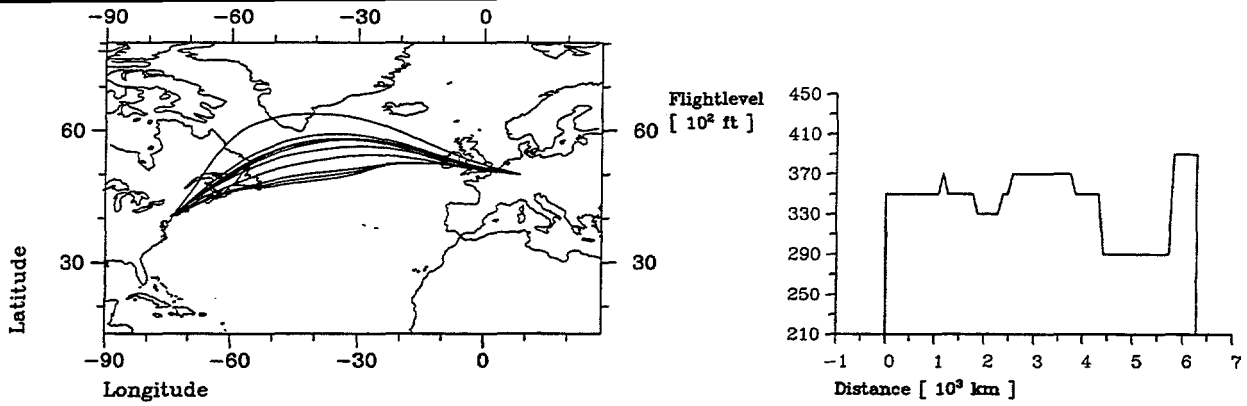

Fig. 4 - Optimal flight routes from FRA to JFK with respect to penalty function at fixed flight level 230, 250, 270, ..., 410 (left) and an example hight profile with $\alpha_{en} = 0.3$ (right).

penalty score is 4.7 % less. We can conclude that the extra way would be favourable with respect to environmental reasons only. Things are not so clear on the other flight levels. In *Figure 4 left* the northern routes correspond to the higher flight levels 330 to 410. The results for the lower flight levels 230 to 310 stay very close to the great circle. This shows that environmental aspects are more important in the upper than in the lower flight levels.

In *Figure 4 (right)* an example height profile is presented for the same mission but now the flight level is not fixed and the environmental factor is 0.3. A value of 0.0 would lead to an ordinary step clime profile and a value of 1.0 would force the aircraft to stay at flight level 230 all the way. The value 0.3 gives a flight level of 350 and 370 for the first part of the way. In the last part of the course the aircraft enters the cyclone area. Here the environmental component forces the plane down to flight level 290. When it has passed the critical area the aircraft is allowed to climb to flight level 390 for the last part of the way before reaching JFK. Also this vertical profile does not seem good for practise it becomes clear what the result of environmental aspects would be.

In *Figure 5* it is shown how fuel consumption, NO_x–emissions, environmental impact and travel time change as the political weight factor α_{en} (*Equation 2*) changes from one extrem position (environmetal impact is of no importance, $\alpha_{en} = 0.0$) to the other extrem position (environmental impact is of very high importance, $\alpha_{en} = 1.0$). As the environmental impact goes down by 64 % the fuel consumption goes up by 20 %. At the same time the NO_x–emissions go up by 21 % and travel time will become longer by 6 % (about 25 minutes on a flight from FRA to JFK). The most interesting part of the diagrams is the interval from $\alpha_{en} = 0.2$ to $\alpha_{en} = 0.6$ where the main changes occur. Despite the higher fuel consumption and NO_x–emission for $\alpha_{en} = 1.0$ the environmental impact is lower because the pollutants are released at a location, where they are less harmful.

4. Conclusions

In our principle study it is demonstrated that flight routes and flight levels can be optimized such that the effects of air traffic on the environment becomes minimal. An adequate ecological penalty function was constructed. It is based on the simplified hypothesis that emissions are harmful only if they are found in the stratosphere 10 days after release. In order to take into account both environmental and economic aspects the ecological penalty function and the economic penalty function are suitably normalized, weighted by "political" factors, and summed to form the total penalty function. The optimal flight routes and flight

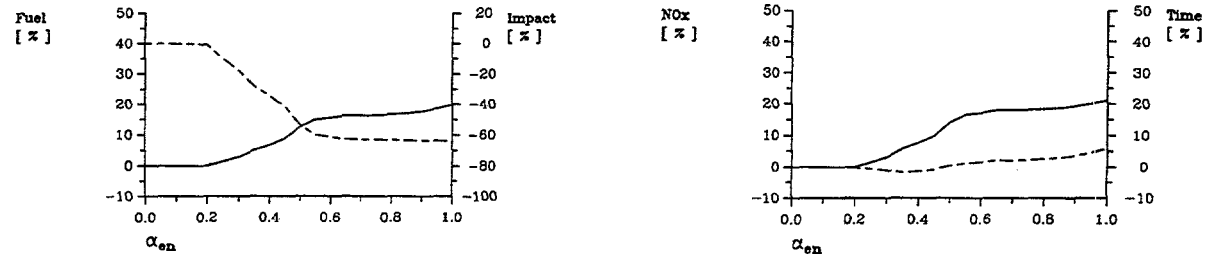

Fig. 5 - Relative changes [%] of fuelconsumption (left, solid), environmental impact (left, dashed), NO_x–emissions (right, solid) and travel time (right, dashed) for a flight from FRA to JFK.

levels are then optained by minimizing the line integral over the total penalty function. This procedure is applied in selected case studies. It has been shown that the environmental pollution, according to our criteria, may be clearly reduced without simultaneously increasing the operating costs.

But anyhow it became clear that there are some critical points that demand attention before this method is ready for practical use. Our assumption about the environmental impact of aircraft pollutants are very crude while some other aspects like contrails are neglected. The mormalisation problem and the political factors, which strongly influence the results, can not solved and found by purely scientific methods. A more detailed version of this work is available from Sausen et al. (1996).

Acknowledgements. This study was carried out for and supported by the Umweltbundesamt through grant UBA–FB 104 02 646.

References

DEIDEWIG, F. and M. LECHT, 1994: NO_x Emissions from Aircraft/Engine Combinations in Flight. In U. Schumann und D. Wurzel (eds.): *Impact of Emissions from Aircraft and Spacecraft upon the Atmosphere. DLR–Mitteilung 94–06*, ISSN 0939–298X, 44–49.

LAND, C., 1994: Transportberechnungen für Luftbeimengungen mit dem globalen Modell ECHAM. Diplomarbeit, Universität Hamburg, 60 S.

PONATER, M., S. BRINKOP, R. SAUSEN and U. SCHUMANN, 1996: Simulating the global atmospheric response to aircraft water vapour emissions and contrails — A first approach using a GCM. *Ann. Geophys.*, in press.

SAUSEN, R., B. FENEBERG and M. PONATER, 1996: Climatic impact of aircraft induced ozone changes. *This issue.*

SAUSEN, R., D. NODORP, C. LAND and F. DEIDEWIG, 1996: Ermittlung optimaler Flughöhen und Flugrouten unter dem Aspekt minimaler Klimawirksamkeit. DLR Forschungsbericht 96–13.

SCHUMANN, U. (ED.), 1995: AERONOX – The Impact of NO_x Emissions from Aircraft upon the Atmosphere at Flight Altitudes 8 – 15 km. EC–DLR Publication on Research Related to Aeronautics and Environment, Oberpfaffenhofen

Remote gas analysis of aircraft exhausts using FTIR-emission-spectroscopy

J. Heland, K. Schäfer
Fraunhofer Institute for Atmospheric Environmental Research, Kreuzeckbahnstraße 19,
D-82467 Garmisch-Partenkirchen, F.R.G.

Abstract. FITR emission spectroscopy as a remote sensing multi-component analyzing technique was investigated to determine the composition of aircraft exhausts at ground level. A multi-layer radiative transfer interpretation software based on a line-by-line computer algorithm using the HITRAN data base was developed. Measurements were carried out with different engine types to determine the traceable gas species and their detection limits. Finally validation measurements were made to compare the results of the system to those of conventional equipment.

1. Introduction

To predict the impact of today's and future air traffic global models are in need of precise emission inventories. Currently these inventories map the total emissions based on flight data, fuel consumption, and the emission indices of the most common airplane/aeroengine combinations. The emission indices of the engines at different altitudes are obtained using correlative calculations based on test bed measurements of the aircraft designers.
In this work FTIR-emission-spectroscopy as a remote sensing multi-component measurement method for aircraft exhausts is investigated. Ground-based measurements were carried out with different engine types and evaluated with a further developed line-by-line software which takes an axial-symmetric, cylindrical layered plume for the retrieval into account. The detection limits of several compounds were obtained considering a typical exhaust gas mixture for the simulations and a measured background of an aircraft body. Validation measurements were made with a propane gas burner at typical exhaust gas temperatures with CO and NO mixed into the fuel to determine the overall accuracy of the system.

2. Experimental

The used K300 spectrometer is a mobile industrial double-pendulum Michelson-interferometer working with unapodized spectral resolutions up to 0.06 cm^{-1} in a wavenumber range between 700 and 4000 cm^{-1}, depending on the detector configuration. The diameter of the telescope is 15 cm with a divergence of 3 mrad. It has been used before in different measurement modes to evaluate smoke stack emissions and ambient air measurements in different polluted areas that have been reported elsewhere [1]. Most of the experiments were performed with an unapodized resolution of 0.2 cm^{-1}, which is near to the line width of the molecules under standard atmospheric conditions. Typically 30-50 interferograms were co-added to obtain one spectrum of the exhaust gas, corresponding to a measurement time of about 2 minutes including the time for the data storage on a PC.
During all measurements the line of sight of the instrument was perpenticular to the exhaust flow. The telescope was pointed from a distance of 20 to 60 m at several downstream positions of the plume and adjusted to receive the maximum signal, which was then believed to be a position in the center of the plume.

3. Data analysis

To simulate the IR emissions from the background (aircraft body for ground-based measurements) through the different hot layers of the exhaust plume and the foreground one has to divide the optical path into discrete homogeneous layers m in which local thermodynamic equilibrium can be assumed. In case of an optical thick gas (transmission: $\tau = 0$), the intensity of the thermal radiation at the wavenumber σ is that of a black-body at the same temperature, i.e. the Planck function $B_\sigma(\sigma, T)$. For a discrete path after the mth layer towards the detector the radiative transfer equation becomes [2]

$$I_{\sigma,m} = \tau_m I_{\sigma,m-1} + (1-\tau_m) B_\sigma(T_m). \quad (1)$$

The heart of the line-by-line calculation of the transmission is the sum over all single transitions of the species in a wavenumber interval $\Delta\sigma$ to determine the monochromatic absorption coefficient at σ. Included are the line strengths and the line shape functions (Voigt approximation by Matveev [3]). The necessary molecular parameters are taken from the HITRAN data base [4] and converted to the actual values with respect to the populations of the involved molecular states.

Since the emission spectra are calculated in absolute radiance units and the raw instrument spectra are in relative intensity units, one has to convert these by a special calibration procedure. The intruments intensity is a composition of the source intensity and the self-radiation of the instrument and can be calibrated using two measured reference (black-body) spectra at different temperatures with known intensities. In case of the K300 spectrometer the self-radiation in the mid-infrared was found to have a black-body equivalent temperature of about 10°C. Thus, comparing the resulting intensities to that of a 200°C black-body source, the self-radiation term is about 2 % of the black-body intensity and can be neglected for our purposes. Thus a calibration with one reference source is sufficiently accurate for aircraft exhaust analyses.

In some of the measured aircraft spectra an elevated wavenumber independent background radiation was found which could not be described with the available gas parameters alone. This continuum transmission is caused by far line wing contributions of the main combustion products CO_2 and H_2O, aerosole particles and contributions of species and lines not included in the calculations. At those wavenumbers at which the total gas transmissions should be almost unity a quantitative continuum description is possible using the simple radiative transfer equation (homogeneous plume) with an effective temperature [2]. Assuming temperature independence a continuum absorption coefficient can be defined which is proportional to the number of gas molecules in the plume. The changes in the results of the retrievals when using this procedure compared to not taking a continuum into account are about a few percent.

Due to the entrainment of cold air into the hot exhaust stream a strong gradient in the plume profile was expected, thus for the interpretation of downstream spectra a special line-by-line algorithm with up to 20 possible plume layers was developed We use the actual number of the gas molecules Z_i in the field of view of the telescope, and a parallel layer configuration.

The retrieval algorithm is based on the CO_2-spectral region around 2400 cm^{-1} where the plume temperature T was found to determine the 'total height' of the spectrum and the molecule numbers n in the plume define the 'fine' structure of the single lines among each other. Quantitatively, the calculation leads to the expression

$$\frac{dI_\sigma}{I_\sigma} \approx 6 \times \frac{dT}{T} \approx 0.4 \times \frac{dn}{n}. \quad (2)$$

Since a certain relative change in temperature means a six times larger change in the relative intensity, the same relative change of the number density of the molecules leads to an about one

order of magnitude lower change of the relative intensity. Thus, these two parameters can be treated separately for the first order determination of the temperatures T and concentrations n. The T_i- and n_i-profiles for a given number of plume layers are being derived from the simulations of about 10 cm^{-1} in the CO_2 region with up to 19 individual transitions with different quantum numbers and different temperature dependencies. Assuming the same T_i and n_i distributions along the plume diameter and knowing the CO_2-concentration profile along the diameter of the plume the profile of the other compounds can be obtained by the simulations.

4. Results

4.1. Detection limits, uncertainties

The detection limits of the FTIR-system were determined semi-empirically by using a typical background measurement of a B-737 aircraft body taken with a MCT detector. The trace limits were defined as the mixing ratios in a 'typical' plume with a diameter of ϕ=50 cm where the simulated emission lines with varying gas temperature were 50 % more intense than the measured background radiation. For the interferences worst case values of 4 % for CO_2 and H_2O, and 500 ppmv for CO were assumed.
For all coumpounds decreasing values were found when the temperature was increased. In *table 1* the possible gas species, some relevant retrieval parameters, and the obtained detection limits are summarized for the above defined 'typical' aircraft plume at T = 380°C.
Beside the uncertainties in the molecular line parameters ($\leq \pm$ 15 %) [4] the errors in the calculations arise mainly because of the conversion of the line data to the actual conditions, to the width of the spectral range for the line-by-line calculations, and uncertainties within the instrumental line shape function. All in all a total uncertainty of about ± 30 % can be estimated.

Table 1: Possible gas compounds, spectral regions, interferences, expected mixing ratios and detection limits for the analysis of the FTIR-emission spectra for a plume temperature of 380°C with a diameter of 50 cm ($^{(*)}$: already detected in aircraft plumes).

	Spectral region [cm^{-1}]	Interferences	Exp. mixing ratios [ppmv]	Detection limits, 380°C [ppmv]
$CO_2^{(*)}$	2380-2400	---	$1...4 \cdot 10^4$	60
$H_2O^{(*)}$	1965-1985	(CO)	$2...6 \cdot 10^4$	7000
$CO^{(*)}$	2160-2180	H_2O, (CO_2)	10 - 3000	20
$NO^{(*)}$	1890-1910	H_2O, (CO, CO_2)	10 - 200	90 (> 60)
NO_2	1620-1640	H_2O	10 - 100	60
$N_2O^{(*)}$	2180-2200	CO, H_2O, CO_2	≤ 7	10
SO_2	1350-1370	H_2O, CO_2, (HC)	≤ 10	340
HCHO	2805-2825	H_2O, (CH_4 +...)	< 15	50
CH_4	3055-3075	H_2O	< 10	150 (> 100)

4.2. Aircraft measurements

The ground-based FTIR-emission measurements were performed with several aircraft engine types listed in *table 2* which were in use for different flight applications. If possible the foreground concentrations of the relevant molecules were determined by long-path absorption measurements with an additional IR source and the MAPS software [5]. These values were used

as inputs for the foreground layers during all plume calculations for one engine.

Table 2: List of engines used for the FTIR-spectroscopic analyses.

Engine Type	Bypass ratio	Diameter of nozzle	Max. thrust	Usage
M701-TZ	---	23 cm	?	former military
Bypass engines	1 : 1	60 cm	?	military
GE CF700-2D2	1.9 : 1	44 cm	19 kN	civil bus. jets
RR M45H	3 : 1	≈ 40 - 60 cm	34 kN	civil bus. jets
JT8D-15 (Hush Kit)	1 : 1	108 cm	70 kN	civil, med. range
CFM56-3B	5 : 1	50 - 80 cm	95 kN	civil, med. range
CFM56-5C2	5 : 1	140 cm	140 kN	civil, long range

The first measurements were made with the old military engine M701-TZ (Φ=23 cm, no bypass) at different thrust levels at a number of downstream positions behind the nozzle exit. The goal of these measurements was to test the equipment under the harsh conditions of an engine run and to demonstrate the feasibility of FTIR-emission measurements. *Figure 1* shows the CO emission indices of the M701-TZ engine for two engine speeds, 65 % and 90 %, respectively, obtained with a homogeneous plume model (dashed lines) at a downstream position of about 30 cm behind the engine compared to the 4-layer-model results at different downstream positions behind the engine. For the 90 % engine speed the models give comparable results whereas the values for the lower thrust level and very high CO indices scatter considerably. The temperature retrievals with the two models at the downstream positions agree well within the measurement uncertainties.

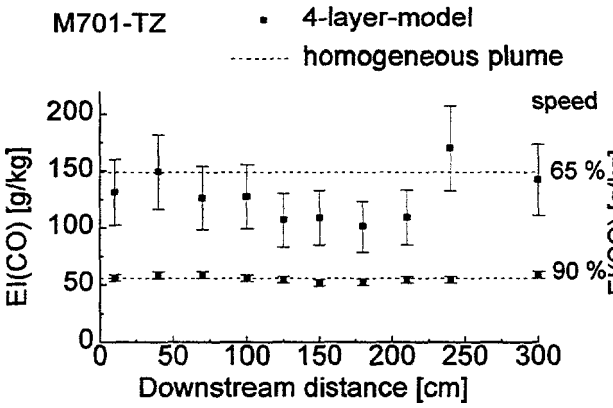

Figure 1: CO emission indices for two engine speeds at several downstream positions behind a M701-TZ engine.

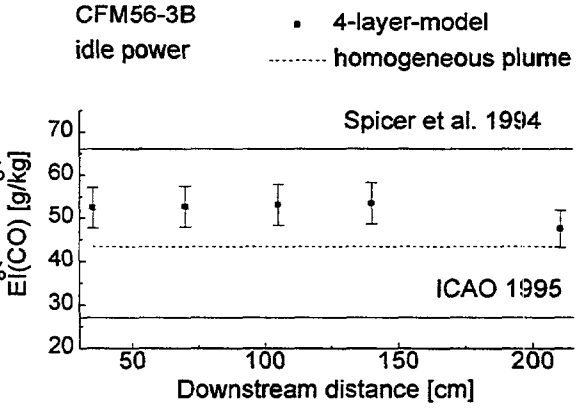

Figure 2: CO emission indices at idle power of a CFM56-3B engine obtained with different plume models compared with those of other authors.

Measurements at two thrust levels and at several downstream positions were performed with a modern CFM56-3B engine (bypass ratio 5:1), usually installed on medium-range aircrafts like the B-737 or the A320. *Figure 2* illustrates the results of the spectra retrievals for CO at idle power obtained with a homogeneous plume model for a measurement position 70 cm behind the engine and those of the 4-layer-model at several downstream distances. Also included are the results given by Spicer et al. [6] and those given by the ICAO [7] for the same engine type at this thrust level. In line with the results from the M701-TZ engine the different plume models for the CFM56-3B analysis show agreement within ± 15 % for the different downstream positions at least up to 3 m behind the engine.

4.3. Validation measurements

To validate the emission measurement results demonstration measurements were carried out using a propane gas burner whose fuel inlet was prepared to mix additional gases (NO and CO) into the propane. The main goal was to achieve gas temperatures very close to those found in an aircraft plume. After some modifications a gas temperature of about 400°C was achieved in a constant exhaust flow of about 26 cm in diameter. In a routine procedure the samples were taken by a probe installed about 20 cm behind the gas exit, pumped through a heated tube, dried and filled into evacuated canisters [8]. The analyses of the samples were done by the means of FTIR-absorption-spectroscopy using calibration gases [8]. The FTIR-emission measurements were carried out directly behind the gas exit of the burner, not influenced by the intrusive method. The data collection time for the spectrometer was adjusted to the sample taking time of about 4 minutes. *Table 3* summarizes the comparison of single measurements made for different gas mixtures in the fuel. Due to the different measurement positions of the two systems the results are given similar to the emission indices in g/kg. The results in brackets were obtained with a homogeneous plume model, the others with a 4-layer-model. However, since both systems were working at their detection limits, the overall agreement of the results is about ± 20 %.

Table 3: Comparison of the results of the demonstration measurements (FTIR-emission-spectroscopy vs. conventional techniques). The results in brackets were obtained with a homogeneous plume model, the other FTIR data from a 4-layer-model.

Sample number		added compound	CO [g/kg]	NO_x [g/kg]
1:	this work	CO	9.8 (≈ 8.2)	< 23.1
	others	CO	8.5 ± 2.4	---
2:	this work	NO	< 9.3 (< 9)	≈ 51.2 (≤ 48.9)
	others	NO	5.7 ± 1.7	50 ± 11
3:	this work	NO	< 9.8 (< 9)	≈ 35.5 (≤ 36.4)
	others	NO	9.8 ± 3.3	46 ± 15
4:	this work	NO	≈ 7.5 (≈ 7)	≈ 51.1 (≤ 52.4)
	others	NO	8.9 ± 2.0	≤ 60 ± 12
5:	this work	NO	< 10.4 (---)	≤ 92 (≤ 91.2)
	others	NO	9.1 ± 2.1	≤ 89 ± 19
6:	this work	CO	≈ 8.8 (< 9.5)	< 11.9 (< 11)
	others	CO	6.3 ± 1.4	---
7:	this work	CO	≈ 8.5 (≈ 8.7)	< 16 (< 11.9)
	others	CO	7.2 ± 3.0	---

5. Conclusions

FTIR-emission-spectroscopy as a remote sensing multi-component exhaust analyzing technique was used to determine the traceable gas species in aircraft exhausts and to test the sensitivity of the system at ground level. A further developed line-by-line computer program with a multi-layer radiative transfer algorithm was used to analyze the spectra.

Measurements were made with military, business and medium range aircraft engines to develop the software and to determine the detection limits for single gas species. Validation measurements were carried out in order to compare the results with those obtained by standard measurement equipment. These measurements showed good agreement within 20 %. In this

work CO_2-, H_2O-, CO-, NO-emissions, and the temperature of the gas could be quantified from the spectra of aircraft engine exhausts with a typical accuracy of ± 30 %. The error margin results mainly from the uncertainties of the line parameters in the available spectral data. Improvements are expected from the HITEMP data base which is about to update the CO_2-, H_2O-, CO-, and NO-HITRAN data for high temperatures in the near future.
Future investigations will focus on further validations of this technique, on emission changes due to engine aging, and on the software development to make the software commercially available. Future applications, for the turbine/combustor design at early stages of the development and the engine-status control after a certain flight time will be possible. In flight measurements are planned for 1998.

6. Acknowledgments

This research is supported by the German Science Foundation (DFG) under the Project No. DFG II C 9 - Scha 571/2 - 2. We thank Prof. Dr. W. Seiler, Prof. Dr. K. H. Becker., Dr. P. Wiesen, Dr. R. Kurtenbach, and everyone involved in making the engine measurements possible.

7. References

[1] Haus, R.; Schäfer, K.; Bautzer, W.; Heland, J.; Mosebach, H.; Bittner, H.; Eisenmann, T., "Mobile Fourier-transform infrared spectroscopy monitoring of air pollution", Appl. Opt., Vol. 33, No. 24, 5682-5689 (1994)

[2] Heland, J., "FTIR-Emissionsspektroskopie an Flugzeugabgasen", Wissenschafts-Verlag Dr. W. Maraun, ISBN 3-927548-81-2 (1996)

[3] Haus, R.; Goering, H., "Atmosphärenphysikalische Grundlagen der infrarotspektroskopischen Luftanalyse", Interner Bericht des Heinrich-Hertz-Institutes für Atmosphärenforschung und Geomagnetismus, Berlin (1991) (in geman, available from the authors)

[4] Rothman, L. S.; Gamache, R. R.; Tipping, R. H.; Rinsland, C. P.; Smith, M. A. H.; C. Benner, D.; Malathy Devi, V.; Flaud, J.-M.; Camy-Peyret, C.; Perrin, A.; Goldman, A.; Massie, S. T.; Brown, L. R.; Toth, R. A., "The HITRAN molecular database: editions of 1991 and 1992", J. Quant. Spectrosc. Radiat. Transfer, 48, 469-508 (1992)

[5] Schäfer, K.; Haus, R.; Heland, J., "Inspection of Non-CO2 Greenhouse Gases from Emission Sources and in Ambient Air by Fourier-Transform-Spectrometry: Measurements with FTIS-MAPS", Kluwer Academic Publishers, Environmental Monitoring and Assessment 31, 191-196 (1994)

[6] Spicer, C. W.; Holdren, M. W.; Riggin, R. M.; Lyon, T. F., "Chemical composition and photochemical reactivity of exhaust from aircraft turbine engines", Annales Geophysicae 12, 944-955 (1994)

[7] ICAO, International Civil Aviation Organization, "Engine Exhaust Emissions Databank", ICAO Doc. 9646, 1st edition, ICAO Document Sales Unit, 1000 Sherbrooke Street West, Suite 400, Montreal, Quebec, Canada H3A 2R2 (1995)

[8] Kurtenbach, R.; Wiesen, P., personal communication (1995)

Trends in Aircraft Emissions: Simulation of two Air Traffic Scenarios in Sweden

Lars-Gunnar Larson and Anette Pålsson, FFA, The Aeronautical Research Institute of Sweden, sponsored by LFV, The Swedish Civil Aviation Administration

Abstract

The developing trends of emissions from aviation in Sweden have been studied by means of flight and emissions simulation. The objective was to investigate whether technical improvements will allow Swedish air traffic to increase, without exceeding national regulations for pollution in the future. It was found that, due to development of aircraft engines and, to some extent, improvement of aerodynamic designs, the fuel consumption and thus the emissions of carbon dioxide will decrease in the future. The decrease of nitrous oxides is predicted to be significant due to advances in engine technology.

1. Introduction

As is well known, the burn of fossil fuels impacts the environment and causes damage to the atmosphere. It is well known that carbon dioxide — CO_2 — contributes to the greenhouse effect. The atmospheric impact of nitrous oxides — NO_x — is more complex. NO_x affects the ozone production in the atmosphere differently depending on altitude. To diminish the damages in a long time period, international and national regulations to limit the emissions are stipulated. The Swedish national goal is to restore the total emission of CO_2 and NO_x by some year in the beginning of next century, to the level of 1990.

The contribution from the air traffic to the total amount of emitted CO_2 and NO_x is small. However, prognoses indicate a substantial growth in air traffic the next decades, and thus an increased quantity of emissions. LFV, the Swedish Civil Aviation Administration, is developing methods to assign emissions and in the future restrain them.

1.1. Objective

The objective of this study is to show the technological potential of allowing an increase in transport capacity within an emissions limit. The base year to which emissions changes should be referred is 1990.

1.2. Choice of Methodology

Information about the emissions of 1990 can be obtained from the national environmental reports. These data are impractical to use because new traffic prognoses and corresponding emissions would have to be calculated for every future case. Instead, a relative method is used; a *traffic scenario* describing the technology and the traffic in the base year is created. The traffic work of the base year scenario is performed with new technology representing a future scenario and the emissions are compared. This future scenario refers to some year in the beginning of next century, not exactly defined.

To model flight profiles and calculate emissions flight simulation is used, including data for aircraft, engine power and exhaust emissions.

2. Simulation Methods

Two computer programs are used for the simulations, *PCP* and *Handy*.

2.1. Flight Simulation

The Programmable Commercial Pilot, *PCP*, is a flight simulation program specially designed for environmental studies [2]. A flight path is defined by a *flight plan*, generating a collection of pre-defined designs, *segments*. For each segment the appropriate values for the parameter pertaining to the segment are supplied. Each

segment generates a motion program that performs an integration of the equations of motion with a set of aerodynamic forces and thrust acting on a point mass. The execution of the flight plan is then processed segment by segment. For each time step in the integration, a set of parameters (position, velocity, thrust, attitude, fuel consumption rate, load factor etc.) is determined by the motion program.

The flight profile is created with respect to the aircraft's specific demands for velocities and Mach numbers at climb, altitude and velocity for changing aerodynamic configuration, indicated air speed, angle of climb etc. A model of the Standard Atmosphere is connected to PCP.
While executing the flight plan PCP gives warnings, e.g. stall warning or need for aerodynamic braking, if aircraft limitations are exceeded.

2.1.1. Tailoring a Flight Profile

The first step of tailoring a flight profile is defining the points where one segment ends and another starts. The numerical data for other fundamental parameters — such as velocities for retracting/extracting flaps, desired velocities at a certain altitude and breaking points for the different flight stages — are supplied. The flight stages consist of a variety of segments. A flight plan for DC9-41 is shown in Fig. 2.1.

2.1.2. Input Data

Each aircraft type is represented by an aircraft model and an engine model which are both connected to PCP. The aircraft model (Lift-Drag model) contains aerodynamic characteristics for different combinations of undercarriage, flaps and slats. The engine model contains propulsion data associated to Mach number, altitude and thrust [3].

The flights are based upon normal domestic traffic with the most frequently used flaps and slats configuration, takeoff weight, fuel quantity, throttle and flight profile applied to the simulations.

```
(START 0.0)
(SET-STEP 2.0)
(SET-ATYPE DC9-41 JT8D-11)
(SET-CONFIG 5)
(SET-STATE (0.0 0.0 0.0) (0.1 0.0 0.0) 4250.5)
(TAKE-OFF 0.90 0.0 40.0 62.8)
(TURN-TO-DIR (1.0 0.0 0.12) 15.0)
(SET-CONFIG 4)
(SACCELERATE 0.90 0.0 100.0 76.3)
(TURN-TO-DIR (1.0 0.0 0.10) 15.0)
(SET-CONFIG 2)
(SACCELERATE 0.90 0.0 100.0 91.5)
(SET-CONFIG 1)
(TURN-TO-DIR (1.0 0.0 0.08) 15.0)
(SACCELERATE 0.87 0.0 48.0 150.0)
(CLIMB-OUT 1233.76 0.87 0.0 0.76 10000.0)
(TURN-TO-DIR (1.0 0.0 0.0) 9.0)
(TURN-ONTO-LINE (405500.1 0.0 10007.5) (1.0 0.0 -0.04) 9.0)
(DESCEND 1233.76 0.0 0.0 0.76 914.3)
(TURN-TO-DIR (1.0 0.0 -0.0525) 11.0)
(SET-CONFIG 7)
(SDECELERATE 0.1 0.0 100.0 65.0)
(TURN-ONTO-LINE(0.0 0.0 0.0) (1.0 0.0 0.0) 11.0)
(BRAKE -0.1 0.0 30.0 0.0 40.0)
(BRAKE 0.1 0.0 30.0 0.6 10.0)
```

Fig. 2.1. Flight plan for DC9-41

2.2. Emission Simulation

PCP produces a file containing time, position, velocity, thrust, attitude, fuel consumption rate, load factor etc. for each time step. This file can be used as input for *Handy* [2]. Handy is a software tool for describing emissions where the flight path and desired parameters can be plotted as a function of flight distance or time for example, see Figure 2.2.

Handy simulates the corresponding emissions and produces a results file which contains the emissions and parameters such as position, velocities, accelerations and thrust. The conclusive file contains the total emissions of carbon dioxide (CO_2), carbon monoxide (CO), hydrocarbon (HC) and nitrous oxides (NO_x).

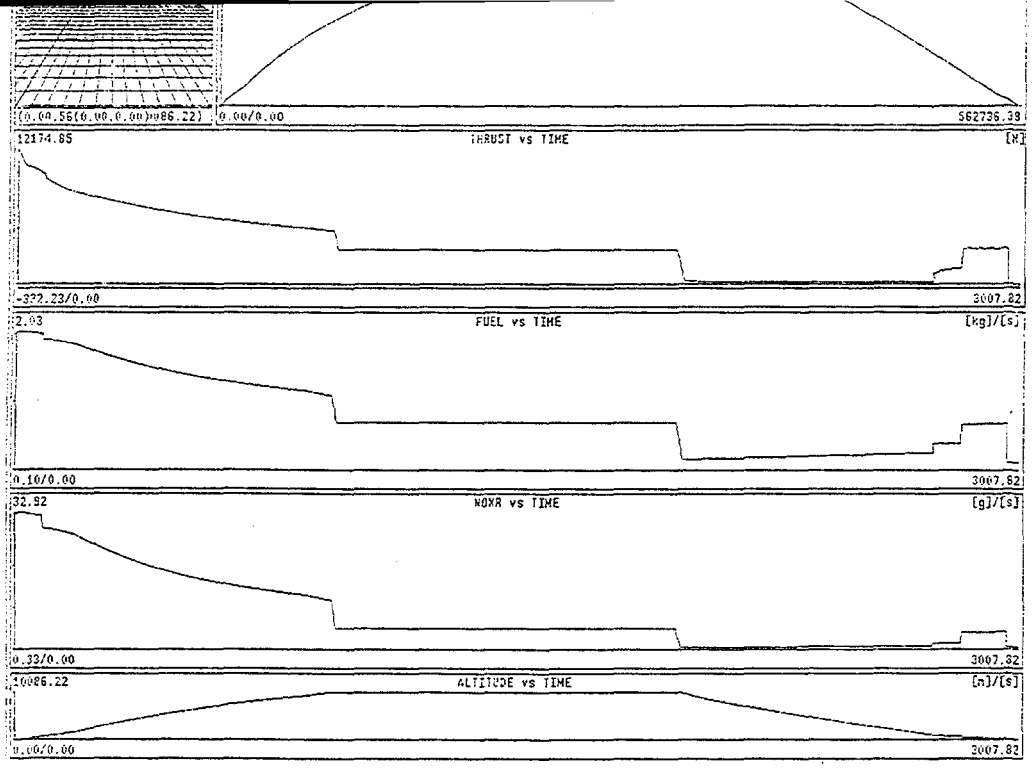

Figure 2.2. Example of graphical presentation of emissions by Handy

2.3. Results Example

To illustrate the simulation method, different aspects of a DC9-41 flight are presented in Figures 2.3-2.5.

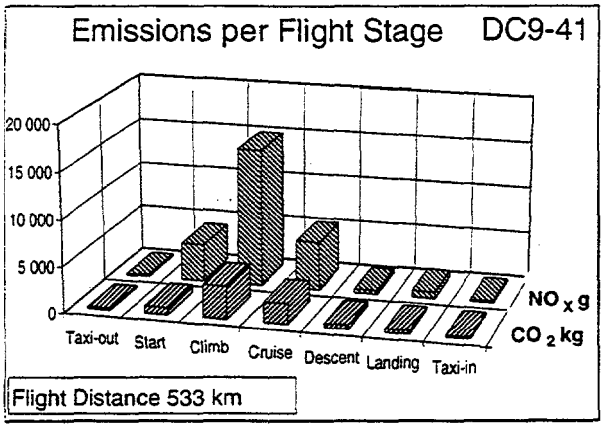

Figure 2.3.

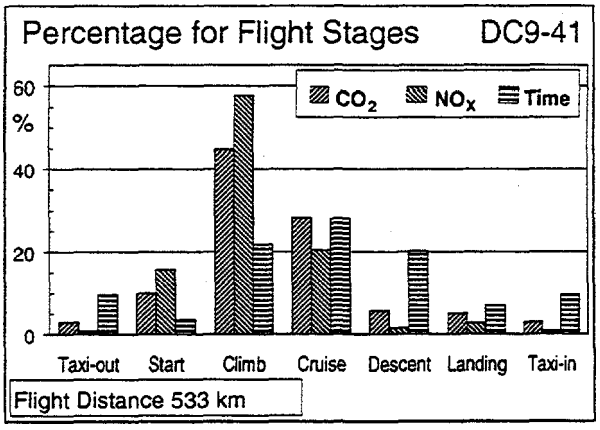

Figure 2.4.

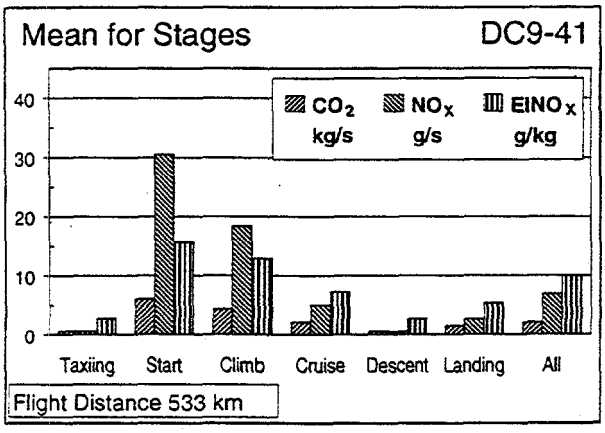

Figure 2.5.

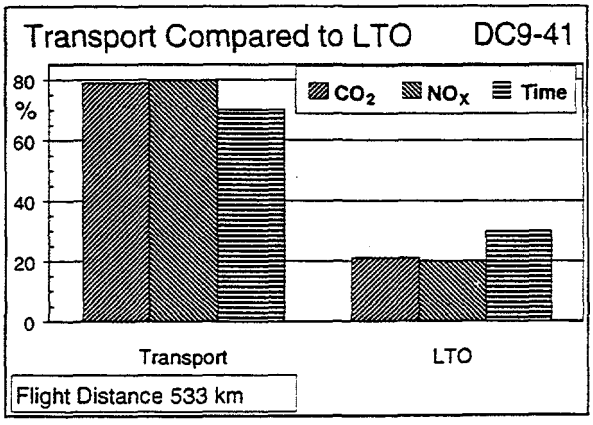

Figure 2.6.

3. Definition of the Base Year Scenario

The air traffic in Sweden is strongly linked to Stockholm Arlanda Airport. Hence, the aircraft types in traffic at Arlanda 1990 can be considered representative for the air traffic in Sweden that year. About two thirds of the most frequent flights were performed by four aircraft types only:

- Fokker F28
- DC9-41
- MD82
- Boeing 737-500

These four aircraft types will be representative for the technology level of *domestic* air traffic in Sweden that year.

The aircraft's engine type, number of aircraft movements, average flight distances and number of passengers (cabin factor ≈2/3) for domestic traffic are shown in Table 3.1.

Tab. 3.1. Scenario for domestic air traffic 1990

Aircraft	Engine	Aircraft movements	Average flight [km]	Seats occupied
F28	PEY - MK555	36 000	380	57
DC9-41	JT8D-11	5 500	533	82
MD-82	JT8D-217C	9 700	530	105
B737-500	CFM56-3B1	7 900	459	88

The product of aircraft movements, average distance and occupied seats for each aircraft conform to the traffic work measured in *passenger kilometre, pkm.* The distribution of pkm on the aircraft types is shown in Figure 3.1.

4. The Base Year Scenario

Data from flights representing the technological level of 1990 are composed in a traffic scenario for this year. Average values of the emissions for F28, DC9, MD82 and B737-500 in 1990 are calculated with respect to number of starts and flight distances.

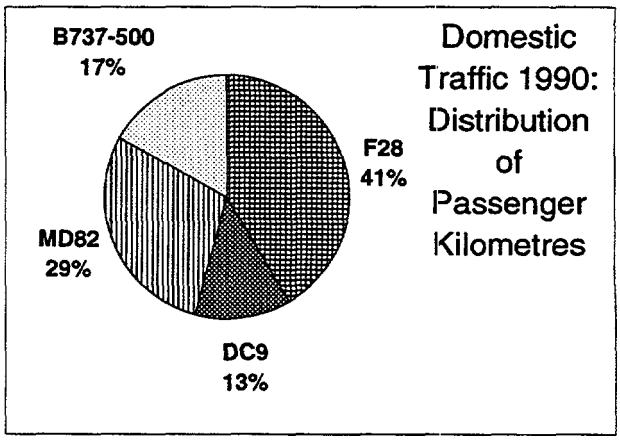

Fig. 3.1. Distribution of passenger kilo metres on different aircraft types at Arlanda 1990

In Figure 4.1 these results are presented for each aircraft and for the "average" aircraft per pkm. The latter represents the "result".

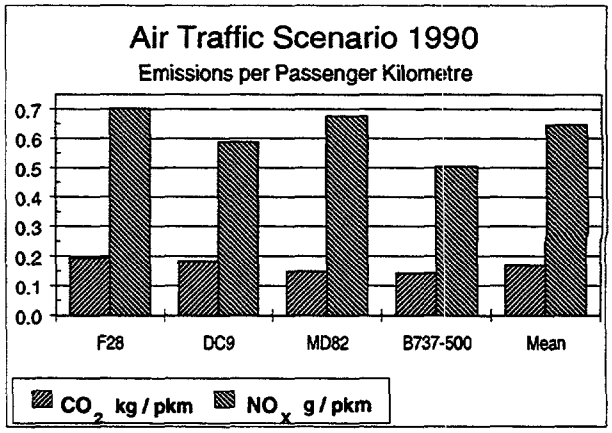

Figure 4.1. Emissions per passenger kilo metre for flight traffic scenario 1990

5. The Future Year Scenario

The results from the B737-600 flights are composed in a future scenario to be compared with the base year scenario. In the future scenario, B737-600 is replacing the other aircraft to represent equivalent flights but with future technology.

The aircraft types included in the study do not have the same number of seats. B737-600

can therefore not replace their flights exactly. Here, two different ways of approaching the problem could be used:

- the future aircraft performs the same number of flights as each of the replaced aircraft
- the future aircraft ships passengers equivalent to the number of passengers in the replaced aircraft flights

The first scenario will show changes in both transport capacity and emissions, the second will show changes in emissions only. We chose the second for our evaluation for the sake of explicity.

Both scenarios produce somewhat fictive measures as capacity and traffic intensity on different routes cannot be fully regarded. This ensues from the fact that only one aircraft of a specific size is used in the simulations when in reality the airlines will use different modern aircraft of various sizes to fulfil their needs.

In the future scenario the same number of passenger kilometres per route will be fulfilled, see Table 5.1.

Table 5.1.

Aircraft	Aircraft movements	Average flight distance [km]	Seats occupied
F28	23 318	380	88
DC9-41	5 125	533	88
MD-82	11 574	530	88
B737-500	7 900	459	88

The results of Scenario 2000 are found in Figure 5.1.

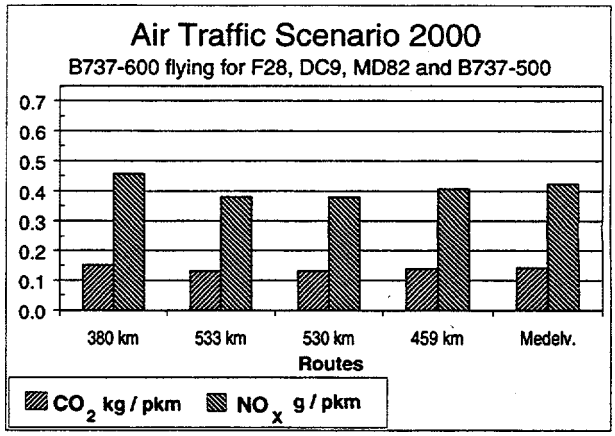

Figure 5.1. B737-600 replacing old air craft in the future scenario

6. Evaluation

6.1. Scenario Comparison

The emissions for the future scenario are now compared to the base year scenario, see Figure 6.1. The differences are significant.

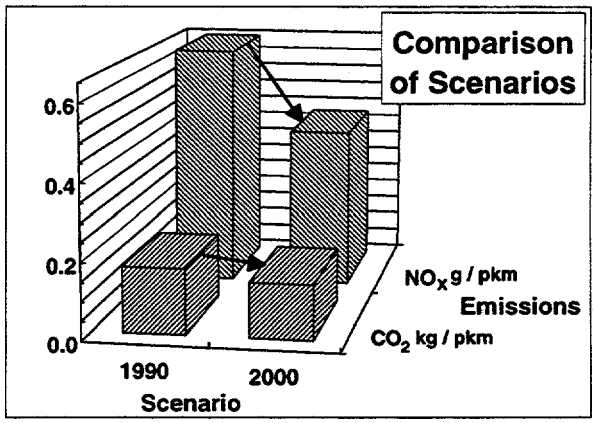

Figure 6.1. Comparison of average emission levels for the two scenarios

The results are presented in numbers in Table 6.1. Also the percentage improvement, which is the result of the study, is shown.

Table 6.1. Comparison of future and base year scenario

	CO_2 kg/pkm	NO_x g/pkm
Scenario 1990	0,17	0,63
Scenario 2000	0,14	0,41
Emissions	**CO_2**	**NO_x**
Decrease	18 %	36 %

6.2. Margins for Air Traffic Growth

Assume that the legislation in the future will limit the total amount of emissions to the values of 1990. This study provides information about which air traffic growth could possibly be allowed depending on which emission — carbon oxide or nitrous oxide — being restraining. The relation of air traffic growth and allowed emission level is illustrated in Figure 6.2. The upper limit corresponds to the results of the study while the bottom limit is estimated to reflect the uncertainties by which the study is impaired.

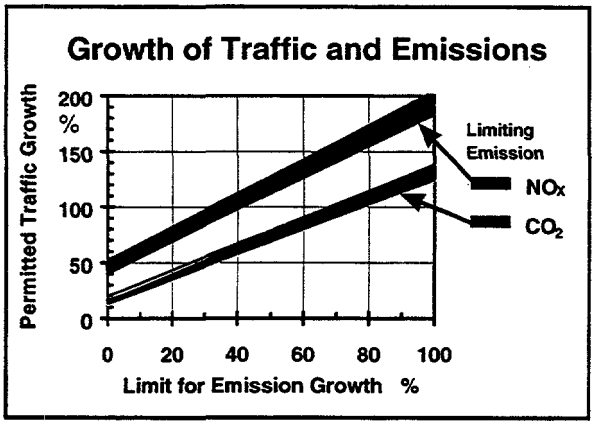

Figure 6.2. Permitted air traffic growth as a function of emission growth limit

7. Conclusions

Aiming to show the technological tendencies, this study declares that improved technology already available can give:

- a decreased fuel consumption, and thus an decrease of emitted carbon dioxide around 15%
- reduced emissions of nitrous oxides around 30%

The improvements in fuel consumption can be ascribed to more efficient engines and aerodynamic improvements that decrease the drag and thus decrease the required thrust. The excessive improvement in emitted nitrous oxides can be ascribed to the new engine technology with double burners reducing the temperature peaks. The aerodynamic improvements also contribute, with decreased drag and thus decreased fuel consumption.

7.1. Traffic Margins

If the emissions of the base year should be used as limit, it can be established that the improvements would allow for:

- traffic increase around 20% if the emissions of carbon dioxide are limiting
- traffic growth around 50% if the emission of nitrous oxides are limiting

7.2 Most Important Flight Stages

This study also illuminates that the emissions during the climb stage constitute a large part of the total emissions in the Swedish air space, where distances for cruise are limited.

7.3. Airport Emissions

Also the emissions at and around airports will decrease due to the new technology which leads to decrease the production of nitrous oxides. To quantify the LTO emissions more detailed studies are necessary.

7.4. Developing the Method

During the studies, the calculations and simulation methods have been improved. The work also has indicated which possibilities there are to further improve the methods.

References

[1] "ICAO Engine Exhaust Emissions Data Bank", ICAO, Doc 9646-AN/943, (1995)

[2] Händig, Anders, "Tools for Aircraft Emissions Simulation and Analysis", FFA TN 1995-07, (1995)

[3] Kläth, Yngve, "Motorprestanda och emissionsdata för några civila motorer", Volvo Aero Corporation, 6250-469, (in Swedish), (1995)

[4] Hasselrot, Anders, "Further Development of an Empirically Based Computer Program to Aircraft", FFA TN 1992-25, (1992)

Environmental Compatibility of

CRYOPLANE

the Cryogenic-Fuel Aircraft

H.G. Klug
(Daimler Benz Aerospace Airbus,
Postfach 95 01 09, 2111 Hamburg, Germany)

Extended Abstract

1. What is CRYOPLANE

"CRYOPLANE" is the project name for an aircraft powered by cryogenic fuel, either Liquid Natural Gas (LNG, mainly consisting of methane, -160°C) or Liquid Hydrogen (LH_2, -253°C). The name "CRYOPLANE" is used by German and Russian companies working jointly on the subject since 1990.

2. Reasons for working on CRYOPLANE

After the depletion of economic crude oil "reserves" expected within 40 years and of less economic "resources", kerosene could be produced from oil sands, shale, or synthesized from gas or coal, but certainly at a higher price, and with increasing damage to the environment. Prices for oil based products, under a plausible scenario, will rise significantly in the 2010 - 2020 period, and will facilitate the change to a new fuel.

The real driver for introduction of a new fuel will be the need to protect the atmosphere from everincreasing emission of fossil-fuel based CO_2, as internationally accepted at the Rio de Janeiro Summit 1992. Aviation cannot claim an exemption, and concern is prowing in the aviation community that governmental action will endanger further traffic growth, or even threaten current business volume.

Why Liquid Hydrogen ?

Hydrogen can be produced by electrolysis of water on the basis of any renewable energy; when burnt the only primary combustion product is water again ("closed cycle"). Hydrogen contains 2.8 times more energy per mass than kerosene.

3. Status of CRYOPLANE

ANTK Tupolev (airframe) and TRUD (engine) have demonstrated the basic feasiblity of the concept by flying the experimental aircraft TU-155 in 1988. Russia currently favours LNG as an intermediate step, while Western interest concentrates upon LH_2. The two technologies are close enough for a very useful cooperation. At this moment, German, Russian, and Canadian partner companies are defining a demonstrator aircraft based upon the regional airliner Do 328, planning for a first flight in 2000.

4. Environmental Aspects

Emission of CO_2, Unburnt Hydrocarbons, soot and sulfur will be completely avoided by hydrogen combustion. LH_2 is an extremely pure liquid.

Emission of water as a primary combustion product is increased by a factor of 2.6. While water vapour is a potent greenhouse gas, its residence time in the atmosphere is relatively short (< 0,5 ... 1 year in low stratosphere) compared to CO_2 (~ 100 years). Simple parametric assessment shows that at flight altitudes equal or below 10 km, burning hydrogen has a much smaller impact in terms of greenhouse effect upon the atmosphere than burning kerosene.

Complex simulations by a General Circulation Models have shown that current water emission by aircraft must be increased by a factor of 10 000 to produce a significant effect on the climate.

Aircraft emit NO_x directly into the atmosphere at high cruise altitudes where NO_x, by a catalytic process, causes the formation of ozone which is a strong greenhouse gas. For kerosene fueled aircraft, the contribution of NO_x / ozone to the greenhouse effect is of similar magnitude as the effect from CO_2.

In the context of the European / Canadian "Euro Québec Hydro Hydrogen Pilot Project" (EQHHPP), it has been demonstrated that by premixing and very lean combustion of hydrogen, the emission of NO_x can be reduced by a factor of 10 or even more compared to current kerosene engines.

Taking the greenhouse effects from CO_2, H_2O, and NO_x / ozone into account, it can be shown that

- LH_2 fueled aircraft cause less greenhouse effect than kerosene aircraft at all practical flight altitudes;
- at 11 km (60 % of all aviation fuel is burnt between 10 and 12 km) the advantage of hydrogen is very significant;
- at 10 km and less, the effect of the hydrogen aircraft is negligible.

No final statement can be made at the moment with regard to the effect of contrails. (3) Exhaust gases behind hydrogen engines contain more water than behind kerosene engines, and hence can form contrails under a wider range of atmospheric conditions. →

However, simulations available suggest that, due to the lack of condensation nuclei, particle number / size will be different, and the radiativ effect of such contrails less pronounced. This is one of the predictions hopefully to be confirmed by flight test of the planned demonstrator aircraft. If, against current expectations, such contrails turn out to be a problem, they could be avoided by lowering the flight level under critical meteorological conditions, or by meteorological navigation, albeit at a fuel consumption penalty.

5. CO_2 Reduction Targets

No CO_2 reduction targets specific to aviation have been formulated yet. Qualitativ requirements can be stated as follows:

- CO_2 output can be allowed to grow only for a limited time period
- CO_2 output in the midterm must go down again significantly below 1990 level
- Content of CO_2 accumulated in the atmosphere must stabilize within the next century.

6. "Business as Usual"

As a reference case, a scenario is analysed where air traffic grows like projected and kerosene is used indefinitely. Only the airplane side is considered, i.e. CO_2 emissions during more and more complicated production is neglected. Existing traffic / fleet projections were extended into the long term future by assuming a 3 % p.a. traffic growth beyond the year 2020 (a moderate assumption compared to the app. 5 % p.a. of the last decades). Fuel consumption and CO_2 emission were calculated for a rate of technical progress of 2 % p.a., i.e. each year the average fuel consumption per seat-km goes down by 2 %. While this was roughly true for the last decades (including the change from the pure jet to the high-bypass-ratio fan engine), it is extremely optimistic for the future.

Nevertheless, CO_2 output under this scenario grows year by year, thus completely missing the target. No stabilization of the CO_2 content of the atmosphere caused by aviation is achieved.

7. Soft Transition to Hydrogen

As a possibility preferrable for many economic and practical reasons, this scenario was defined taking into account the extremely long life cycle of aircraft programs, and the 25 year life of any individual aircraft.

It is assumed that

- Transition starts successively in different regions of the word, offering more or less favourable conditions in terms of environmental awareness, technical capacilities, and availability of LH_2 from renewable sources. Governmental action to stimulate the change to LH_2 will be required at least in the early phases.
- Transition starts successively for regional, short / medium, and long haul traffic.

The transition process, under such a scenario, will start in 2005 in niche markets, but takes place on a really large scale only in the 2020 ... 2030 period, and is virtually concluded by 2050.

Fuel consumption and CO_2 emission were calculated, allowing for the same rate of technical progress (2 % p.a.) as before. The result clearly showed that under such a scenario, aviation cannot meet the CO_2 reduction targets until the period 2030 ... 2040. A stabilization of the CO_2 content of the atmosphere caused by aviation is achieved around the year 2050, when near-zero CO_2 emission is realized. Lateron, CO_2 content is going down again.

8. "Crash Transition"

Finally, a scenario was considered, where within the period 2010 ... 2030, the complete fleet of civil airliners is switched from kerosene to LH_2 propulsion.

Such a scenario could only be realized under the impact of some catastrophic event, e.g. major crude oil reserves become no longer accessible for political reasons, or dramatic effects of anthropogenic greenhouse effect cause governments to enforce transition to renewable energies.

Under this scenario, the CO_2 content of the atmosphere due to aviation, reaches its maximum by 2030. While it may be desirable for ecological reasons, such a scenario might prove an economic catastrophe to civil aviation, with devastating results, or might turn out not to be practical at all.

9. Conclusions

Liquid Hydrogen fueled aircraft promise big advantages relativ to kerosene aircraft in terms of environmental compatibility.

Transition to LH_2 will take a long time if extreme economic penalties are to be avoided. Under such a "soft scenario", transition would start in regional niche markets after 2005, and would be completed only beyond 2050. CO_2 accumulated in the atmosphere would reach a maximum around 2050, and would then go down again, as aviation reaches the ideal target of "zero CO_2 emission".

To actually initiate such a soft transition in the 2005 ... 2010 period, further technological preparation is urgently required, including realization of an LH_2 Demonstrator aircraft.

Non–intrusive measurement of emission indices — A new approach to the evaluation of infrared spectra emitted by aircraft engine exhaust gases

E. Lindermeir, P. Haschberger, and V. Tank
Deutsche Forschungsanstalt für Luft- und Raumfahrt (DLR),
Institut für Optoelektronik, Postfach 1116, 82230 Wessling, Germany

Abstract

A non-intrusive method is used to determine the emission indices of a research aircraft's engine in-flight. The principle is based on the Fourier Transform Infrared Spectrometer MIROR which was specifically designed and built for operation aboard aircrafts. This device measures the spectrum of the infrared radiation emitted by the hot exhaust gas under cruise conditions. From these spectra mixing ratios and emission indices can be derived. An extension to previously applied evaluation schemes is proposed: Whereas formerly the plume was assumed a homogeneous layer of gas, temperature and concentration profiles are now introduced to the evaluation procedure.

1 Introduction

World wide air traffic is expected to double in the next decade [1]. Consequently there is a need of estimating the effects of aircraft upon the environment. Especially effects on global climate and the ozone layer are being discussed. In 1992 the German Federal Ministry for Education, Science, Research, and Technology (BMBF) started the project "Pollutants from Air Traffic" (Schadstoffe in der Luftfahrt) in order to scientifically investigate if the large rates of growth of air traffic might cause future problems.

For an accurate estimate of the pollutants emitted by aircraft it is necessary that emission indices (ratio of gramme mass of trace gas per kilogramme mass of burnt fuel) of commonly used engines are available. Emission indices not only depend on the engine, they are also functions of an aircraft's flight condition. Currently there are no legal requirements to measure the emissions of an engine under cruise conditions. On the other hand, on long distance flights the major part of the NO_x emissions, for example, occurs during cruise. Therefore one task of the above mentioned project is to develop and operate a measurement system to determine the amount of pollutants emitted by an engine in-flight.

After a short description of the principle of the method that was employed for this type of measurement this paper will focus on the way the measured data are evaluated.

2 Physical principle of the measurement

For in-flight measurements non-intrusive methods are most suitable for the detection and quantification of the emitted gases. The method described here is based on the fact that hot, hetero-atomic gases emit infrared radiation. The wavelength of the emitted radiation

is specific for a certain molecule. Thus, the spectrum of the radiation emitted by hot exhaust gases consist of many, very narrow lines. The shape (intensity and line-width) of these depends on the gas species, their concentration, gas temperature, and pressure. For the determination of the concentrations of the exhaust gas species and their temperature, spectra of the emitted infrared radiation are measured and by application of a suitable evaluation procedure the interesting quantities are obtained.

3 Experimental setup

To evaluate the emission lines in the measured infrared spectra high spectral resolution ($< 0.2\ \mathrm{cm}^{-1}$) is necessary. Therefore a Fourier transform infrared spectrometer is used. Usually these optical devices are mechanically quite sensitive. Commercial instruments are manufactured for use in laboratories only. Therefore it was necessary to design and build a rugged FTIR instrument specifically for operation aboard an aircraft. For this task the FTIR principle "Michelson Interferometer with Rotating Retroreflector" (MIROR) [3] was chosen, because it is based on the continuous rotation of one retroreflector whereas all other optical components can be fixed tightly with reference to each other.

Fig. 1 shows a sketch of the instrument installed in the cabin of the DLR research aircraft ATTAS (VFW 614) which was used to demonstrate the technique. The infrared radiation emitted by the exhaust passes through a germanium window to the receiving telescope of the spectrometer. The data are recorded at a frequency of approximately 1.5 measurements per sec.

4 Current Data Evaluation

Principle. After radiometric calibration of the acquired data, spectra in physical units of spectral radiance ($\mathrm{W/cm^2\ sr\ cm^{-1}}$) are obtained. These are compared to calculated infrared spectra which are the result of modelling the measurement setup. These simulated spectra are functions of the interesting parameters, i.e. the plume's temperature and the concentrations of the emitted gases. By applying a non-linear least squares fit, these parameters are varied until the differences between simulated and measured spectra are minimised (cf. [4] for a description of the algorithm).

For in-flight measurements the model consists of three major parts: the plume, the germanium window, and the atmosphere in the aircraft's cabin. Simulations [2] show, that radiation emitted from the atmosphere behind the plume is negligible, as is the influence of the gases between plume and germanium window. The reason for this is the temperature of about 240 K in flight levels around 9 km which is very low compared to temperatures of more than 600 K in the exhaust.

Measurements. In-flight measurements of the infrared radiation emitted by the exhaust gas were performed on 8th June 1995. While data were collected engine parameters which affect the mixing ratios in the plume, like thrust, fuel flow, temperature, etc., were kept at constant values. The exact flight conditions are reported in [5]. The top of Fig. 2 shows the region of the measured spectrum, in which emission lines of CO occur. A model

MIROR on board VFW 614

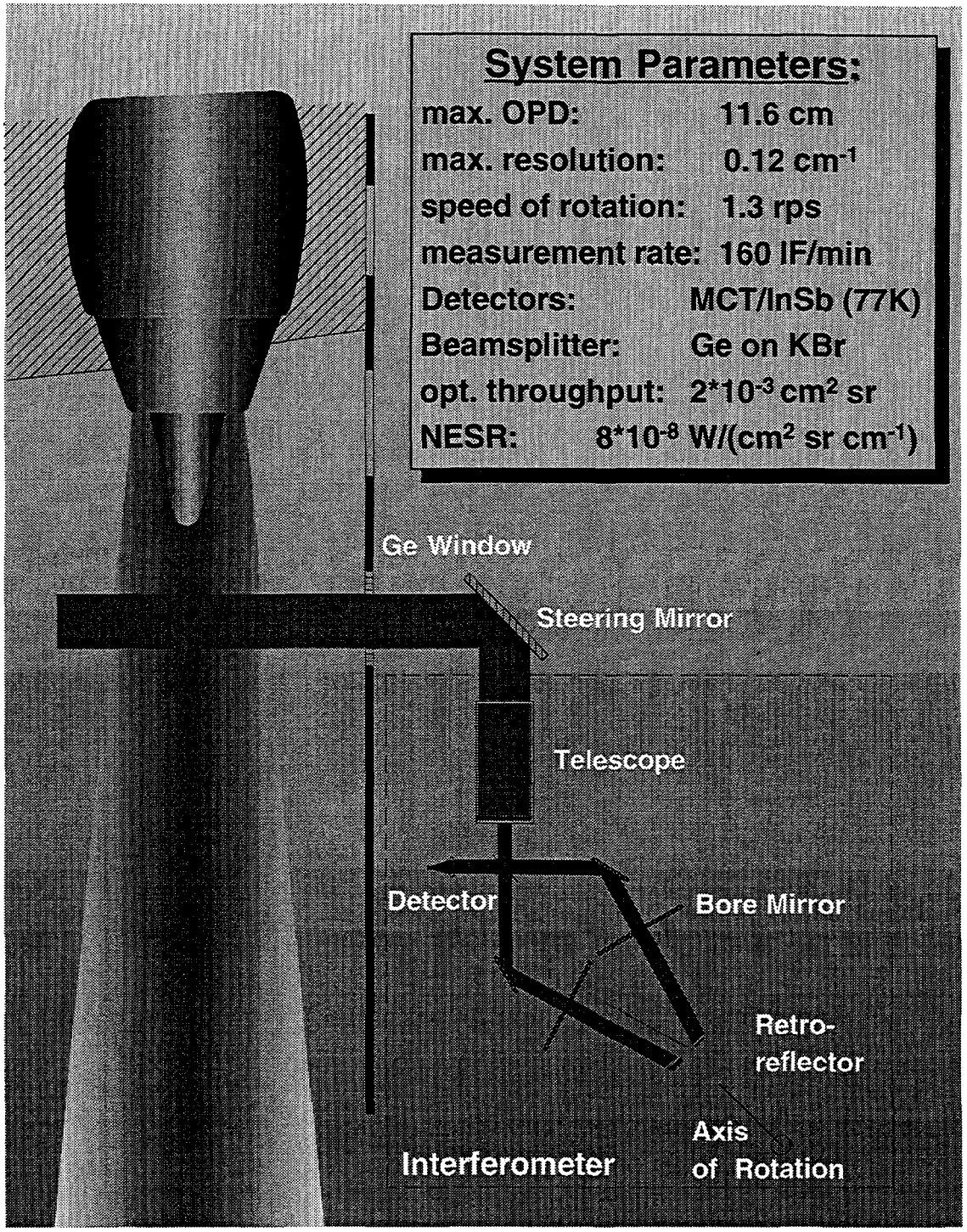

Figure 1: Experimental setup: The Fourier Transform Infrared Spectrometer MIROR installed in the cabin of the DLR research aircraft ATTAS (VFW 614).

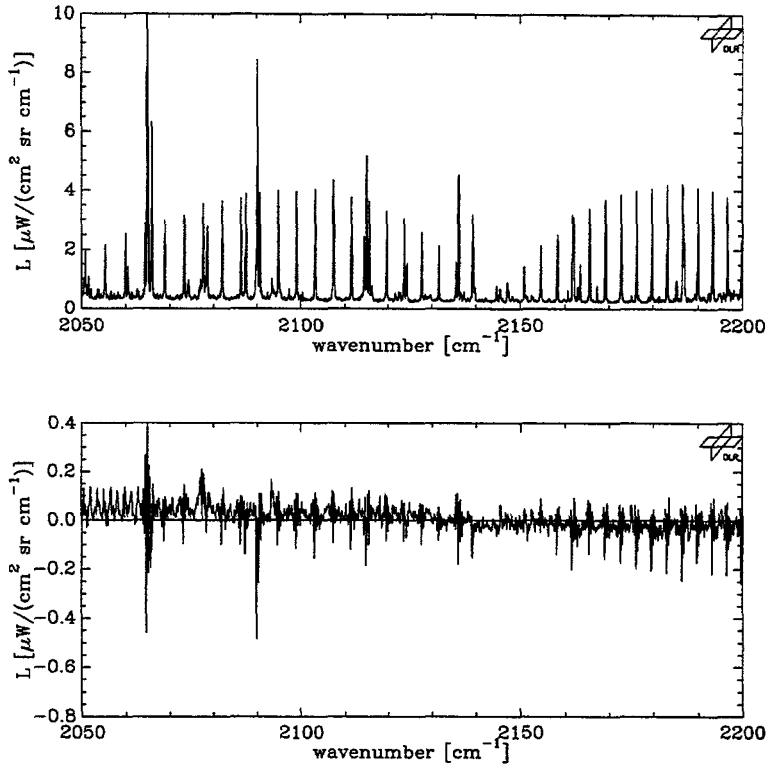

Figure 2: Top: Regions of the measured and fitted spectra where CO emission lines occur. Bottom: Absolute difference: Calculated spectrum – measured spectrum.

spectrum (also included in the top of Fig. 2) was fitted in order to determine the concentration of the gases and their temperature. For this model the plume was represented by a homogeneous layer of gas. In the bottom of the figure the absolute deviations between measurement and fitted model can be seen. Table 1 shows the resulting parameter values. They were derived under the assumption of stoichiometric combustion, i.e. the emission index of CO_2 was set to 3150 g/kg.

Parameter	Value
temperature T	631.3 K
concentration CO_2	28600 ppmv
concentration CO	238 ppmv
emission-index CO	16.7 g/kg

Table 1: Parameters obtained by a least squares fit of a model to the measured spectrum.

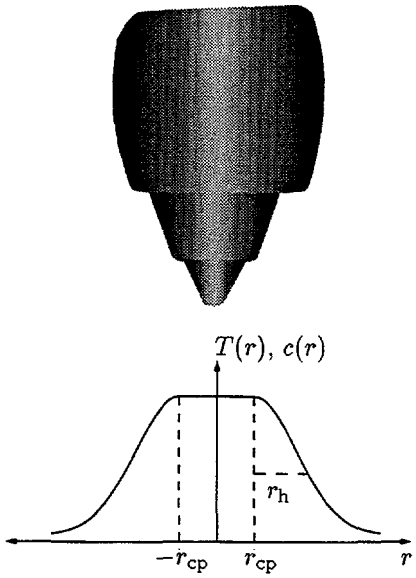

Figure 3: Radial profiles for temperature and concentration.

5 New Evaluation procedure

The assumption that the plume can be represented by an homogeneous layer of gas is valid only if the investigated region of the exhaust gas is very close to the nozzle exit. This condition was fulfilled for the measurements at the research aircraft ATTAS, where the measurement spot was approximately 1 m downstream from the nozzle exit.

In continuation of the project investigations will focus on the engine of an Airbus A340 which is expected to be of relevance for the global climate. For this aircraft the assumption of a homogeneous layer will lead to averages which may deviate considerably from the true values. Therefore a new evaluation scheme, presented in this paper, must be applied.

The radiation emitted by the plume will be modelled by use of radial temperature and concentration profiles as depicted in Fig. 3. These are symmetric to the axis of the engine, and, according to flow field simulations [2], there is an inner region of constant plume properties (limited by a *constant property radius*, r_{cp}), and an outer region, where temperature and concentrations decay according to a Gaussian function. The temperature profile, for example, is given by the following equation:.

$$T(r) = T_{\max} \qquad \text{for } |r| \le r_{\mathrm{cp}} \tag{1}$$

$$\frac{T(r)-T_\infty}{T_{\max}-T_\infty} = \exp\left[-\ln(2)\left(\frac{|r|-r_{\mathrm{cp}}}{r_{\mathrm{h}}}\right)^2\right] \qquad \text{for } |r| > r_{\mathrm{cp}} \tag{2}$$

where $T(r)$ is the temperature at radius r, $T_{\max}$ is the temperature in the constant property region, T_∞ is the ambient temperature, and r_h is the half-width radius of the Gaussian part.

Because it can be assumed that the Prantl and Schmidt numbers are equal to 1 [2], the expressions for the ratios of the concentration differences (analog to Eq. (2)) are the same as for the ratio of the temperature differences. Thus for the profiles of M gases and the temperature to be determined, there are $2M+4$ parameters in the plume model. These

are: parameters for the max. and the ambient values of each profile, the constant property radius, and the half-width of the Gaussian part of all profiles.

Of course, for radiometrically modelling the plume the profiles must be sampled. The big advantage of the use of a profile is that the number of unknown parameters which must be determined by a least squares fit, is independent of the number of samples, while, on the other hand, the accuracy of the plume-model increases with the number of samples. At the same time this number may not be too large, as it considerably increases the CPU-time needed for the calculation of the modelled spectrum. Calculations show that an acceptable trade-off is achieved with approximately 10 samples.

6 Conclusion

A method for non-intrusive in-flight measurements of emission indices and exhaust gas temperature of aircraft engines has been briefly described. The currently used evaluation procedure is applicable for measurements on board the DLR research aircraft ATTAS, which was used to demonstrate the technique. The achieved accuracies are estimated to about 20% for NO and H_2O, 10% for CO_2 and CO, and 2% for the temperature.

In a next step measurements of the exhaust gases of an engine which is of interest in estimating global effects of present and future air traffic will be performed. Therefore experiments aboard an Airbus A340 are scheduled in 1997. For these measurements the evaluation software has been extended to determine radial profiles of temperature and concentrations. First results of these calculations will be shown at the conference.

References

[1] Schumann, U., On the effect of emissions from aircraft engines on the state of the atmosphere, in *81st Symposium on Fuel and Combustion Technology for Advanced Aircraft Engines, AGARD Conf. Proc., 536,* pp. 1-19, 1993.

[2] Beier, K. and F. Schreier, Modeling of aircraft exhaust emissions and infrared spectra for remote measurement of nitrogen oxides, *Ann. Geophys., 12,* 920–943, 1994

[3] Haschberger, P. and V. Tank, Optimization of a Michelson interferometer with a rotating retroreflector in optical design, spectral resolution, and optical throughput, *J. Opt. Soc. Am. A., 10,* 2338-2345, 1993.

[4] Lindermeir, E., Evaluation of infrared spectra of aircraft exhaust with the FitFas software, *Ann. Geophys., 12,* 417-421, 1994.

[5] Haschberger, P. and E. Lindermeir, Spectrometric inflight measurement of aircraft exhaust emissions: First results of the June 1995 campaign, *J. Geoph. Research,* in press, 1996

Fuel Consumption and Exhaust Emissions of Aircrafts

Ralf Büchler, Institute of Flightmechanics, TU Braunschweig

1. Introduction

Within one century the human race succeeded in turning the 'dream of flying' into a modern aircraft industry. Since World War II the technology and air traffic showed an explosive development. This brought many adventages such as high mobility of people and goods, but also negative effects such as air pollution and noise molestation, which raise discussions about environmental protection.

	passengers (Mio)	pass. Km (Mio)
1950	31	28
1970	307	387
1990	1154	1888
1995	1850	3000

Table 1:Number of passengers during the last 45 years /1/

Only a few years ago aircrafts were neglected as pollutants, because their emission amount is only about 2% of all anthropogene exhausts. Jet air traffic is the called to account for contamining the upper troposphere and lower stratosphere.. This is because exhausts in those altitudes (10-13 km) have a huge influence on the stability of the ozone layer. Chemical investigations have shown, that ozone can easily be taken to pieces by nitrogen compounds (NO_x), a part of aircraft exhausts.

This paper investigate the reduction of contamination of sensitive atmospheric layers by improved flight planning steps, is investigated → p-425

2. Atmosphere

The atmosphere is a higly sensitive and complex system to many local and time variables. In order to estimate the influence of aircrafts on the atmosphere, a mathematic model has to be found. In this investigation the U.S. Standard Atmosphere Supplements /2/ is used. Atmospheric investigations showed that stay periods of pollutants above the tropopause are multiple higher than underneath. Therefore the location of the tropopause is the most interesting part. The potential of damage is much higher in the stratosphere than in the troposphere. For futher consideration the tropopause is accepted as a kind of bound function with regard to environmental damage.

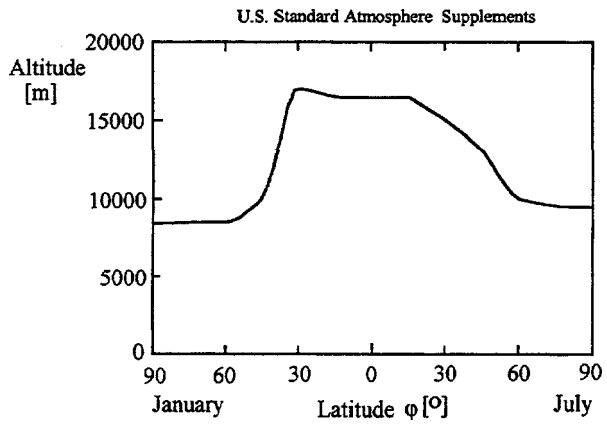

Fig. 1 Altitude of the tropopause on the northern hemisphere /2/

3. Flightmechanics

The operation point of an engine respectively the required thrust level results from the combination of altitude and mach number. *Figure 2 and 3* show the characteristic curves for thrust, specific fuel consumption and emission indices (emission amount related to burned fuel). The calculation of the output parameters is based on a general flight performance program coupled with an engine synthesis program /3/.

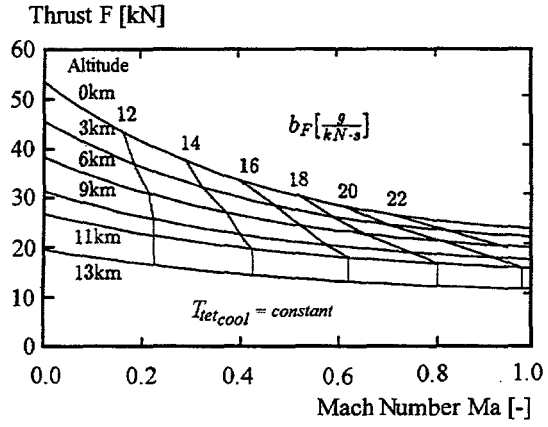

Fig. 2 Characteristic curves of thrust and specific fuel consumption

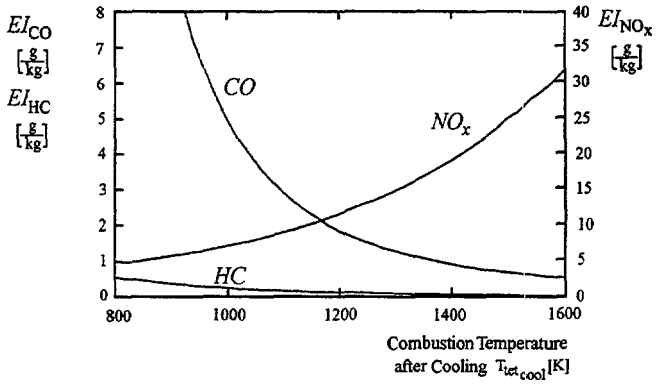

Fig. 3 Characteristic curves of the emission indices

Emissions of carbon dioxide (CO_2), water (H_2O) and sulphur dioxide (SO_2) are coupled directly to the fuel consumption. Minimizing the burned fuel optimizes simultaneously aforesaid emitted particles. Nitrogen compounds (NO_x), carbon monoxide (CO) and hydrocarbon (HC) additionally depend on the operation point of the engine.

4. Influence of altitude limitations on fuel consumption and emissions

Exhaust gas in sensitive regions of the atmosphere should be avoided, because it destroys ozone in the upper troposphere and lower stratosphere. Therefore, flight level restrictions should be installed. It is assumed that the environmental damage caused by aircrafts could be reduced considerably by avoiding stratospheric flights.
However, the optimal flight altitude of most jet aircrafts is placed in those regions, because otherwise, higher fuel consumption and emissions will be expected. The following table shows the output data of a B747-400 from Frankfurt to New York, flying in different altitudes.

altitude h [m]	consumption m_{fuel} [kg]	emission $m_{emission}$ [kg]
10000	67137	829
9000	70064	907
7000	81664	1156
5000	100983	1657

Table 2:Fuel consumption and exhaust emissions in different altitudes (Frankfurt to N.Y.)

At first sight the introduction of altitude limitations seems to be a contradiction to the reduction of environmental pollution. Consumption and emissons increase and the economic effiency becomes worse. On the other hand stay periods of those particles, especially NO_x, in the atmosphere reduce considerably. This correlation can be described by the following quality function:

$$P_{harm} = f(\sum m_{emission}, t_{stay})$$

P_{harm} = potential of damage

$\sum m_{emission}$ = sum of emissions

t_{stay} = stay period

A detailed analysis of the components of this equation has to be done by chemists. Investigations by engineers only calculate the amounts of exhausts along the trajectory. The following picture shows the additional expenditures for trajectories avoiding the stratosphere. The example shows a B747-400 flight along a constant degree of longitude from the equator to the north pole.

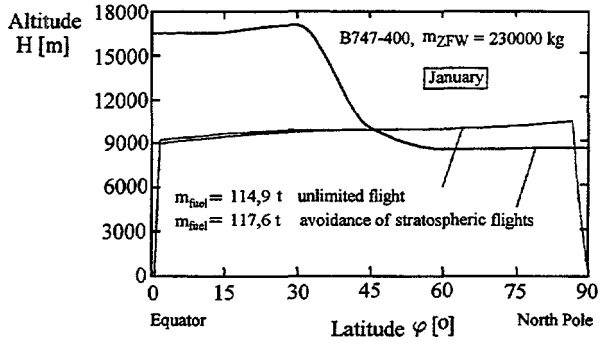

Fig.4 Flight trajectories of allowed and avoided stratospheric flights

As a result a tropospheric flight requires ca. 2.3% more fuel and produces just as much emissions than a flight without altitude limitation. In the northern hemisphere flight directories from north to south are for altitude limited flights more economic than the other way round. This is because there is a smaller gap between this flight trajectory and the optimal flight.

5. Effects on fuel consumption and emissions by varying flight structures and flight profiles

The main task of flight control planning is the organization of the air traffic. An organization schedule should minimize the risks of accidents and reduce the noise and exhaust loads for the people in the air and on the ground. Therefore, aircrafts have to fly on given flight tracks. These tracks are estimated daily, influenced by weather and the amount of air traffic.

5.1 Inspection of global main air routes

Investigations in global air routes allow to quantify the emission of aircrafts into the atmosphere. *Table 3* shows fuel consumption, emissions and parts emitted above the tropopause for flight calculations between Europe and different cities on different continents accompanying.

route (B747-400)	$m_{consumption}$ [kg]	$m_{emission}$ [kg]	percentage above tropop.	$m_{consumption}$ [kg]	$m_{emission}$ [kg]	percentage above tropop.
	winter			summer		
Frankf.-L.A.	110338	1464	92.9 %	110042	1469	46.1 %
Frankf.- N.Y.	72658	914	90.1 %	72967	935	-
Frankf.-Mex.C	119907	1533	57.5 %	117223	1521	-
Frankf.-B.Aires	147306	1922	-	137715	1846	-
Frankf.-Nairobi	64898	912	8.5 %	68339	930	-
Frankf.-Ar Riad	42073	622	36.0	44512	637	-
Frankf.-Singapur	106991	1580	-	114895	1682	-
Frankf.-Tokyo	102315	1440	89.9 %	104472	1454	54.4 %
Frankf.-L. Palmas	36388	475	38.2 %	35243	487	-

Table 3 Consumption and emission of a B747-400 on main air routes

More than a third of intercontinental aircraft movement happens across the North Atlantic Ocean. A long distance of the trajectory between Europe antd the USA is situated above the tropopause, because of the northern position of the system. Consequently environmental pollution is very high in this region /4/. Investigations of the North Atlantic Track-Sytem (NAT) allow to classify the influence of aircrafts on the atmosphere.

5.2 North Atlantic Track-System (NAT)

The NAT-System is set twice a day by the air traffic control service in Prestwick (Scotland) and Gander (Canada). The position and number of tracks can vary every day, depending on the weather (polar front jet stream) and the announced flights. For a general investigation of the track-system between Europe and the East Coast of the USA an average winter day is used because of the low tropopause. For this day an 6x5 constellation is given, i.e. 5 flight levels and 6 horizontal tracks.

There is no special interest on single trajectories, but in the effects of the whole system, i.e. in what way fuel consumption and emission amounts are influenced by moving or changing the structure of the system. *Figure 5* shows the optimal position with regard to consumption and exhausts for westbound flights on a normal winter day. The cross section is equal to the 30th degree of latitude. This is the most northern point of the track-system. *Figure 6* shows the same system avoiding stratospheric flights. The NAT-System was set four flight levels lower (ca. 2600m). This results in higher consumption and exhausts.

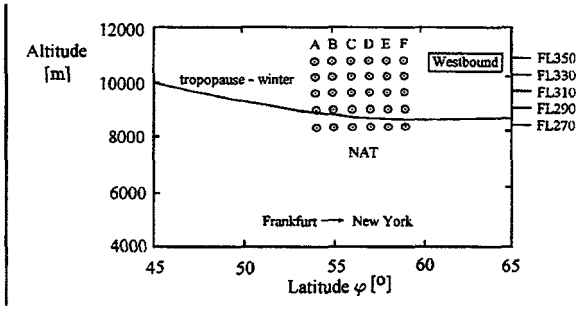

Fig. 5 Example, optimal position of the NAT-System for flights in wintertime, Westbound, 30th degree of latitude

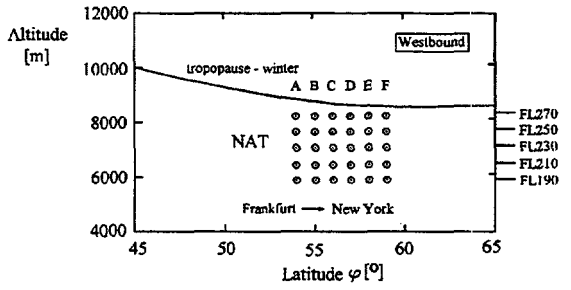

Fig. 6 NAT-System to avoid stratospheric flights

With regard to economic reasons a downward shift of the NAT-System causes a higher fuel consumption. The extra fuel comsumption is shown in *table 4*. Another possibility is to modify the 6x5 block constellation, to spread the system. Investigations have shown that a horizontal shift of a flight track causes lower consumption as a vertical shift. A vertikal jump over one flight level results in the same consumption and emission amount than a horizontal shift over three tracks. This leads to the assumption that the track-system should be spread and arranged in accordance with atmospheric boundaries. *Figure 7* shows such a modified track-system.

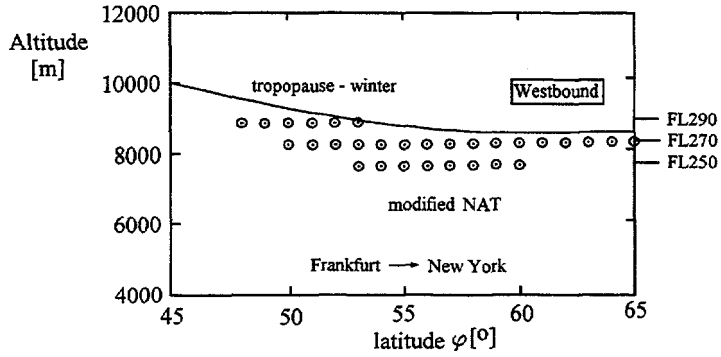

Fig.7 Modified track-system with 30 tracks

Separation of the tracks provides an elliptic arrangement of flight paths underneath the tropopause. Even if the distance of single trajectories increases, consumption reductions are calculated. In order to avoid stratospheric flights the fuel consumption is about 6.3t lower for the modified case compared to the shifted system for flights Frankfurt - New York in winter time. *Table 4* shows the characteristics of consumption and emission behaviour for different cases.

direction	season	reference system, today, fig. 5	shifted system fig. 6	modified system fig. 7
Frankfurt-New York	winter	$m_{fuel} = 75.0t$ $m_{emission} = 954.3kg$	+ 13.29% + 14.91%	+ 4.78% + 4.92%
Frankfurt-New York	summer	$m_{fuel} = 74.9t$ $m_{emission} = 932.0kg$	+ 3.27% + 3.25%	- 0.22 % - 0.12%
New York-Frankfurt	winter	$m_{fuel} = 63.6t$ $m_{emission} = 915.3kg$	+ 19.84% + 21.23%	+ 5.95% + 6.01%
New York-Frankfutrt	summer	$m_{fuel} = 65.1t$ $m_{emission} = 933.0kg$	+ 6.35% + 6.60%	+ 0.21% + 0.34%

Table 4 *Fuel consumption and emission by avoidance of stratospheric flights related to the NAT-System*

The table shows that the modified structure of the NAT-System decreases the additional fuel comsumption and emissions extremely, if stratospheric flights are avoided. The disadvantages in general are higher during winter time, because of the low tropopause. The average value is 2-3% of additional fuel and emission amount during the whole year, but without pouring any exhausts into the stratosphere. The potential of damage can be decreased by a flexible arrangement of the flight tracks.
After licensing satellite navigation systems (GPS) for air navigation in the near future, aircrafts are able to follow trajectories in a more accurate way. This makes it possible to move single tracks closer together, without repealing actual security standards. A smaller track-system can reduce consumption and emissions additionally.

6. Conclusion

Above calculated results have shown, that a further development of flight track planning allows considerable improvements on fuel consumption and exhaust emissions. In consideration of new aircrafts and new engine technology the emission rate per distance decreases. Even if air traffic will further increase, optimistic investigations prognose a reduction of the environmental damage by aircraft exhausts, if the effects of improved flight track arrangement and engine innovations will be combined.
After licensing GPS for air traffic, aircrafts can follow curved trajectories more exactly. Therefore, flight tracks can be accomodated economically to the actual weather conditions, i.e. tail wind situations can be used and head wind situations can be avoided much better than now. This leads to additional economies of less comsumption and less emissions.
This investigation is a basic work to give information for the atmospheric chemistry. In order to give the chemists detailled information, how much and where the exhausts are poured into the atmosphere. Moreover airlines and flight control institutions can use the result of this investigation to minimize the potential of dammage by aircrafts without reducing air safety and economic output.

7. Literature

/1/	W.Pompl	Air Traffic - An Economical Introduction, Springer Publisher, Berlin, Heidelberg, 2. Edition, 1991
/2/		U.S. Standard Atmosphere Supplements, U.S. Government Printing Office, Washington D.C., 1966
/3/	F. Deidewig	Program VARCYCLE for Engine Analysis, Institute of Drive Technics, DLR, Cologne, April 1993
/4/	P.H. Zimmermann	The Impact of Aircraft Released NO_x to the Tropospheric Ozone Budget: Sensitivity Studies with a 3D Global Transport/Photochemistry Model. Max-Planck-Institute for Chemistry, Mainz, DLR-Info 94-06, 1994

Contrail observations from space using NOAA-AVHRR data

Hermann Mannstein
Institut für Physik der Atmosphäre
DLR Oberpfaffenhofen
D-82234 Weßling, Germany

Abstract

The infrared channels of the Advanced Very High Resolution Radiometer (AVHRR) onboard of the weather satellites of the NOAA series allow the detection of contrails. An automated detection scheme is described and tested against computer aided visual classifications by two experts. The algorithm seems to identify contrails within the satellite data with a skill comparable to the human observers.

Clusters of contrails within the satellite images are connected to outline regions where the atmospheric properties are favourable for the existance of observable contrails. Air traffic data shows, that over Middle Europe at least in the main flight levels most of these regions should be marked by detectable contrails. The mean areal coverage of these regions is estimated to be in the range of 10% to 20%, the cloud coverage by detected contrails was 0.9% in 60 AVHRR scenes covering Central Europe.

1. Introduction

Whether there is a relevant climatic impact of contrails is still an open question. High and optical thin cirrus clouds and also aged contrails may have a positive correlation to the radiation budget of the combined surface and atmosphere system. An increase of coverage by contrails may thus lead to warmer surface temperatures while all other cloud types lead to surface cooling. The global mean coverage by contrails is not known. Bakan [1] derived from visual inspection of AVHRR ('Advanced Very High Resolution Radiometer') data the contrail coverage of the North Atlantic region and found values up to 2% depending on season and location.

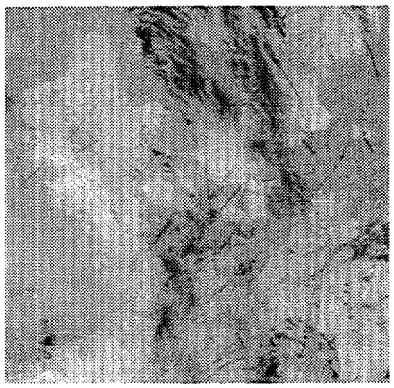

Fig. 1: NOAA-12, T(Ch. 5), May 4th, 1995. 07:43 UT.

Fig. 2: NOAA-12, T(Ch.4) - T(Ch. 5), May 4th, 1995. 07:43 UT.

Fig. 3: Regional standard deviation of T5.

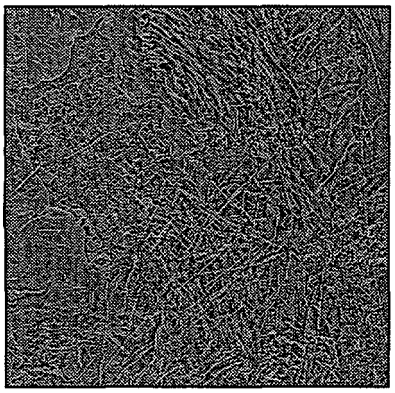

Fig. 4: Normalized temperature Ch.5.

Fig. 5: Large scale maximum gradient of T5.

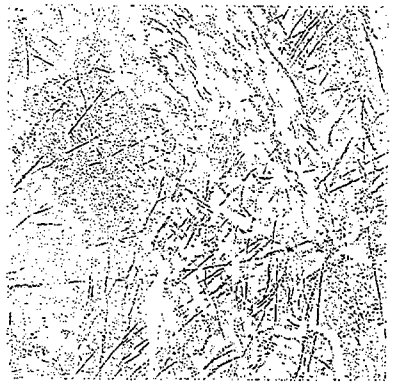

Fig. 6: first guess Mask for detection of contrails.

Local area coverage (LAC) images recorded by the AVHRR onboard of the weather satellites of the NOAA series show often linear structures which can be identified as contrails without any doubt. Best suited to identify contrails are the channels in the thermal infrared part of the spectrum i.e. channel 4 (10.3 to 11.3 μm) and channel 5 (11.5 to 12.5 μm) and the difference of the blackbody temperatures derived from this channels [2, 1]. Figs. 1 und 2 show an extreme case of contrail coverge over Denmark, southern Sweden, northern Germany and the western part of Poland. This small part of an AVHRR scene is used in the following to illustrate the contrail detection algorithm.

2. Contrail Detection Algorithm

2.1. Description

Input data for the detection algorithm are the equivalent blackbody temperature derived from channel 5 (T5) and the temperature difference between channel 4 and 5 (TD). To avoid interference with artefacts produced by remapping we use the data in the original satellite projection. Figs. 1 and 2 show an example of this data. Both datasets are filtered with an highpass kernel and normalized with the regional standard deviation STD5 and STDD(Fig. 3).

T5 is inverted. From the resulting normalized images N5 and ND (Fig. 4), the large scale maximum gradient of T5 (G5) (Fig. 5) and TD we derive a mask shown in Fig 6, which marks all pixel fulfilling each of the following requirements:

- $N5 + ND > 1.5$ (This value depends on the type of normalisation)
- $G5 < 2. * STD5 + 1$ to avoid the interpretation of edges as lines
- $TD > 0.2$

The fixed parameters this requirements where derived by an evolutionary algorithm which maximized the correlation of the resulting mask with the visual analysis of some test cases.

The sum of the normalized images $N5+ND$ is input for further filtering. We convolve the data with a line filter of 19 x 19 pixel in 16 different directions. Because of the normalization of the input data, a single threshold is sufficient to isolate connected regions, which are treated as seperate objects. Each of this objects is checked against the mask described above. To be regarded as a contrail, the remaining pixel in each object have to fulfill the following criteria:

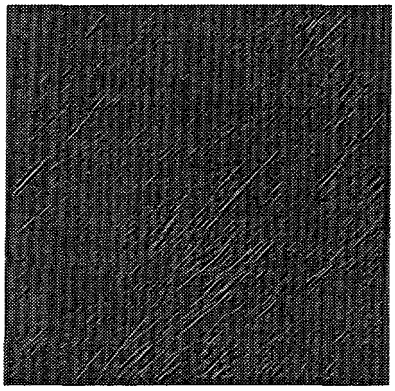

Fig. 7: Sum of normalized images convolved with line detection kernel for 45°.

Fig. 8: contrails derived for the direction 45°.

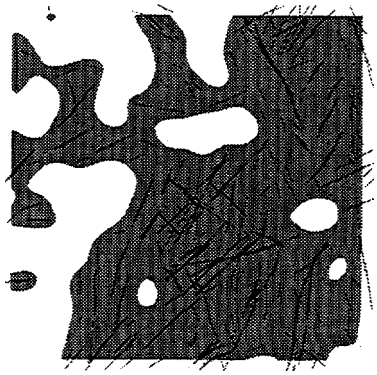

Fig. 9: Result from the contrail detection scheme.

- Ten or more pixel form the object
- the length has to be more then 16 pixel distances
- the correlation of the coordinates must be greater then 0.975

Using morphological functions we fill interrupted contrails. The results for each direction are added. The whole algorithm is then applied to the same dataset sampled every second element and line to detect wider contrails. Fig. 9 shows the result.

2.2. Verification: Comparison with visual classification

For the comparison we used AVHRR Data of the noon overpasses for the months of July and October 1990. The data covers Middle Europe. Due to the changeable satellite position the width of the dataset and the spatial resolution varies. The data has been classified by two observers using an interactive computer program, which allows to mark and store lines of variable width within an image. The result of these two classifications is given in Fig. 10. Fig. 11 shows the result of the automated classification in comparison to the mean value of the two human observers. The variability within the two datasets is comparable.

3. Regions of potential contrails

Over Middle Europe we detect contrails usually in clusters. The typical width of these clusters is in the order of 100 km, the shape is often elongated. We conclude, that these clusters mark regions where the state of the atmosphere within the cruising levels is suitable for the formation of persistent contrails. The atmospheric conditions for contrail formation are extensively described in [3]. For the persistence of contrails a steady lifting of the air parcel seems to be an additional requirement.

Under unchanged atmospheric conditions, the areal extent of these regions sets an upper limit to contrail coverage in case of increased air traffic. Due to the uncertainties in the humidity measurement of radiosondes in this altitudes, and the subsynoptic scale of this regions of potential contrails, a direct determination from standard observational data seems to be not feasible.

Due to the dense air traffic over Middle Europe, we can assume that most of the regions of potential contrails are also marked by them. The scheduled flights from May 4th 1995 from 1.5 h before the satellite overpass at 7:43 UT are schown in Fig. 12. The flightroutes

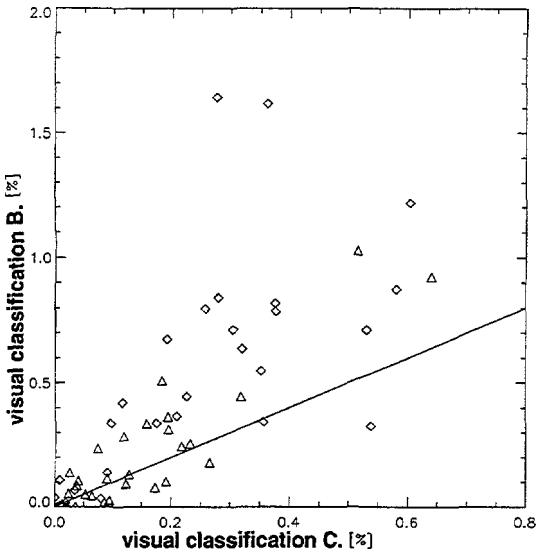

Fig. 10: Comparison of two independent visual classifications

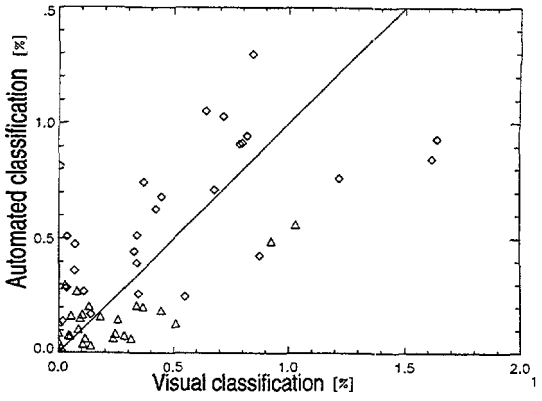

Fig. 11: Comparison of the automated contrail detection scheme to the mean value of the two visual classifications

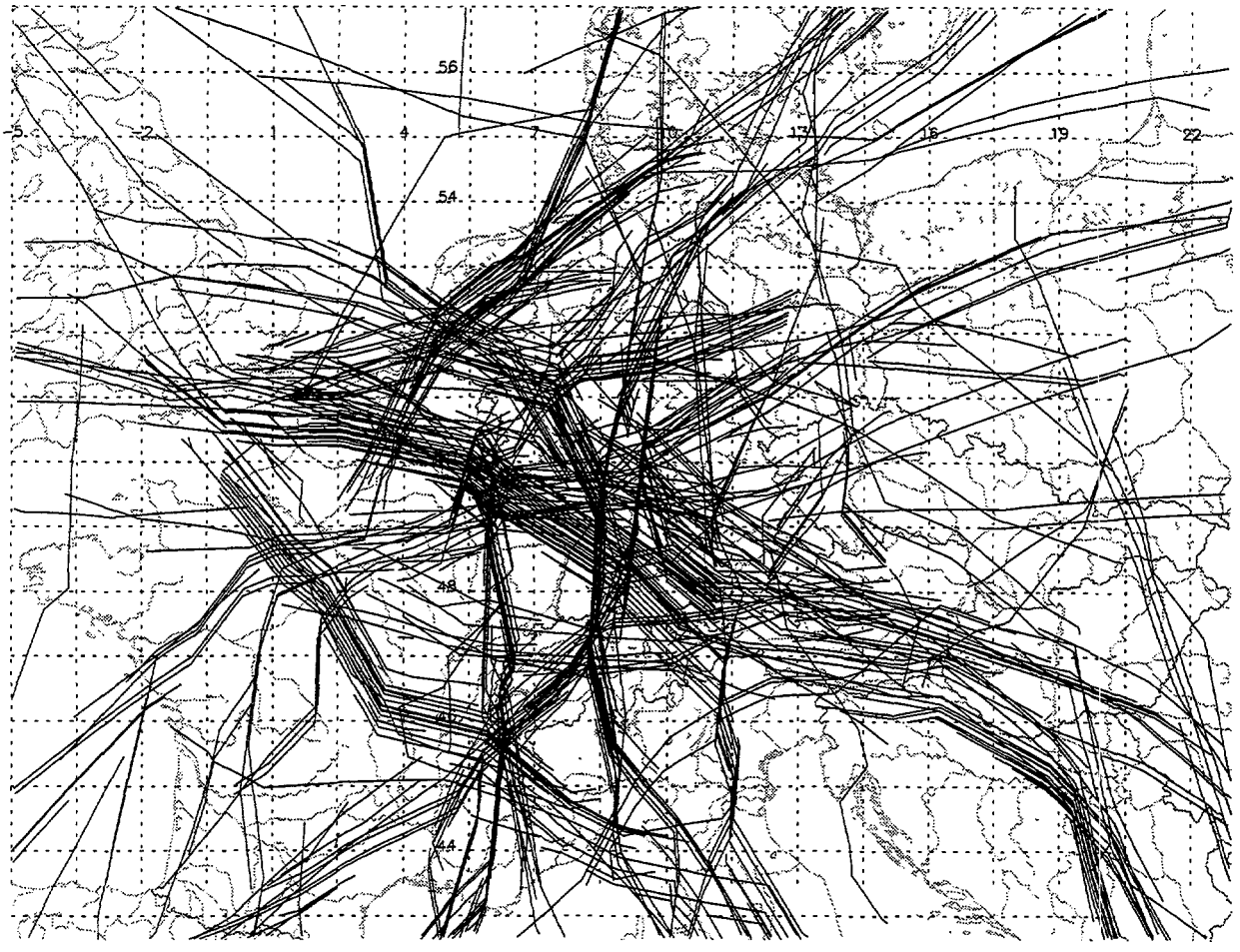

Fig. 12: Air traffic over Middle Europe May 4th 1995, 06:13 - 07:43 UTC, only flights above flight level 200 (20000 feet). A windspeed of 30 kn from NNE is assumed for the whole area.

are shifted to simulate a windspeed of 40 kn from NNE, which was measured on this day over northern Germany in the 300 hPa level To estimate the minimum extent of those regions we use the morphological image processing operators "erode" and "dilate" with a circular template of 25 pixels radius. The result is shown in grey in Fig 9: The regions where the algorithm found contrails are connected, while those regions without contrails within a distance of 25 pixels are left blank. The preliminary inspection of 60 AVHRR scenes from July and October 1990 over Central Europe showed that this regions cover about 10%, while the coverage with contrails is 0.9%. These numbers are preliminary, but longer time series are now being processed, which will lead to statistically significant data.

4. Conclusions

An algorithm was developed, which allows the automated detection of contrails from AVHRR LAC data. As the AVHRR is flown on the operational meteorological satellites of the NOAA series since 1979, and the LAC data are received and archived at numerous receiving stations around the world, this algorithm makes it possible to produce worldwide statistics on contrail coverage. In regions with dense air traffic it is also possible to estimate the regions of potential contrail.

Acknowledgements: Parts of this work were supported by the BMBF (German Federal Ministry for Education, Science, Research and Technology) within the DLR-BMBF project "Schadstoffe in der Luftfahrt". I wish to express my thanks to EUROCONTROL for the "flight profiles" and to Caroline Vogt for handling this data.

References

[1] S. Bakan, M. Betancor, V. Gayler, and H. Grassl. Contrail frequency over Europe from NOAA-satellite images. *Annales Geophysicae*, 12:962–968, 1994.

[2] Thomas F. Lee. Jet contrail identification using the AVHRR infrared split window. *Journal of Applied Meteorology*, 28:993–995, 1989.

[3] U. Schumann. On conditions for contrail formation from aircraft exhaust. *Meteorologische Zeitschrift, N.F.*, 5:4–23, 1996.

EXTRAPOLATION OF CONTRAIL INVESTIGATIONS BY LIDAR TO LARGER SCALE MEASUREMENTS. ANALYSIS AND CALIBRATION OF CCD CAMERA AND SATELLITE IMAGES

R. SUSSMANN, F. HOMBURG, V. FREUDENTHALER, AND H. JÄGER
Fraunhofer-Institut für Atmosphärische Umweltforschung, IFU
Kreuzeckbahnstrasse 19, D-82467 Garmisch-Partenkirchen, Germany
FAX: +49 8821 73573, e-mail: sussmann@ifu.fhg.de

ABSTRACT

The CCD image of a persistent contrail and the coincident LIDAR measurement are presented. To extrapolate the LIDAR derived optical thickness to the video field of view an anisotropy correction and calibration has to be performed. Observed bright halo components result from highly regular oriented hexagonal crystals with sizes of 200 µm - 2 mm. This is explained by measured ambient humidities below the formation threshold of natural cirrus. Optical thickness from LIDAR shows significant discrepancies to the result from coincident NOAA-14 data. Errors result from anisotropy correction and parameterized relations between AVHRR channels and optical properties.

1. INTRODUCTION

A major role in the radiation balance of the earth is attributed to natural cirrus clouds which on average cover about 20 % of the globe.[1] In the last years research activities have been strongly extended to investigate the role of anthropogenically induced cirrus (contrails) and the possible impact on climate[2,3] resulting from an additional surface coverage of at most 2 % on long term average.[4,5] The critical climate effect results from the highly non-linear dependence of solar backscattering and solar absorption from cloud coverage and optical thickness (OT).[6] For this, we address the following questions of particular interest: i) Is there, in *persistent* contrails, any significant difference in radiative impact compared to natural cirrus; *i.e.*, are there differences in optical properties, *e.g.*, particle shapes and orientations? Information on this topic can be derived from halo observations within persistent contrails.[7] ii) How can changing cloud coverage and OT accurately be determined within surface areas as large as possible? We report on possibilities to combine high accuracy techniques to derive OT (LIDAR) with surface covering techniques (CCD camera and satellite imaging).

2. COINCIDENT IMAGING BY LIDAR AND CCD CAMERA

The objective of the experimental analysis described in this section is to derive a 3D 40° field of view (FOV) image of clouds or contrails with a pixel grey scale representing the OT.

2.1 EXPERIMENT

The experiments are performed with the IFU fast scanning backscatter-depolarisation LIDAR optimized for contrail investigations[8] (Nd:Yag Laser 532 nm/550 mJ, 52 cm Cassegrain telescope, Chopper, 2 polarisation orientations, PMT's with range gate switch, 4 channels simultaneous analog sampling) in combination with a CCD camera (Sony, 756×581 pixel, video processor (AEG), framegrabber (Matrox)) mounted collinear to the laser axis.

In *Figure 1* the CCD image is displayed that had been taken on 23 April 1996 during the campaign "Contrail" from an aged contrail (age ~ 0.5 h) produced by the research aircraft FALCON. For the LIDAR cross section measurement the drift speed of the contrail has to be predetermined from LIDAR sounding (height) and video imaging (angular velocity). By these data the LIDAR-CCD-camera scanning mount is computer controlled to track the drifting contrail. The scanning direction can then be marked

via 3 mouse clicks (*Figure 1*). The cross section of *Figure 2* had been scanned *via* 30 scanning points (10 laser pulses each). To get a contrail cross section the LIDAR return signals are interpolated in between the separated laser directions (grey scale in *Figure 2*).

2.2 CORRECTION FOR BIDIRECTIONAL ANISOTROPY

As a first step towards a 3D image of the FOV area versus OT, we derive from the LIDAR return profiles the changing OT of the contrail along the different laser pointing directions (*Figure 3*). Using the pixel intensities of corresponding pointing directions we can then transform the whole CCD pixel intensity image (*Figure 1*) to an image, where the grey scale represents the OT. However, several nonlinearity and anisotropy effects have to be taken into account: i) aerosol and subvisible cirrus scattering contributing to the visible contrail brightness, ii) muliple scattering effects influencing the OT, iii) nonlinearities in the CCD camera pixel intensity response, and iv) bidirectional anisotropy of the scattering phase function. We found experimentally the points i) - iii) be negligible; *i.e.*, we found for a certain observation geometry the pixel intensitis of a CCD camera image being linear related to the OT. However, consideration of (iv) is of striking quantitative importance, as pointed out in the following.

Both for spherical particels and for randomly oriented nonspherical particles the scattering phase function is *unidirectional*. Typical for this are the ring type 22° and 46° halos. Away from these ring halos and away from the forward scattering peak, however, typical *unidirectional* scattering phase functions display flat and monotoneous behavior. Thus, within a large variety of observation geometries, the scattering probability does not change significantly within the CCD camera FOV. However, when ice crystals tend to orient, the scattering probability becomes a *bidirectional* property; *i.e.*, the scattering phase function additionally displays a strong dependence on the relative azimuth angle between the solar path and the observation direction. One example for this is displayed in *Figure 4*.

Thus the procedure for deriving a 3D image of OT within our 40° FOV is to first normalize the CCD-camera pixel array by dividing by a bidirectional scattering phase function typical for cirrus and/or contrail. The LIDAR derived values of OT are then plotted versus the normalized pixel values at corresponding pointing directions. From this the calibration relation results. A possible offset in the pixel value corresponding to zero OT points to the existence of a natural cirrus at another height level.

2.3 WHY DO CONTRAILS DISPLAY BRIGHT HALOS?

In this section we want to discuss what can be learned from halo observations within persistent contrails with respect to optical properties. From photographs (one displayed in *Figure 4*) we obtained proof, that the observed phenomena resulted from hexagonal plates oriented horizontally. This can be concluded from comparison to computer simulations of halo phenomena by ray-tracing techniques (geometrical optics).[9] Nearby radio soundings displayed ambient humidities well below 100 % with respect to ice (RH_i = 79 % and 65 %, respectively).

Plate shaped particles tend to fall oriented[10] for Reynolds numbers between 1 and 100.[11] For ice plates falling oriented in air, diameters between 200 μm and 2 mm have been found.[10] *Table 1* gives an overview on the previous halo observations in contrails found in the literature. We learn, that *most of the halo observations are due to oriented plates with diameters between 200 μm and 2 mm.*

Generally, the occurrence of halo phenomena results from the simplest crystals (hexagonal plates and columns) and the most regular crystal shapes. We *can* observe halos in contrails, and this probably even *more pronounced* than in natural cirrus: Already in one of the first contrails ever produced (11 May 1919 above Munich) a halo had been observed; furthermore we want to cite a statement by Weickmann on his early flight observations: "We remember several contrails where the most wonderful halo phenomena developed, we ever saw". Also the statements by Boerner and aufm Kampe point to the observation of unusual bright halo phenomena in contrails (see *Table 1* for references). This might be also confirmed by our observation of the 120° parhelion within a contrail (*Figure 4*), a component which has rather rarely been observed even in natural cirrus.

Persistent contrails obviously often consist of unusual regular crystals. This seems to be surprising, considering the state of the art knowledge of the initial growth phase of a contrail.[3] There is a rapid freecing,[12] particles form at least partly by condensation on soot particles. The early growth of these

sublimation nuclei in the young contrail can then be determined by high water supersaturation caused by the engines, which results in an irregular early crystal growth.

However, the late growth of contrails depends on the ambient humidity just as in case of natural cirrus. Assume a region with low relative humidities near 100 % (or even below) with respect to ice, as found in our two observations. In such a region natural cirrus will *not* be favored to form, since for formation of *natural* cirrus a minimum relative humidity *significantly above* 100 % with respect to ice has been found.[13-15] However, a contrail *can be forced to form* in this region,[16] and grow fast until all water vapour from the airplane in excess of the ambient relative humidity is deposited on the ice particles. It can then become persistent and grow extremely slow according to low relative humidity (around or *even below* ice saturation) of the entrained ambient air. We like to point out, that at the moment there is no evidence available that a contrail can not become persistent at ambient relative humidities below 100 % with respect to ice (surface effects). So a contrail may find more probably ideal conditions for a regular crystal growth.

3. COINCIDENT LIDAR AND SATELLITE IMAGING

In order to evaluate the change of the radiation budget of the earth caused by contrails, large scale imaging of their OT and surface coverage is required. Both can in principle be derived from multispectral data of the NOAA Advanced Very High Resolution Spectrometers (AVHRR).[17,18] The derivation of contrail OT from reflectance channels has, *e.g.*, been implemented in the program package APOLLO developed by DLR, with an OT error estimated to be in the range of ±50 %.

There have been only few validations of satellite derived OT of natural cirrus by conicident LIDAR measurements,[19,17] and only one validation in case of a contrail:[20] All are showing significant deviations in the range of the above mentioned error (±50 %). We are currently running measurements to get a variety of LIDAR data coincident to satellite overpasses. One of these LIDAR measurements has been discussed above (*Figures 1* and *2*); it had been taken coincident to a NOAA-14 overpass. We found a discrepancy to satellite OT significantly larger than ±50 %.

The major error sources in the satellite retrieval of OT are: i) Contributions to the contrail OT caused by natural cirrus layers at height levels close to the contrail level (*Figure 2*). ii) Optical properties like the OT can only be calculated from the *directional* hemispherical reflectance of the cloud. However, the observable quantity is the *bidirectional* reflectance. The anisotropy correction factors currently used are the cause of uncertainties since they are based on global averages.[17] iii) The parameterization of the relation between reflectance and OT is based on a simple model und thus a main error source.

In the investigation at hand the error is mainly caused by using the automatized retrieval algorithm of OT from the satellite data which was designed for cases where OT > 0.5.

4. SUMMARY AND CONCLUSIONS

Using a scanning backscatter-depolarisation LIDAR the OT along a contrail cross section was derived. From these data a CCD camera image taken coincident and collinear to the laser axis is calibrated to display a grey scale that represents the changing OT across the image. Our observation of extreme azimuthal anisotropies in the images (halo components) points to the need that the resulting OT image is corrected for bidirectional anisotropy.

Most of the halo observations within persistent contrails are due to hexagonal plates oriented horizontally with diameters 200 µm - 2 mm. Nearby radio soundings display ambient relative humidities well below 100 % with respect to ice. We assume the possibility of contrail persistence at an ambient humidity even below 100 % with respect to ice. This is in line with the repeated observations of unusual bright halo phenomena within persistent contrails, which points to a very slow thus regular crystal growth. In a more general context, the observed azimuthal anisotropies point to the need of a 3D radiative transfer model.

LIDAR validation of contrail OT derived from satellite measured reflectance shows discrepancies above the ±50 % error range. The main errors in the satellite data analysis are due to the anisotropy correction of top of cloud reflectance and to the parameterization which relates cloud reflectance to OT.

Our future work will focus on the open questions outlined in this paper: i) For improved anisotropy corrections (both for CCD images and AVHRR reflectance) the knowledge of bidirectional scattering phase functions typical for cirrus/contrails is required. Up to now, there had been only theoretical studies

of bidirectional phase functions for distinct crystal types, sizes, and orientations (ray-tracing calculations). However, typical phase functions observed in reality are composed from various contributions that can only be derived from experimental studies planned at the moment. ii) Onother subject of our ongoing work is to derive experimentally parameterizations of the relations between AVHRR reflectance data and the LIDAR-derived OT, especially for small values (OT < 0.5) typical for contrails. For this we will analyze a larger set of LIDAR measurements and satellite data from coincident overpasses. The OT calibrated CCD images can serve as an intermediate step, as they provide LIDAR-derived mean values of the OT over areas comparable to the size of one NOAA-AVHRR pixel (1×1 km).

ACKNOWLEDGMENT

The authors like to thank P. Wendling and R. Busen (DLR) for valuable discussions. This research has been supported by the German Bundesministerium für Bildung, Wissenschaft, Forschung und Technologie within the joint project "Schadstoffe in der Luftfahrt (Pollutants from Air Traffic)" and by the Comission of the European Union within "AEROCONTRAIL" of the Environment and Climate Programme.

1. K.N. Liou, "Influence of cirrus clouds on weather and climate processes: A global perspective," Mon. Wea. Rev. **114,** 1167-1199 (1986).
2. K.N. Liou, S.C. Ou, and G. Koenig, "An investigation on the climatic effect of contrail cirrus," in Air-Traffic and the Environment, U. Schumann, ed., Vol. 60 of Lecture Notes in Engineering (Springer, Berlin, 1990), pp. 154-169.
3. U. Schumann, "On the effect of emissions from aircraft engines on the state of the atmosphere," Ann. Geophys. **12,** 365-384 (1994).
4. S. Bakan, M. Betancor, V. Gayler, and H. Grassl, "Contrail frequency over Europe from NOAA-satellite images," Ann. Geophys. **12,** 962-968 (1994).
5. U. Schumann and P. Wendling, "Determination of contrails from satellite data and observational results," in Air-Traffic and Environment, U. Schumann, ed., Vol. 60 of Lecture Notes in Engineering (Springer, Berlin, 1990), pp. 138-153.
6. M. Ponater, S. Brinkop, R. Sausen, and U. Schumann, "Simulating the global atmospheric response to aircraft water vapour emissions and contrails - A first approach using a GCM," Ann. Geophys., subm.
7. R. Sussmann, "Optical properties of contrail induced cirrus. Discussion of an unusual halo phenomenon," Appl. Opt., subm.
8. V. Freudenthaler, F. Homburg, and H. Jäger, "Ground-based mobile scanning LIDAR for remote sensing of contrails," Ann. Geophys. **12,** 956-961 (1994).
9. See, *e.g.*: K.-D. Rockwitz, "Scattering properties of horizontally oriented ice crystal columns in cirrus clouds, Part I," Appl. Opt. **28,** 4103-4111 (1989), and references therein.
10. A. Ono, "The Shape and Riming Properties of Ice Crystals in Natural Clouds," J. Atmos. Sci. **26,** 138-147 (1969).
11. K. Sassen, "Remote sensing of planar ice crystal fall attitudes," J. Meteorol. Soc. Jpn. **58,** 422-429 (1980).
12. B. Kärcher, Th. Peter, and R. Ottmann, "Contrail formation: Homogeneous nucleation of H_2SO_4/H_2O droplets," Geophys. Res. Lett. **22,** 1501-1504 (1995).
13. K. Sassen and G.C. Dodd, "Haze particle nucleation simulations in cirrus clouds, and applications for numerical modeling and lidar studies," J. Atmos. Sci. **46,** 3005-3014 (1989).
14. H. Grassl, "Possible climatic effects of contrails and additional water vapor," in Air Traffic and the Environment-Background, Tendencies and Potential Global Atmospheric Effects, U. Schumann, ed. (Springer, Berlin Heidelberg New York, 1991), pp. 124-137.
15. A.J. Heymsfield and L.M. Miloshevich, "Relative humidity and temperature influences on cirrus cloud formation: Observations from wave clouds and FIRE II," J. Atmos. Sci. **52,** 4302-4326 (1995).
16. H. Appleman, "The formation of exhaust condensation trails by jet aircraft," Bull. Amer. Meteorol. Soc. **34,** 14-20 (1953).
17. K.T. Kriebel, R.W. Sounders, and G. Gesell, "Optical Properties of Clouds Derived from Fully Cloudy AVHRR Pixels," Beitr. Phys. Atmosph. **62,** 165-171 (1989).
18. M. Betancor Gothe and H. Grassl, "Satellite Remote Sensing of the Optical Depth and Mean Crystal Size of Thin Cirrus and Contrails," Theor. Appl. Climatol. **48,** 101-113 (1993).
19. C.M.R. Platt, D.W. Reynolds, and N.L. Abshire, "Satellite and Lidar Observations of the Albedo, Emittance and Optical Depth of Cirrus Compared to Model Calculations," Mon. Wea. Rev. **108,** 195-204 (1980).
20. M. Kästner, K.T. Kriebel, R. Meerkötter, W. Renger, G.H. Ruppersberg, and P. Wendling, "Comparison of Cirrus Height and Optical Depth Derived from Satellite and Aircraft Measurements," Mon. Wea. Rev. **121,** 2708-2717 (1993).
21. L. Weickmann, "Wolkenbildung durch ein Flugzeug," Naturwissenschaften **7,** 625 (1919).
22. A. Schmauss, "Bildung einer Cirruswolke durch einen Flieger," Randbemerkungen IV. - Meteorol. Z. **36,** 262-265 (1919).
23. J. Küttner, "Beobachtungen an Kondensfahnen," Z. Meteorol. **1,** 183-185 (1946).
24. D.S. Hancock, "A mock sun in vapour-trail cloud," Quart. J. Roy. Meteorol. Soc. **69,** 46 (1943).
25. H. Boerner, "Haloerscheinungen an Kondensfahnen," Z. angew. Meteorol. **60,** 397 (1943).
26. H.J. aufm Kampe, "Die Physik der Auspuffwolken hinter Flugzeugen," Luftwissen **10,** 171-173 (1943).
27. H. Weickmann, "Die Eisphase in der Atmosphäre," Berichte des Deutschen Wetterdienstes in der US-Zone **6,** 3-54 (1949).
28. K. Sassen, "Iridescence in an aircraft contrail," J. Opt. Soc. Am. **69,** 1080-1083 and 1194 (1979).

Table 1. Halo observations in contrails

Author, date	Report (*verbally, manual drawing, photograph*)	Halo component	Crystal type and orientation
L. Weickmann,[21] Schmauss,[22] May 1919	*verbally*: "part of sun ring"; "northern and southern part of ring at distance of 22°"[a]	not unique:[a] *22° halo* (or possibly: *22° parhelia*)	*no distinct type*[d] (or possibly: *oriented plates*)
Küttner,[23] April 1942	*verbally*: "horizontal circle, in any case circumzenithal circle, whose extrapolation does approximately pass the sun"[c] *manual drawing*: northern 30% part of a ring whose extrapolation passes the sun[c]	not unique:[c] *parhelic circle*	*oriented plates* and/or *singly oriented columns*
Hancock,[24] Dec 1942	*verbally*: "mock sun of faint red color"[b]	not unique:[b] *22° parhelion* (or possibly: *22° halo*)	*oriented plates* (or possibly: *no distinct type*[d])
Boerner,[25] 1943	*verbally*: "side suns (of small ring) and circumzenithal arc (upper tangent arc of large ring) very bright colored, weak parts of 22° ring"	*22° parhelia, circumzenithal arc, weak 22° halo*	*oriented plates* and further crystals with *no distinct type*[d]
aufm Kampe,[26] 1943	*photograph:* no additional information *verbally:* "most beautiful and manifold halos"	not unique: *circumzenithal arc* or *upper tangent arc*?	*oriented plates* (or possibly: *singly oriented columns*)
H. Weickmann,[27] 1949	*verbally (flight report)*: "we remember several contrails where the most wonderful halo phenomena developed we ever saw"	no statement	-
Sassen,[28] Oct 1974	*photograph*	*upper 22° tangent arc, weak 22° halo,*	*singly oriented columns* and *oriented plates* and further
This work, Jan 1996	*verbally*: "parhelia of 22° halo" *photograph* with *angle measurement*	*22° parhelia, 120° parhelion*	crystals with *no distinct type*[d] *oriented plates*
This work, June 1996	*photograph*	*22° parhelion*	*oriented plates*

[a]The second statement could be taken as an indication for the occurrence of *22° parhelia* rather than parts of the *22° halo*.
[b]The *22° parhelia* (mock suns) usually contain all colors, whereas the *22° halo* is just red inside the ring.
[c]The manual drawing points to a *parhelic circle*, which forms in the north opposite to the sun. Contrary to the verbal note, we exclude *circumzenithal arc* and *circumhorizontal arc*, which would be centered around the sun azimuth angle (we calculate azi_{sun} = 215° from the observation time 14:00 MEZ 3 April 1942, Augsburg, Germany) and extend at most a third around the horizon; furthermore the latter are restricted to elevation angles above 58° and below 32°, respectively. This does not fit the sun elevation of 47.6° we calculate from the observation time.
[d]Nearly all randomly oriented crystals show the *22° halo*; however, circular halos do not necessarily require random orientation.

FIGURES

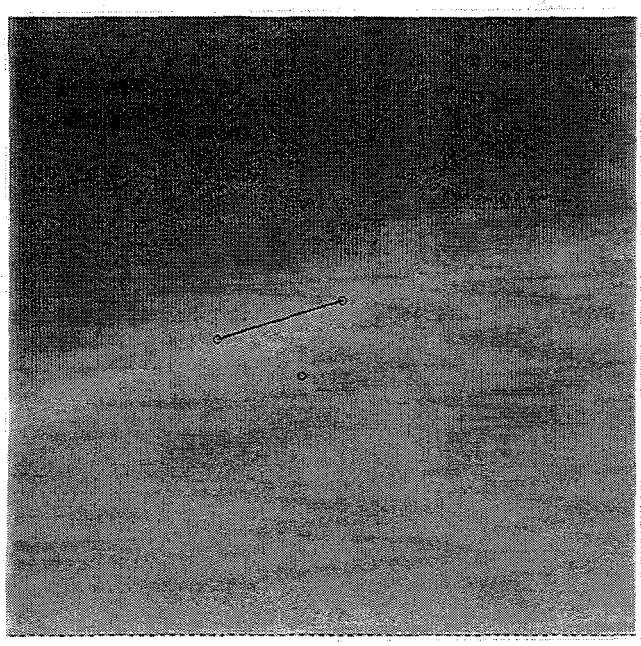

Figure 1. CCD image of a persistent contrail produced by the research aircraft FALCON on 23 April 1996. The LIDAR scanned contrail cross section is perpendicular to the line. The start of the LIDAR scanning cross section is marked (o). Imaginghad been performed coincident to a NOAA-14 overpass.

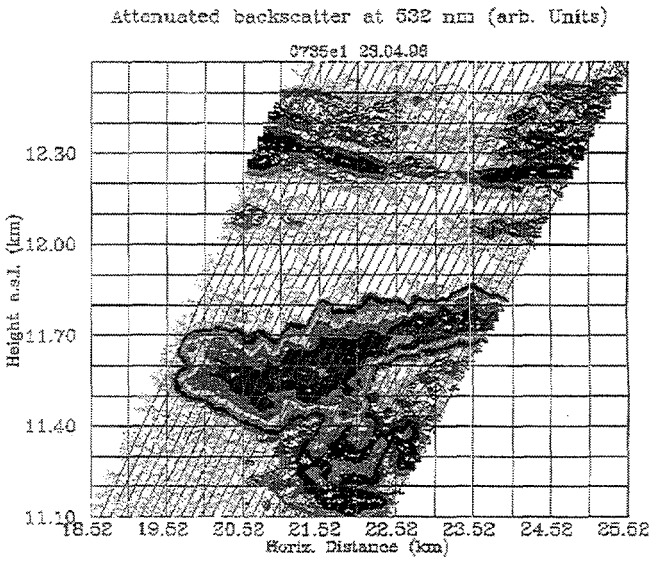

Figure 2. LIDAR attenuated backscatter signal from 30 different laser pointing directions (lines) along the contrail cross section (Figure 1). Note also a thin natural cirrus around 12.3 km height.

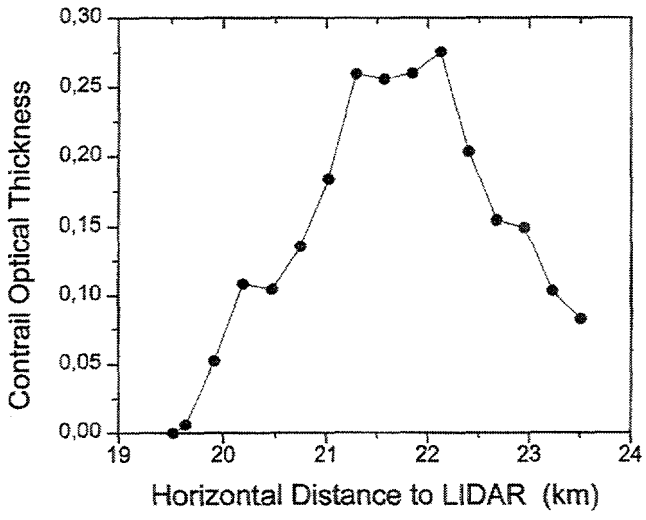

Figure 3. Contrail optical thickness derived from the LIDAR backscatter signal along the pointing directions marked in Figure 2. An extinction-to-backscatter ratio of 20 was used.

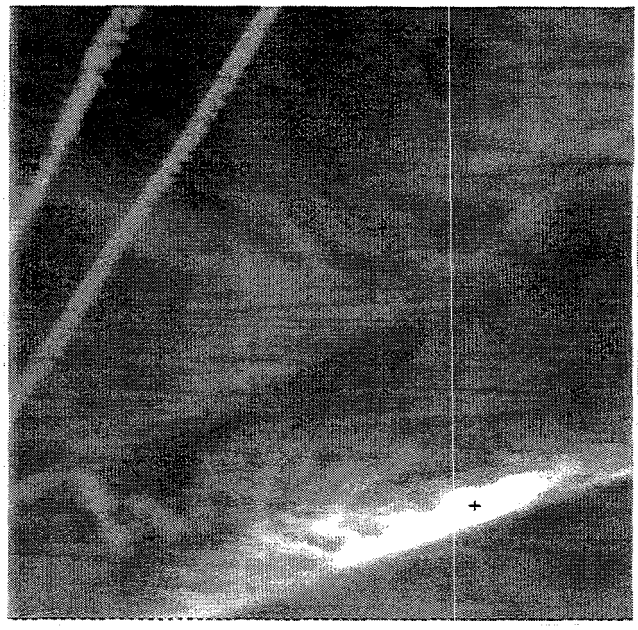

Figure 4. CCD camera image of a 120° parhelion (+) in a persistent contrail observed from Garmisch-Partenkirchen (47.7° N, 11.1° E, 730 m a.s.l.) at a zenith angle of 71.1° and a +315.0° azimuth at 12:25 UTC 18 Jan 1996. From radio soundings a relative humidity with respect to ice of RH_i = 79 % is calculated.

Remote Sensing of Contrails and Aircraft Altered Cirrus Clouds

R. Palikonda[1], P. Minnis[2], L. Nguyen[1], D. P. Garber[1], W. L. Smith, Jr.[1], D. F. Young[2]

[1]Analytical Services and Materials, Inc.
Hampton, Virginia, USA

[2]Atmospheric Sciences Division
NASA Langley Research Center
Hampton, Virginia, USA

Analyses of satellite imagery are used to show that contrails can develop into fully extended cirrus cloud systems. Contrails can advect great distances, but would appear to observers as natural cirrus clouds. The conversion of simple contrails into cirrus may help explain the apparent increase of cloudiness over populated areas since the beginning of commercial jet air travel. Statistics describing the typical growth, advection, and lifetime of contrail cirrus is needed to evaluate their effects on climate.

1. INTRODUCTION

Contrails may have a significant impact on the regional energy budget by blocking outgoing longwave radiation and reflecting incoming solar radiation. Such effects may also alter weather and climate patterns. The overall impact depends on many factors including the contrail areal coverage, lifetime, time of formation, microphysical properties, altitude, and background. A variety of studies have suggested that cloud cover has risen due to contrails caused by increasing air traffic leading to reduced surface sunshine [1] or to surface warming [2]. Although several papers have been devoted to assessing the frequency of contrail occurrence, knowledge of the areal extent of contrail clouds is minimal. An examination of contrails by Bakan et al. [3] showed a maximum coverage of only 2% over a relatively small part of Europe and the northeast Atlantic. That study and others generally assume that contrail clouds are only those that are the familiar, narrow linear streaks in the sky or in a satellite image. As contrails are usually observed only in the air traffic routes and the routes only cover a small portion of the globe, it is difficult to reconcile the small fraction of cloudiness attributable to contrails and the larger increases in thin cloudiness if only the fresh, linear contrails are considered.

Bakan et al. [3] noted that many of the contrails they observed in a given NOAA Sun-synchronous satellite Advanced Very High Resolution Radiometer (AVHRR) image could be seen in other images 6 to 48 hours later. From the surface, it is possible to observe the transformation of contrails into cirrus clouds having little resemblance to their original linear shape. Given these observations, it is highly probable that some long-lived contrails cannot be recognized as such and will increase the amount of cloudiness caused by jet aircraft exhaust. This paper examines the problem of determining if and how much additional cloud cover can be attributed to contrails. AVHRR and Geostationary Operational Environmental Satellite (GOES) data are used to track contrails for a few select cases and evaluate their areal and optical properties as they develop.

2. DATA AND ANALYSIS

NOAA-12 1-km AVHRR data and GOES-8 at 75°W and GOES-9 at 135°W taken at 15-minute intervals provide a variety of views for studying contrail development. The AVHRR data used here comprise the visible (VIS; 0.65 μm), solar-infrared (SI; 3.75 μm), infrared (IR; 10.8 μm), and

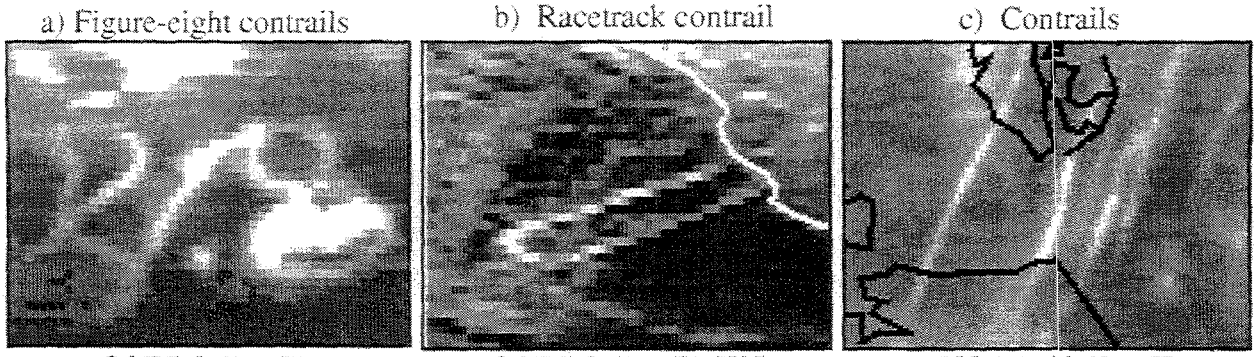

Fig. 1. Satellite thermal imagery (a) 1945 UTC, 11 April 1996 over the Gulf of Mexico. (b) 2330 UTC, 12 May 1996 off the coast of California. (c) 1214 UTC, 26 September 1996 over eastern Virgina.

split window (WS; 12.0 μm). The 4-km GOES imager has similar channels except that the SI central wavelength is 3.9 μm. The GOES VIS data can also be obtained at 1-km resolution. Temperature and humidity soundings from the nearest National Weather Service station were used to relate temperature to altitude.

During the NASA Subsonic Contrails and Clouds Effects Special Study (SUCCESS) conducted over the U.S. during Spring, 1996, two extraordinary contrail systems were observed off the coast. One was a series of figure eights from an unknown source over the Gulf of Mexico during 11 April (Fig. 1a). The eights were originally 30 km wide and extended ~70 km from north to south The other system was a 100-km long oval or race track produced over the Pacific Ocean by the NASA DC-8 as it sampled contrails produced by commercial airliners and its own exhaust (Fig. 1b). These two sets of contrails are ideal for tracking because they are extensive and easily distinguishable from natural clouds. The third case involves linear contrails produced by commercial aircraft over the east coast of the U.S. 26 September 1996 seen over mouth of the Chesapeake Bay in the AVHRR imagery in Fig. 1c.

The data were analyzed with the multispectral techniques of Minnis et al. [4] to derive the phase, effective ice particle diameter D_e, optical depth τ, temperature T_{cld}, and altitude z of the high-altitude clouds within a box defined to include only the clouds arising from the subject contrail systems. The box was also selected to include the portions of the background to compute the clear-sky VIS clear-sky reflectance and IR, SI, and WS clear-sky temperatures T_{CS}. During daytime, the VIS-IR-SI technique (VIST) was used to determine the values for each parameter, while the SI-IR-WS (SIRS method) was applied at all hours [4]. The cloudy pixels were identified over ocean as those having temperatures $T < T_{CS}$(IR) -1.5K. Over land, the temperature threshold depression varies up to 6K depending on the variability of the backround temperature. The parameters were computed only for the pixels corresponding to the contrail cloudiness. Screening other cloudy pixels can be subjective and difficult, however, some objective criteria were applied to eliminate non-contrail clouds. Clouds having $T_{cld} > 273$K were assumed to be low clouds and clouds with $\tau > 1$ were assumed to be pre-existing cirrus. Cloudy pixels with indeterminate particle size results were assumed to belong to the contrail because those results usually occur for optically thin clouds or those along the edge of a larger cloud. The areal contrail coverage is the number of contrail pixels multiplied by the mean area of a pixel at the given viewing angle. Actual area was computed for the entire cloud ensemble for the racetrack and figure-eight contrails because they remained relatively distinct entities. Fractional area was computed for the linear contrails using a constant box size of 20 x 30 pixels or ~ 13,600 km^2.

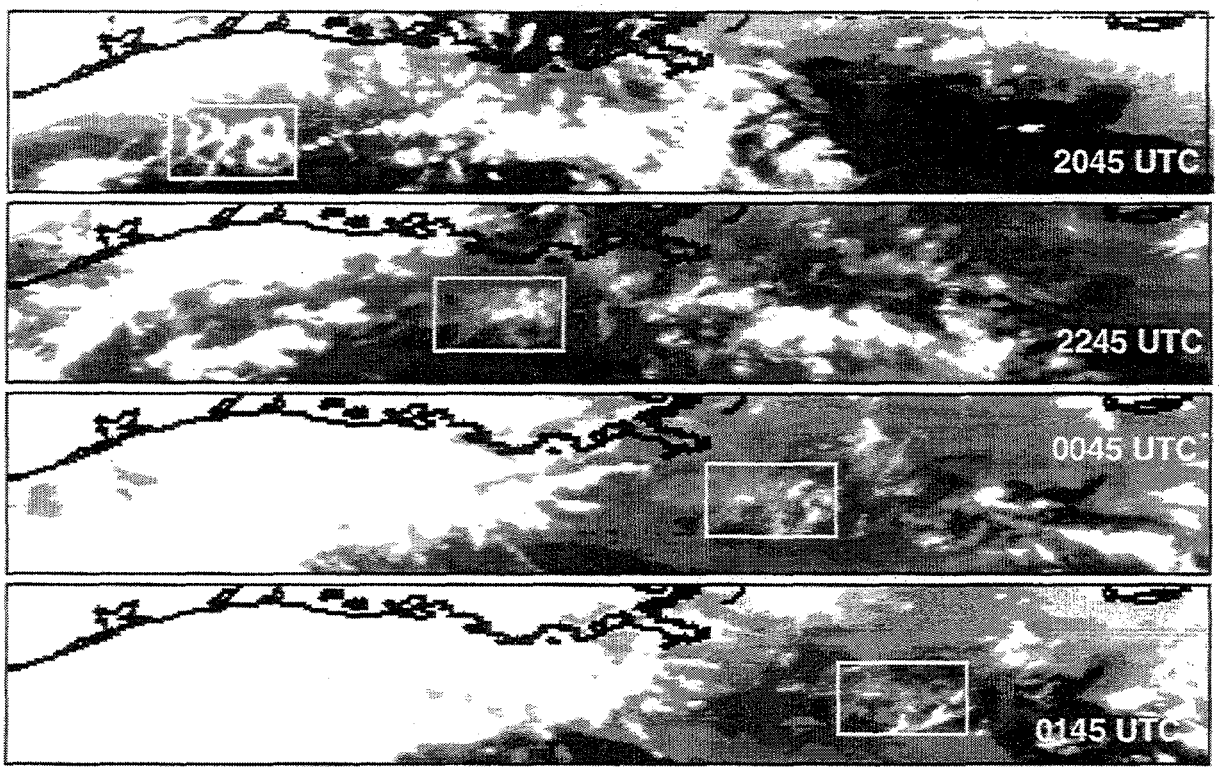

Fig. 2. GOES-8 infrared imagery showing transformation and dissipation of the figure-eight contrails from 2045 UTC, 11 April 1996 to 0145 UTC, 12 April 1996 over the Gulf of Mexico.

3. RESULTS

The transformation and dissipation of the figure-eight contrails can be seen in the GOES IR imagery in Fig. 2. At 2045 UTC, the arms of the eights were 2-4 pixels or ~12 km wide. The eights gradually diffused, filled, and became indistinguishable from other cirrus by 2245 UTC. They advected a total of ~750 km before disminishing to a small area south of the western tip of Florida by 0145 UTC, 12 April. During most of that time, the contrail clouds were too thick or dispersed to be recognizable as contrails from either the satellite or surface perspective. Figure 3 shows the analysis results using the two techniques applied to the GOES data within the analysis boxes. The initial VIST results yield a relatively small average particle size that increases as the contrails advect. At 1915 UTC, shortly after the contrail formed, the VIST-derived cloud temperature is estimated at 247 K. According to a 1200 UTC, 11 April sounding taken at Lake Charles, Louisiana, that temperature corresponds to an altitude of 7.8 km. The sounding also showed that the troposphere above 7 km is extremely moist indicating that an altitude of 7.8 km is reasonable for this contrail. The VIST cloud temperature increased slightly after 3 hours suggesting that the contrail decreased in altitude as it spread. Optical depth remained relatively constant. The SIRS analysis yields a different picture of the cloud parameters with T_{cld} decreasing until 2115 UTC before increasing again. Although the initial values are nearly the same, the optical depths are smaller and D_e is larger, on average, than the VIST results. The SIRS analysis is less reliable during the day than at night so the retrievals after 0000 UTC are more accurate. When lower clouds are absent, the VIST results are more accurate than the SIRS data. Thus, the parameter variations given by the VIST are a better representation prior to 2300 UTC. The results for τ and D_e after 2300 UTC are probably accurate to $\pm$ 50%. The areal coverage increases steadily until it reaches ~24,000 km^2 at 0000 UTC. The mean contrail cloud optical depths decreased after 0000 UTC as the cloud dissipated.

The 12 May, DC-8 contrail forms over a background of low stratocumulus and advects over a clear portion of the ocean along the coast before passing over the land at 0045 UTC, 13 May (Fig. 4).

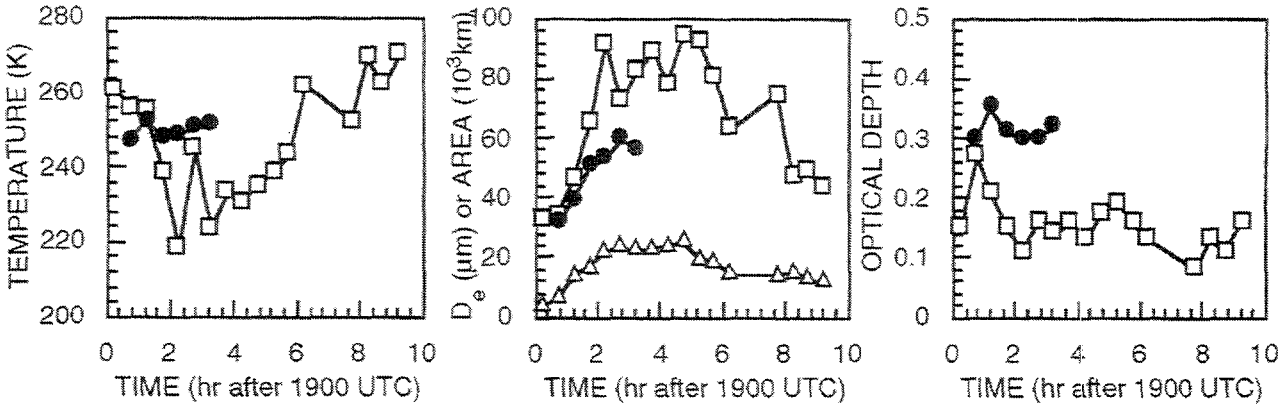

Fig. 3. Cloud parameters from figure-eight contrails over Gulf of Mexico for 11-12 April 1996. Closed symbols from VIST analysis. Open symbols from SIRS. Triangles refer to area.

It also fills and spreads as it moves with the wind. At 0300 UTC, over the foothills of the Sierra Nevada, the oval structure is gone, replaced by a somewhat amorphous shape. When the system reaches the mountains (0445 UTC), the cloud seems to thicken before dissipating over Nevada at 0545 UTC. The analysis results in Fig. 5 show the cloud starting near 230 K and apparently dropping in altitude to warmer temperatures. The particle initially is ~30 μm in diameter and increases

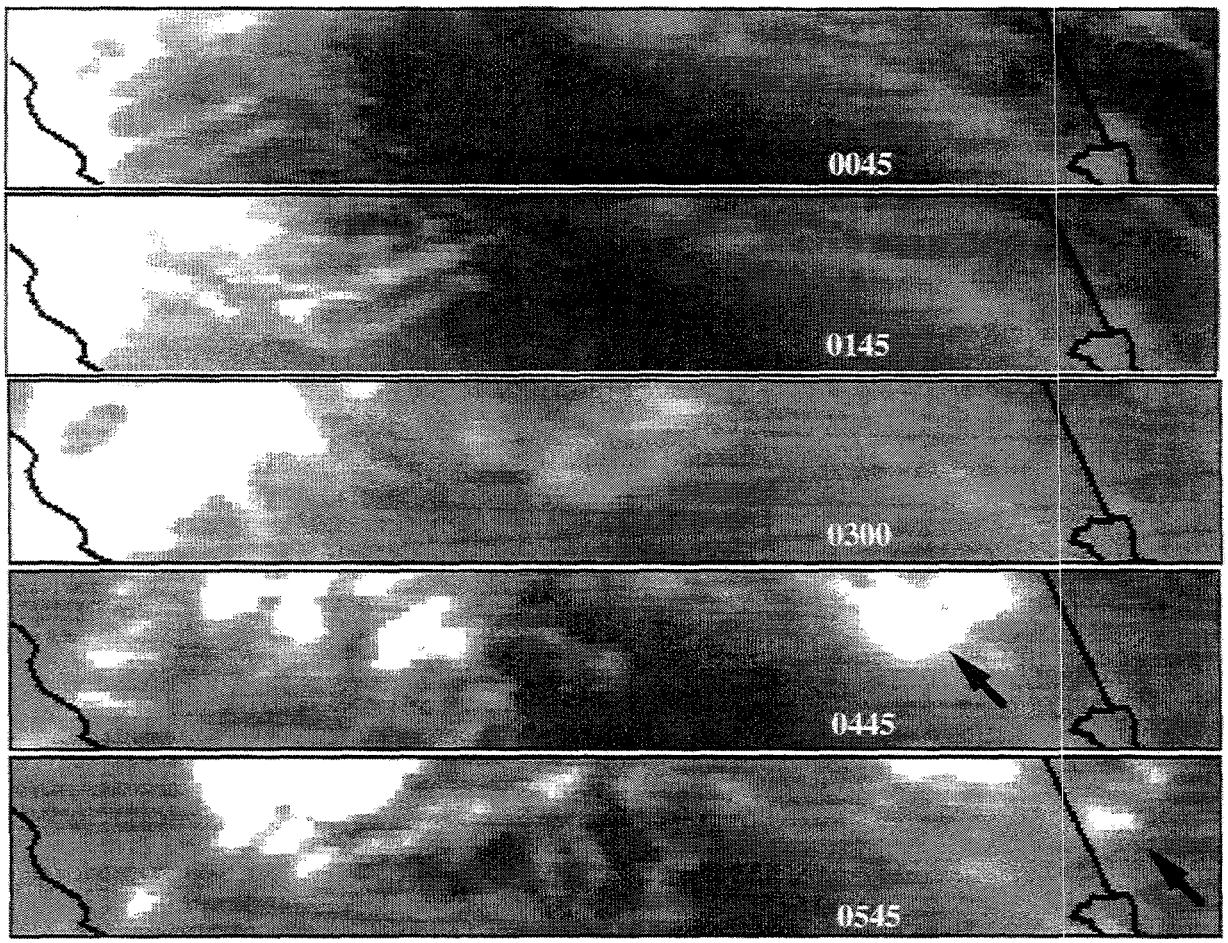

Fig. 4. GOES-9 IR imagery showing transformation and dissipation of the DC-8 racetrack contrail from 0045-0545 UTC, 13 May 1996 over northern California to the Nevada border.

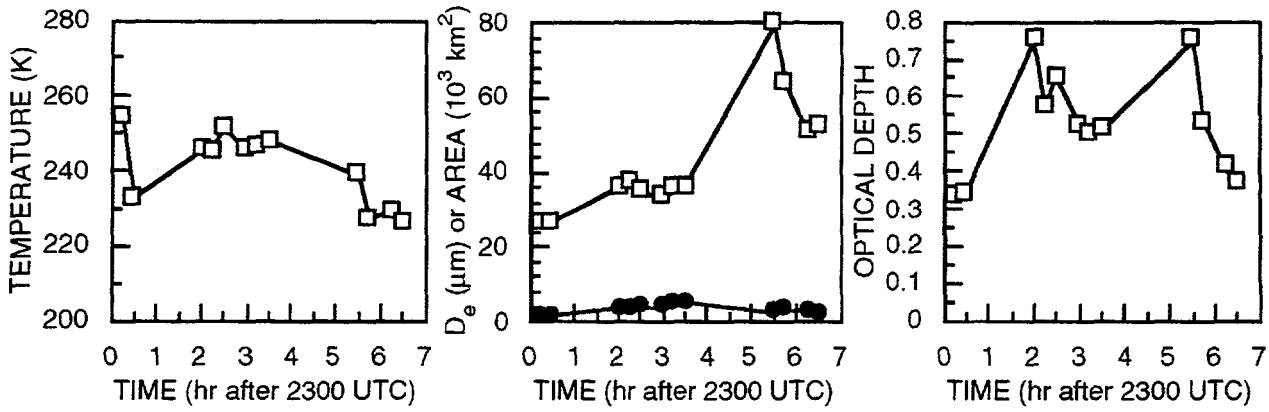

Fig. 5 Cloud parameters computed for racetrack contrail from GOES-9 data 12-13 May 1996. Solid symbols refer to contrail area. Temperature refers to contrail temperature.

to ~ 40 μm for several hours and to larger values over the mountains. The optical depths, which average ~ 0.5, far exceed those seen for the figure-eight contrails. Areal coverage by this contrail-cirrus system reaches a peak of ~ 5000 km^2 at 0230 UTC. The missing hours in Fig. 5 were not analyzed because of the variability in the background temperatures. The DC-8 flew at an altitude near 10 km which corresponds to ~ 229K on the nearest sounding. Thus, it appears that T_{cld} for the contrail was overestimated by more than 10K for much of the cloud's lifetime. The magnitude of this potential error is not surprising given the changing background: low clouds, clear ocean, mountains, and valley. This variability precluded the use of the VIST for all of the contrail.

The linear contrails in Fig. 1c advected over the Atlantic Ocean and were tracked with a constant-area box using GOES-8 data. Figure 6 shows the cloud parameters derived from GOES-8 for the constant-area box. The cloud temperature remained relatively steady near 245K for the first few hours, then decreased as the cloud optical depth diminished. These temperature changes correspond to height increases from 8 to 10 km. Unlike the previous two cases, the mean particle sizes are more typical of natural cirrus, although they appear to be more like contrails during the most rapid growth of the cloud around 1430 UTC. The contrails in Fig. 1c were observed from the surface around 1230 UTC and occurred with scattered, thin natural-looking cirrus. Therefore, some of the larger particles may be due to pre-existing cirrus. The optical depths are significant, averaging around 0.3 for the study period. The contrails appear to have developed from ~30% coverage in the box at 1245 UTC to 80% 6 hours later. Examination of the surrounding areas in the GOES-8 imagery yielded little cirrus coverage. These same parts of the air mass lacked the original contrails seen at 1230 UTC in the AVHRR imagery suggesting that the contrails were responsible for much of the observed cloudiness in the box which was generally clear before 1200 UTC.

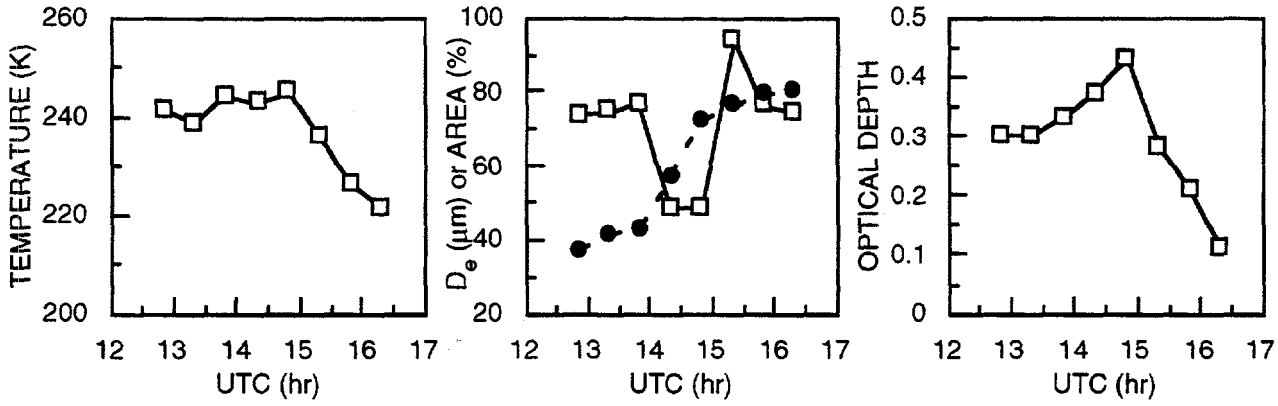

Fig. 6. Cloud parameters computed from GOES-8 data with VIST for a moving 20x30 pixel box containing contrails during 26 September, 1996. Temperature refers to cloud temperature.

4. DISCUSSION

Accurate determination of the cirrus microphysical properties is difficult for clouds with such small optical depths. The sensitivity of the retrievals to variations in background reflectance and temperatures is greatest when the clouds are thin ($\tau < 0.5$). However, the effective particle sizes in Figs. 3 and 5 change as expected for contrails: initially very small particles because of the abundance of nuclei followed by crystal growth as the cloud diffuses into cleaner air. The different behavior seen in Fig. 6 may be due to errors in the analyses for the lower sun angles before 1400 UTC. A closer examination of the data is required to determine if the retrievals are accurate. Similarly, the apparent underestimation of the racetrack cloud height will require further investigation. Because the DC-8 took microphysical measurements during the initial formation of that contrail, it will be possible to estimate the retrieval errors for the first few data points.

The cloud growth rates seen in Figs. 3, 5, and 6 are remarkable. Peak coverage occurs approximately 3 hours after the contrail is detectable from the satellite. The contrail clouds dissipate slowly both in horizontal and vertical extent. The ends of the contrail lifetimes were not totally observed in these results. Significant areal coverage remained in all three cases after 5 to 9 hours. Additional tracking could reveal re-growth or continued dissipation. Assumptions about contrails remaining in the air routes are not supported by these results. Contrail cloudiness can advect considerable distances from their source, substantially increasing the area affected by manmade clouds.

5. CONCLUDING REMARKS

It is clear from these results that contrail areal coverage is much greater than that derived from analyses relying on narrow linear features like those in Fig. 1c. Such analyses provide a minimum estimate of contrail cloud cover. The results found here are not necessarily typical of all contrails. Given the difficulty in analyzing these relatively distinct cases, it may be concluded that objective tracking or automated retrieval of advecting contrail properties will require substantial additional research. Until more automated procedures become available, it will be possible to acquire a more representative statistical base of contrail characteristics by performing analyses similar to the present one using a much larger satellite dataset. Such statistics are crucial elements for understanding the impact of contrails on climate. This study is just an initial glimpse of the potential changes in cloudiness induced by modern air travel.

6. REFERENCES

[1] Angell, J. K., 1990: Variation in United States Cloudiness and Sunshine Duration between 1950 and the drought year 1988. *J. Climate*, **3**, 296-308.

[2] Liou, K. N., S. C. Ou, and C. Koening, 1990: An Investigation on the climatic effect of contrail cirrus. *Lecture Notes in Engrg.*, **60**, Springer, Berlin, 138-153.

[3] Bakan, S.; Betancour, M.; Gayler, V.; and Grassl, H. 1994: Contrail Frequency Over Europe From NOAA-Satellite Images. *Annal. Geophys.*, **12**, 962-968.

[4] Minnis, P., D. P. Kratz, J. A. Coakley, Jr., M. D. King, R. Arduini, D. P. Garber, P. W. Heck, S. Mayor, W. L. Smith, Jr., and D. F. Young, 1995: Cloud optical property retrieval (Subsystem 4.3). "Clouds and the Earth's Radiant Energy System (CERES) Algorithm Theoretical Basis Document, Volume III: Cloud Analyses and Radiance Inversions (Subsystem 4)", *NASA Reference Paper RP-1376 Vol. 3*, 135-176.

In-situ observations of interstitial aerosol particles and cloud residues found in contrails

Johan Ström

Department of Meteorology, Stockholm University
S-106 91 Stockholm, Sweden

1. Introduction

In spring 1994 a series of flights were conducted in cirrus clouds and contrails over southern Germany. One of the aims of this campaign was to study the phase partitioning of aerosols and water in these clouds. To acheave this seperation of particles two coplementary sampling probes were mounted on the research aircraft Falcon. These are the Counterflow Virtual Impactor (CVI) or supermicrometer inlet, and the interstitial inlet or submicrometer inlet. The submicrometer inlet, is a 1/4" stainless steel tube which is tapered to give an effective opening cross section of 3.8 mm^2. The opening of the inlet is turned opposite to the flight direction which results in cloud particles not being sampled due to their inertia carrying them past the inlet. Thus, only the interstitial aerosol (unactivated particles in between the cloud elements) will be sampled. The upper cut-off for this inlet is estimated to be just under 1 μm aerodynamic diameter [1]. The CVI is a device that inertially separates cloud elements larger than a certain aerodynamic size from the surrounding atmosphere into a warm, dry and particle free air [2]. Water vapor and residue particles left behind by the evaporated cloud elements, are subsequently sensed and sampled by instruments downstream of the CVI. The calculated 50% sampling efficiency for the probe used in this experiment is 4.5 μm diameter.

Inside the aircraft the sample air from the two inlets is distributed to different sensors. The concentration of ambient aerosol and residual particles larger than 0.018 μm diameter was measured by two TSI-3760 condensation particle counters (TSI Inc., St. Paul MN, USA) modified for aircraft use [1]. Residual particles are non-volatile material remaining after evaporating the condensed water from the cloud particles. Assuming that each cloud element leaves behind only one residue particle, these measurements yield an equivalent number concentration for cloud particles having an aerodynamic diameter larger than the lower cut size of the CVI. The size distribution of the sampled aerosol and residual particles between 0.1 to 3.5 μm diameter was measured by a PMS PCASP (Passive Cavity Aerosol Spectrometer) working alternatively on both inlets. A dual-beam Lyman-α hygrometer [3] was used to measure the evaporated water from the sampled cloud element, which corresponds to the condensed water content (CWC) in cloud particles larger than the lower cut size of the CVI. The gasphase water vapor content was measured by a cryogenic frost point mirror [4].

2. Measurements

The results presented below are all from 21 March 1994. This was a day on which many persistent contrails were formed over southern Germany. In the measuring area the lower levels were covered by an almost compact stratocumulus cloud. At high altitude, the wind was northerly and the sky was almost clear except for occasional patches and streaks of visible cirrus clouds. To the north the cirrus clouds became more homogeneous, and to the south, over the Alps, the sky was completely free of clouds. The contrail measurements were done by chasing commercial aircraft in the flight corridors over southern Germany. The Falcon aircraft would position it self above the contrail and descend slowly through the exhaust. Once below the

contrail the Falcon aircraft ascended to the side of the exhaust and repeated the descent. The contrails were about 2 minutes old at the time of sampling and the ambient temperature were typically -55°C.

Figure 1 show an example of a vertical profiles in and near the exhaust of a B767. The thicker solid and dashed lines correspond to the first and second descent through the exhaust, respectively. The thin lines show the measurments made during the ascents outside the contrail.

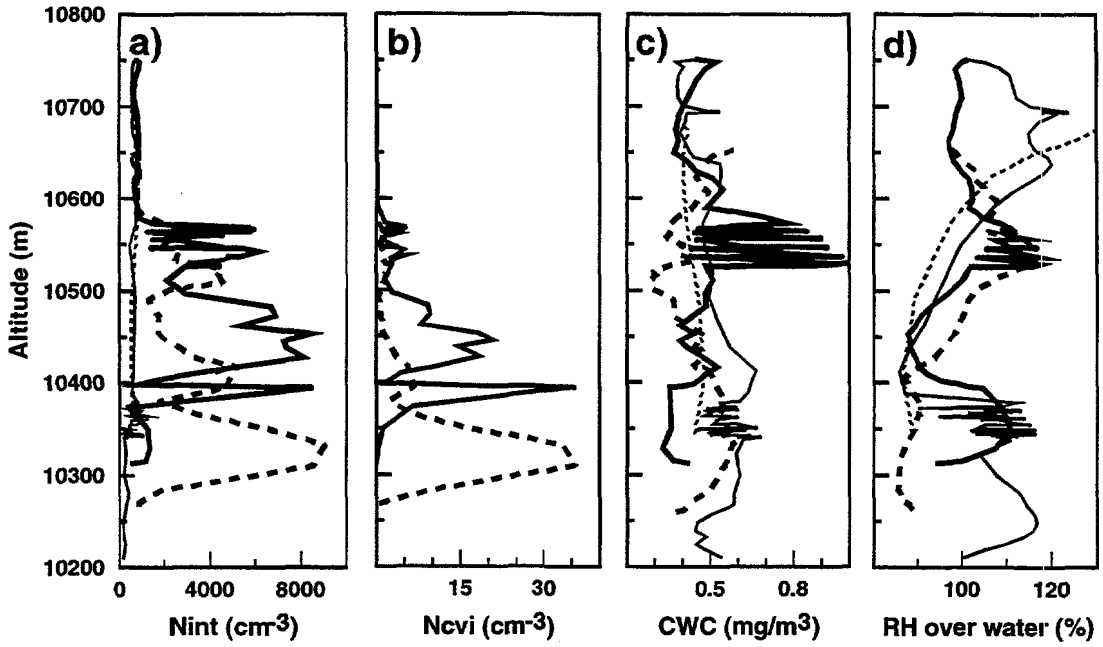

Figure 1. Vertical profiles through a B767 contrail of: a) interstitial aerosols b) cloud particles c) cloud water content d) relative humidity with respect to water.

Although the upper and lower bound of the contrail can be clearly distinguished by the particle data the different parameters show large variations inside the contrail. Maximum concentrations for particles larger than 0.018 μm diameter reach almost 10000 cm^{-3}. For cloud particles larger than 4.5 μm diameter the peak concentrations exceed 30 cm^{-3}. In Table 1 below, data from measurements made in contrails from four different aircraft are summerized. Instead of reporting ambient particle concentrations we have normalized the average concentration from one descent with the plume cross section.

Table 1. Contrail properties

Aircraft	Boeing 767		Boeing 767		B-747	MD-80		
Contrail	1a	1b	2a	2b	3	4a	4b	
Time in contrail (s)	144	105	105	48	93	75	36	
Diameter (m)	290	333	245	215	403	181	230	**Median values**
#/m (CVI)*10^{10}	41	64	11	5.7	16	1.7	4.1	**11**
#/m (INT) *10^{13}	23	30	6	5.7	16	1.7	3.9	**6**
CE fraction (%)	0.18	0.21	0.18	0.1	0.1	0.1	0.1	**0.1**
DMM (μm)	5.3	5.0	5.5	5.5	2.4	5.8	4.7	**5.3**

Contrail properties measured on 21 March 1994. The cloud element (CE) fraction is the number of particles per meter (#/m) sampled by the CVI-inlet devided by the number of aerosol particles sampled by the interstitial inlet (INT). The diameter of mean mass is given from the CWC and number concentration of crystals larger than 4.5 μm diameter.

The plume cross section is not known explicitly and had to be estimated from the observed diameter in the vertical and assuming a cylindrical shape of the contrail. By taking the ratio between the cloud particle and the interstitial aerosol concentrations, we can calculate the fraction of particles that grew to a size larger than 4.5 μm diameter. This value did not change very much between the different measurements and ranged between about 0.1 and 0.2. From the observed values we can calculate a diameter of mean mass (DMM), defined as the cube root of $(CWC/N_{cvi})(6/\pi)$, which give a hint on the sizes of these particles. In all the contrail passes except number 3 the DMM is around 5 μm diameter. For the B-747 case there is something wrong because the DMM is smaller than the lower cut-off size for the CVI. We think that the problem is due to noise in the hygrometer measurement during this passage. We can compare the observed DMM values from the other cases with a calculated value using a B-737 as an example. The aircraft burn 2300 kg/h and fly at a speed of about 800 km/h. This results in 3.45 g water emitted per meter flown using an emission index for water of 1200 g/kg. If this water is distributed on the number of particles observed in passes 2a and 2b the resulting DMM is 4 and 5 μm, respectively. Values that compare well with observations.

Figure 2 show the residual aerosol size distribution for the B-767 and B-737 contrails along with a cirrus and sub-visible cirrus case measured on the same day. Note that a residual particle is what remain after the condensed water on the crystal is evaporated. In the Fig.2, all the crystals were larger than 4.5 μm diameter. Clearly the contrail distributions differ from the cirrus cases in that the almost all residual particles are smaller than 0.1 μm diameter. For larger residual particle sizes the contrail distributions resembles the sub-visible case. This is perhaps not so surprising if one concider that part of the ambient air is mixed into the contrail and that persistent contrails form in conditions that are close to trigger cirrus cloud formation. Thus, we believe that the residual particles larger than 0.1 μm in the contrail are mainly from crystals entrained from the ambient air.

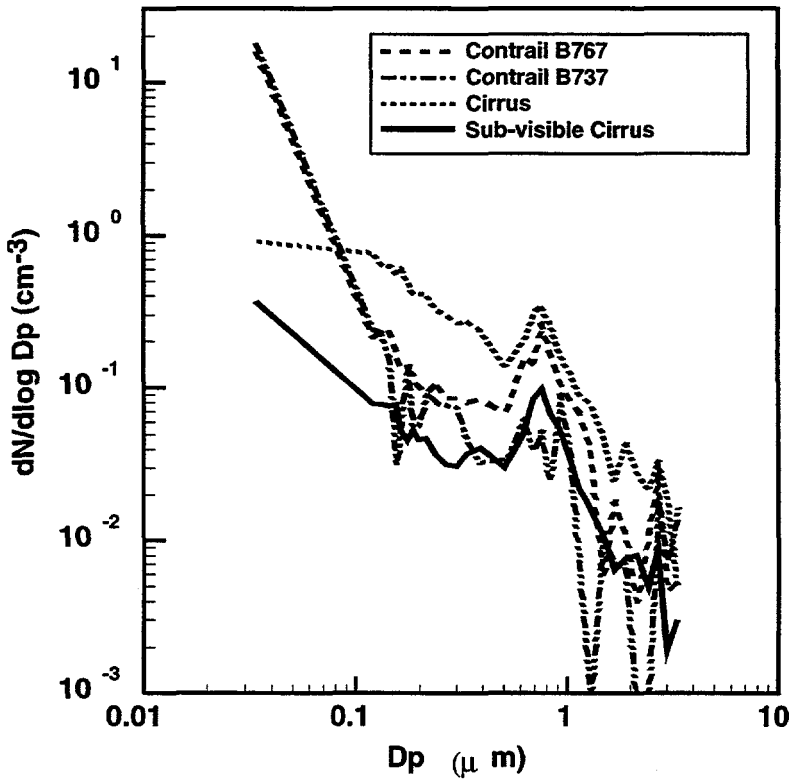

Figure 2. The residual particle size distribution as measured by the CVI for two different contrails and two different types of cirrus clouds.

3. Summary

The measurements presented above suggests that in a few minutes old contrails:

- A significant portion of the water that make up the crystals and the particles on which the crystals form are emitted by the aircraft.
- The number of particles larger than 0.018μm diameter emitted by the aircraft is on the order of 10^{13}-10^{14} per meter flight.
- The number of particles larger than 4.5μm diameter formed in the aircraft exhaust is on the order of 10^{10}-10^{11} per meter flight.
- The fraction of particles acting as CCN show little variation between different aircraft types and have a central value of 0.1%.
- Due to the large number of particles emitted by the aircraft and the limited water supply the crystal should typically be smaller than 10 μm diameter.

Reference

1 Schröder, F., and J. Ström, 1996: Upper tropospheric aerosols. *Atmos. Res.* (in press).

2 Ogren, J.A., J. Heintzenberg, and R.J. Charlson, 1985: In-situ sampling of clouds with a droplet to aerosol converter. *Geophys. Res. Lett.*, **12**, 121-303.

3 Zuber, A. and G. Witt, 1987: Optical hygrometer using differential absorption of hydrogen Lyman-Alpha radiation. *Appl. Opt.* **26**, 3083-3089.

4 Busen, R., and A. L. Buck, 1993: A high performance hygrometer for aircraft use: Description, installation, and flight data.,Report No. 10, Institut für Physik der Atmosphäre, 29pp.

A NUMERICAL SIMULATION OF A CONTRAIL

L. LEVKOV, M. BOIN, D. MEINERT
GKSS Forschungszentrum, Max-Planck-Straße
D-21502 Geesthacht, Germany

Abstract

In this study the formation of a contrail from an aircraft flying near the tropopause is simulated using a three-dimensional mesoscale atmospheric model including a very complex scheme of parameterized cloud microphysical processes. The model predicted ice concentrations are in very good agreement with data measured during the International Cirrus Experiment (ICE), 1989. Sensitivity simulations were run to determine humidity forcing on the life time of contrails.

Keywords - International Cirrus Experiment; Contrail; Ice nucleation

INTRODUCTION

Theoretical studies on the climatic changes of the Earth due to pollution have emphasized the role of high and cold cirrus clouds. Model calculations have shown that a 2 % increase in the occurance of cirrus clouds can produce a 1 K rise in Earth temperature (Barrett,1992).

It is known that condensation trails (contrails) formed in the exhaust of aircrafts can trigger cirrus clouds. In particular contrails from aircrafts flying in the upper troposphere may affect changes in the climate of our planet.

The effect of the cirrus clouds on the Energy Radiation Budget (ERB) of the Earth strongly depends on their microphysical properties and, in this respect, on the microphysics of the contrails.

In this study the formation of a contrail from an aircraft flying near the tropopause is simulated using a three-dimensional mesoscale atmospheric model including a very complex scheme of parameterized cloud microphysical processes.

MODEL AND CLOUD SCHEME

The model used in this study is the three-dimensional, time-dependent, non-hydrostatic mesoscale model GESIMA (GEesthacht SImulation Model of the Atmosphere). The dynamical part is based on the anelastic approximation (Kapitza and Eppel, 1992).Predicted variables of this complex model are the three velocity components u, v and w, the potential temperature θ, the mixing ratio for water vapour q_V and the mixing ratios q and number concentrations N for the cloud species. The parameterizations of the microphysical processes is based upon Levkov et al.,1992.

Fig.1 gives an overview of all cloud microphysical processes which are included in the model in a parameterized form.

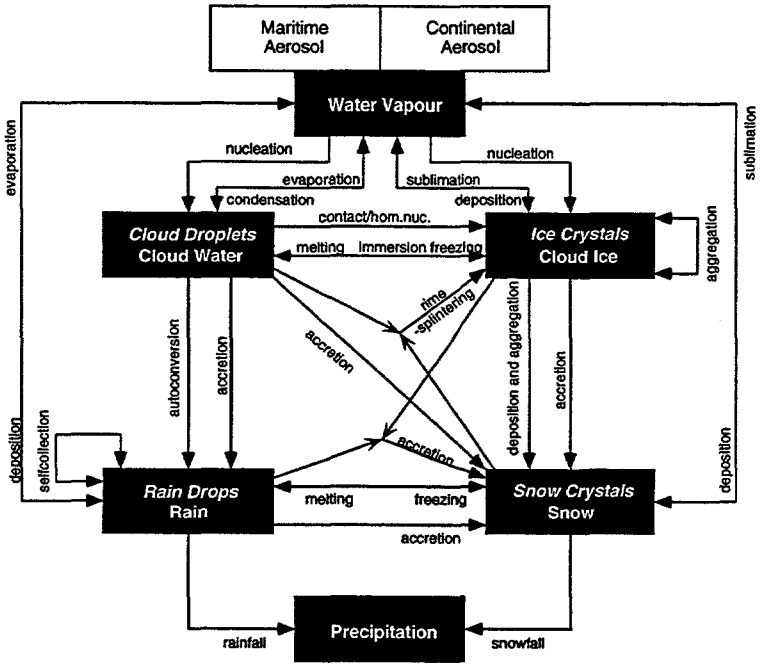

Figure 1: *Water species and cloud processes included in the cloud scheme.*

The continuity equations for grid volume average mixing ratio of species X of water (q_X), potential temperature deviation (Θ') and number concentration (N_X) of cloud particles, and number concentration of aerosol particles (N_A) can be written as follows:

$$\frac{\partial q_X}{\partial t} = ADV(q_X) + DIF(q_X) + \frac{\partial}{\partial z}(q_X U_X) + Q_{q_X} \quad (1)$$

$$\frac{\partial \Theta'}{\partial t} = ADV(\Theta') + DIF(\Theta') + Q_{\Theta'} \quad (2)$$

$$\frac{\partial N_X}{\partial t} = ADV(N_X) + DIF(N_X) + \frac{\partial}{\partial z}(N_X U_X) + Q_{N_X} \quad (3)$$

$$\frac{\partial N_A}{\partial t} = ADV(N_A) + DIF(N_X) - N_W \quad (4)$$

The subscript X stands for cloud water, rain water and vapor.

"ADV" represents the advection and with "DIF" are denoted the eddy diffusion term. U_X is the mass weighted mean velocity for rain drops and Q_{q_X}, Q_{N_X} and $Q_{\Theta'}$ denotes the change of the water species and temperature due to microphysical and radiative processes.

INITIALISATION AND RESULTS

The radiosonde soundings of the vertical profiles of temperature, humidity and wind velocity from Helgoland (14:00 GMT, 24th Sept. 1989) completed by data measured during the International Cirrus Experiment (ICE) mission ICE 206 (Hennings et al., 1990) are used as initial conditions for the presented simulations.

Fig.2 shows the relative humidity over ice and the total ice mixing ratio for one grid box at the elevation of the flight at different time stages, predicted by the cloud scheme.

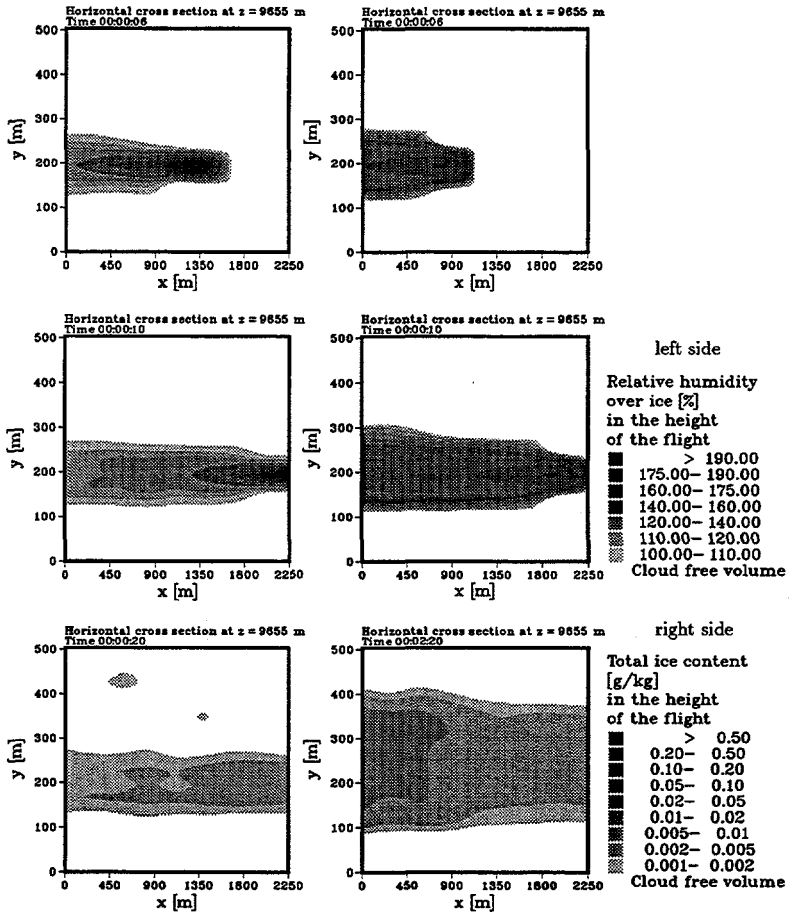

Figure 2: *Horizontal cross section of the relative humidity over ice and the total ice content in the height of the flight at different time steps.*

An updraft of the contrail is found in the simulation data. This rising up of the contrail can be explained taking into account the release of energy during the nucleation and the temperature perturbation due to the energy exhausted by the aircraft.

During the International Cirrus Experiment (ICE) 1989 mission ICE206 in-situ measurements were taken when the contrail was about 8 minutes old (Albers et al., 1990). At this time an ice concentration of $3.5 \cdot 10^{-5} kg/kg$ was measured in the contrail. The simulated ice mixing ratios at this stage of contrail development are $0.9 \cdot 10^{-6} kg/kg$. The measurements lead to a crystal number of $1.5 \cdot 10^{5} m^{-3}$; the model computed a number of $3 \cdot 10^{5} m^{-3}$.

A numerical fit is done proposing the following exponential function for the calculation (Fig. 3) of the life time of faint contrails in case of known ambient humidities:

$$\text{Life time [s]} = \exp\left(\frac{(RH[\%] - f)\ln 10}{g}\right) \tag{5}$$

where f=54.1108 and g=16.0675. The square of the correlation coefficient R for this fit is

0.82; the saturation range is from 70 to 130% with respect to ice by temperature between -40 and $-50°C$. The threshold values of $0.004gm^{-3}$ total ice content and $0.167gm^{-2}$ ice water path are used.

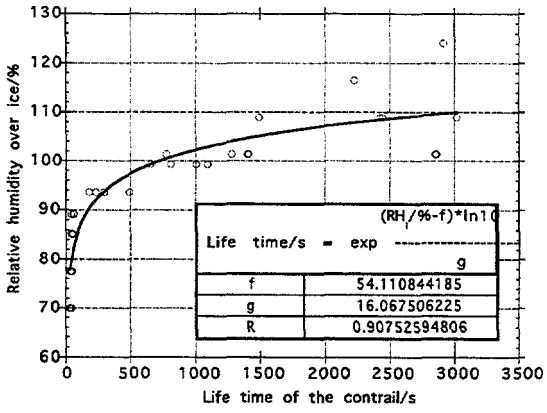

Figure 3: *Scatter plot of the pairs of ambient humidity and simulated contrail life time for the threshold values for faint contrails. Exponential function fitted to these data.*

Figure 4: *Contrails observed from environmental satellites*

CONCLUSIONS

In this paper a cloud scheme is exercised in a meso-scale environment with moist processes generating a contrail in a region with subsaturated air. The simulated ice concentrations are derived from the mixing ratios and number concentrations of the water species. The parameterizations lead to a time of persistence of the contrail of about 10 minutes. The general feature of the contrail (ice mass and concentration) seems to be well reproduced with the cloud scheme.

An updraft of the contrail is found in the simulation data. This rising up of the contrail can be explained by taking into account the release of energy during the nucleation and the temperature perturbation due to the energy produced by the aircraft exhaust.

During the International Cirrus Experiment (ICE) 1989 mission ICE 206 in-situ measurements were taken when the contrail was about 8 minutes old (Albers, 1990). At this time an ice concentration of $3.5 \cdot 10^{-5} kg/kg$ was measured in the contrail. The simulated ice mixing ratios at this stage of contrail development are $0.9 \cdot 10^{-6} kg/kg$. The measurements lead to a crystal number of $1.5 \cdot 10^{5} m^{-3}$; the model computed a number of $3 \cdot 10^{5} m^{-3}$.
In further studies we will try to compare our results to observations of contrails from satellite images.

The simulation results indicate an exponential variation of the life time of the contrail with changes in the moisture of the ambient air. Future studies will examine the possibility to extrapolate this relation to different atmospheric conditions.

References

Kapitza, H., and D. P. Eppel, The non-hydrostatic mesoscale model GESIMA. Part I: Dynamical equations and tests, *Contr. Atmos. Phys.*, **65**, 129–145, 1992.

Levkov, L., B. Rockel, H. Kapitza, and E. Raschke, 3D meso-scale numerical studies of cirrus and stratus clouds by their time and space evolution, *Contr. Atmos. Phys.*, **65**, 35–58, 1992.

Hennings, D., M. Quante, and R. Sefzig, *International Cirrus Experiment 1989*, Field Phase Report, University of Cologne, 1990.

Albers, F., M. Quante, and E. Raschke, Aircraft measurements in high altitute contrails during ICE 1989, *7th Conference on Atmospheric Radiation*, 23th–27th July 1990, San Francisco, 1990.

Authors email: levkov@gkss.de, dieter.meinert@gkss.de

A MODEL STUDY OF THE SIZE AND COMPOSITION DISTRIBUTION OF AEROSOLS IN AN AIRCRAFT EXHAUST

A.A. Sorokin

SRC "ECOLEN", 2 Aviamotornaya str.,111250, Moscow, Russia

1. ABSTRACT

A two-dimensional, axysimmetric flowfild model which includes water and sulphate aerosol formation represented by moments of the size and composition distribution function is used to calculate the effect of radial turbulent jet mixing on the aerosol size distribution and mean modal composition.

2. INTRODUCTION

Observations of aerosols in aircraft wakes have indicated that the size distribution of particles formed in the jet plume may be important for the processes involved in the further evolution of aerosols in the wake. Visual observations of the short contrails from a jet aircraft operating under cruise conditions and in young jet exhaust plumes at ground levels have shown also that besides the sulphuric acid and water vapour binary nucleation other factors are possibly responsible for early contrail formation. Processes of water vapour condensation on activated soot particles, homogeneous nucleation on ions, also freezing of water droplets and ice particles formation, and turbulent radial mixing may also be important. Existing models can not given information about the aerosol size distribution evolution in the turbulent plume because of both the number of size and composition bins, and the using of a trajectory assumption for particles motion in a turbulent flow. The large number of coupled diffusion equations required for size bins approximations makes their direct solution intractable. Here we present a first preliminary results of calculations with a specific aerosol model which includes water droplets formation on soot particles represented by moments of the size distribution function with direct modelling of their radial turbulent mixing.

3. AEROSOL DYNAMIC

The jet phase of near field plume is modelled using a parabolised isobaric Navier Stokes equations with a two equation turbulence model [1]. Gasdynamical equations are supplemented by two diffusion equations for passive scalar (or dilution factor) and dispersion of passive scalar fluctuations. For turbulent jets with condensation processes a nucleation rate in mixing layer is in most cases a very strong function of the thermodynamical parameters. So, for such flows the nucleation rate must be averaged by using an appropriate probability density function for the turbulent characteristics, which just includes the mean value and dispersion of passive scalar as parameters. However, in the plume of modern aircraft the process of water vapour homogeneous nucleation is not important in comparison with the condensation on soot particles or ions and sulphate nuclei. A second order numerical scheme was used for the radial direction.

As in the most of preceding models [2,3] it is assumed that condensate particles are well able to follow the gas motion. Also, as in the model by Brown et al. [3]

coagulation of soot and condensed particles is neglected since the time scale of coagulation is much longer than the time associated with the jet regime of plume. The process of soot activation is not known sufficiently well for present time. So, part of activated soot particles is considered as an input parameter.

For jet exhaust mass transport of formatted aerosol is effected by convection and turbulent diffusion in the radial direction. In principle, one needs to incorporate a general kinetic equation for size distribution function **f(x,y,r)** [4] in the total system of turbulent diffusion equations. Here **x** and **y** are axial and radial directions, **r** is radius of particles. But due to an additional independent variables (radius and also in many cases the composition of particles) the computational requirement of such models tent to be substantial. The using of size bins models [3] also is ineligible because of the number of discrete entities (few tens or more) tracked in solving the two dimensional diffusion equations.

An alternative approach to the size bins models is a description of the aerosol dynamics through the evolution of a moments of the size distributions function. Such model has an advantage of a simplicity and that most notably in essential reduction of the number of coupled diffusion equations required for solution.

The governing equations for moments G_i [4] , where

$$G_i = \int_0^\infty f(r,x,y) r^i dr \ , \ i = 0,1,2,... \qquad (1)$$

are given by an infinite system of nonclosed diffusion equations [1]:

$$\rho U \frac{\partial G_i}{\partial x} + \rho V \frac{\partial G_i}{\partial y} - \frac{1}{y}\frac{\partial}{\partial y}\left(\rho y \frac{\varepsilon}{Sc_t}\frac{\partial G_i}{\partial y} \right) = \rho i \int_0^\infty R_c\, r^{i-1} f\, dr \qquad (2)$$

where R_c is a growth rate of droplets as result of water vapour condensation, ρ is gas density, **U** and **V** are respectively axial and effective transverse velocities, ε is turbulent viscosity and Sc_t is turbulent Schmidt number.

Approximating the shape of the aerosol size distribution by an unimodal lognormal function,

$$f(r) = \frac{G_0}{\sqrt{2\pi}\, r \ln\beta} \exp\left[-0.5 \frac{\ln^2(r/r_g)}{\ln^2\beta} \right] \qquad (3)$$

a closure of the system (2) can be achieved, when mean modal radius r_g and deviation β are known functions of the some first moments. In our modelling in the most cases we used moments G_0 (total particles concentration), G_2 (total surface density) and G_3 (aerosol volume mixing ratio) for the definition of the function of $f(r; G_0, G_2, G_3)$ in equations (2). Also, for the testing of model sensibility to the choice of moments number we used for $f(r)$ definition the moments G_0, G_4 and G_5 or even the system of moments $G_0 \div G_5$. In the last case we considered two functions as (3). The results of modelling of water vapour condensation on soot in the jet exhaust of subsonic aircraft have shown the closely related surface density and mass mixing ratio of formatted water aerosol for all cases.

In common case the total size distribution is result of action by a several contributors of condensation nuclei (soot particles, nucleation of sulphuric acid, ions hydration, condensation on

In common case the total size distribution is result of action by a several contributors of condensation nuclei (soot particles, nucleation of sulphuric acid, ions hydration, condensation on ambient sulphate particles and so on). Hence, it is appropriate to consider the corresponding groups of moments equations as system (2) with the corresponding to each group approximating unimodal function, as (3). The total size distribution will be a sum of local functions.

The problem of aerosol composition modelling in moment's approach is more complex, because we don't know a possible type of distribution over the composition for given radius of particles. So, as a preliminary result, we considered the mean mass composition of aerosols and its variation from equilibrium composition for the case of sulphuric acid and water vapour condensation on activated soot particles.

4. MODEL TESTING FOR LABORATORY DATA

An investigation of fog formation in flow field of the turbulent water-vapour/air jet that issued into a room was conducted in [5]. The data allow the behaviour of the jet fog formation was characterised by the competing mechanisms of heterogeneous nucleation on entrained nuclei, growth of droplets and its turbulent radial diffusion. Fog jets were generated with effluent temperatures of 62°C and 85°C, corresponding to a vapour mass fraction , of 0.14 and 0.45, respectively. The data and modelling supported expectations that the fog formed due to heterogeneous condensation on the particles in the room.

While condensation tends to narrow a polydisperse distribution of droplets, condensation with mixing and particle entrainment results in the opposite - a broader distribution. The given Moment-Condensation-Mixing model incorporate these processes to explain the axial trends in the shape of the measured droplet size distributions. Figure 1 show that model predict the experimentally detected droplets size distribution in the main region of the jet.

5. JET EXHAUST MODELLING

The plume flowfield was treated for a subsonic aircraft B707 at an altitude of 12.2 km for the same initial conditions and nozzle geometry as in a recent paper by Brown et al. [3]. Soot particles distribution used in the work was as in measurements [6] with mean modal radius, r_g=0.03 μm, deviation β=1.6, and soot emission index, EI(soot)=10^{-4}.

Saturation profiles, calculated in the present work are in the some difference from the result by Brown et al. [3]. For example, saturation at the plume axis is reach at a downstream distance of 172 meters(147 meters in [3]). This difference is connected with the different models of turbulence used in the works and as a consequence different rates of mixing.

In existing trajectory models diffusion of particles formed on a particular path to other parts of the plume is not account in contrast to given diffusion model. Figure 2 shows the mass fraction of water that condenses at plume axis when 10% of the exhaust particulates are activated for trajectory model of particles motion with size-bin and size-moment approximation of particles growth, and for diffusion model with moment approach. The profiles of bin and moment approximation for trajectory model coincide very closely, but are displaced 25 meters downstream relative to the profile of diffusion model in the initial phase of aerosol formation and far exceed the moment diffusion solution when condensed water is decrease due to further dilution. This result show the importance of diffusion effect on water condensate distribution in the plume.

Figure 3 illustrates the effect of ambient and core condensation nuclei on the size distribution of contrail droplets on condition that all ambient particles (number density in air is of 100/cc) and only 2% of core soot particles are condensation nuclei. Simulation is performed with two systems of moment equations, as (2) for two distribution function of water droplets.

6. CONCLUSION

The results presented here indicate that moment approximation of aerosol size distribution as alternative approach to size bins models is usable as efficient method of aerosol dynamics simulation in the plumes marked by the essential turbulent diffusion of formed aerosols from one to other parts of plume.

The aerosol dynamics model presented here is currently being extended and combined with a chemical plume model to enable the characterisation of the size distribution, phase and non-equilibrium composition of plume aerosols.

7. ACKNOWLEDGMENTS

The author acknowledge Richard Miake-Lye and Richard Brown for helpful discussion of this work . This work was supported in part by Russian Foundation of Fundamental Investigations Grant 96 - 01 - 01450 .

8. REFERENCES

[1] Vatazhin A.B. and Sorokin A.A., " Aircraft's atmosphere aerosols and ecology problems", Fluid Dynamics, v.27, pp.57-77, 1992.

[2] Karcher B., Peter Th., and Ottmann R., " Contrail formation : Homogeneous nucleation of H_2SO_4 / H_2O droplets ", Geophys. Res. Lett., v.22, pp.1501-1504, 1995.

[3] Broun R.C., Miake-Lye R.C., Anderson M.R. , Kolb C.E., and Resch T., " Aerosol dynamics in near-field exhaust plumes ", J. Geophys. Res., in press, 1996.

[4] Friedlander S.K., Smoke, Dast and Haze, John Wiley and Sons, New York, 1977.

[5] Strum M.L. and Toor H.L., Microphysical measurements of fog in a turbulent jet, 49 p., Carnegie Mellon University, Pittsburgh, 1991.

[6] Whitefield P.D., Trueblood M.B., and Hagen D.E., " Size and hydration characteristics of laboratory simulated jet engine combustion aerosols ". Particulate Science and Technology, v.11, pp. 25-36, 1993.

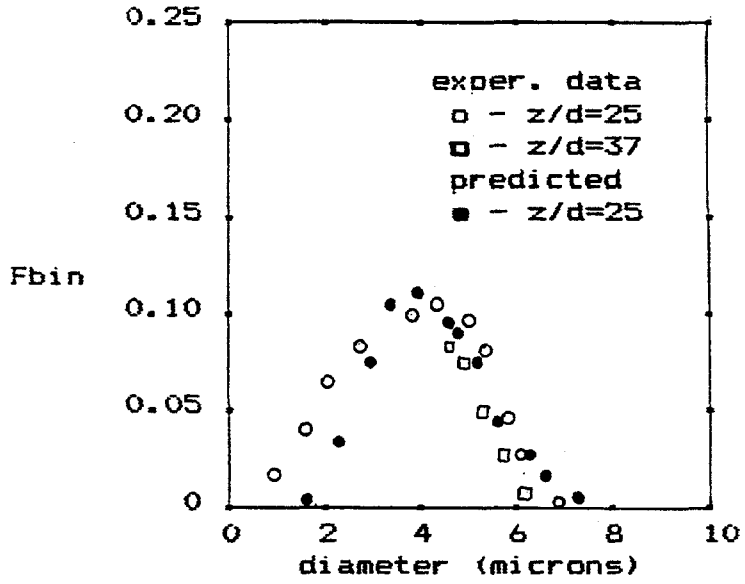

Figure 1. Comparison of the size distribution in the unseeded 62 C jet along the jet centerline.

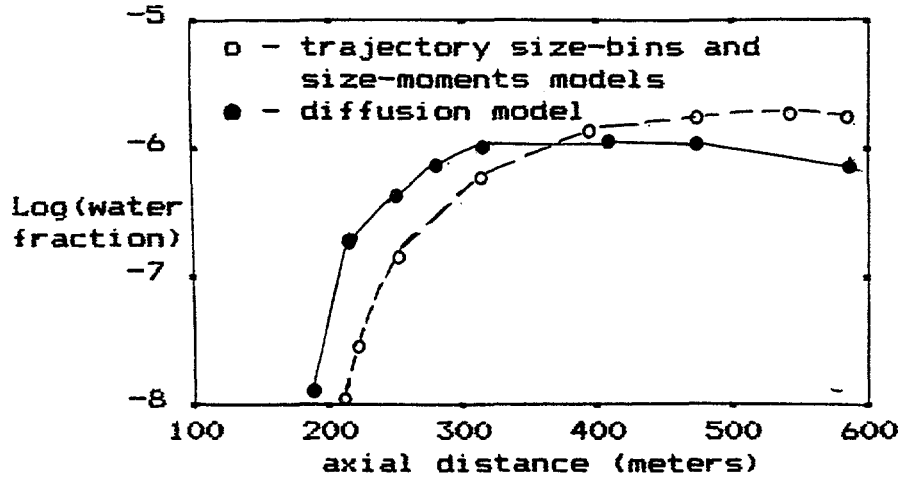

Figure 2. Water mass fraction for jet centerline for trajectory and diffusion models of simulation.

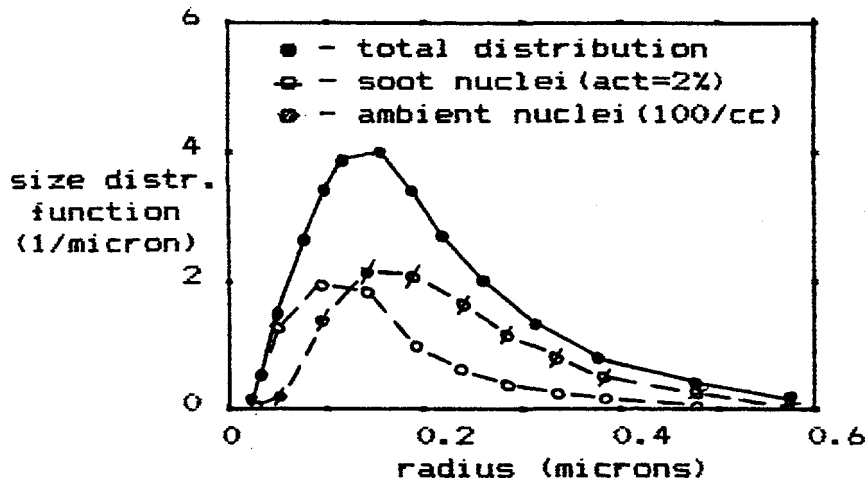

Figure 3. Aerosol size distribution for water vapour condensaton on soot particles (activation=2%) and ambient aerosols (N=100/cc).

Effect of Aircraft Exhaust Sulfur Emissions on Near Field Plume Aerosols

Submitted to Geophysical Research Letters, July, 1996

R.C. Brown, R.C. Miake-Lye, M.R. Anderson, and C.E. Kolb
Center for Chemical and Environmental Physics
Aerodyne Research, Inc.
Billerica, MA 01821

Abstract

Based on estimated exit plane sulfur speciation, a two dimensional, axisymmetric flowfield model with coupled gas phase oxidation kinetics and aerosol nucleation and growth dynamics is used to evaluate the effect of fuel sulfur oxidation in the engine on the formation and growth of volatile H_2SO_4/H_2O aerosols in the near field plume. The conversion of fuel sulfur to sulfur trioxide and sulfuric acid in the engine is predicted to significantly increase the number density and surface area density of volatile H_2SO_4/H_2O aerosols and the chemical activation of exhaust soot particulates. This analysis indicates the need for experimental measurements of exhaust SO_X emissions to fully assess the atmospheric impact of aircraft emissions.

INTRODUCTION

Field measurements of the aerosols in jet engine exhaust wakes have indicated high levels of sulfuric acid. *Hofmann and Rosen* [1978] reported close to total conversion of the fuel sulfur to sulfuric acid in an SR-78 aircraft plume sampled 18 hours after emission at an altitude of 23 km. Estimates of between 12 % and 45 % sulfur conversion have been reported for the Concorde wake after approximately 16 minutes at 16.2 km based on in-flight aerosol measurements by the instrumentation aboard the ER2 [*Fahey et al.*, 1995]. Additionally, preliminary data garnered under the SUCCESS program have indicated a high level of small volatile aerosols whose number density varies with the mass loading of fuel sulfur [*Ballenthin et al.*, 1996].

In stark contrast, modeling studies of aircraft plume chemistry have predicted that the net conversion of fuel sulfur to sulfuric acid is limited to between 0.5% - 2% [*Miake-Lye et al.*, 1993, 1994; *Kärcher et al.*, 1994, 1995]. These numerical estimates are based on current emission scenarios for sulfur speciation which assume that fuel sulfur is emitted from the engine as SO_2 and is subsequently converted to sulfuric acid by gas phase reactions in the exhaust plume. The growing consensus between the results of field measurements points to a fundamental discrepancy between observations and the homogeneous and heterogeneous kinetic mechanisms currently thought to govern sulfur chemistry in the modern jet aircraft engines and exhaust plumes.

The extent to which fuel sulfur is converted to volatile aerosol precursors during combustion and the subsequent turbine flow in supersonic and subsonic aircraft engines was recently estimated numerically [*Brown et al.*, 1996a]. The results of that analysis pointed to between 2% and 10% conversion of the fuel sulfur to SO_3 and H_2SO_4 in the engine. The range in the estimated values is due to the limitations of the models used in that study to accurately characterize the oxidative pyrolysis of typical jet engine fuels and 3-dimensional fluid dynamics for real combustors and turbines, and the lack of high temperature kinetic data for important sulfur oxidation reactions. Although there is little experimental data currently available to

validate these model results, it is important to note that the estimated conversion is consistent with measured values for a gas turbine at ground level burning diesel fuel [*Harris*, 1990].

The present paper extends the analysis of sulfur oxidation in the engine by providing an estimated of the effect of exit plane sulfur emissions on aerosol formation and growth processes in the near field plume. Both engine and plume results are important in addressing the field measurement results First, the analysis of oxidation in the engine will better define the extent of sulfur conversion required in the wake by gas phase or heterogeneous oxidation mechanisms to account for the estimated percent conversion derived from in-flight measurements. Second, the analysis of the effect of speciated sulfur oxide emissions at the exhaust exit on the number density, size distribution and composition of near field aerosols will provide an estimate of the aerosol surface area density for subsequent evaluation of heterogeneous oxidation mechanisms in the wake.

EFFECT OF SO_3 AND H_2SO_4 EMISSIONS ON VOLATILE EXHAUST AEROSOLS

To illustrate the effect of SO_x emissions at the exhaust exit on the formation, growth and chemical processing of near field plume aerosols, parametric studies were performed for the Concorde exhaust under the ambient conditions reported for the in flight wake measurements by the ER-2 over New Zealand in 1994 [*Fahey, et al.*, 1995]. Since direct measurements of the level of S(VI) (SO_3 and H_2SO_4) at the exhaust exit have not been reported, the percent conversion was varied between 2 % and 20 %. This range encompasses both the model estimates described previously [*Brown et al.*, 1996b], as well as experimental measurements for hydrocarbon flames [*Merryman and Levy*, 1971] and gas turbine exhausts [*Hunter*, 1982; *Harris*, 1990].

The near field plume is modeled using the JANNAF Standard Plume Flowfield model (SPF-II) [*Dash et al.*, 1979]. SPF-II is an axisymmetric Parabolic Navier Stokes (PNS) flow code with a two equation turbulence model. A second order numerical scheme is used for the radial direction. The flow dynamics is coupled to the gas phase kinetics, binary H_2SO_4/H_2O

nucleation and aerosol coagulation by an implicit treatment of chemical source terms in which the product of species concentrations are linearized over each spatial step.

Gas phase HO_X, NO_X and SO_X chemistry and aerosol formation and growth is modeled using the Plume Nucleation and Condensation (PNC) model described previously [*Brown et al.*, 1996b]. The PNC model includes binary H_2O/H_2SO_4 homogeneous and heterogeneous nucleation using classical nucleation theory with hydrate interactions and acid aerosol growth by vapor condensation and coagulation. In subsaturated plumes, the growth of both acid aerosols and soot/acid aerosols by vapor condensation is assumed to be driven by H_2SO_4 condensation. The aerosol weight percent and size than follows by assuming equilibrium between the aerosol and the gas phase water vapor. Similarly for coagulation, the number of acid molecules is conserved while the aerosol volume is allowed to adjust to its equilibrium value. If critical saturation is achieved, then acid and water vapor condensation are followed kinetically and both acid and water molecules are conserved in a coagulation event.

Figure 1 shows the number density of volatile H_2O/H_2SO_4 aerosols, averaged over the plume cross section 5 km downstream assuming that 2%, 5%, 10% and 20% of the fuel sulfur is emitted at the exit plane as SO_3. As would be anticipated, the number density and mean radius of volatile aerosols is seen to increase as the exhaust emission level of SO_3 increases. It is interesting to note that the size distribution in Figure 1 for high exhaust emission levels of SO_3 tends toward better agreement with preliminary volatile aerosol measurements under the recent SUCCESS campaign [*Anderson*, 1996].

A natural and important consequence of the high number density of small H_2O/H_2SO_4 aerosols is a significant increase in aerosol surface area. As an example, Figure 2 shows the volatile aerosol surface area density along the plume axis as a function of downstream axial distance for the runs with 2%, 5% and 10% conversion at the exhaust exit. The large increase in surface area early in the plume is notable. Since the critical saturation ratio for water condensation is not achieved in the Concorde plume, persistent contrail particles do not form and water vapor condensation on activated soot particulates is limited to that needed to bring the

volatile component on activated soot particulates into equilibrium with the gas phase. However, in supersaturated plumes, the growth of water droplets and/or ice crystals is significant and would result in additional surface area density to that shown in Figure 2.

Lastly, Figures 3a and 3b show the number of H_2SO_4 molecules adsorbed per exhaust soot and the ratio of the resulting soot/sulfuric acid aerosol radius, r, to the radius of the insoluble soot core, r_c, as a function of the core radius. The results presented are for the plume axis 5 km behind the aircraft. As seen in Figure 3a, the model predicts a substantial number H_2SO_4 molecules on each soot particle, which can be interpreted as chemical activation of the exhaust soot particles. Early in the plume, activation results from both binary (H_2SO_4 and H_2O) heterogeneous binary nucleation [*Zhao and Turco*, 1995] and coagulation with acid aerosols formed through homogeneous binary nucleation [*Brown et al.*, 1996]. Relative to these two mechanisms, gas phase adsorption (assuming a clean soot surface accommodation coefficient of unity) is negligible. As the surface of soot particulates is modified by the addition of acid, further acid uptake occurs by both coagulation and acid vapor condensation. While acid uptake rates are larger for larger soot particulates, as seen by the larger number of acid molecules per soot CN in Figure 3a, the effect on the particle size is largest for the smaller particles as shown in Figure 3b.

CONCLUSIONS AND SUMMARY

This paper has investigated the effect of S(VI) (SO_3 and H_2SO_4), vapor emissions at the engine exit on the nucleation and growth of volatile H_2SO_4/H_2O aerosols and the chemical processing of exhaust soot particulates in the near field plume. Model results for the near field Concorde exhaust plume indicate that the formation of SO_3 in the engine results in dramatic increases in the volatile aerosol number density and surface area density, as well as in the chemical activation of exhaust soot particulates.

The relevance of these results to the potential atmospheric impact of aircraft exhaust aerosols is threefold. First, the two dimensional global modeling study of *Weisenstein et al.*

[1996], predicts an increase in the stratospheric aerosol surface area by factor of two due to sulfuric acid nucleation in supersonic High Speed Civil Transport (HSCT) plumes if 10% of the emitted SO_2 is converted to H_2SO_4 shortly after emission. Since SO_3 is readily converted to H_2SO_4 within the first few milliseconds after emission, the oxidation of fuel sulfur in the engine could have an important effect on the stratospheric sulfate aerosol surface area density, irrespective of any further homogeneous or heterogeneous oxidation in the exhaust wake. Second, oxidation of fuel sulfur to SO_3 in the engine is predicted to significantly increase the volatile aerosol surface area in the near field (within the first kilometer) plume. Thus, while 2% to 10% oxidation in the engine would not account for the high level of sulfuric acid estimated from in flight aerosol measurements for the Concorde plume [*Fahey et al.*, 1995], it may play a fundamental role if there is further heterogeneous sulfur oxidation in the wake. Third, conversion to acid aerosol precursors in the engine is predicted to result in relatively fast chemical activation of exhaust particulates providing copious active water condensation sites and altering their surface properties for heterogeneous interactions.

Although the extent to which exhaust soot particulates require chemical activation to condense water in saturated plumes is not known, laboratory studies have indicated that carbon black samples are hydrophobic, requiring a much higher saturation ratio to condense water than more hydrophilic particulates, but that water uptake is enhanced in the presence of sulfuric acid vapor [*Wyslouzil, et al*, 1994]. If aircraft exhaust soot exhibits similar properties, then model results indicate that H_2SO_4 activation through heterogeneous nucleation [*Zhao and Turco*, 1995] and acid aerosol coagulation [*Brown et al.*, 1996b] would provide an extremely facile mechanisms for activating soot particles as water or ice condensation nuclei. This was previously noted in model results for a High Speed Civil Transport and B707 exhaust assuming that fuel sulfur is emitted at the exhaust exit as SO_2 and that the formation of H_2SO_4 vapor is limited to hydroxyl radical oxidation in the plume [*Brown et al.*, 1996b]. The present study reinforces that effect and, more importantly, indicates that the potential role of sulfuric acid in the formation of contrails would be difficult to discern from only modest reductions in the fuel

sulfur content. This is due in part to the potential for much higher, nonlinear conversion of S(IV) to S(VI) in the engine compared that currently calculated for hydroxyl radical oxidation in wake. In addition, however, the thermodynamic and kinetic constraints on sulfur oxidation kinetics during combustion and flow through the engine turbine are such that the level of SO_3 may not scale linearly with the level of fuel sulfur and the percent conversion may increase sharply as fuel sulfur is increased [*Brown et al.*, 1996a]. Consequently, in-flight measurements with respect to the effect of "low" and "high" sulfur fuels on the formation of contrails or the emission of volatile aerosols such as those reported by *Busen and Schumann* [1995] and *Schumann et al.*, [1996] require quantitative data for speciated sulfur oxide emission indices and/or very significant fuel sulfur reductions for accurate interpretation.

ACKNOWLEDGMENTS

The authors wish to acknowledge NASA for the support of this work under the Atmospheric Effects of Aviation Subsonic Assessment through contract NAS1-20273.

REFERENCES

Anderson, B., personal communication. 1996

Brown, R.C., M.R. Anderson, R.C. Miake-Lye, C.E. Kolb, A.A. Sorokin, and Y.I. Buriko, Aircraft Exhaust Sulfur Emissions, Geophy. Res. Letters, submitted, 1996a.

Brown, R.C., R.C. Miake-Lye, M.R. Anderson, C.E. Kolb and T. Resch, "Aerosol Dynamics in Near-Field Exhaust Plumes," J. Geo. Res., in press, (1996b).

Busen, R. and U. Schumann, Visible contrail formation from fuels with different sulfur contents, Geophys. Res. Lett. 22 (11), 1357-1360, (1995).

Ballenthin, J.O., T.M. Miller, W.B. Knighton, E. Trzcinski, J.F. Borghetti and G.S. Fderico, In-situ mass spectrometric sampling of jet aircraft exhaust wakes, American Geophysical Union, Spring Meeting, Baltimore, MA, 1996.

Dash, S.M., H.S. Pergament, D.E. Wolf, N. Sinha, M.W. Taylor, and M.E. Vaughn, The JANNAF standard plume flowfield code version II (SPF-II), Vol. I and II, US Army Missile Command, TR-CR-RD SS 90-4, 1990.

Fahey, D.W., E.R. Keim, K.A. Boering, C.A. Brock, J.C. Wilson, H.H. Johnson, S. Anthony, T.F. Hanisco, P.O. Wennberg, R.C. Miake-Lye, R.J. Salawitch, N. Louisnard, E.L. Woodbridge, R.S. Gao, S.G. Donnelly, R.C. Wamsley, L.A. Del Negro, S. Solomon, B.C. Daube, S.C. Wofsy, C.R. Webster, R.D. May, K.K. Kelly, M. Loewenstein, J.R. Podolske, and K.R. Chan, Emission measurements of the Concorde supersonic aircraft in the lower stratosphere, Science 270, 70-74 (1995).

Harris, B.W., Conversion of sulfur dioxide to sulfur trioxide in gas turbine exhaust, J. Engin. for Gas Turbines and Power, 112, 585-589 (1990).

Hofmann, D.J. and J.M. Rosen, Balloon Observations of a Particle Layer Injected by Stratospheric Aircraft at 23 km. Geophys. Res. Lett. 5, 511-574 (1978).

Hunter S.C., Formation of SO_3 in gas turbines, Trans. ASME 104, 44-51 (1982).

Kärcher, B., Transport of exhaust products in the near trail of a jet engine under atmospheric conditions. J. Geophys. Res. 99, 14,509-14,517 (1994).

Kärcher, B., Th. Peter and R. Ottmann, Contrail formation: Homogeneous nucleation of H_2SO_4/H_2O droplets. Geophys. Res. Lett. 22 (12), 1501-1504 (1995).

Merryman, E.L. and A. Levy, Sulfur trioxide flame chemistry - H_2S and COS flames, Thirteenth Symposium (International) on Combustion, The Combustion Institute, p. 427-436, (1971).

Miake-Lye, R.C., M. Martinez-Sanchez R.C. Brown, and C.E. Kolb, Plume and wake dynamics, mixing and chemistry behind a high speed civil transport aircraft, J. Aircraft 30 (4), 467-479 (1993).

Miake-Lye, R.C., M.R. Anderson, R.C. Brown, and C.E. Kolb, Calculations of condensation and chemistry in an aircraft contrail, in DLR-Mitteilung, 94-06, pp. 274-279, DLR, D-51140, Koln, 1994.

Schumann, U., J. Strom, R. Busen, R. Baumann, K. Gierens, M. Krautstrunk, F.P. Schroder, and J. Stingl, In situ observations of particles in jet aircraft exhausts and contrails for different sulfur-containing fuels, J. Geophys. Res. 101, 6853-6869 (1996).

Weisenstein, D.K., M.K.W. Ko, N.-D. Sze and J.M. Rodriguez, Potential impact of SO_2 emissions from stratospheric aircraft on ozone, Geophys. Res. Lett. 23, 161-164 (1996).

Wyslouzil, B.E., K.L. Carleton, D.M. Sonnenfroh, W.T. Rawlins and S. Arnold, Observation of hydration of single, modified carbon aerosols, Geophys. Res. Lett. 21 (19), 2107-2110, (1994).

Zhao J and R.P. Turco, Nucleation simulations in the wake of a jet aircraft in stratospheric flight, J. Aero. Sci. 26 (5), 779-795 (1995).

Figure Captions

Figure 1. Volatile H_2O/H_2SO_4 aerosol number density versus aerosol radius 5 km downstream of the exhaust exit. The number density has been averaged over the plume cross sectional area. Profiles are shown assuming 2%, 5%, 10% and 20% of the fuel sulfur is converted to SO_3 in the engine.

Figure 2. Volatile H_2O/H_2SO_4 aerosol surface area density along the exhaust plume axis as a function of downstream distance. Profiles are shown assuming 2%, 5% and 10% of the fuel sulfur is converted to SO_3 in the engine.

Figure 3. (a) Number of H2SO4 molecules per exhaust soot CN and (b) ratio of the soot radius to he initial core radius as a function of the core radius along the exhaust plume axis as a function of downstream distance. Profiles are shown assuming 2%, 5% and 10% of the fuel sulfur is converted to SO_3 in the engine.

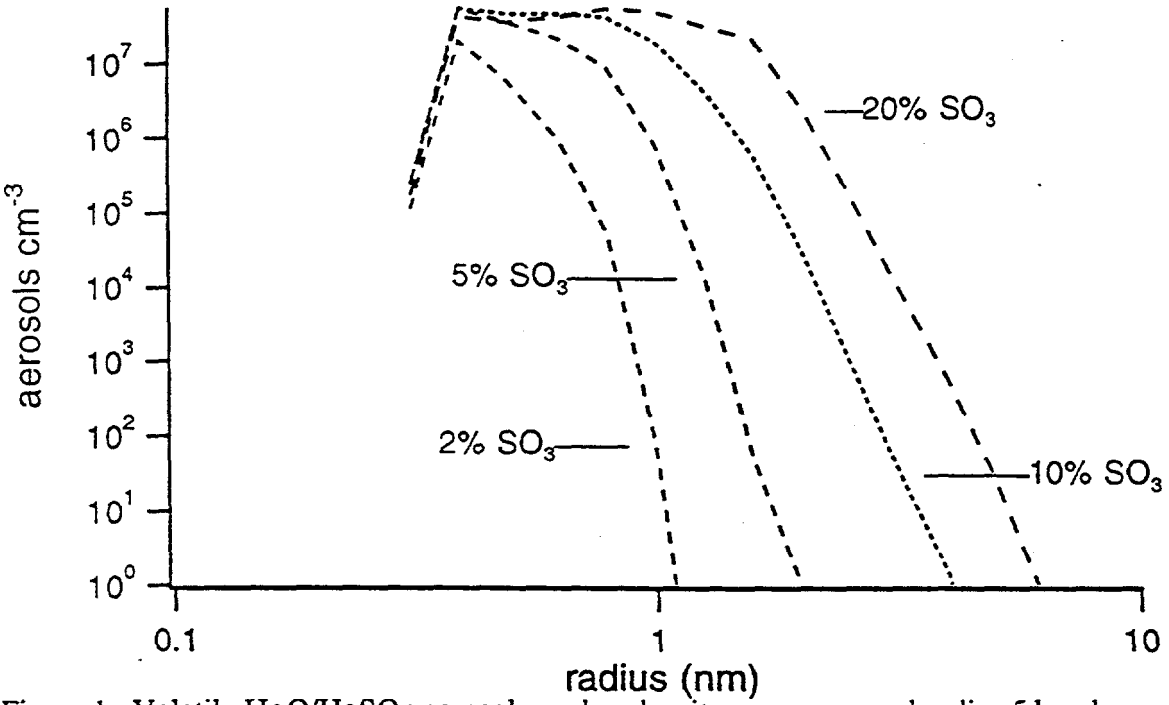

Figure 1. Volatile H_2O/H_2SO_4 aerosol number density versus aerosol radius 5 km downstream of the exhaust exit. The number density has been averaged over the plume cross section. Profiles are shown assuming 2%, 5%, 10% and 20% of the fuel sulfur is converted to SO_3 in the engine.

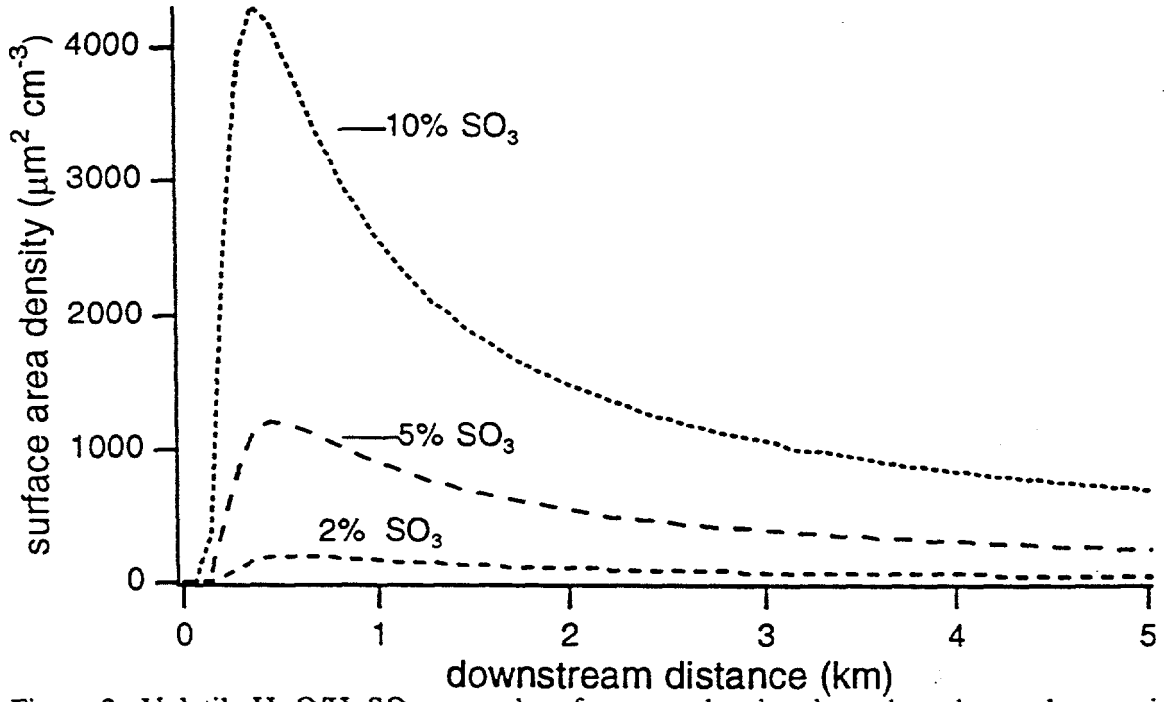

Figure 2. Volatile H_2O/H_2SO_4 aerosol surface area density along the exhaust plume axis as a function of downstream distance. Profiles are shown assuming 2%, 5% and 10% of the fuel sulfur is converted to SO_3 in the engine.

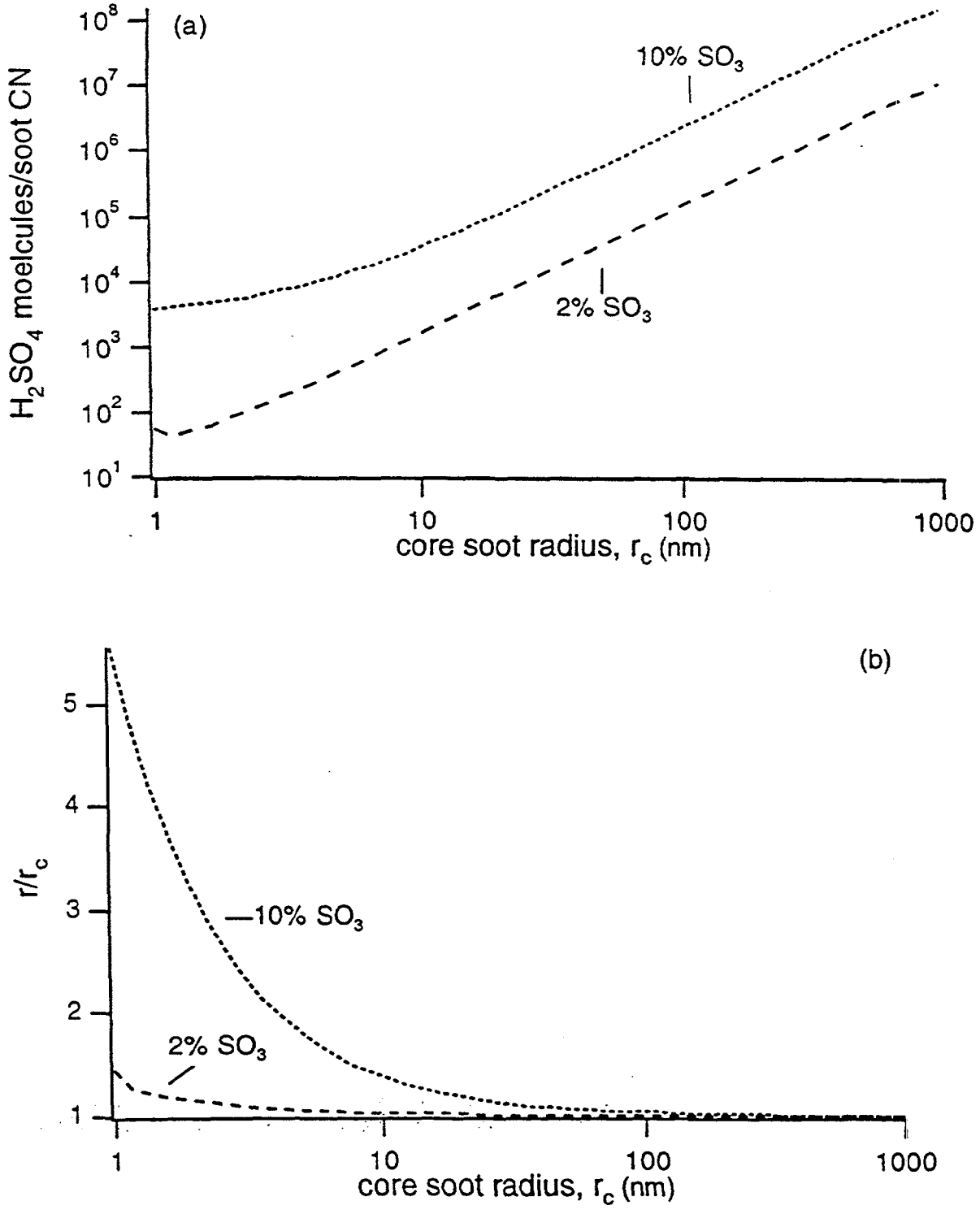

Figure 3. (a) Number of H2SO4 molecules per exhaust soot CN and (b) ratio of the soot radius to he initial core radius as a function of the core radius along the exhaust plume axis as a function of downstream distance. Profiles are shown assuming 2%, 5% and 10% of the fuel sulfur is converted to SO3 in the engine.

GASDYNAMICS, OPTICS AND CHEMISTRY OF AN AIRCRAFT CONDENSABLE WAKE

Emil S. Grinats, Alexei V. Kashevarov, Albert L. Stasenko
(Central Aerohydrodynamic Institute, Russia)

Prediction of the properties of a jet-and-vortex wake from an individual airplane is of great interest [1-3] as the first step to assessment of the possible global changes in the atmosphere due to the world civil aviation as a whole [4,5]. In this report, several mathematical models of the different regions of an aircraft wake and corresponding numerical results are presented.

The axisymmetric exhaust jet was simulated on the base of the well-known k-ε model of turbulence. The following set of parameters was chosen for a nozzle exit section: temperature T_a=561 K, exhaust velocity u_a = 1320 m/s, condensation nuclei density $n_a = 10^{13}$ m^{-3}, kinematic turbulent viscosity for nozzle circumference ν_{Ta} = 22.5 m^2/s, nozzle exit radius r_a = 1 m. The corresponding values in the co-flowing atmosphere were T_∞ = 216.7 K, u_∞ = 708 m/s, n_∞ = 0, $\nu_{T\infty} = 10^{-2}\nu_{Ta}$. The mass density of surrounding gas at the flight altitude ρ_∞ = 0.12 kg/m^3, the water vapour mass fraction $c_{v\infty} = c_{vs}(T_\infty)$, where c_{vs} corresponds to saturation vapour. Most of these values was close to those of paper [4], but we deliberately chose some higher water vapour concentration at the nozzle exit (mole fraction $X_{va} = 0.1X_a$) to make condensation more pronounced (this value may be real, for example, if not only kerosene but hydrogen also is used as a fuel).

All the nuclei of condensation were divided into three groups nuclei of: $n_{a1}=n_{a2}=n_{a3}=n_a/3$ with the different condensation coefficients: α_{c1} = 0.1, α_{c2} = 0.5, α_{c3} = 1. (Such a difference may arise, for example, because of the different degree of "treating" of these nuclei with acid vapours.) Hence, these groups of particles the generating drops had the different rates of condensation growth or evaporation. Another reason for varying the drop radii was collisions resulting in drop coalescence or break-up. The result of interaction between s and j droplets (s being a target, j – projectile, $s \geq j$) was described by the semi-empirical formula for the probability η_{sj} as a function of Re_{sj}, Lp_s, a_s/a_j. This formula is an interpolation of a collection of experiments on the drop pair collision [6], Reynolds Re_{sj}, and Laplace Lp_s numbers depending on the relative droplet velocity $|\boldsymbol{V}_s - \boldsymbol{V}_j|$, their viscosity, density, surface tension, and radii a_s, a_j.

As an example, *Fig. 1a,b* present the radial distributions of the number density and drop radius of the major fraction (s =3) for three cross-sections of the axisymmetric jet. The dash-and-dotted lines correspond to the case of no coagulation ($\eta_{sj} \equiv 0$), and the solid lines to the coagulation/break-up probability $\eta_{sj} \neq 0$. One may see that at the nearest section to the nozzle exit (x/r_a = 100) the number density and drop radius s = 3 are almost independent on the collisions, but at the far sections the influence of aglomeration is remarkable. Note the decrease of the minor fraction concentrations (n_1 and n_2) to be more pronounced than that of the major one (n_3).

Jet chemistry was investigated on the base of kinetic scheme of the gas phase reactions of Ref. [4], enriched by including chemisorption by water droplets of several species [5] (especially such as No_x) and by taking into account of the photochemical processes. The numerical investigations were carried out in the vast region of species concentrations, condensation nuclei densities, temperatures and other governing parameters.

As far as the change of ozone content is of the most environmental interest , the function was calculated

$$\Delta\Psi_{O_3}(x) = \frac{1}{M_{O_3}} \int_0^\infty \rho u (c_{O_3}^{ch} - c_{O_3}^{no\,ch}) 2\pi r dr, \quad \frac{mol}{s}$$

where M_{O_3} is ozone molar mass, $c_{O_3}^{ch}$ and $c_{O_3}^{no\,ch}$ – mass fraction in the presense or absence of the chemical reactions. (Note that ozone is absent at the nozzle exit cross-section but may occur in the jet because of diffusion from surrounding atmosphere, even without of chemical reactions.) The calculations show that at some distance from the nozzle exit $\Delta\Psi_{O_3}$ almost ceases to depend on this distance, so $x = 350$ was chosen to illustrate the influence of exhaust chemical content on the ozone, see *Fig. 2*.

The light circles correspond to the basis set of molar fractions γ_j, the curves show the change in $\Delta\Psi_{O_3}$ if only one of the species j (marked near the corresponding curve) changes its mole fraction (see horizontal scale), the others being unchangeable. The dash-and-dotted straight line means the consumption rate of ozone at the engine inlet (– 0.014 mol/s).

One can see that at the basis set of species concentration, ozone is partially restored due to chemistry (up to +0.006 mol/s). But the most interesting evidence of *Fig. 2* is the possibility to exceed ozone consumption rate by the engine, if one could augment the exit mole fraction of OH by two orders of magnitude. If so, the jet would turn to be an ozone generator. Of course, this fact does not mean that all will be all right with the other exhausted species on the global atmosphere scales and time intervals.

(4) In the *3D far wake* model the numerical results for distribution of species exhausted by the engines and entrapped by the velocity field of two parallel vortices are shown in *Fig. 3a*. The back sight distribution of total water concentration (vapour plus liquid water) is presented for two cross sections of the wake (in this case the scale for x-axis is equal to $L_x = 4600$ m). The input set of parameters corresponds to the perspective Russian SST-2 [7] fueled with hydrogen: weight G=225 tons, wing span $b = 54$ m, $r_a = 0.87$ m, u_a= 1000 m/s, $T_a = 417$ K, $c_a^{H_2O} = 4.55 \cdot 10^{-2}$, the flight conditions (at altitude ~ 18 km) are $\rho_\infty = 0.12$ kg/m^3, $T_\infty = 216.7$ K, $c_\infty^{H_2O} = 2.61 \cdot 10^{-6}$.

The system of coordinates is connected with the middle point ($\eta = 0$, $z = 0$) between two descending trailing vortices, so aircraft is gradually lifting in this system, the vortex core centers (0, ±1) remaining immovable. Finally, in *Fig. 3b,c* the scattering densities ~ na^6 at the wake section $\tilde{x} = 0.5$ in vertical and horizontal scanning are shown. The signal level is normalized by its maximum value.

The authors are thankful for financial support of the work by the International Science and Technology Center (in the frame of the Project 200). We are especially grateful to the Technical Program Committee of the International Colloquium "Impact of Aircraft Emissions upon The Atmosphere" for granting our participation in the meeting.

1. Stolarski R.S., Wesoky H.L. NASA's high-speed research program: a status report on the atmospheric effects of stratospheric aircraft, Int. Symp. on Space, Aeronautics and Atmospheric Environment, ANAE, Toulouse, France, 1994.
2. Ramaroson R.A., Louisnard N. Potential effects on ozone of future supersonic aircraft – 2D simulation. Ann. Geophys., 1994, 12, p. 986–995.
3. Schumann U. On the effect of emission from aircraft engines on the state of the atmosphere. Ann. Geophys., 1994, 12, p. 365–384.
4. Miake-Lye R.C., Martinez-Sanchez M., Brown R.C., Kolb C.E. Plume and wake dynamics, mixing and chemistry behind HSTC aircraft. J. Aircraft, 1993, 30, p. 467–479.
5. Stasenko A.L. Contribution to the theory of chemisorption of nitrogen oxides by water drops in a jet of stratospheric aircraft. Preprint of TsAGI, N 51, 1991, 36 p. (in Russian).

6. Vasenin I.M., Arkhipov V.A., Butov V.G., Glazunov A.A., Trofimov V.F. Gasdynamics of two-phase flows in nozzles. Tomsk, Ed.: Tomsk University. 1986, 264 p. (in Russian).
7. Vasiliev L.E., Popov S.I., Svishchev G.P. Supersonic civil aircraft of the second generation. Air Fleet Technology. 1994, N 1-2, p. 14–17.

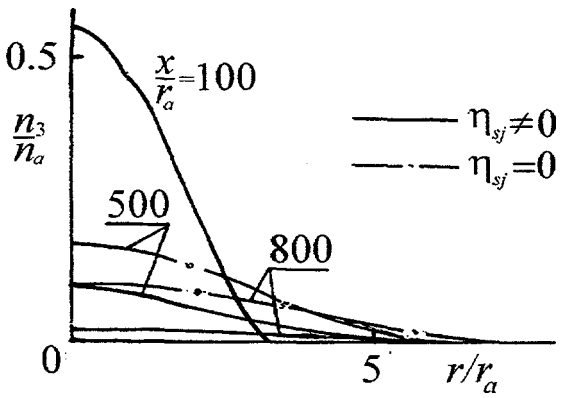

Fig.1a – Distributions of major fraction number density

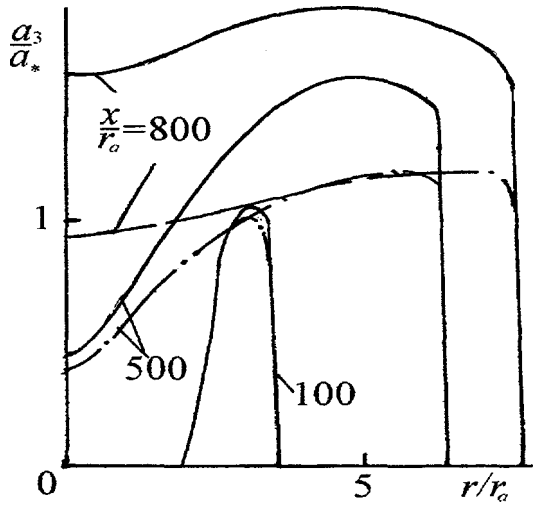

Fig.1b – Distributions of drop radius

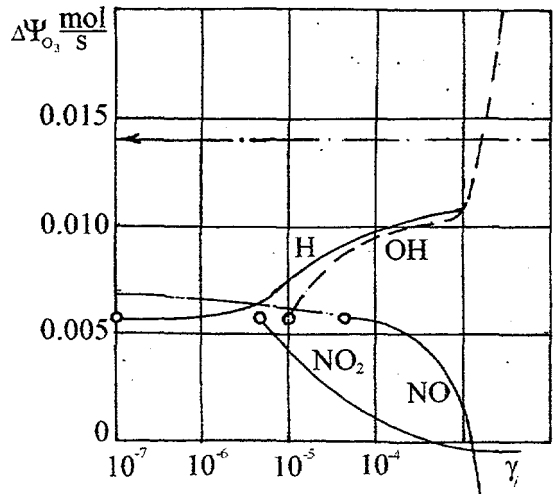

Fig.2 – Influence of exhaust chemical content on ozone

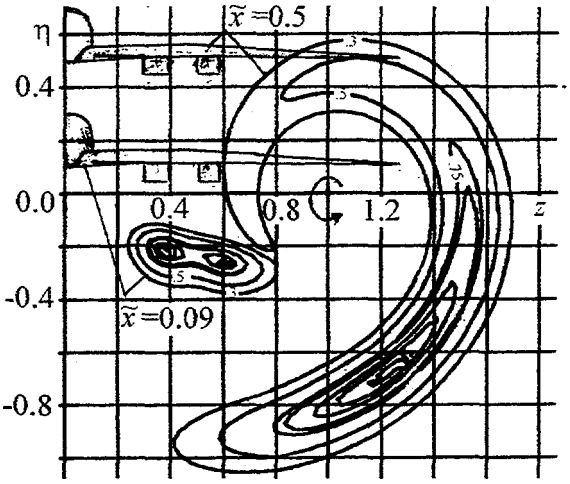

Fig.3a–Distribution of total water concentration in the flow field of two parallel vortices

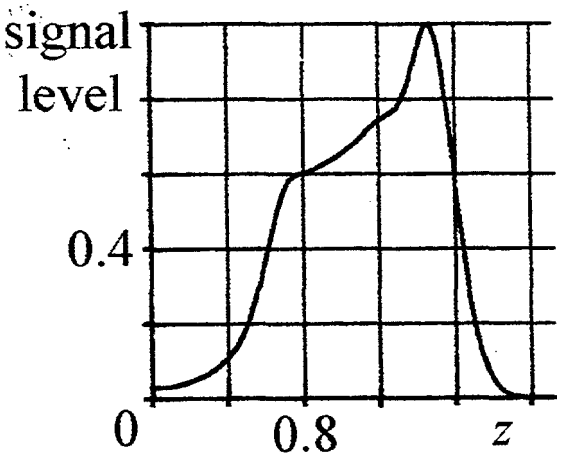

Fig.3b – Scattering density in vertical scanning

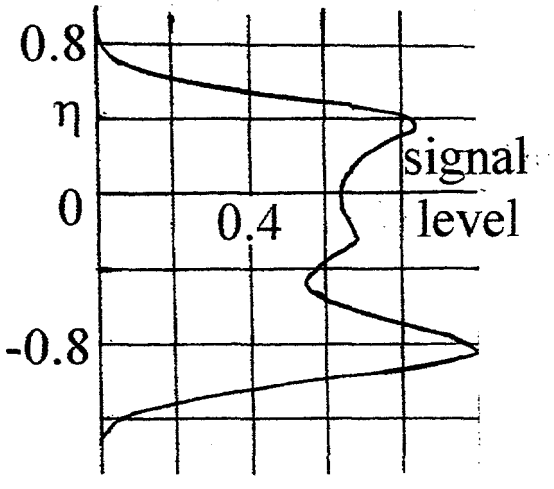

Fig.3c – Scattering density in horizontal scanning

Numerical modelling of the internal mixing by coagulation of black carbon particles in aircraft exhaust

Sofia Ohlsson and Johan Ström

Department of Meteorology, Stockholm University
S-106 91 Stockholm, Sweden

1. Introduction

When exhaust gases from an aircraft engine mix with ambient air the humidity may reach water saturation and water droplets will form on the available cloud condensation nuclei (CCN). These droplets then freeze to ice particles and form a visible trail, a so called condensation trail or contrail. Depending on the ambient conditions the contrail may remain visible for a long time or evaporate quickly. It is still not resolved if the CCN, on which the cloud droplets form, are mainly particles present in the ambient air or particles emitted by the aircraft. In the exhaust from a jet engine the particles are believed to consist mainly of black carbon (BC) and sulfate [1]. Sulfur in the fuel is oxidized to SO_2 in the combustor and a fraction of this gas will react in the exhaust to form sulfuric acid, which eventually condenses to form aerosol particles [2]. The BC particles are the result of unburned hydrocarbon compounds in the exhaust and consist of more than 90% carbon. Pure carbon particles are hydrophobic and will form CCN only under high supersaturation. This means that the BC particles are unlikely to contribute to the CCN population in the exhaust unless they upon mixing with water-soluble material transform into "new" particles that are more hygroscopic and can act as CCN. This pathway is supported by measurements made by Parungo et al. [3] and Lammel and Novakov [4]. Parungo et al. found that BC particles coated with sulfuric acid might provide a source for CCN and the measurements by Lammel and Novakov showed that the hygroscopicity of BC particles from diesel combustion in diffusion flames increased when a sulfur containing compound was added to the fuel. Also studies from Wyslouzil et al. [5] suggest that, depending on how the H_2SO_4 is distributed between the BC particles and the sulfuric acid particles (formed by homogeneous nucleation), the fraction of carbon particles that act as CCN could be significant. The transformation of particles due to mixing of two different compounds, in this case of soluble and insoluble material, may take place through; gas-to-particle conversion directly during combustion, condensation of soluble material on insoluble particles or by coagulation between soluble and insoluble particles.

The aim of this paper is to study, with the help of a numerical model, how a two-component aerosol (i.e. BC and sulfate) in an exhaust trail may be transformed in terms of hygroscopicity by coagulation mixing and how this may depend on the sulfur content in the fuel.

2. The model

2.1. Model description

For the simulation of mixing by coagulation a numerical model described by Ström et al. [6] was used. The two component (soluble and non-soluble) aerosol in the model is initially externally mixed. The number density distributions of the two components are approximated by 46 discrete radius intervals or size classes in the radius range 0.000891 μm to 35.48 μm. Each size class is characterized by its geometric mean radius. The aerosol size distribution composed of

a mixture of the two compounds is actually described as a two dimensional field, where the number density function is dependent on the particle size and the size of the non-soluble particle.

In the original model the Cunningham slip correction factor was assumed only to be pressure dependent. In this study, however, we used a different expression for the slip correction that is both pressure and temperature dependent [7]:

$$S_c = 1 + \lambda / r\,(1.246 + 0.42 \exp(-0.87\, r / \lambda) \qquad (1)$$

where r is the radius of the particle and λ is the free mean path of the gas (in this case the air), given by [8]

$$\lambda = k\,T / (2\,\pi\, d_m\, p) \qquad (2)$$

k is the Boltzmann constant, T the temperature, p the pressure and d_m the mean molecular diameter.

2.2. Model input parameters

The model is simulating the emissions from a jet aircraft, flying on a pressure level of 300 hPa at an ambient temperature of 225 K. Its cruising speed is 250 m s^{-1} and the fuel consumption is 2500 kg per hour. We assume the shape of the BC size distribution to be fixed immediately behind the engine. Thus, the number of particles is determined by the so called emission index for BC, EI_{BC}, which is the mass in grams of BC formed per kg fuel burned. The value of EI_{BC} depends on, among other things, engine type and power setting, but in this study we used a fixed EI_{BC} value of 0.02 g kg^{-1}. Two different shapes of initial BC distribution was used: one monodisperse distribution with particles of 0.0158 μm radius, (referred to as BC1), and one log-normal distribution with r_g=0.0158 μm and σ=1.5 [9], [10] (referred to as BC2).

Kärcher et al. [11] suggested on basis of model studies of binary H_2SO_4 / H_2O nucleation in contrails, that sulfur dioxide will oxidize to sulfate and form particles through gas-to-particle conversion even after the plume onset. In total a fraction of 0.5% of the fuel sulfur will have converted to sulfate. This value is consistent with measurements by Reiner and Arnold [12] and is also used in our calculations. However, in our model we assume all sulfate particles to form immediately behind the engine (as for the BC particles). This deviates most likely from reality but enables us to but an upper bound on the mixing by coagulation. The size distribution for sulfate particles in the aircraft exhaust is not well known, thus the shape had to be assumed. In order to get a fell for the sensitivity, we tried two different shapes both with small particles and narrow distributions having the following log-normal parameters: r_g=0.00158 μm and σ= 1.3, and r_g=0.00251 μm and σ= 1.4, referred to as S1 and S2, respectively. With the parameters given above the number concentration of sulfate particles is given by the sulfur content in the fuel. This content in jet fuels is typically 100 - 2000 ppm by mass [13]. One of the aims of this study is to examine whether there is any significant difference in particle coagulation for low or high sulfur content in aviation fuel, why we run the model for 100 ppm(m) (case 1a, 2a and 3a) and 1000 ppm(m)(case 1b, 2b and 3b). The different cases are summerized in Table 1.

Other parameters that influence the particle concentrations in the wake of the aircraft are: the aircraft speed, fuel consumption, and the dilution and mixing with the background aerosol in the ambient air. Since this later process was not included in the original model it had to be added. The growth of the cross section area during a time increment dt is estimated from model results by Gierens [14], suggesting the cross section area of the plume to increase from $5 \cdot 10^4$ m^2 to roughly $40 \cdot 10^4$ m^2 in 30 min corresponding to about 200 m^2 s^{-1}. The diluting air is, however, not particle free, and therefore an amount of the background aerosol corresponding to the dilution must be added to the particle population at each time step. This distribution was taken as the sum of two log-normal distributions Ström et al. [15]. The background aerosol is assumed to be soluble, and thus added to the sulfate size distribution.

Table 1. Case descriptions.

Case	Black carbon distr.	Sulfate distr.	EI_{BC} ($g\ kg^{-1}$)	Sulfur (ppm(m))
1a	BC1	S1	0.02	100
1b	BC1	S1	0.02	1000
2a	BC2	S1	0.02	100
2b	BC2	S1	0.02	1000
3a	BC2	S2	0.02	100
3b	BC2	S2	0.02	1000

4. Results

The results show similar properties for the different size distributions (of sulfate particles), why we only will show the results for case 2a and 2b.

As seen in *Fig. 1* (case 2a) the number concentration of mixed particles reach a maximum after about 0.1 s plume age. At this point the source of mixed particles through coagulation and the reduction in number concentration through dilution by plume dispersion are equal. After this short time period the number concentration of the mixed particles begins to decrease and the mixing of particles by coagulation should become less important. This can also be seen in*Fig. 2*, where the number concentrations are normalized with the cross section area of the plume. After only 2 s the mixed particles have reached 50% of an asymptotic value of about 10^{12} particles per meter.

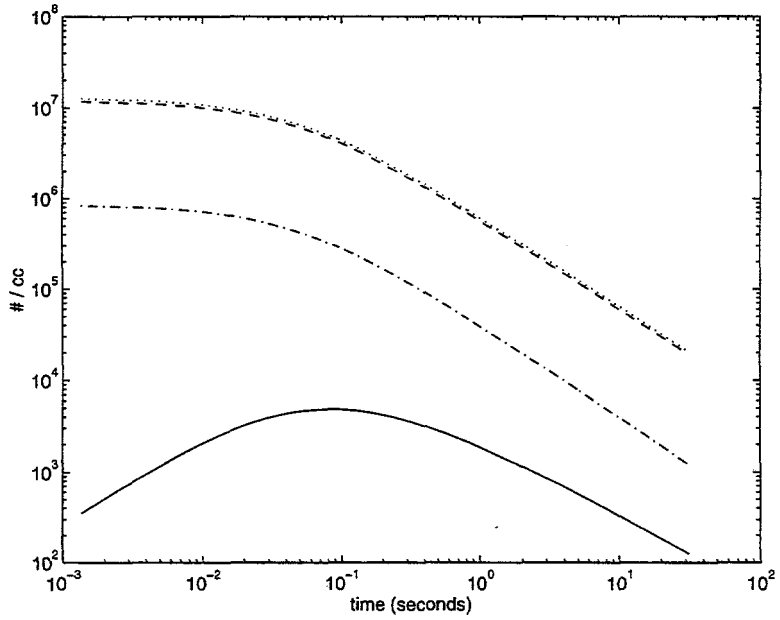

Fig. 1 - Number concentrations as a function of time; mixed particles (solid), BC particles (dashed-dotted), sulfate particles (dashed) and total pa ticle concentration (dotted line).

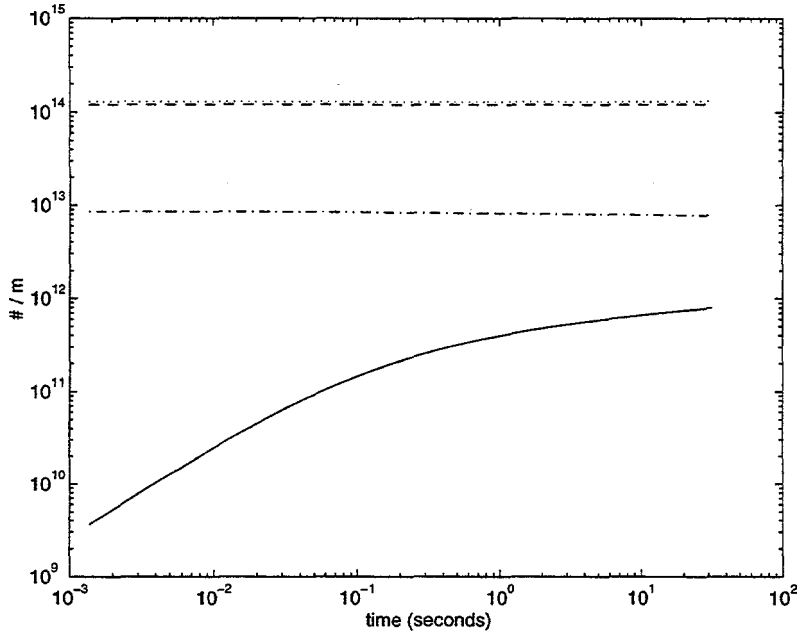

Fig. 2 - Number concentration normalized with the cross section area of the plume; mixed (solid), BC (dashed-dotted), sulfate (dashed) and total particle concentration (dotted line).

Fig. 3 shows the number fraction of each of the three types of aerosols (sulfate, BC, and mixed) after 30 s. The aerosol smaller than 0.004 μm and larger than 0.04 μm consist mainly from sulfate particles, and the aerosol in the size range in between (i.e from 0.004 to 0.04 μm) consist mainly from BC particles. The mixed particles form only a small fraction of the total particle number concentration (0.6 %). The mixed number fraction shows two maximums around 0.025 μm and 2 μm radius, respectively. The small particles are composed by a large fraction of BC and a very small fraction of sulfate, while the conditions are the opposite for the larger particles (a very large fraction of sulfate and a little fraction of BC). The geometrically averaged volume fraction of BC as a function of particle size is presented in *Fig. 4*. Note that for a given particle size, the volume fraction of BC may be different for different particles.

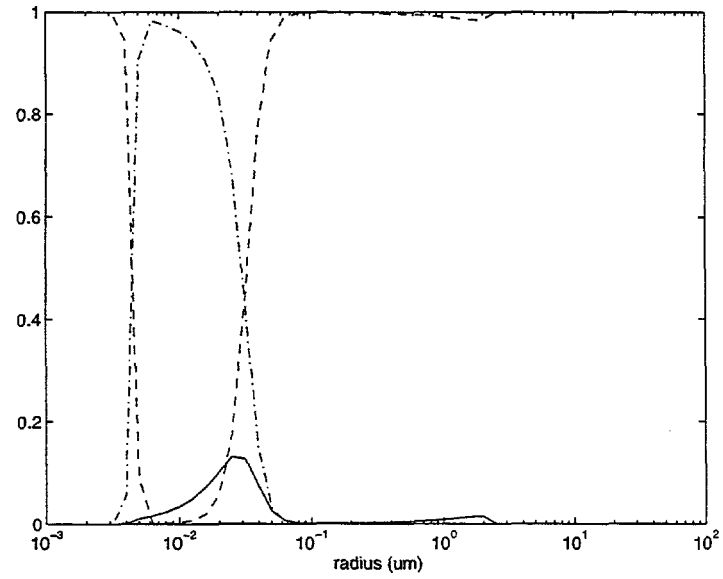

Fig. 3 - Number fraction of the three aerosol types; mixed (solid), BC particles (dasehed-dotted) and sulfate particles (dashed line).

The high sulfur case 2b (1000 ppmm sulfur) show qualitatively the same features as case 2a. The main differences are that the number concentration of sulfate particles increases with increasing sulfur content, which lead to a higher number fraction of mixed particles around 0.025 μm. The number fraction of mixed particles around 2 μm remain unaffected by the change in sulfur content. These mixed particles are a result of BC particles coagulating with the ambient aerosol. The total number of mixed particles are proportional to the change in sulfur content and reach about 10^{13} particles per meter.

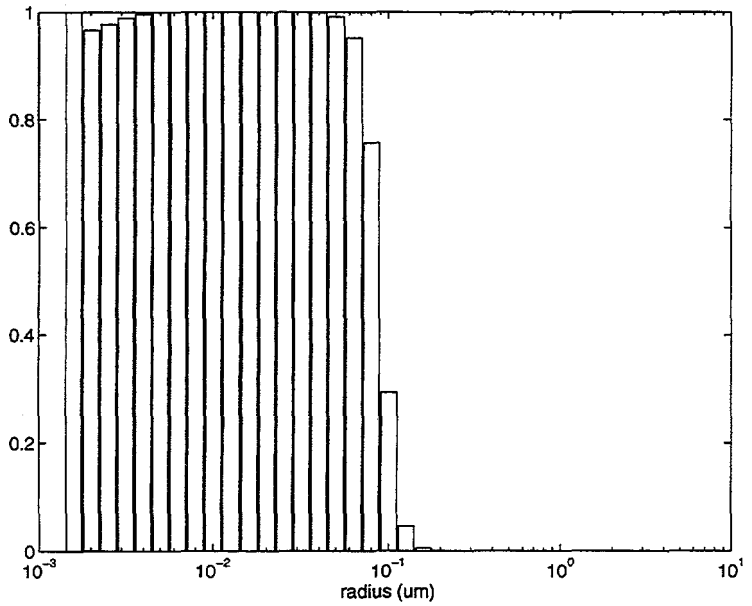

Fig. 4 - Geometrically averaged volume fraction of BC in mixed particles as function of particle size.

5. Summary

Although our treatment of the initial aerosol is crude and we consider only one type of process in the model the results are enlightening.

* The coagulation process is important during a very short time period on the order of a few seconds.
* Our choices of size distribution for the sulfate and BC particles formed in the exhaust seems to be of little importance for the result.
* An increase in fuel sulfur content will lead to an increase in total number concentration, and the amount of BC particles that will take part in the coagulation process increases. Thus, the total number concentration of mixed particles also increase.
* The largest number fraction of mixed particles is found around 0.025 μm radius, while a smaller peak is found for particles around 2 μm radius.
* Even though the number concentration of mixed particles increase with increasing fuel sulfur content, the fraction of mixed particles in the size range 0.8 - 2.5 μm is unaffected by the sulfur content in the fuel.
* These particles may be very effective in forming cirrus clouds since the inclusion of an insoluble core can stimulate ice formation through immersion freezing.
* The mixed particles formed by coagulation constitutes only a very small fraction of the total number concentration in the plume (less than 1 %).

References

1. Schumann, U., J. Ström, R. Busen, R. Baumann, K. Gierens, M. Krautstrunk, F. P. Schröder and J. Stingl, In situ measurements of particles in jet aircraft exhaust and contrail for different sulfur-containing fuels, *J. Geophys. Res.*, 101, 6853-6869, 1996.
2. Fahey, D. W., E. R. Keim, E. L. Woodbridge, R. S. Gao, K. A. Boering, B. C. Daube, S. C. Wofsy, R. P. Lohmann, E. J. Hintsa, A. E. Dessler, C. R. Webster, R. D. May, C. A. Brock, J. C. Wilson, R. C. Miake-Lye, R. C. Brown, J. M. Rodriguez, M. Loewenstein, M. H. Proffitt, R. M. Stimpfle, S. W. Bowen and K. R. Chan, In situ observations in aircraft exhaust plumes in the lower stratosphere at midlatitudes, *J. Geophys. Res.*, 100, 3065-3074, 1995.
3. Parungo, F., B. Kopcewicz, C. Nagamoto, R. Scnell, P. Sheridan, C. Zhu and J. Harris, Aerosol properties in the Kuwait oil plumes: Their morphology, size distribution, chemical composition, transport and potential effect on climate, *J. Geophys. Res.*, 97, 15867-15882, 1992.
4. Lammel, G. and T. Novakov, Water nucleation properties of carbon black and diesel soot particles, *Atmos. Environ.*, 29, 813-823, 1995.
5. Wyslovzil, B. E., K. L. Carleton, D. M. Sonnenfroh and W. T. Rawlins, Observations of hydration of single modified carbon aerosols. *Geophys. Res. Lett.*, 22 1501-1504, 1994.
6. Ström, J., K. Okada and J. Heintzenberg, On the state of mixing of particles due to Brownian coagulation, *J. Aerosol Sci.*, 23, 467-480, 1992.
7. Walter, H., Coagulation and size distribution of condensation aerosols, *Aerosol Sci.*, 4, 1-15, 1973.
8. Wayne, R. P., Chemistry of atmospheres, (2nd edition). *Oxford University Press Inc., New York.*, 1993.
9. Burtscher, H., Measurement and characteristics of combustion aerosols with special consideration of photoelectric charging and charging by flame ions., *J. Aerosol Sci.*, 23, 549-595, 1992.
10. Whitby, K. T., Size distribution and physical properties of combustion aerosols. *Proceedings Carbonaceous Particles in the Atmosphere. National Science Foundation and Lawrence Berkely Laboratory*, 1979.
11. Kärcher, B., Th. Peter, R. Ottman, Contrail formation: Homogeneous nucleation of H_2SO_4/H_2O droplets, *Geophys. Res. Lett.*, 22, 1501-1504, 1995.
12. Reiner, T. and F. Arnold, Laboratory flow reactor measurements of the reaction $SO_2+H_2O+M-> H_2SO_4+M$: Implications for gaseous H_2SO_4 and aerosol formation in the plumes of jet aircraft, *Geophys. Res. Lett.*, 20, 2659-2662, 1993.
13. Busen, R. and U. Schumann, Visible contrail formation from fuels with different sulfur contents, *Geophys. Res. Lett.*, 22, 1357-1360, 1995.
14. Gierens, K. M., Numerical simulations of persistent contrails, *J. Atmos. Sci.*, In Press, 1996.
15. Ström, J., B. Strauss, T. Anderson, F. Schröder, J. Heintzenberg and P. Wendling, In-sit observations of the microphysical properties of young sirrus clouds, submitted to *J. Atmos. Sci*, 1996.

ENGINE JET ENTRAINMENT IN THE NEAR FIELD OF AN AIRCRAFT

F. GARNIER, L. JACQUIN, A. LAVERDANT

Office National d'Etudes et de Recherches Aérospatiales, 29 avenue de la Division Leclerc, 92 320 Châtillon- France

Abstract

A simplified approach has been applied to analyse the mixing and entrainment processes of the engine exhaust through their interaction with the vortex wake of an aircraft. ~~Our~~ These investigations are focused on the near field, extending from exit nozzle to the beginning of the vortex phase (*i.e.* to about twenty seconds after the wake is generated). This study is performed using an integral model and a numerical simulation for a two-engine large civil aircraft. The properties of the wing-tip vortices on the calculation of the dilution ratio (defined as a tracer concentration) have been shown. The mixing process is also affected by the buoyancy effect, but only after the jet regime, when the trapping in the vortex core has occurred. Qualitative comparison with contrail photography shows similar features. Finally the distortion and stretching of the plume streamlines inside the vortices can be observed, and the role of the descent of the vortices on the maximum tracer concentration has been discussed.

1. Introduction

The interaction of engine exhausts with the trailing vortices of an aircraft is an important topic for aviation impact on the atmosphere. Aircraft exhaust contains gases resulting from combustion, usually designated as major species (CO_2, CO, H_2O, NOx), associated with a number of minor effluents (like H_2SO_4, HNO_3...), in gas or solid phase. Several recent studies (Brown *et al.*, 1995, Taleb *et al.*, 1996) have shown the important part played by the system water vapour-sulphuric acid on the aerosol formation in the wake.

These emissions can lead to ice nucleation and growth processes that will form contrails in the atmosphere. These contrails may have an impact on the cloudiness and may modify the earth's radiative budget balance.

However, the origin of contrails remains unclear, even though this problem has received a large attention for many years (Appleman, 1953, Scorer and Davenport, 1970, Maxworthy, 1975, and Schuman, 1996). One of the causes is the lack of knowledge of accurate partial vapour pressures of different species (mainly water and sulphuric acid) in the wake vortex. So for assessing these local variables which control the dispersion and dilution of the aircraft emissions, we have had to investigate the mixing process throughout the wake. The effect of trailing vortices on the mixing and chemistry of the jet engine has been studied by several authors (Miake-Lye *et al.*, 1993 and Garnier *et al.*, 1996). But a detailed modelling of this phenomenon has never been accurately achieved.

In the present paper, we use an integral model and a two-dimensional direct simulation of convection-diffusion equation (2D-DNS) to investigate the evolution of the mixing along the wake of a typical large transport aircraft, extending from exit nozzle of the engine to the beginning of the vortex phase. Attention is concentrated on the evaluation of the surrounding mass flow (*i.e.* the vortical flow) which is radialy drawn towards the jet engine across its conical surface.

2. The nearfield interaction

The wake of an aircraft is composed of two counter rotating wing tip vortices. The vortical motion is generated by strong radial pressure gradients. One generally admits that the exhaust emissions are captured by the vortices. At the early stage of vortex formation, the axial velocities are appreciable in the core of the vortices. But the details of this flow are not well known. As shown by Jacquin and Garnier, 1996, if the jet is not too close to the vortex axis, it is initially almost insensitive to the details of the vortex flow. However, the axial velocities in the cores of the vortices decay more rapidly downstream than the tangential velocities. So, at least as a first approximation, the three-dimensional (3-D) vortices evolve in time to the two-dimensional (2-D) vortices (Govindaraju and Saffman, 1971).

For modelling purpose, it is useful to define three regions in the entrainment and mixing process : a nearfield jet regime, a deflection regime and a shearing regime. The nearfield jet regime is characterised by physical processes of usual co-flowing jets. For example, by means of the trajectory box model, Kärcher, 1995 has studied the expansion and cooling of the engine jets of a subsonic B 747.

The deflection regime corresponds to the entrainment of the jet engine towards the vortex core. From the studies on the jets in crossflow (Rodi, 1982, and Jacquin, 1994), one assumes that the two basic parameters are the jet specific momentum flux (for plumes there is an analogous quantity, the specific buoyancy flux) and the vortex flow velocity. So the exhaust jet flow is submitted to a balance of a centripetal force induced by the vortical motion and a inertial force induced by the specific momemtum flux at the exhaust. The buoyancy body force generated by the non-uniform density (*i.e.* temperature difference) is based on the Boussinesq approximation.

The shearing regime describes the shape of the plume submitted to the shearing processes. This mechanism takes place as soon as the vortical motion is significant across the plume surface. This occurs if the jet is sufficiently close to the vortex core, far behind the deflection regime.

3. Theoretical analysis

An integral model has been developed to take continuously into account the jet mixing during the first two regimes described above, *i.e.* up to its entrainment into the vortex core.

This approach is described in a Lagrangian framework and uses the control volume concept to integrate the conservation laws of mass, momentum and energy. The details of the basic equations are given in Jacquin and Garnier, 1996. The vortex wake is represented by the superposition of two gaussian vortices and it has been shown that the engine jets have a weak influence on global dynamics of the wake. The turbulent diffusion and its effect on the expansion and cooling of the jet is based on the Morton-Taylor-Turner analysis. This approach is generalised to account for the transversal shear generated by the vortical motion. Change in the mean concentration of a tracer in a jet is intimately tied to the rate of entrainment, i.e. the rate at which vortical ambient fluid is included within the jet boundaries. The expression of the entrainment function writes:

$$E = \tilde{\rho}\left[\alpha_s\left(V_s - \tilde{V}_s\right) + \alpha_n\sqrt{\tilde{V}_n^2 + \tilde{V}_b^2}\right]D$$

where subscript s, n and b denote respectively the velocity components tangential, normal and binormal to the jet path; D the jet diameter and ρ the density. The tilde is referenced as the ambient fluid. From experiments on coaxial gas jets (Forstall and Shapiro, 1950), the coefficient α_s is taken equal to 0.15. The value of α_n is close to one and is determined from experiments on the study of jets in a crossflow (Jacquin, 1994, Rodi, 1982).

After the integral model is run, the transport and dispersion of the polluant is analysed by solving the convection-diffusion equation in an eulerian framework. From Williams, 1985, it is convenient to introduce the dilution ratio Z (or the mixture variable) defined as a passive scalar which is initially assumed to have a value of one inside the plume and zero in the ambient air. This variable satisfies the following equation:

$$\rho\frac{\partial Z}{\partial t} + \rho v.\nabla Z = \nabla.(\rho D \nabla Z)$$

where D is the diffusivity of the scalar. The passive scalar field Z does not influence the flow dynamics. The velocity field is represented by the superposition of two Lamb-Oseèn vortices, with a descent (translation) velocity taken to $\frac{\Gamma}{2\pi d}$, where d denotes the separation between the two trailing vortices. By assuming the load distribution on the wing to be elliptic, d is given by: $d = \frac{\pi}{4b}$, where b denotes the wing span.

This simulation is performed in laminar case, using a Peclet number of the order of 600 based on the circulation $\frac{\Gamma}{\upsilon}$, or a Reynolds number because the Prandtl number is equal to 1. So, the laminar vortex core grows only by viscous diffusion. At high Reynolds number (flight conditions) the turbulence must be considered but its precise role is unclear. Furthermore Zeman, 1995 showed that the turbulence has a weak influence on the persistence and the growth of the vortices.

The computations are performed on a fine-grid of 601 × 601 nodes in order to resolve the details of the plume structure. The numerical method adopted here is an implicit finite-

difference scheme, developed by Peyret, 1983. A more complete description of this method is given in Laverdant and Candel, 1988.

3.1 Initial conditions

The aerodynamics aircraft parameters and flight conditions are described in *table 1* for a two engine civil transport aircraft: an Airbus A-330. The thermodynamics conditions at the exit of a typical engine are given in *table 2*. The initial vortex core radius is taken arbitrarily constant, equal to one meter. The computation with the integral model is stopped when the jet boundary encounters the vortex centre. There, the jet has become largely dominated by the shearing process. When the direct numerical simulation runs, a plume gaussian distribution of a scalar (dilution ratio) is introduced in the surrounding of two Lamb-Oseén vortices. The initial plume, shown in *figure 5a* , is such that 1% of effluent encounters the vortex centre. The gaussian plume width and amplitude are calculated from the integral model results.

Table 1: Parameters for the two engine Airbus A-330 study

Flight conditions: Altitude (km)	10
Ambient Temperature (K)	220
Ambient pressure (Pa)	0.24
Ambient density (kgm^{-3})	0.38
Span b (m)	60.3
Aspect Ratio	9.3
Wing surface (m^2)	361.3
Circulation $\Gamma(m^2s^{-1})$	540
Lift coefficient	0.5
Aircraft velocity (ms^{-1})	252
Engine/vortex centre (m)	14

Table 2: Thermodynamic conditions at the exit of typical engine

Nozzle Diameter Primary Flux (m)	0.6
Jet Exhaust Temperature (K)	480.3
Jet Exhaust Velocity	580

4. Results and discussion

In this study the wing-tip vortices of the A-330 are assumed fully rolled-up and the generation region is not taken into account by the modelling. *Figure 1* shows a large aircraft contrail observed from ground a few seconds after the passage of the aircraft. The feature of this observation depends strongly on the ambient relative humidity and temperature. If these values are low enough, in the early stage of the wake one only sees the ice crystals formed by the aircraft exhaust trapped in the vortex core. A qualitative comparison with the calculations of the tip-vortex/jet exhaust interaction using the integral method shows the deflection of the engine jet streamlines generated by the centripetal force.

Figure 2 depicts the effect of the buoyancy body force on the dilution ratio and temperature. These averaged variables, known as 'top-hat' variables are calculated with and without the buoyancy force. It is apparent that this force enhances the mixing but only after about three wing spans behind the aircraft. Then, the specific buoyancy flux becomes large enough to balance the jet specific momentum flux, when the trapping in the vortex core has occurred. It corresponds to the end of the jet regime defined in section 2. *Figure 3* denotes the results obtained when considering an isolated jet flow (*i.e.* without vortex) and an interaction with a single vortex and with the two wing-tip vortices. Comparisons show that the action of the counter rotating system increase the mixing and entrainment processes and make the deflection and trapping of exhaust jet more efficient than in a single vortex.

Figure 4 and *figure 5* show the results given by the numerical simulation of a convection-diffusion equation. The dilution ratio (considered as a tracer concentration) is calculated at different locations inside the wake vortex. The maximum tracer concentration (squares in *figure 4*) follows the exhaust hot plume throughout the wake. After twenty second plume age, the dilution ratio is the order of 10^{-4}. This value and the one calculated by a Large Eddy Simulation (Gerz and Kärcher, 1996, in this present issue) are in close agreement in the early stage of the wake. The rapid decrease of the dilution ratio at the initial plume centre shows the rapid distortion and entrainment of the exhaust emissions towards the vortex core (triangles in *figure 4*). *Figure 5 (a)* to *(d)* shows the evolution in time of the crossflow distribution of dilution ratio field. The drawing of the aircraft is shown for scale and does not represent the location relative to the wake. The entrainment and mixing processes in this case show a stretching and a distortion of the interface between plume and ambient air (*figure 5 b*), followed by a relatively large scale engulfment into the vortex core (*figure 5 c* and *d*). The vortices descent under mutual interaction and a part of the hot plume is trapped downward. This is the beginning of the detrainment process and the mixing is then driven by the descent velocity (see also the evolution of the maximum tracer concentration plotted in *figure 4*).

5. Conclusion

We have used an integral model and a direct numerical simulation of a passive tracer field to investigate the entrainment and mixing between the hot exhaust jet and the surrounding air. This analysis is performed in the near field of the wake vortex of a Airbus 330, up to about twenty seconds after the wake is generated. But it was expected that the mixing process in the early stage of the wake could modify the microphysical properties of the contrails at a later time.

The calculations of the dilution ratio have been compared with the results given by a more complete model: a Large Eddy Simulation. Comparison between the two models are in good agreement. However, our work is obviously limited to the near field regime.

Atmospheric effects (stratification, turbulence, shear) are not included in this study but dominate the dynamics and the mixing of the aircraft exhaust in the far field.

References

Appleman, H., 1953: The formation of exhaust condensation trails by jet aircraft. *Bull. Amer. Meteorol. Soc.* **34**, 14-20.

Brown, R. C., Miake-Lye, R. C., Anderson, M. R., Kolb, C. E. and Resh T. J., 1996: Aerosol dynamics in near field aircraft plumes. *J. Geophys. Res.* in press.

Forstall, W. JR. and Shapiro A. H., 1950: Momentum and mass transfer in coaxial gas jets. *J. App. Mech.*, 399-408.

Gerz, T. and Kärcher, B., 1996: Dilution of aircraft exhaust and entrainment rates for trajectory box models. *Impact of Aircraft Emissions upon the Atmosphere*. Paris, October 15-18 (in this issue).

Garnier, F., Baudoin, C., Woods, P., Louisnard N., 1996: Engine emission alteration in the near field of an aircraft. *Atm. Environment.* In press.

Govindaraju, S. P. and Saffman, P. G., 1971: Flow in a turbulent vortex. *Phys. Fluids* **14**, 2074-2080.

Jacquin, L., 1994: Phenomenological description and simplified modeling of the vortex wake issuing from a jet in a crossflow. *La Rech. Aéro.*, **2**, 117-133.

Jacquin, L. and Garnier, F., 1996: On the dynamics of engine jets behind a transport aircraft. In: *The Chararacterization and Modification of Wake from Lifting Vehicles in Fluids*, Trondheim (Norway), May 20-23.

Kärcher, B., 1995: A trajectory box model for aircraft exhaust plumes. *J. Geophys. Res.* **100**, 18835-18844.

Laverdant, A. and Candel, S., 1988: A numerical analysis of a diffusion flame-vortex interaction. *Comb. Sc. and Tech.* **60**, 79-96.

Maxworthy, T., 1975: The motion of aircraft trailing vortices. *J. Appl. Mech.* **42**, 2.

Miake-Lye, R. C., Martinez-Sanchez, M., Brown, R. C., and Kolb, C.E., 1993: Plume and wake dynamics, mixing, and chemistry behind a high speed civil transport aircraft. *J. Aircraft* **30**, 467-479.

Peyret, R. and Taylor, T. D., 1983: Computational Methods for fluid flow. Springer-Verlag, New-York, 68.

Rodi, W., 1982: Turbulent buoyant jets and plumes. *Pergamont Press.*

Schumann, U., 1996: Contrail formation from aircraft exhausts. *Meteorol.* Z., N.F. **5**, 4-23.

Scorer, R. S. and Davenport, L. J., 1970: Contrails and aircraft downwash. *J. Fluid Mech.* **43**, 451-464.

Taleb, D., McGraw, R., Mirabel, Ph., 1996: Microphysical study of aerosol formation in the wake of an aircraft. Submitted to *J. Geophys. Res.*

Zeman, O., 1995: The persistence of trailing vortices: A modeling study. *Phys. Fluids* **7**, 135-143.

Williams, F. A., 1985: Combustion Theory. 2nd ed., Benjamin Cummings Publ.,CA.

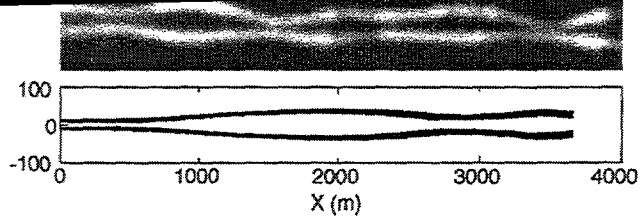

Fig.1 : Engine jets trajectory behind a typical large aircraft. Qualitative comparison with a contrail photography.

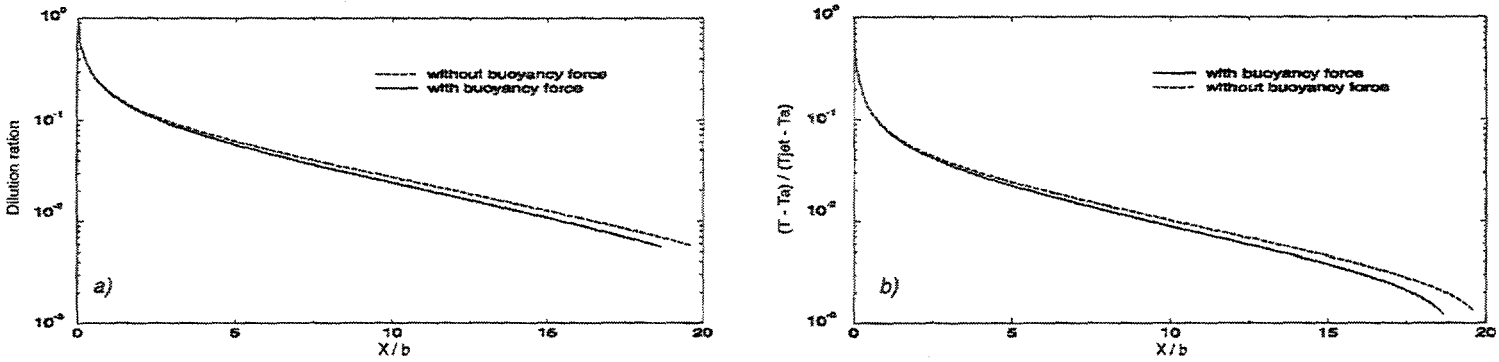

Fig. 2 : Effect of the buoyancy force on the dilution ratio (a) and normalized temperature (b), plotted versus x / b (b being the span) for a two-engine Airbus A-330. (using the integral model)

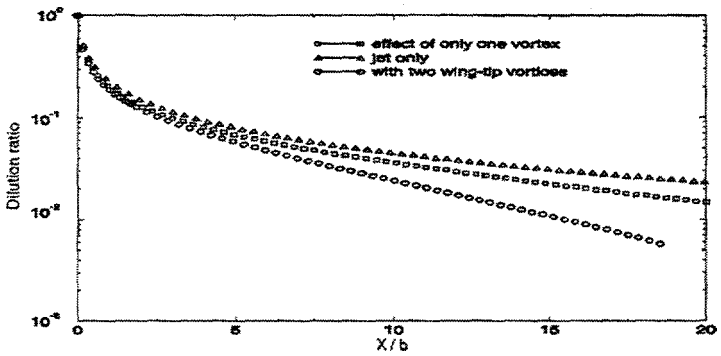

Fig. 3 : Wing-tip vortices effect on the dilution ratio, obtained using the integral model.

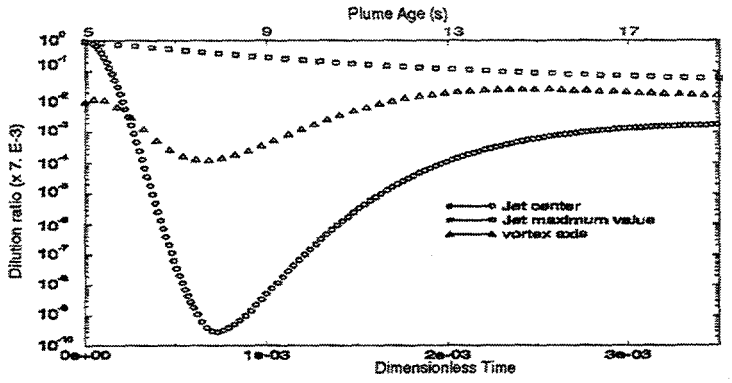

Fig. 4 : Dilution ratio profiles at different locations inside the wake vortex. (using 2D-DNS). The squares denote the maximum of tracer concentration

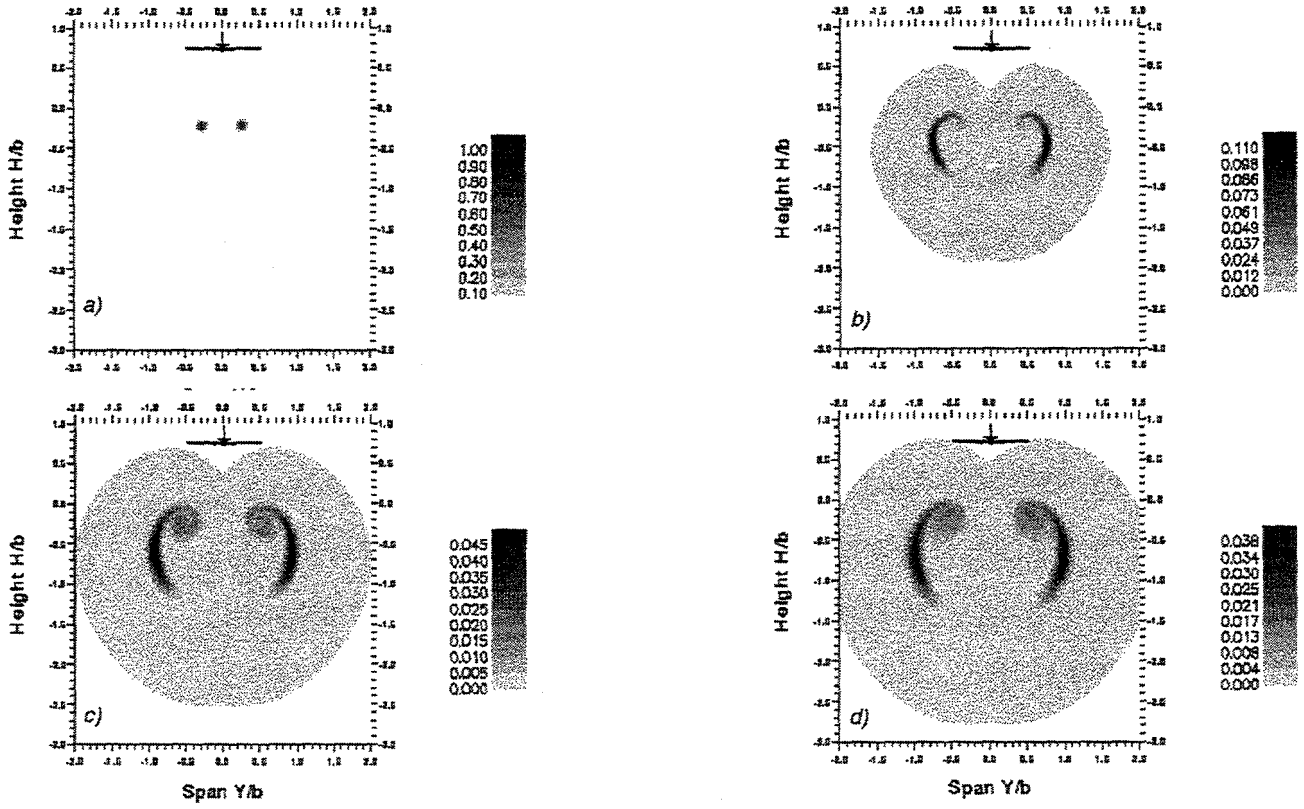

Fig. 5 : Direct numerical simulation of a tracer concentration (dilution ratio x 7. 10^{-3}) convected and diffused into the wake vortex. a) initial conditions calculated from integral method b) plume age 14 s c) plume age 22 s d) plume age 26 s

KINETICS OF CONTRAIL PARTICLES FORMATION AND HETEROGENEOUS REACTIONS ON SUCH PARTICLES

M.N.Kogan, A.V.Butkovsky, A.I.Erofeev, O.G.Freedlender, N.K.Makashev
Central Aerohydrodynamic Institute (TsAGI)
Zhukovsky, Moscow Region, 140160 Russia

The research of impact of aircraft emissions upon the atmosphere is a very complex and difficult problem. More than two decades of intensive investigations of the problem of ozone decay do not permit to make definite conclusions. Many important problems still remain unsolved in the aircraft/atmosphere interaction: engine, nozzle, jet, jet/vortex system interaction, vortex breakdown, contrail formation, meso-scale and global processes, their effects on climate. The particles formation and heterogeneous reactions play an important role in some of these processes. ~~The present report is devoted to~~ these problems, are discussed.

1. CONDENSING PARTICLES INTERACTION.

In the paper [1] it was shown that condensing particles attract each other. It was shown also [2] that due to this effect the diameters of water particles in the process of coagulation in a jet of supersonic aircraft in stratospheric conditions become approximately two times larger (*Fig. 1*). In this figure d^* is a some characteristic value, x/r_a and r/r_a are normalized axial and radial coordinates with origin at the center of nozzle exit with radius r_a. The dashed-point lines are present results when coagulation was not taken into account, the dashed lines correspond to the case when coagulation without attracting forces was taken into account and solid lines show the results with attracting forces. This result was obtained for free-molecular conditions, i.e. when Knudsen number $Kn_d=\lambda_\infty/d$ (λ_∞-molecular free path at the infinity, d-particle diameter) is large. This report presents an example of Monte-Carlo direct simulation(DSMC) results for smaller Knudsen number. It is seen that attracting force increases when Knudsen number decreases (*Fig. 2*).

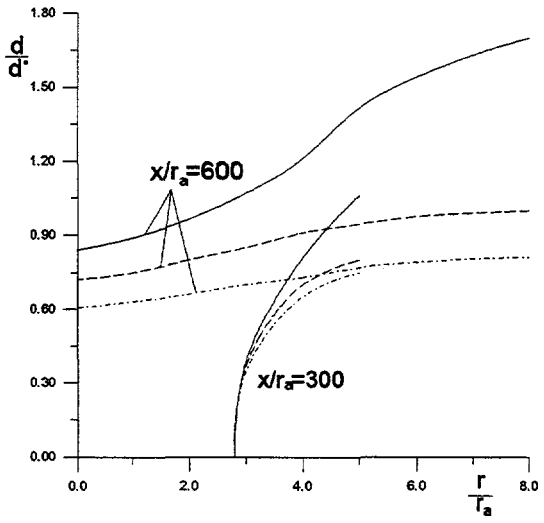

Fig. 1 - Particles size in a jet.

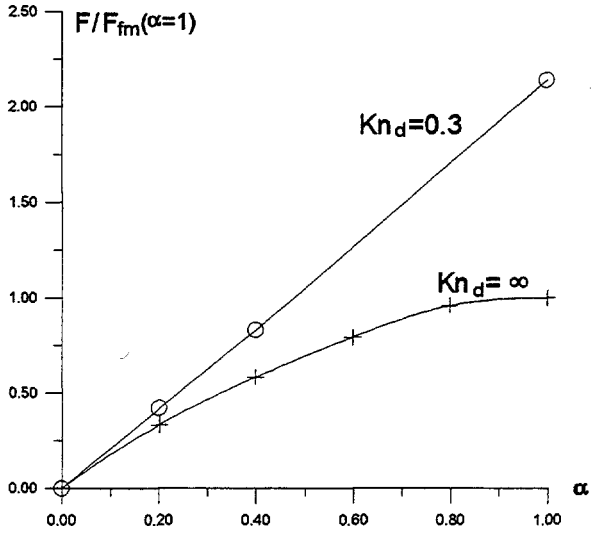

Fig. 2 - Attractive force between two condensing spheres.

Here the attraction of the two spherical particles with equal diameters is considered; the distance between centers of the particles l=2d, α is the condensation coefficient. The case

of strong supersaturation is considered. This result was obtained for the gas phase consisting of the water vapor only. In the real jet or in a contrail water vapor is only small part of a complex mixture. In a free molecular case realizing in a jet of stratospheric aircraft, each gas of the mixture interacts with particles independently - so that the curve $Kn_d=\infty$ in *Fig. 2* valids also for a mixture. At smaller Knudsen numbers collisions of water molecules with other molecules of the mixture prevent water molecule interaction with particles. Due to this the above mentioned effect of attraction becomes weaker. The solution of this problem is in progress now.

2. CONDENSATION IN POROUS MEDIA.

The second problem is concerned with the porous structure of the ice particles. Quite a little is known about the morphology of the ice in the atmosphere. Even less is known about the structure of the ice particles formed at nonequilibrium conditions of jets or contrails. However, many laboratory experiments indicate that the ice films have porous structure [3]. It is important to know the total surface area and fraction of it available for reaction(condensation, evaporation, chemical reactions). To obtain some insight into the problem a simple 2D porous model is considered. This model consists of infinite number of the plane channels with absolutely thin walls (*Fig. 3*). Gas motion in channels is investigated for various Knudsen numbers $Kn_d=\lambda_\infty/d$, that is for various gas rarefaction or channel width, d. Far to the left and right from the ends of channels (strictly speaking at the infinity) there are uniform flows with Maxwellian molecule velocity distribution function. In calculations presented here the temperature of these flows T_∞ was taken equal to the temperature of the channel walls T_w. There are transition layers (TL) between this uniform flows and flows at the entrances of the channels. The interaction between the channels takes place in these transition layers. To demonstrate the influence of this interaction the flow through porous model is considered first for a given pressure difference $\Delta p=kT_\infty\Delta n$.

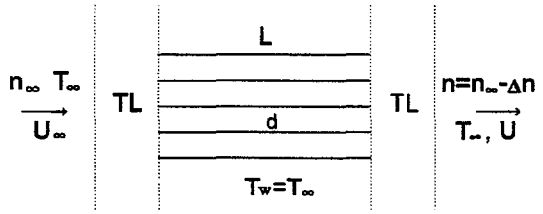

Fig. 3 - Plane porous bed model

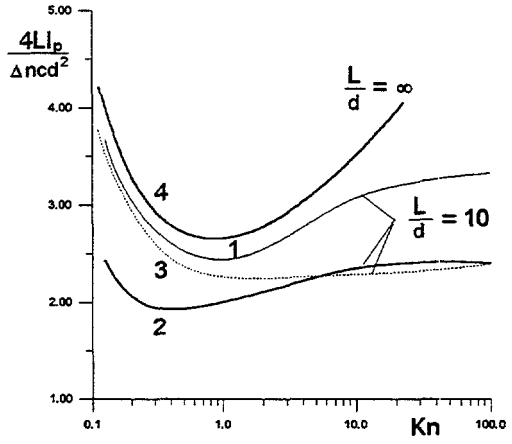

Fig. 4 - Gas flow through plane channel

The normalized molecule number flux through one channel against Knudsen number is shown in *Fig. 4*. For example the data are presented for L/d=10. Here $I_p=n_\infty U_\infty d$ is molecular number flux, $c=(8kT/\pi m)^{1/2}$ -mean molecular velocity, m-molecule mass. The curve 1 corresponds to the case when TL is taken into account. The curve 2 corresponds to the case when transition layers are ignored, i.e. it is supposed that at the ends of channel we have Maxwellian distribution functions with parameters n_∞, T_∞, $U_\infty=0$ and $n_\infty-\Delta n$, T_∞, U=0 for molecules coming into the channel. The curve 3 is calculated for the gas flow through the single channel which connects two vessels with different pressure [4]. The

curve 4 shows the result for classical Poiseuille flow in infinitely long channel [5]. The data comparison shows that neglection of transition layers gives us the error about 30%. The same error may arise in the interpretation of experimental data on accomodation coefficients measurements with the help of capillary sieve [6].

Let us now considere the flow caused by condensation on the plate walls of the channels. Let $\Delta n=n_\infty-n_e(T_w)$, where n_e is the saturation vapor molecular number density and n_∞ is the number density of the vapor at infinity on both sides of the porous model. The problem was solved by DSMC method for various values of condensation coefficient α equal to the evapotation coefficient γ, relative channel length L/d and various flow regimes(or Knudsen numbers). The solution was obtained for small value of supersaturation. For example the value of condensing gas flux is plotted against channel length and flow regime in channel(*Fig. 5*, $\alpha=0.1$). Here I_c is molecular number flux into one channel from one side of porous model. These data show that at $L/d\approx 20$ the condensing flow is stabilized, i.e. the flux doesn't increase at larger L/d values. It means that active surface increases no more. The asymptotic results at small value of α and Kn are agree with the numerical data.

3. EVAPORATION AND CONDENSATION COEFFICIENTS.

Accomodation coefficients are the third issue of the paper. Let I_l and I_i are the number of molecules leaving and impinging on the gas/condensed phase interface. It is supposed usually that

$$I_l = \gamma I_e(T_w) + (1-\alpha) I_i \tag{1}$$

where γ and α are evaporation and condensation accomodation coefficients, respectively, and

$$I_e(T_w) = \frac{P_e(T_w)}{\sqrt{2\pi m k T_w}} \tag{2}$$

i.e. saturation values of equal I_l and I_i at surface temperature T_w with $P_e(T_w)$ being the saturation pressure and k,m being the Boltzmann constant and mass of molecule. As at equilibrium $I_i=I_l=I_e(T_w)$ it follows from(1) that $\alpha=\gamma$. If one supposes that α and γ are functions of T_w only then $\alpha=\gamma$ for noneqilibrium conditions also. In this case evaporation rate can be presented as

$$R = I_l - I_i = \alpha(I_e - I_i) \tag{3}$$

as was assumed in section 2. Today values of α and γ can be obtained only experimentally. Even the well-known system of water vapor/ice gives us the wide range of α and γ values from 0.006 to 1(see references in [7]). It is occurred because different kinds of ice and different methods were used in different experiments. It seems that experiments described in [7] are the unique investigation in which coefficients α and γ for water vapor/ice system have been measured by the same technique. The conclusion made in the paper [7] is that α and γ are approximately equal. But there are objection against that conclusion. The most part of experiments in [7] were performed for "pure" condensation and "pure" evaporation. That means that one can neglect I_l in the first case and I_i in the second case. For "pure" evaporation

$$\gamma = \frac{R}{I_e(T_w)} \tag{4}$$

The ice thickness growth rates proportional to R were measured using optical interference technique. But to calculate I_e the quasi-equilibrium pressure(the vapour pressure at R=0, $T_w\neq T_g$, where T_g is the temperature of vapour) P_g was used in eq.(2) instead of saturation pressure $P_e(T_w)$. But the difference between these values should be taken into account. *Fig .6* displays the difference of data with $P_e(T_w)$ taken from paper [8] and P_g -from [7].

Now, for example, if we use in eq.(4) the saturation pressure value given in the *Fig. 6* at Tw=185K we obtain γ=0.27 instead of value γ=0.63 obtained in [7] using P_g. Of cause we can not insist on presented particular values. The types of ice can be different and measurements can be carried out by different techniques. But the presented example shows a great probability to meet situations with unequal α and γ coefficients.

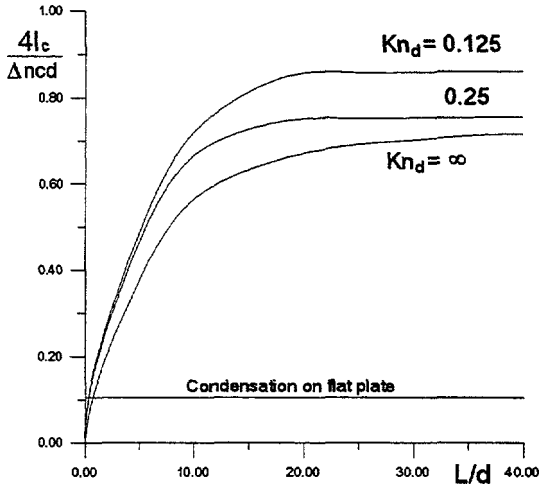

Fig. 5 - Flux due to condensation on the walls of channels

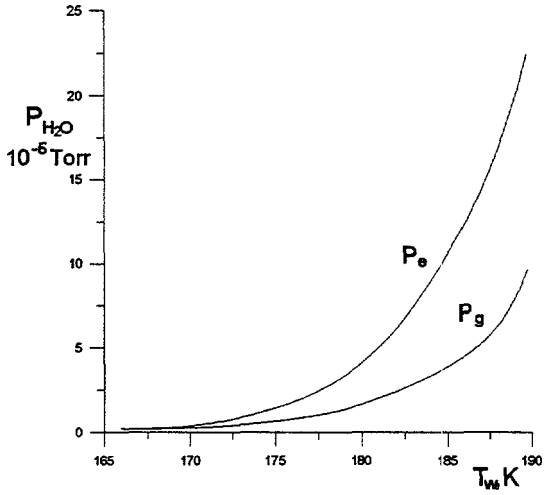

Fig. 6 - Dependences of saturation pressure and gas pressure on the wall temperature.

The solution of the Boltzmann equation in the Knudsen layer connects flow parameters at the outer boundary of this layer with condition on the surface. The relations in a general case have the following form

$$\frac{n}{n_e(T_w)} = \phi(M,\alpha,\gamma),\ T/T_w=\psi(M),\ 0<M<1 \qquad \text{for evaporation}$$

$$\frac{n}{n_e(T_w)} = \phi_c(M,\alpha,\gamma,T/T_w),\ M<0 \qquad \text{for condensation}$$

Here n, T, M are the molecular number density,vapour temperature and Mach number at the outer boundary of the Knudsen layer; $n_e(T_w)=P_e(T_w)/kT_w$. These relations for $\alpha=\gamma=1$ can be found, for example, in [9,10]. To obtain the relations for a general case the approach proposed in [11] was used. Using this approach we obtain for evaporation

$$\frac{n}{n_e(T_w)} = \frac{\gamma\phi(M,1,1)}{\alpha+(1-\alpha)\phi(M,1,1)M\sqrt{2\pi\kappa\psi}} \qquad (5)$$

For condensation ϕ(M,1,1) must be replaced by ϕ_c(M,1,1,T/T_w). The obtained results show great sensibility of evaporation/condensation rates to values of accomodation coefficients α and γ. If, for example, we accept presented above value γ=0.27 instead of γ=0.63 we must have more than two times smaller supersuturation to obtain the same condensation rate, i.e. the same Mach number. Consequently very careful measurements of these coefficients are necessary.

4. CONCLUSION.

Only few kinetic fundamental problems are considered in this presentation. A large number of such problems one meets on each stage of the investigation beginning from

engine up to global scale problems. As it was shown above each one may introduce significant errors and the sum of them may drastically change the final conclusions.

ACKNOWLEDGEMENTS

The authors are thankful for financial support of the work by the International Science and Technology Center (in the frame of the Project 200) and the Technical Program Committee of the International Colloquium "Impact of Aircraft Emissions upon the Atmosphere" for granting our participation in the meeting.

REFERENCES

1. Kogan M.N., Bobrov I.N., Cercignani C., Frezzotti A. Interaction of evaporating and condensing particles in the free-molecular regime. Physics of Fluids,7,N7,1775-1781(1995).
2. Kashevarov A.V., Kogan M.N., Stasenko A.L. Influence of vapour condensation upon droplets coagulation in a jet of high-altitude aircraft. Proc. of 1st Intern. Conference on «Fundamental Research in Aerospace Science».Sept. 22-24(1994), in press.
3. Kolb C.E. et al. Laboratory studies of atmospheric heterogeneous chemistry. In «Progress and Problems in Atmospheric Chemistry», J.R. Barker,ed. World Scientific Publishing Co.,771-875 (1995).
4. Akinshin V.D.,Makarov A.M., Seleznev V.D., Sharipov F.M. Rarefied gas flow in plane short channel at arbitrary Knudsen number. Prikladnaya Mehanika i Tehnicheskaya Fizika,N5,48-53 (1989),(in Russian).
5. Ohwada T., Sone Y., Aoki K. Numerical analysis of the Poiseuille and thermal transpiration flows between two parallel plates on the basis of the Boltzmann equation for hard-sphere molecules. Physics of Fluids A,1,N12,2042(1989).
6. Akinshin V.D., Borisov S.F., Porodnov B.T., Suetin P.E. Experimental investigation of rarefied gas flows in capillary sieve at different temperatures. Prikladnaya Mehanika i Tehnicheskaya Fizika,N2,45-49 (1974),(in Russian).
7. Haynes D.R.,Tro N.J., George J.M. Condensation and evaporation of H_2O on Ice Surface. J. Phys. Chem.,96,8502-8509(1992).
8. Tschudin K. Die Verdampfungsgeschwindigkeit von Eis. Helv. Phys. Acta,19,91-102 (1946).
9. Kogan M.N. Kinetic theory in Aerothermodynamics. Prog. Aerospace Sci.,29,271-354(1992).
10. Kogan M.N. Evaporation/Condensation kinetics. Harvey J. and Lord G., Eds., Rarefied Gas Dynamics,253-262,Oxford University Press(1995).
11. Kogan M.N., Makashev N.K. The role of the Knudsen layer in the theory of surface reactions. Izv. Akad. Nauk SSSR, Mech. Zhidk. i Gaza,N6,3-11(1971), (in Russian). See also: Fluid Dynamic,6,913(1971).

Numerical modelling of the Concorde wake during ZEBRE

Klaus Gierens

DLR, Institut für Physik der Atmosphäre,
Oberpfaffenhofen, Germany

Abstract

Numerical simulations of the Concorde contrail during the ZEBRE experiment have been performed. ~~It is~~ The main goal of the simulations to reproduce the fast vanishing of the contrail which disappeared 20-30 s after exhaust. It is difficult to evaporate ice crystals during the jet and vortex phase of the aircraft wake, when the exhaust products are trapped in the vortex cores. The trapping also excludes spatial dispersion of the ice crystals as an explanation of the short contrail lifetime. The disappearance of the contrail within 20-30 s requires that a substantial part of the exhaust gases escapes from the region that is lateron trapped in the vortex cores.

1. Introduction

The project ZEBRE was one flight of the Concorde during the SESAME campaign of winter 94/95. The flight took place on 30 January 1995 from Paris northward along the western coast of Scandinavia to about 70°N latitude and back. Objectives of ZEBRE were to determine: contrail evolution, horizontal and vertical diffusion, particle dimensions (size distribution, shape, surface area) and nature (type, phase), thermodynamic time constants, sedimentation, etc. The idea behind this effort was to see whether water vapour, exhausted by supersonic aircraft at high altitude in the cold winter stratosphere with typical background humidity close to saturation, would condense and then provide sites for heterogeneous chemical reactions with the possibility of catalysing ozone loss.

In order to aid physical interpretation of the observational results obtained during the ZEBRE experiment, numerical modelling studies of the Concorde wake were performed. A disappointing feature of the experiment was the short lifetime of the (visual) contrail which did not exceed 30 s. Contrary to the expectation, the stratosphere was much drier (rel. humidity 5% relative to liquid water) than necessary for ice saturation. There are two possibilities for the disappearance of the contrail: evaporation of the ice crystals or their spatial dispersion via the downward travelling vortex pair. The explanation of the quick disappearance of the Concorde contrail is the goal of the present contribution.

2. Setup of the experiments

For the simulations, the Large-Eddy model MESOSCOP [1] including bulk cloud microphysics [2] has been applied. The microphysics scheme has been adapted for contrail simulations [3]. The model is run in a 2-D mode (cross section through the wake) with high spatial (1.75 m) and temporal (0.02 s) resolution. The initial wake (computed by T. Gerz, DLR) is approximated by a pair of Lamb vortices with a circulation of 595 m^2s^{-1} each, which leads to sinking of the wake with 4.7 m/s. The wake is situated at about 16 km altitude at an ambient pressure of 85 hPa and a temperature of -71°C. The initial flow field (corresponding to 4.7 s after exhaust) is shown in *Figure 1*. The atmospheric profiles of temperature, wind, and humidity were obtained from a balloon measurement (Andoya, 30 Jan 1995, 1847 UTC). The simulation pursues the wake evolution for 30 s since the contrail got invisible about 20 - 30 s after exhaust.

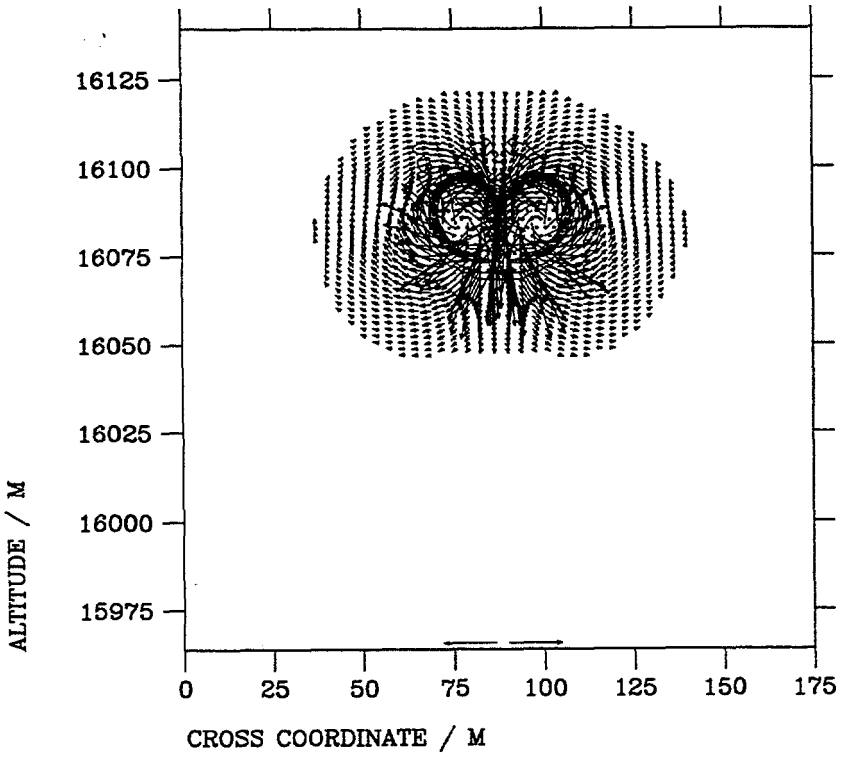

Fig. 1 - Initial flow field (arrows) and ice distribution (contours and stipples). The arrows at the bottom indicate a velocity of 10 m/s. The initial state for the present simulations refers to a time 4.7 s after exhaust.

Assuming an emission index of 1.225 kg water vapour per kg fuel, a speed of 591 m/s, and a fuel flow rate of 5.14 kg/s (from Air France data), one yields an exhausted amount of M_{H2O}=10.6 g water vapour per meter of flight path. However, without a detailed modelling of the nucleation and depositional ice crystal growth in the jet immediately behind the exhaust, the resulting partition of the emitted water into vapour and ice is unknown. An analytical thermodynamic calculation of the expansion-condensation trajectory of the moist exhaust air in the (e,T)-phase space, assuming maximum condensation, yields a transient maximum ice content of 8.36 g/m in the plume, which is reached when the plume temperature is -64 °C. The simulations, however, start at a later time, when the ice mass is already decreasing because of decreasing total water mixing ratio. The plume ice content is then less than 7.5 g/m, even with maximum condensation assumed for the initial jet phase. Also the number of ice crystals in the wake is unknown. Fahey et al. [4] determined an emission index for non-volatile particles of $2\text{-}9\times10^{16}$ per kg of fuel in the plume of a Concorde. It may further be estimated that the soot particle emission index is 2-20 times smaller [5]. If we assume that all soot particles trigger formation of an ice particle, then we may estimate a range of $0.9\text{-}39\times10^{13}$ ice crystals per meter of flight path. The higher of these numbers is probably unrealistically large, because then the mean size of an ice crystal would be of the order 0.2 μm which would give rise to a faint brown hue of the contrail [6], yet this was not observed. On the other hand, the lowest possible ice crystal number means a crystal size of the order 1 μm, which would yield a clearly visible hueless contrail. However, it should be noted that even a crystal number of 10^{13} per meter of flight path is about two orders of magnitude more than measured so far in contrails of commercial aircraft [7]. The evaporation of ice crystals is modelled via a Koenig-type parameterization [8], i.e. $dm/dt=am^b$, where m is the mass of an ice crystal in kg and $a=7.764\times10^{-7}(\rho_v - \rho_{sat,ice})/(\rho_{sat,ice} - \rho_{sat,liq})$ [kg/s] and b=0.65.

3. Results and Discussion

3.1. Complete trapping of water vapour

In order to cover the possible range of initial conditions (ice vs. vapour mass, number of crystals), simulations have been performed with M_{ice}=0.1 and 0.6×M_{H2O}, correspondingly M_{vap}=0.9 and 0.4×M_{H2O}, and N_{ice}=10^{13} and 10^{14} m^{-1} in the plume. For these four simulations identical spatial distributions of ice and vapour mass and number density of ice crystals were used (cf. *Figure 1*), where these exhaust products were distributed over an initial area of 1115 m^2. It turned out however, that with identical spatial distributions of vapour and ice, the ice cannot evaporate within 30 s. Instead, the ice content is growing.

In an open system with 5% relative humidity an ice crystal would evaporate fast: Having initially a mass of 10^{-14} g, it would loose 90% of it within 20 s or so. However, during the jet and vortex phase, a contrail isn't an open system. The emitted exhaust products are at least partially trapped in the vortex cores [9]. For the simulations this means that the initial ice particles are situated in an immediate environment with large ice-supersaturation. The ice-supersaturation reaches quite high values: 6 and almost 15 for the cases with M_{vap}=0.4 and 0.9×M_{H2O}, respectively. This is much more than known from simulations of the jet and vortex regime of subsonic airliners [10]. After 30 s, i.e. at the end of the simulations the supersaturation is used up almost completely since the ice crystals were growing during whole the simulation time. The ice mass reached after 30 s of simulation (about 5 g/m) depends only little on the initial ice vs. vapour partitioning and also little on the number of ice crystals in the plume. *Figure 2* shows the ice mass distribution for the case with M_{ice}=0.6×M_{H2O} and N_{ice}=10^{13} m^{-1} reached after 30 s of simulation. It is seen that the bulk of the ice is trapped within the vortex cores. But there is also a tail extending from the original emission altitude down to the current location of the contrail. This tail indicates that the exhaust material is not trapped completely inside the vortex cores. If a significant part of the exhaust products could during the early jet phase escape from the region that is later trapped in the vortex cores, the contrail could probably evaporate within 30 s from exhaust, as observed.

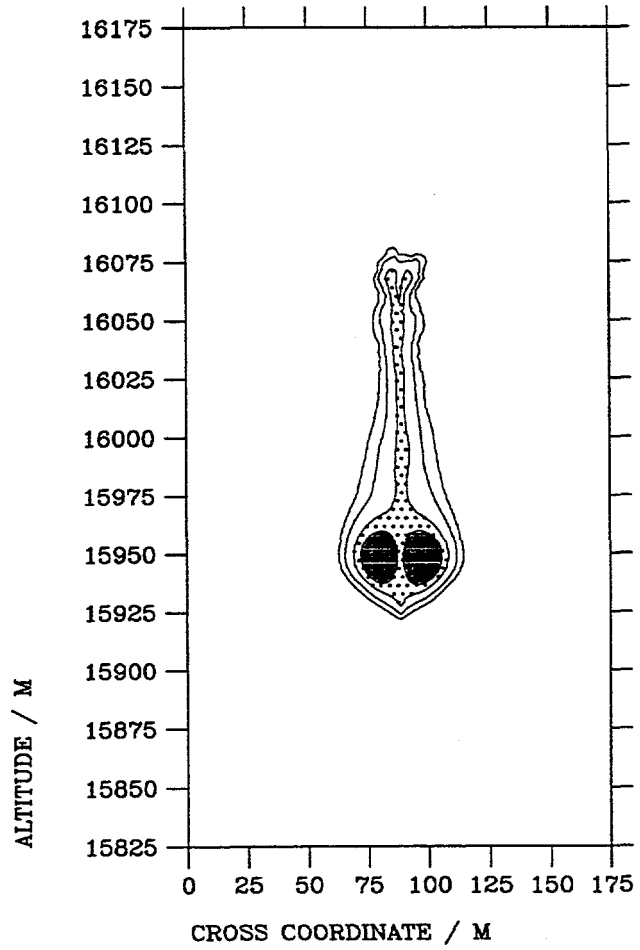

Fig. 2 - Contours of ice water content (IWC) reached after 30 s of simulation for a case with initially 6.4 g/m of ice and 10^{13} m^{-1} ice crystals in the plume. Ice and vapour share the same initial spatial distribution, i.e. they are confined to the core region of the lamb vortices. The exhaust material is almost completely trapped in the vortex system. This circumstance inhibits the complete evaporation of the ice. Instead, an equilibrium state with ice crystals in an ice saturated environment is approached. Contour values are 10^{-2}, 10^{-1}, 10^{0} (sparse stipples), and $10^{0.5}$ mg/m^3 (dense stipples).

3.2. Incomplete trapping of water vapour

Two additional simulations have been performed with M_{ice}=0.1 and 0.6×M_{H2O} and N_{ice}=5×10^{13} m^{-1} in the plume. For these experiments, the ice has been placed again inside the initial vortex core (area 1115 m^2), however, the exhausted water vapour was assumed to be only partially trapped in the vortex cores. It was instead equally distributed over an area of almost 20,000 m^2, which was selected using a kinetic energy criterion: the kinetic energy of the flow had to be at least one percent of its overall maximum in the vortex system where the exhaust vapour was distributed.

In the case with M_{ice}=0.6×M_{H2O} the ice crystals do not vanish completely within 30 s. At the end of the simulations there are still 1.81 g/m of ice in the plume, giving an optical depth τ of 0.62 in the visual wavelength region (the initial value of τ is 2.3 in this case), which is a far above the perception threshold of τ_{min}=0.02. In the other case with M_{ice} = 0.1×M_{H2O} , however, the ice evaporates completely and the optical depth reaches the perception threshold after 15 s of simulation, i.e. about 20 s after exhaust. The initial value of τ is 1.03 in this case. *Figure 3* shows a series of IWC (ice water content) contour plots for this simulation, one for every second, the lowest contour value being 10^{-10} kg m^{-3}. These plots show clearly the both vortex cores, the sinking of the contrail, and its evaporation. From this simulation it may be concluded that during the jet phase of the Concorde wake a significant part of the exhaust material escapes from the wake and is lateron not trapped in the vortex cores.

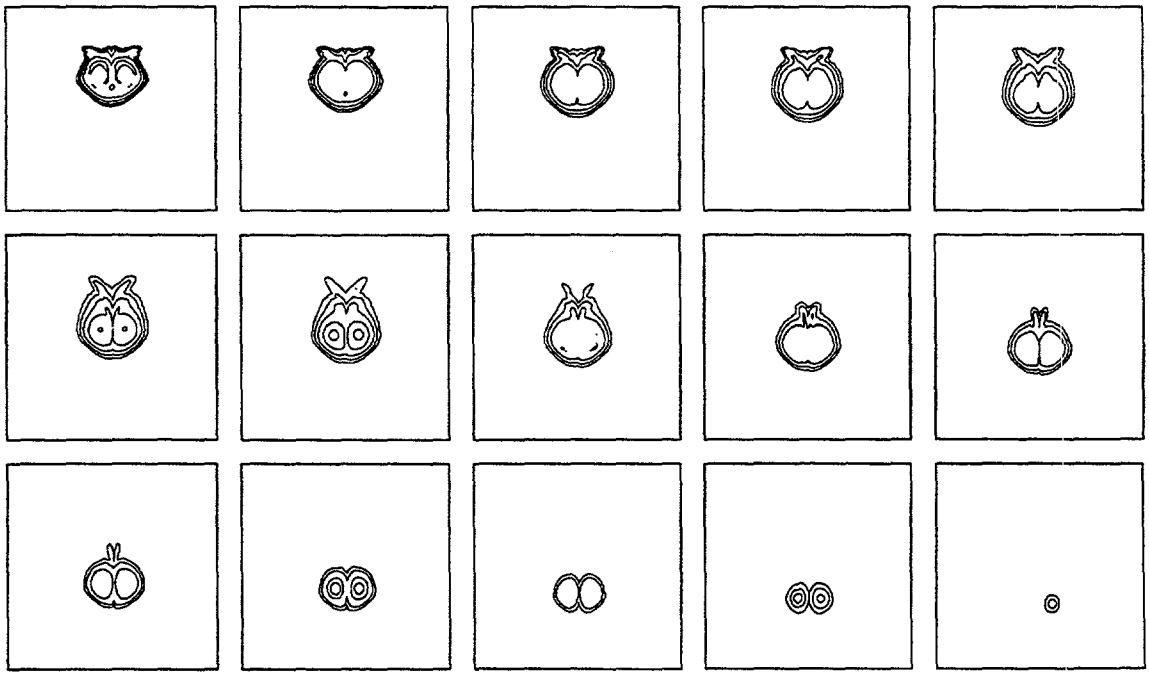

Fig. 3 - Time series of IWC contour plots for the case with partial trapping of the exhaust water vapour. The lowest contour means a value of 10^{-4} mg m^{-3}, the step from one contour to the next means a factor of 10, the highest contour value is 1 mg m^{-3}. The first plot corresponds to 5.7 s after exhaust, and the timestep between two plots is 1 s. The double vortex structure , its sinking, and the ice evaporation can clearly be seen. The coordinates are as in Figure 1.

3.3. Incomplete trapping of water vapour and ice

Finally, two simulations have been performed with both the vapour and ice distributed equally over the larger area of almost 20,000 m^2. The ice vs. vapour masses and crystal numbers are chosen as before. In these two cases the ice evaporates completely within 30 s. The perception threshold is reached after 16 s of simulation in the case with M_{ice}=0.6×M_{H2O}, and after 9 s in the case with lower initial ice mass in the plume. However, the initial maximum optical depths of τ=0.48 and τ=0.22,

respectively, seem to be too low to explain the bright appearance of the contrail in its initial phase.

4. Conclusions

This contribution describes the numerical modelling of the Concorde wake during ZEBRE. Major objectives of ZEBRE, like contrail evolution, horizontal and vertical expansion, etc., could not be addressed in the evaluation process since, unfortunately, the experiment was conducted in rather dry air. Accordingly, the lifetime of the contrail was very short. It was the main purpose of the present contribution to explain the early disappearance of the Concorde contrail. It turned out difficult to let evaporate the ice in the model contrails, since the exhaust water (vapour and ice) was substantially trapped within the vortex core region. This leads to an equilibrium state with ice crystals situated in an ice-saturated environment. Because of the trapping it is not possible either to explain the disappearance of the contrail with spatial dispersion of the ice crystals. Instead, it must be concluded that a substantial portion of the exhaust material is able to escape during the early jet phase from the region that is lateron trapped within the vortex cores. Such a situation has been simulated here with rather *ad hoc* assumptions about the initial distributions of exhaust vapour and ice. However, they at least demonstrate that it is in possible to let the contrail disappear in the model, when a significant part of the exhaust products do not become trapped in the vortex cores.

The uncertain role of trapping and the unknown initial partitioning of the exhaust water between vapour and ice clearly indicates the need for numerical models of the early jet and vortex phase that combine dynamics and microphysics.

Acknowledgements - I thank T. Gerz for the calculation of the initial flow field, and W. Renger, J.P. Pommereau, and B. Nardi for providing data of the Concorde flight.

References

[1] Schumann, U. *et al.*, 1987: A mesoscale model for simulation of turbulence, clouds and flow over mountains: formulation and validation examples. *Beitr. Phys. Atmos.*, **60**, 413-446.
[2] Höller, H., 1986: Parameterization of cloud-microphysical processes in a three dimensional convective mesoscale model. DFVLR-FB 86-02, 82 pp.
[3] Gierens, K.M., 1996: Numerical simulations of persistent contrails. *J. Atmos. Sci.*, in press.
[4] Fahey, D.W., *et al.*, 1995: Emission measurements of the Concorde supersonic aircraft in the lower stratosphere. *Science*, **270**, 70-74.
[5] Schlager, H. *et al.*, 1996: In situ observations of airtraffic emission signatures in the north atlantic flight corridor. Institut für Physik der Atmosphäre, Report No. 59, ISSN 0943-4771, 13 pp.
[6] Gierens, K.M., and U. Schumann, 1996: Colors of contrails from fuels with different sulfur contents. *J. Geophys. Res.*, **101**, 16,731-16,736.
[7] Ström, J., *et al.*, 1994: Recent measurements in cirrus clouds and contrails using the MISU CVI-payload during ICE94. 7th EUCREX-2 workshop, Lille, France, 83-85.
[8] Koenig, L.R., 1971: Numerical modelling of ice deposition. *J. Atmos. Sci.*, **28**, 226-237.
[9] Miake-Lye, R.C. *et al.*, 1993: Plume and wake dynamics, mixing, and chemistry behind an HSCT aircraft. *J. Aircraft*, **30**, 467-479.
[10] Kärcher, B., 1994: Transport of exhaust products in the near trail of a jet engine under atmospheric conditions. *J. Geophys. Res.*, 99, 14509-14517.

BUILDUP OF AEROSOL PRECURSOR GASES AND SULFUR-INDUCED ACTIVATION OF SOOT IN NASCENT JET AIRCRAFT EXHAUST PLUMES

B. KÄRCHER, T. GERZ*, M.M. HIRSCHBERG & P. FABIAN

Lehrstuhl für Bioklimatologie und Immissionsforschung, Universität München
Hohenbachernstr. 22, D-85354 Freising, Germany

**Institut für Physik der Atmosphäre, DLR Oberpfaffenhofen*
Postfach 1116, D-82230 Wessling, Germany

ABSTRACT. Research issues concerning the chemical transformation of exhaust trace gases are summarized. The photochemical evolution of NO_x early in the plume is strongly coupled to plume mixing. Substantial amounts of HNO_3 are generated in nascent plumes even if no NO_2 is emitted. The production of H_2SO_4 becomes very efficient if part of the fuel sulfur is emitted as SO_3. Each emitted soot particle can acquire $1 - 10\,\%$ by mass fully oxidized sulfur molecules prior to binary homogeneous nucleation, if a few percent of the exhaust SO_x are emitted as SO_3, indicating an important activation pathway for soot, and leading to a marked enhancement of new aerosol formation and growth rates.

1. INTRODUCTION

A sound assessment of the chemical impact of aviation on the global atmosphere relys on a proper understanding of chemical processes in the aircraft wake on spatial scales too small to be resolved by current regional or global models. The situation is complicated by the fact that turbulence, by which ambient air is mixed into the wake and which leads to a dilution of the exhaust species, can interact with chemical reactions. This point is especially important up to the dispersion regime and is adressed by *Gerz and Kärcher* (this issue), where we describe how we introduce entrainment rates, extracted from sophisticated dynamical models that compute plume mixing properties starting at the nozzle exit plane of the jet engines, into our coupled photochemical-microphysical trajectory box model [1,2]. We focus here on the fate of NO_2 in the vortex regime constrained by measurements in the wake of a B 747 [3], discuss the chemical transformations of emitted NO_x into HNO_3 and of exhaust SO_x into H_2SO_4 (both acids are known to participate in particle formation in jet plumes [4,5]), and investigate possible pathways of sulfur and soot interaction in young plumes. In the light of new experimental data suggesting that adsorption of SO_2, NO_2, and HNO_3 on soot is characterized by sticking coefficients well below 0.1 (Leah Williams, personal communication, 1996), adsorption of fully oxydized sulfur species can be expected to play a key role concerning the chemical activation of exhaust soot. This is supported by recent model results indicating much higher emissions of SO_3 than previously thought [6].

2. PHOTOCHEMICAL EVOLUTION OF NO_2

During the POLINAT-mission nitrogen oxides and ozone (among other species) have been measured in the near-field plumes of several commercial airliners in the North Atlantic flight corridor. Here, we simulate the evolution of NO, NO_2, and O_3 for one specific case (the KLM flight 746 at November 13, 1994; B 747 with CF6-80C2B1F engines). The dilution data used in the model is constrained by the measured CO_2 (15 ppmv above background at a plume age $t = 83$ s) within the aircraft vortex; the calculated temperature evolution is also consistent with the observations (see contribution by *Gerz and Kärcher* in this volume and

[3]). Measured background abundances of key species are used as boundary conditions for the plume mixing calculation. The measured emission index of NO_x, $EI(NO_x) = 12.3 \pm 1.8\,g\,kg^{-1}$, has been inferred by relating the observed NO_x abundance to the CO_2 emission index. This implies that NO_x behaves like a chemically passive tracer; however, the $[NO_2]/[NO]$ ratio may vary with time. We assume $[OH]_0$=10 ppmv at the nozzle exit plane, use $EI(NO_x)$ to initialize the model, and treat the unknown value $[NO_2]_0$ as a free parameter.

Figure 1 depicts the time history of NO, NO_2, and O_3 in the vortex core. Measured values for NO ($\sim$ 60 ppbv) and NO_2 ($\sim$ 1.5 ppbv) at 83 s are shown as upper and lower black dots. Ozone builds up and overshoots the background level of 45 ppbv early in the plume due to the perturbed HO_x chemistry, but rapidly approaches the ambient value. A few percent of exhaust NO is directly converted to HNO_2 within the first milliseconds (not shown); the rest dilutes like a passive tracer and approximately hits the observed value taken during the vortex crossing. Note that [NO](t) levels off around 30 s, when entrainment is strongly suppressed after the formation of the vortex is completed. The dashed line shows $[NO_2](t)$ using $n = [NO_2]_0/[NO_x]_0 = 0.05$; the dashed line with open dots assumes $n = 0$, i.e., no emission of NO_2. Values up to $n = 0.013$ lead to NO_2 histories similar to the latter case for $t > 0.1$ s. In both runs, we prescribe a rate $J = 10^{-2}\,s^{-1}$ for the photolysis of NO_2. At the time of observation, both model results exceed the measured value. Only for $n < 0.013$ and with an additional enhancement of J by a factor 3 (see dashed line with open triangles) can photolysis deplete NO_2 more rapidly than it is formed by the NO + O_3 recation at $t = 83$ s. In this case, the model value for $[NO_2]/[NO_x]$ (0.03) agrees quite well with the observation (0.02). The fact that the sky was covered with thick clouds just below the source aircraft might give a reasonable explanation for such a marked enhancement of the photolysis rate, which has been calculated for clear sky conditions. In any case, the comparison with the observations points to relatively low, if any, emissions of NO_2 of the order of 1 % of the exhaust NO_x in this plume event, in contrast to the common assumption $n = 0.1$ previously used in plume chemistry models. Further measurements are needed to investigate the possible range of the NO_2 emission index.

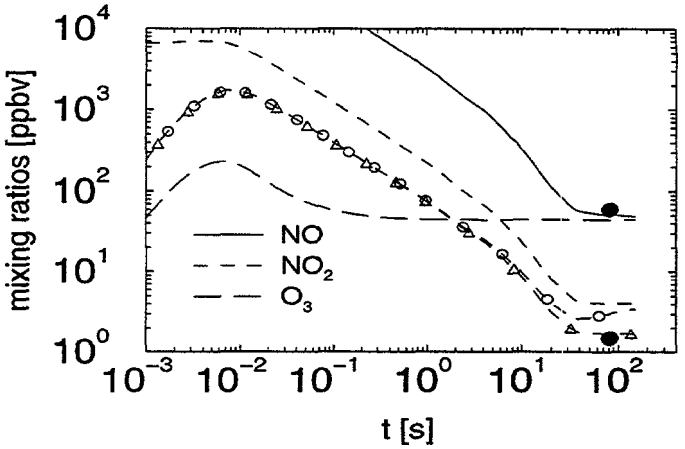

Fig.1. Photochemical evolution of NO, NO_2, and O_3 in a B 747 vortex core. Measured values for NO, NO_2 at $t = 83$ s are shown as black dots. We assume 5 % (− − −) and 0 % (− ∘ −) of the NO_x emitted as NO_2 and an NO_2 photolysis rate $J = 10^{-2}\,s^{-1}$. Best agreement with the observation is found for less than 1.3 % initial NO_2 and $J \times 3$ (−△−).

3. CONVERSION OF NO_x TO HNO_3

The buildup of HNO_3 out of NO_2 takes place *via* the reaction with exhaust OH. Thereby, $[HNO_3]_{max}/[NO_2]_0$-ratios up to $4 - 6$ % can be reached for values of the nozzle exit plane mixing ratio $[OH]_0$ up to 10 ppmv. For higher HO_x emissions, strong coupling of HO_x and NO_x reactions lead to an enhanced increase of HNO_3, with $[HNO_3]_{max}/[NO_2]_0$ =20 % for $[OH]_0 = 100$ ppmv [2]. We also concluded that secondary HNO_3 can be produced even if

no NO_2 is emitted (see Fig.11 in Ref.[2]). Because in this case several oxidations steps are necessary to produce NO_2, mainly the reactions of NO with entrained O_3 and emitted HO_2, the conversion of exhaust NO into HNO_3 is expected to be less efficient. We evaluate the maximum conversion efficiencies $\eta(n, [OH]_0) = [HNO_3]_{max}/[NO_x]_0$ of emitted NO_x = NO + NO_2 into HNO_3 as a function of $n = [NO_2]_0/[NO_x]_0$ and for several values of $[OH]_0$ for the Airbus A 310 (flight during the German SULFUR 4-mission in March 1996), see Fig.2.

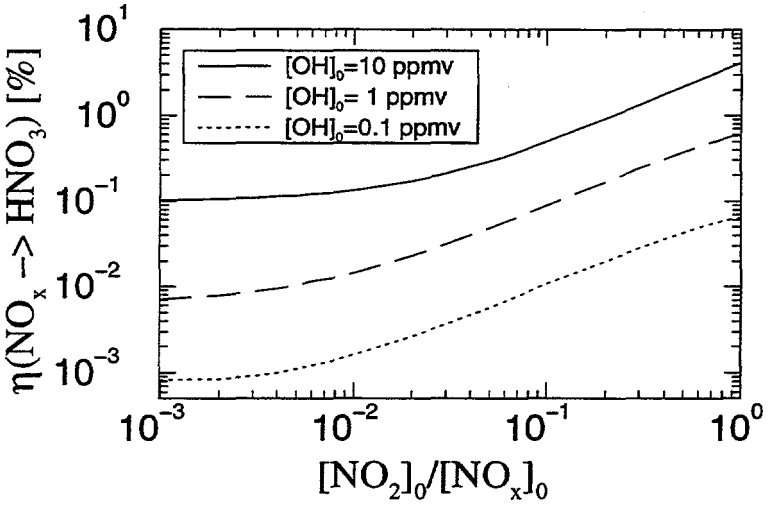

Fig.2. Maximum conversion efficiency η of emitted NO_x to HNO_3 in the jet plume vs the NO_2 to NO_x exit plane ratio for various values of emitted OH for the A 310.

When no NO_2 is emitted (n = 0), η values stay below 0.1 %. However, these values depend on the NO emission index (we use EI(NO_x)=8 g (as NO_2) per kg fuel), especially for high HO_x emissions due to the increased importance of HO_x-NO_x-reactions, see above. Conversion efficiencies start to increase markedly for $n > 10^{-2}$, but there is currently no observational evidence for values $n >$ 0.1. Although η values increase by nearly two orders of magnitude between $n = 0$ and $n = 1$, the production of gaseous HNO_3 out of emitted NO_x is always limited by exhaust HO_x. For typical exhaust NO mixing ratios 10 – 100 ppmv and a 'reasonable' value $[OH]_0$=10 ppmv, still 10 – 100 ppbv HNO_3 is produced in the jet plume even for $[NO_2]_0$=0. Strong interaction of HNO_3 with liquid H_2SO_4/H_2O aerosols [5] is expected especially if part of the NO_x exits the jet engines in the form of NO_2.

4. CONVERSION OF SO_x TO H_2SO_4

During combustion of kerosene in the gas turbines, the fuel sulfur is converted to SO_2 and, as model calculations [6,7] indicate, to SO_3. We investigate the transformation of emitted $SO_x = SO_2 + SO_3$ to H_2SO_4 in the young plume for the subsonic A 310 and for the Concorde supersonic aircraft. When no SO_3 is emitted, oxidation of SO_2 by emitted OH builds up a transient steady-state level of SO_3 that quickly reacts with H_2O to form H_2SO_4 within a few milliseconds after the exhaust exited the engines. In this way, depending on $[OH]_0$, typical SO_2 to H_2SO_4 conversion efficiencies $[H_2SO_4]_{max}/[SO_2]_0 < 1-2$ % are reached until OH is depleted by concomitant reactions with emitted NO_x [2,4]. We extend these studies and investigate the maximum SO_x to H_2SO_4 conversion efficiencies, $\eta(s, [OH]_0) = [H_2SO_4]_{max}/[SO_x]_0$, as a function of $s = [SO_3]_0/[SO_x]_0$ and for several values of $[OH]_0$, see Fig.3. Note that, as in the NO_x case, this definition of η only adresses transformation in the gas phase and does not take into account possible heterogeneous losses on soot.

We first discuss the A 310 case (thin lines). In the limit $s \to 0$, H_2SO_4 production is initiated by oxidation of SO_2 as noted above, and the dependence $\eta([OH]_0)$ is identical to that discussed previously [2]. The rate limiting reaction of SO_2 with OH causes η to be bound between 0.01% and 0.5% for low (dotted line) to rather high (solid line) $[OH]_0$ levels. With increasing amount of directly emitted SO_3, η increases because the fast reaction SO_3 +

H_2O immediately leads to H_2SO_4 and bypasses the slower SO_2 + OH reaction pathway. For $s < 10^{-2}$, η shows a pronounced $[OH]_0$ dependence, because the SO_3 concentration produced in the plume *via* SO_2 + OH is greater than, or similar to, the emitted $[SO_3]$. However, for $s > 10^{-2}$, η increases substantially because direct conversion of $[SO_3]_0$ to H_2SO_4 takes over the dominant part and the $[OH]_0$ dependence diminishes. In this case, production of gaseous H_2SO_4 becomes very efficient and is no longer constrained by the available exhaust OH.

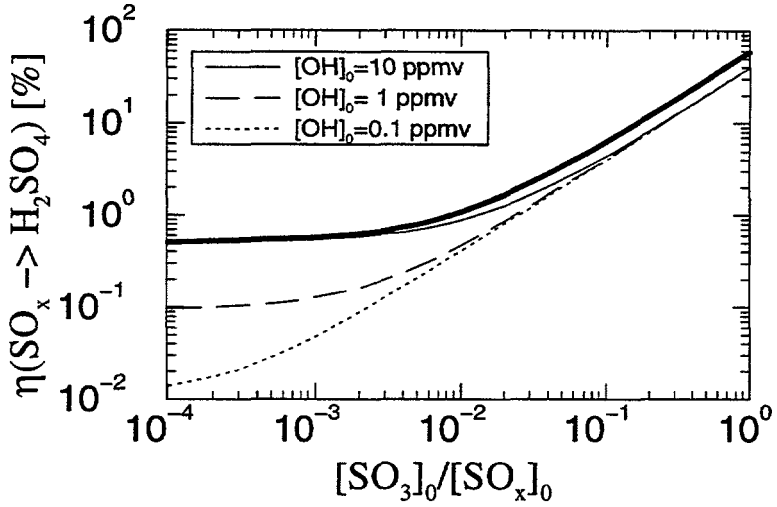

Fig.3. Maximum conversion efficiency η of emitted SO_x to H_2SO_4 in the jet plume vs the SO_3 to SO_x exit plane ratio for various values of emitted OH. Thin lines: for the A 310; bold line: for the Concorde with $[OH]_0$=9 ppmv.

If the fuel sulfur would be completely oxidized to SO_3 before leaving the engines ($s = 1$), a maximum conversion efficiency of 40 % (60 %) can be read off from Fig.3 for the A 310 (Concorde). We note that η = 100 % is not reached since mixing reduces SO_3 while being converted to H_2SO_4. The conversion efficiency for the Concorde (calculated for $[OH]_0$ = 9 ppmv) exhibits a very similar dependence on s, with slightly higher values for comparable OH levels compared to the subsonic case (turbulent mixing of the Concorde wake is weaker and less efficient in diluting the species up to this plume age).

5. SOOT AND SULFUR INTERACTION

It is important to estimate how much of the emitted SO_3 can be adsorbed by soot instead of being chemically converted to H_2SO_4 in the gas phase as assumed above. Similarly, we need to know how many H_2SO_4 molecules are adsorbed and therefore not available for binary homogeneous nucleation. Upon striking the soot surface, molecules (number density $n(0)$) are adsorbed according to a sticking probability $\gamma \leq 1$ and only a fraction f remains in the gas phase. Vapor species (ambient concentration n_a) and soot dilute in the jet plume, driven by the entrainment rate $\omega(t)$. To determine $f(t)$, we consider the equation $dn/dt = -\omega(n - n_a) - \gamma n \bar{v} A_s/4$, whereby $\bar{v}$ is the thermal velocity of the molecules and $A_s(t) = 4\pi r_s^2 n_s(t) \exp(2 \ln^2 \sigma_s)$ is the soot surface area density. This equation for dn/dt, which generalizes the simpler approach presented in Ref.[8], approximately describes the competition between mixing and adsorption in the jet regime. (It strictly holds only for mixing ratios [1].) The characteristic timescales are $t_m = 1/\omega_{max}$ and $t_{ad} = 4/(\gamma \bar{v} A_s(0))$, respectively, which we combine to the parameter $\tau = t_m/t_{ad}$. We use $\gamma = 1$ and $\bar{v} = 2.5 \times 10^4\,\mathrm{cm\,s^{-1}}$, giving $t_{ad} = 0.3 - 3\,\mathrm{s}$ (with $r_s = 10 - 30\,\mathrm{nm}$, $n_s(0) = 10^7 - 10^6\,\mathrm{cm^{-3}}$, $\sigma_s = 1.4$), and assume $n(t) \gg n_a$ and $n_{s,a} = 0$, for simplicity. The mixing rate can well be approximated by $\omega(t \leq t_m) = 0$ and $\omega(t > t_m) = \alpha/t$. Typically, $t_m = 5 - 50\,\mathrm{ms}$ and $0.8 \leq \alpha \leq 1$. Coagulation between soot particles is slow compared to dilution as long as $n_s < 4 \times 10^7\,\mathrm{cm^{-3}}$, assuming Brownian (thermal) coagulation. Hence, $dn_s/dt = -\omega n_s$, yielding $n_s(t) = n_s(0)\mathcal{D}(t)$, with $\mathcal{D}(t) = \exp(-\int_0^t \omega dt)$. With these assumptions, the loss equation for n can be integrated analytically. Introducing the dimensionless time $\theta = t/t_m$, we find $f(\theta) = \exp[-\tau\phi(\theta)]$, whereby $\phi(\theta \leq 1) = \theta$, $\phi(\theta > 1) = 1 + (\theta^{1-\alpha} - 1)/(1 - \alpha)$ if

$\alpha < 1$, and $\phi(\theta > 1) = 1 + \ln(\theta)$ if $\alpha = 1$. The universal function $f(\theta)$ is displayed in Fig.4 for various values of τ for $\alpha = 0.9$. Results for any particular problem can easily be read off this general solution after conversion to the scaled variables τ and θ. If adsorption is faster than mixing ($\tau > 1$), f decreases rapidly; otherwise ($\tau < 1$), a large fraction of molecules remains in the gas phase and will not be taken up by the soot particles in the early plume.

The chemical conversion is completed within the lifetime of emitted OH (determined by reactions with exhaust NO_x) and the timescale of the $SO_3 + H_2O$ reaction, that is, for $t_{SO_3} \simeq 20\,\text{ms}$ after emission. This yields $\theta_{SO_3} = 0.5 - 5$ and $\tau = 0.01 - 0.2$, giving $f(\theta_{SO_3}) = 0.92 - 0.99$ for the range of mixing properties and soot characteristics as given above. At least 92 % of the exhaust SO_x stays long enough in the gas phase to be partially (SO_2) or fully (SO_3) converted to H_2SO_4. This means that H_2SO_4 can efficiently be build up in the gas phase out of emitted SO_2 and SO_3, since only a very small amount of SO_x can be removed by uptake on soot. Sulfuric acid in turn gets adsorbed by soot until it is depleted by homogeneous nucleation and condensation starting around $t_{H_2SO_4} = 0.05 - 0.3\,\text{s}$ or $\theta_{H_2SO_4} = 2 - 30$; hence, $f(\theta_{H_2SO_4}) = 0.7 - 0.92$. At most 30 % of the emitted or chemically produced H_2SO_4 is not available for homogeneous nucleation and growth. Uptake of species is more effective for large soot surface area densities and/or slow plume mixing rates. For the range of average sulfur contents in jet aviation fuel $0.1 - 1\,\text{g}\,\text{kg}^{-1}$, this leads to heterogeneous losses of SO_3 and H_2SO_4 on soot of the order $10^3 - 10^5$ fully oxydized S(VI) molecules, or soluble mass fractions around $0.1 - 10\,\%$, per soot particle, depending on the assumed maximum conversion efficiency $\eta(SO_x \rightarrow H_2SO_4)$, or s, within the first $\sim 0.1\,\text{s}$ after emission and on the soot surface area. Mass fractions $\mu \simeq 8\,\%$ on fresh soot taken directly behind the engines have indeed been measured [9], very likely made up of sulfur species due to an observed correlation of the soluble mass with the fuel sulfur level. Further, laboratory experiments with carbon particles have shown that H_2SO_4 mass fractions around 10 % per soot particle lead to a very marked increase in H_2O adsorption compared to a pure graphitic surface [10]. We add that values of μ of a few percent are only achieved assuming $s \simeq 0.1$, which would point to much larger emissions of SO_3 than previously used in modeling aerosol dynamics in aircraft plumes, resulting in dramatically enhanced binary nucleation and droplet growth rates compared to the $s = 0$-case.

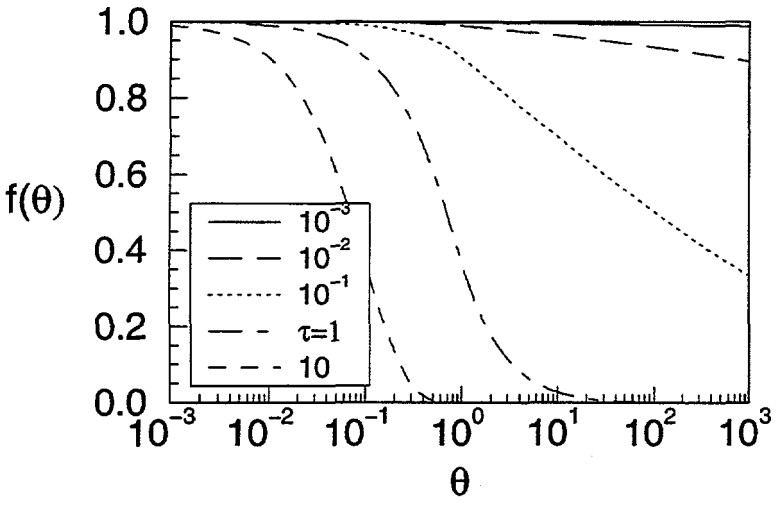

Fig.4. Fraction f of molecules that remain in the gas phase and are not adsorbed by soot vs the dimensionless time θ. The parameter τ is the ratio of mixing to adsorption timescale.

Together with adsorbed water vapor, the H_2SO_4 nucleates heterogeneously and likely creates a liquid soot coating [5,8]. Note that our estimate gives the maximum number of adsorbed molecules because the gas kinetic flux $\gamma\tilde{n}v/4$ is an upper bound of the binary heterogeneous nucleation rate. Values larger than $\tau \simeq 0.2$ are hardly reached; $\tau \simeq 10^{-2}$ is representative for modern subsonic aircraft, leading to $f_{\min} \simeq 0.7$ from Fig.4. Hence, we conclude: volatile gas-to-particle conversion is not limited by heterogeneous losses of SO_3 and H_2SO_4 on soot, because

heterogeneous nucleation of H_2SO_4 and H_2O cannot deplete the gaseous H_2SO_4 prior to binary homogeneous nucleation due to the limited soot surface area. We finally remark that after the onset of binary homogeneous nucleation, scavenging of the freshly nucleated volatile droplets will serve as an additional pathway for soot activation [8,11].

ACKNOWLEDGEMENT. We gratefully acknowledge financial support by BMBF and UBA. Results given in Sections 4 and 5 are partly taken from material submitted for publication in *Atmospheric Research.*

REFERENCES

1. Kärcher, B.
A trajectory box model for aircraft exhaust plumes
J. Geophys. Res. **100**, 18835–18844, 1995.

2. Kärcher, B., Hirschberg, M.M. and Fabian, P.
Small–scale chemical evolution of aircraft exhaust species at cruising altitudes
J. Geophys. Res. **101**, 15169–15190, 1996.

3. Gerz, T. *et al.*
Transport and chemistry of emissions in the wake of subsonic aircraft
J. Geophys. Res. (in preparation) 1996.

4. Miake-Lye, R.C., Brown, R.C., Anderson, M.R. & Kolb, C.E.
Calculations of chemistry and condensation in an aircraft contrail
DLR-Mitt. **94-06**, 274–279, Dtsch. Forsch. Luft- u. Raumfahrt, Köln, Germany, 1994.

5. Kärcher, B.
Aircraft-generated aerosols and visible contrails
Geophys. Res. Lett. **23**, 1933–1936, 1996.

6. Brown, R.C. *et al.*
Aircraft exhaust sulfur emissions
Geophys. Res. Lett. (submitted) 1996.

7. Hunter, S.C.
Formation of SO_3 in gas turbines
Trans. ASME J. Eng. Power **104**, 44–51, 1982.

8. Kärcher, B., Peter, Th., Biermann, U.M. and Schumann, U.
The initial composition of jet condensation trails
J. Atmos. Sci. **53**, 3066–3083, 1996.

9. Hagen, D.E., Whitefield, P.D.
A field sampling of jet exhaust aerosols
Part. Sci. Technol. **10**, 53–63, 1992.

10. Wyslouzil, B.E., Carleton, K.L., Sonnenfroh, D.M., Rawlins, W.T., Arnold, S.
Observation of hydration of single modified carbon aerosols
Geophys. Res. Lett. **21**, 2107–2110, 1994.

11. Brown, R.C. *et al.*
Aerosol dynamics in near field aircraft plumes
J. Geophys. Res. (in press) 1996.

POTENTIAL TRANSFORMATION OF TRACE SPECIES INCLUDING AIRCRAFT EXHAUSTS IN A CLOUD ENVIRONMENT. THE "CHEDROM MODEL".

Ozolin, Y.E.*, R. Ramaroson**, I.L. Karol*.
*Main Geophysical Observatory, 7 Karbyshev st., St. Petersburg, 194021, Russia.
**Office National d'Etudes et de Recherches Aerospatiales, 8 rue des Vertugadins, 92190,Chalais Meudon.

Abstract. Box model for coupled gaseous and aqueous phases is used for sensitivity study of potential transformation of trace gases in a cloud environment. The rate of this transformation decreases with decreasing of pH in droplets, with decreasing of photodissociation rates inside the cloud and with increasing of the droplet size. Model calculations show the potential formation of H_2O_2 in aqueous phase and transformation of gaseous HNO_3 into NO_x in a cloud. This model is applied for exploration of aircraft exhausts evolution in plume inside a cloud.

1. Introduction.

One of the large uncertainties which need to be assessed for the potential transformation of the aircraft exhausts is their interaction with cloud droplets in the lower and middle troposphere and formation of aqueous phase species. This phase constitutes the main potential sink for soluble gases and for radicals so that the classical production rate of tropospheric gaseous species may be strongly affected. Many papers, for example [1-4], had mentioned the importance of aqueous phase on a global scale on ozone production and loss rate. It has been published [1] that OH or HO_2 species are lightly soluble in pure water but their production inside droplets is significant, so that consequently H_2O_2 is potentially highly produced in aqueous phase. Also gaseous phase species can be produced due to chemical reactions in aqueous phase with following volatilization in gaseous phase. So the processes in clouds are the key processes which should be included in the tropospheric gas phase photochemistry model. In this work, the box model with detailed chemistry in gaseous and aqueous phases is described. This model was used for sensitivity studies to explore the potential effects of the cloud environment on various chemical species and especially on the nitrogen and hydrogen chemistry. Simulations were conducted by varying such parameters as pH of the cloud, the radius of the droplets, the spectral representation of the droplets in the cloud and the photodissociation rates of species in gaseous and aqueous phases. Results from these sensitivity studies are presented below.

This box model for coupled gaseous and aqueous phases chemistry was applied for model study of local scale impacts of aircraft exhausts in the lower and middle troposphere. The plume model is based on model [5] of local dispersion and photochemical transformations of aircraft exhausts with new chemistry of this work including aqueous phase. The results of calculations are analyzed.

2. Description of the model.

The set of gaseous chemistry includes oxygen, nitrogen, hydrogen, chlorine, sulfur species, detailed methane chemistry and chemistry of volatile organic compounds from C_2 to C_6. Variable compounds in gas phase are: O_3, O, $O(^1D)$, OH, HO_2, H_2O_2, NO, NO_2, NO_3, N_2O_5, HNO_3, HO_2NO_2, HNO_2, Cl, ClO, Cl_2O_2, HCl, HOCl, $ClONO_2$, CH_2O, CH_3O_2, $C_2H_5O_2$, CH_3CHO, CH_3COO_2, PAN($CH_3COO_2NO_2$), $C_3H_7O_2$, $C_4H_9O_2$, $C_4H_7O_3$, O_2CH_2OH, HCOOH, HS, H_2S, SO, SO_2, SO_3, HSO, HSO_2, HSO_3, H_2SO_4, COS, CH_3OH, $C_3H_7O_3$, $C_3H_7O_2$, $C_6H_{13}O$, $C_6H_{13}O_2$, CHO, CH_3O, C_2H_5O, CH_3CO, C_3H_7O, C_4H_9O.

The aqueous phase takes into account the uptake on the surface of cloud droplets, the diffusion (equilibrium) inside the droplets and the aqueous chemistry in the droplets. The mass transfer limitation for the aqueous phase OH is included in model according to proposition [6]. In aqueous phase variable not dissociated species are: O_3a, OHa, NO_2a, NOa, NO_3a, CH_3OOHa, CH_3O_2a, C_3H_6Oa, PANa, CH_2Oa, CH_2OHOHa, SO_4^-, HSO_5^-, SO_5^-, CO_3^- , and families of variable dissociated species are: $SO_2t=SO_2a+HSO_3^-+SO_3^=$, $SVI=H_2SO_4a+HSO_4^-+SO_4^=$, $HNO_3t=HNO_3a+NO_3^-$, $HNO_2t=HNO_2a+NO_2^-$, $CO_2t=CO_2a+HCO_3^-+CO_3^=$, $H_2O_2t=H_2O_2a+HO_2^-$, $HO_2t=HO_2a+O_2^-$, $HClt=HCla+Cl^-$, $NH_3t=NH_3a+NH_4^+$, $HCOOHt=HCOOHa+HCOO^-$, $CH_3SO_4t=CH_3SO_4^-+CH_2SO_4^=$.

The following long-lived gaseous species are fixed in the model: N_2, O_2, CO_2, H_2, NH_3, H_2O, N_2O, CCl_4, CH_3Cl, CH_3CCl_3, $CFCl_3$, CF_2Cl_2, CO, CH_4, C_2H_6, C_3H_8, C_4H_{10}, C_6H_{14}. CH_3OOH, C_2H_5OOH, CH_3COO_2H, C_3H_7OOH, C_4H_9OOH, C_3H_6O, C_4H_8O, C_3H_6.

Parameters of gas phase reactions were taken from [7] and parameters of aqueous phase reactions as well as gas-aqueous and aqueous phase equilibrium were taken from [3]. The photodissociation coefficients are held fixed in this work during the term of model calculations. Cross sections from [8] were used for estimation of photodissociation rates inside droplets.

The system of differential equations describing the transformation of gas (C_g) and aqueous (C_a) phase species in a cloud may be written as:

$$\begin{aligned} dC_g/dt &= Q_g - S_g - C_g*L*K_t + C_a*K_t/(He*R*T) \\ dC_a/dt &= Q_a - S_a + C_g*L*K_t - C_a*K_t/(He*R*T) \end{aligned} \quad (1)$$

where Q_g and S_g are gas phase specie source and sink, Q_a and S_a are the same for aqueous phase, T is temperature, L is liquid water content, He is effective Henry's law constant, R is universal gas constant, K_t is gas-transfer coefficient:

$$K_t=(r^2/(3*D_g)+4*r/(3*V*\alpha))^{-1} \quad (2)$$

where r is radius of droplet, D_g is gas-phase diffusion constant, V is mean molecular velocity, α is accommodation or sticking coefficient.

When we have an ensemble of droplets of different sizes in a cloud, we need to write separate equations for aqueous species transformation in every class of droplets with radius r_i. In this case we will have following set of equations for gas phase and aqueous phase species:

$$\begin{aligned} dC_g/dt &= Q_g - S_g - C_g*\sum_i L_i*K_{ti} + \sum_i C_{ai}*K_{ti}/(He*R*T) \\ dC_{ai}/dt &= Q_{ai} + S_{ai} + C_g*L_i*K_{ti} - Ca_i*K_{ti}/(He*R*T) \end{aligned} \quad (3)$$

Wide sensitivity studies were carried out with coupled gas and aqueous phases chemical box model. Initial conditions for gas phase species in equation (1) were taken at first from 1-D global photochemical model [9] and then corrected by box model calculations of diurnal variations during few days for gases chemistry only. For aqueous phase compounds the initial concentrations were taken equal to zero. Calculations at altitude 4 km were carried out with following model parameters used in equations (1) and (2): L=3 10^{-7}, D_g=0.1 cm^2/s.

3. Results and discussion.

Evolution of gas and aqueous species in cloud depend on large number of internal parameters of model, the principal of which are rates of chemical reactions, photodissociation values, pH value, size of the droplets in cloud.

As the usual value of pH inside the cloud's droplets is between 3 and 7, we carried out model calculations with fixed pH for these limits. We obtained that chemical process in aqueous phase is more active in droplets with larger value of pH (and smaller concentration of H^+). This effect follows from aqueous phase equilibrium for dissociated species, when smaller concentration of H^+ leads to larger concentration of ions and solubility of gases which can be dissociated to ions in aqueous phase. The dependence of gas and aqueous phases transformation in cloud on pH value is especially prominent for sulfuric species (*Fig.1a*). For pH=7 we can see interesting effect of increasing H_2O_2t due to its chemical formation in aqueous phase after few hours of cloud conditions (*Fig.1b*). Concentration of gaseous H_2O_2 , which is in equilibrium with aqueous phase begins to grow simultaneously.

Model sensitivity study was carried out for the estimation of possible effect of cloud on photochemical processes due to changing of photodissociation values. A comparison of results, obtained with standard photodissociations and with ten times smaller values of them has shown that the decrease of photodissociation rates leads to approximately proportional decrease of short lived gases such as O, OH, HO_2, NO, SO, HSO and others. Also decrease aqueous phase species such as OHa, HO_2a, NOa , which are in equilibrium with gas phase. We have find very interesting effect of aqueous phase photodissociation of NO_3^- ($NO_3^- + h\nu \rightarrow NO_2a + OHa + OH^-$) [8] on the transformation of HNO_3 and NO_x in cloud (*Fig.2*). Even small value about 10^{-5} s^{-1} (in standard variant) of this photodissociation changes process of HNO_3 transformation significantly because of regenerating NO_2 in aqueous phase, which is saturated and volatilized in gaseous phase.

For the study of the effect of spectral distribution of droplets by size in a cloud on chemical processes, the numerical experiment with cloud that have 3 classes of droplets was carried out. Radii of droplets: $r1$=10^{-2}, $r2$=10^{-3}, $r3$=10^{-4} cm were hold constant. Water content of every class was equal to 1/3 of the total amount L=3·10^{-7}. The results of calculation of the partition of some aqueous phase species between these classes as well as their concentrations in cloud with droplets of single size (r=10^{-3} cm) are presented at *Fig.3*. This picture illustrates that the large part of aqueous phase compounds with large solubility constant *He* is in the small droplets. For species with small solubility such as NO_2 we have the equal concentration of compounds in every class of droplets . This is because of fast establishment of equilibrium between the aqueous and gaseous phases of species with small solubility constant when the aqueous phase specie is determined by its gas phase.

Model calculations for study of local impact of aircraft exhausts were carried out with use of local dispersion model [5] and photochemical box model described in this work. Following aircraft exhausts (mol/cm) were taken for numerical experiments: $(NO)_e$=10^{18},

$(NO_2)_e=10^{17}$,$(OH)_e=4\cdot10^{16}$, $(SO_2)_e=5\cdot10^{16}$. Results of calculations are presented at *Fig.4* and show smaller increase of HNO_2 comparing with clear atmosphere and fast decrease of HNO_3 in a cloud air due to solution of these gases in water droplets. The effect of increasing NO_x in a cloud is connected with the process of transformation of background HNO_3 into NO_x which was pointed above.

4. Conclusions.

Calculations describe the transformation of the soluble gases into aqueous phase inside the cloud droplets. The rate of this transformation decrease with decreasing of pH in droplets, with decreasing of photodissociation rates inside the cloud and with increasing of the droplets size.

Model calculations show potential formation of H_2O_2 in aqueous phase after few hours of cloud conditions.

The aqueous phase photodissociation of NO_3^- with formation of NO_2a is very important for nitrogen chemistry in cloud. By this way it is possible transformation of gaseous HNO_3 into NO_x inside the cloud.

For a cloud that consists of several classes of droplets the large part of aqueous phase compounds with large solubility constant is concentrated in small droplets.

Aqueous phase chemistry leads to decreasing of HNO_2 , HNO_3 and HO_x compounds and to increasing of NO_x (if $J(NO_3^-) \neq 0$) in plume inside cloud comparing with cloudless troposphere.

References .

1. Chameides, W. L., The photochemistry of a remote marine stratiform cloud, *J.Geophys.Res.*, **89**, 4739-4755, 1984.
2. Jacob, D. J., Chemistry of OH in remote clouds and its role in the production of formic acid and peroxymonosulfate, *J.Geophys.Res.*, **91**, 9807-9826, 1986.
3. Pandis, S. and J. H. Seinfeld, Sensitivity analysis of a chemical mechanism for aqueous phase atmospheric chemistry, *J.Geophys.Res.*, **94**, D1, 1105-1126, 1989.
4. Lelieveld, J. and P. J. Crutzen, The role of clouds in tropospheric photochemistry, *J. Atmosph. Chem.*, **12**, 229-267, 1991.
5. Karol I.L. and Y.E. Ozolin, Small- and medium scale effects of high flying aircraft exhausts on the atmospheric composition. *J. Ann. Geophysicae*, **12**, 979-985, 1994.
6. Schwartz, S.E. and Freiberg, J.E., Mass-transport limitation to the rate of reaction of gases in liquid droplets: application to oxidation of SO_2 in aqueous solutions, *Atmos. Environ.*, **15**, 1129-1144, 1981.
7. DeMore, W. B. , S. P. Sander, R. F. Hampson, M. J. Kurilo, D. M.Golden, C. J. Horward, A.R. Ravishankara, and M. J. Molina, Chemical kinetics and photochemical data for use n stratospheric modeling, Evaluation 10, J.P.L., Publ., 1992.
8. Graedel, T.E. and Weschler, C.J., Chemistry within aqueous atmospheric aerosols and raindrops, *Rev. Geophys. Space Phys.* **19**, 505-539, 1981.
9. Ramaroson, R., M. Pirre, and D. Cariolle, A box model for on-line computations of diurnal variations in 1-D model: potential for application in multidimensional cases, *J.Ann.Geophysicae*, **10**, 416-428, 1992.

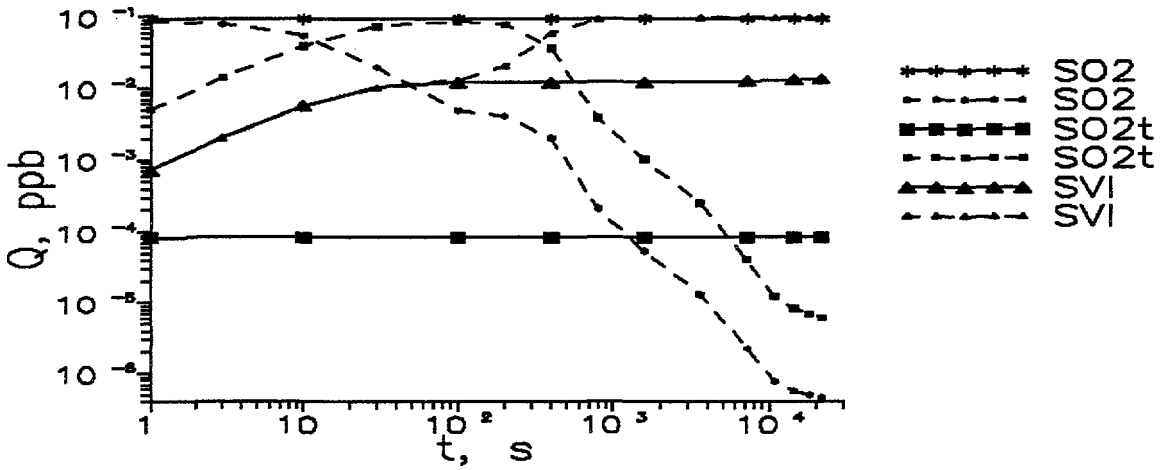

Fig.1a. Evolution of gaseous and aqueous phases in cloud ($r=10^{-3}$ cm) for pH=3 (solid) and pH=7 (dashed).

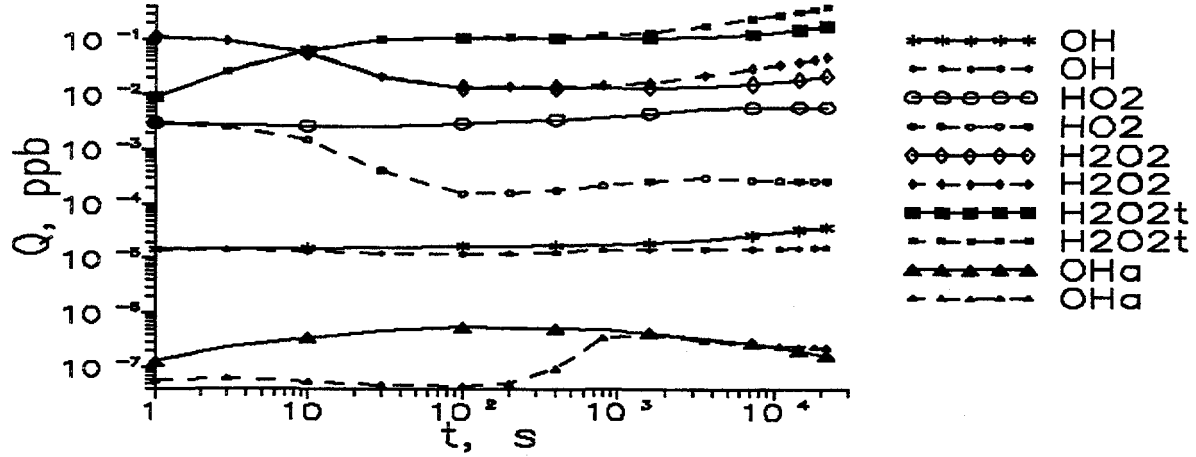

Fig.1b. Evolution of gaseous and aqueous phases in cloud ($r=10^{-3}$ cm) for pH=3 (solid) and pH=7 (dashed).

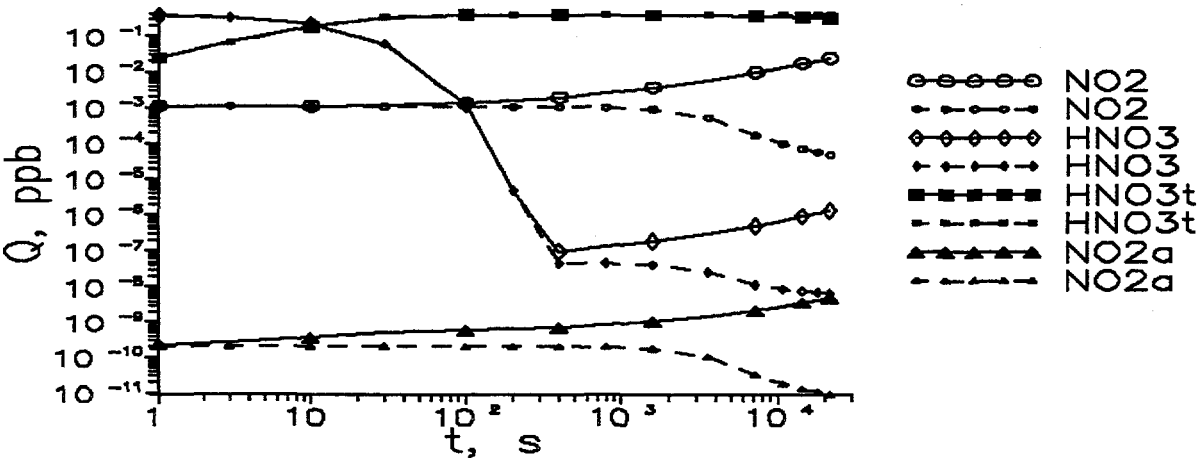

Fig.2. Evolution of gaseous and aqueous phases in cloud ($r=10^{-3}$ cm, pH=5) for $J(NO_3^-)$standard (solid) and $J(NO_3^-)=0$ (dashed).

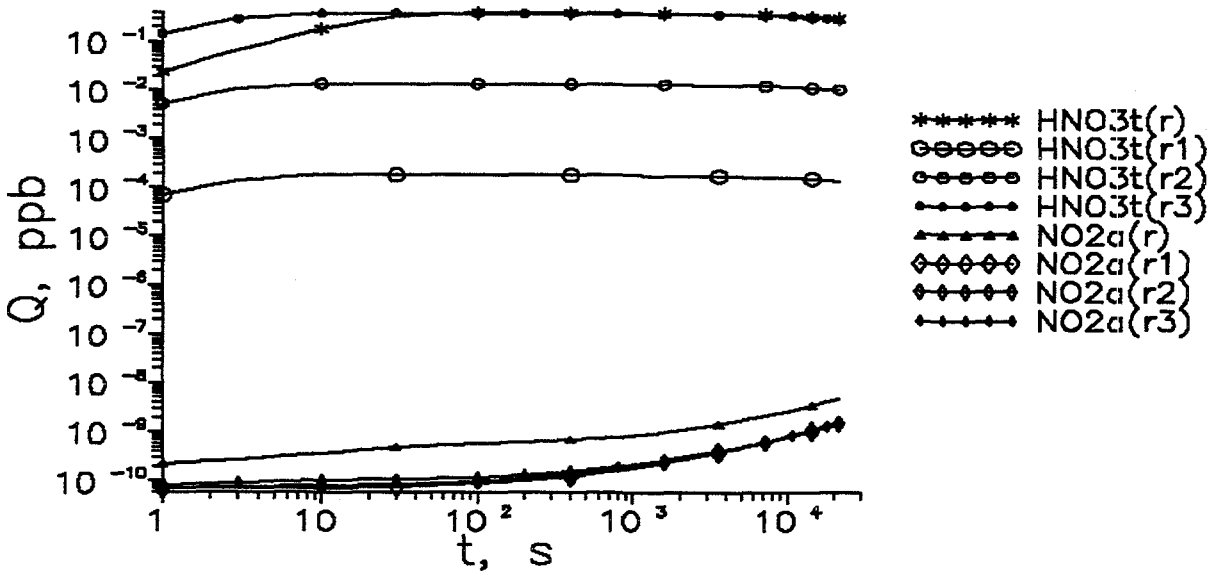

Fig.3. Evolution of aqueous phase in cloud with single class of droplets ($r=10^{-3}$ cm, pH=5) and in cloud with 3 classes of droplets ($r1=10^{-2}$, $r2=10^{-3}$, $r3=10^{-4}$ cm, pH=5).

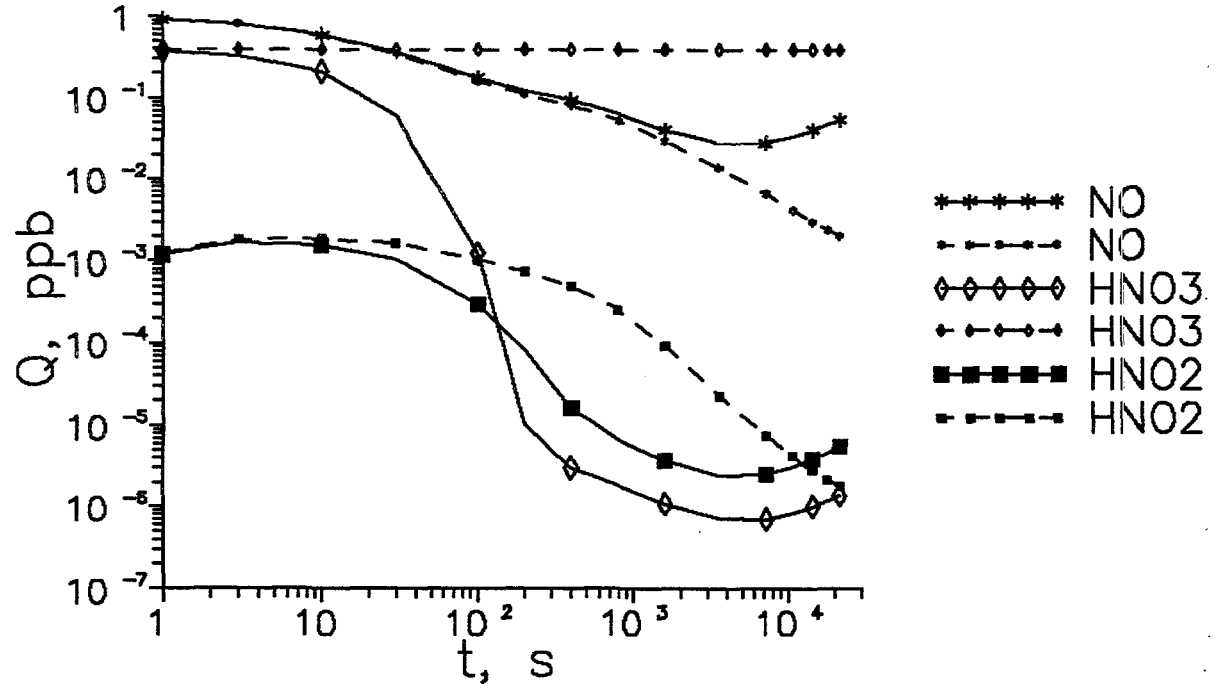

Fig.4. Evolution of gases in plume inside cloud ($r=10^{-3}$ cm, pH=5) (solid) and in cloudless atmosphere (dashed).

Hydrogen chloride heterogeneous chemistry on frozen water particles in subsonic aircraft plume: laboratory studies and modelling

Persiantseva N.V., Popovitcheva O.B., Rakhimova T.V.
Moscow State University, 119899, Russia

Abstract

Heterogeneous chemistry of HCl, as a main reservoir of chlorine content gases, has considered after plume cooling and ice particle formation. The HCl, HNO_3, N_2O_5 uptake efficiencies by frozen water were obtained in Knudsen-cell flow reactor at the subsonic cruise conditions. The formation of ice particles in the plume of subsonic aircraft is simulated to describe the kinetics of gaseous HCl loss due to heterogeneous processes. It is shown that the HCl uptake by frozen water particles may play the more important role in the gaseous HCl depletion in the aircraft plume.

1. Introduction

Interaction of acidic gases such as HCl and HNO_3 with ice particles of polar stratosphere clouds (PSC) is a key step in chemistry of ozone hole in Antarctic. The effect of the emission of NO_x, H_2O, and solid particles on O_3 loss [1,2] is one of the main potential problems of the atmosphere perturbation by aircraft. The large emission indexes for H_2O and non-volatiles particles [2] create the conditions for heterogeneous nucleation and growth of water particles due to supersaturation in the plume. After the engine exhaust enters the surrounding atmosphere, temperature decreasing are accompanied by increasing to ambient value the chlorine content in the plume gas and the HCl concentration as a basic chlorine containing component of the atmosphere. So , probably the problem of heterogeneous HCl interection becomes actual for the effective HCl uptake by ice particles and proceeding the following heterogeneous reactions similar to ones on PSC

$$HCl + ClONO_2 \rightarrow Cl_2 + HNO_3, \quad (1)$$

$$HCl + N_2O_5 \rightarrow ClNO_2 + HNO_3, \quad (2)$$

$$HCl + HOCl \rightarrow Cl_2 + H_2O, \quad (3)$$

which transfer chlorine from chemically passive forms into active chlorine radicals.

The present work is devoted to investigation of hydrogen chloride heterogeneous process on the ice particle surface at the subsonic aircraft cruise conditions. The formation of ice contrail particles inside aircraft plume occur as result of the heterogeneous nucleation of water vapor on the combustion particles, the condensational growth and the freezing at the plume temperature near the ambient value. Laboratory studies of HCl, HNO_3 and N_2O_5 uptake efficiency by frozen water are carried out under the typical cruise conditions. These results are applied for consideration of HCl uptake by frozen water particles and estimation of the time constant for the gaseous HCl depletion in the plume. The chemical transformation inside aircraft plume due heterogeneous reactions on the ice contraile particles is simulated using the results on exhaust product evolution of the nonequilibrium photochemical model of the subsonic aircraft plume [3].

2.HCl uptake by ice. Laboratory studies.

The HCl uptake efficiency is defined by the fractional collision frequency that leads to the reactant loss on ice surface. At present, the single laboratory measurements of HCl uptake efficiency, $\gamma \approx 0.4$, by ice at T=200K was produced in [4]. But the problem how to interpolate this result to the atmosphere conditions is essential because the high HCl vapor pressure $p = 2 \cdot 10^{-4}$ Torr has been used.

In our work the laboratory investigations of HCl uptake efficiency by ice over wide range of HCl pressures and ice temperatures has been carried out. The experimental technique developed is some version of a Knudsen cell flow reactor [5]. The Knudsen cell consists of two chambers separated by a valve. The lower chamber is a stainless steel cup with the teflon rod inside.The upper chamber is coupled to a three dimentional quadrupole high frequency ion trap working as a mass spectrometer.

In this work we have chosen the special technology of ice film preparation. Ice has been created by freezing the distilled and deionized water. The thick film (≈ 60 μm) has been frozen on the teflon rod surface and stretched out at the temperature ≈ 230K. The rate of cooling has been near 10 K s^{-1} , water have supercooled and rapidly crystallized to fine grain ice [6]. We have varified that the surface area of the produced film is near geometrical one.

The series of operations with a valve have allowed us to detect the water vapor behavior above ice before and under HCl exposure and to measure the HCl uptake efficiency. We could see that opening the valve under the ice surface leads to the water vapor pressure increasing due to ice sublimation. The HCl vapor admission into the Knudsen cell chamber decreases the water pressure on 15 % that is mean the suppression of ice sublimation at HCl uptake by ice. Changes in the HCl mass spectrometer intensity when the valve is opened under HCl exposure define the HCl uptake efficiency [5]. The typical duration of HCl interaction with ice was near 10 minutes. But a few results was produced when HCl exposure was being proceeding for 2.5 hours. .

Results and discussions. The measurements of HCl uptake efficiency , γ, by frozen water were carried out at initial pressure of HCl vapor in the range $p \approx 10^{-7}$ - 10^{-4} Torr and ice temperature 150 -240K. The dependenices of γ on the final HCl pressure are shown at T=188, 208 and 240K in Fig.1. At the temperatures $\approx$ 188 - 208K the two pressure regions of the different characteristic values of γ are observed. Only at lower HCl pressure in the range $p = 3 \cdot 10^{-7}$ - 10^{-6} Torr, $\gamma \approx 0.1 \pm 0.02$ for all over temperature range. For higher pressure $\gamma \approx 0.5 \pm 0.1$ is characteristic value for T$\approx$ 188 -208K. For each value of temperature there is the transition area between the characterictic values of γ . The position of the transition area is displaced to lower pressure at the temperature decreasing.

Existing the different characterictic values of HCl uptake efficiency at the different pressure and temperature has indicated the possible structure and phase changing of ice surface at the HCl pressure increasing. This assumption is confirmed by Fourier transform infrared studies of HCl - ice interaction. Infrared spectra (IR) of ice at T=155K after 40 - min exposure to HCl pres-sure $8 \cdot 10^{-7}$ Torr were produced in [7]. It was shown that these spectra resemle that for the crystalline compound $HCl \bullet 6H_2O$. At similar conditions $\gamma \approx 0.5$ was observed by us.

From comparing of our results with [7] the conclusion may be made that the low value $\gamma \approx 0.1$ corresponds to HCl vapor interaction with pure ice, the value $\gamma \approx 0.5$ indicates the

formation of HCl hexahydrate with increase of HCl pressure. So we see that the measurements of HCl uptake in [4] was conducted at HCl hexahydrate formation on ice surface.

Essential problem at the HCl uptake analysis is the determination of HCl amount absorbed on the ice surface. In many works [8,9] the HCl - ice interaction is considered only as a surface process. In the fast flow reactor experiments [8] the HCl molecules are suggested to be absorbed creating a near monolayer concentration $C_s \approx 10^{15}$ cm^{-2} on ice surface at T ≈ 200K and HCl stratosphere pressure p≈$7 \cdot 10^{-8}$ - $2 \cdot 10^{-6}$ Torr. As the other studies have shown [9,10], the surface coverage may be dependent on HCl pressure and the ice film thickness.

At the conditions of our Knudsen cell flow reactor we could observe the process of HCl uptake proceeding quasistationary during long time with the low constant level of HCl pressure above ice. It is mean that no saturation of ice surface and the film bulk was in our experiments.The HCl molecules were not accumulated on the surface and penetrate into the bulk.The flow of the HCl molecules into the ice bulk due to diffision should sustain the low surface concentration. This conclusion can be confirmed by results [10] on observation of the low $C_s \approx 10^{13}$ - $2 \cdot 10^{14}$ cm^{-2} for 10^{-7} - 10^{-6} Torr of HCl pressure.

The model of HCl dissolution in the ice film was suggested in [11]. Integration of the above results on investigation of the uptake efficiency with this model would be appropriate for modelling of the HCl interaction with ice particles in the atmosphere.

Adsorption of HNO_3 and N_2O_5 , as the most important for heterogeneous chemistry nitrogen components in the plume, may influence on rate of HCl heterogeneous processes. A number of experiments was carried out by us for obtaining γ for HNO_3 and N_2O_5 in the range p ≈ 10^{-6} - 10^{-4} Torr. We have obtained $\gamma \approx 6 \cdot 10^{-3}$ Torr for HNO_3 and $\gamma \approx 3 \cdot 10^{-2}$ for N_2O_5. These values are less γ for HCl that is mean that HCl uptake will take place on realy clear ice surface.

3. Kinetics of HCl uptake by ice particles.

The produced results can be appled for description of HCl uptake by ice particles at the cruise conditions. On the altitudes of subsonic aircraft cruise ≈10 km the HCl pressure is near 10^{-7} - 10^{-6} Torr and T ≈ 223 K. According to a phase diagram of the HCl/H_2O system the gaseous HCl is in the thermodynamic equilibrium with pure "ice" at the stratospheric conditions. For this case the value of $\gamma = 0.1 \pm 0.02$ (see Fig.1).

For description of kinetics of HCl - ice particle interaction after aircraft emission it is necessary to define the plume particle parameters which are not well characterized for subsonic aircraft exhaust.

Formation of ice contrail particles. It is needed to simulate the nucleation and condensational growth of water particles in the plume and then their freezing to obtain the size and the total ice particle surface area.

The high emission index of subsonic aircraft engine for combustion (or soot) particles defines their initial concentration n ≈10^5 - 10^6 cm^{-3} and particle size $R_o \approx 0.01$ - 0.1 μm [1]. We conclude that the formation of the water particles in the aircraft exhaust occur by heterogeneous nucleation, probably on combustion particles, but not on stratospheric aerosols or exhaust sulfate particles [2], due to very high combustion particle concentration.

To estimate the size which can be reached by water particles under water supersatu-

ration of aircraft exhaust, we have used the results of nonequilibrium model [3] for transformation of exhaust products in the plume of subsonic aircraft with hydrocarbon combustion engines. Evolution of H_2O concentration and temperature along the plume for CH_4 fuel was analysed. The simple thermodynamics approach was applied for estimations.

A maximum of water vapor supersaturation in the plume [3] takes place after colling below temperature ≤ 300K. The size of the water particles formed is more reasonable to be estimated at T = -20C, when the heterogeneous freezing of water particles should be occured. For the spherical particles the radius is given by equation

$$R = \sqrt[3]{R_0^3 + \frac{3m(N_0 - N_s)}{n\rho 4\pi}}, \qquad (4)$$

where N_o, N_S are the water vapor saturation concentrations for T = 300K and 253K, correspondently; m, ρ are the molecular mass and density of water. For the concentration of activited combustion particles $n \approx 10^5$ cm^{-3} we have the particle radius $R \approx 2.8$ μm.

The futher temperature decreasing to ambient value (223K for 10 km) takes place inside aircraft plume on the distance ≈ 100 m from exit plane. But the vapor condensation on the frozen water particles is appeared to be neglected for the radius estimate on (4) equation gives the R increasing only on 0.1 μm. So we consider that the ice contrail particles in the plume are the frozen water particles. And at the considered conditions we have the total surface area $S \approx 0.08$ cm^2/cm^3 of air and mass $M \approx 7 \cdot 10^{-6}$ g·ice/cm^3 of air .

HCl uptake by frozen water particles. Entering the engine exhaust into the surrounding atmosphere and plume cooling are accomponied by increasing of HCl content in the plume to ambient value on the distance ≈ 100 m from an exit plane of aircraft engine. So we see that a maximum of HCl is reached when the frozen water particles of plume have their maximum size.

So it is simple to estimate the time constant for the HCl uptake by ice particles $\tau = (\gamma w S/4)^{-1}$, where w is the mean kinetic HCl velocity. Then we have $\tau \approx 0.01$ s. Kinetics of the gaseous HCl uptake by frozen water particles is shown in Fig.2. The calculations were started after the size of ice particles has reached a maximum.

The total mass of ice contrail particles M is available for incorporation of all gaseous HCl into the ice particle volume.This result is contrary to a case of HCl interaction with PSC [10] when the gaseous HCl can be depleted only by heterogeneous reactions.

4. HCl heterogeneous reactions on ice particles.

It is likely that the HCl uptake by ice is the first step of heterogeneous reaction 1)-3) proceeding on the ice surface. It is necessary to study each of the elementary reaction steps to describe the surface - mediate chemical transformation. But at present, this approach is not elaborated and reactions 1)-3) are described by an integrated parameter, as reaction probability γ_r. Laboratory studies of γ_r has been carried out on the ice surface either contained the apparent mole fraction of HCl [4] or treated with HCl untill its saturation uptake capacity [13]. The gas - phase HCl concentration maintained at twice or more the $ClONO_2$, N_2O_5, or HOCl concentrations [8,12,13]. As a result, the approach is elaborated for the calculation of gaseous HCl loss rate where it is defined by γ_r and flow of the other react component of 1)-3) [14].

Under of aircraft emissions upon the atmosphere the situation is far from conditions of the model laboratory experiments [4,8,12,13]. First, the surface concentration C_s of HCl adsorbed by ice contrail particles for time τ is very low . For the considered above case, $C_s \approx 10^{10}$ cm^{-2} that is very far from surface saturation. So the question arises about effectivity of reactions 1)-3) and availability of the measured γ_r. Second, a maximum of HCl concentration N_{HCl} in the plume can be less the other react components. Then the approach [14] can not be used and the HCl loss rate may be defined by ice uptake.

In this work we have simulated the kinetics the heterogeneous reactions 1)-3) in the plume after the size of frozen water particles has reached a maximum. At the considered above conditions [3] on the distance ≈ 100 m from an exit plane of engine $N_{HCl}>N_{N2O5}>N_{HOCl}>N_{ClONO2}$ and we can apply the approach [14] for HCl loss description in heterogeneous reactions (1-3). Standart γ_r values were taken [1].

Fig.2 demonstrates the gaseous HCl loss by ice particle uptake and in the heterogeneous reaction with N_2O_5 (2). We can see that the ice particle uptake provides for a sink of gaseous HCl with more rate than depletion in the heterogeneous reaction. These results are neccesary for construction of comprehensive photochemical model of aircraft contrail.

5. Conclusion.

The laboratory studies and analysis of subsonic aircraft conditions have shown that the HCl uptake by frozen water particles may play the more important role in the heterogeneous chemistry of hydrogen chloride. The approch [14] is not applied for the full description of gaseous HCl depletion in the plume. The consistent consideration of the heterogeneous reactions needs in the step -by-step studies at any relations of reactant concentrations.

References

1.Danilin M.Y., Ebel A., Elbern H., and Petry H. J.Geophys.Res. **1994.** *99.* 18951

2.Fahey D.W., Keim E.R. et.al. Science. **1995**. *270.* 70

3.Starik A.M., Dautov N.G., Titova N.S. in "Atmospheric effects of aviation", Proc. of Annual Meeting. Virginia 1995.

4. Leu M.T. Geophys.Res.Lett. **1988**. *15,* 17

5. Quinlan M.A., Reihs C.M. et al. J.Phys.Chem. **1990**. *94,* 3255

6. Johari G.P., Pascheto W., and Jones S.J. J.Phys.D. **1995**. *28,* 112

7. Koehler B.G., McNeill L.S., Middlebrook A.M., and M.A.Tolbert. J.Geophys.Res. **1993**. *98.* 10563

8. Hanson D.R., Ravishankara A.R. J.Phys.Chem. **1992**. *96,* 2682

9.Chu L.T., Leu M.T., and Keyser L.F. J.Phys. Chem. **1993** .*97.* 7779

10.Domine F., Chaix L., Thibert E. in "Polar stratospheric ozone". Proc. of 3rd European workshop. Germany 1995.; European Comm. **1996.** 736.

11.Popov A.M., Popovicheva O.B. et.al. Russian J.of Phys.Chem.**1995** *69.* 1823

12. Hanson D.R., Ravishankara A.R J.Geophys.Res. **1991**. *96,* 5081

13.Chu L.T., Leu M.T., and Keyser L.F. J.Phys.Chem. **1993.** *97.* 12798

14. Turco R.P., Toon O.B., and Hamill P. J. Geophys.Res. **1989**. *94* . 16493

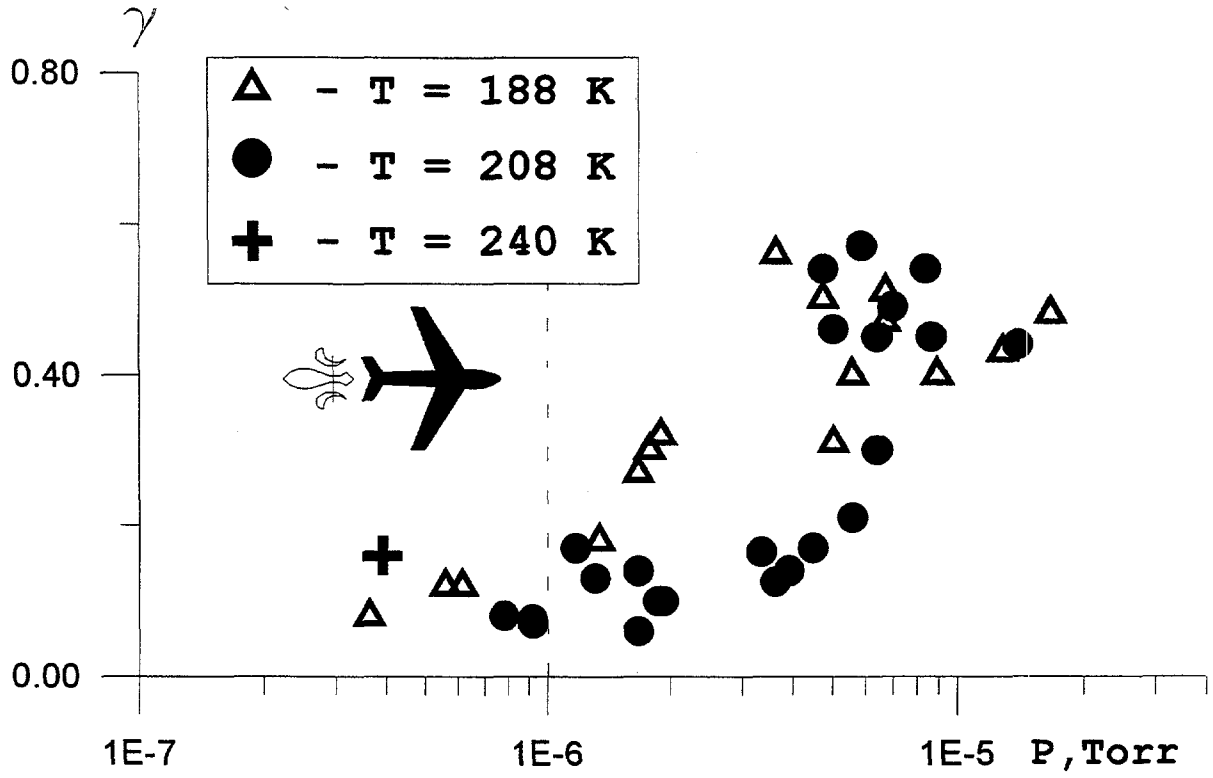

Fig.1 - Dependence γ on the HCl pressure over ice surface. The region for aircraft conditions is shown by dashed vertical line.

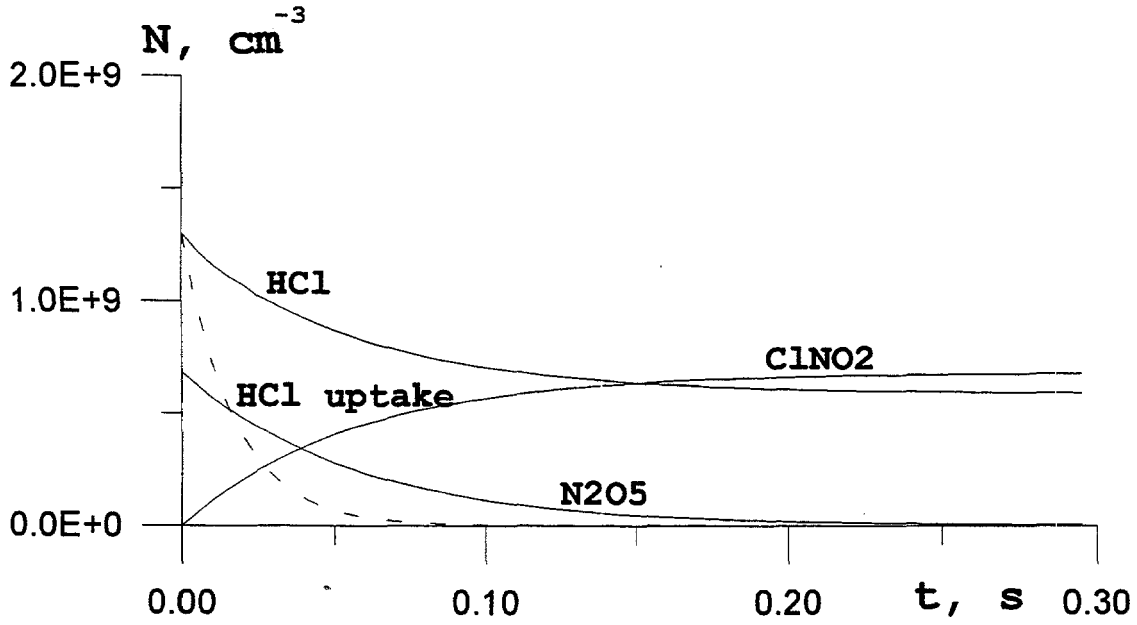

Fig.2 - Temporal evolution of HCl, N2O5, ClNO2 in the heterogenious reaction (2) after the size of ice particles has reached a mixmum. Dashed line corresponds to HCl loss by ice particle uptake.

Model analysis of the chemical conversion of exhaust species in the expanding plumes of subsonic aircraft

M.Möllhoff, J.Hendricks, E.Lippert, H.Petry
Universität zu Köln, Institut für Geophysik und Meteorologie, 50923 Köln, FRG

R.Sausen
DLR, Institut für Physik der Atmosphäre, Oberpfaffenhofen, 82234 Weßling, FRG

Abstract: A box model and two different one-dimensional models are used to investigate the chemical conversion of exhaust species in the dispersing plume of a subsonic aircraft flying at cruise altitude. The effect of varying daytime of release as well as the impact of changing dispersion time is studied with special respect to the aircraft induced O_3 production. Effective emission amounts for consideration in mesoscale and global models are calculated. Simulations with modified photolysis rates are performed to show the sensitivity of the photochemistry to the occurence of cirrus clouds.

1. Introduction

By investigating the chemical transformation of aircraft emissions with the aid of mesoscale or global models a general problem arises: Aircraft plumes need a certain time until they are dispersed to larger scales. The models are not capable to resolve the subgrid structures of young plumes. Instead the emissions commonly are diluted spontaneously and homogeneously to the concerned model grid boxes. As a consequence the high pollutant concentrations in the young plumes are not represented. Because the net ozone production rate is a strong nonlinear function of the NO_x-concentration significant errors in the simulated aircraft induced changes of ozone may occur.

In this study a mesoscale box model and three different plume models are applied to investigate the chemical conversion of pollutants in the expanding plumes of subsonic jets at cruise altitude. Plume simulations are carried out for different daytimes of exhaust release and for differnt dispersion strengths or dispersion times, respectively. From the results effective emission amounts are calculated which can be used in mesoscale or global models to take plume effects into account. Contrails or cirrus clouds may influence the actinic flux within the plume. The sensitivity of the aircraft induced O_3 production to the resulting change of the photolysis rates is evaluated by additional model runs.

2. Description of model and simulations

The simulations are performed with four different model approaches: **1.)** The photochemical conversions are simulated with the box version of the mesoscale EURAD system [1,2,3]. In this case the plume expands spontaneously to a volume of 50km x 50km x 1km which corresponds to the gridsize of the EURAD model system. This technique represents the way emissions are commonly handled in mesoscale and global models and is termed as spontaneous expansion. **2.)** A box model with expanding volume is applied. According to published diffusion parameters of aircraft exhaust plumes near the tropopause [4] the growth of the plume is simulated following Gauss theory. The initial size corresponds to that at the end of the vortex regime. This approach is termed as 0D continuous expansion. **3.)** As a new tool a 2D model was developed. A system of shells is arranged around the plume axis. The growth of each shell as well as the initial emission distribution is calculated analogous

to approach 2 following Gauss theory. The one shell version of this model corresponds to approach 2. **4.)** The gaussian models are restricted to handle non reactive tracers. Another approach is the use of a 1D Eulerian model which explicitly solves the diffusion equation for each reactive trace constituent. By this approach as well as by using approach 3 the pollutant distribution perpendicular to the plume axis is taken into account.
The chemistry mechanism applied in all models is the Chemistry module for the lower Stratosphere and the Troposphere CHEST [5]. The simulations were carried out for june conditions at $50°N$ and $10.7km$ altitude. The considered aircraft exhausts are the NO_x and CO emissions of a B747 at cruise stage [6].

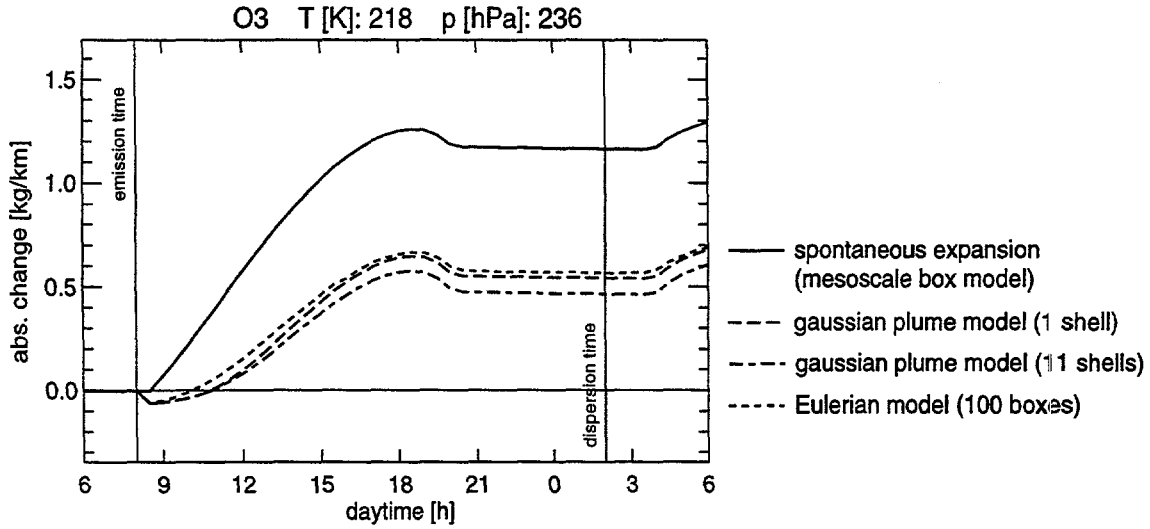

Fig.1 - Absolute change of O_3 mass per unit plume length [kg/km] caused by the emissions of a B747, released at 8h local time. Simulations with the four different model approaches.

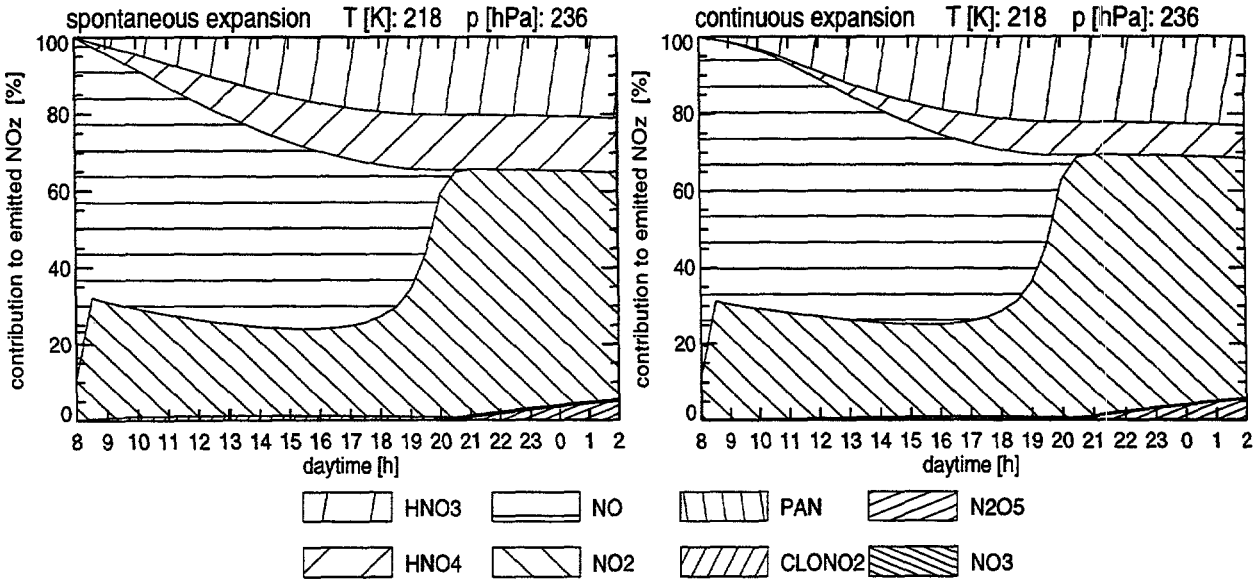

Fig.2 - Transformation of emitted NO_x as simulated with the mesoscale box model (left frame) and the 0D plume model (right frame). Expressed as realtive contributions of nitrogen containing species to the total nitrogen change, caused by the emission of a B747, released at 8h local time.

3. Comparison of the different model approaches

Fig.1 shows the absolute change of O_3 mass per unit plume length [kg/km] caused by the emissions of a B747, released at 8h local time. Results obtained with the four different model approaches are plotted as a function of daytime. One clearly recognizes that the

plume models (approach 2-4) simulate a considerably less aircraft induced O_3 production than the mesoscale box model (approach 1). The appearence of the absolute O_3 change is quite similar in the simulations with the three plume models. This statement also holds for the relevant nitrogen species (not figured in this paper). The results of the 0D plume model (1 shell) show more similarity to the values of the Eulerian model than the results of the shell model with 11 shells. The simulations reveal that the consideration of the distribution of species perpendicular to the plume axis has no relevant effect. For this reason the 0D continuous expansion model is used for the following investigations.
The conversion of the emitted NO_x to other nitrogen containing constituents is presented in *Fig.2* for the simulation with the mesoscale box model and the 0D plume model. After a dispersion time of 18 hours (see chapter 4) about 40% of the emitted NO_x is transformed into reservoir species like HNO_3, HNO_4 and nighttime N_2O_5. The results of the plume model show that the production of HNO_3, which in general is more stable than HNO_4 or N_2O_5, is more effective as suggested by the mesoscale box model.

4. Varying release time, changing dispersion time

In the following the results of the mesoscale box model (approach 1) will be compared to those of the 0D plume model (approach 2). For comparison entrainment is not considered in simulations with the mesoscale box. In the plume model dispersion is represented until the plumes cross section reaches the mesoscale.

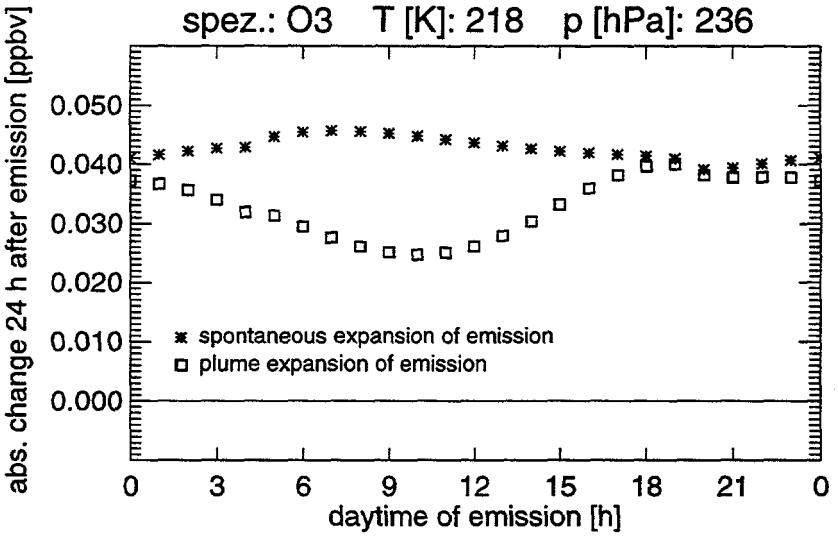

Fig.3 - Absolute change of O_3 [ppbV] caused by emissions of a B747, 24 hours after emission release at different daytimes. Simulated with the mesoscale model (spontaneous expansion) and the 0D plume model.

To get an impression of how the aircraft induced effects vary with the daytime of emission release simulations have been conducted for emission releases at each full hour of a day. In *Fig.3* the response of ozone 24 hours after emission as simulated with the mesoscale box model and the plume model is displayed. In the case of the simulated plumes the area of the plumes cross sections has dispersed to that of the mesoscale box after 24 hours [7]. Consequently after this time period, which is called dispersion time in this paper, the results of the two models can be compared in terms of mixing ratios.
The ozone production is much smaller in the plume model, when the emissions are released at daytime. The discrepancies are small for nighttime releases because in this case the most effective dispersion takes place in the absence of photochemical activity.

In the simulations presented above a dispersion time of 24 hours is assumed. To investigate the sensitivity of the results to a more rapid disperion additional simulations with dispersion times of 18 hours and 12 hours were carried out. *Fig.4* shows the results of simulations which were performed with the mesoscale box model and the 0D plume model assuming dispersion times of 12, 18 and 24 hours, respectively. The release time is chosen to be 8h local time. The absolute aircraft induced O_3 change at the end of the day increases with decreasing dispersion time. As expected the O_3 changes as simulated with the mesoscale box and the plume model converge with increasing dispersion efficiency.

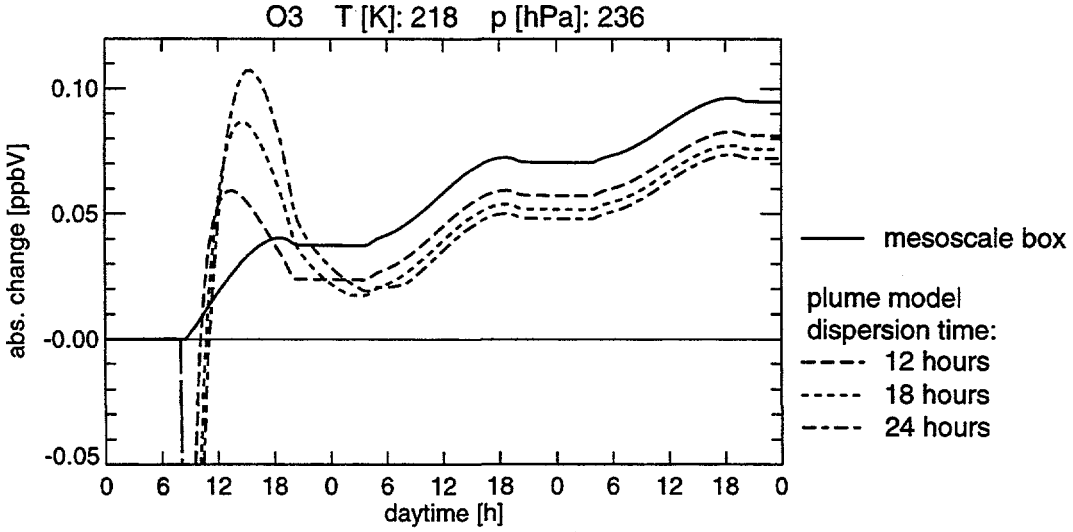

Fig.4 - Absolute change of O_3 [ppbV] caused by the emissions of a B747, released at 8h local time. Simulations with the mesoscale box model and the plume model assuming dispersion times of 12, 18 and 24 hours.

5. Effective emission amounts

In mesoscale and global models emissions generally are treated by a spontaneous mixing over the concerned grid boxes. The effects of the plume dispersion could be taken into account by using corrected emission amounts which are termed as effective emission amounts. In this study the necessary corrections are determined by variation calculations. Simulations with the mesoscale box model are performed for a wide range of modified NO_x (represented as NO) emission amounts. To guaranty conservation of the released nitrogen amounts the modification of NO_x is compensed by corresponding emissions of HNO_3 and HNO_4. To account for the less effective O_3 production of the plume model a varying negative emission amount of O_3 was taken into account. The results are compared to those of the 0D plume model. To obtain a maximum agreement the minimum of the mean root square deviation F:

$$F = \sqrt{\sum_{i=1}^{n}(X_{ic} - X_{is})^2}\ , \qquad (1)$$

is searched. Here X_{ic} and X_{is} are the mixing ratios of a species i after the dispersion time for continuous expansion (0D plume model) and for spontaneous expansion (mesoscale box), respectively. In the present study n=4 and $(X_1,\ldots,X_4) = (O_3,\ NO_x,\ HNO_3,\ HNO_4)$ was assumed. Further details are described in [7].

The diurnal variation of the effective emission amounts is calculated under conditions of a clean background as well as for the case of emission into a polluted highly frequented flight corridor. The results are representative for the conditions described in the 2nd chapter. *Fig.5* exemplarly shows the effect of using corrected emission amounts on the aircraft induced O_3

change for a release of aircraft exhausts at 8h local time into an unpolluted background. After the dispersion time of in this case 18 hours the results of the mesoscale box simulation using the corrected emission amounts match those of the plume model quite well. This statement even holds for the following two days.

Fig.6 presents the effective emission amounts of NO and O_3 for the conditions of an originally polluted flight corridor. For the calculations a disperion time of 18 hours is assumed. The corrected emissions are expressed as relative fractions of the uncorrected NO_x change caused by the B747. Corrections for each daytime are suggested.

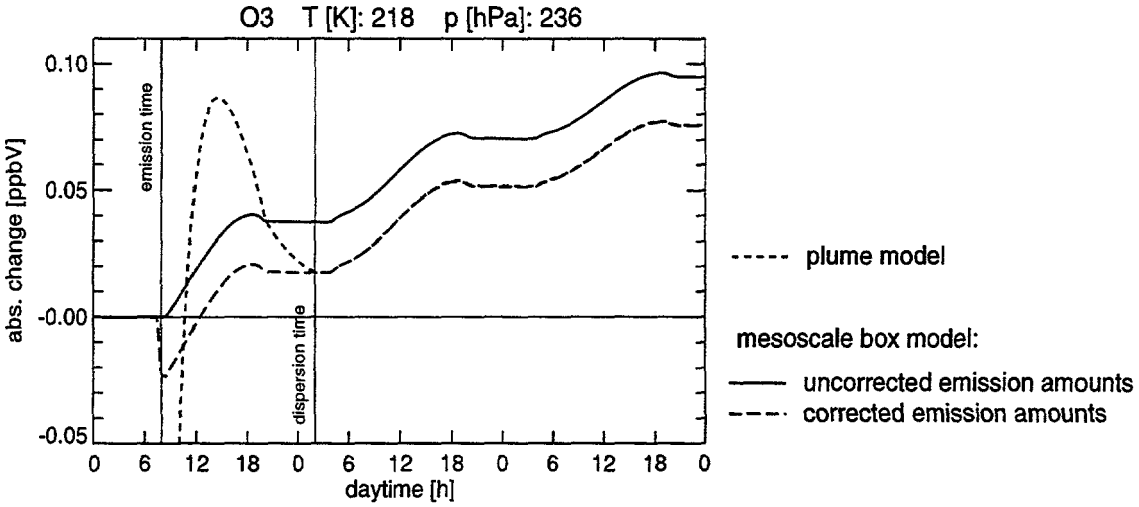

Fig.5 - Absolute change of O_3 [ppbV] caused by the emissions of a B747, released at 8h local time. Simulations with the plume model and the mesoscale box model under consideration of uncorrected and corrected aircraft emission amounts. Dispersion time: 18 hours.

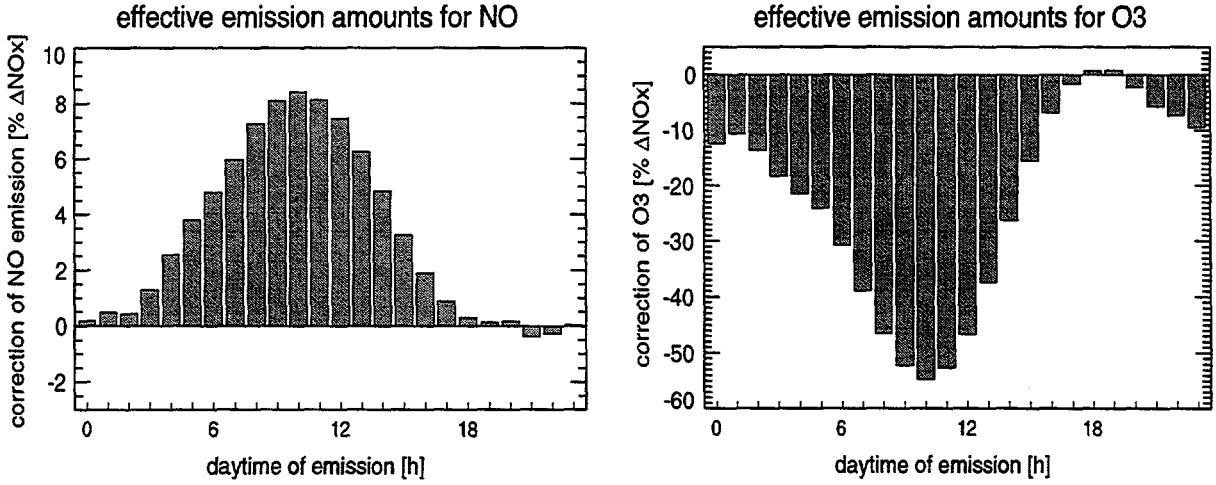

Fig.6 - Effective emission amounts for NO (left frame) and O_3 (right frame) relative to original NO_x emission, for different daytimes of release into a polluted flight corridor. The emission amounts have to be interpreted in terms of mixing ratios. Dispersion time: 18 hours.

6. Enhanced actinic fluxes

The formation of contrails is a frequently observed phenomenon evoked by the emissions of high flying subsonic jets. The possibility of the formation of cirrus clouds triggered by the occurence of contrails has been a central point of many discussions concerning the impact of aviation on the atmospheric radiation budget. The presence of cirrus clouds may cause considerable changes of the actinic fluxes in the concerned regions. As a consequence of the corresponding change in the photolysis rates of atmospheric constituents, which are coupled

linearly to the actinic flux, the transformation of aircraft exhausts above, below or within the cirrus may be influenced, too. The theoretical highest enhancement of the actinic flux below or above a cloud amounts to factors of 5 or 3, respectively [8].
To study the effect of the changed photolysis rates on the aircraft induced O_3 production simulations with the 0D plume model were performed considering enhancement factors for the actinic flux of 0.5, 2 and 5. *Fig.7* shows the results of these model runs. The aircraft induced O_3 production shows a considerable increase under conditions of enhanced photolysis rates. An approximately linear dependence is observed.

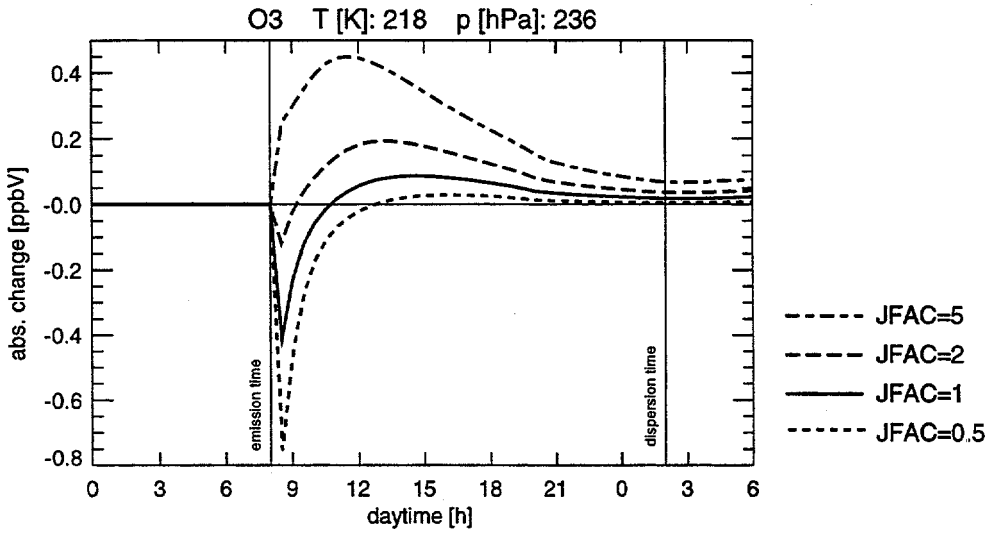

Fig.7 - Absolute change of O_3 [ppbV] caused by the emissions of a B747, released at 8h local time. Simulations with the plume model under consideration of varying actinic fluxes. The standard photolysis rates were multiplied by factors of 0.5, 1, 2 and 5 for the respective simulations. Dispersion time: 18 hours.

References

1. Petry, H., H.Elbern, E.Lippert, R.Meyer, 1994: Proceedings of an International Scientific Colloqium, Köln, April 18-20, 1994, U.Schumann and D.Wurzel, Eds., DLR, 329-335.
2. Petry, H., A.Ebel, V.Franzkowiak, J.Hendricks, E.Lippert, M.Möllhof, 1996: *this volume.*
3. Hendricks, J., A.Ebel, E.Lippert, H.Petry, 1996: *this volume.*
4. Schumann, U., P.Konopka, R.Baumann, R.Busen, T.Gerz, H.Schlager, P.Schulte, H.Volkert, 1995: *J. Geophys. Res.*, **100**, 14147-14162.
5. Lippert, E., J.Hendricks, H.Petry, 1996: *this volume.*
6. Deidewig, F., 1992: DLR, IB-325-4-92. 89 pp.
7. Möllhoff, M., 1996: Modellierung der chemischen Umwandlung reaktiver Flugzeugabgase im Tropopausenbereich unter Berücksichtigung ihrer Dispersion. Thesis, Univ. Köln.
8. Madronich, S., 1987: *J. Geophys. Res.*, **92**, 9740-9752.

Analysis of nonequilibrium chemical processes in the plume of subsonic and supersonic aircraft with hydrogen and hydrocarbon combustion engine.

A.M. Starik, A.B. Lebedev, N.S. Titova

On the basic of quasi one dimensional mixing model the numerical analysis of nonequilibrium chemical processes in the plume of subsonic and hypersonic aircraft is presented. It was found that species HNO, HNO_3, HNO_4, N_2O_5, ClO_2, CH_3NO_2 could be formed as a result of nonequilibrium processes in the plume and their concentrations can essentially exceed both background values in free stream of atmosphere and their values at the nozzle exit plane.

The environmental perturbation caused by exhaust of subsonic and supersonic aircraft depend on deposition altitude and amount and composition of emissions. In order to define real emission of pollutant components in the atmosphere the analysis of nonequilibrium processes in gas engine elements and in plume is required.

In this report the results of such analysis for subsonic and hypersonic aircraft with hydrocarbon and hydrogen combustion engine are presented.

The model that was used for analysis of photochemical nonequilibrium processes in the plume contains the gasdynamic block in which the gasdynamic parameters are calculated taking into account the turbulent mixing of internal flow from nozzle with free stream of atmosphere air containing all gas small components and the kinetic block in which change of concentration of components along the plume is calculated using quasi one-dimensional approximation and average values of velocity and temperature.

In according with such method the change of the concentration of species i along the plume with the cross section $A(x)$ is defined by the equation [1]

$$\frac{d(\rho_i u A)}{dx} = \frac{d(\rho_{i\infty} u A)}{dx} + A m_i G_i \qquad (1)$$

$$G_i = \sum_{q=1}^{M} S_{iq} + \sum_{l=1}^{M_1} J_{il}, \quad S_{iq} = \left(\alpha_{iq}^- - \alpha_{iq}^+\right)\left[R_q^+ - R_q^-\right]$$

$$R_q^{+(-)} = k_{+(-)} \prod_{j=1}^{n_q^{+(-)}} N_j^{\alpha_{iq}^{+(-)}}, \quad J_{il} = \sum_k \beta_{il} I_{lk} N_k$$

Here m_i is the molecular mass of the species i, ρ_i is the partial density of the species i averaged over the area of the plume, $\rho_{i\infty}$ is the constant partial density of the species i on the boundary of the plume, u is the air velocity in a system of coordinates connected with the aircraft, M is the number of the chemical reactions, M_1 is the number of the photochemical reactions, resulting in the formation or destruction of the species i, α_{iq}^+ and α_{iq}^- are the stoichiometric coefficients of the chemical reaction q, and β_{il} is the stoichiometric coefficient of the photochemical reaction l, $n_q^{+(-)}$ is the number of the species taking part in the forward (+) and backward (-) chemical reaction, $k_{+(-)q}$ is the rate constant of these reactions, I_{lk} is the rate of photochemical reaction l of the species k, $N_i = m_i \rho_i$. It is comfortable to input the molar concentration of the species i $\gamma_i = N_i / N$, where $N = \sum_{i=1}^{S} N_i$, S is the number of atomic and molecular species in the mixture and rewrite the equation (1) in the following form

$$\frac{d\gamma_i}{dx} = \frac{1}{Nu}\left(G_i - \gamma_i \sum_{j=1}^{S} G_j\right) + \left(Q_i - \gamma_i \sum_{j=1}^{S} Q_j\right), \quad Q_i = \frac{N_{i\infty} - N_i}{AN}\frac{dA}{dx} \qquad (2)$$

The solution of the equations' system (2) was carried out numerically with the using of implicit different scheme of the second order precision.

The fields of hydrodynamic parameters of subsonic coflowing jet were determinate by using the simple algebraic method. In this method, the nonisobaric jet first replaced by a hypothetical isobaric jet with a different Mach number M_1 and radius R_c that were determined from the condition that the total pressure and gas flow rate through the nozzle in the real and hypothetical cases were equal [2]. The influence of turbulent of external flow on the mixing was taken into account by increasing of turbulent viscosity coefficient and turbulent diffusivity coefficient of coflowing jet. This effect was determined by changing of momentum-loss thickness. The near field plume extending from the exhaust exit plane to the plane of interaction between exhaust plume and wing vortices considered here. The extend of this region corresponded approximately to a downstream of 1000-1500 nozzle diameters for subsonic aircraft.

The fields of hydrodynamics parameters of hypersonic coflowing jet were determined by numerical solution parabolic equations for axisymmetric compressible turbulent flow, using second order numerical implicit scheme [3]. We considered flow behind hypersonic aircraft with aerodynamic scheme such as "Hotoll". This aircraft had only one exhaust and ogive form. The nonisobaric jet was replaced by a hypothetical isobaric jet so as for coflowing jet of subsonic aircraft. We considered four turbulent models, that were taken into account the effect of compressibility to turbulent supersonic flows: two of them were two-equation turbulence models [3,4] and two ones were one-equation turbulence models [3,5].

When we have elaborated the kinetic scheme of processes in the plume for subsonic and hypersonic aircraft we have taken into account that the temperature along the plume can change from *1900 K* to *200 K*, and the combustion products can enter into reactions with the small species of atmosphere during the process of mixing. So the elaborated scheme of chemical processes includes reactions characterized both for the high temperature conditions [6] and for the atmospheric photochemistry [7] and contains 240 chemical and 28 photochemical reactions with participation of 61 components: H_z, N_z(z=1,2), O_x (x=1...3), H_zO_z, NO_x, HNO_y (y=1...4), $O(^1D)$, $O(^3P)$, N_2O, N_2O_5, CO_x, CH_q (q=3,4), CH_yO_x, HCN, CN, NCO, CH_3NO_{z+1}, SO_x, HSO_3, H_2SO_4, Cl_z, ClO_z, CF_zCl_x, CCl_q, $ClNO_3$, $CH_{z+1}Cl$, $Cl_2(F)CO$, F_2, ClF, HCl, HOCl. Values of photodissociation rates were taken from Ref. [8].

To obtain the quantitative information about the variation of the gas chemical composition along the plume it is important to set the probable values of gas composition in the atmosphere and at the nozzle exit plane. The point is that the small species of the combustion products (OH, H, O, H_2O_2, HO_2, HNO_3, HNO_4, N_2O_5, C, C_2, CN, CH_4 and etc.) which concentrations can essentially change in the plume by photochemical reactions influence on the change of the state of atmosphere and Earth ozone layer. Moreover, the penetration of background species (example, Cl-containing) from atmosphere into the plume can result in the formation of the new products, which are contained neither combustion products nor atmosphere. Unfortunately at the present time the enough full data about the composition even main small species don't exist. Their concentrations change according to the high, latitude and longitude. Such information is absent for the gas composition at the nozzle exit plane too.

So for the subsonic aircraft two model tasks have been considered. For the first task the boundary conditions were taken from [9], and for the second task its were taken from the calculation of the combustion of C_8H_{18}+air mixture with the equivalence ratio 1/4. This calculation was carried out with using enough full kinetic scheme, including 435 reversible reactions with participation of 66 components: N, N_2, H, H_2, O, O_2, O_3, OH, H_2O, H_2O_2, NO, NO_2, NO_3, N_2O_5, HNO, HNO_2, HNO_3, HNO_4, C, C_2, CO, C_nH_m, $C_nH_mO_z$, C_xH_y, $C_xH_yN_z$, $C_xH_yN_zO$ (n=1,...4; m=1,...10) [6]. Concentration values of small species of atmosphere were taken from [8].

The data for the change of γ_i and T along the plume that were obtained for these two variants is given in *Table 1*. The flight conditions were following: Max number of flight M_∞ =0.55, altitude of flight H=10 *km*, T_∞=223 *K*, P_∞=35 *kPa*, Max number at the nozzle exit plane M_n=0.97, diameter of the nozzle exit plane D_n=1,04 *m*. Analysis of present results shows that the formation of N-containing (HNO, HNO_2, HNO_3, HNO_4, N_2O_5) and S-containing (SO_3, HSO_3, H_2SO_4) species and decreasing of the concentration of O, OH, HO_2 and H takes place in both cases. These processes proceed especially actively on the initial plume part where the temperature and density of the gas are great. It should be note that the change of the N- and H-

Table 1. The change of the temperature and gas composition at the various planes of the plume of subsonic aircraft under M_∞=0.55, H=10 km.

x, m	0.0	0.0	*atmosphere*	1.0		100		1000	
Var.	1	2	-	1	2	1	2	1	2
T, K	450	450	223.1	444.6	444.5	238.8	238.9	224.7	224.7
H_2O	3.59(-2)	3.500(-2)	5.768(-5)	3.608(-2)	3.508(-2)	3.631(-3)	3.584(-3)	3.584(-4)	3.535(-4)
O_2	1.56(-1)	1.618(-1)	2.002(-1)	1.568(-1)	1.621(-1)	1.958(-1)	1.963(-1)	1.998(-1)	1.998(-1)
H_2	1.03(-6)	5.522(-7)	9.378(-7)	1.035(-6)	5.538(-7)	9.474(-7)	8.991(-7)	9.386(-7)	9.345(-7)
OH	3.40(-6)	9.478(-5)	1.071(-13)	1.617(-13)	4.934(-12)	1.089(-14)	2.890(-13)	8.237(-15)	2.046(-13)
H	6.12(-9)	5.179(-8)	2.35(-20)	1.058(-17)	2.373(-17)	2.810(-20)	1.240(-19)	5.780(-21)	5.617(-20)
O	1.55(-7)	6.054(-6)	1.664(-15)	9.988(-11)	1.728(-10)	5.437(-13)	6.890(-12)	6.338(-14)	4.793(-13)
N_2	7.68(-1)	7.746(-1)	7.995(-1)	7.718(-1)	7.759(-1)	7.967(-1)	7.971(-1)	7.993(-1)	7.993(-1)
HO_2	9.77(-8)	3.223(-7)	1.406(-11)	4.113(-17)	4.647(-14)	1.100(-15)	8.005(-15)	5.088(-16)	1.138(-15)
H_2O_2	2.44(-8)	1.346(-8)	8.793(-10)	2.854(-8)	5.321(-6)	3.624(-9)	5.365(-7)	1.110(-9)	4.581(-8)
N	0.0	1.206(-13)	4.228(-28)	1.682(-22)	1.356(-22)	9.103(-23)	7.838(-23)	8.555(-23)	7.343(-23)
NO	2.81(-3)	2.728(-4)	1.003(-11)	2.820(-3)	2.402(-4)	2.797(-4)	2.413(-5)	2.348(-5)	2.034(-6)
NO_2	8.73(-6)	1.103(-4)	6.027(-12)	8.964(-6)	1.324(-4)	1.004(-6)	1.337(-5)	1.462(-7)	1.111(-6)
HNO_2	0.0	1.799(-5)	3.879(-14)	3.445(-6)	2.593(-5)	3.418(-7)	2.610(-6)	2.877(-8)	2.184(-7)
N_2O	4.30(-7)	4.648(-5)	2.811(-7)	4.321(-7)	4.656(-5)	2.961(-7)	4.940(-6)	2.824(-7)	6.720(-7)
HNO	0.0	4.736(-11)	0.0	7.770(-10)	1.580(-8)	7.708(-11)	1.587(-9)	6.490(-12)	1.332(-10)
O_3	0.0	6.463(-9)	7.275(-8)	7.174(-10)	7.696(-7)	9.490(-9)	6.268(-8)	1.330(-8)	7.908(-8)
HNO_3	4.07(-8)	2.983(-8)	2.271(-10)	6.739(-8)	2.561(-5)	6.892(-9)	2.580(-6)	7.904(-10)	2.172(-7)
NO_3	0.0	2.226(-5)	3.598(-15)	2.893(-15)	1.053(-10)	5.083(-16)	2.484(-13)	7.192(-16)	1.372(-13)
N_2O_5	0.0	0.0	1.653(-13)	1.457(-17)	7.632(-12)	2.672(-13)	1.074(-9)	4.952(-13)	8.619(-10)
HNO_4	0.0	2.738(-25)	1.061(-10)	1.023(-19)	1.904(-15)	9.553(-11)	9.668(-11)	1.053(-10)	1.058(-10)
CH_3	0.0	5.343(-15)	1.855(-21)	0.0	2.514(-27)	1.104(-20)	7.208(-21)	3.890(-21)	1.817(-21)
CH_4	0.0	3.467(-15)	1.496(-6)	1.921(-21)	3.461(-15)	1.347(-6)	1.345(-6)	1.483(-6)	1.483(-6)
CO	1.09(-5)	1.017(-6)	2.283(-7)	1.095(-5)	1.008(-6)	1.292(-6)	3.068(-7)	3.178(-7)	2.348(-7)
CO_2	3.24(-2)	2.645(-2)	3.092(-4)	3.256(-2)	2.649(-2)	3.509(-3)	2.945(-3)	5.785(-4)	5.304(-4)
HCO	0.0	2.102(-16)	8.074(-23)	6.745(-26)	3.459(-25)	6.437(-22)	4.737(-22)	3.986(-22)	2.482(-22)
CH_2O	0.0	3.792(-15)	1.900(-11)	3.242(-21)	1.836(-15)	1.712(-11)	1.710(-11)	1.884(-11)	1.893(-11)
CH_3O	0.0	2.572(-18)	8.917(-18)	0.0	1.310(-26)	6.282(-19)	6.636(-18)	6.395(-19)	5.766(-18)
CH_3OH	0.0	8.950(-18)	0.0	0.0	2.894(-15)	7.471(-22)	2.916(-16)	5.825(-21)	2.605(-17)
CH_3O_2	0.0	1.190(-18)	2.710(-12)	3.127(-28)	3.036(-25)	2.688(-16)	3.110(-15)	2.748(-16)	2.954(-15)
CH_3NO_2	0.0	0.0	0.0	3.156(-27)	2.069(-15)	2.485(-12)	2.299(-12)	2.951(-12)	2.478(-12)
CH_3NO_3	0.0	0.0	0.0	0.0	7.848(-18)	1.016(-15)	1.501(-13)	2.711(-15)	2.515(-13)
SO_2	6.91(-6)	6.91(-6)	0.0	6.941(-6)	6.742(-6)	6.887(-7)	6.788(-7)	5.796(-8)	5.695(-8)
SO_3	0.0	0.0	0.0	9.541(-10)	6.172(-8)	8.000(-15)	2.066(-13)	6.358(-15)	1.567(-13)
HSO_3	0.0	0.0	0.0	6.875(-18)	1.993(-16)	4.440(-19)	1.158(-17)	3.535(-20)	8.625(-19)
H_2SO_4	0.0	0.0	0.0	1.926(-9)	1.175(-7)	2.861(-10)	1.805(-8)	2.421(-11)	1.517(-9)
Cl	0.0	0.0	2.316(-16)	7.854(-28)	9.313(-28)	4.627(-13)	2.866(-13)	2.472(-13)	1.054(-13)
ClO	0.0	0.0	6.578(-13)	5.351(-29)	1.745(-28)	3.354(-17)	5.897(-16)	7.644(-17)	1.658(-15)
ClO_2	0.0	0.0	0.0	0.0	0.0	7.797(-14)	4.811(-14)	1.069(-13)	4.562(-14)
$ClNO_3$	0.0	0.0	3.407(-13)	4.378(-28)	5.916(-28)	3.072(-13)	3.614(-13)	3.391(-13)	5.974(-13)
HCl	0.0	0.0	1.934(-10)	2.485(-25)	3.313(-25)	1.743(-10)	1.741(-10)	1.921(-10)	1.920(-10)
HOCl	0.0	0.0	4.138(-12)	5.316(-27)	7.088(-27)	3.727(-12)	3.721(-12)	4.101(-12)	4.100(-12)
CH_2Cl	0.0	0.0	0.0	0.0	0.0	8.620(-17)	6.061(-17)	5.329(-16)	3.005(-16)
CH_3Cl	0.0	0.0	5.442(-10)	6.992(-25)	9.323(-25)	4.902(-10)	4.894(-10)	5.397(-10)	5.396(-10)
Cl_2	0.0	0.0	3.834(-18)	0.0	0.0	6.899(-18)	5.896(-18)	3.898(-17)	3.108(-17)
Cl_2CO	0.0	0.0	0.0	0.0	0.0	3.277(-24)	2.218(-23)	7.166(-23)	4.349(-22)
CCl_3	0.0	0.0	0.0	0.0	0.0	2.879(-22)	7.284(-21)	1.646(-21)	2.679(-20)
CCl_4	0.0	0.0	1.214(-10)	1.560(-25)	2.080(-25)	1.094(-10)	1.092(-10)	1.204(-10)	1.204(-10)
ClF	0.0	0.0	0.0	0.0	0.0	7.423(-24)	5.025(-23)	1.624(-22)	9.855(-22)
$CFCl_2$	0.0	0.0	0.0	0.0	0.0	1.810(-23)	1.610(-22)	3.613(-22)	2.250(-21)
$CFCl_3$	0.0	0.0	1.406(-10)	1.806(-25)	2.408(-25)	1.266(-10)	1.264(-10)	1.394(-10)	1.394(-10)
FClCO	0.0	0.0	0.0	0.0	0.0	7.423(-24)	5.025(-23)	1.624(-22)	9.855(-22)
F_2CO	0.0	0.0	0.0	0.0	0.0	4.147(-24)	2.808(-23)	9.073(-23)	5.506(-22)
CF_2Cl	0.0	0.0	0.0	0.0	0.0	1.956(-23)	2.291(-22)	3.408(-22)	2.224(-21)
CF_2Cl_2	0.0	0.0	2.339(-10)	3.005(-25)	4.006(-25)	2.107(-10)	2.103(-10)	2.319(-10)	2.319(-10)

containing species concentrations at the initial plume part don't connect with the penetration atmospheric gases into the flow.

Interaction of the relatively hot gases plume with the coflow of cold air results in the sufficiently quick decrease of the temperature and the appearance in the plume the small atmosphere species that capable to interact with the combustion products of the fuels.

The decrease of the temperature results in the change of the dependence character $\gamma_{N_2O_5}(x)$ and $\gamma_{HNO_4}(x)$, $\bar{x}=x/D$, where D is the diameter of the nozzle exit plane. The quick decrease of $\gamma_{N_2O_5}$ and γ_{HNO_4} in the interval $10^{-2}<\bar{x}\leq 4$ is stopped and then their values begin to increase. It takes place because the role of recombination reactions resulting in the formation HNO_4 and N_2O_5 is increased on cooling of the gas until $T<300$ K. The HNO_4 concentration reaches its background value in the atmosphere and N_2O_5 concentration exceeds its background value essentially. The decrease of the temperature is accompanied by the formation of new species CH_3NO_2, CH_3NO_3 which are contained neither combustion products nor background atmosphere. The other interesting and important process caused by penetration into the flow of small gas species is the interaction Cl-containing species with nitrogen oxides realizing on the lengths which greater than the characteristic scale of the mixture. When the $\bar{x}$ ($4\leq\bar{x}\leq 10^{-2}$) is increased the essential increasing of the concentrations of Cl, Cl_2, ClO_2, $ClNO_3$, CH_2Cl by comparison with background values and the decreasing ClO concentration takes place. The analysis of the reaction rates in which all Cl-containing species take part has shown that at the beginning of mixture zone ($\bar{x}=4$) the formation of free chlorine takes place as result of interaction ClO and NO, which concentrations are essentially in 10^6 times greater in the plume than in the atmosphere.

Because of considerable (in 10^3 times) increase of Cl concentration the acceleration of the formation ClO_2 takes place. The recombination ClO and NO_2 resulting in the formation $ClNO_3$ is essentially more slow process.

Under $\bar{x}>10^2$ the situation changes. The values γ_{Cl} and γ_{ClO_2} begin to increase after achievement their maximum values whereas the concentrations of $ClNO_3$, Cl_2, CH_2Cl and ClO continue to grow. Nevertheless the free chlorine concentration essentially exceeds its background value as far as the interaction of the plume with the pair of whirlwinds leaving the ends of wings.

The change of flight altitude (H=20 *km*) don't result in some new qualitative regularities although in consequence of change of the pressure and background composition of the atmosphere the quantitative values of component concentration are somewhat changed. It should be mentioned that at $\bar{x}>10$ the photodissociation processes begin to influence on the formation of the free atoms and radicals at flight altitude H≥18 *km*. Neglect of these processes can result in essential (until 10^4 times) mistakes of values γ_{OH}, γ_O, γ_H, γ_{HSO_3} and some products of CFC's disintegration too. It should be noted that considered regularities remain just one qualitatively at somewhat other boundary conditions at the nozzle exit plane corresponding [9].

Under analysis of nonequilibrium processes in the plume of hypersonic aircrafts with H_2+air combustion engine the following flight regime has been chosen: $M_\infty=6$, H=29 *km*, $P_n=P_\infty$ =1,372 *kPa*, $T_\infty=216$ *K*. Here P_n is the pressure at the exit nozzle plane. The gas composition and temperature at the nozzle exit plane was taken from reference [10] in which the chemical nonequilibrium flow in the gas engine elements was calculated with the use of full kinetic scheme containing 152 reversible reactions. The calculation of the fields of hydrodynamic parameters was carried out with taking into account the presence of external and internal boundary layers at exit of the nozzle surface. The estimations that were carried out have shown that the thicknesses of these layers are equal $0.4R_n$ and $0.05R_n$ accordingly, R_n is the radius of the nozzle exit plane ($R_n=1.09$ *m*). The plume boundary r_p was determined from the condition $[h_0(r_p)-h_{0\infty}]=0.1[h_0(r=0)-h_{0\infty}]$. Here h_0 is the full mixture enthalpy, $h_{0\infty}$ is the enthalpy of the atmospheric air. The comparison of the fields of hydrodynamic parameters calculated with the utilization of different turbulent models showed that one-equation models result in the considerable errors for similar plumes. So calculations were carried out with the utilization of two-equation models [4].

The results of the calculation of the variation of the different species concentration along the hypersonic aircraft plume are presented in the *Table 2*.

The results which were obtained for subsonic and hypersonic aircrafts indicate on the considerable change of the composition of the gas mixture along the plume. Moreover this change can be caused not only by the mixture of combustion products with the atmosphere air but by proceeding of whole complex of nonequilibrium photochemical reactions. Besides the

Table 2. The change of the temperature, radius and gas composition at the various planes of the plume of hypersonic aircraft with hydrogen combustion engine under M_∞=6, H=29 km.

x, m	0.0	*atmosphere*	2.0	200	2000
T, K	1651	216	1650.9	481.7	246.61
r, m	1.07	-	1.07	2.35	5.21
H_2O	2.98(-1)	3.249(-6)	3.00(-1)	1.174(-1)	4.336(-2)
O_2	1.31(-2)	1.998(-1)	1.467(-2)	1.280(-1)	1.733(-1)
H_2	7.06(-3)	6.661(-7)	6.541(-3)	1.795(-3)	6.587(-4)
OH	4.86(-3)	1.070(-11)	1.638(-4)	2.683(-5)	2.208(-11)
H	1.81(-3)	2.097(-17)	3.849(-3)	5.728(-6)	2.676(-14)
O	8.9(-4)	1.843(-10)	6.285(-4)	2.856(-6)	1.096(-9)
N_2	6.67(-1)	7.999(-1)	6.668(-1)	7.497(-1)	7.814(-1)
HO_2	1.69(-7)	7.044(-11)	6.674(-8)	2.496(-7)	2.184(-14)
H_2O_2	2.41(-7)	2.274(-10)	4.056(-9)	1.825(-6)	6.034(-7)
N	1.04(-8)	8.682(-17)	8.925(-15)	2.723(-15)	1.421(-15)
NO	7.41(-3)	1.990(-9)	7.453(-3)	2.863(-3)	1.047(-3)
NO_2	1.35(-5)	4.041(-9)	1.836(-8)	7.501(-6)	1.077(-5)
HNO_2	2.98(-5)	2.255(-12)	4.195(-7)	1.061(-5)	6.205(-6)
N_2O	1.78(-7)	1.149(-7)	1.317(-7)	5.934(-8)	9.441(-8)
HNO	1.75(-7)	0.0	1.312(-7)	7.904(-7)	1.785(-7)
O_3	1.79(-10)	1.081(-5)	2.102(-11)	3.479(-7)	1.315(-6)
HNO_3	4.71(-9)	1.403(-9)	5.880(-9)	1.184(-7)	1.019(-7)
NO_3	3.25(-9)	2.604(-12)	2.199(-13)	5.123(-12)	2.324(-13)
N_2O_5	0.0	1.209(-9)	5.604(-28)	9.099(-13)	6.667(-10)
HNO_4	6.87(-27)	1.895(-10)	4.853(-24)	3.819(-12)	1.165(-10)
CH_3	0.0	1.671(-18)	0.0	1.470(-12)	2.271(-18)
CH_4	0.0	8.190(-7)	0.0	3.967(-7)	6.624(-7)
CO	0.0	2.662(-8)	0.0	4.931(-8)	3.478(-8)
CO_2	0.0	2.326(-4)	0.0	1.430(-4)	1.995(-4)
HCO	0.0	1.040(-22)	0.0	5.101(-14)	1.879(-19)
CH_2O	0.0	4.614(-11)	0.0	9.375(-11)	5.548(-11)
CH_3O	0.0	9.937(-16)	0.0	2.364(-12)	1.243(-17)
CH_3OH	0.0	0.0	0.0	2.146(-14)	5.564(-21)
CH_3O_2	0.0	1.452(-12)	0.0	3.760(-13)	1.754(-16)
CH_3NO_2	0.0	0.0	0.0	6.519(-8)	2.479(-8)
CH_3NO_3	0.0	0.0	0.0	4.561(-14)	4.549(-14)
SO_2	6.91(-6)	0.0	6.91(-6)	2.653(-6)	9.777(-7)
SO_3	0.0	0.0	3.135(-10)	7.737(-9)	8.877(-14)
HSO_3	0.0	0.0	3.641(-11)	1.922(-11)	6.340(-17)
H_2SO_4	0.0	0.0	4.141(-12)	1.067(-8)	8.558(-9)
Cl	0.0	8.190(-14)	0.0	3.705(-11)	3.635(-11)
ClO	0.0	1.458(-10)	0.0	1.325(-13)	2.817(-14)
ClO_2	0.0	0.0	0.0	1.028(-16)	1.753(-13)
$ClNO_3$	0.0	5.351(-11)	0.0	1.925(-11)	4.042(-11)
HCl	0.0	5.979(-10)	0.0	4.867(-10)	6.278(-10)
HOCl	0.0	1.556(-10)	0.0	4.317(-11)	1.128(-10)
CH_2Cl	0.0	0.0	0.0	2.085(-11)	8.140(-12)
CH_3Cl	0.0	1.581(-10)	0.0	7.636(-11)	1.275(-10)
Cl_2	0.0	7.071(-15)	0.0	4.404(-15)	9.690(-15)
Cl_2CO	0.0	0.0	0.0	2.402(-24)	7.183(-22)
CCl_3	0.0	0.0	0.0	9.305(-14)	3.521(-14)
CCl_4	0.0	6.825(-12)	0.0	4.104(-12)	5.820(-12)
ClF	0.0	0.0	0.0	1.323(-23)	3.958(-21)
$CFCl_2$	0.0	0.0	0.0	2.538(-14)	9.447(-15)
$CFCl_3$	0.0	1.160(-11)	0.0	7.110(-12)	9.944(-12)
FClCO	0.0	0.0	0.0	1.323(-23)	3.958(-21)
F_2CO	0.0	0.0	0.0	1.083(-23)	3.240(-21)
CF_2Cl	0.0	0.0	0.0	1.743(-13)	6.494(-14)
CF_2Cl_2	0.0	6.880(-11)	0.0	4.213(-11)	5.896(-11)

change of the gas composition in the plume the phase transformations can take place. For example in the plume of subsonic aircraft flying at a oltitude of 10 *km* under 75% water steams can turn into the liquid phase if $\bar{x} \geq 250$.

In the regions of the plume where $T<233$ *K* the water drops can freeze and turn into the ice particles. The estimations show that the freezing zone of water drops is found in outside jet region. So sufficiently large (by comparison with background one) concentrations of the species N_2O_5, HNO_3, $ClNO_3$, SO_3, H_2SO_4 are in the plume, the rates of following heterogeneous processes can increase in perturbation region of atmosphere (here index "s" corresponds to the proceeding of the reactions on the surface of the solid particle)

1. $N_2O_5 + H_2O(s) \rightarrow 2HNO_3(s)$
2. $HNO_3 + H_2O(s) \rightarrow HNO_3(s)$
3. $SO_3 + H_2O(s) \rightarrow H_2SO_4(s)$
4. $H_2SO_4 + H_2O(s) \rightarrow H_2SO_4(s)$
5. $ClNO_3 + H_2O(s) \rightarrow HOCl(s,g) + HNO_3(s)$

The penetration into the plume of HCl can initiate the heterogenions reactions that proceed with the generation of gaseous Cl.

6. $HCl + H_2O(s) \rightarrow HCl(s)$
7. $HCl(s) + ClNO_3 \rightarrow Cl_2 + HNO_3(s)$

However at present time sufficiently strict consideration of these processes is impossible because the reliable models of ice formation in the plume of the jet engine and values of probabilities of processes in corresponding conditions are absent.

References

1. Matloff G.L., Hoffert M.I. AIAA-Journal. 1977. V.15. №8. p.1205.
2. Kozlov V.E., Secundov A.N., Smirnova I.P. Fluid Mechanics-Soviet Research. 1988. V.17. №1. p.93.
3. Kozlov V.E., Secundov A.N., Smirnova I.P. Fluid Dynamics. 1986. V.21. №6. p.875.
4. Fujiwara H., Aracawa C. Engineering turbulence modelling and experiment 3. / ed. Rodi W., Bergles G. Creece. 1996. p.151.
5. Shur M., Strelets M., Zaiikov L. et. al. AIAA-paper 95-0863.1995.
6. Dautov N.G., Starik A.M. Fizika gorenia i vzriva. 1996. V.32. №1. p.94.
7. Baulch D.L. Cox R.A., Crutzen P.J. et. al. J. Chem. Phys. Ref. Data. 1982. V.11. №2. p.327.
8. Shimazaki T. J.Atmosph. Terr. Phys. 1984. V.46. №2. p.173.
9. Miake-Lye R.C., Martinez-Sanchez M., Brown R.C., Kolb C.E. Journal of aircraft. 1993. V.30. №4. p.467.
10. Dautov N.G., Starik A.M. Teplofizika vysokih temperatur. 1995. V.33. №2. p.219.

CHEMISTRY IN AIRCRAFT PLUMES

A.G. Kraabøl[1], P.Konopka [2], F. Stordal [1] and S. Knudsen [1]
[1] Norwegian institute for Air research,
N-2007 Kjeller, Norway
[2] DLR, Institute of Atmospheric Physics,
D-82230 Wessling, Germany

ABSTRACT

An expanding plume model with chemistry has been used to study the chemical conversion of NO_x to reservoir species in aircraft plumes. The heterogeneous conversion of N_2O_5 to HNO_3(s) has been investigated when the emissions take place during night-time. The plume from an B747 has been simulated. During a ten-hour calculation the most important reservoir species was HNO_3 for emissions at noon. The heterogeneous reactions had little impact on the chemical loss of NO_x to reservoir species for emissions at night.

1. INTRODUCTION

Subsonic aircraft cruise at altitudes from 8-12 km, near the tropopause. One main concern about the emissions is the effect of NO_x emissions on ozone. These emissions cause a larger production of ozone in this altitude range, compared to man made NO_x emission at the surface. An ozone change near the tropopause will in turn have a stronger impact on radiative forcing.

In order to study the long term and global effects of NO_x emission on ozone it is important to quantify the chemical loss of NO_x, before the aircraft plume is spread to a larger scale. The purpose of the present study has been to investigate the chemical transformations of NO_x in the plume from a B747 from a few seconds after the emissions and up to ten hours. Consequently, we start our calculations after the jet-regime, which in our case is assumed to last for 4 s. The emphasis has been placed on the conversion of NO_x to HNO_3, PAN and HNO_4.

In flight corridors with heavy traffic several aircraft will fly through essentially the same air mass. The chemical conversions in a new plume inside old plumes of ages up to two hours have therefore been investigated. The new plume has been assumed to mix with the surrounding air from the core of the old plume. The impact of heterogeneous chemistry with respect to the conversion of N_2O_5 to the more stable compound HNO_3 has also been investigated for emissions at night.

2. THE MODEL

The model describes both the dispersion and chemical transformation in aircraft plumes. Since the plume is not well mixed from a cross sectional point of view, the plume is divided into several cross-sectional layers to resolve the inhomogeneous distribution *(Figure 1)*. The axes from the plume centre to the boundary of the different layers are given as

$$a_i = f_i \cdot \sigma_{major}, \qquad b_i = f_i \cdot \sigma_{minor} \tag{1}$$

where $f_i = 0.5i$, $i = 1,....8$. σ_{minor} and σ_{major} denote the standard deviation of the minor and major principal axis of the plume, respectively ([1] and [2]). The plume is treated in segments with a length set equal to the distance the aircraft travels in one second.

The concentration gradients within the plume give rise to mixing, which is described in terms of diffusion. The model thus consists of the following modules: calculations of the horizontal and vertical dispersion of the plume in the vortex and dispersion regimes, calculation of diffusion between the layers, and calculations of a detailed photochemistry for the free troposphere in the layers. The whole plume is advected along pre-calculated trajectories, based on actual winds. There is no diffusion between the outermost layer and the background air, providing mass balance of the emitted species within the plume. The model is further described in [3].

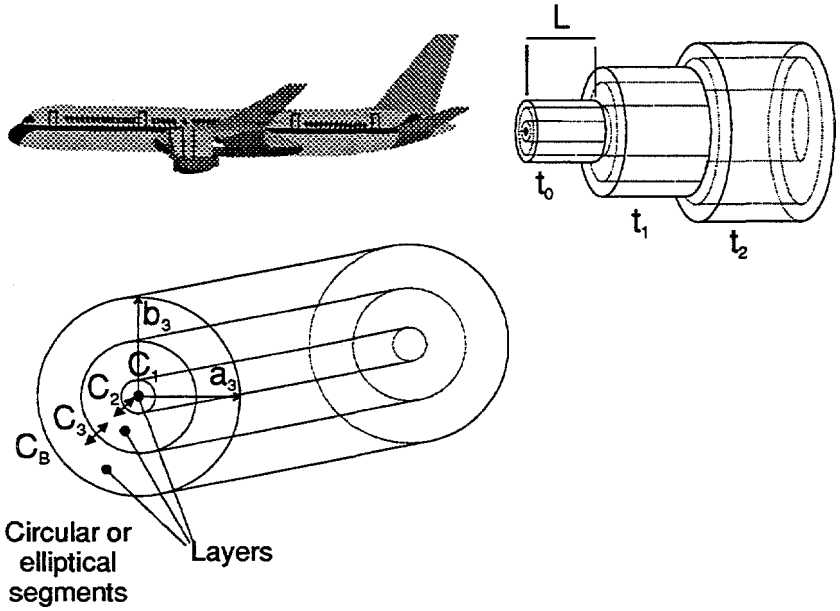

Fig. 1 - The upper part shows the plume from a side view at different times (t_0, t_1...t_n). The lower part shows a cross section of the plume. C_1 to C_3 indicate the concentration in the plume. (Only three of eight layers are shown.) The arrows indicate diffusion between the layers in the plume. (The figure is taken from [2].*)*

3. RESULTS

3.1. Experimental data and initial conditions

The emission indices for the B747 are given in *Table 1*. Of the total emissions, 75% are distributed in the 3 innermost layers, 20% in the fourth layer and 5% in the fifth layer, in broad agreement with a Gaussian distribution. The outermost layers of the plume are initialised with background values. The initial horizontal and vertical standard deviation of the plume was set to 6 m. *Table 2* gives the values of some initial key species in the plume and in the background atmosphere. The initial value of OH and HO_2 are taken from studies done within the AERONOX project [3, chapter 4], and the HNO_2 value is based on observations in young exhaust plumes [4].

3.2. Chemical conversion of the NO_x emissions

The size of the plume and the NO_x concentrations after ten hours of calculations are shown in *Figure 2*. The NO_x level in the outermost layers of the plume has reached background level after this time period, while the NO_x in the core of the plume was more than twice that of the background concentration.

Table 1 - Engine type, air speed, emission indices and fuel consumption for the considered B747, cruising height, pressure and temperature of the atmosphere.

Parameter	Units	Value
Engine type		CF6-80C2B1F
Air speed, V	m/s, Ma	247.0, 0.84
EI(H_2O)	g/kg	1242.0
EI(CO_2)	g/kg	3153
EI(SO_2)	g/kg	1.0
EI(CO)	g/kg	1.5
EI(NO_x)	g/kg	12.5
EI(HC)	g/kg	0.2
Fuel consumption	kg/km	12
Temperature	K	214
Density	kg/m^3	0.358
Cruising height	km	11.25

Table 2 - Initial values of some key species in the plume and the background atmosphere. The NO_x values are given for the 5 inner layers in the plume. The rest of the listed species have the same value in all the layers in the plume.

Species	Plume	Background
NO_x (ppbv) layer 1-3	772	0.16
layer 4	252	
layer 5	52	
O_3 (ppbv)	77.7	77.7
HNO_2 (molecules·cm^3)	$4.7\ 10^9$	$4.0\ 10^6$
OH (molecules·cm^3)	$2.1\ 10^7$	$2.1\ 10^6$
HO_2 (molecules·cm^3)	$3.8\ 10^6$	$3.8\ 10^7$

The chemical conversion of NO_x to reservoir species during the ten-hour time period was studied for a summer situation for emissions at noon (Case 1). The difference in the number of molecules for the odd nitrogen species (NO_y=NO+NO_2+HNO_2+PAN+HNO_4+$2N_2O_5$+HNO_2+CH_3NO_3+$C_3H_5NO_2$+$C_4H_9ONO_3$+$CH_3O_2NO_2$) in the plume was found between a run with emissions (run A) and in a run without emissions (run B). In run B we follow a 'plume' with the same dispersion and mixing with the ambient air as in run A. The purpose was to avoid taking into account an increased level of reservoir species like e.g. HNO_3 which was mixed into the plume from the surrounding air, due to a chemical diurnal variation in the background air. Consequently, the difference in NO_y between the two runs is equal to the sum of the emitted NO_x and the initial value of HNO_2 during the whole ten-hours calculation. By comparing the decrease in the NO_x emitted and the corresponding increase in reservoir species after ten hours it is possible to quantify the chemical loss of in NO_x in the plume.

Sensitivity studies were also performed for situations where an aircraft enters air masses which have already been exposed to aircraft emissions. The new plume was mixed with the surrounding air from the old plume. This was studied for emissions in one hour and two hours old plumes, respectively. The chemical evolution in the plume was also investigated for emissions at night.

The results for the above described experiments are shown in *Table 3*, were the difference in number of molecules for the odd nitrogen species between run A and B are listed. The emitted initial NO_x in the plume amounts to $4.85 \cdot 10^{23}$ molecules. The last column shows the percentage loss of NO_x during the ten hour period. In Case 1, 10.4 % was lost due to chemical conversion to

reservoir species. The most important species after ten hours was HNO_3. Since night time chemistry started to dominate at the end of the calculations, N_2O_5 was the second most important reservoir. The sum of the formation of NO_3 and organic nitrates were more important than e.g. conversion of NO_x to PAN and HNO_4. In fact the level of HNO_4 was lower in run A compared to run B. At the start of the calculations HO_2 was lost due to reaction with the emitted NO in run A. This again influenced the formation of HNO_4 in the plume.

In Case 2 a young plume was mixed with the surrounding air from a plume of age one hour. The chemical conversion of NO_x was considerably less compared to Case 1. This was mainly due to less chemical conversion of NO_x to HNO_3. The OH level in the old plume was lower compared to the background air due to chemical conversion of NO_x to HNO_3. This again caused a lower OH concentration in the new plume that was mixed with the old plume. In addition the dilution of NO_x was slower in the new plume since the surrounding air had a higher NO_x level in this case. This increased the ozone loss in the initial phase of the plume. The lower O_3 level caused a less production of OH through the reactions

$$O_3 + hv \rightarrow O^1(D) + O_2 \quad (2)$$

$$O^1(D) + H_2O \rightarrow 2OH \quad (3)$$

In Case 3 a new plume mixes with a plume of age two hours. The chemical conversion of NO_x was somewhat higher compared to Case 2, but was still low compared Case 1.

For emissions at night (Case 4) the most important reservoir was N_2O_5. The total chemical loss of NO_x was half of the loss in Case 1. The conversion of NO_x to HNO_4 was higher in this case however. At the end of the calculations daytime chemistry started to dominate, and the HO_2 level increased in the plume mainly due to mixing with surrounding air. This caused a faster conversion to HNO_4 at the end of the calculations compared to Case 1.

3.3. Heterogeneous chemistry

The emissions of SO_2, H_2O and soot particles can lead to formation of ice and sulphate particles in aircraft plumes. Heterogeneous reactions can take place on the surface of these particles and influence the conversion of NO_x to HNO_3. The impact of the reaction

$$N_2O_5(g) + H_2O(g) \rightarrow 2HNO_3(s) \quad (4)$$

on both ice and sulphate particles was therefore studied for emission at night. N_2O_5 is formed during night by the reaction

$$NO_2(g) + NO_3(g) \rightarrow N_2O_{5(g)} \quad (5)$$

This compound is more rapidly dissociated by UV-light than HNO_3. Reaction (4) will therefore lead to an decrease in the NO_x concentration in the plume.

The total surface area of ice particles in the plume after 4 s has been estimated as $1.8 \cdot 10^{-6}$ cm^2/cm^3 [3, chapter 4.2.2.2]. It was further assumed that the ice particles in the plume would decrease due to plume expansion and mixing with ambient air. The total area was close to zero after about one hour *(Figure 3)*. The total area of sulphate particles was estimated as

$$A_{sulphate} = 2.5 \cdot SO_2 \frac{M_{wH_2SO_4}}{N_a \cdot \rho_{H_2SO_4}} \cdot \frac{V_{H_2SO_4}}{A_{H_2SO_4}}, \quad (6)$$

where $M_{wH_2SO_4}$ and N_a are the molecular weight and Avogadros number, respectively. Furthermore, $\rho_{H_2SO_4} = 1.8$ g/cm^3 is the density of sulphuric acid and $V_{H_2SO_4}$ and $A_{H_2SO_4}$ are the volume and area of the particles, respectively. The radii of the sulphate particles were considered to be $5.6 \cdot 10^{-6}$ cm. *Figure 3* shows the total area of sulphate particles in the innermost layer of the plume during the ten-hour period.

The last two rows in *Table 3* shows results for emissions at night-time. In Case 4 only gas phase chemistry was included, and in this case 5.6% of the NO_x was converted after ten hours. In Case 5 reaction (4) was included. The loss of NO_x then increased to 6.4%. The level of N_2O_5 was higher in run B compared to run A. This was because reaction (2) caused a higher loss of N_2O_5 in the plume when heterogeneous chemistry was included.

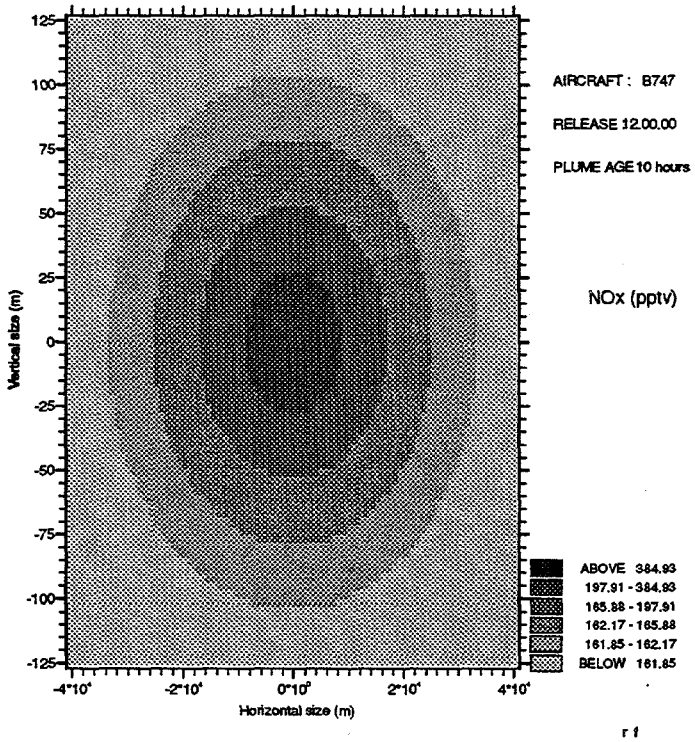

Fig. 2 - The level of NO_x in the plume and the size of the plume after ten hours.

Table 3 - The difference in number of molecules between a run with and without emission after ten hours. The differences are given in 10^{20} molecules, and is calculated for all the odd nitrogen species in the chemistry scheme in the entire plume volume. ORG is the sum of NO_3 and the organic nitrates CH_3NO_3, $C_2H_5NO_2$ and $C_4H_9ONO_3$. Case 1: The reference study. Case 2: A new plume within an old plume of age one hr. Case 3: A new plume within an old plume of age two hr. Case 4: Emissions at night. Case 5: Emissions at night with heterogeneous chemistry.

Case	ΔNO_x	ΔHNO_3	ΔPAN	ΔHNO_4	$\Delta 2N_2O_5$	ΔORG	ΔHNO_2	loss of NO_x(%)
1	4345.6	459.2	2.4	-1.0	31.1	13.0	0.9	10.4
2	4788.4	34.3	-0.2	-2.3	32.6	-3.7	0.1	1.3
3	4767.1	61.4	-0.5	-5.2	33.6	-6.5	0.2	1.7
4	4578.6	44.8	0.4	12.3	200.4	3.9	7.2	5.6
5	4540.5	44.8	0.4	12.2	-153.1	3.8	7.1	6.4

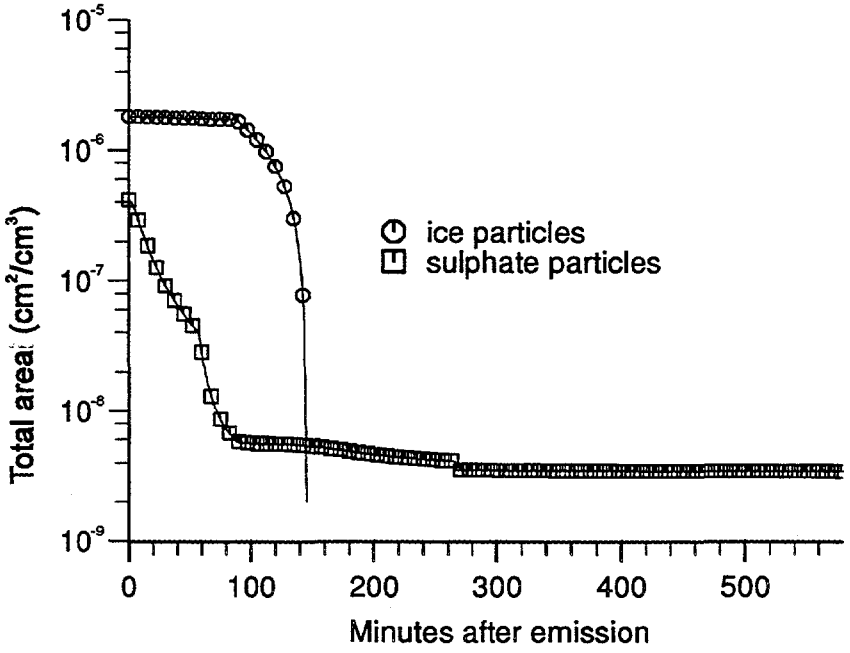

Fig. 3 - The total area of ice and sulphate particles in the plume during the ten hour period.

5. CONCLUSIONS

A plume model with chemistry has been used to study the chemical conversion of NO_x to reservoir species from a few seconds and up to ten hours after the emissions. When the plume was mixed with background air the chemical conversion amounted to 10%, and the most important reservoir species was HNO_3. The conversion of NO_x was reduced by a factor 10 when a new plume was mixed with old plumes of some hours. This suggests that in flight corridors with heavy traffic, there is a possibility that the chemical conversion of emissions will be less than for emissions in less trafficated flight corridors. To study this closer detailed flight statistics must be taken into account.

The chemical evolution in the plume for a night time case was simulated, including also the conversion of N_2O_5 to HNO_3(s) on ice and sulphate particles. Crude estimates have been made of the total area of ice and sulphate particles in the plume. In a case without and with heterogeneous chemistry 5.6% and 6.4% of the emitted NO_x was converted to reservoir species after ten hours, respectively. This reaction had therefore relatively little influence on the chemical conversion of NO_x compared to the gas phase chemistry on the ten hour time scale.

6. REFERENCES

[1] Konopka, P., 1995: Analytical Gaussian solutions for anisotropic diffusion in a linear shear flow. *J. Non-Equilib. Thermodyn.*, **20**, 78-91.

[2] Kraabøl, A.G., P. Konopka, F. Stordal and S. Knudsen: Chemistry and dispersion of aircraft plumes. *J. Geophys. Res*, submitted 1996.

[3] Schumann, U., editor, 1995: *AERONOX- The impact of NO_x Emissions from Aircraft upon the Atmosphere at Flight Altitude 8-15 km.* EC-DLR, Publications on Research Related to Aeronautics and Environment.

[4] Arnold F, T. Stilp, T. Scheidt, H. Schlager and M.E. Reinhardt, 1992: Measurements of jet aircraft emissions at cruise altitude I: The odd nitrogen gases NO, NO_2, HNO_2 and HNO_3. *Geophys. Res. Lett.*, **19**, 2421-2424.

FOR THE ESTIMATION OF STRATOSPHERIC AIRCRAFT EFFECT ON OZONE LAYER

E.Kadygrov, M.Sorokin, A.Troitsky
Central Aerological Observatory,
Dolgoprudny, Moscow region, 141700 Russia

ABSTRACT

The objective of present report is to contribute A remote sensing capability for measurement of temperature fluctuation and some important gases species concentration at the wake vortex and wake dispersion regimes behind the supersonic aircraft at cruise altitude. Proposed new method of observation is based on the measurement of radiobrightness contrast between the ambient atmosphere and perturbated area behind the aircraft by using millimeter or submillimeter wave scanning spectroradiometers with the specially selected spectral parameters. The qualitative estimations of the sensitivity of measurement to the temperature fluctuation, the changing in concentration of ozone, water vapour, nitrogen oxide and sulfur dioxide were calculated. The preliminary test of a new equipment were conducted from high-altitude balloon (temperature profiles and fluctuation and ozone concentrations) and from the ground (sulfur dioxide relative concentration) measurements.

1.INTRODUCTION

A number of reputable scientific studies have suggested that aviation may contribute to detrimental chemical changes of the atmosphere (particularly ozone content) and to climate change. Much of the emphasis of present studies of atmospheric effect of aviation has been of supersonic transport : development of model and real-time observations. One of the importent part of observations is the knowledge of local influence for ozone content resulting from a jet exhaust of a single aircraft at real flight conditions. Behind the aircraft processies occur in three physically identifiable regimes: a) exhaust plume (0-0.6 sec time since emission; 0-0.14 km distance behind plume), b) the wake vortex (0.6-91 sec, 0.14-22 km) and c) the vortex break-up and wake dispersion (> 91 sec, > 22 km) [1] . These near-field regimes are of interest becouse they contein far higher concentrations of reactive, exhaust-derived, chemical species families that critical to a wide range of atmospheric chemical processes. At the present time observations at b) and c) region is possible only by in-situ sensors from other aircraft which flight in the wake of supersonic aircraft " through flights" or flight with episoding crossing of wake.

At our report the possible using of millimeter and submillimeter wave spectroradiometers for measurement at the wake vortex region of temperature fluctuations, fluctuation in concentration of ozone, water vapour, sulfur dioxide and nitroxen oxide are discussed. Most of gases which is connected with aircraft emission (NO_X, H_2O, SO_2, O_3) has a spectral lines in millimeter and submillimeter wavelenghts [2]. All this gasis has also a spectral lines at submillimeter region. Temperature profiles and fluctuation measurements can be provided by measurement of molecular oxygen emission which has a set of strong spectral lines in millimeter and submillimeter region.

2. AIRBORNE MICROWAVE REMOTE SENSING METHOD OF LOCAL OZONE VARIATION MEASUREMENT.

Applications of microwave spectroradiometer is based at the using special form of antenna beam and spectral parameters of the spectroradiometer. Variations of ozone concentrations at the wake vortex regime to attain by measurement of radiobrightness contrast, when antenna beam is scanning at horizontal plain from the ambient atmosphere over perturbed region behind aircraft (Fig.1).

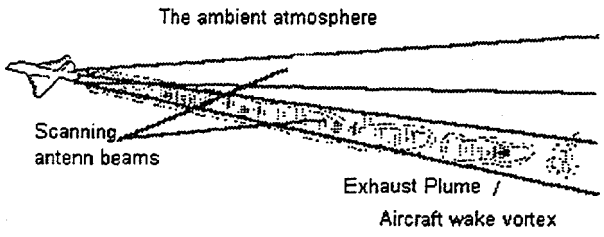

Fig. 1 The position of the antenna beam.

As well known from observations the component of aircraft exhaust can be the long time (from the several minutes up to several hours) conserved at the narrow region along the aircraft trace and the diameter of this region is approximately 1 ÷ 6 Km. The wide of antenna beam can be selected with the reason that the more part of aircraft trace will be inside of this beam. As shown at Fig. 2, the wide of antenna was selected according

are L = 110 or 220 Km for antenna beamwidth q = 1° or 0.5° accordingly. Antenna beamwidth at the distance L from aircraft include practically all region of wake vortex and wake despersion regimes. Some problem is present if the speed of aircraft is ~ 2 Mach or more - in this case the flight time at the distance L will be only 3 ÷ 6 minute, so it is no simple mode for scanner.

The scanning angle is inside the region $\pm 2q$ to the right and to the left from aircraft trajectory directions, which gives the possibility to measure the radiobrightness temperature of unperturbation ambient atmosphere and made corrections of direction to the perturbation region of the atmosphere.

The another part of antenna beam consist the atmospheric layer which is above flight altitude. The thermal emission from this part of the atmosphere not give the information by aircraft exhaust perturbed atmosphere, but contrary, decrees the radiobrightness contrast, which is necessary to measure. It is possible to except the influence of this part atmosphere thermal emission by using optional frequency band of radiometer according dependence of molecular absorption spectral line from pressure (DSB-mode, 4 spectral channels, double frequency convertation, using of "roll up" of spectral bands, as was shown at [3,5]).

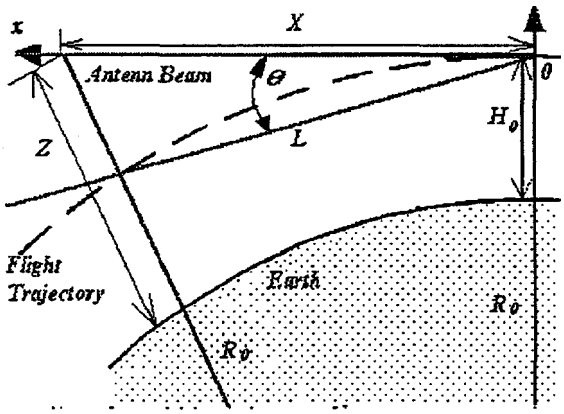

Figure 2 The microwave remote sounding geometry.

As possible to see from Fig. 2, microwave sounding in our case have many common in scanning geometry with limb sounding from satellite, but possible to call it as "inverse limb sounding". For radiobrightness temperature, which will measure from aircraft possible to write following equation

$$T_b(\nu,H) = \int_0^\infty T(x)\gamma\ (\nu,x)Exp(-\tau\ (\nu,x))dx \tag{1}$$

where x - co-ordinate along tangent for observation point; ν - frequency of radiometer; $\gamma(\nu,x)$ - molecular absorption coefficient; $\tau(\nu,x)$ - optical depth of the atmosphere at the observation line. For direction, which is shown at Fig. 2, where R_0 - radius of Earth, H - flight altitude, can be written

$$(R_0+H)^2 + x^2 = (R_0+z)^2$$

$$\frac{dx}{dz} = f(z) = \frac{R_0+z}{\left[(R_0+z)^2-(R_0+H)^2\right]^{1/2}} \tag{2}$$

and for T_b

$$T_b(\nu,H) = \int_H^\infty T(z)\gamma\ (\nu,z)Exp(-\tau_\nu\ (H,z))f(z)dz \tag{3}$$

where

$$\tau_\nu(H,z) = \int_H^z \gamma\ (\nu,z')f(z')dz' \tag{4}$$

account the frequency band of radiometer, for radiobrightness temperature possible to received equation

$$T_b(H) = \int_{\Delta\nu} T_b(\nu, H) F(\nu) d\nu \tag{5}$$

where *F(n)* - frequency parameters of radiometer; $\Delta\nu$ - frequency difference from the center of the spectral line.

. Usually the frequency characteristic is consider as even distribution inside the frequency band of radiometer.

The dependence of ozone absorption spectral line halfwidth from altitude is shown at Fig. 3, in the same place mark out the frequency region corresponding to altitude range 16 ÷ 24 Km. It should be noted that excessive narrow frequency band of radiometer will bring the loss of radiometer sensitivity. So it is necessary to bring into proper correlation the radiometer sensitivity and altitude range, which do not give the contribution to the radiobrightness temperature. Indicated in Fig. 3 altitude range is closely to optimal, because in real operation of the radiometer will be additionally limited by middle antenna beam.

Final expression for radiobrightness temperature will be written with taken into account real antenna beam $\Gamma(\Omega)$

$$T_b = \int_{\Delta\Omega} T_b(\Omega)\Gamma(\Omega) d\Omega \tag{6}$$

over solid angle Ω. In this case, the shown at Fig. 2 geometry is complicate, and expression (2) are incorrect, but on the whole, expression for radiobrightness temperature (3) to stay correct and more, peculiarity of quadrature (3) in point $z = H$ take off by averaging over antenna beam.

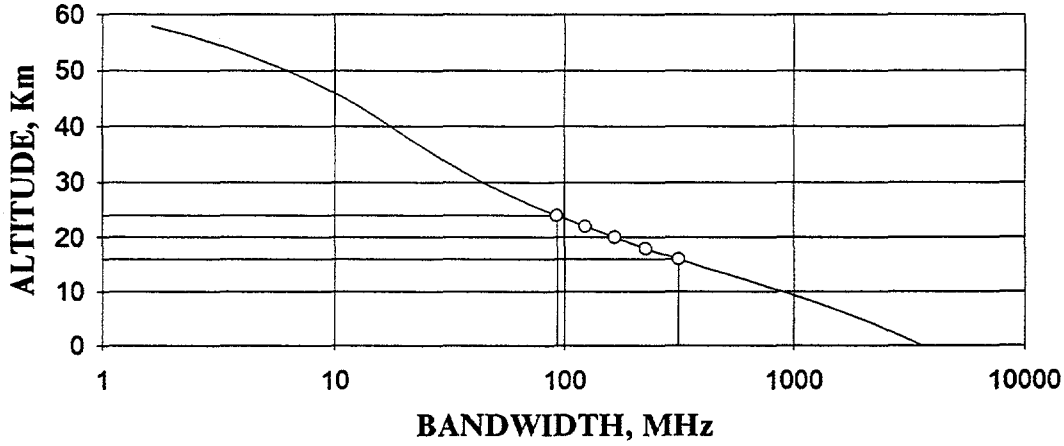

Figure 3 The Altitude dependence of the ozone line bandwidth.

Using the method presented above, qualitative estimates of brightness contrast can be calculated without complicated and unwieldy calculations. Frequency offset relative to line center was chose $\Delta\nu$ = 200 MHz and according bandwidth, that corresponding atmosphere layer $\delta h << H$, also will be considered antenna beam infinitesimal narrow. Then expression (4) for optical depth can be written approximately

$$\tau_\nu(H) = \int_{H}^{H+\delta h} \gamma(z) f(z) dz \approx \gamma_0 \int_0^X dx \approx \gamma_0 L \tag{7}$$

where γ_0 molecular absorption coefficient at flight altitude, which be considered permanent in atmosphere layer δh. Therefore for the radiobrightness temperature (3) can be written

$$T_b(H) \approx T(H)(1 - Exp(-\gamma_0 L)) \tag{8}$$

water vapour absorption's that is, γ_0 - the ozone absorption coefficient only, can be calculated:

for the ozone line absorption 110 GHz - $T_b \approx 5 \div 9°$ K

for the ozone line absorption 142 GHz - $T_b \approx 12 \div 17°$ K.

Considering the uniform atmosphere at horizontal plain within the limits scanning range, for division of the radiobrightness temperature: of the ambient atmosphere and wake vortex region

$$\frac{T_b^0}{T_b} = \frac{1 - Exp(-\gamma_0^0 L)}{1 - Exp(-\gamma_0 L)} \approx \frac{\gamma_0^0}{\gamma_0} = \frac{n_{o3}^0}{n_{o3}} \qquad (9)$$

where n^0_{o3} and n_{o3} - the ozone concentration, accordingly in the ambient atmosphere and in the region behind aircraft perturbed by the engine exhaust. If the sensitivity of radiometer is equal 0.1° K, that is the minimum of the brightness contrast $T^0_b - T_b \approx 0.1°$ K registered by the radiometer. Accordingly minimum of the registered ozone content variation is equal approximately 2% at the cylindrical range behind the aircraft on the extension L and diameter equal antenna beamwidth.

Undoubted merit of the presented method in technical aspect, is appeared double sideband mode (DSB) of the radiometer operating, that essentially are simplified front end of the radiometer and are increased it sensitivity. After accorded modification radiometer, which can be used by the presented method, was written at [5,8,9]. This radiometer has small dimensions 32 * 21 * 18 cm and low weight of 10 kg (without scanner), that make it very suitable for the Stratospheric Aircraft experiment. Same measurements of differencies between ambient atmosphere and in the region behind aircraft perturbed by the engine exhaust possible to made for water vapor, where also expected contrast of radiobrightness temperature is about 10÷15 K.

3. STATISTICAL ESTIMATION OF MEASUREMENT CONDITIONS.

In present report we also proposed the method of statistical processing of radiobrightness temperature which will measure along of exhaust from individual aircraft wakes. Our evaluate shows that by using of this method it is possible to measure differencies in No_x and SO_2 concentration between ambient atmosphere and engine exhaust. At least in this case radiobrightness contrast will be about 2-3 K, which is approximately the same with the natural variability of the radiobrightness temperature according to atmospheric turbulence an airplane wake.

For statistical consideration of measurement conditions we assume, that from motionless point at flight altitude H flow out jet aircraft plumes, which has approximately constant trajectory in relation of spherical Earth Surface (Fig. 1).

Inside the wake there are perturbated zone with temperature T and mixing ratio r, which fluctuated over ambient atmosphere at the same altitude. Equation for radiobrightness temperature T_b along the axis l will be following [6]

$$T_b(\nu,\theta) = \int_0^\infty r(l)T(l)K(\nu,\theta,l)dl \qquad (10)$$

where θ- angle between horizontal direction at point H and the axis, l - absorption coefficient of No_x with mixing ratio r(l);

$$K(\nu,\theta,l) = \frac{\gamma_1(\nu,T,P)}{\cos(\theta)} \exp(-\tau(\nu,l)/\cos(\theta)) \qquad (11)$$

$$\tau(\nu,l) = \int_0^l \gamma(\nu,T(l'),P(l'))dl' \qquad (12)$$

$$\gamma = r(l)\gamma_1(\nu,T,P) \qquad (13)$$

In this case perturbated atmosphere will be in area HL at the beam, and fluctuated part of radiobrightness temperature will be determined by the first integral in equation:

$$T_b(\nu,\theta) = \int_0^L r(l)T(l)K(\nu,l,\theta)dl + \int_L^\infty r(l)T(l)K(\nu,\theta,l)dl \qquad (14)$$

For the first part of equation (14) will take the solution of energy transfer equation for radiobrightness temperature variations, which was received at [6]. If take in account, $T_b(l) << T$, we can received:

$$\delta T_b = T_b(l) - \overline{T_b} \qquad \delta\gamma = \gamma(l) - \overline{\gamma}(l) \qquad (15)$$

$$\delta T_b = \int_0^L \delta\gamma\{T(l) - T_b(l)\}K(l)dl + \int_0^L \delta l\overline{\gamma}(l)K(l)dl \qquad (16)$$

$$\delta T_b = \overline{T}\int_0^L \frac{\delta r}{\overline{r}}\overline{\gamma}(l)K(l)dl + \int_0^L \delta l\overline{\gamma}(l)K(l)dl \qquad (17)$$

possible to receive:

$$\left\langle \delta T_b \delta T_b' \right\rangle = \frac{\overline{T}^2}{\overline{r}^2}\left\langle \hat{\delta r}\hat{\delta r}' \right\rangle + \left\langle \hat{\delta T}\hat{\delta T}' \right\rangle \qquad (18)$$

Equation (18) is correspond to accumulation of the signal during the flight with constant altitude (which is equal the increasing of integration time for usual measurement). If we will know the middle temperature of aircraft wake, the dispersion of it fluctuation on the wake, and dispersion of fluctuation NO_x concentration at the wake, it is possible to made evaluation of middle mixing ratio of NO_x at the wake of aircraft. The middle temperature of the atmosphere in the wake and its dispersion is possible to indicate at the same aircraft and with the same measurement geometry by using microwave radiometer in molecular oxygen band (60 Ghz, 118 Ghz or 298 Ghz). By the amount of dispersion fluctution of molecular oxygen radiation it is possible to made evaluation: is flight conditions all right for accumulation of the signal or not:

$$\overline{r}^2 = \frac{\overline{T}^2\sigma_r^2}{\left(\sigma_{T_b}^2 - \sigma_T^2\right)} \qquad (19)$$

If σ_T in (19) is very large, then equation (19) will be uncertain. For evaluation of fluctuations of NO_x concentrations it is possible to use results of model calculations [7].

4. SOME RESULTS OF PRELIMINARY TESTING OF EQUIPMENT

As the first step of verifications of this method in real observations experimental equipment was tested at seven high-altitude balloon flights with two microwave spectroradiometers [8,9]. 5-mm microwave spectroradiometer for temperature measurement has total weigt 5 kg and 6 spectral channels. 2.7 spectroradiometer for measurement of ozone concentration has 12 spectral channels and total weight 10 kg. Maximum flight altitude of the balloon was about 20-32 km. As example of measurement at Fig.4-Fig.6 shown temperature profiles which was received by 5-mm spectroradiometer with different geometry of measurement: Fig.4 - zenith sounding; Fig.5 - horizon sounding. At Fig.6 is shown results of comparison of ozone profile measurement by using 2.7 mm spectroradiometer and ozonozonde.

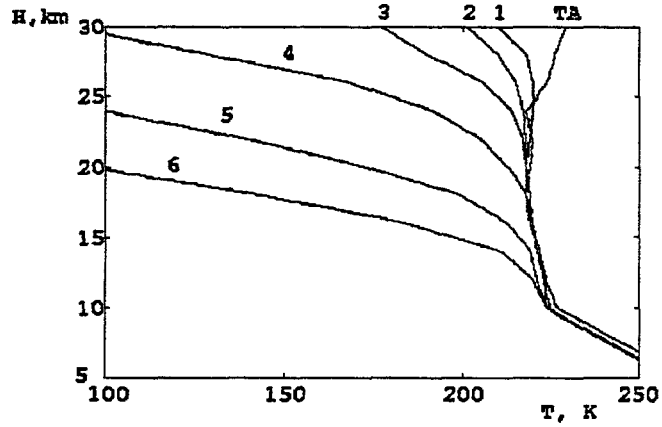

Figure 4. Zenith sounding.

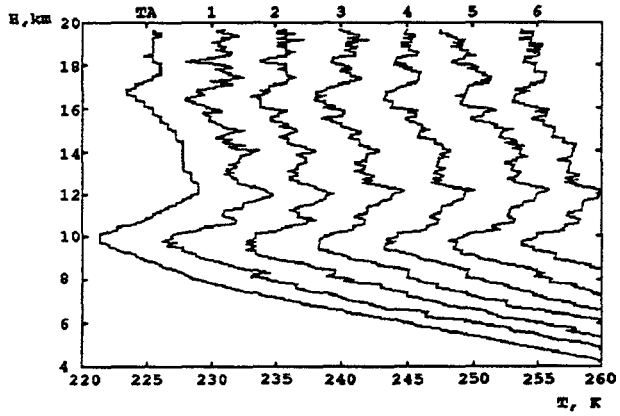

Figure 5. Horizon sounding.

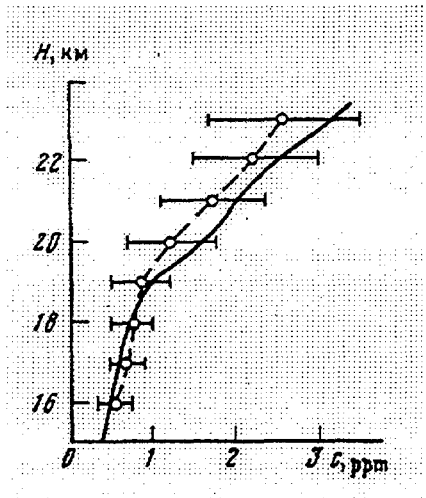

Figure 6 Result of ozone concentration measurement from high altitude balloon (- - spectroradiometer data, - ozonesonde data).

Results of testing flights shows, that for aircraft with flight altitude about 20 km 5-mm spectroradiometers gives the possibility to measure temperature and it's dispersion at flight altitude (horisontal sounding), and temperature profiles in the range of ±5 km from flight altitude (scanning sounding). Ozone profile measurement

conducted by using of spectroradiometer with central frequency 131 GHz. Spectroradiometer has 4 spectral channels: to channel was at ± 500 MHz from the central frequency and two channel was at ±4 GHz from the central frequency. The sensitivity of the radiometer was 0.2 K at the 1 sec integration time. At the spectroragiometer were used DSB mode and also "roll up" of the spectral line [5].

Measurement were conducted at October 1995 near region were SO_2 concentration was sometimes quite more than in ambient atmosphere. At the presents of SO_2 clouds spectroradiometer measured 12-17 g/m^2 of SO_2 concentration at the troposphere.

CONCLUSION

As was shown at present report, the aircraft-borne microwave spectroradiometers can be a useful instrument for measurement of H_2O, O_3, NO_x, SO_2 and temperature fluctuations in wake from individual aircraft . For real observations they can be installed, for example, at russians supersonic aircraft TU-144 and subsonic aircraft "Geophysica" (which has maximum flight altitude 21 km, cruise speed 750 km/h and payload weight 1500 kg). The simple estimates show that NO_x , H_2O and SO_2 emissions from stratospheric aircraft will made such changes of O_3 concentrations in the ambient atmosphere, which can be detected by the microwave techniques installed at the stratospheric aircraft.

REFERENCES

1. Thompson A.M, Friedl R.R, Wesoky H.L. (editors). Atmospheric Effects of Aviation: First report of the Subsonic. NASA Reference Publication N 1385, 1996.
2. Poynter R.L., Pickett H.M. Submillimeter, millimeter and microwave spectral line catalogue. App. Optics, 1985, v. 24, N 14, pp. 2235-2240
3. Aniskovich V.M., Budilovich N.V., Strukov I.A. et all. Balloon-borne millimeter wave spectroradiometer for ozone concentration measurement. In: Proc. All-Union Symposium of propapation of mm and submm wave in the atmosphere. 1991, Nygny Novgorod,Russia,pp.200-201.
4. Kadygrov E.N., Kokin G.A., Potapov A.A. Microwave devices for investigation of ozone layer. - The World Radioelectroniks, N10, 1989, pp.52-62 (in Russian)
5. Vlasov A.A., Kadygrov E.N., Shaposhnikov A.N. Radiophysical aspects of thermal sounding the stratosphere from satellites on the O_2 absorption lines in the frequency range 55-65 GHz. Radiophysic, 1991,v.34, N3, pp 240-247.
6. Markina N.N., Naumov A.P., Sumin M.I. Retrieval processing in microwave remote sensing of the atmosphere. - Prepr. N 149, N. Novgorod, Russia, RFI, 1981, p. 47 (in Russian)
7. Kasibhatla P.S. NO_x from subsonic aircraft emissions: A global three - dimensional model study, Geophys. Res. Lett, 20, 1707-1710, 1993
8. Vlasov A.A., Kadygrov E.N., Sorokin M.G. Balloon measurements of the middle atmosphere parameters using microwave spectrometers. - 10-th ESA Symp, ESA SP-317, France, 1991, pp. 219-222
9. Kadygrov E.N., Sorokin M.G., Vlasov A.A. Ozone concentration determination by microwave measurement from balloons in the stratosphere. - Earth research from space, N 3,1993, pp.102-106 .

Development and application of a chemistry mechanism for mesoscale simulations of the troposphere and lower stratosphere

E.Lippert, J.Hendricks and H.Petry
University of Cologne, Institute for Geophysics and Meteorology,
50923 Cologne, FRG

Abstract: A new chemical mechanism is applied for mesoscale simulations of the impact of aircraft exhausts on the atmospheric composition. The temporal and spatial variation of the tropopause height is associated with a change of the trace gas composition in these heights. Box and threedimensional mesoscale model studies show that the conversion of aircraft exhausts depends strongly on the cruise heights as well as on the location of release in relation to the tropopause. The impact of aircraft emissions on ozone is strongly dependent on the individual meteorological situation. A rising of the tropopause height within a few days results in a strong increase of ozone caused by aircraft emissions.

1. Introduction

As commercial jets cruise mainly in midlatitude regions at tropopause altitudes their exhausts are released both in the lower stratosphere and in the upper troposphere [1]. The emitted NO_x play a dual role in these regions. On the one hand NO_x contributes to the catalytic ozone destruction, on the other hand NO_x controls the atmospheric concentration of several constituents [2]. To study the impact of aircraft emissions with a chemistry–transport–model (CTM) the model must be able to treat tropospheric as well as stratosperic chemical processes in detail. Due to the strong variability of the tropopause height a model must resolve the main cruising range between 9 and 13 km accurately. The impact of aircraft emissions crucially depend on the atmospheric background concentrations of reactive trace gases. To guarantee an adequate representation of the background composition the initialization and boundary conditions of a mesoscale model have to be adjusted to the individual meteorological situation or tropopause height, respectively.
In the present paper the new developed CTM is introduced coming up to all these requirements. Model results concerning the impact of aircraft exhausts on the composition of the atmosphere are presented. Simulations investigating the effects of shifting the main cruising altitudes to lower heights have been performed and are discussed as well as findings about the influence of varying tropopause height. The signification of the background conditions and the dependence of the impact of the emissions on the meteorological situation are shown.

2. Model description

The *Eur*opean *A*irpollution *D*ispersion (EURAD) model is a system of modules to treat the transport and chemical transformation of trace species on the mesoscale. The EURAD system consists of three main modules, the MM5, EEM and CTM. The meteorological PSU-NCAR mesoscale model MM5 [3] delivers hourly meteorological fields as input for the CTM. Surface emissions are preprocessed by the *E*URAD *E*mission *M*odel EEM [4], whereas aircraft emissions are prepared separately as input for the CTM [5]. The CTM is a threedimensional Eulerian *C*hemistry *T*ransport *M*odel [6], solving a set of chemical species conservation equations:

$$\frac{\partial C_i}{\partial t} = \nabla \left(\nabla \underline{\underline{K}} C_i - \underline{u} C_i \right) + P_i - L_i + E_i + \frac{\partial C_i}{\partial t}|_{clouds.} + \frac{\partial C_i}{\partial t}|_{drydep.} \qquad (1)$$

The temporal change of the mixing ratio of a species i is calculated taking turbulent diffusion, advection, chemical transformation (production (P_i) and loss rate (L_i)), emissions (E_i), cloud effects including redistribution, scavenging and aqueous chemistry and dry deposition into account.

For applications to the chemistry of the tropopause region and aircraft effects respectively a new chemical mechanism named CHEST (*Ch*emistry module for the lower *S*tratosphere and the *T*roposphere) has been developed [7]. The mechanism was developed out of RADM2 [6,8], which is originally developed for simulation of tropospheric chemical processes, especially for simulations in the planetary boundary layer. Two main points had to be taken into account:
1. Due to the huge computing time requirements of the threedimensional model and because organic chemistry plays a minor role in tropopause regions the organic part of RADM2 was reduced. On the other hand the inorganic part was extended by processes representing stratospheric chemistry. Thus inclusion of chlorine and hydrogen chemistry was necessary. The oxygen as well as the HO_x- mechanism of RADM2 was extended for better handling the ozone chemistry in the upper troposphere and stratosphere. Table 1 summarizes the species and reactions of both RADM2 and CHEST.

	RADM2	**CHEST**
calculated chemical species	63	60
inorganics	21	31
organics	42	29
photolysis reactions	21	26
homogeneous collision reactions	137	160
heterogeneous reactions	1	2

Table 1 - Species and reactions of RADM2 and CHEST

CHEST calculates the transformation of 60 species divided into 31 inorganics and 29 organics, which are represented by 26 photolytic decompositions, 160 homogeneous and 2 heterogeneous reactions. CHEST was tested against other chemical mechanisms [7] designed especially for applications either in the troposphere or in the stratosphere by running a box model for different atmospheric regions and conditions. The tests showed that CHEST works well both under tropospheric and stratospheric conditions. The comparison also pointed out that RADM2 is not suitable for applications in stratospheric regimes. Thus the implementation of CHEST into the EURAD model system for applications in tropopause regions is justifiable. Besides the box model tests a threedimensional comparison with satellite data was done [7]. The results gained with RADM2 in contrast to those obtained with CHEST pointed out that RADM2 overestimates the ozone concentrations in stratospheric regions. A comparison of the results obtained with model runs investigating the impact of aircraft emissions was also done. The CTM using CHEST calculates a slightly higher (about 10% higher on average) emission induced ozone increase in the main cruise altitudes during an October episode than the CTM running RADM2 as chemical mechanism.

The initialization and the treatment of the lateral boundary conditions of the model have been improved by adjusting the considered concentration profiles to the individual meteorological situation or tropopause height, respectively. This is done by coupling the standard initial profiles to the actual potential vorticity field. The left frame of Fig.1 illustrates the dynamical situation on 25th of April, 1986 at 12 GMT showing the potential vorticity on the 300 hPa surface in grey code. One can find high PV- values northwest of Spain, in the region around the Black Sea and also in the north western boundary domain of the model.

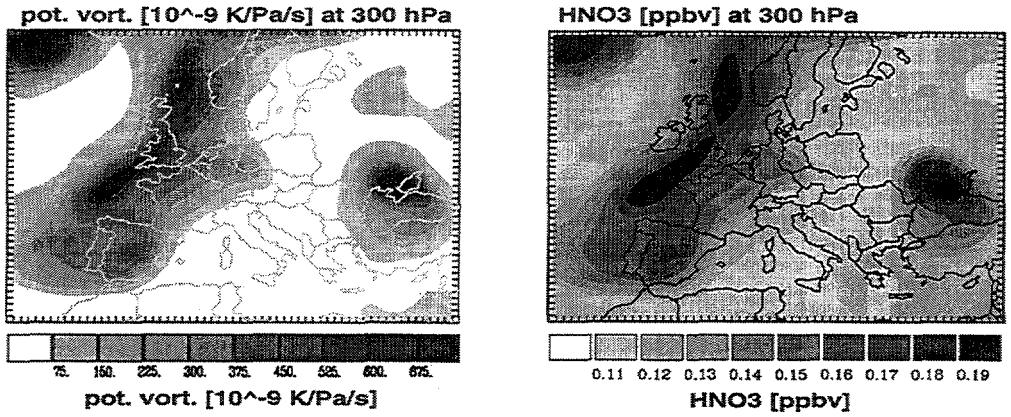

Fig.1 - Potential vorticity [$10^{-9}\,\frac{K}{Pa \cdot s}$] calculated with MM5 and initial HNO_3 concentration field [ppbv] (CTM) on April 25th, 1986, 12 GMT at 300 hPa.

The high PV- values in these regions reveal a low tropopause. A similar structure can be seen in the initialized HNO_3- concentration field with high values in the discussed regions. In contrast to the former used static initialization technique, where the trace gases are homogeneously initialized in a model level, the dynamically adapted method leads to a more realistic distribution which is adjusted to the meteorological situation. The same technique is used for cross boundary inflow conditions. For the present as well as for other studies [9,10] the 3D- model domain of the CTM covering the North Atlantic and western parts of Europe is divided into 56 × 46 grid points with a horizontal resolution of 50 × 50 km^2 each. In the vertical the model extends up to 10 hPa with 29 terrain following σ- levels. The vertical resolution of the model in tropopause altitudes ranges between 500 and 1000 m.

3. Results and Discussion

3.1 Box model studies

To estimate the chemical impact of aircraft emissions on atmospheric background constituents box model simulations have been carried out. Model runs were performed for different emission scenarios as well as for various heights of aircraft exhaust release [10,11,12].

In this paper the effect of reducing the main cruising altitude from about 11.5 km to 10 km

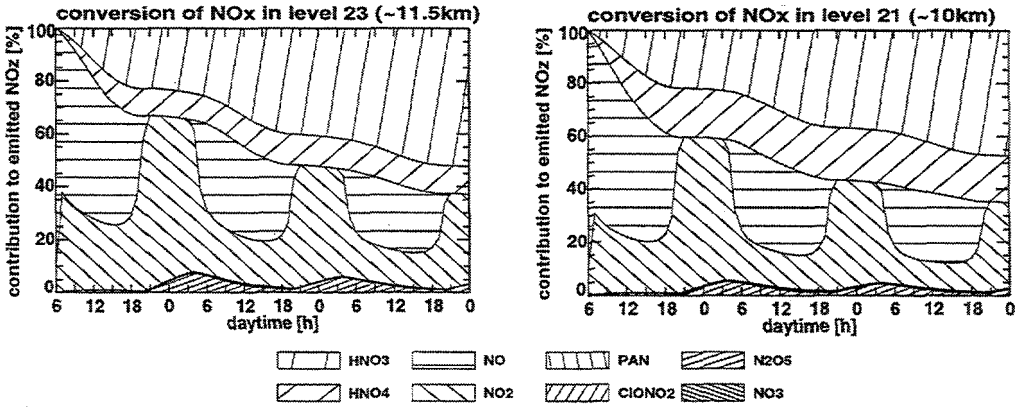

Fig.2 - Box model studies: chemical conversion of the emitted NO_x of a B747 to NO_z calculated for 11.5 km (left frame) and 10 km altitude. No entrainment is considered.

height will be discussed. The emissions considered here are those of a single B747 at cruise stage [10]. The exhausts are released into a box volume of $50 \times 50 \times 1\,km^3$ at 6 h local time in the morning. The simulations are representative for June 21st and 50° N. The reduction of the cruise altitude results in a much stronger emission induced ozone production [10].

Otherwise the NO_x- emissions undergo chemical conversion into other nitrogen containing constituents. The main portion of the NO_x released in 11.5 km altitude is converted into nitric acid (about 50%) after 3 days of simulation (Fig.2, left frame). A significant part of the emitted NO_x reacts to HNO_4 (about 10%). Only about 35% of the NO_x- emission is not converted 3 days after release. Releasing the exhausts in lower regions of the model atmosphere results in a change of the conversion behaviour of NO_x (Fig.2, right frame). The NO_x released in 10 km altitude is more effectively converted to HNO_4 (about 20%). Otherwise less HNO_3 is produced compared to the other case study. These discrepancies in the conversion behaviour are caused by the different atmospheric composition in the two altitudes (in 10 km altitude more HO_x especially HO_2 is available than in 11.5 km height). Consequently the shift of the main cruise levels to lower atmospheric regions yields in a change of the chemical conversion of the emitted NO_x into reservoir species.

3.2 3-D mesoscale model studies

3.2.1 The influence of varying tropopause height

The threedimensional simulations were performed for a real episode starting on Oct. 11th at midnight and ending on Oct. 21st 1993 at 0 GMT. The episode is characterized by a

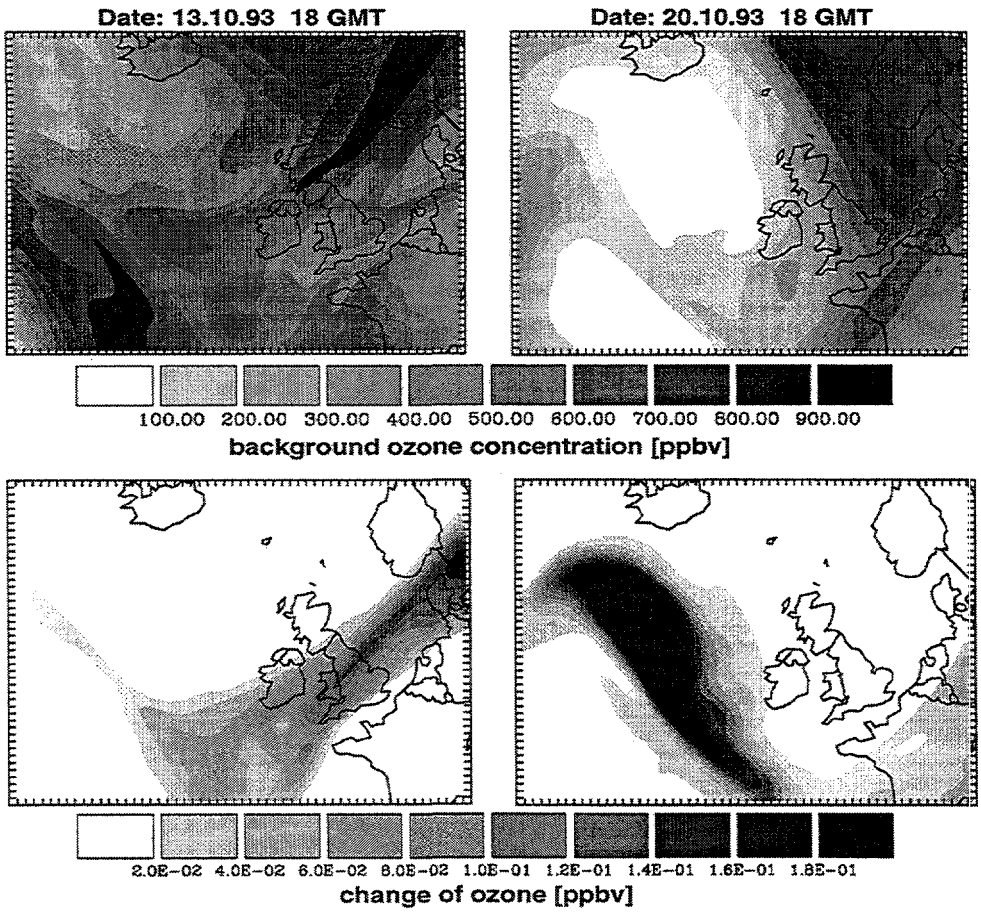

Fig.3 - Calculated background ozone [ppbv] (upper frames) and change of O_3 [ppbv] (lower frames) caused by aircraft emissions in model level 23 (11.5 km) on Oct. 13th, 18 GMT (left frames) and Oct 20th, 18 GMT (right frames).

comparably low tropopause (below 250 hPa) during the first 8 days. On the last 2 days (19. – 20.10.) a rising of the tropopause up to more than 200 hPa takes place which is caused by the evolution of a ridge over the North Atlantic [9]. In the upper frames of Fig.3 the calculated background ozone concentration [ppbv] for Oct. 13th, 18 GMT and 20th, 18 GMT

in 11.5 km altitude is shown. The high O_3 values on Oct. 13th (left frame) correspond to the low tropopause whereas the low ozone concentrations on Oct. 20th (right frame) especially in the North Atlantic corridor illustrate a high tropopause. This means that on the beginning of the episode the aircraft emissions are mainly released into stratospheric air masses whereas during the last 2 days the exhausts are emitted into tropospheric regimes. The resulting ozone changes in 11.5 km altitude can be seen in the lower frames of Fig.3. On Oct. 20th the increase of O_3 due to aircraft emissions in the corridor is much stronger than on Oct. 13th. Higher HO_x- concentrations (more H_2O) and a greater $\frac{NO}{O_3}$- ratio in the upper troposphere compared to the stratosphere are responsible for these effects. The results demonstrate the strong influence of the individual meteorological situation on the impact of aircraft emissions. A comparison of the model results obtained with the former static initialization technique and those discussed above showed strong differences in the aircraft emission induced ozone increase. Using the static method for initialization and boundary conditions the CTM estimates a much stronger (about 2 times higher averaged over the whole episode) ozone production caused by exhausts compared to the CTM applying the new dynamically adapted initialization method. Thus the representation of the atmospheric background conditions in the model is very important investigating the impact of aircraft exhausts on the atmosphere.

3.2.2 The impact of varying cruise height

In another threedimensional study the effect of shifting the main cruise altitudes from between about 10.5 and 12.5 km down to about 9 – 11 km is investigated. The results for HNO_3 [tons (N)] (upper frame) and O_3 [tons (O_3)] (lower frame) are shown in Fig.4. Here

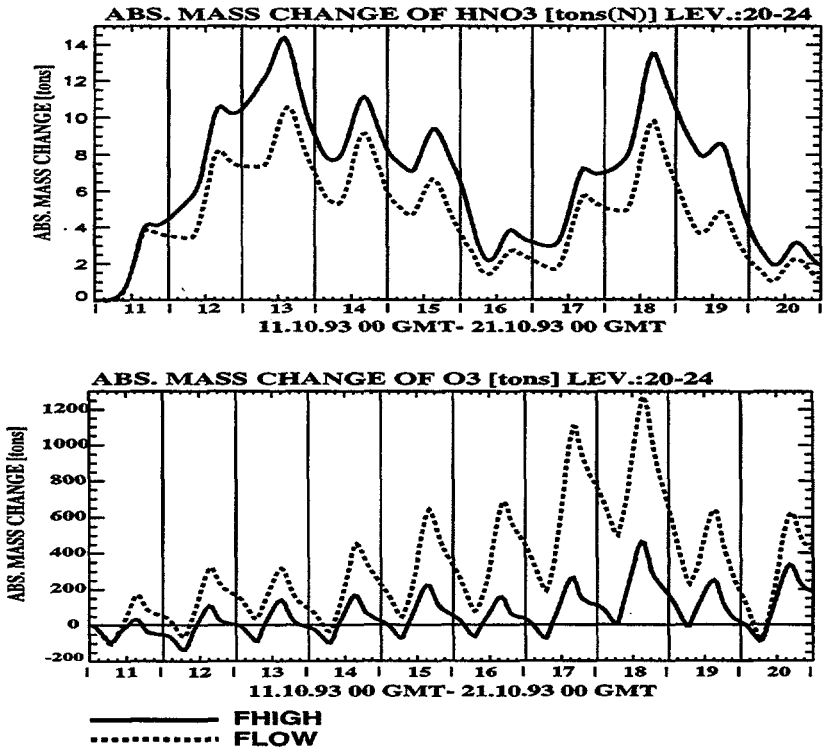

Fig.4 - Aircraft induced change of HNO_3 [tons (N)] (upper frame) and O_3 [tons (O_3)] (lower frame) during the whole episode. The dotted curves represent the results gained with lowered emission height scenario, whereas the solid curves show the results obtained with the high altitude emission case. Integration range: total CTM domain, 9–13 km.

the integrated change of HNO_3 and O_3 summed up over the whole model domain between

9 and 13 km altitude is shown as a function of time. The solid curves represent the aircraft induced change for the case of main cruising between 10.5 and 12.5 km whereas the dotted lines show the results of the simulations considering lowered emission heights. As has to be expected from the box model studies (s.a.) the reduction of the cruising altitudes results in a change in the chemical conversion of the NO_x- exhausts to reservoir species. If aircrafts cruise at lower levels less HNO_3 is produced due to the emissions. On the other hand more HNO_4 is produced (not shown).
Not only the conversion of NO_x is modified by the reduction of the emission heights moreover an enhanced ozone production (about 3 times higher than the high altitude emission case, Fig.4, lower frame) due to aircraft emissions can be observed. Other episodic studies [9,10] showed similar effects.
Thus a general reduction of the main cruise altitudes of the subsonic traffic results in a much higher emission induced ozone production.

References

1. Hoinka, K.P., M.E.Reinhardt, W. Metz, 1993: *J. Geophys. Res.*, **98**, 23113-23130.
2. Ehhalt, D.H., F.Rohrer, 1994: Proceedings of the 7th BOC Priestly Conference.
3. Jakobs, H.J., H.Feldmann, H.Hass, M.Memmesheimer, 1995: *J. Appl. Met.*, **34**, 1301-1319.
4. Memmesheimer M., J. Tippke, A.Ebel, H.Hass, H.J. Jakobs, M.Laube, 1991: Proceedings of the EMEP workshop on Photooxidant Modelling for Long-Range Transport in Relation to Abatement Strategies. Berlin, April 16-19, 1991, 307-324.
5. Franzkowiak, V., H. Petry, A. Ebel, 1996: *this volume.*
6. Hass, H., 1991: Mitteilungen aus dem Institut für Geophysik und Meteorologie der Universität zu Köln, A.Ebel, F.M.Neubauer, P.Speth, Eds., Heft 83, 100 pp.
7. Lippert, E., 1996: Der Einfluß von Flugzeugabgasen auf die Zusammensetzung der Atmosphäre: Untersuchungen mit einem mesoskaligen Chemie–Transport–Modell. PhD thesis, Mitteilungen aus dem Institut für Geophysik und Meteorologie der Universität zu Köln, A.Ebel, M.Kerschgens, F.M.Neubauer, P.Speth, Eds., Heft 109.
8. Stockwell, W.R., P.Middleton, J.S.Chang, 1990: *J. Geophys. Res.*, **95**, 16343-16367.
9. Hendricks, J., A. Ebel, E. Lippert, H. Petry, 1996: *this volume.*
10. Petry, H., A.Ebel, V.Franzkowiak, J.Hendricks, E.Lippert, M.Möllhof, 1996: *this volume.*
11. Lippert, E., J.Hendricks, B.C.Krüger, H.Petry, 1994: Proceedings of an International Scientific Colloqium, Köln, April 18-20, 1994, U.Schumann and D.Wurzel, Eds., DLR, 348-353.
12. Möllhoff, M., J. Hendricks, E. Lippert, H. Petry, R. Sausen, 1996: *this volume.*

On the influence of temporal and spatial resolution of aircraft emission inventories for mesoscale modeling of pollutant dispersion

V. Franzkowiak, H. Petry and A.Ebel
University of Cologne, Institute for Geophysics and Meteorology,
Albertus-Magnus-Platz, 50923 Cologne, Germany

Abstract: The sensitivity of a mesoscale chemistry transport model to the temporal and spatial resolution of aircraft emission inventories is evaluated. A statistical analysis of airtraffic in the North-Atlantic flight corridor is carried out showing a highly variable, fine structured spatial distribution and a pronounced daily variation. Sensitivity studies comparing different emission scenarios reveal a strong dependency to the emission time and location of both transport and response in chemical formation of subsequent products. The introduction of a pronounced daily variation leads to a 30% higher ozone production in comparison to uniformily distributed emissions.

1. Introduction

Mesoscale chemistry transport models applied to study the impact of aircraft emissions upon the atmosphere may cover the gap between micro- and global-scale investigations. Until now mesoscale model sytems use only transformed global aircraft emission inventories as input data to assess the impact of pollutants from airtraffic. The goal of the presented study is to evaluate the sensitivity of a mesoscale model system to the temporal and spatial resolution of aircraft emission data.

A statistical analysis of airtraffic in the North-Atlantic flight corridor covering 8 days shows a highly variable and fine structured distribution. These features cannot be resolved by global emission inventories[1]. Based on such an inventory modifications are performed step by step to implement some of the analysed fine structure characteristics. These newly generated datasets are used as input data in sensitivity studies for a regional chemistry and transport model covering the main part of North-Atlantic flight corridor. The analysis presented in this paper is restricted to NO_x-emissions and their impact on ozone and on the reservoir species nitric acid (HNO_3). Furthermore transport studies with a passive tracer are carried out on an expanded model domain to investigate the sensitivity of both long range horizontal and vertical transport to the resolution of emission data and to assess the importance of inflow through the domain boundaries. The consistency of all calculations is obtained by keeping the total amount of NO_x-emissions (resp. tracermass) constant in all case studies.

In conclusion some requirements of a future aircraft emission inventory to meet the specific demands of mesoscale modelling are formulated.

2. Modeldescription, domain, episode

The *Eur*opean *A*ir Pollution *D*ispersion (EURAD) model system consists of three major modules: the PSU-NCAR model MM5 [2], the EURAD emission module EEM [3] and the chemistry transport model CTM [4]. The MM5 provides the meteorological input data for the CTM. The EEM generates surface emissions. Another module calculates different aircraft emission szenarios on regional scale using global emission inventories and airtraffic control data [5]. All modules operate on an Eulerian grid. Because of computational restriction the CTM operates only on a smaller part of the MM5 domain.

The horizontal grid resolution of the EURAD model version applied for this study is $50 \times 50 km^2$. The vertical range reaches from the surface to $10 hPa$ divided in 29 layers with a

thickness of $\Delta z \sim 500 - 1000m$ in the tropopause region which is for various reasons of special interest for these investigations (see next chapter). The location of the model domain can be depicted in figure 5. The presented episode covers nearly 11 days from October 11th to 21st, 1993 (CORRIDOR-episode, 258 h model time).
The results of this particular study has been derived with the original chemical mechanism CTM2 [6]. Therefore they are not directly comparable to studies using the newly developed, more sophisticated CHEST algorithm [7].

3. Analysis of airtraffic in the North-Atlantic flight corridor

The North-Atlantic is one of the most highly frequented flight corridors of todays subsonic airtraffic. The following analysis is based on aproximatly 5300 flight movements through Shanwick Control area covering the eastern part of the North- Atlantic flight corridor. The time period of the registered flights is 8 days in October 1993 (14th–21st). The data and additional information is provided by DORA (Dircetorate of Operatinal research And Analysis)[6]. The following figures (1–4) summarize the most striking characteristics of airtraffic in the North-Atlantic flight corridor.

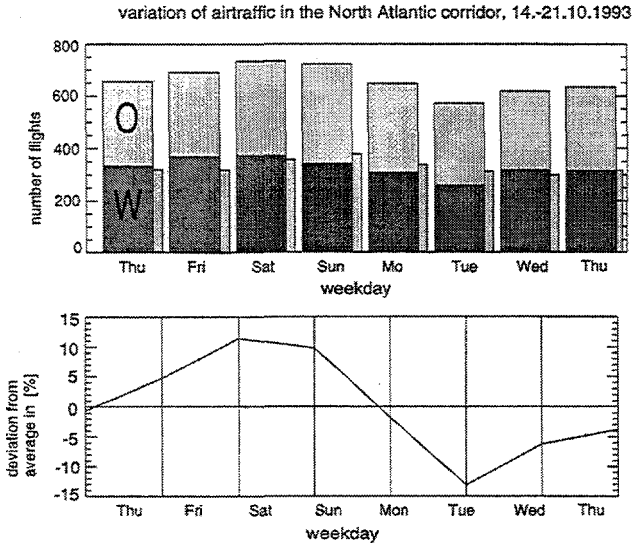

Fig.1 - Weekly variation of airtraffic in the North-Atlantic flight corridor by total number of fligts per day (upper frame) and deviation from weekly average (lower frame), data provided by Shanwick Control.

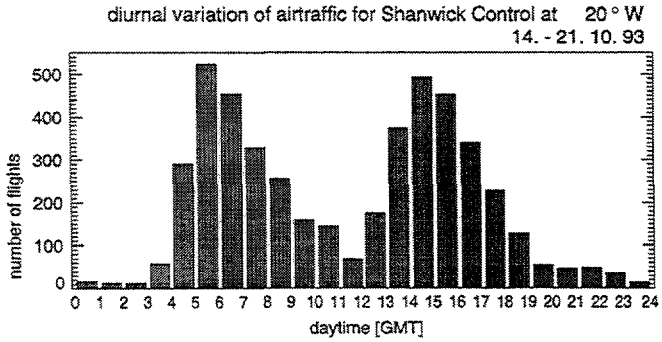

Fig.2 - Diurnal variation of airtraffic in the North-Atlantic flight corridor at 20° W, data provided by Shanwick Control. Airtraffic between 0 and 12 GMT represents mostly eastbound flights whereas westbound flights dominate between 12 and 23 GMT.

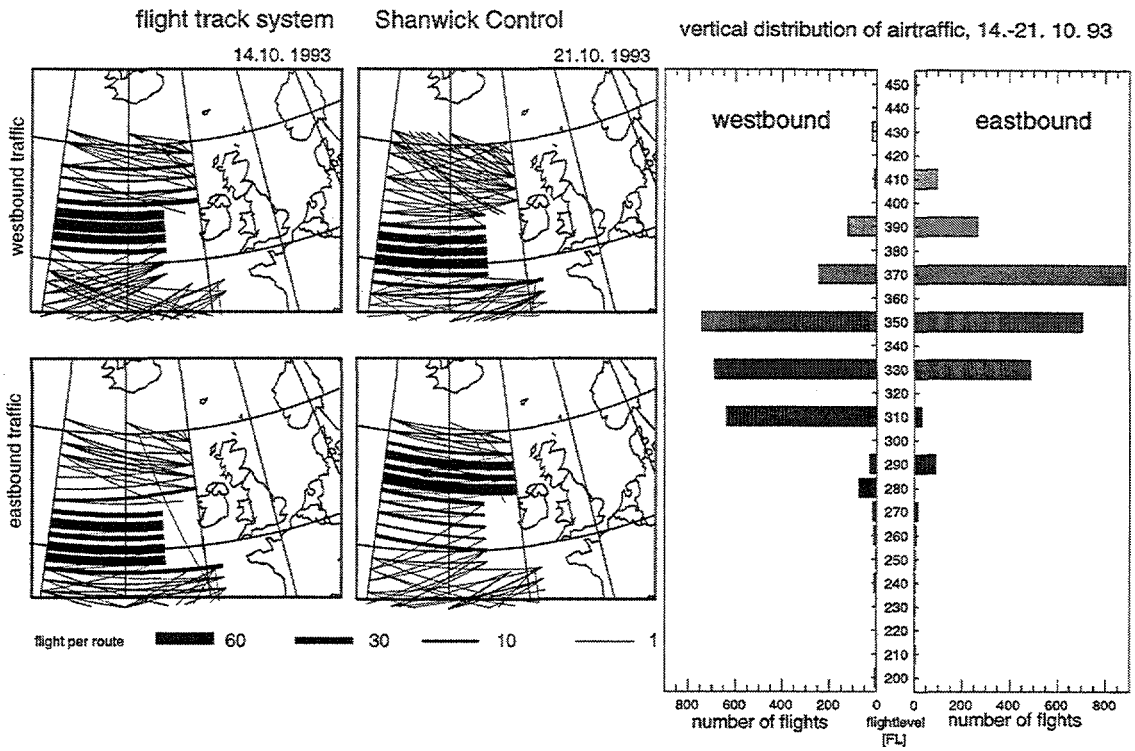

Fig.3 - Flight track system for east- and westbound airtraffic in the North-Atlantic flight corridor for two different dates: October 14th and 21st, 1993 (left frames). Vertical distribution of airtraffic, FL 200–450 (right frame), data from Shanwick Control.

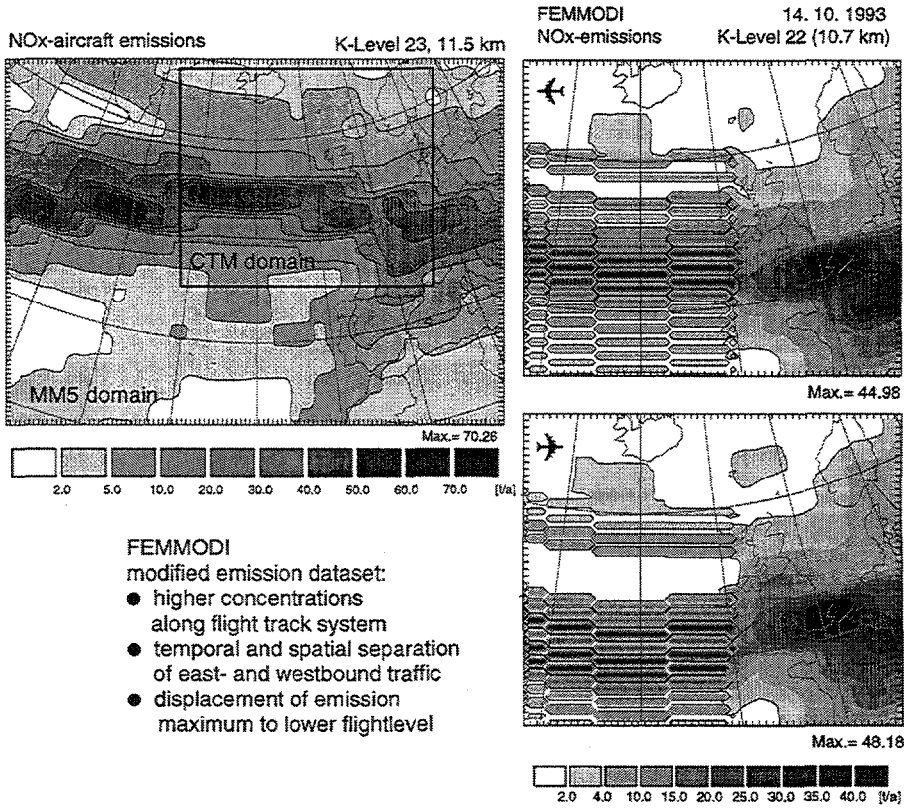

Fig.5 - NO_x aircraft emissions transformed from a global inventory (WSL) (left frame) and modified emission dataset for October 14th, 1993 (upper right frame: eastbound traffic, lower right frame: westbound traffic) on CTM domain. The cross sections are drawn in the corresponding main emission level (right frame: 11.5 km; left frames: 10.7 km)

One can recognize a pronounced weekly and diurnal variation of the airtraffic. Furthermore a fine structured, highly variable lateral distribution of the flight track system is obvious. Airtaffic is mostly restricted on a few highly frequented flight tracks. The vertical staggering shows a clear separation between both flight directions and a concentration of traffic on a few selected flight levels in the tropopause region (9–12 km).

4. Aircraft emission inventories

The basic global emission inventory used for this study is published by the Warren Spring Laboratory, WSL[1]. In a first instance this dataset (horizontal resolution aprox. 2.8°) is transformed to the mesoscale domain and grid ($50 \times 50\,km^2$). Thereafter some modifications are carried out to implement some of the analysed charcteristics of the airtraffic. These include horizontal and vertical redistribution of the emissions onto a flight track system and introduction of a diurnal variation. A comparison of two datasets is shown in Figure 5.

5. Sensitivity studies

Several sensitivity studies were carried out with different emission scenarios as input data. Some of the results are summarized in the following figures (6–8). The analysis is divided into transport studies using a passive tracer representing aircraft emissions and studies with the CTM focussing on the response of ozone and HNO_3 towards the different input data.

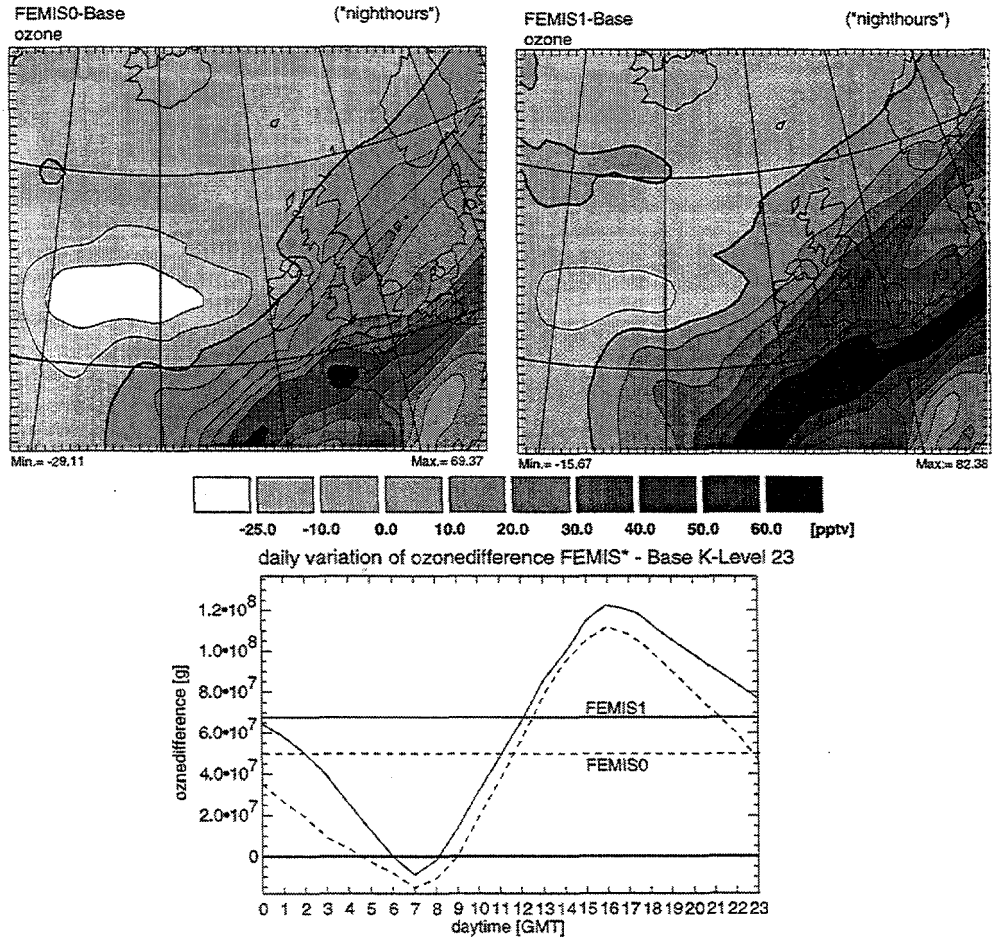

Fig.6 - Upper frames: Averaged response of ozone to NO_x aircraft emissions under night time conditions calculated for the complete CORRIDOR episode (258 h). Left frame: uniformily distributed emissions (FEMIS0), right frame: diurnal variation (FEMIS1). Lower frame: averaged daily variation of ozone response to different emission scenarios (FEMIS0,1)

5.1 Studies with the CTM

One major aspect of these CTM-studies is the introduction of a pronounced daily variation of the emission data (FEMIS1). Even on the restricted domain for the mesoscale chemical studies the effect on the ozone production is obvious. The deviation between both case studies (FEMIS0: no variation vs. FEMIS1: daily variation) occurs mainly under nighttime conditions, which leads to a more pronounced ozone reduction in the case of uniformily distributed emissions (fig.6, upper frames). The areas of ozone surplus in both cross sections (thick solid line marks the zero-contour) are due to preceding production under daylight conditions. In the case study FEMIS0 the portion of nighttime emissions is higher inrelation to case stdy FEMIS1 . This results finally in a 30% lower net ozone production averaged over the whole episode and calculated in the main emission level (fig.6, lower frame).
The redistribution of emissions onto a fine structured and highly variable flight track system even increases the deviation in the ozone production (fig.7, thin solid line). This is mainly due to a lower emission height in the modified NO_x-dataset (s.a).
Because of the more distinct dependency on the day-/night-cycle of the (photo-) chemical

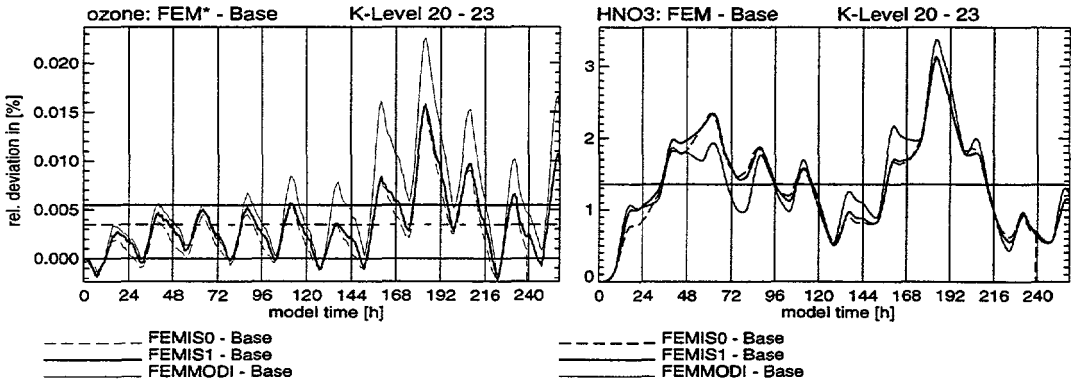

Fig.7 - Timeseries of the response of ozone and HNO_3 to different NO_x aircraft emission scenarios for the complete CORRIDOR episode (258 h). FEMIS0: uniformily distributed emissions, FEMIS1: diurnal variation, FEMMODI: flight track system and diurnal variation.

pro- and reduction-processes (NO_x–O_3–cycle) , ozone is much more sensitiv to the modification of NO_x input data than HNO_3 (fig.7). Noteworthy the relative deviation in the latter case is in the order of 2 magnitudes higher (0.02% vs. 2%). It is important to note that further studies reveal a strong seasonal dependency for the production rate of subsequent products [8].

5.2 Transport studies with a passive tracer

To quantify the significance of inflow through the domain boundaries tracer studies on a expanded model domain were compared to corresponding calculations on the restricted CTM domain. In the latter case no inflow is taken into account. Figure 8 (upper frames) clearly underlines the importance of the inflow especially through the western boundary. The inflow is very variable in time and depends strongly on the dynamical situation (fig.8 lower frame). Another study on the expanded domain (not shown here) investigates the influence of time, location and resolution of emission data on longrange horizontal and especially vertical transport. It shows signifcant sensitivity for downward transport during a tropopause folding event in response to modified input data.

6. Conclusions and outlook

The presented model system is very sensitive to the implemented modifications of the NO_x input data. It produces – even on a small, restricted domain – significantly different results. Some requirements of an aircraft emission inventory which meet the demands of mesoscale

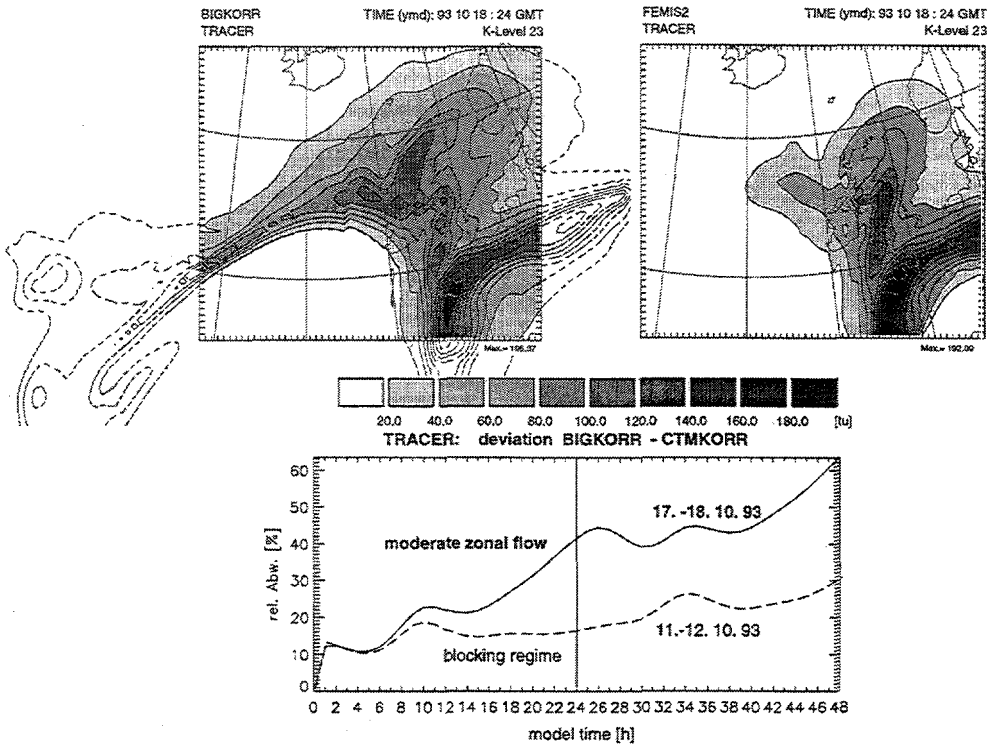

Fig.8 - Upper frames: Comparison of tracer studies between standard CTM-domain (right frame, 56 x 48 gridboxes) and expanded model domain (left frame, 109 x 79 gridboxes). Stippeld lines mark concentration field on the expanded domain. Lower frame: timeseries of the deviation between tracermass in the CTM-domain with and without inflow. Solid line marks the deviation for moderate zonal flow regime (shown in the upper frames), stippled line marks deviation for blocking regime (not shown here).

modelling are: diurnal variation in the model domain, emissions on flight track system, separation of east and westbound traffic, high resolution data directly transformed to a mesoscale grid and extended emission inventories (outbound of the model domain) for initial and boundary conditions.

In the meantime further investigations were carried out which implement a new boundary initialization taking into account the inflow through the domain boundaries using a parametrizational approach [9].

References

1. McInnes, G., C.T.Walker, 1992: Warren Springs Laboratory, Report LR 872 (AP).
2. Jakobs, H.J., H.Feldmann, H.Hass, M.Memmesheimer, 1995: *J. Appl. Met.*, **34.**
3. Memmesheimer M., J. Tippke, A.Ebel, H.Hass, H.J. Jakobs, M.Laube, 1991: Proceedings of the EMEP workshop on Photooxidant Modelling for Long-Range Transport in Relation to Abatement Strategies. Berlin, April 16-19, 1991, 307-324.
4. Hass, H., 1991: Mitteilungen aus dem Institut für Geophysik und Meteorologie der Universität zu Köln, A.Ebel, F.M.Neubauer, P.Speth, Eds., Heft 83, 100 pp.
5. V. Franzkowiak, 1995: *Diploma thesis, Univ. Köln.*
6. Davies, L., D. Harrison, 1990: *DORA Communications,* **8936**, *CAA.*
7. Lippert, E., J.Hendricks, H.Petry, 1996: *this volume.*
8. Petry, H., A.Ebel, V.Franzkowiak, J.Hendricks, E.Lippert, M.Möllhof, 1996: *this volume.*
9. J.Hendricks, A.Ebel, E.Lippert, H.Petry, 1996: *this volume*

AEROSOL CHARACTERIZATION DURING PROJECT POLINAT

Donald E. Hagen, Alfred R. Hopkins, Jonathan D. Paladino,
and Philip D. Whitefield
Cloud and Aerosol Sciences Laboratory
University of Missouri-Rolla
Rolla, MO 65409-0430 USA
and
Harvey V. Lilenfeld
McDonnell Douglas Aerospace-East
St. Louis, MO 63166 USA

1. INTRODUCTION

The objectives of the aerosol/particulate characterization measurements of project POLINAT are: (1) to search for aerosol/particulate signatures of air traffic emissions in the region of the North Atlantic Flight Corridor; (2) to search for the aerosol/particulate component of larger scale enhancement ("corridor effects") of air traffic related species in the North Atlantic region; (3) to determine the effective emission indices for the aerosol/particulate component of engine exhaust in both the near and far field of aircraft exhaust plumes; (4) to measure the dispersion and transformation of the aerosol/particulate component of aircraft emissions as a function of ambient condition; (5) to characterize background levels of aerosol/particulate concentrations in the North Atlantic Region; and (6) to determine effective emission indices for engine exhaust particulates for regimes beyond the jet phase of plume expansion.

2. EXPERIMENTAL APPROACH

The University of Missouri-Rolla Cloud and Aerosol Sciences Laboratory (UMR/CASL) has developed a Mobile Aerosol Sampling System (MASS) specifically designed for airborne characterization measurements of poly-dispersed particulates and aerosols. In particular, the MASS permits realtime characterization of aerosol/particulate in the size range 0.01 to 1.0 micron (dia) and under all ambient atmospheric conditions between sea level and 42,000 ft. In project POLINAT aerosol measurements were made using the MASS installed on the German Aerospace Research Establishment (DLR) Falcon research aircraft. The MASS is a flight worthy mobile aerosol sampling system assembled from laboratory instrumentation. It has been used extensively in airborne field studies such as NASA's projects FIRE, SUCCESS, and SNIF. Its main component consists of two EAC's (Electric Aerosol Classifier) configured in series with a water saturator in between. With this system we can acquire total aerosol concentration, size distribution, volatility, and condensation property (critical supersaturation) information for aerosols in the dry size range 10-300nm. During the POLINAT campaigns the MASS was divided into two components: (1) the flight rack and, (2) the ground rack. The flight rack had the capability to measure total CN and non-volatile CN concentrations and acquire size distributions in realtime. It also had the capability of taking tank samples either for quasi-realtime size analysis in-flight or

post flight size and hydration property analysis. In the latter case the ground rack was coupled to the flight rack. The MASS methodology has been described in detail else where and will not be described here.[1-4]

3. MAIN RESULTS AND CONCLUSIONS

3.1 CN data in the POLINAT data bank. Total CN and non-volatile CN versus time profiles for all flights are recorded. Over 70 aerosol size distribution measurements were made and are recorded. These distributions include both total CN and non-volatile CN for aged plumes encountered in the corridor, young plumes detected in the near field missions, and the corridor background. Hydration properties are recorded as fractional populations for 80nm dry size particle samples versus soluble mass fraction. The specific attributes of all these data are discussed in the following sections.

3.2 CN measurements as signals of air traffic emissions in the North Atlantic region. CN measurements were among the best tracers of aircraft effluents. The measured peak concentrations (appearing as peaks in the CN vs. time profiles) exceeded background levels typically by factors of five. Calculations of predicted plume positions revealed that these peaks are often due to the superposition of more than one aircraft plume of variable age. These plume ages ranged from 0.5 to 5 hours.[5] Volatility ratios of the aerosol samples taken show significant increases for both new and aged aircraft exhaust plumes. Typical background volatility ratios were less than 3:1, whereas ratios as high as 50:1 were observed in moderately aged plumes. The superimposition of plumes of different ages significantly affects the appearance of the size distributions recorded in these plumes, especially when they are compared to those for younger single plumes investigated during the near-field flights (30 June, 3 July, and 5 July 1995). In the case of the aged plumes there is evidence of decreasing CN concentration at small particle diameters (below 30 nm) and the generation of a peak in the size distribution occurring in the range 35-50 nm (Figure 1). The distributions characteristic of young plumes from single aircraft sources are Junge type (Figure 2). Thus, this technique shows promise as an extremely sensitive diagnostic for identifying aircraft emissions in-flight.

3.3 Corridor effects. To date in project POLINAT it has not been possible to extend the range of the Falcon to make measurements outside the region of intense air traffic in the North Atlantic corridor (i.e. in a north-south traversing) while operating out of Shannon. Large scale enhancement of CN concentration were observed during an anti-cyclonic weather pattern that persisted in the measurement area for up to 5 days during the campaign. The stability of the air parcels and the pronounced increase in CN as a function of air traffic provide indirect evidence for a corridor effect. Figure 3 is a plot of the average total and non-volatile CN concentrations from four subsequent flights at 10.7 km during the period of the stagnant anti-cyclone in the measuring area. Size distributions taken in the corridor background exhibited the expected Junge type distributions in both the total CN and non-volatile data.

3.4 Near-field exhaust measurements. During the near field encounters the MASS methodology was applied to samples acquired in young plumes from single aircraft sources. The size distributions for these young plumes were all Junge type except for one penetration where a log-normal distribution was recorded. Two penetrations were recorded for encounter number 9,

a B747 with CF6-50E2 engines. The size distributions for each penetration are given in Figures 4 and 5. The first penetration (Figure 4) exhibits a log-normal shape, whereas the second penetration (Figure 5) exhibits a Junge type shape common to the other penetrations observed in the near field encounters. These results are of particular interest because for the first penetration the population at small CN diameters is much smaller than that for the second penetration. This is consistent with a lesser degree of gas-to-particle formation in the first penetration compared to the second. Based on studies by Schumann *et al.*[6] where one dimensional CN concentration profiles have been measured for perpendicular passes through plumes, it is likely that the first penetration was sampled from the center of the plume whereas the second penetration occurred on the fringe.

3.5 Emission indices. The near field plume encounters in project POLINAT provided simultaneous measurements of CO2, NOx, and CN. From these data emission indices for CN have been calculated for the total and non-volatile aerosol (see *Table 1*) and represent the first such data measured in-flight at cruise altitudes for modern commercial wide body aircraft.

Nr	Type	Engine	TCN:NVCN	EICN (tot) 10^{15}/kg	EICN (nv) 10^{15}/kg
5	B747	JT9D-7J	6.9	5.8	2.7
6	DC10	CF6-50C	5.2	4.5	0.46
7	B747	JT9D-7J	8.7	9.9	0.45
8	B747	JT9D-7A	-	0.81	0.57
9	B747	CF6-50E2	2.2	1.8	0.53
10	EA34	CFM56-5C2	21.1	2.9	1.6

Table 1: Summary of Near Field plume measurements for which both total and non-volatile emission indices were calculated.

The method described by Schlager *et al.*[7] and Fahey *et al.*[8] was used to calculate the emission indices from the plume encounter CN data. These were found to range from 0.8 - 10 x 10^{15}/kg and 0.5 - 3 x 10^{15}/kg for total and non-volatile CN respectively. These values are at least an order of magnitude smaller than those reported for the Concorde's Rolls Royce Olympus engines from ground based and in-flight measurements.[8,9] A mass-based emission index will be developed from the size distribution data recorded in the POLINAT data base, along with the assumption of particle sphericity and density.

3.6 Exhaust particle hydration measurements. The soluble mass fractions of particulates collected during POLINAT were studied by measuring their deliquescence behavior. 80 nm dry size particles were extracted from tank samples acquired under different conditions including young plumes, aged plumes, and corridor background. The 80 nm class of particles was chosen since this diameter falls in the median size range for typical jet engine exhaust. The moist environment in the deliquescence experiment put a limit on the upper range of voltages that could be used in the

differential mobility analysis of the deliquesced particles. Thus soluble mass fractions above 0.23 were not accessible. Within these limits a clear correlation between plume age and solubility was observed. In young plumes the fractional population of totally insoluble particles was small (<20%). This contrasts with aged plumes and corridor background samples where much larger fractional populations (>40%) were observed.

3.7 Dispersion inferences from CN measurements. The CN data provide a complementary resource for horizontal and vertical diffusivity calculations using the methods described by Schumann *et al.*[10]

REFERENCES

1. Hagen, D.E., M.B. Trueblood, and J. Podzimek, "Combustion Aerosol Scavenging", *Atmos. Env.* **25A**, 2581, (1991).
2. Hagen D.E., M.B. Trueblood, and P.D. Whitefield, "A Field Sampling of Jet Exhaust Aerosols", *Particle Sci. & Techn.*, **10**, 53-63 (1992).
3. Hagen D.E., J. Podzimek, and M.B. Trueblood, "Upper Tropospheric Aerosol Sampled During Project 'FIRE IFO II", *J. Atmos. Sci.*, **52**, 4196 (1995).
4. Hagen D.E. and P.D. Whitefield, "Particulate Characterization in the Near Field of Commercial Transport Aircraft Exhaust Plumes Using the UMR MASS, Part 1", *J. Geophys. Res.*, In Press November 1995.
5. Konopka P., "Analytical Gaussian solutions for Anisotropic Diffusion in a Linear Shear Flow", *J. Non-Equilib. Thermodyn.*, **20**, 78 (1995).
6. Schumann, U., J. Strom, R. Busen, R. Baumann, K. Gierens, M. Krautstrunk, F. Schroder and J. Stingl, "In situ Observations of Particles in Jet Aircraft Exhausts and Contrails for Different sulfur Containing Fuels", DLR Institut fur Physik der Atmosphare Report No. 35, Oberpfaffenhofen, June 1995
7. Schlager H, P. Konopka, P. Schulte, U. Schumann, H. Zereis, F. Arnold, D. Hagen, P. Whitefield, and J. Ovarlez, "In Situ Observations of Air Traffic Emission Signatures in the North Atlantic Flight Corridor", *J Geophys. Res.* Submitted July 1996.
8. Fahey, D.W. *et al.*, "Emission Measurements of the Concorde Supersonic Aircraft in the Lower Stratosphere," *Science* **270**, 70-73, (1995).
9. Whitefield, P.D., D.E. Hagen, H.V. Lilenfeld, and M.B. Trueblood, "Ground-Based Particulate Emissions Measurements on the Concorde Olympus Engines", Proc. Combustion Institute Symposium, St. Louis, May 1996.
10. Schumann, U., P. Konopka, R. Baumann, R. Busen, T. Gerz, H. Schlager, P. Schulte, and H. Volkert, "Estimate of Diffusion Parameters of Aircraft Exhaust Plumes Near the Tropopause from Nitric Oxide Turbulence Measurements", *J. Geophys. Res.*, **100**, 14147-14162, (1995).

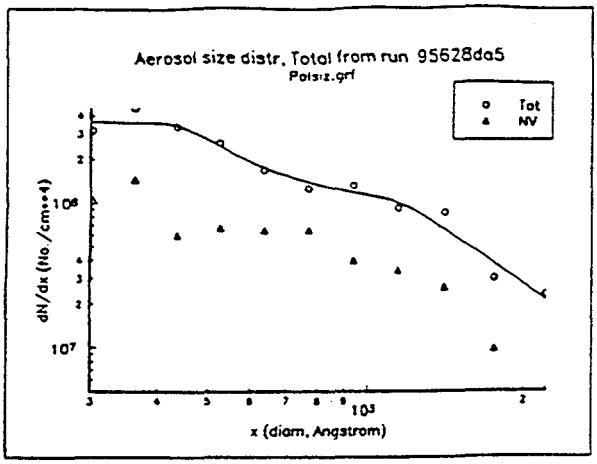

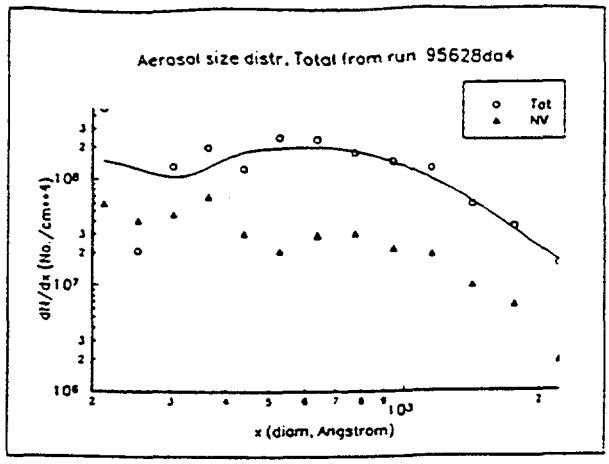

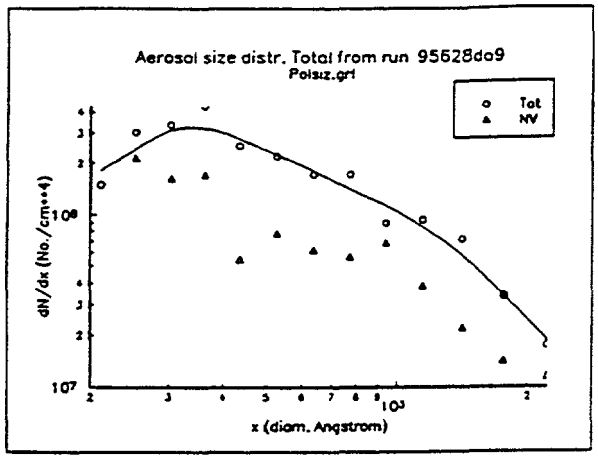

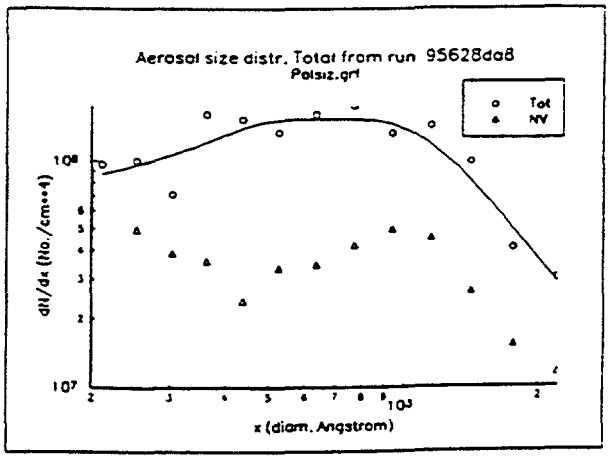

Fig. (1) Size distributions for aged plumes during project POLINAT

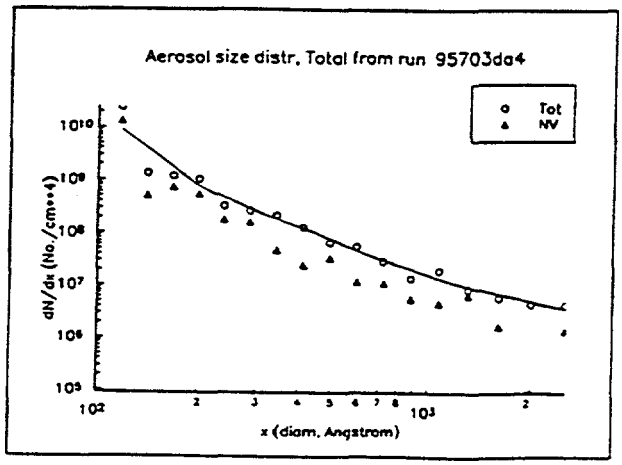

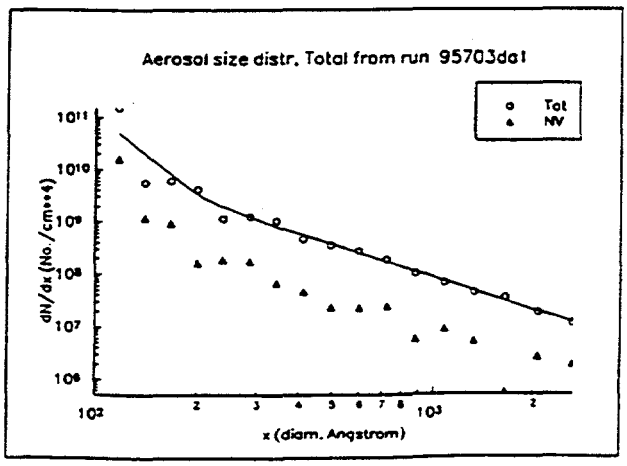

Fig. (2) Size distributions for young plumes during project POLINAT

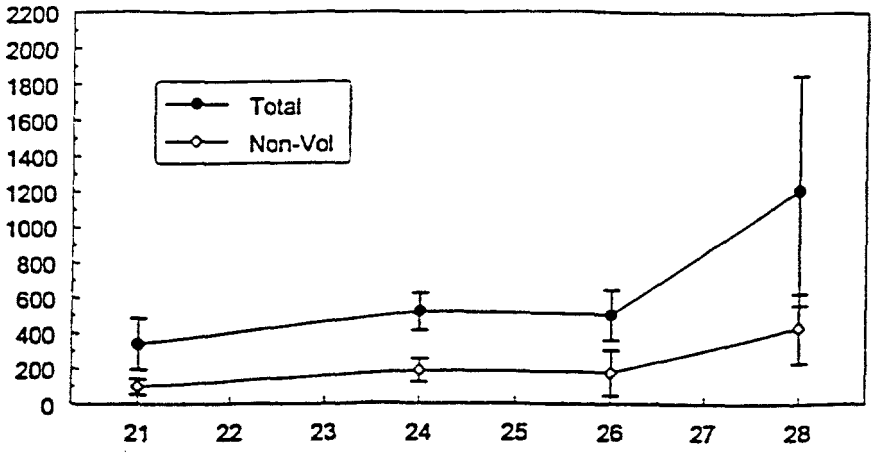

Fig. (3) Total and Non-volatile CN concentrations during anticyclonic weather pattern.

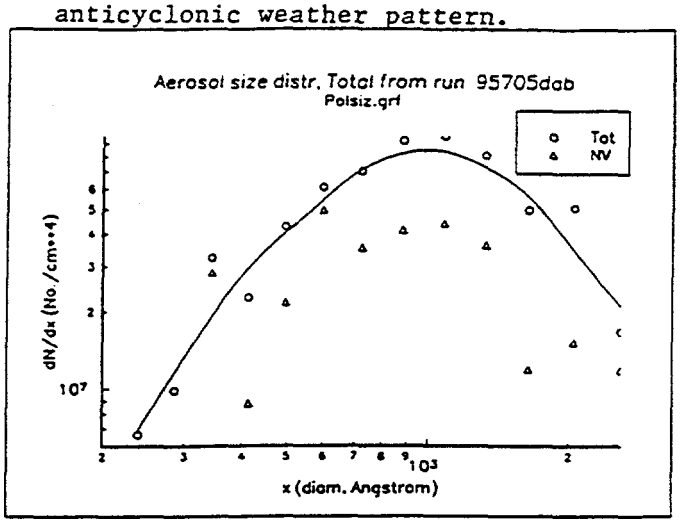

Fig. (4) Size distribution for penetration (1) July 1995

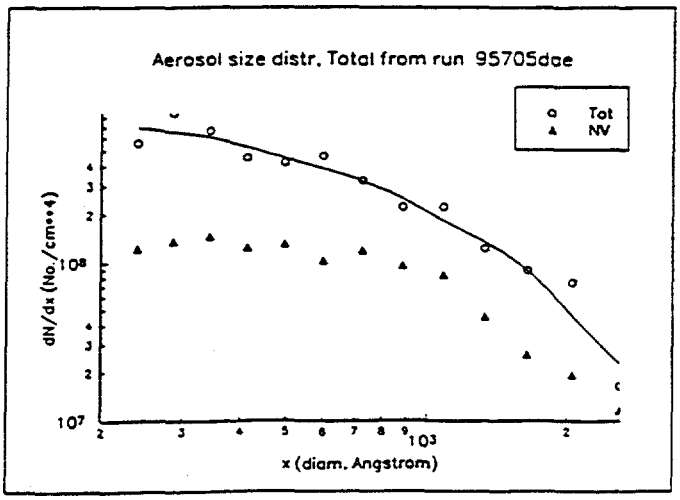

Fig. (5) Size distribution for penetration (2) July 1995

WATER VAPOUR MEASUREMENTS DURING POLINAT 1

Joëlle Ovarlez, Henri Ovarlez
Laboratoire de Météorologie Dynamique du CNRS, Ecole Polytechnique,
91128 Palaiseau cedex, France

ABSTRACT

The POLINAT 1 experiment has been performed within the framework of the Environment Programme of the Commission of the European Community. It was devoted to the study of the pollution from aircraft in the North Atlantic flight corridor. For that experiment the water vapour content was measured with a frost-point hygrometer on board of the DLR Falcon research aircraft. This instrument is described, and some selected results are given.

1. Introduction:

The POLINAT (POLlution from aircraft emissions IN the North ATlantic flight corridor) experiment has been performed during 1994-1995. The aim of this experiment was to investigate the impact of pollutants emitted by aircraft on the concentrations of ozone and other trace gases in the upper troposphere and lower stratosphere. The emissions of pollutants from aircraft engines could contribute to anthropogenic climate changes (Schumann, 1994; Fortuin et al, 1995; Rind and Lonergan, 1995). In the upper troposphere the water vapour emitted by aircraft can enhance the greenhouse effect by increasing the cloud cover by the formation of contrails (Liou et al, 1990). Around the tropopause radiative forcing is very sensitive to changes in humidity (Shine and Shina, 1991). In the stratosphere the additional water vapour may lead to enhanced formation of polar stratospheric clouds that contribute to ozone destruction (Peter et al, 1991; Considine et al 1993).

During the POLINAT campaigns trace gas measurements were made with instruments on board the Falcon research aircraft of DLR (Deutsche Forschungsanstalt für Luft-und-Raumfahrt), as described by Schlager et al (1996). Concentration of trace species were measured, in the North Atlantic flight corridor, at cruise altitudes of commercial aircraft, i.e. in the upper troposphere and lower stratosphere, during two campaigns, one in November 1994, the other in June/July 1995, and some results of POLINAT project are given by Schumann et al (this issue). The Falcon aircraft was operated from Shannon airport, west of Ireland. The water vapour content measurement on board the Falcon has been carried out with a frost-point hygrometer designed and operated by LMD. Meteorological planning and analysis were performed by KNMI using output from the ECMWF (European Centre for Medium-range Weather Forecasts) model.

2. Description of the hygrometer:

Water vapour content was measured by a cryogenic frost-point hygrometer that is based on the same concept as the instruments used previously by Spyers-Duran (1991) and by Busen and Buck (1995) on board of aircraft. It has originally been designed for stratospheric balloons (Ovarlez, 1991, Ovarlez and Ovarlez, 1994). For POLINAT, it has been adapted to the Falcon aircraft installation and certification requirements. The hygrometer is based upon the well-known chilled mirror technique. The block diagram of the aircraft-borne instrument is shown in figure 1: The onset of condensation on a cooled mirror is detected optically, and the mirror is maintained at the temperature of

condensation by controlling the heating and cooling of the mirror. The measurement of the mirror temperature gives the frost-point temperature of the air passing over the mirror. The cooling is realized with the help of a copper rod immersed in liquid nitrogen enclosed in a dewar container. The heating is produced by a resistance wire wrapped around the rod. The air flow is generated by the difference between the dynamic pressure at the aircraft air inlet and the static pressure of the ambient air. A pressure sensor measures the air pressure at the sensor head of the hygrometer to allow for determination of the water vapour mixing ratio. This mixing ratio is calculated as the ratio between the water vapour saturation pressure over ice and the air pressure (WMO 1984). In order to avoid contamination when flying through dense low level clouds, the instrument is activated by the experimenter after the first kilometres of the aircraft ascent. From then, it works in an automatic mode. The range of frost-point temperatures of the instrument is -90 C to -10 C. The accuracy of the measurement of the water vapour mixing ratio is estimated to be less than 5% under the circumstances of the POLINAT observations, which ranged from -70 C to -10 C in frost-point temperature, and from 10 to 3000 ppmv in water vapour mixing ratio. The relative humidity is calculated by using the air temperature from the standard Falcon measurements, which are described by Fimpel (1987). Then, the relative accuracy on relative humidity determination is 10%.
The LMD hygrometer was used for the first time on board an aircraft during the POLINAT experiment. Mixing ratios as low as 5 ppmv were measured in the stratosphere for frost-point temperatures down to -75 C.

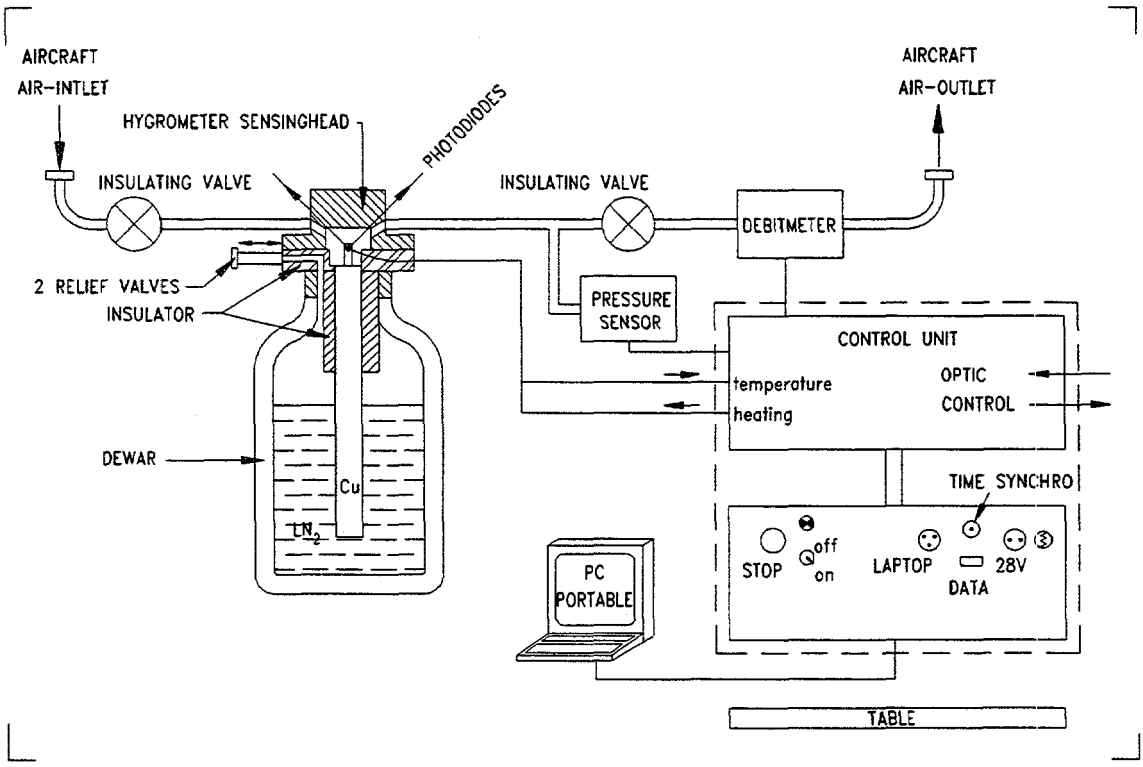

Fig.1- Block diagram of the frost-point hygrometer used onboard the DLR Falcon aircraft during the POLINAT experiment

General observations:

The water vapour measurement gave for each flight the background conditions as they are very changeable with respect to meteorological situation.

The residence time of pollutants from the air traffic and their consequences on the atmospheric pollution depends strongly on whether these pollutants are emitted in the stratosphere or in the troposphere. Therefore it is important to determine when the measurements from POLINAT flights are made above or below the tropopause level. The water vapour measurements clearly identify the transition between tropospheric and stratospheric air masses as shown for a typical example in figure 2.

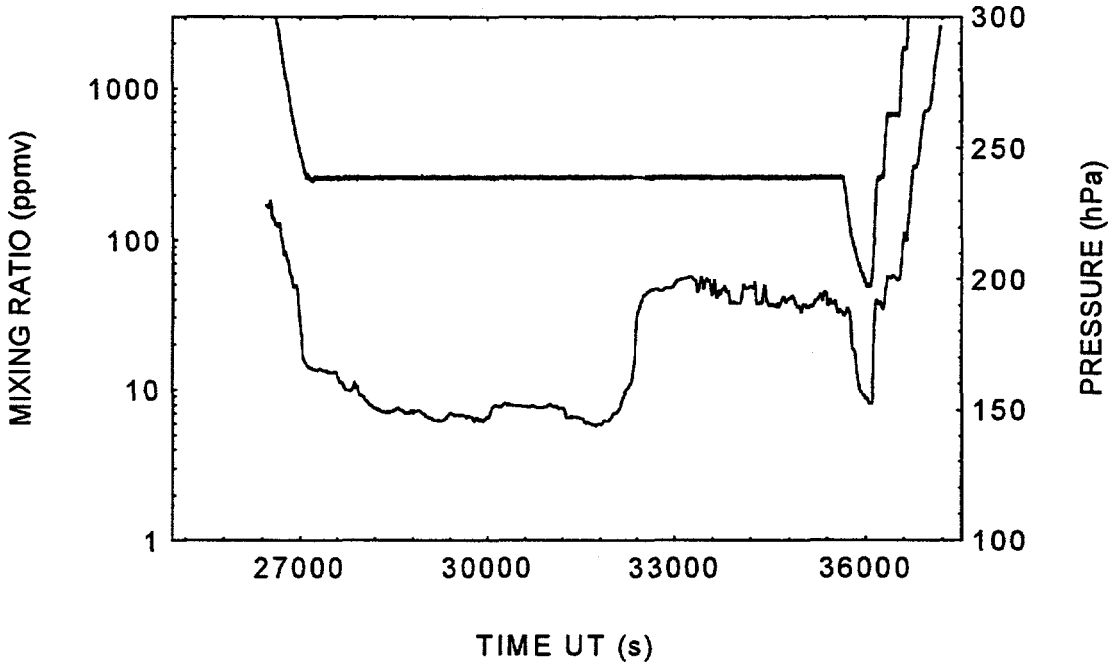

Fig.2. At constant pressure level of the Falcon aircraft, the water vapour mixing ratio is below 10 ppmv during the first part of the flight showing that the aircraft is in stratospheric air. Then suddenly the mixing ratio increases up to about 50 ppmv showing that the aircraft flew in tropospheric air for the same pressure level. In addition, the steep variations show the ability of the instrument to follow the fast changes in the water vapour content.

Other particular meteorological situations were observed and well identified by the water vapour measurements such as a cold through and high perturbations after the occurrence of a thunderstorm (Ovarlez J. et al, 1996).

On another hand the analysis of the difference between measured humidity and predicted humidity retrieved from ECMWF analyses along the aircraft trajectories by KNMI has been made (Ovarlez J. and P. van Velthoven, 1996).

Observations in young plumes

Usually the upper troposphere and lower stratosphere are very dry. Nevertheless in two cases during the winter campaign, very high humidity values sometimes exceeding ice

saturation were measured, as persistent contrails and natural cirrus clouds were visible. The Falcon could chase some contrails events for those flights. The time of the chasing of the plumes is identified from NO measurements performed by the DLR instrument (Schlager et al, submitted).

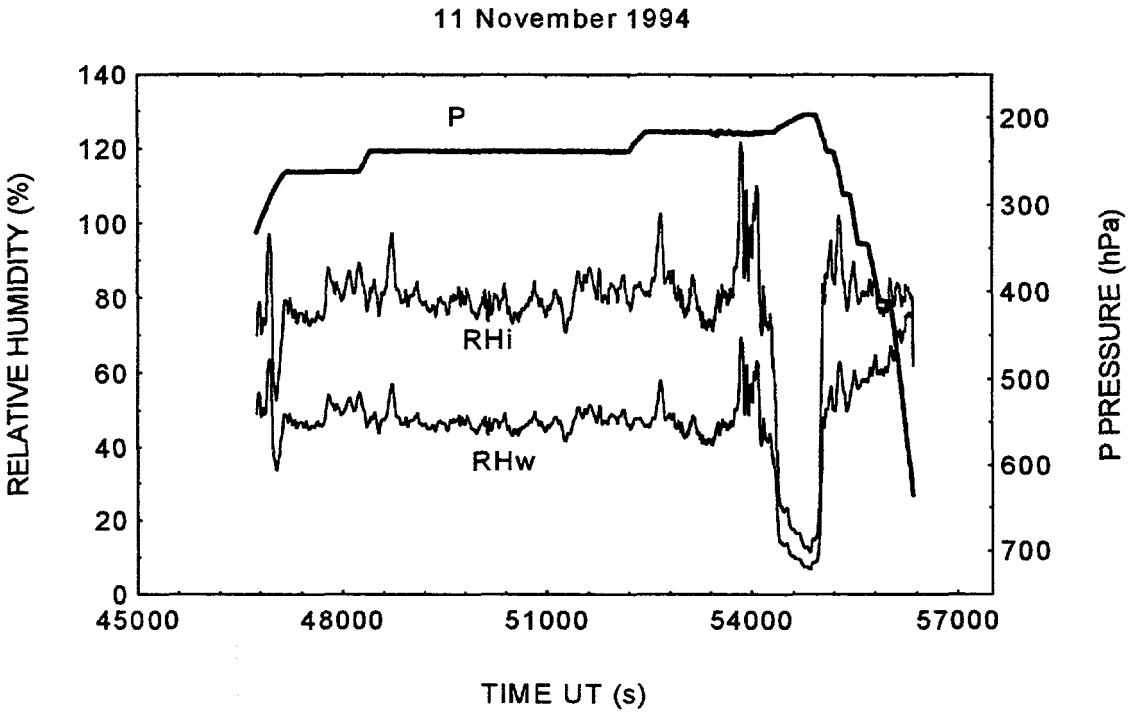

Fig.3: Humidity of the environment during the 11 November flight. P is the pressure level of the aircraft. At tropospheric level, the background relative humidity is higher than 80% over ice (RHi), and around 50% over water (RHw).Before descent for landing, the aircraft went at stratospheric level for a short period of time as shown by the low humidity measured.

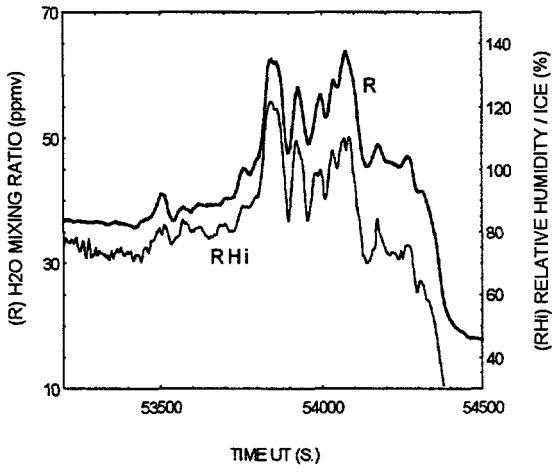

Fig. 4 -Contrail observation during the flight performed on 11 November, with measurements of oversaturation with respect to ice and high increase in the water vapour content with respect to the background. Air temperature perturbations (not shown) were observed at the same time.

Figure 3 shows the water vapour measurements during the 11 November flight, when the frost-point and air temperatures are very close together and the relative humidity with

respect to ice (RHi) is very high, over 80% in the tropospheric part. The detail of a plume chasing from a B747 aircraft measured during that flight is shown in Figure 4.
This plume was also well identified by the other pollutants measurements. When entering the plume a fast increase in the water vapor content is found and then perturbations inside the plume. Relative humidity with respect to ice increases up to 120%, and that oversaturation induces ice particles formation. The presence of a contrail was confirmed by visual observation during that chasing. This observation is being more carefully investigated as there is a general agreement that contrails become persistent only when the ambiant air is oversaturated with respect to ice, otherwise the life of the contrail is very short and the ice particles evaporate rapidly.
During the other winter flight performed is very humid air, and devoted to young plume chasing high oversaturation with respect to ice was also measured in the plumes, but in an environment already saturated and under the visual observation of cirrus clouds.
Near field plume measurements were also performed during the summer campaign, but in conditions quite far from saturation. From the enhancement of water vapour content inside the plume, compared to that of CO2 (measurements performed by DLR), the water vapour emission indice was calculated. It is found to be between 1.28 and 1.39 kg/kg , that is not far from the expected value.

Summary and conclusion

An accurate and reliable cryogenic frost-point hygrometer has been developped to be used for in situ measurements from aircraft. It has been used in the frame of the European project POLINAT 1, and will be used during the POLINAT 2 campaign during summer 1997. Background concentration of water vapour has been measured at aircraft flight levels, in the eastern part of the North Atlantic corridor, under several meteorological conditions. Measurements in young plume have been performed and oversaturation with respect to ice have been measured during some young plume chasing in high background humidity condition as contrails and cirrus were observed.

Acknowledgements: This work was supported by the Commission of the European Community under contract EV-5V-CT93-0310 (DG12 DTEE). We thank the Flight Operation Department of DLR for the operation of the Falcon aircraft. We are also grateful to Hans Schlager for the organisation of the field campaign and to Ulrich Schumann for coordination of the Project.

REFERENCES

Busen, Reinhold and Arden L. Buck, 1995: A high performance hygrometer for aircraft use: description, installation, and flight data. *J. Atmosph. and Oceanic Technology*, 12, 1, 73-84.

Considine, David B., Anne R. Douglass and Charles H. Jackman, 1994: Effect of polar stratospheric cloud parametrization on ozone depletion due to stratospheric aircraft in a two dimensional model, *J. Geophys. Res.*, 98, D12, 23,141-23,164.

Fortuin, J.P.F., R. van Dorland, W.M.F. Wauben and H. Kelder, 1995: Greenhouse effects of aircraft emissions as calculated by a radiative transfer model, *Ann. Geophys.* 13, 413-418.

Fimpel, Hans P., the DFVLR meteorological research aircraft Falcon-E: Instrumentation and examples of measured data, Proceedings of the sixth Symposium on Meteorological Observation and Instrumentation, Amer. Meteorol. Soc., 1987.

Gutzler David S., Uncertainties in Climatological Tropical Humidity Profiles 1993: Some implications for Estimating the Greenhouse Effect, *J. of Climate*, 6, 978-982.

Liou, K.N., S.C. Ou and G. Koenig, 1990: An investigation of the climatic effect of contrail cirrus, Air traffic and the Environment, vol 60, U.Schumann Ed., Spring-Verlag, 138-153.

Ovarlez Joëlle, 1991: Stratospheric Water Vapor Measurement in the Tropical Zone by means of a Frost Point Hygrometer on Board Long-Duration Balloons, *J. Geophys. Res.*, 96, D8, 15541-15545.

Ovarlez J. and H. Ovarlez, 1994: Stratospheric water vapour content evolution during EASOE, *Geophys. Res. lett.* 21, 13, 1235-1238,.

Ovarlez J, H. Ovarlez, R.M. Philippe and E. Landais,Water vapor measurements during the POLINAT campaigns, Air Pollution Report N° 58, CEC, Bruxelles, in press, 1996.

Ovarlez Joëlle and Peter van Velthoven, Comparison of water vapour measurements with data retrieved from ECMWF analyses during the POLINAT experiment, submitted J. appl. Meteor., 1996.

Peter, Th., C. Brühl and P.J. Crutzen, 1991: Increase in the PSC formation caused by high flying aircraft, *Geophys. Res. Lett.*, 18, 8, 1465-1468.

Rind, D. and P. Lonergan, Modeled impacts of stratospheric ozone and water vapor perturbations with implications for high-speed civil transport aircraft, J. Geophys. Res. 100, 7381-7396, 1995.

Schlager H., et al, Airborne observations of large scale accumulation of airtraffic emissions in the north atlantic corridor within a stagnant anticyclone, *this issue*.

Schlager H., P. Konopka, P. Schulte, U Schumann, H. Ziereis, F Arnold, D. Hagen, P. Whitefield and J. Ovarlez, 1996: In situ observations of Airtraffic Emission Signatures in the North Atlantic Flight Corridor, submitted *J. Geophys. Res.*.

Schumann Ulrich, 1994: On the effect of emissions from aircraft engines on the state of the atmosphere, *Ann. Geophys.*, 12, 365-384.

Schumann U. et al, Pollution From Aircraft Emissions In The North Atlantic Corridor - Overview on the Results of the POLINAT project, *this issue*.

Shine, K.P. and A. Sinha, 1991: Sensitivity of the Earth's climate to height dependent changes in the water vapour mixing ratio, *Nature*, 354, 382-384,.

Spyers-Duran, P.A., An airborne cryogenic frost-point hygrometer, 1991: Proceedings of the seventh symp. on Meteorological Oservations and Intrumentation, A. M. S., 303-306.

WMO Technical Regulations,1984: Basic document N 49.

Presented at: Impact of Aicraft Emissions upon the Atmosphere
International colloquium Paris, October 15-18, 1996

Gaseous ion-composition measurements in the young exhaust plume of jet aircraft at cruising altitudes: Implications for aerosols and gaseous sulfuric acid

F. Arnold[1], K.-H. Wohlfrom[1], M. Klemm[1], J. Schneider[1], K. Gollinger[1], U. Schumann[2], R. Busen[2]

1: Max-Planck-Institute for Nuclear Physics (Atmospheric Physics Devision), P. O. Box 103980, D-69029 Heidelberg, Germany

2: DLR, Institute for Atmospheric Physics, P. O. Box 1116, D-82230 Wessling, Germany

Abstract. ~~We have made~~ (were made) mass spectrometric measurements in the young exhaust plume of an Airbus (A310) at cruising altitudes at distances between 400 and 800 m behind the Airbus (averaged plume age: 3.4 sec). The measurements indicate that gaseous sulfuric acid (GSA) number densities were less than $1.3 \cdot 10^8$ cm^{-3} which is smaller than the expected total sulfuric acid. Hence the missing sulfuric acid must have been in the aerosol phase. ~~Our~~ These measurements also indicate a total aerosol surface area density $A_T \leq 5.4 \cdot 10^{-5}$ cm^2 per cm^3 which is consistent with simultaneously measured soot and water contrail particles. However, homogeneous nucleation leading to $(H_2SO_4)_x(H_2O)_y$-clusters can not be ruled out.

Introduction

Jet engines produce gaseous sulfuric acid (GSA) from fuel sulfur (c.f. Reiner and Arnold, 1993). GSA may undergo bi-molecular nucleation leading to sulfuric acid-water (AW) condensates (c.f. Zhao and Turco, 1994; Kärcher et al., 1995; Fahey et al., 1995; Schumann et al, 1996a). Nucleation may proceed via a homogeneous (HONU), heterogeneous (HENU, on soot), and a chemiion (CINU) mechanism (Frenzel and Arnold, 1994; Arnold et al., 1997). While HONU and CINU lead to new "pure" AW-aerosols HENU does not produce new particles but may lead to an AW-coating of soot particles (SP) and thereby convert "bare" probably hydrophobic SP to hydrophilic SP which may act as CCN. For a high fuel-sulfur content (FSC) HONU possibly can become very efficient and rapidly deplete GSA by converting it to A_xW_y-clusters (A denotes H_2SO_4, W denotes H_2O).

The present paper reports on an experimental search for GSA in a young exhaust plume (plume age: 3.4 s) of an Airbus (A310) at cruising altitude. Our mass spectrometer measurements set an upper limit to the GSA-number density which is significantly lower than the expected total sulfuric acid (TSA) concentration. This is consistent with model results obtained by Kärcher (1996). The measured total aerosol surface area density was $A_T \leq 5.4 \cdot 10^{-5}$ cm^2 / cm^3 which is roughly consistent with soot and ice contrail particle measurements. Hence our measurements indicate GSA-depletion which can be due to HENO, HONU or possibly even GSA-scavenging by ice contrail particles.

Measurements

The analytical concept underlying our present search for GSA and A_T in a young jet aircraft plume at cruising altitude builds on ambient atmospheric gaseous negative ions which are used as probes for GSA and A_T. Such ions belong mostly to two families: $NO_3^-(HNO_3)_m$ and $HSO_4^-(HNO_3)_m$ (c.f. Heitmann and Arnold, 1983) of which the former is usually dominant. In the background atmosphere

the abundance ratio R_B of ions with HSO_4^--"cores" to ions with NO_3^--"cores" ranges between about 0.05 and 0.5. R_B is controlled mostly by the ambient GSA-concentration which converts $NO_3^-(HNO_3)_m$ to $HSO_4^-(HNO_3)_m$ via:

$$NO_3^-(HNO_3)_m + H_2SO_4 \xrightarrow{k1} HSO_4^-(HNO_3)_m + HNO_3 \quad (1)$$

The rate coefficient k depends on m. Since for ambient $NO_3^-(HNO_3)_m$ usually m = 2 an effective $k_1 = 1.1 \cdot 10^{-9}$ $cm^3 s^{-1}$ (Viggiano et al., 1982) is used for GSA-detection. Considering a steady-state of HSO_4^--formation via (1) and HSO_4^--loss via ion-ion recombination, we obtain the expression

$$(GSA)_B = \frac{R_B}{k_1 \tau_R} \quad (2)$$

τ_R=200 s : ion-ion recombination lifetime (around 10 km altitude)

Ambient ions like ambient gases become entrained into a young jet aircraft exhaust plume where they may become depleted by attachment to aerosols whose total surface area density A_T may be very much larger than in the "background" atmosphere. Ion attachment to HONU-produced clusters of the type A_xW_y leads to electrically charged clusters which should be detectable by an ion mass spectrometer with a sufficiently large mass range. Ion attachment to soot particles (SP) leads to charged SP which are too massive to be detected by mass spectrometry.

A_T is related to the measured ratio of total ion concentrations inside and outside the plume n_p/n_B by the expression:

$$\frac{n_p}{n_B} = \exp\left(-\frac{\alpha \tau_{res} A_T \bar{v}}{4}\right) \quad (3)$$

α : sticking probability assumed to be 1

$\bar{v}$: mean thermal velocity of ions ($2 \cdot 10^4$ cm/s)

τ_{res} : effective residence time of entrained ions in the plume which are detected at the plume age τ_p = 3.4s

To estimate τ_{res} we use a plume dilution model given by Schumann (1996b). In this model, the plume cross section (and thereby the dilution factor N) is proportional to t^a leading to $\tau_{res} = \tau_p /(1+a)$. A series of measurements with $\tau \geq 0.2$ s is reproduced well by this model using a = 0.8. Therefore, we find a mean τ_{res} = 1.9 s. This method gives an upper limit to A_T since it yields a mean value for the time ($\tau_p - \tau_{res}$) to τ_p and A_T decreases with plume age due to the plume dilution.

Entrained $NO_3^-(HNO_3)_m$ ions will also react with plume-GSA which is more abundant than in the "background" atmosphere. Neglecting for a moment ion-scavenging by aerosols the following scenarium emerges: After entrainment of an NO_3^--containing ion it may react with GSA (reaction (1)) and become converted to a HSO_4^--containing cluster ion. Hence the number density of ions with NO_3^--"cores" (n_1) would obey the expression

$$\frac{(NO_3^-)_P}{(NO_3^-)_B} = \exp\left(-k_1 \tau_{res} (GSA)_P\right) \quad (4)$$

if (GSA) would not vary with τ_p. In reality however (GSA) decreases with increasing τ_p and therefore expression (4) yields only a mean (GSA) for the plume ages between (τ_p–τ_{res}) and τ_p where $(NO_3^-)_p$ is measured. Correspondingly to the decrease of NO_3^--containing ions the number density of HSO_4^--containing ions should increase.

In reality however additional ion scavenging by aerosols may also occur leading to a decrease of the total ion number density and necessarily a decrease of both (NO_3^-) and (HSO_4^-) by the same factor. A

combination of ion-scanvenging by aerosols and reaction (1) should lead to a decrease of (HSO_4^-) which is less than the decrease of (NO_3^-) and the total ion concentration.

We have used an aircraft-based ion mass spectrometer (IOMAS) for the measurements of n_p, n_B, and ion composition. IOMAS which was developed, built, and operated by MPIK-Heidelberg has a mass range of 1000 amu (atomic mass units) and is pumped by a liquid-neon cooled cryopump. For details of the IOMAS-instrument see Krieger and Arnold (1994).

In general, measurement of gaseous sulfuric acid may be affected by wall losses. The present ion-based method avoids wall losses, because the important ion-molecule reactions take place in the ambient atmosphere.

Air temperature is measured with platinum resistance thermometers mounted at the nose of the Falcon fuselage (Schumann et al., 1996a). Integrated into the sampling tube of the IOMAS-instrument was a condensation nucleus counter (CNC TSI 3010) which measured CN with radii equal to or larger than 10 nm. Since soot particles emitted by the jet engines have a mean radius of about 30 nm they can be detected by the CN-counter and serve as tracers for the plume. Peak values inside the plume are lower limits caused by coincidence.

Results and discussion

Figure 1 shows a time plot of the temperature difference (ΔT) between plume air and background air and a time plot of the CN-number densities measured by the CN-counter which was mounted into the sampling-line of the IOMAS-instrument. The measurements to be reported here took place at 10.4 km altitude in the young exhaust plume of an Lufthansa Airbus (A310, engine-type: CF6-80C2A2) when the IOMAS flew onboard of the DLR-research aircraft "Falcon" 400 m - 800 m behind the Airbus (averaged plume age: 3.4 s). The ambient "background" conditions were: Temperature: 215 K and relative humidity: 22%. Hence persistent water ice contrails or cirrus clouds were not expected. As indicated by greatly increased CN-concentrations and temperature elevations of up to 1 K exhaust plume air of the Airbus was frequently sampled between 10:12:30 and 10:15:45 UTC (FSC = 850 ppmM, phase 1) and between 10:20:00 and 10:24:00 UTC (FSC = 2700 ppmM, phase 2).

Also given in figure 1 are total negative ion countrates (C) measured outside (C_B) and inside (C_p) the plume during plume penetration phase 1. Outside the plume, C_B ranges between 130 and 170 per second (average: $\overline{C}_B = 140 \pm 20$ per second) which is similar to previous measurements. Inside the plume C_p is only 80 ± 16 per second. Hence $C_P / C_B = n_P / \overline{n}_B = 0.6 \pm 0.2$. Expression 3 leads to $A_T \leq 5.4 \cdot 10^{-5}$ cm^2 per cm^3 inside the plume at $\tau_p = 3.4$ s.

Also given in figure 1 are partial count rates (C_1 and C_2) for the ion families containing NO_3^- and HSO_4^-. In the plume these decrease by the factors 0.59 ($\pm$ 0.2) and 0.47 ($\pm$ 0.32), respectively. These factors are not significantly different from the factor 0.56 ($\pm$ 0.18) by which the total contrate C decreases. This indicates that (GSA) is not large enough to change NO_3^- and HSO_4^- by reaction (1). Considering an uncertainty of 23 % for C_{1P} expression (4) yields an upper limit (GSA)$\leq 1.3 \cdot 10^8$ cm^{-3}.

From the difference ΔT between background and plume temperature we infer the dilution factor N (Schumann 1996a):

$$N = \frac{Q(1-\eta)}{c_p \cdot \Delta T} \qquad (5)$$

$Q(1-\eta)$: effective specific combustion heat with propulsion efficiency η

c_p : specific heat capacity of air

With $Q = 4.3 \cdot 10^7$ Jkg^{-1}, $\eta = 0.28$ and a measured mean ΔT of 0.3 K one obtains $N = 1 \cdot 10^5$. The expected total sulfuric acid concentration can be calculated as follows:

$$(TSA) = \frac{FSC \cdot \varepsilon \cdot 29 \cdot n_{air}}{32 \cdot N} \qquad (6)$$

ε : efficiency for sulfur-fuel conversion to GSA

n_{air} : number density of the ambient air ($0.8 \cdot 10^{19}$ cm^{-3})

ε was experimentally determined by the MPIK-Heidelberg group in a jet engine test channel (Arnold et al., 1997). For FSC = 850 ppmM and ε=0.02 we obtain (TSA) = $1.2 \cdot 10^9$ cm^{-3}. This exceeds our above experimental upper limit of $1.3 \cdot 10^8$ cm^{-3} by a factor of 9.

Hence the missing sulfuric acid must have been in the aerosol-phase. The measured upper limit for the total aerosol surface area density of $A_T \leq 5.4 \cdot 10^{-5}$ cm^2 per cm^3 compares well to other particle measurements. A SP-concentration of $\leq 1 \cdot 10^5$ cm^{-3} (Pitchford et al., 1991; Fahey et al., 1995) would imply a total SP-surface area density of $\leq 1 \cdot 10^{-5}$ cm^2 per cm^3. Measurements of ice particles made on the same flight (see Busen et al., 1996) indicate a total surface area density for these particles of $1.5 \cdot 10^{-5}$ cm^2 per cm^3. Hence soot- and ice contrail-particles can account for the GSA- and ion-depletion indicated by our present measurements; however HONU can not be ruled out.

Attachment of entrained negative ions (mostly $NO_3^-(HNO_3)_m$) to A_xW_y-clusters should lead to measurable negatively charged clusters. Hence ion attachment should produce charged clusters of the type $[NO_3(HNO_3)_mA_xW_y]^-$. For m=2 and x=2 one expects a series of cluster ion species $[NO_3(HNO_3)_mA_2W_y]^-$ with different y. Possibly even different m and x may occur due to desorption of H_2SO_4 and HNO_3 upon ion attachment. For m=2, x=2, and y=0 the mass number of the charged cluster would be 384. This is within the mass range of IOMAS (1000 amu). Probably entrained ions upon attachment to A_xW_y become distributed among numerous A_xW_y species with different mass numbers and small concentrations and thereby lead to numerous but only small mass peaks. Hence detection of such charged clusters by IOMAS may be difficult since the small mass peaks may fall below the ion detection limit. A more sensitive detection of numerous clusters with low partial number densities is to run IOMAS in a high-pass (integral) mode.

Summary and conclusions

The present IOMAS-measurements in the young plume of an Airbus may be summarized as follows:

- The GSA-number density was less than $1.3 \cdot 10^8$ cm^{-3} which is 9 times less than expected for total sulfuric acid. This indicates that the missing sulfuric acid must have been in the condensed (aerosol-) phase.
- The total aerosol surface area density A_T is less than $5.4 \cdot 10^{-5}$ cm^2 per cm^3 which is consistent with that of soot and ice.

Future mass spectrometric plume measurements should include TSA and large ions formed by the attachment of entrained $NO_3^-(HNO_3)_m$ ions to A_xW_y-clusters. It has been proposed (Arnold et al., 1997) to measure TSA by IMR-MS with a vaporizer and large ions by an IOMAS-instrument operated in a high-pass mode and with a large mass range of say 2000 amu. Future IOMAS-measurements should also take place in the absence of a water contrail preferably above the tropopause.

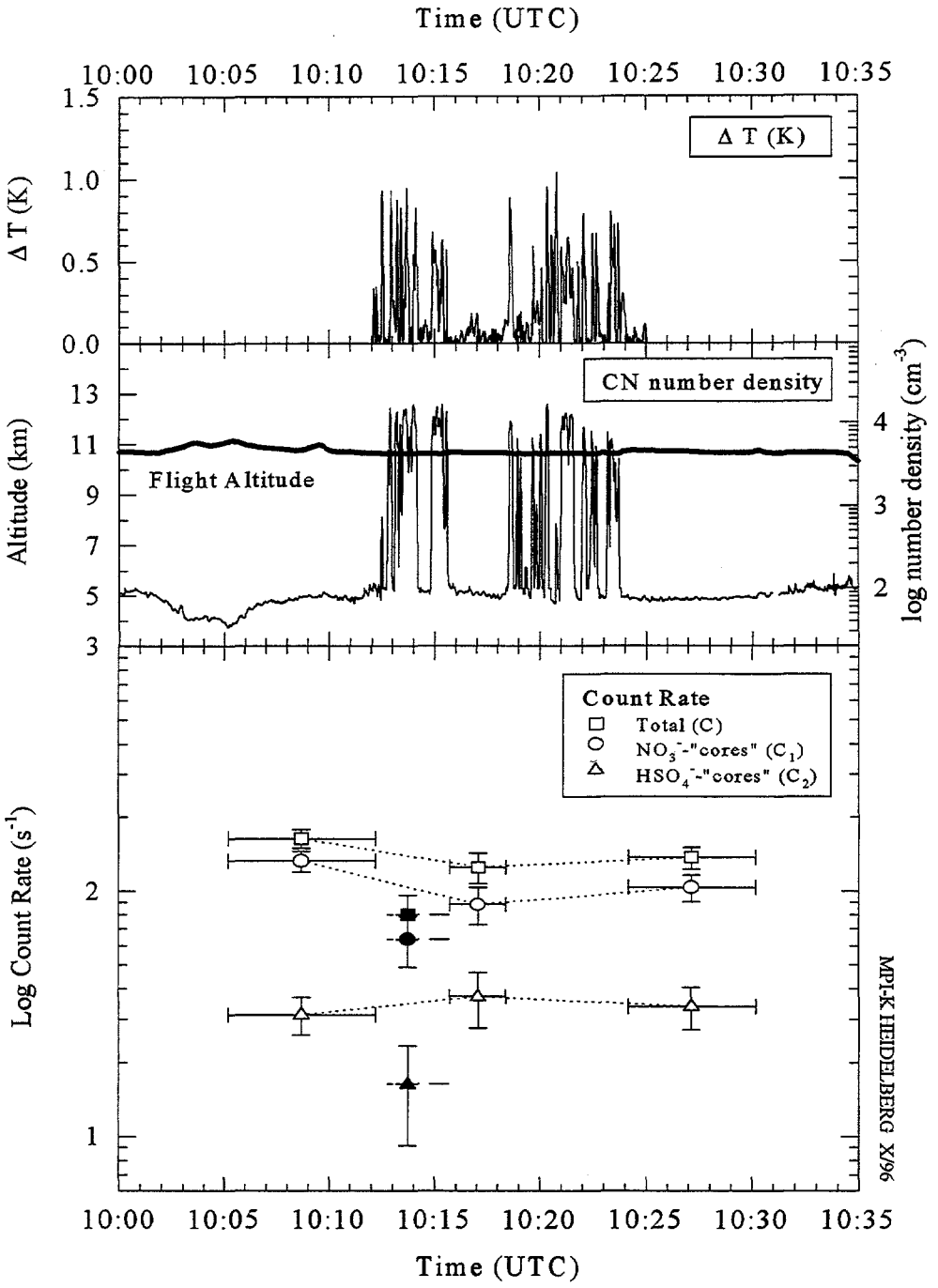

Figure 1: Time plots of the difference ΔT between background and plume temperature, and CN-number densities measured by the CN-counter which was integrated into the IOMAS instrument. Also given are total countrates C and countrates of ions with NO_3^-- and HSO_4^--cores measured by IOMAS outside (open symbols) and inside the plume (filled symbols).

Acknowledgments. We greatly appreciate support by DLR-Abteilung Flugbetrieb, Deutsche Lufthansa, and the technical staff of MPIK-Heidelberg and DLR. Parts of this project were funded by BMBF and DFG.

References

Arnold, F., Scheid, J., Stilp, T., Schlager, H., and Reinhardt, M.E., Measurements of jet aircraft emissions at cruise altitude I: The odd nitrogen gases NO, NO2, HNO2, and HNO3, Geophys.Res.Lett. 19, 2421-2424, 1992

Arnold, F., Stilp, T., and Wohlfrom, K.-H., Sulfuric acid cluster-ion detection in jet engine exhaust: implications for the formation of gas phase sulfuric acid, contrails and clouds, to be submitted to *J.Geophys.Res.*, 1997

Busen, R., Hagen, D., Kuhn, M., Petzold, A., Schröder, F., Schumann, U., Ström, J., and Whitefield, P., Experiments on contrail formation from fuels with different sulfur content. *Proc. Intern. Coll. "Impact of Aircraft Emissions upon the Atmosphere,"* Paris, 15-18 Oct. 1996, pp. 6, 1996.

Fahey, D.W., et al., Emission measurements of the Concorde supersonic aircraft in the lower stratosphere, *Science* 270, 70 - 74, 1995

Frenzel, A., and Arnold, F., Sulfuric acid cluster ion formation by jet engines: implications for sulfuric acid formation; in *Schumann and Wurzel* 1994, 106-112, 1994

Heitmann, H., and Arnold, F., Composition measurements of tropospheric ions, *Nature* 306, 747-748, 1983

Kärcher, B., Peter, Th., and Ottmann, R., Contrail formation: homogeneous nucleation of H_2SO_4/H_2O droplets; *Geophys.Res.Lett.* 22 (12), 1501-1504, 1995

Kärcher, B., Aircraft-generated aerosols and visible contrails, *Geophys.Res.Lett.*, 23, 1933-1936, 1996

Krieger, A., and F. Arnold, First composition measurements of stratospheric negative ions and inferred gaseous sulfuric acid in the winter Arctic vortex: implications for aerosols and hydroxyl radical formation; *Geophys.Res.Lett.* 21 (13), 1259-1262, 1994

Reiner, Th., and F. Arnold, Laboratory flow reactor measurements of the reaction $SO_3 + H_2O + M \rightarrow H_2SO_4 + M$, *Geophys.Res.Lett.* 20, 2659-2662, 1993

Pitchford, M., Size and critical supersaturation for condensation of jet aircraft exhaust particles, *J. Geophys. Res.* 96, No. D11, 20787-20793, 1991

Schumann, U., and Wurzel, D. (eds.), Impact of aircraft and spacecraft upon the atmosphere. *Proc.Intern.Coll*, Cologne April 18-20 1994, DLR Mitteilung 94-06, 1994

Schumann, U., J. Ström, R. Busen, R. Baumann, K. Gierens, M. Krautstrunk, F. P. Schröder, and J. Stingl, In situ observations of particles in jet aircraft exhausts and contrails for different sulfur-containing fuels. *J. Geophys. Res.*, 101, 6853-6869, 1996a.

Schumann, U. et al., Pollution from aircraft emissions in the North Atlantic flight corridor / Overview on the results of the POLINAT project. Proc. Intern. Coll. "Impact of Aircraft Emissions upon the Atmosphere," Paris, 15-18 Oct. 1996, pp. 6, 1996b.

Viggiano, A., et al., Stratospheric negative-ion reaction rates with H_2SO_4, *J.Geophys.Res.* 87 (C9), 7340-7342, 1982

Zhao, J., Toon, O.B., and Turco, R.P., Origin of condensation nuclei in the springtime polar stratosphere, *J.Geophys.Res.*, 100, 5215-5227, 1995

Tropospheric mixing ratios of NO and NOy obtained during TROPOZ II in the latitude region 67°N-56°S

Franz Rohrer, Dirk Brüning and Dieter H. Ehhalt

Institut für Atmosphärische Chemie, Forschungszentrum Jülich, Jülich, Germany

Abstract: Tropospheric mixing ratios of NO and NOy were measured along the flight track of the TROPOZ II aircraft campaign (~~Figure in January 1991~~. These measurements cover regions along the east coast of North America, the Pacific and Atlantic coast of South America and the Atlantic coast of North Africa and Europe. The meteorological conditions are close to the climatological mean: westerly winds at high and mid latitudes, variable and weak winds at low latitudes.

1 RESULTS

The NOy data obtained during TROPOZ II are supplementary to the NO measurements performed during the STRATOZ III [1] and TROPOZ II campaigns along the same flight track at two different seasons. Despite the longer atmospheric lifetime of NOy, all three datasets show the large influence of continental nitrogen oxide sources, especially for the upper troposphere over the continents during summertime. Owing to the general wind pattern, the nitrogen oxide data obtained during TROPOZ II show large scale outflow of NO/NOy enriched air along the east coasts of the North and South American continents and inflow of clean maritime air over the west coasts of South America, North Africa and Europe. The NO concentrations in the free tropospheric air flowing out from the (winter) North American continent lie between 100 and 300 pptv with a weakly C shaped vertical profile. The air coming off the (summer) South American continent has a factor of 3 lower NO mixing ratios, between 40 to 100 pptv, but a more pronounced C shaped vertical profile with NO mixing ratios of up to 200 pptv in the upper troposphere of the tropics. The NOy distributions show a similar pattern.

2 MODEL CALCULATIONS

The NO distributions measured during the TROPOZ II and STRATOZ III [1] campaigns can be compared to the results of a global chemical tracer model [2]. The model includes a simple linear NOx/HNO_3 chemistry with prescribed OH and O_3 fields. The NO distributions are calculated with emissions from fossil fuel combustion, biomass burning, soil microbial activity, lightning, aircraft exhausts and stratospheric influx. For the STRATOZ III campaign, the model reproduces most of the salient features of the observed NO distribution, especially the high NO mixing ratios in the upper troposphere at northern mid-latitudes. This good overall agreement between observation and model calculation is also found for the TROPOZ II campaign, but only in the southern hemisphere. The high NO mixing ratios observed west of the North American continent are not reproduced by the model calculations. The reason for this discrepancy is yet unknown.

References

[1] J. W. Drummond, D. H. Ehhalt, and A. Volz. Measurements of nitric oxide between 0-12 km altitude and 67°N to 60°S latitude obtained during STRATOZ III. *J. Geophys. Res.*, 93:15,831–15,849, 1988.

[2] A. B. Kraus, F. Rohrer, E. S. Grobler, and D. H. Ehhalt. The global tropospheric distribution of NOx estimated by a three-dimensional chemical tracer model. *J. Geophys. Res.*, 101:18587–18604, 1996.

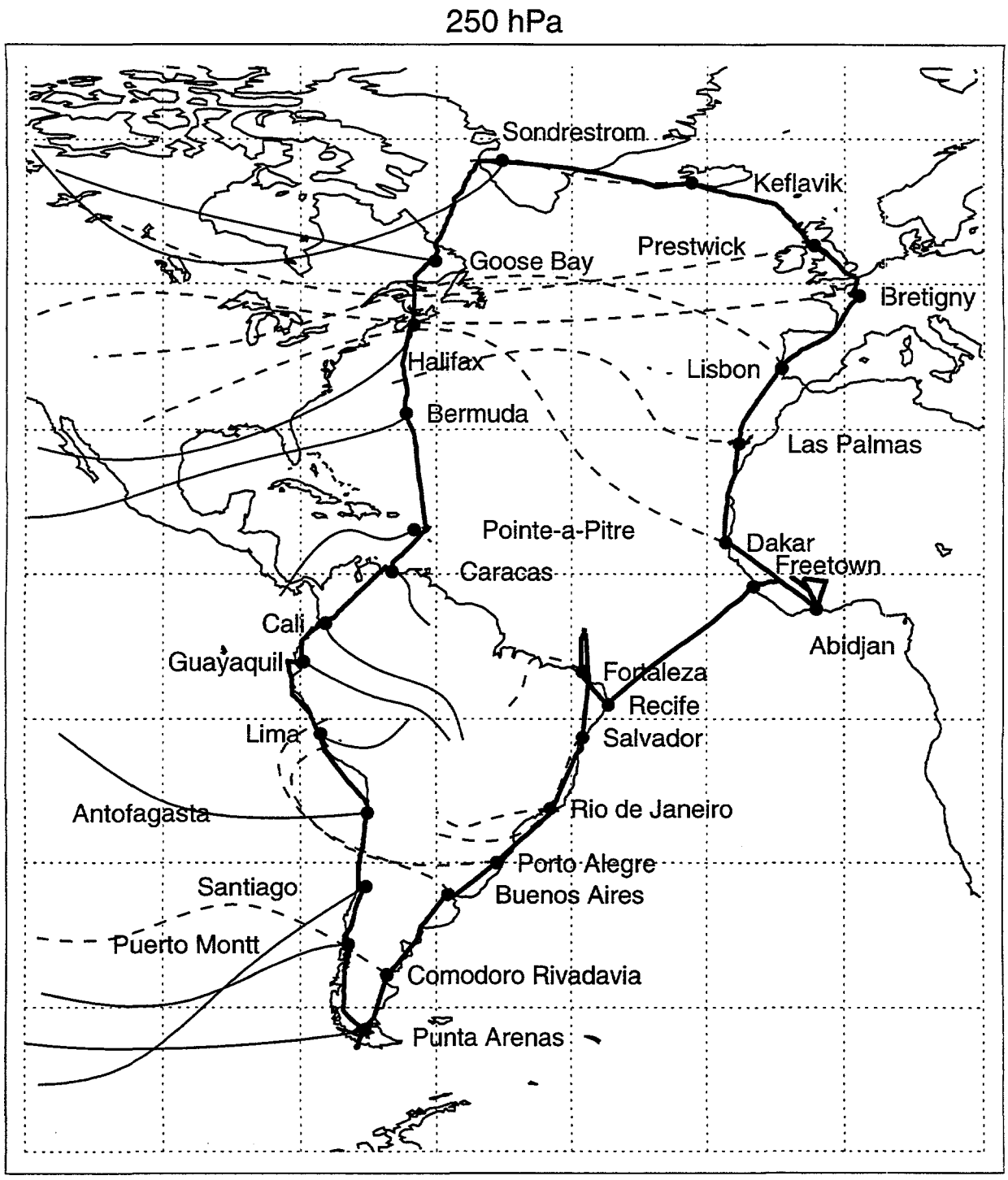

Figure 1: Flight track of the TROPOZ II expedition, January 1991. The thin lines indicate three days backtrajectories (ECMWF).

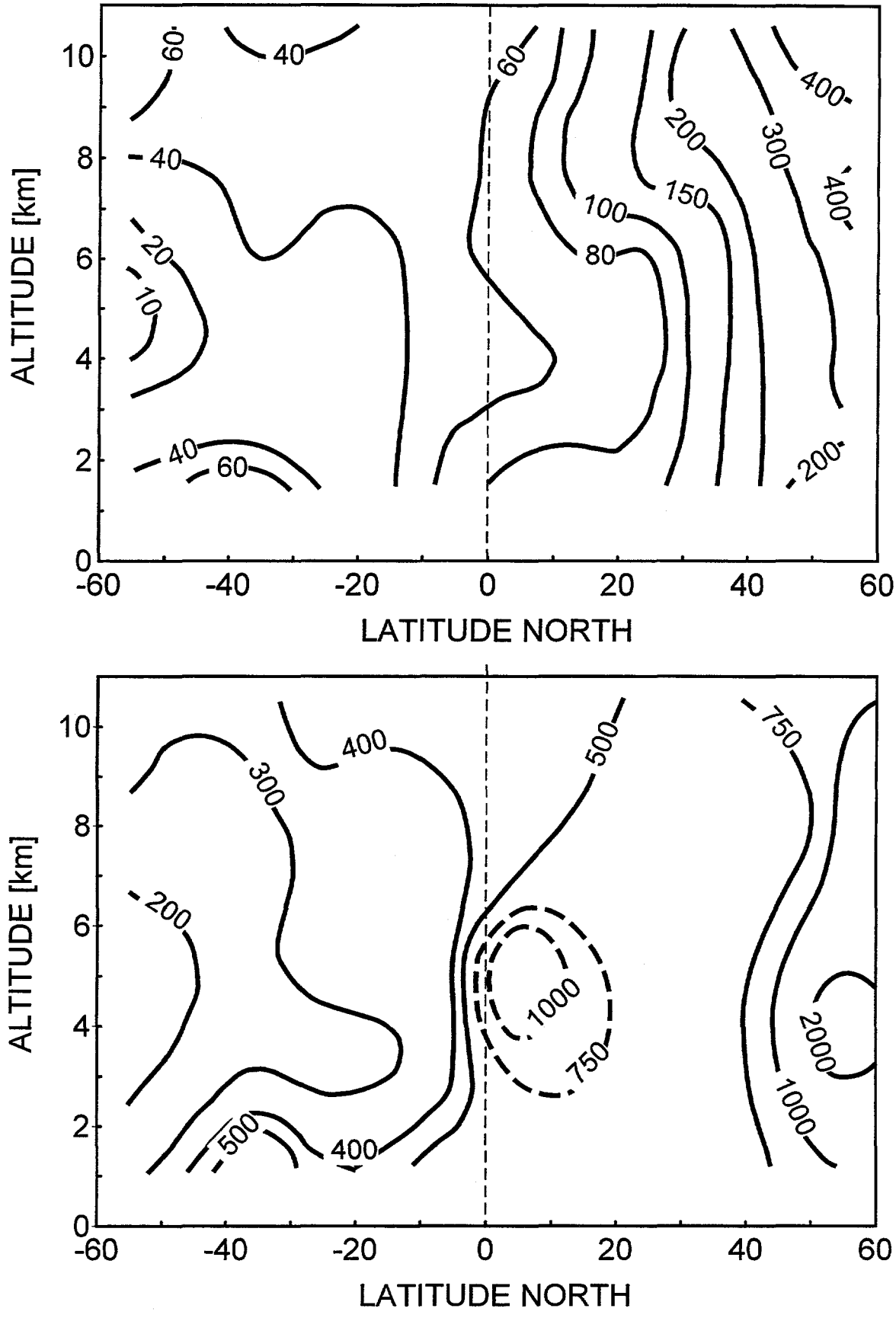

Figure 2: Averaged latitude-altitude cross sections of NO (upper panel) and NOy (lower panel) during TROPOZ II, southbound flights

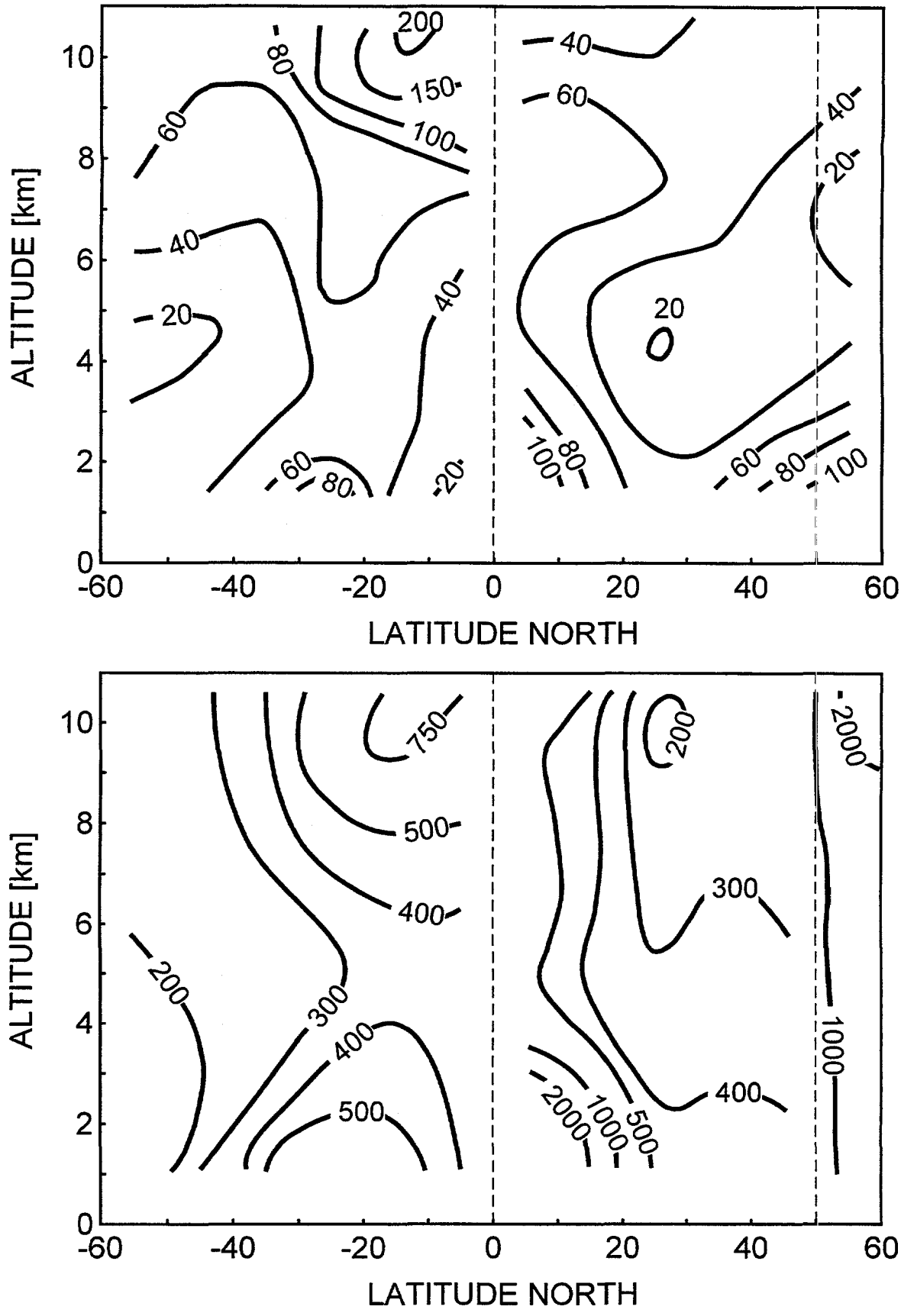

Figure 3: Averaged latitude-altitude cross sections of NO (upper panel) and NOy (lower panel) during TROPOZ II, northbound flights

Instrumentation for Tropospheric Aerosol Characterization

Z. Shi, S. E. Young, C. H. Becker, and M. J. Coggiola
SRI International, Menlo Park, CA 94025
H. Wollnik, University of Giessen, Giessen, Germany

A new instrument has been developed that determines the abundance, size distribution, and chemical composition of tropospheric and lower stratospheric aerosols with diameters down to 0.2 μm. In addition to aerosol characterization, the instrument also monitors the chemical composition of the ambient gas. More than 25,000 aerosol particle mass spectra were recorded during the NASA-sponsored Subsonic Aircraft: Contrail and Cloud Effects Special Study (SUCCESS) field program using NASA's DC-8 research aircraft.

1. INTRODUCTION

A new instrument has been developed that determines the abundance, size distribution, and chemical composition of tropospheric and lower stratospheric aerosols with diameters down to 0.2 μm. In addition to aerosol characterization, the instrument also monitors the chemical composition of the ambient gas. The instrument is based a time-of-flight mass spectrometer (TOFMS), coupled with an aerosol sampling system and a laser scattering particle detector. A direct sampling method and differential vacuum pumping scheme is used to introduce the aerosols into the mass spectrometer. Volatilization of aerosols on a heated surface within the ion source volume followed by complete and quantitative mass spectrometric analysis of the resulting vapors using electron impact ionization yields the desired chemical composition information.

2. INSTRUMENT DESCRIPTION

Figure 1 shows our instrument as it was configured during the Spring 1996 NASA SUCCESS mission. Our design for the particulate mass spectrometer consists of (1) a particle beam generated by a three-stage, differential pumping system that brings the directly sampled particles into a vacuum environment; (2) a small diode-laser-based OPC that provides a timing trigger; (3) a heated

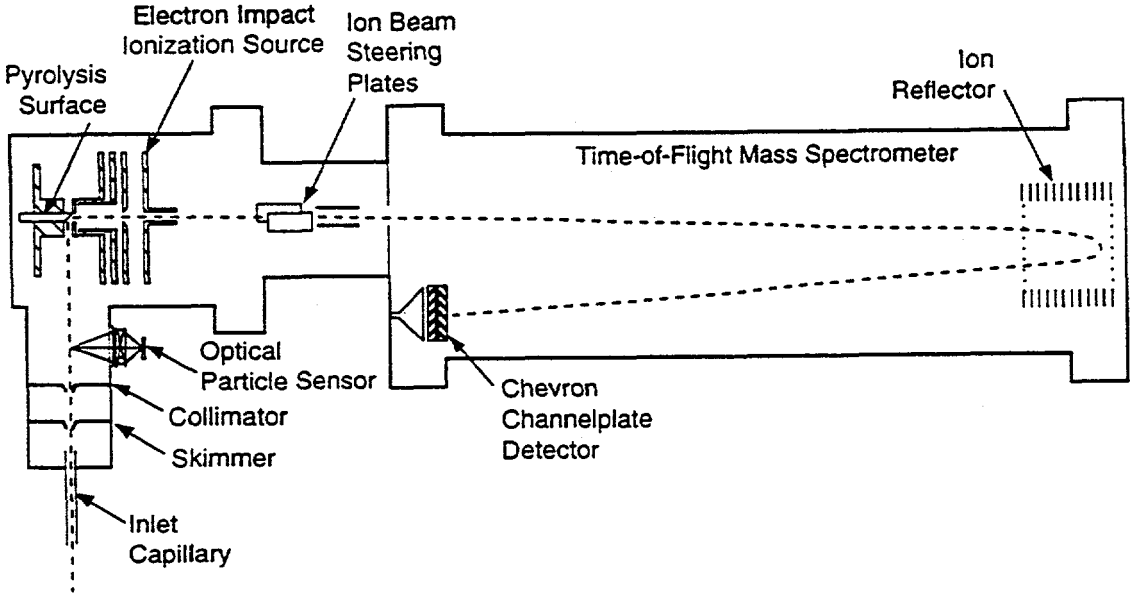

Fig. 1 - Schematic of the SRI real-time aerosol particle characterization system.

surface for rapid vaporization of the particle; (4) a reflectron, TOF, mass spectrometer using pulsed EI to detect all species; and (5) a data acquisition and experiment control computer.

2.1 AMBIENT AEROSOL SAMPLER

For the SUCCESS mission, we used a simple, forward-facing external sampling probe that extended 30 cm from the surface of the DC-8. A conical diffuser probe tip with a 0.635 cm sample orifice and a 20.2° half-angle was added to the end of the probe, based on a design provided by the Desert Research Institute. Aerosols sampled through this probe were transported through approximately 1 m of 0.635-cm-id, conductive silicone tubing (TSI, St. Paul, MN) to the instrument inlet. A portion of the 4 l/min air stream was drawn inside the instrument via the particle beam generator for analysis by mass spectrometry. The remaining, unsampled gas stream was exhausted externally through a separate port on the probe flange.

2.2 PARTICLE BEAM GENERATOR

The particle beam generator (PBG) serves the dual purpose of acquiring a representative sample of the air passing through the instrument and causing the particles in this sample to take the form of a beam – a beam that ultimately strikes the heated surface within the ion source of the mass spectrometer. Our PBG design was adapted from the system developed and used by D. Murphy (NOAA, Boulder, CO). Murphy's design uses a glass-lined, stainless steel, capillary to both restrict the volumetric gas flow entering the vacuum system and to aerodynamically focus the particles near the centerline of the flow.

Under the typical operating conditions encountered during SUCCESS, a 25-cm length of 750-μm-diameter capillary produced a pressure drop of approximately a factor of 200 from an ambient pressure of 150 Torr to a pressure in the first differential region of 0.7 Torr. The first differential pumping region was defined by the exit of the capillary and a Teflon disk with a 0.1-cm-diameter sampling orifice located 1 cm from the capillary. An 8 l/s mechanical pump was used to remove the excess gas flow from this region. Aerosols and background gas entering the second differential pumping region again traversed a distance of 1 cm before encountering a second Teflon disk with a 0.1-cm diameter orifice. Pumping in this region was provided by a 3.3 l/s mechanical pump, yielding a typical operating pressure of 5 mTorr. Upon exiting the second differential pumping region, the remaining aerosol particles passed through the observation region of a Vaculaz-2 OPC (Particle Measuring Systems, Boulder, CO). This OPC is specifically designed to operate at reduced pressures, and all of the laser-diode and array detection optics are located external to a vacuum housing equipped with sapphire windows.

2.3 VOLATILIZATION

In its current configuration, our instrument uses an indirectly heated, stainless steel surface inclined 45° with respect to the incident aerosol beam. Spot welded onto the front of the target surface are multiple layers of nickel mesh (Buckbee-Meers, MN). The mesh provides numerous wells, wherein aerosols are trapped, forcing them to undergo multiple collisions with the heated surfaces. This technique significantly enhances the probability that an aerosol particle accommodates on the surface long enough to be heated to the nominal target temperature of 600° C, and hence long enough to volatilize. With this design, an upper temperature limit of 600° C was found experimentally, restricted by the operating limit of the 0.3-cm-diameter cartridge heater.

A portion of the vapors produced during the volatilization enter directly into the electron impact ion source of the instrument. The ion optical axis of the source is also at a 45° angle to the volatilization target surface, and hence perpendicular to the aerosol beam. The electrostatic grid that forms the back side of the ion source is located immediately in front of the volatilization target surface, thereby maximizing the transfer of vapors into the source region. The ionization and subsequent mass analysis of these vapors in our apparatus is described briefly below.

2.4 MASS SPECTROMETRY

The mass spectrometric requirements of our instrument are modest: an upper mass range of 500 amu, with unit mass resolution or better. Typical EI-TOF mass analyzers can meet these requirements using a simple, linear flight path combined with a short duration, pulsed, ion source. The low signal levels that result from the use of very narrow ion injection pulses are compensated for by signal averaging using multiple scans. With our instrument, this mode of operation is not possible because the sample vapor is present for a relatively short period of time. Achieving high mass resolution with a TOF instrument is straightforward when pulsed laser ionization is used.[1-3] However, high resolution is more complicated to achieve with EI due to the significantly wider spatial, temporal, and energy spread of the nascent ions. Without some form of compensation, EI-TOF would not have been suitable for our instrument. The most common approach to overcome this difficulty is to use an ion mirror, or reflectron-type TOF.[4,5] The properties of this device are well known, and a number of computer codes have been developed to assist with their design.[6] Resolving powers ($m/\Delta m$) of more than 1000 can be readily obtained using a reflectron with a pulsed EI source.

A significant improvement in resolution and signal level can also be obtained through the careful design of the ion source itself. Wollnik and co-workers (University of Giesen, Germany) have developed a storage ion source for TOF spectrometers. This source uses the space charge well created by a magnetically confined, DC electron beam to form and trap positive ions. A combined extraction and ion bunching scheme is then used to produce a narrow ion burst of ~10 ns duration. As a result of the ion bunching, however, the ion burst has a wide energy spread (typically 100 eV). Again, the use of a reflecting ion mirror to provide sufficient energy compensation to achieve high mass resolution (>8000 at 28 amu) has been demonstrated.[7]

This source is ideally suited to our system because it can generate and store ions over a time period (~ 1 ms) commensurate with the duration of the particle volatilization, thus maximizing the fraction of neutral molecules that are ionized. With the generous assistance of the Giesen group, we were able to duplicate their ion source design with appropriate modifications to accommodate our volatilization target surface and aerosol inlet. This source functioned reliably during the entire SUCCESS mission, requiring only minor, periodic maintenance.

2.5 DATA ACQUISITION SYSTEM

The most critical requirement of the data acquisition system is the speed at which the signal can be digitized. Given the fixed flight path of 1.6 m, the nominal ion energy of 1.7 keV, and the desired mass range of 500 amu, an analog-to-digital (ADC) converted speed of 500 MHz was required. This capability was provided by a DA500A ADC manufactured by Signatec, Inc. (Corona, CA). This unit operates in an IBM-compatible computer, and provides 8-bit digitization with 256 kB of local data storage. Each mass scan required 32 kB of data storage. The instrument control software was responsible for transferring the raw spectral data from the DA500A local storage, and storing the results in a disk file along with selected instrument and flight parameters. The former included the operating pressures in the aerosol inlet, and the vaporization temperature, while the latter included location, altitude, and true ground speed of the DC-8.

3. SUCCESS MISSION RESULTS

Of the more than 25,000 aerosol mass spectra obtained during the 19 SUCCESS mission flights, approximately 5,700 have been more closely examined. These spectra were chosen based on two criteria: (1) a normally functioning instrument with good sensitivity and (2) an integrated ion intensity that was significantly above the average. The former criterion eliminated data obtained when the instrument was not producing quantifiable data due to an operational problem (such as a dirty ion source or a reduced gain ion detector). The latter criterion allowed us to rapidly sort through the raw data and identify those spectra that likely contained chemically interesting results.

Each of the examined spectra were classified as to their likely chemical composition based on the observed ions, their distribution, and their relative intensities. Of the 5,700 spectra included in the evaluation, 100 were found to have significant ion intensities associated with materials other than water. All of the remaining spectra showed only evidence of water, with no significant other chemical species apparent above the background. The distribution of chemical compositions that were assigned to these 100 aerosol particles is: sulfate 55%, carbonate 19%, nitrate 8%, sodium 5%, sulfuric acid 5%, and unassigned 8%. In many cases, the counter-ion could also be inferred from the mass spectra. For example, the majority of sulfate aerosols were ammonium sulfate, while the carbonate aerosols appeared to be both ammonium(bi) carbonate and calcium carbonate. All of these assignments must be regarded as tentative until we are able to generate, sample, and analyze authentic samples of these materials in the laboratory to confirm their mass spectral signatures.

Figure 2 shows an example of an aerosol particle most probably containing calcium nitrate. Characteristic peaks are seen at nominal m/z 14 (N+), 16 (O+), 17 (OH+), 18 (H_2O+), 28 (N_2+), 30 (NO+), 32 (O_2+), 40 (Ca+), 46 (NO_2+), and 62 (NO_3+). Despite having a mass resolution (M/ΔM) in excess of 1000, the ion peak at m/z 40 cannot be assigned unambiguously to Ca+ alone (atomic mass 39.9626) because of the isobaric argon ion (atomic mass 39.948). Separation of these ions would require a mass resolution in excess of 2,500. However, because this spectrum was obtained in a single scan, the m/z 40 intensity due to background argon would be very much lower than observed here.

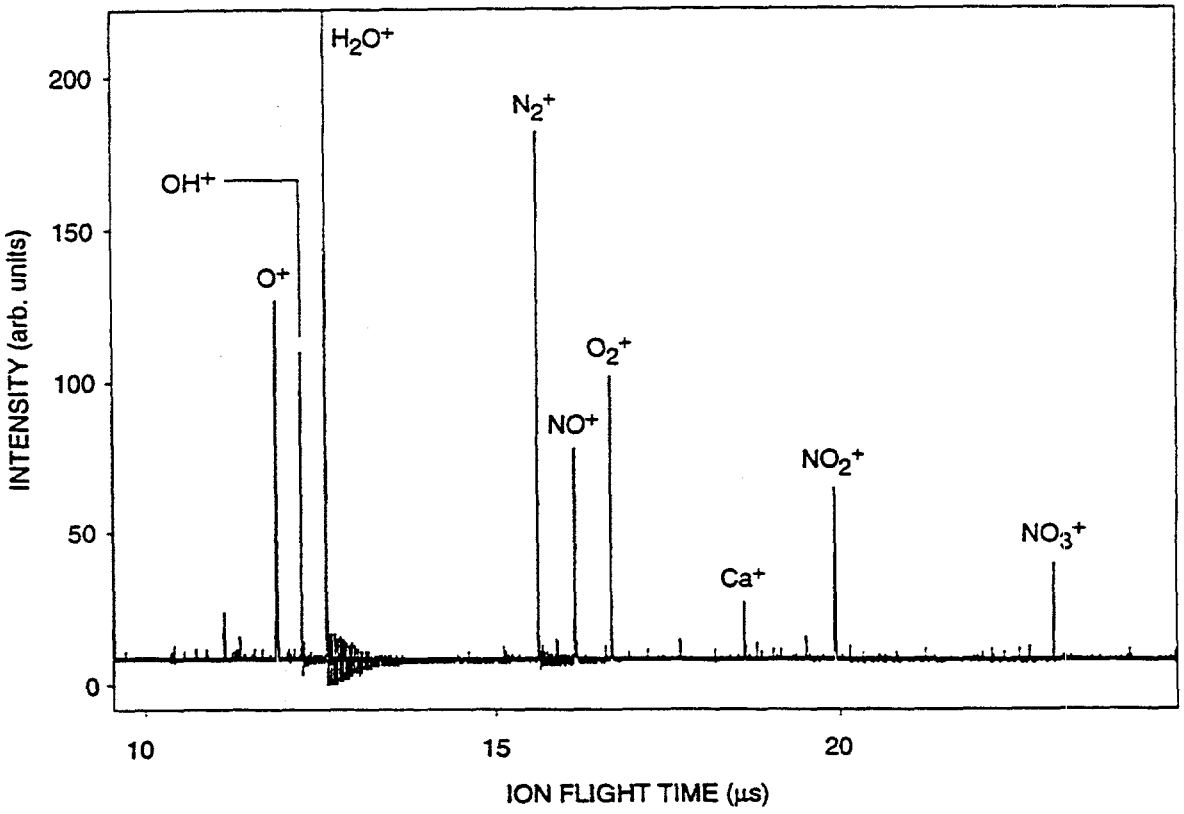

Fig. 2 - Time-of-flight mass spectrum of a single calcium nitrate aerosol particle recorded during SUCCESS flight 960212, May 2, 1996.

Figure 3 shows an example of what appears to be an aerosol particle containing a significant amount of sulfuric acid. This particle was sampled in the wake of the NASA 757 at a separation distance of 5-10 km, corresponding to a plume age of 1 min. In fact, all of the aerosol particles tentatively assigned as sulfuric acid were sampled under similar conditions, lending support to the theory that they were formed in the engine exhaust. The spectra in *Figure 3* shows characteristic

peaks at nominal m/z 16 (O+), 17 (OH+), 18 (H_2O+), 28 (N_2+), 32 (O_2+, S+), 48 (SO+), 64 (SO_2+), 65 (HSO_2+), 80 (SO_3+), 81 (HSO_3+), 96 (SO_4+), 97 (HSO_4+), and 98 (H_2SO_4+).

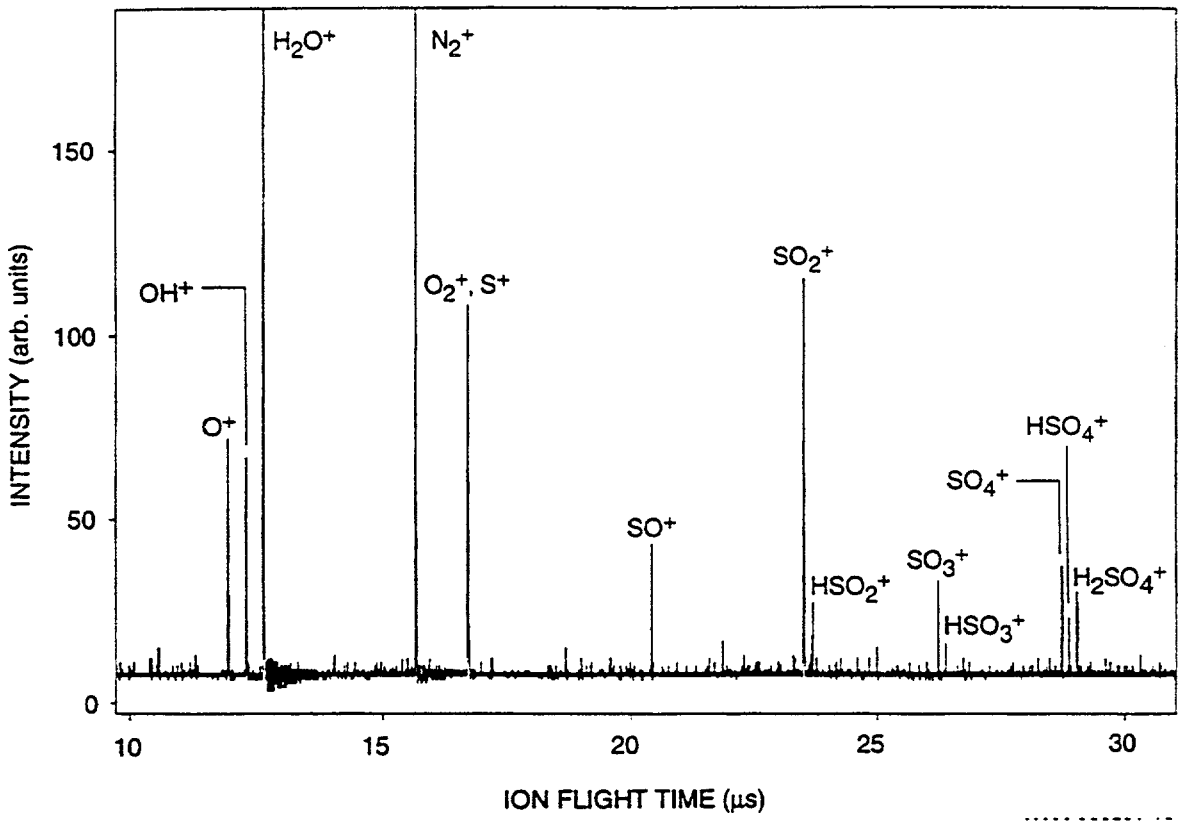

Fig. 3 - Time-of-flight mass spectrum of a single aerosol particle containing sulfuric acid recorded during SUCCESS flight 960213, May 3, 1996.

4. CONCLUSION

A new instrument has been successfully used to chemically characterize tropospheric aerosol particles in real-time. The results of its first deployment as part of the SUCCESS mission demonstrate the usefulness of this approach for atmospheric research in general, and the study of aircraft emissions and their impact on the atmosphere, in particular.

5. REFERENCES

1. H. Wollnik, *Nuc. Instrum. and Methods* **A298**, 156 (1990).
2. G. R. Kinsel, J. M. Grundwuermer, and J. Grotemeyer, *J. Am. Soc. Mass Spectrom.* **4**, 2 (1993).
3. R. Grix, R. Kutscher, G. Li, U. Grüner, and H. Wollnik, *Rapid Comm. Mass Spectrom.* **2**, 83 (1988).
4. R. T. Short and P. J. Todd, *J. Am. Soc. Mass Spectrom.* **5**, 779 (1994).
5. R. Kutscher, R. Grix, G. Li, and H. Wollnik, *Int. J. Mass Spectrom. Ion Proc.* **103**, 117 (1991).
6. T. Bergmann, T. P. Martin, and H. Schaber, *Rev. Sci. Instrum.* **61**, 2592 (1990).
7. R. Grix, U. Grüner, G. Li, H. Stroh, and H. Wollnik, *Int. J. Mass Spectrom. Ion Proc.* **93**, 323 (1989).

A new project, SPIRALE : Balloon-borne *in situ* multi-component measurement using infrared diode lasers

Guy Moreau (PI), M. Pirre, C. Robert (PM), LPCE/CNRS
3A Avenue de la Recherche Scientifique, 45071 Orléans Cedex 02
B. Rosier, Y. Louvet, R. Ramaroson, ONERA, FRANCE
Fort de Palaiseau, 91120 Palaiseau, FRANCE
C. Camy-Peyret, LPMA
Université P & M Curie 75252 Paris Cedex 05, FRANCE
Y. Macleod, SA
Université P & M Curie 75252 Paris Cedex 05, FRANCE
D. Courtois GSMA
Faculté des Sciences 51062 Reims Cedex, FRANCE

for stratospheric studies — (are presented)

~~We present~~ the scientific goals and the description of a new experiment SPIRALE, which is a balloon-borne instrument, able to measure *in situ* several air components (up to 10). ~~We take advantage of the existence of~~ Infrared diode laser spectroscopy, ~~which can~~ monitors simultaneously atmospheric trace gases at high rate, ~~given~~ its specificity, sensitivity, and wide range of compounds to which it can be applied.

is described. — is applied for

1 - Introduction : The existing instruments for stratospheric studies are either balloon-borne or air-borne. Above 20 km, the balloon is the only carrier used for *in situ* measurements. Up to now for given objectives in a campaign, several *in situ* instruments are put together, each measuring generally one or two parameters. Multi-instrumented flights frequently took place in the past. They have given quite good data and permitted to understand the chemistry of several local systems such as transitions at twilight, polar ozone holes, etc.. Now, the question arises whether a single instrument can fulfil the goals of several instruments, i.e., able to perform *in situ* measurements of several molecules at high rate in the stratosphere, especially in the lower stratosphere.

The need of such instrument can be justified through an insight of several current scientific objectives :

1 - To derive vertical profiles of fast and reactive evolving species, and to check them with models, seasonal and long term evolution of stratospheric key species (O3, NOx, HCl, etc.) being reliably monitored by ground-based and satellite instruments.

2 - To study a given chemical family in measuring active, sink and source species to provide local mass balance. Furthermore, these experimental concentrations will serve as inputs in models, which in turn give the concentrations of non measured species.

3 - From aerosol (natural or anthropogenic) measurement, and species related to aerosols like chlorine and bromine compounds, to understand their influence on ozone chemistry in the lower stratosphere.

4 - To study the impact of aircraft on ozone in the lower stratosphere (16-25 km), in dense airline zones, at flying altitudes, by monitoring locally species rejected by fuel combustion, like NOx, methane, and hydrocarbons or species produced from their degradation. Particularly, concurrent determination of ozone, chlorine, and nitrogen reservoir species (HCl, $ClONO_2$, N_2O_5, HNO_3, HO_2NO_2, ..), will help to assess the influence of NO_x exhaust. Detailed profiles are then required to take into account the subsequent chemistry.

5 - In the lower stratosphere, the dynamical processes of the troposphere-stratosphere exchanges, to measure simultaneously ozone and its precursors (CH_4, CO, H_2O, N_2O), with additional anemometric measurements.

Among the variety of multi-constituent measurement techniques, remote or *in situ* sensing has been extensively used : UV/visible [1], infrared spectrometers [2], FT-infrared spectrometers [3], mass-spectrometers. A balloon-borne *in situ* tunable diode laser absorption spectrometer, named BLISS, has already been developed at JPL [4]. BLISS has provided numerous results on stratospheric species from balloon measurements as well as airplane measurements. However, the vertical resolution of BLISS, greater than 200 m, does not match the requirement of detailed vertical profiles.

The SPIRALE project, will exploit the balloon-borne instrument SPIRALE, whose assigned scientific goals are several of those listed above in stratospheric studies. The measurement of species is made through absorption technique, with infrared diode lasers as light sources. This technique has been chosen because of its great potentialities. It is the only technique able to measure simultaneously *in situ* several trace species. It justifies the SPIRALE acronym : « **SP**ectrométrie **I**nfra-**R**ouge pour l'étude de l'**A**tmosphère par diodes **L**aser **E**mbarquées ». The SPIRALE project has been presented by several French laboratories (list above). It benefits of technical skills in project management for several of them. It includes also, besides scientific aeronomic objectives, complementary studies in molecular spectroscopy which are needed for several species, so that to reduce uncertainties. Presently, the instrument assembly is close to its achievement (1st Phase). LPCE manages the project, while ONERA has diode laser emission and detection in charge. LPMA and GSMA contribute to the spectroscopy work. The first flight of the SPIRALE instrument is planned for autumn 1997, with 4 species measured from 3 absorbed laser beams. The instrument will be completed with 6 lasers installed on board, enabling the measurement of 10 species at most (2nd Phase).

2 - Instrument set-up : *Figure 1* presents a simplified overview of the SPIRALE optics. Three nitrogen dewars contain up to 6 diode lasers and 12 infrared detectors (InSb or HgCdTe). Only one light beam is drawn in figure 1. The combination of mirrors collimate the beam from the laser into the entrance hole in the front mirror of the vertical Herriott cell where absorption takes place. The second mirror, or back mirror of the Herriott cell is located lower at a distance d not greater than 4 m. Laser beam is reflected N times on the two mirrors of the Herriott cell after a path length $L = N \cdot d$. Then, it passes through the same entrance hole, and is collimated on detector. Diode lasers generally have several modes, therefore a monochromator is inserted before entering Herriott cell, whose dispersive element is a grating, the input and output conjugated points being respectively the diode laser and a calibrated hole. After mode filtering, but before Herriott cell, a beam splitter drives away a part the beam toward an absorption cell containing molecules of the selected specie. This beam is used as an optical frequency reference, and as a concentration reference when it is available. Therefore there are two detectors for the measurement of one specie.

The originality of SPIRALE instrument lies in the open absorption cell, enabling measurements of unstable trace species, that is normally difficult with instruments where air is pumped. The back mirror is moved to its work position only above tropopause, where the occurrence of ice or water deposition is impossible. The Herriott cell is common to all beams, with the same path lengths, but reflection spots are different. Optical adjustments are mediumly critical. The back mirror of the Herriott cell is less critical than the entrance mirror, that makes possible its use. The maximum absorption length can be set up to 350 m.

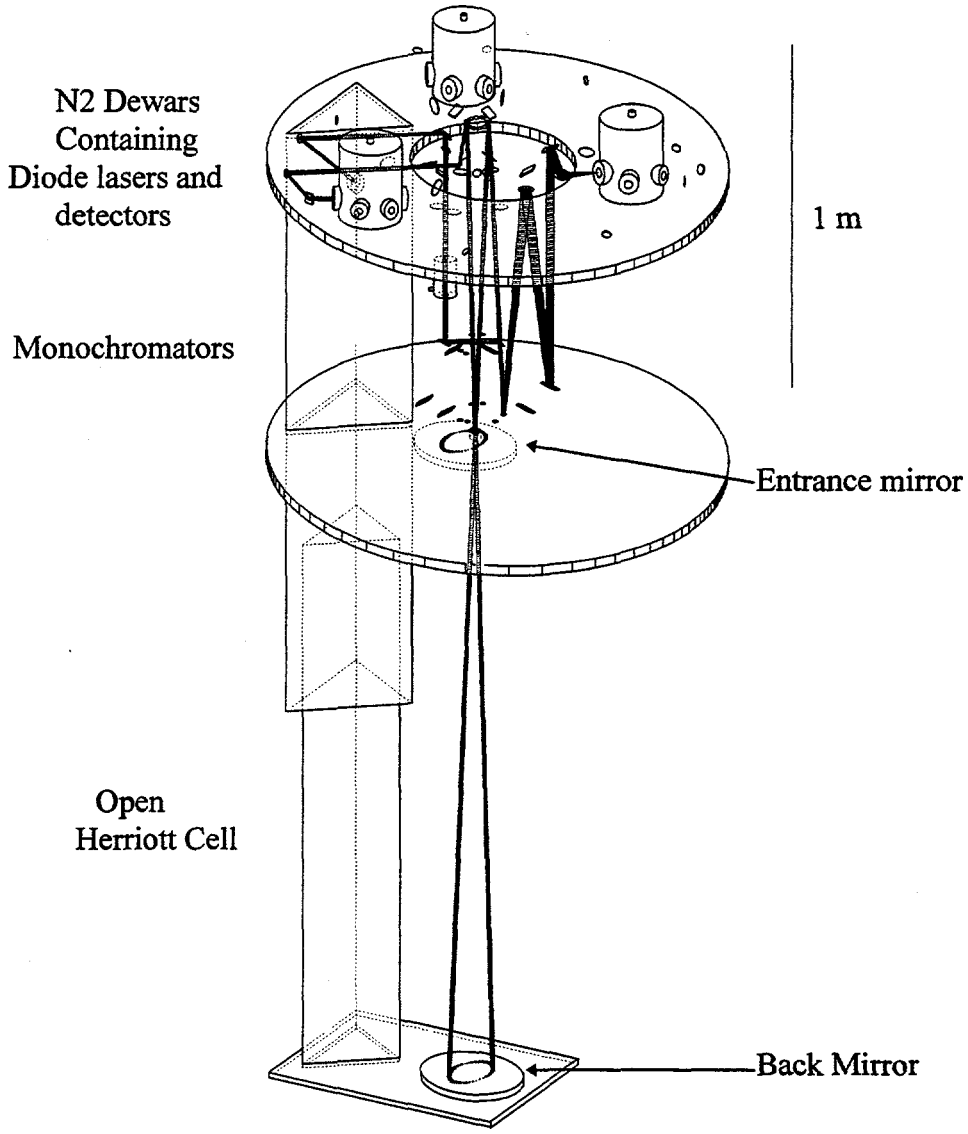

Figure 1 : SPIRALE Optics Schematic. Only one laser beam is shown for clarity

The concentration, for a given specie, is derived from the absorbed beam detector signals, by application of the Beer law. Signals consist in absorption spectra, following frequency tuning of the diode laser back and forth one absorption line specific of the specie. When different species have close absorption lines, they can be measured with the same laser. The sweep frequency of the laser is fixed to 1 kHz, the sampling rate being 1024 per sweep. The signals are added together during 1 second on board, and send to the ground, because telemetry rate cannot sustain raw signal rate. The secondary effect is to decrease noise. However, during 1 second, there is no optical frequency control. The only result is to get larger absorption lines due to frequency shift or jitter. One Hz sampling rate for species is convenient with a fair vertical resolution. We can expect the detection and the measurement of species with absorption as low as 10^{-4} (relative absorption). We have access therefore, to molecules as : CO_2, H_2O, CO_2, O_3, CH_4, N_2O, CO, NO_2, NO, HCl, but the two latter have a poor S/N ratio. For the first flight, 3 diode lasers will be installed.

Other parameters are projected to be measured : of course temperature and pressure, but also aerosols, etc.. In the design of the instrument, volume have been kept unoccupied and reserved to small instruments, for their validation for instance.

3 - SPIRALE EVOLUTION AND IMPROVEMENT : The first flight is planned for autumn 1997 in Aire Sur L'Adour (France). The measured species will be NO, NO_2, $CO+O_3$. The main goal is to test the instrument in retrieving the vertical profiles of these species, which are rather well known,. The scientific program in the coming year is largely devoted to the lower stratosphere. However, at low altitude, pressure line broadening effect reduces dramatically S/N ratio. It may imply than for altitude between 11 km and 15 km, a pressurized closed Herriott cell be used instead an open one.

The mission of SPIRALE is also to measure trace species whose absorption is lower than 10^{-4}. Optical frequency modulation technique has proved to be valuable in detecting absorption as low as 10^{-6} [6]. It means that species like HNO_3, CH_2O, H_2O_2, F_2CO, HOCl, HO_2 can be measured. In the 2nd Phase of SPIRALE project, the 3 next detection channels will be reserved to them, using frequency modulation technique, and one channel will be ready for flights in 1998. A R & T program on this detection technique, financed by CNES, common to LPCE and ONERA, has prepared the way of their installation on SPIRALE instrument.

References :

[1]L. E. Mauldin & Al , (SAGE experiment II), Optical Ingeneering, **24**, 307-3012 (1985) ; J. P. Naudet, C. Robert, D. Huguenin, (AMON experiment), Proc. 14th ESA Symp. Eur. Rocket & Balloon Programs and Related Res. Montreux, ESA SP-355, 165-168 (1994)

[2] R. L. Baker, L.E. Mauldin, J. M. Russel, (HALOE Remote sensor), Infrared Technologies, Proc. Soc. Photo-Optical Eng. Vol. 685, 181-191, (1986) ; A. Girard, & Al, (Grille Spectrometer), J. Geophys. Res. 88, 5377 (1983)

[3]C. B. Farmer, O. F. Raper, F. G. O'Callaghan, (Final Report on the first flight of the ATMOS Instrument) JPL Publication 87-32, (October 87) ; C. Camy-Peyret & Al, (LPMA Fourier Transform Spectrometer), Proc. 12th ESA Symp ; European Rocket and Balloon Programmes and related Research, Lillehammer, 29 May - 1 June 1995

[4] C. R. Webster and R. D. May, J. (BLISS instrument) Geophys. Res. **92**, 11931 (1987)

[5] J.A.Silver (Frequency Modulation), Applied Optics, 31, 707-717 (1992)

The SPIRALE project is financed jointly by CNES (Centre National d'Etudes Spatiales, and by INSU (Institut National des Sciences de l'Univers, department of Centre National de la Recherche Scientifique -CNRS-)

Influence of interannual variations of stratospheric dynamics in model simulations of ozone losses by aircraft emissions

E.A.Jadin

Central Aerological Observatory, Dolgoprudny, 3 Pervomayskay Str., 141700, Russia

1.Abstract

The questions of model predictions of aircraft emission impacts on the ozone variations are considered. Using the NMC data it is shown that the stratospheric circulation underwent the abrupt transition to a new regime in summer 1980. The strong correlations are found between the monthly mean total ozone and stratospheric angular momentum anomalies during 1979-1991. The natural long-term changes of transport processes are necessary to take into account in model simulations of anthropogenic impacts on the ozone layer.

2.Introduction

The model predictions of the ozone layer depletion by CFC's and aircraft emission impacts [WMO/UNEP,1994] have the significant shortcoming. Indeed, they do not take into account interannual and interdecadal changes of the stratospheric circulation and wave activity. The ozone variations from year to year can be caused not only by man-made activities, but long-term natural changes of stratospheric dynamics may play a big role in observed ozone trends too. Regarding to model predictions of aircraft emission impacts on ozone layer Jadin and Bromberg [1994] have shown that the 2D - model simulations with chemical eddies result in less ozone losses, than without. Because the eddy transport processes depend strongly on the wave activity variations, the effects of its interannual changes can lead to large differences in results of model simulations.

The questions that will be considered in this work are as follows - are there the long-term changes of stratospheric dynamics from late 70's to early 90's and how are these changes associated with the observed ozone trends on the global scale?

3.Data and Method of Analysis

For the diagnostics of zonal changes of the atmospheric dynamics were used the calculated variations of the relative atmospheric angular momentum [Rosen and Salstein, 1985]

$$AAM = \frac{2\pi a^3}{g} \int_{p_b}^{p_t} \int_{-\frac{\pi}{2}}^{\frac{\pi}{2}} \bar{u} \cos^2 \varphi d\varphi dp \qquad (1)$$

where a is radius of the Earth, g is gravity acceleration, $\bar{u}$ zonal wind, p pressure, φ latitude, p_b, p_t pressure at lower and upper boundaries of an atmospheric layer respectively.

It is well known that on seasonal and interannual time scales (up to 2 - 3 years) the AAM changes are connected with the length of day (LOD) variations by the simple relation [Rosen and Salstein, 1985]

$$LOD = 1.68 AAM \qquad (2)$$

where LOD is in millisecond units and AAM in $10^{26} \kappa g \times m^2/sec.$

The calculations of AAM changes were conducted using the daily NMC wind data on standard levels 1000 hPa -100 hPa and the MMC/CAC geopotential height data for 100 hPa - 0.4 hPa in 1979 - 1992. For the stratosphere the zonal mean winds were calculated by the gradient wind approximation. In the $10^o N - 10^o S$ belt the wind values were found using the linear interpolation between the hemispheres. The monthly mean anomalies of stratospheric angular momentum were calculated for each month during 14 years 1979 - 1992. The results are presented in the millisecond units using relation (2). The TOMS data (version 6) were used for the calculations of the correlations between the interannual variations of the stratospheric (100 hPa - 0.4 hPa) angular momentum (SAM) and total ozone anomalies in 1979-1991.

4.Results

In order to indicate the long-term changes of atmospheric dynamics as whole the global stratospheric and tropospheric AAM(1000 hPa - 100 hPa) angular momentum anomalies were calculated (*Fig.1*). The positive (westerly) anomalies of the tropospheric momentum are associated with the El Niño events in 82/83 , 86/87 and 90/92. The ENSO signal is also seen in the stratosphere, but there are large differences in the behavior of the

stratospheric and tropospheric anomalies. The large negative (easterly) SAM anomalies are observed in 79/early 80 and 90/92 in contrast with the westerly AAM(100) anomalies. Conversely, the westerly (easterly) anomalies of the stratospheric (tropospheric) momentum were indicated in the second half of 1985. The long-term downward trend with the QBO signal in the global SAM anomalies takes place during 1981-1992, while it is not remarkable in the tropospheric angular momentum changes. These differences can be explained by the interference between the quasibiennial (QB) and low-frequency (LF) components of the interannual changes in the stratospheric and tropospheric circulation [Jadin, 1996b]. The large easterly global SAM anomalies in 79/early 80 are caused by the unusual "easterly cat eyes" structure of the zonal wind anomalies in the subtropics (*Fig.2*). That structure is not observed during 1981-1990, however, it is recurred in 91/92 in the upper and middle stratosphere near equator.

Figure 3 shows the long-term propagation of the SAM anomalies for October in 1979-1992. The striking feature of this propagation resembles the V - structure that has been indicated by Dickey et al.,[1992] in the low-frequency propagation of the tropospheric momentum. The disturbances of stratospheric circulation are generating near equator and then they are slowly propagating to middle and high latitudes during winter/spring times, when the planetary waves can penetrate into the stratosphere. The V - structure may give a basis for empirical predictions of the future behavior of ozone layer [Jadin, 1995, 1996a]. If the strong easterly SAM anomalies generated near equator in 1991/92 will be able to propagate to middle and high latitudes of the Nothern (NH) and Southern (SH) Hemispheres during following years, it can result in a gradual recovery of ozone layer to the previous state. *The disappearance of ozone hole over the Antarctic may start in 1996-1998 already.*

The westerly anomalies are dominated in the high and midlatitudes of the SH except 1979-1981, 1984 and 1988. It is interesting that the westerly (easterly) SAM anomalies in $50^{o}S-60^{o}S$ band are in a good accordance with the decrease (increase) of the total ozone in the Antarctic [Jadin, 1996a]. This can mean that the natural interannual and decadal variations of stratospheric dynamics and wave activity affect strongly polar vortex isolation and ozone trends over the Antarctic. The similar features are observed for the Arctic and the middle latitudes of the NH in January - March during 1979-1991 [Jadin, 1996a].

The results of the singular value decomposition (SVD) analysis of the relations between the interannual variations of the SAM and total ozone anomalies are shown in *Figure 4* [Jadin and Diansky, 1996]. The correlations between the total ozone anomalies and the time series of the leading SVD mode of the SAM anomalies are very high in the high latitudes of the SH and middle to high latitudes of the NH during winter/springtimes. The features of the first SVD mode of total ozone anomalies resemble the ozone trend fit of the regressions calculated by Randel and Cobb [1994], while the behavior of the leading SVD mode and its time series of the SAM anomalies hints on a decadal decrease of the stratospheric wave activity in the middle and high latitudes in 1979-1991.

The results of these analyses were used in the numerical experiments with the 2-D model of gas-phase chemistry and residual circulation and the planetary wave model. The observed variations of the monthly mean zonal wind were incorporated into these models to study the response of ozone layer to the interannual variations of the stratospheric dynamics using some simple parametrizations. The preliminary results showed that the decrease (increase) of the stratospheric planetary wave activity results in the decrease (increase) of ozone amounts in high latitudes during winter/spring seasons. The further calculations are conducting to take into account the observed interannual variations of stratospheric dynamics in model predictions of the response of ozone layer to the aircraft emissions.

5.Concluding remarks

The main question of the recent state of ozone problem is to distinguish the influence of natural and anthropogenic impacts on the ozone layer depletion. On the one hand, the presented results give evidences of sharp changes of stratospheric circulation in the beginning of 80's and, on the other hand, its strong relations with total ozone anomalies during 1979-1991. The analysis of the linear trend of zonal mean wind at 100 hPa in the high latitudes of the SH showed that the largest increase of westerlies occurred in June - August, not in October, when ozone reductions are most prominent [Jadin, 1996b]. This can imply that the long-term changes of stratospheric dynamics are *unlikely* caused by variations in the radiative budget of the lower stratosphere. Probably, decadal changes of the stratospheric wave activity, which can be associated with a large increase of the sea surface temperature (SST) in the Pacific, Atlantic and Indian ocean in the end of 70's [Smith

et al., 1994], may be a primary reason both of the stratospheric circulation anomalies and ozone trends. The decadal decrease of wave activity can create favorable conditions for chemical mechanisms of ozone layer destruction and a decrease of eddy ozone exchange. The large correlations between the SST anomalies in the central Pacific and ozone hole development in the Antarctic [Angell, 1988; Kodera and Yamazaki, 1989], as well as between the SST's in the North Atlantic and total ozone anomalies over the Europe [Jadin,1992] argue in favor this point of view. The results presented here can be used for model predictions of the future behavior of ozone layer taking account the interannual and decadal variations in the coupled ocean-atmosphere system.

6.References

1. Angell,J.K., 1988, *Geoph. Res. Lett.*, 15, 915-918.
2. Dickey,J.O., S.L.Marcus, and R.Hide, 1992,*Nature, 357*, 484-488.
3. Jadin,E.A.,1992, *Meteorology and Hydrology, 7*,22-26.
4. Jadin,E.A., and D.V.Bromberg, 1994, *J. Atm. Terr. Phys., 56,9*,1091-1093.
5. Jadin, E.A., 1995, *Meteorology and Hydrology, 7*, 48-55.
6. Jadin, E.A., 1996a, *Meteorology and Hydrology, 7*, 43-55.
7. Jadin,E.A., 1996b, *Meteorology and Hydrology*, submitted.
8. Kodera,K., and K.Yamazaki, 1989, *J.Met.Soc.Japan, 67*, 3, 465-472.
9. Randel,W.J., and J.B.Cobb, 1994, *J.Geoph.Res., 99*, 5433-5447.
10. Rosen,R.D.,and D.A.Salstein, 1985, *J.Geoph.Res. 90*, 8033-8041.
11. Smith,T.M., R.W.Reynolds, and C.F.Ropelewski, 1994, J.Climate, 7, 949-964.
12. WMO/UNEP international report" Scientific Assessment of Ozone Depletion": 1994.

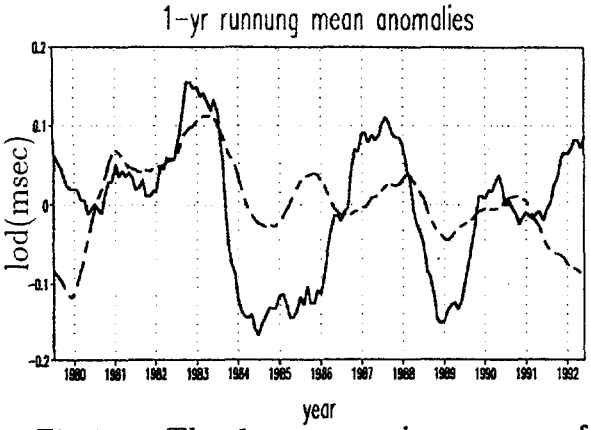

Fig.1. - The 1-year running means of the tropospheric (solid) and stratospheric (dashed) angular momentum anomalies (msec).

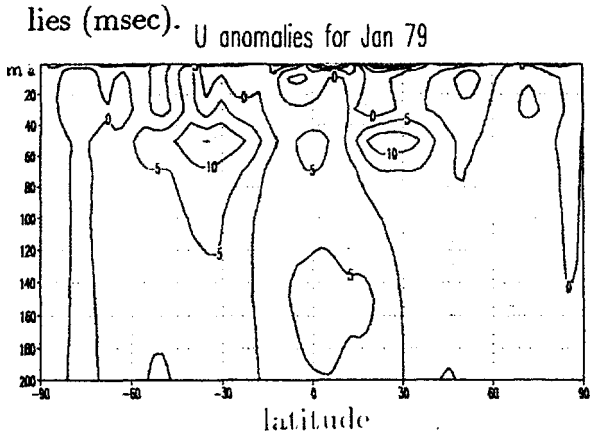

Fig.2. - Monthly mean anomalies (m/sec) of zonal wind in January 1979 for 1979-1992.

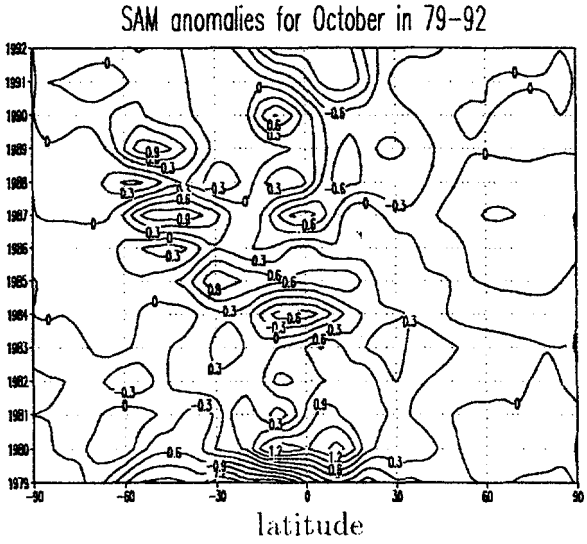

Fig.3. - Monthly mean anomalies of the stratospheric momentum for October 1979-1992 (in 0.01 msec units).First point of each year is corresponding to October.

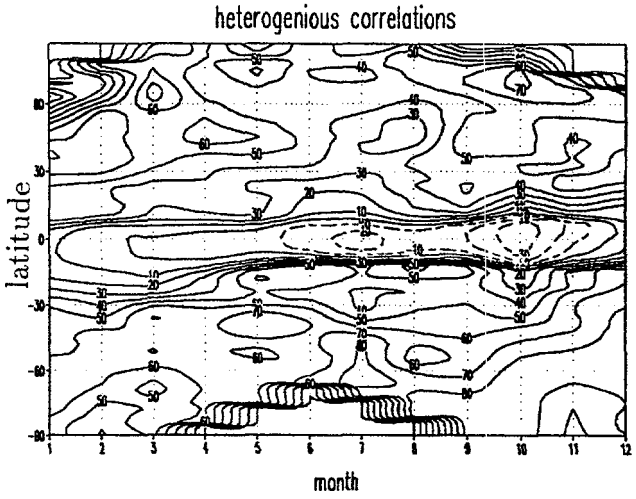

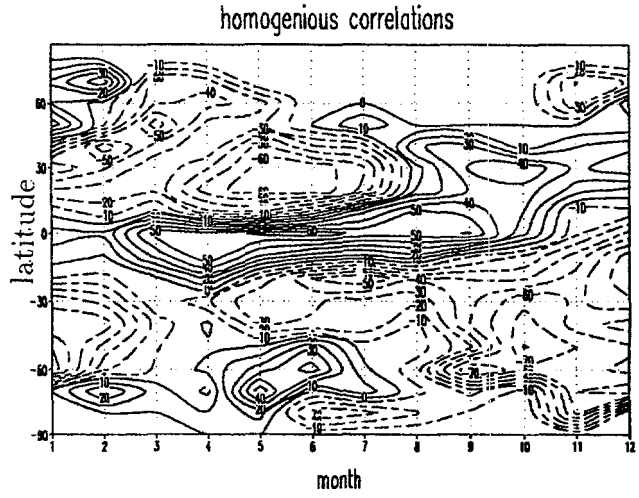

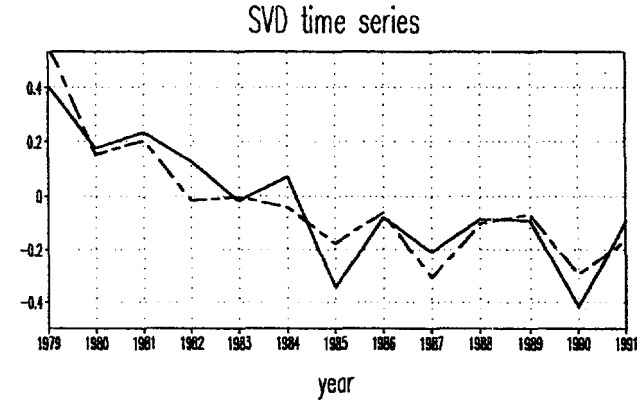

Fig.4. - The correlations (%) between time series of the leading SVD mode of stratospheric momentum anomalies and the total ozone anomalies (top) and stratospheric momentum anomalies (middle) for 1979 - 1991.(Bottom) The time series of the leading SVD modes of the total ozone anomalies (solid) and the stratospheric momentum anomalies (dashed).Units are arbitrary.

EFFECTS OF NO_X AND SO_2 INJECTIONS BY SUPERSONIC AVIATION ON SULFATE AEROSOL AND OZONE IN THE TROPOSPHERE AND STRATOSPHERE

I. G. Dyominov, A. M. Zadorozhny
Novosibirsk State University, Novosibirsk, 630090, Russia
N. F. Elansky
Institute of Atmospheric Physics, RAS, Moscow, 109017, Russia

Abstract. The impact of supersonic aviation on atmospheric ozone and sulfate aerosol is examined with the help of a two-dimensional dynamical/radiative/chemical model of ozonosphere including aerosol physics. For SO_2 emissions from aircraft as gas, gas/particles (90%/10%) mix, and particles of 0.01μm radius the sulphate aerosol surface density at maximum of changes increases against its background value by ~50%, ~75%, and ~200%, respectively. This effect of SO_2 emissions with insignificant NO_x injection leads to a significant decrease of total ozone by 2015 in the entire atmosphere. For NO_x emissions which are anticipated in future ($EI(NO_x)$ = 15) any kind of SO_2 emission results in significant weakening of supersonic aviation impact on ozone layer in the Northern Hemisphere.

1. INTRODUCTION

As we approach the age of High Speed Civil Transport (HSCT, commercial flights are scheduled at the beginning of the 21st century), the possible impact of aviation on atmospheric ozone arouses constantly growing interest. These flights will go along existing routes at heights from 15 to 24 km. These heights are known to be those where maximums in distribution of ozone and aerosol sulfate particles are formed. Therefore, this stratospheric region is the most sensitive to changes in gas and aerosol composition of the atmosphere.

By now, many authors [1, 2] have shown that surface heterogeneous processes on background sulfate aerosol are decisive for global impact of stratospheric aviation on ozone. Evaluation of ozone destruction which takes into account these processes gives 3 to 5 times less estimates than the prediction based on only gas-phase processes [3]. The effect is mostly caused by hydrolysis of N_2O_5 on sulfate aerosol particles

$$\text{(R1)} \quad N_2O_5 + H_2O(\text{aerosol}) \rightarrow 2HNO_3.$$

As a result, ozone destruction in nitrogen catalytic cycle is drastically reduced.

Some works which include aerosol physics considerations [2, 4-7] also indicate that the heterogeneous effect becomes still stronger if we take into account the impact of SO_2 emission from aircraft engines on atmospheric sulfate aerosol layer.

Notice that all the above works fail to include a factor of conversion of aircraft injected gas components into the other state. Some other findings [8] indicate that conditions existing in the stratospheric region of HSCT flights stimulate formation in the aircraft plume of sulfate aerosol particles from SO_2 molecules containing in aircraft exhausts. Therefore, examination of the impact of SO_2 emission from supersonic aircraft on atmospheric aerosol must include scenarios of either complete or partial conversion of SO_2 into sulfate particles.

Weisenstein et al. [9] were the first who used such scenarios for their research. Their calculation of stratospheric aerosol loading showed that for full conversion of SO_2 from aircraft engine discharges into sulphate particles the impact of the latter on the atmosphere leads to a very large increase in the density of the sulfate aerosol surface. This fact results in a significant change of stratospheric ozone distribution.

Dyominov and Zadorozhny [10] obtained similar results for the scenarios identical to those in [9]. In this work we examine the impact of NO_x and SO_2 emissions from supersonic aircraft (Mach 2.4) on the ozone and sulfate aerosol layers of the atmosphere. The emphasis is given to examining global annual average change of sulfate aerosol and ozone in the troposphere and stratosphere. This approach makes it possible to delineate basic features of buffering properties of atmospheric sulfate aerosol, that is, the ability of sulfate aerosol particles, due to heterogeneous and microphysical processes, to significantly reduce the impact of supersonic aviation on atmospheric ozone.

2. DESCRIPTION OF THE MODEL

The impact of aviation on atmospheric ozone and sulfate aerosol is examined with the help of an interactive numerical two-dimensional zonal averaged model of the ozonosphere. This model is used to calculate diabatic circulation, temperature, gas and aerosol composition of the troposphere and the stratosphere at latitudes from the North to South Poles in a self-consistent way.

Photochemical, radiative, dynamical, and aerosol units of the model are given detailed description in [2, 11-13]. The model calculates 45 minor gas constituents describing the condition of seven families: O_x, HO_x, NO_y, Cl_y, Br_x, CHO_x, and HSO_x. The interaction of all gas constituents is entered into by 157 photochemical reactions. Twenty six of their number describe the interaction of sulfate components DMS, CS_2, H_2S, OCS, S, SO, SO_2, SO_3, HSO_3, H_2SO_4.

The temperature stratification of the atmosphere is determined by the heat balance equation for the entire region. Calculation of the atmospheric heating (cooling) rates takes into account heat fluxes due to convection, turbulent heat exchange, solar and infrared radiation.

Dynamical processes of the atmosphere are represented in the model with residual meridional circulation. The latter is described by the system of equations for zonal averaged horizontal motion and a thermodynamic equation of energy.

Distribution of sulfate aerosol particles with radii 0.0064 μm ≤ r ≤ 5.2 μm is defined from a system of continuity equations for particle size distribution functions n(r):

$$\frac{\partial n(r)}{\partial t} = P\Big|_{nucl} + \frac{\partial n(r)}{\partial t}\Big|_{cond\ and\ vap} + \frac{\partial n(r)}{\partial t}\Big|_{coag} + \frac{\partial n(r)}{\partial t}\Big|_{sed} \frac{\partial n(r)}{\partial t}\Big|_{wash} + \frac{\partial n(r)}{\partial t}\Big|_{transp} \qquad (1)$$

The right-hand terms of equation (1) characterise processes of heterogeneous and homogeneous nucleation, condensation, evaporation, coagulation, sedimentation, and washout of particles, as well as their transport by diabatic circulation and turbulent diffusion. For the purpose of numerical solution of equation (1) the particle size distribution function n(r) is replaced with a discrete function $N_i(r_i, r_{i+1})$, where i is the number of an interval (or bin) on a grid of discrete radii, $r_{i+1} = \sqrt[3]{2}r_i$; $\Delta r_i = (\sqrt[3]{2} - 1)r_i$; $r_n = \sqrt[3]{2^{n-1}} \cdot r_1$. The total number of bins is 30.

Calculations show [2, 11-13] that the model is quite adequate in describing major features of dynamic processes, thermal regime, gas and aerosol composition of the troposphere and stratosphere.

3. SCENARIOS

Calculations of global impact by regular flights of 500 supersonic aircraft on the ozone and sulfate aerosol layers are carried out for the period from 1990 through 2015. Boundary conditions for the atmospheric background of 1990 correspond to the data of [1]. For 2015, new recommendations give CH_3Br, N_2O, CH_4, and CO_2 mixing ratios equal to 15 pptv, 300 ppbv, 1994 ppbv, and 412 ppmv, respectively. Averaged global fuel consumption is 60 megaton a year. Calculations are carried out with the two values of nitrogen oxide emission index ($EI(NO_x)$), 15 g and 5 g of NO_2 equivalent per 1 kg of fuel. Emission index for SO_2, H_2O, CO and CH_4 are

adopted to be 0.4, 1230, 1.5 and 0.2 g per 1 kg of fuel. The ratio of a mean speed of flights to the sound velocity (Mach number) is 2.4. Calculations are carried out with and without account taken for SO_2 emission from aircraft engines. Three kinds of SO_2 emission are used: as 100% gas, gas/particles (90%/10%) mix, and 100% particles. The size of sulphate particles is taken to be 0.01 μm [8, 9]. In addition to reaction R1 our calculation takes into account reactions $ClONO_2$ and $BrONO_2$ hydrolysis on sulfate aerosol particles:

$$\text{(R2)} \quad ClONO_2 + H_2O(\text{aerosol}) \rightarrow HOCl + HNO_3,$$
$$\text{(R3)} \quad BrONO_2 + H_2O(\text{aerosol}) \rightarrow HOBr + HNO_3.$$

The adopted values of γ, a heterogeneous reaction probability, are as follows: $\gamma_1 = 0.1$[1]; $\gamma_2 = 0.006 \cdot \exp(0.15(200-T))$ [1]; and $\gamma_3 = 0.4$ [14]. The prognosis for ozone in 2015 for various scenarios, including combinations of NO_x and SO_2 emissions from aircraft is made for the two states of chlorine background [ClY] in 2015: 3 ppbv and 2 ppbv.

4. RESULTS AND DISCUSSION

The results of self-consistent model calculations show that without SO_2 emission ($EI(SO_2)=0$) the impact of aircraft exhausts on a background value of sulfate aerosol surface density (see *Figure 1a*) is hardly noticeable. This fact allows us to take into account only SO_2 emission for estimation of supersonic aviation impact on the sulfate aerosol layer of the atmosphere. This estimation gives a significant (about 35%-50%) increase of aerosol surface density in the lower Northern stratosphere following SO_2 injection in the gaseous form (*Figure 1b*). Gas/particle (90%/10%) mix gives a still more significant increase (*Figure 1c*). The maximum amounts to ~75 percent. When all SO_2 converts into sulfate particles, the latter cause a catastrophically great

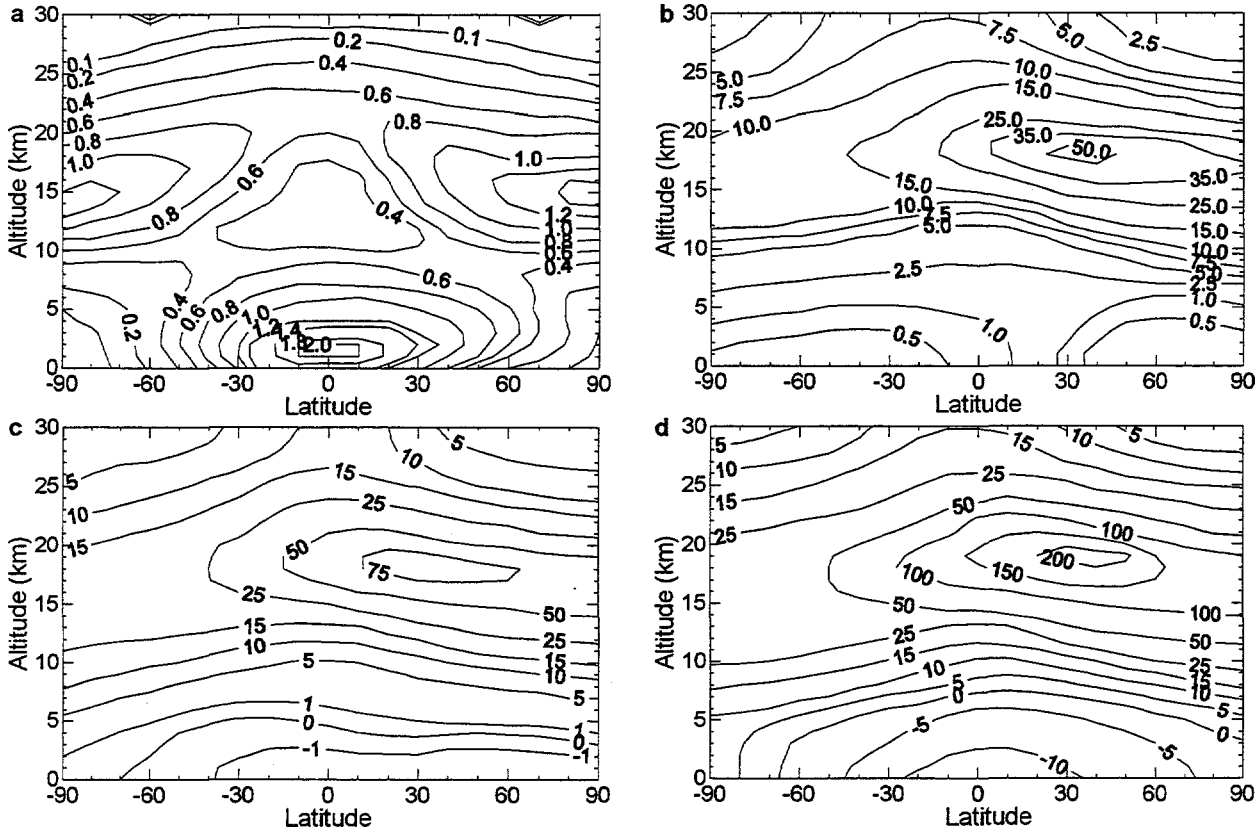

Fig. 1. Calculated annual average aerosol surface density (a) for background conditions (10^{-8} cm^{-1}), and percent difference from background with emission of SO_2 from supersonic aircraft as (b) 100% gas, (c) 90% SO_2 gas and 10% particles, and (d) 100% particles of 0.01 μm radius.

(~100-200%) increase in aerosol surface density (see *Figure 1d*) in a wide range of latitudes (20°S-90°N). All these effects are caused mainly by increased H_2SO_4 content and nucleation, condensation, and, to a lesser degree, by coagulation.

In light of all the above results, prognostic estimates of ozone change by 2015 due to HSCT flights shows that, for the background sulfate aerosol ($EI(SO_2)$)=0), NO_x emission leads to a fairly significant decrease in annual average total ozone (see curve 1 in *Figure 2*). The greatest total ozone decrease is observed at $EI(NO_x)$ = 15 and 2 ppbv [ClY] (see curve 1 in *Figure 2b*), and the smallest decrease is observed at $EI(NO_x)$ = 5 and 3 ppbv [ClY] (see curve 1 in *Figure 2c*). If we take into account that the sulfate aerosol surface changes due to SO_2 emission, we obtain for the two examined chlorine background conditions that nitrogen oxide injection with $EI(NO_x)$=15 leads to a decrease of total ozone depletion in the Northern Hemisphere and an increase in the Southern Hemisphere (see curves 2-4 in *Figures 2a,b*). For the latter case, an increase of ozone depletion is quite significant at 3 ppbv [ClY] and insignificant at 2 ppbv [ClY]. For the two chlorine background conditions and all SO_2 emission scenarios with $EI(NO_x)$=5 leads to an increase of total ozone depletion both in the Northern and the Southern Hemisphere (see curves 2-4 in *Figures 2c,d*).

All the above results are caused mainly by heterogeneous processes. Some of these processes weaken destructive impact of hydrogen, nitrogen, chlorine, and bromine catalytic cycles on ozone, while others strengthen it. To make clear how these processes influence ozone changes during HSCT flights, consider local ozone change at 45°N in June for all scenarios (*Figure 3*). For significant nitrogen oxide discharges ($EI(NO_x)$=15) we see a decrease of ozone depletion (see curves 2-4 in *Figures 3a,b*). It is entirely due to reaction R1. While converting N_2O_5 (and consequently NO_x) into chemically inert HNO_3, this reaction leads to significant weakening of

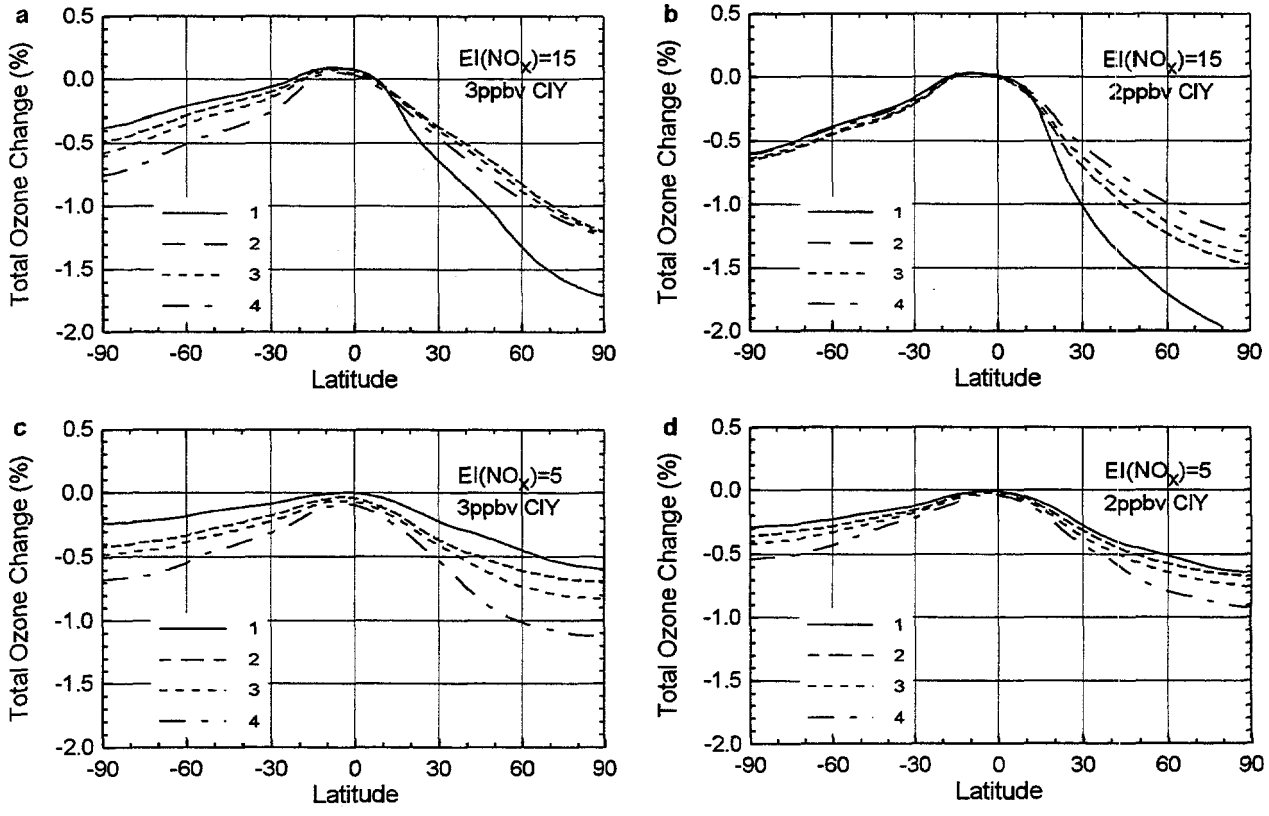

Fig. 2. Percent change in annual average total ozone due to NO_x and SO_2 emission from supersonic aircraft. Curve (1) shows results with no SO_2 emissions. Curve (2-4) include SO_2 emission as (2) 100% gas, (3) 90% SO_2 gas and 10% particles, and (4) 100% particles of 0.01 μm radius.

ozone destruction via the nitrogen catalytic cycle. The higher the sulfate aerosol particle surface density, the greater this weakening of ozone destruction (sf. curves 2-4 in *Figure 3b*). The role of the heterogeneous reaction R1 is greatly reduced due to reactions R2 and R3. The reason is that active HOCl and HOBr that form in these reactions leads to strengthened ozone destruction via hydrogen, chlorine, and bromine catalytic cycles. It is the strengthening of ozone destruction via hydrogen and chlorine catalytic cycles that entirely change the character of a decrease of the ozone depletion at 3 ppbv [ClY] in comparison with that at 2 ppbv [ClY] (cf. curves 2-4 in *Figures 3a and 3b*). For an insignificant nitrogen oxide injection ($EI(NO_x)=5$) and the two examined chlorine background conditions the ozone depletion is increased (see curves 2-4 in *Figures 3c,d*). This increase is entirely caused by the strengthening of ozone destruction via the hydrogen, chlorine, and bromine catalytic cycles. The higher the sulfate aerosol particle surface density, the greater this strengthening of ozone destruction caused by reactions 2 and 3 (cf. curves 2-4 in *Figures 3c,d*).

Shown in the calculations the character of local ozone changes at 45°N is also present at all latitudes of the Northern and the Southern Hemispheres. This fact does determine latitudinal variations of changes in annual average total ozone due to supersonic aviation flight. For example, in the Southern Hemisphere, where the atmospheric discharges of nitrogen oxides (both for $EI(NO_x)=15$ and for $EI(NO_x)=5$) are insignificant, the ozone depletion increase (see curves 2-4 in *Figure 2*) is entirely caused by the strengthening of ozone destruction via the hydrogen, chlorine, and bromine catalytic cycles. The identical effect is seen in the Northern Hemisphere for nitrogen oxide injection with EI(NOx)=5 (cf. curves 2-4 in *Figures 2c,d*).

Only nitrogen oxide injection with $EI(NO_x)=15$ in the Northern Hemisphere results in an ozone depletion decrease. It is caused by the weakening of ozone destruction via the nitrogen

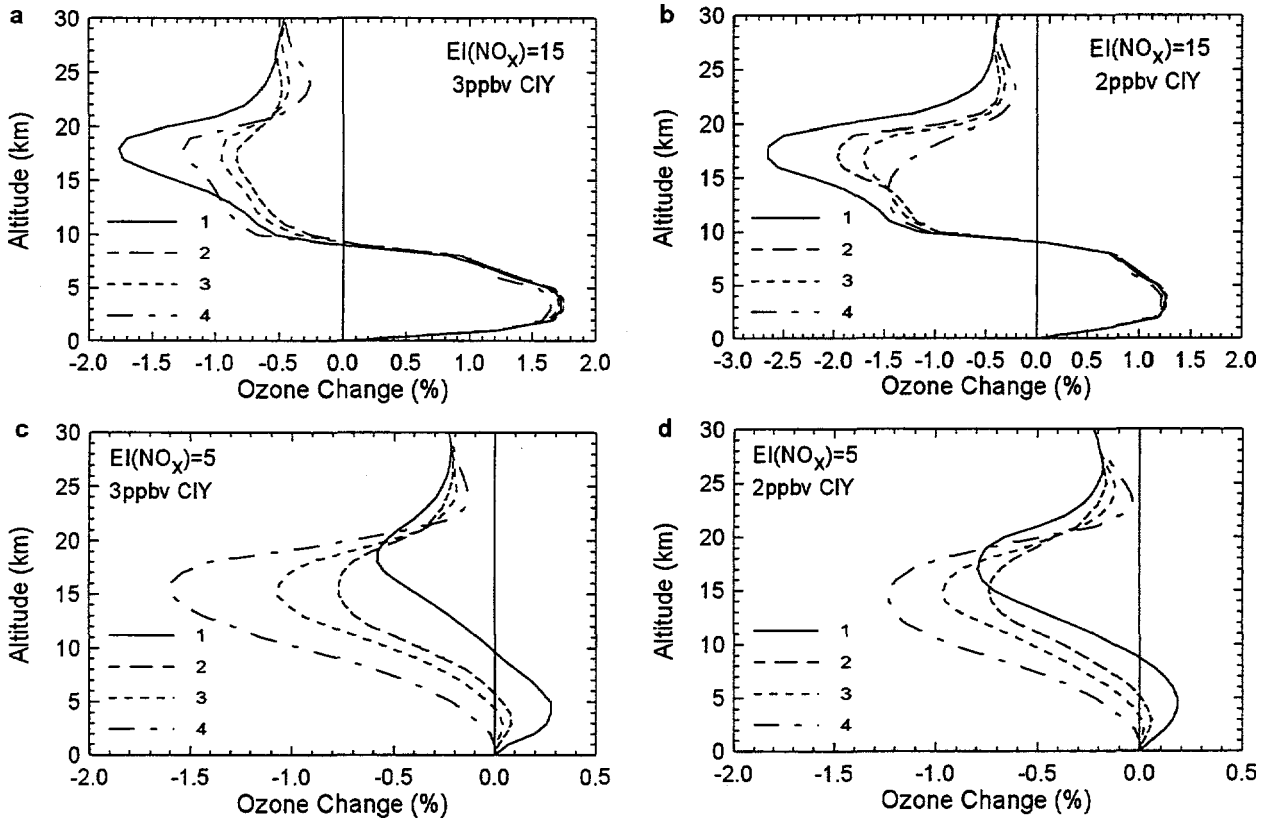

Fig. 3. Percent change in of local ozone for June at 45°N due to NO_x and SO_2 emission from supersonic aircraft. Curve (1) shows results with no SO_2 emissions. Curve (2-4) include SO_2 emission as (2) 100% gas, (3) 90% SO_2 gas and 10% particles, and (4) 100% particles of 0.01 μm radius.

catalytic cycle. So, for NO_x and SO_2 emissions from aircraft engines anticipated in near future (that is, with $EI(NO_x) = 15$ and with $EI(SO_2) = 0.4$) sulfate aerosol layer is a buffer in the atmosphere of the Northern Hemisphere for every kind of SO_2 emission, that is, it leads (due to heterogeneous and microphysical processes) to the weakening of impact of regular flights of supersonic aviation on the ozone layer of the atmosphere.

Acknowledgements. The authors thank very much Debra K. Weisenstein for the data for the scenarios used in this work. The work was supported under Grant No. 94-05-16661 of the Russian Foundation for Basic Research.

REFERENCES

1. Stolarski R. S., and H. L.Wesoky, The Atmospheric Effects of Stratospheric Aircraft: A Second Program Report, *NASA Reference Publication 1293*, 1993.
2. Golitsyn G. S., et al., Study of the tropo/stratosphere gaseous composition changes and its influence on the climate and environment, *Report No.3, IAPh RAS*, Moscow, (in Russian), 1994.
3. Johnston, H. S., D. E.Kinnison, and D. J.Wuebbles, Nitrogen oxides from high-altitude aircraft: An update of potential effects on ozone, *J. Geophys. Res.*, **94**, 16,351-16,363, 1989.
4. Bekki, S., and J. A.Pyle, Potential impact of combined NO_x and SO_x emissions from future high speed civil transport aircraft on stratospheric aerosols and ozone, *Geophys. Res. Lett.*, **20**, 723-726, 1993.
5. Pitari G., et al., High-Speed Civil Transport Impact: Role of Sulfate Nitric Acid Trihydrate and Ice Aerosols Studied with a Two-Dimensional Model Including Aerosol Physics, *J. Geophys. Res.*, **98**, 23,141-23,164, 1993.
6. Tie, X. X., et al., The impact of high altitude aircraft on the ozone layer in the stratosphere, *J. Atmos. Chem.*, **18**, 103-128, 1994.
7. Dyominov, I. G., and N. F. Elansky, The impact of supersonic aviation on the ozone layer: A chemical/microphysical model study, *Ann. Geophys., Part III, Suppl. III*, **13**, 700, 1995.
8. Fahey, D. W., et al., Emission measurements of the Concorde supersonic aircraft in the lower stratosphere, *Science*, **270**, 70-74, 1995.
9. Weisenstein, D. K., et al., Potential impact of SO_2 emissions from stratospheric aircraft on ozone, *Geophys.Res.Lett.*, **23**, 161-164, 1996.
10. Dyominov I. G., and A. M. Zadorozhny, On the role of sulfate aerosols in estimation of the impact of supersonic aviation on the ozone layer, Ann. *Geophys., Part II, Suppl. II*, **14**, 507, 1996.
11. Ginzburg, E. I., and I. G. Dyominov, Numerical dynamical model of ozonosphere, In: *Principles of Creating of Dynamic Model for Upper Atmosphere*, Moscow, Gidrometeoizdat, 61-83, (in Russian), 1989.
12. Dyominov, I. G., et al., The estimation of effects of effects of regular rocket launches "Energia" and "Shuttle" on the ozone layer and earth's climate, *Preprint N1, IAPh RAS*, Moscow, 110pp., (in Russian), 1992.
13. Talrose V. L., et al., Scientific basis for control of environment quality based on analysis of global bio-geochemical cycles for organogenic elements, *Report No.2, INEP ChPh RAS, Moscow*, (in Russian), 1993.
14. Hanson, D. R., and A. R. Ravishankara, Heterogeneous chemistry of bromine species in sulfuric acid under stratospheric conditions, *Geophys. Res. Lett.*, **22**, 385-388, 1995.

The Global Distribution of Tropospheric NO_X estimated by a 3-D Chemical Tracer Model

Annette B. Kraus, Franz Rohrer, and Dieter H. Ehhalt
Institut für Atmosphärische Chemie, Forschungszentrum Jülich, Jülich, Germany

1 Abstract

The global distribution of NO_X in the troposphere is calculated using a three-dimensional chemical tracer model with a simplified chemistry scheme for the tracers $NO_X \equiv NO + NO_2$ and HNO_3. At northern mid- and high latitudes, the calculated tropospheric NO_X content is dominated by the surface source fossil fuel combustion. In the tropical free troposphere lightning discharges provide about 80% of the total NO_X throughout the year. The zonally averaged fractional contribution of aircraft emissions strongly depends on season. ~~The largest contribution of this source, over 60%, occurs during January in the upper troposphere between 45°N and 60°N.~~

The NO mixing ratios determined by the model show good overall agreement with corresponding zonal mean values observed during the STRATOZ III aircraft campaign in June. ~~The same also is true for measurements made in January during the TROPOZ II campaign, but only in the southern hemisphere~~. Over Canada, mixing ratios as high as 0.5-1.0 ppbv NO were measured during TROPOZ II, the origin of which is not yet understood.

2 Introduction

The nitrogen oxides NO and NO_2 play a dual role in tropospheric chemistry: They are a major factor affecting the concentration of the hydroxyl radical, OH, which is the main oxidizing agent in the troposphere. Even more important, they control the tropospheric formation of ozone, O_3. Through their impact on tropospheric chemistry the NO_X - although unimportant greenhouse gases by themselves - do also exert an indirect influence on the earth's radiation budget.

Since the response of tropospheric chemistry is highly non-linear with respect to changes in the NO_X concentration [e.g., *Ehhalt and Rohrer*, 1995], the predicted impact of anthropogenic NO_X emissions strongly depends on the initial NO_X distribution. That distribution is poorly known. Because of its short lifetime, the tropospheric concentration of NO_X is highly variable in space and time, and it takes numerous measurements to characterize the global NO_X distribution. An adequate data base for that purpose still does not exist. Aim of the calculations presented in the following is to fill that gap, at least as far as this is possible at the moment. Calculated distributions of NO_X must have a fair degree of uncertainty, since, for example, some of the sources of NO_X are poorly quantified.

3 Model Description

The Chemical Tracer Model CTM used here [*Prather et al.*, 1987] solves continuity equations:

$$\frac{\partial \rho_i}{\partial t} = -\nabla \cdot (\mathbf{u} \cdot \rho_i) + \left(\frac{\partial \rho_i}{\partial t}\right)_{\text{source}} + \left(\frac{\partial \rho_i}{\partial t}\right)_{\text{dep}_{\text{wet}}} + \left(\frac{\partial \rho_i}{\partial t}\right)_{\text{dep}_{\text{dry}}} + \left(\frac{\partial \rho_i}{\partial t}\right)_{\text{chem}} \quad (1)$$

for chemically reactive tracers $i \in \{NO_X, HNO_3\}$ on an Eulerian grid with a spatial resolution of 10° × 8° (longitude × latitude) and 9 sigma layers in the vertical between the Earth's surface and 10 hPa. The temporal resolution of the CTM is 8 hours for dynamical processes and 1 hour for sources, sinks, and chemistry. The meteorological input data which are necessary to run the CTM are provided by the GISS GCM [*Hansen et al.*, 1983]. The photolysis rates J_{NO_2} and J_{HNO_3} as well as the mixing ratios of O_3 and OH are prescribed as 5-day mean values [for references, see *Kraus et al.*, 1996]. Important consequence thereof is the fact that the model chemistry is linear.

source	emission rate (range of estimates) [Mt N yr^{-1}]	annual cycle
fossil fuel combustion	21.9 (13.1 - 28.9)	no
soil microbial activity	4 (1 - 20)	yes
lightning discharges	5 (2 - 10)	yes
biomass burning	4.4 (2.5 - 16.5)	yes
transport from the stratosphere	0.65 (0.3 - 0.9)	yes
aircraft emissions	0.45 (0.45 - 0.85)	no

Table 1: Sources and emission rates used in the CTM.

The sources included in the CTM are listed in Table 1 together with their emission rates assumed here. Figure 1 shows maps of source distributions during January and July for three types of sources. Details and references of the source parameterizations are given by *Kraus et al.* [1996], except for the new lightning source parameterization used here, which is discussed in *Kraus* [1996].

Dry deposition acts as a sink of NO_X and HNO_3, whereas the wet deposition processes washout and rainout only affect the water soluble species HNO_3. As in *Ehhalt et al.* [1992], these three sink processes are parameterized in very simple manner here.

4 Results

The tropospheric distribution of NO_X is shown in Figure 3 for January and July at three different altitudes. It is characterized in the lowest model layer by mixing ratios on the order of 1-10 ppbv at the main continental source regions at norhtern mid-latidudes. At other continental regions the NO_X mixing ratio is about 100 pptv. In the middle troposphere, peak NO_X mixing ratios of about 50 pptv are reached in regions of strong vertical mixing. In the tropics, most of the NO_X present at 500 hPa is injected directly at that pressure by lightning. Above the main source regions at northern mid-latitudes, most of the NO_X is lifted from the PBL. In the upper troposphere significantly higher NO_X mixing ratios are obtained than in the middle troposphere. This feature occurs since the models's deep wet convection transports polluted air from the boundary layer directly to that altitude; entrainment does not occur. Further, the chemical lifetime of NO_X is about 10 days in the upper troposphere, whereas it is only 1-2 days in the PBL. The difference between the NO_X patterns for January and July mainly reflects the difference in the corresponding convection patterns.

Vertical profiles with relatively high mixing ratios in the lower and in the upper troposphere and relatively low mixing ratios in between often are called "C-shaped" [*Ehhalt et al.*, 1992]. This C-shaped structure of the tropospheric NO_X distribution is clearly visible in Figure 2 which gives zonally averaged monthly mean values. In addition, this figure shows the strong interhemispheric gradient of tropospheric NO_X mixing ratios.

4.1 Contributions of the Individual Sources

Figure 4 shows how large the zonally averaged relative contributions of the surface sources, lightning, and aircraft emissions are during January and July. Combined with Figure 2, this figure gives the corresponding zonally averaged absolute contributions of the three types of sources.

The most important contributions to the total tropospheric burden of NO_X come from the following individual sources:

1. Fossil fuel combustion: in the lower troposphere at northern mid- and higher latitudes (relative contribution of more than 70% in summer and up to 95% in winter). At southern mid-latitudes, they also are the dominant source.

2. Soil microbial activity and biomass burning: in the tropics near the surface and in the upper troposphere (relative contribution of about 40% for both sources together). Soil microbial activity is the stronger source in July and biomass buring it is in January.

3. Lightning discharges: more than 80% in the tropical middle troposphere throughout the year.

4. Aircraft emissions: make a significant contribution only in the upper toposphere at northern mid-latitudes. Their relative contribution strongly depends on the degree of vertical mixing within the troposphere. It is large (up to almost 70%) in winter and less than 20% in summer.

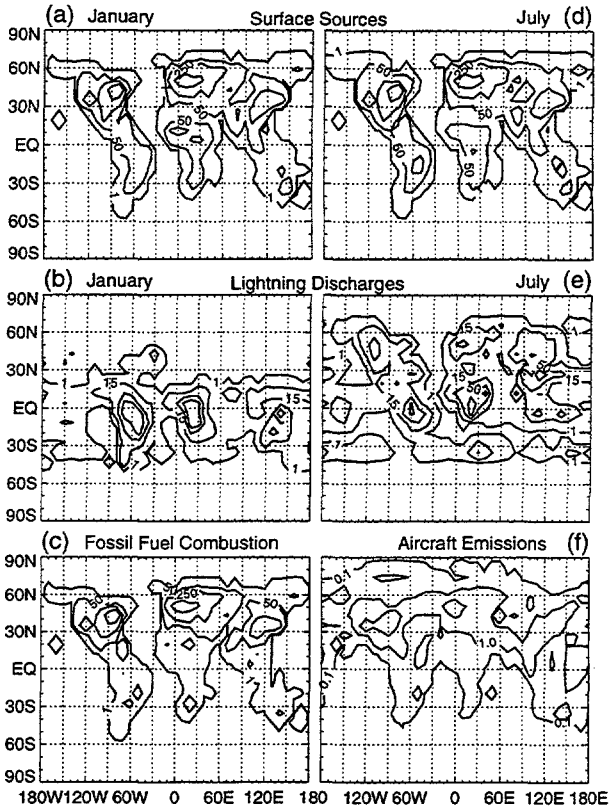

Figure 1: Monthly mean NO_X emission rates with contours at 1, 50, 250, and 1000 mg N m^{-2} yr^{-1} in panels (a), (c), and (d), 1, 15, 50, and 90 mg N m^{-2} yr^{-1} in panels (b) and (e), and 0.1, 1, and 10 pptv in panel (f).

5 Comparison with Observations

Figure 5 shows that the main structure of NO mixing ratios observed in June 1984 during the STRATOZ III aircraft campaign [*Drummond et al.*, 1988] agrees well with corresponding results obtained by the CTM along the flight track. June monthly mean values of the calculation are shown here, because the CTM does not aim at reproducing observed weather situations. Both panels of Figure 5 show a decrease of the NO mixing ratio with altitude in the lower troposphere and an increase when the pressure is lower than about 400 hPa. Both panels also clearly show the interhemipheric gradient of the NO mixing ratio. The CTM underestimates the observed background NO mixing ratio are the southern hemispheric free troposphere and the degree of pollution in the lower troposphere at northen mid-latitudes. On the other hand, it overestimates the amount of NO present in the tropical

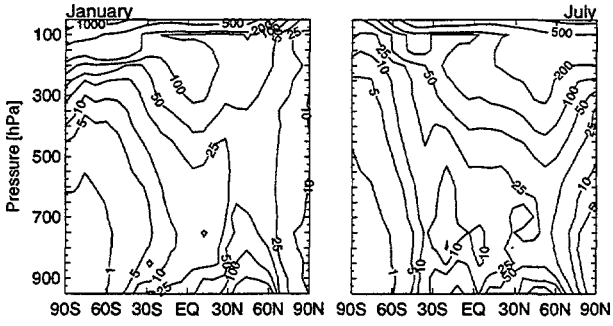

Figure 2: Zonally averaged monthly mean NO_X mixing ratios with contours at 1, 5, 10, 25, 50, 100, 200, 500, and 1000 pptv.

upper troposphere. The latter two features reflect the fact that entrainment processes are missing in the convection parameterization of the CTM. The enhanced NO mixing ratios observed at low altitudes originate in plumes of polluted air close to airports.

Figure 6 shows that the agreement is worse between NO mixing ratios observed in January 1991 during the TROPOZ II aircraft campaign [*Rohrer et al.*, 1996] and corresponding calculated monthly mean values. In the southern hemisphere, the CTM reproduces the structure of the observations quite well, but again underestimates the absolute values. In the northern hemisphere, the observations made during TROPOZ II not necessarily are representative. In fact, NO was considerably enhanced during that campaign in the tropical lower troposphere over Central Africa as a consequence of heavy bush fires. Further, extremely high NO mixing ratios were observed during TROPOZ II in the free troposphere over Canada, the origin of which is unexplained yet. Both these events are local and transient in character and cannot be resolved by the CTM.

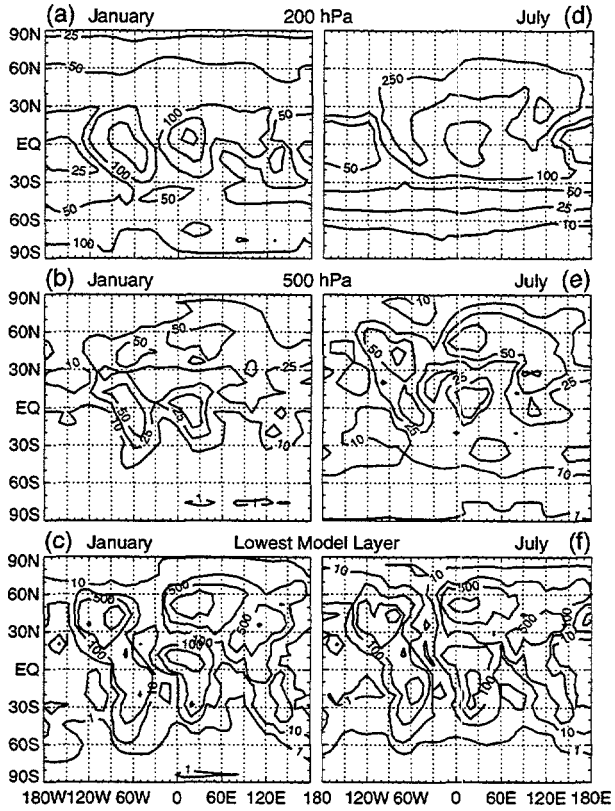

Figure 3: Monthly mean NO_X mixing ratios with contours at 1, 10, 25, 50, 100, 250, and 500 pptv in panels (a), (b), (d), and (e) and at 1, 10, 100, 500, and 2500 pptv in panels (c) and (f).

6 Conclusion

The CTM provides an overview of the global distribution of NO_X in the troposphere.

This distribution is dominated by the surface sources (fossil fuel combustion in particular) at northern mid- and higher latitudes, by lightning acitivity in the tropics, and by aircraft emissions in the winterly upper troposphere at northern mid-latitudes.

The main features of observed NO distributions are reproduced well by the CTM, local effects, however, cannot be resolved.

References

Drummond, J. W., D. H. Ehhalt, and A. Volz, Measurements of nitric oxide between 0-12 km altitude and 67degn-60degs latitude obtained during stratoz iii, *J. Geophys. Res.*, *93*, 15,831–15,849, 1988.

Ehhalt, D. H., and F. Rohrer, The impact of commercial aircraft on tropospheric ozone, in *The chemistry of the atmosphere - oxidants and oxidation in the Earth's atmosphere*, edited by A. R. Bandy, vol. 170 (Spec. Pub.), pp. 105–120. The Royal Society of Chemistry, Lewisburg, PA, USA, 1995.

Ehhalt, D. H., F. Rohrer, and A. Wahner, Sources and distribution of NO_X in the upper troposphere at northern mid-latitudes, *J. Geophys. Res.*, *97*, 3725–3738, 1992.

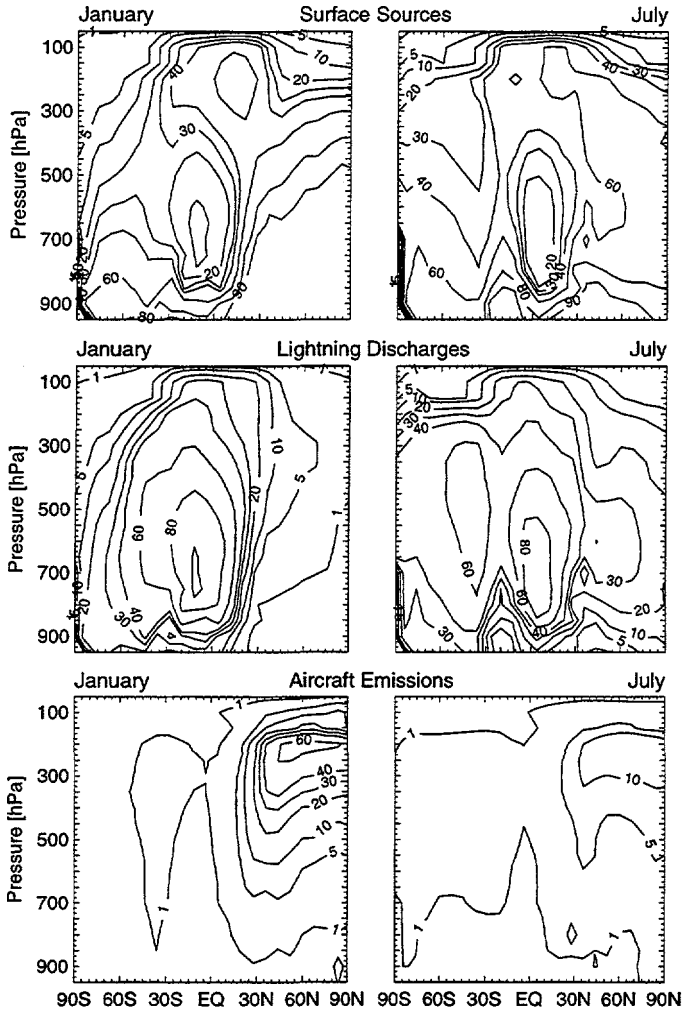

Figure 4: Zonally averaged monthly mean relative contributions of different sources with contours at 1, 5, 10, 20, 30, 40, 60, 80, and 90%.

Hansen, J., G. Russell, D. Rind, P. Stone, A. Lacis, S. Lebedeff, R. Ruedy, and L. Travis, Efficient three-dimensional global models for climate studies: Models I and II, *Mon. Weather Rev.*, *111*, 609–662, 1983.

Kraus, A. B., A three-dimensional model study on the global distribution of tropospheric NO_X, Ph.D. thesis, Universität zu Köln, Köln, Germany, to appear 1996.

Kraus, A. B., F. Rohrer, E. S. Grobler, and D. H. Ehhalt, The global tropospheric distribution of NO_X estimated by a three-dimensional chemical tracer model, *J. Geophys. Res.*, *101*, in press, 1996.

Prather, M. J., M. B. McElroy, S. C. Wofsy, G. Russell, and D. Rind, Chemistry of the global troposphere: Fluorocarbons as tracers of air motion, *J. Geophys. Res.*, *92*, 6579–6613, 1987.

Rohrer, F., D. Brüning, and D. H. Ehhalt, Tropospheric mixing ratios of NO obtained during TROPOZ II in the latitude region 67degn-56degs, *J. Geophys. Res.*, p. submitted, 1996.

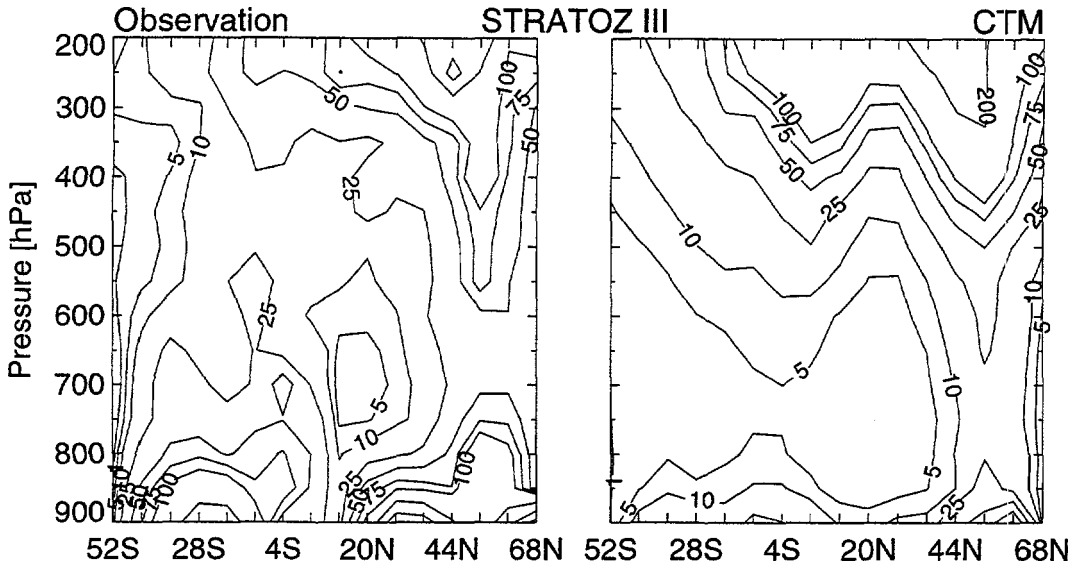

Figure 5: Zonally averaged NO_X mixing ratios with contours at 1, 5, 10, 25, 50, 75, 100, 200, 300, and 400 pptv.
Left panel: Observations from the STRATOZ III aircraft campaign.
Right panel: Monthly mean values calculated by the CTM along the flight track for June.

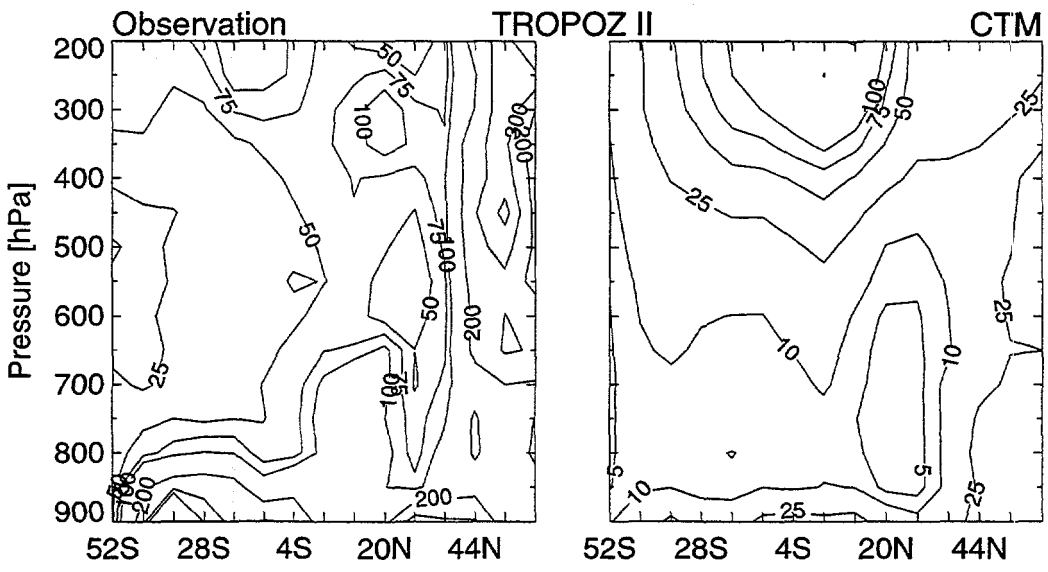

Figure 6: Zonally averaged NO_X mixing ratios with contours at 1, 5, 10, 25, 50, 75, 100, 200, 300, and 400 pptv.
Left panel: Observations from the TROPOZ II aircraft campaign.
Right panel: Monthly mean values calculated by the CTM along the flight track for January.

On the impact of aircraft emitted NOx on upper troposphere photochemistry

Andreas Wahner, Franz Rohrer and Dieter H. Ehhalt

Institut für Atmosphärische Chemie, Forschungszentrum Jülich, Jülich, Germany

Abstract: In a previous paper we showed that emissions by subsonic aircraft contributed about 30% to the burden of nitrogen oxides in the upper troposphere at Northern mid-latitudes [1]. The enhanced nitrogen oxide concentrations influence the photochemical production of ozone as well as to the steady state concentrations of hydroxyl radicals, OH, in the upper troposphere. Current estimates place the resulting zonally averaged increase of summertime ozone around 5%. That increase is small compared to the impact of NO_x from fossil fuel combustion on boundary layer ozone. We have used a simple quasi 2-D model for the latitude band 40°-50° N to analyze the reasons for that. The model includes a simplified CH_4 - CO chemistry and the salient sources of upper tropospheric NO_x, namely lightning, stratospheric input, aircraft emissions and fast upward transport of surface emissions. The differences between the various chemical pathways producing and destroying ozone in the planetary boundary layer on the one hand and in the upper troposphere on the other are closely linked to differences in the local OH chemistry. It is shown that the maximum of net O_3 production and OH concentrations occur at much lower NO_x mixing ratios (200 pptv) than in the lower troposphere. NO_x concentrations in that range are measured at northern mid-latitudes. Therefore, the increase of tropospheric ozone due to increased NO_x by aircraft emissions is expected to be small.

1 PHOTOCHEMISTRY IN THE UPPER TROPOSPHERE

Figure 1 shows the flow diagram describing the major reaction paths controlling the OH concentration and the photochemical ozone production in the upper troposphere. The major differences to the chemistry in the lower troposphere are :

- Because of the low mixing ratio of water vapor, the primary OH formation ($O_3 + h\nu + H_2O$) is up to three orders of magnitude slower.
- The secondary HOx production through oxidation of methane has a much higher yield (about 0.6).
- The removal of HNO_4 by reaction with OH is important (Figure 2).
- The maximum of [OH] and of the ozone production rate is shifted to much lower [NOx] (Figure 3).

2 2-D MODEL CALCULATIONS

To illustrate the effect of the nonlinearities (Figure 3) on the prediction of the changes in the O_3 concentration induced by aircraft emissions we performed a case study with a simple zonal channel model [1]. The model is designed to calculate the altitude by longitude distribution of trace species from 0-14 km altitude in the latitude band 40°-50°N. It calculates transport by advection, vertical eddy diffusion and deep convection. The model includes NO emissions by fossil fuel combustion, biomass burning, soil emissions, lightning, aircraft and stratospheric influx. Due to the fact that over large regions the NO mixing ratios in the upper troposphere (Figure 4) are close to those that produce the maximum OH concentrations, the changes in

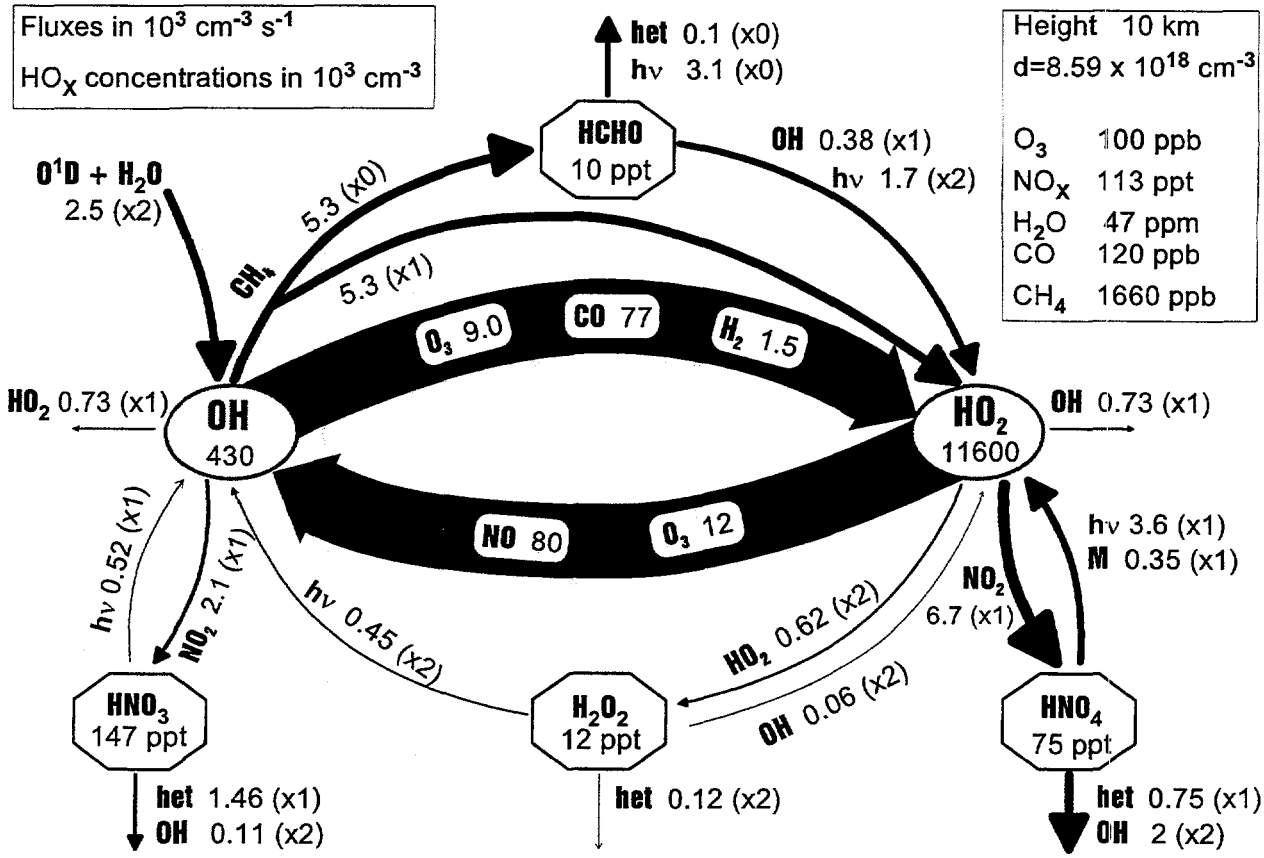

Figure 1: Major reaction paths controlling OH in the upper troposphere

OH due to aircraft emissions (Figure 5) are relatively small and both negative and positive. The changes in the net production of O_3 behave quite similar to the changes in OH. However, because of the long lifetime of O_3 in the upper troposphere, the O_3 mixing ratio increases everywhere (Figure 6). The areas of decreased net O_3 production contribute to the small overall increase of O_3 : on average about 2% at 8-12 km altitude. The major uncertainties in these calculations are:

- Inputs of NOx into the upper troposphere from sources other than aircraft emissions (lightning, fast upward transport of surface emissions).
- The global distributions of H_2O and O_3.
- The photolysis frequencies of O_3, NO_2 and HCHO.
- The products of the reaction of HNO_4 with OH.

References

[1] D. H. Ehhalt, F. Rohrer, and A. Wahner. Sources and distribution of NO_x in the upper troposphere at northern mid-latitudes. *J. Geophys. Res.*, 97:3725–3738, 1992.

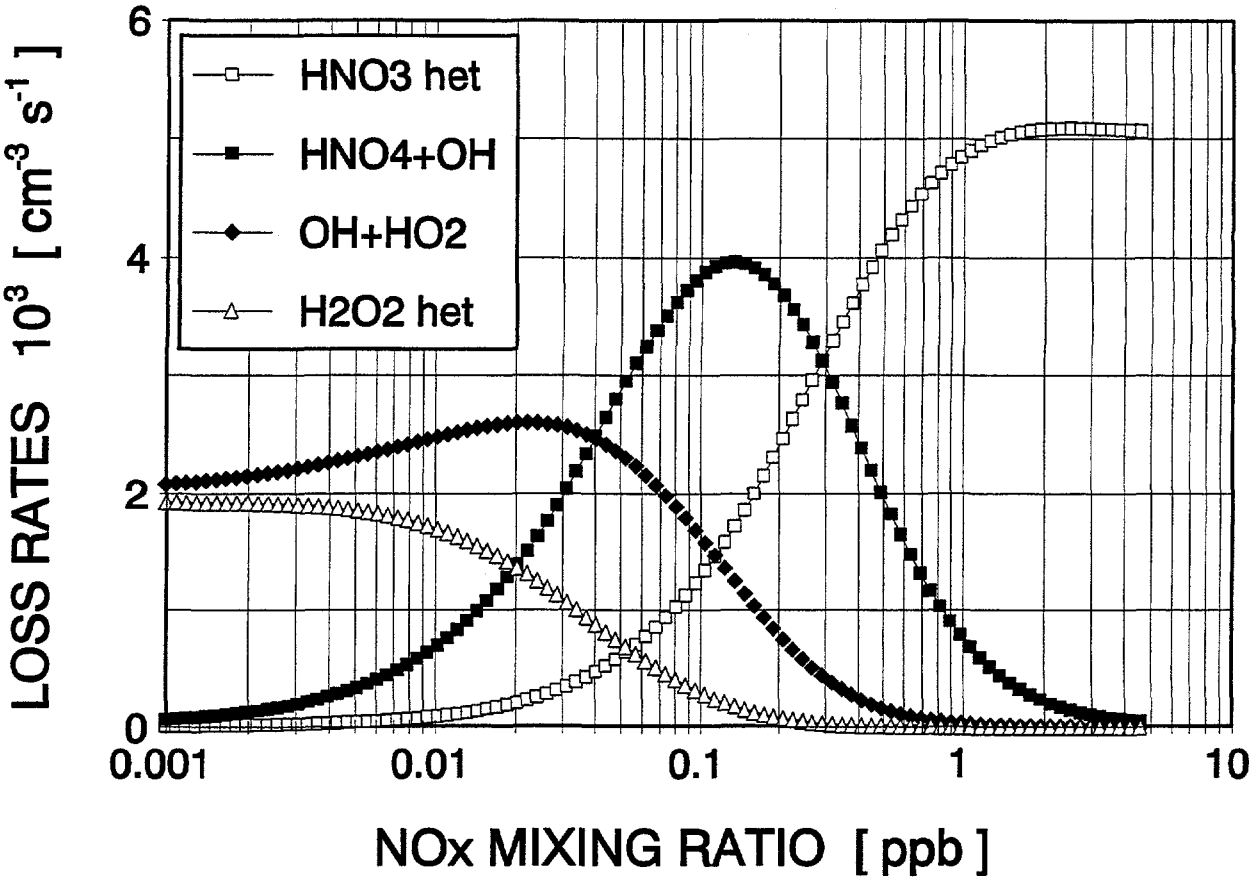

Figure 2: Major net loss reactions of HOx calculated for June, 10 km, 45°N

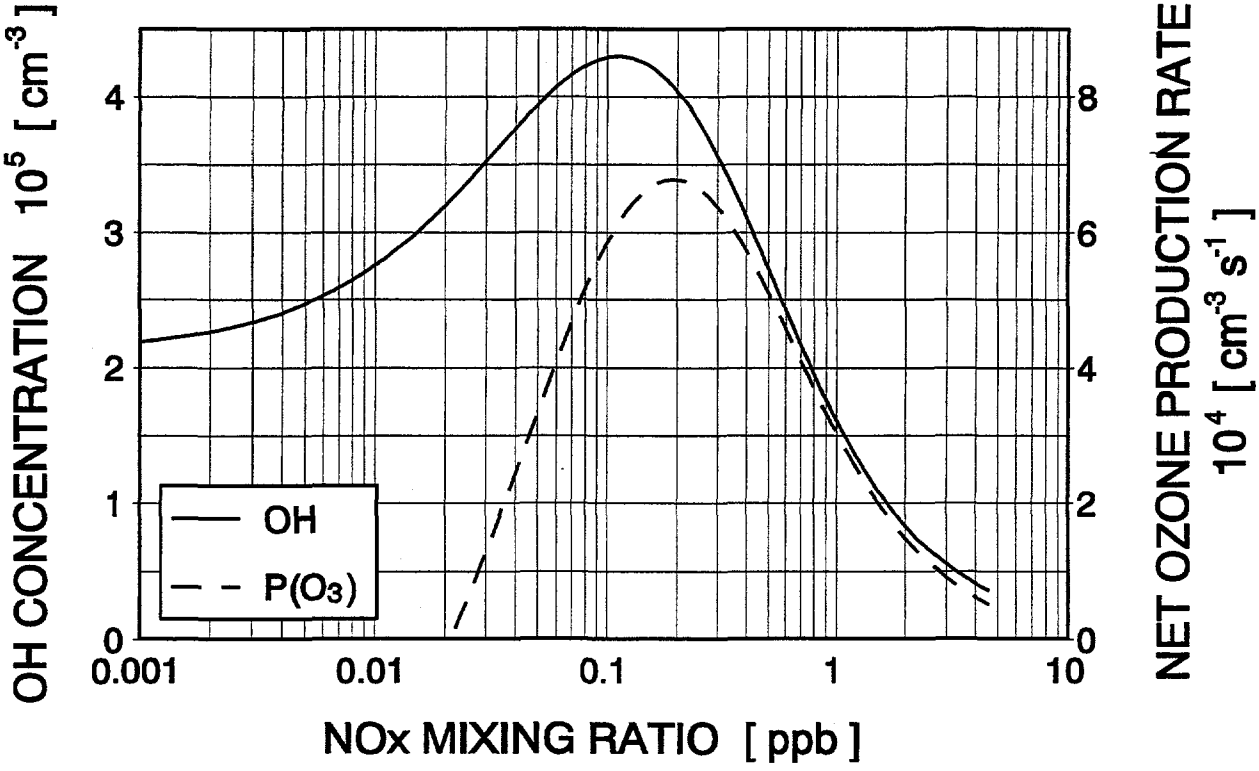

Figure 3: OH and net ozone production vs NOx calculated for June, 10 km, 45°N

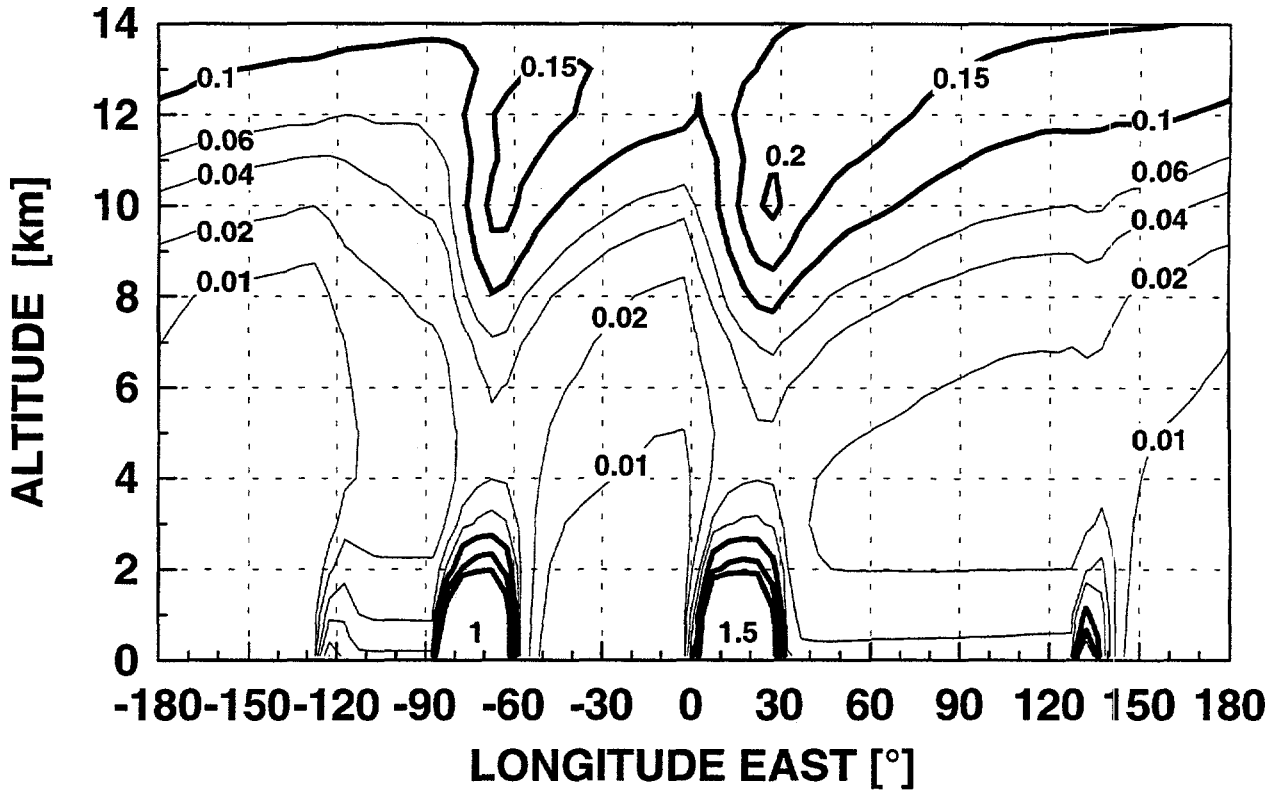

Figure 4: Calculated zonal distribution of NO during June 1984, 45°N

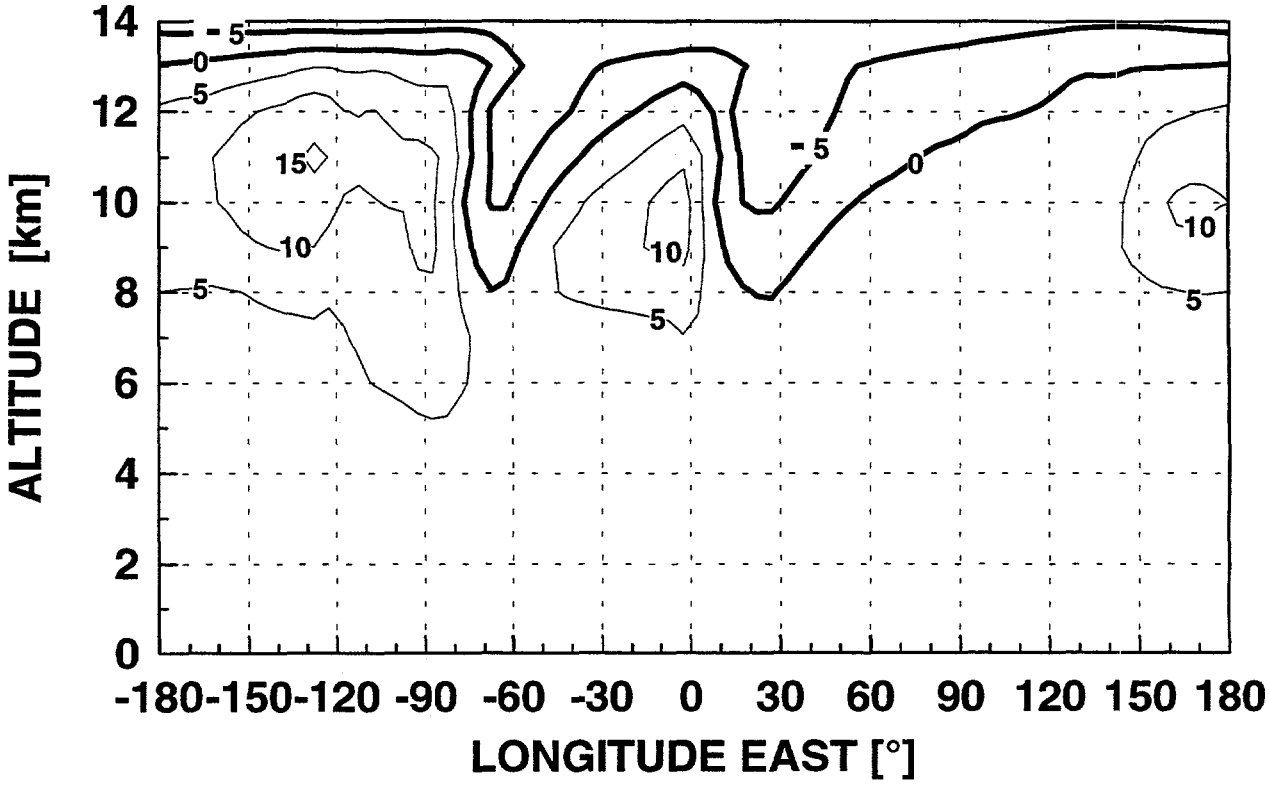

Figure 5: Calculated relative change of OH induced by aircraft emissions of NO (June, 45°N)

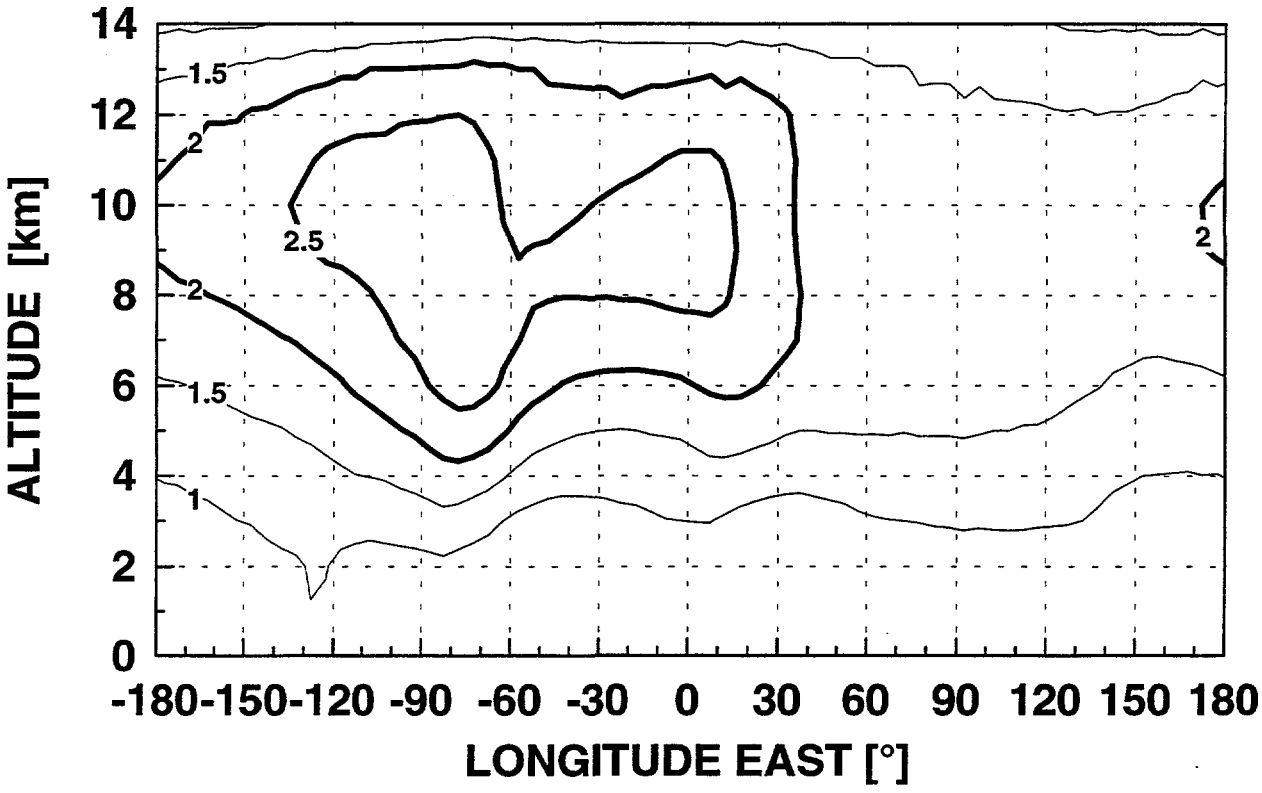

Figure 6: Calculated relative change of O_3 induced by aircraft emissions of NO (June, 45°N)

The role of convective tracer transport for the NO_x content in the North Atlantic flight corridor

Ines Köhler and Robert Sausen
DLR, Institut für Physik der Atmosphäre, Oberpfaffenhofen, Germany

Abstract

The effect of convective tracer transport on the NO_x distribution at cruising altitudes is studied by means of the atmosphere general circulation model ECHAM which was extended by a simplified (linear) NO_x chemistry module. NO_x originates from several sources including aircraft emissions. Two numerical simulations have been performed: one including convective tracer transport and one without this process. The differences in the NO_x distribution of these two runs are discussed~~, in this paper~~.

1. Introduction

Surface sources substantially contribute to the NO_x burden of the upper troposphere at the northern mid latitudes. Brasseur et al. (1996) found that in July ≈25% of NO_x in the upper troposphere of the northern mid latitudes is provided by surface sources. Köhler et al. (1996) show that for the same month more than 55% of the atmospheric NO_x content in the same region originates from these sources. It is well known that convective transport is an important dynamic process with large impact on the vertical structures of temperature, moisture, and mixing ratios of chemical species. In this paper we investigate the quantitative importance of convection to tracer distributions, in particular to the NO_x distributions arising from different sources.

2. Model and Experiments

The investigations were carried out by means of the atmosphere general circulation model ECHAM3/T21 (Roeckner et al., 1992; Lohmann and Roeckner, 1995), which was extended by a simplified (linear) NO_x chemistry modul (Köhler et al., 1996). ECHAM is a state of the art GCM. Tracers are advected by a semi-Lagrangian scheme. Cumulus convection including convection of tracers is parametrized on the basis of a mass flux approach, comprising the effects of deep, shallow, and mid level convection (Tiedtke, 1989).

The simplified chemistry treats NO_x (NO_x=NO+NO_2) and HNO_3 as prognostic variables. The nitrogen compounds are eventually removed from the atmosphere by dry deposition, and HNO_3 additionally by wash–out. The background–concentrations of OH and O_3 are prescribed. Due to the linearity of the chemistry modul, NO_x and HNO_3 from separate sources can be treated independently. This has several advantages with respect to the scientific insight. The relative contribution of individual sources to the total burden of NO_x can be calculated for each source from the results of one single simulation. As the total emissions for various sources are quite uncertain, it might be necessary to rescale the results which can be done easily. Further details about the model can be found in Köhler et al. (1996).

NO_x is mainly produced by fossil fuel combustion, biomass burning, soil microbial activity, lightning, degradation of N_2O in the stratosphere, and aircraft emissions (*Tab. I*). The latter emissions have been specified according to the ANCAT/DLR flight emissions data base (ANCAT, 1995). From the total surface sources data set (Lee et al., 1996), which

Table I - Input of NO_x into the atmosphere from various sources as used in our model simulations.

sources	amounts [Tg (N) yr^{-1}]
aircraft (ANCAT/DLR database)	0.85
total surface sources (industry and surface traffic + + soil microbial activity + biomass burning)	31.2
surface sources USA	5.8
surface sources Europe	8.5
surface sources Asia	5.3
surface sources southern hemisphere	5.2
lightning	5.0
stratospheric production	0.64

includes the NO_x emissions by fossil fuel combustion, biomass burning, and soil microbial activity four different regional data sets were extracted: NO_x surface emissions from the United States, Europe, Asia, and the southern hemisphere.

In order to quantify the role of the convective tracer transport, two ten–year simulations in seasonal cycle mode were performed, in which the convective transport for tracers was either switched on or off. These simulations where preceded by a sufficiently long spin–up period (Köhler et al., 1996).

The resulting June and November[1] mean distributions of NO_x (with and without convective tracer transport) and the relative contributions of the different sources to the total atmospheric NO_x burden are analysed in the North Atlantic flight corridor (NAFC), including the contributions of surface sources from different countries or continents. The difference between the control run (convective tracer transport is switched on) and the run without convective tracer transport gives the effect of this process to the NO_x distribution: positive values indicate an increase of NO_x and negative values a decrease.

3. Results

June and November means of the NO_x concentrations were calculated over a 10–year period. The values in the *Tables II, III,* and *IV* are calculated for the region 28°N to 72°N, 82°W to 14°E, and 175 to 325 hPa, which includes the NAFC and which is contained in the figures.

3.1 Contributions of aircraft and surface emissions to the total NO_x burden of the atmosphere in the North Atlantic flight corridor

Figure 1a shows the distribution of total NO_x at 200 hPa as calculated by ECHAM3 for June (left) and November (right) in the NAFC region (when convection is switched on). In November the NO_x distribution is more zonally homogeneous than in June, as the zonal wind component is larger, and the contributions are much smaller. In June and in November relative maxima with concentrations higher than 375 pptv and 150 pptv, respectively, are found over Europe. The seasonal differences in the NO_x mixing ratios are due to stronger vertical transport in June. In the eastern part of the NAFC the simulated mixing ratios of the total NO_x burden are about 225 pptv in June and 140 pptv in November. These values have been confirmed by the POLINAT campaign (Schlager et al., 1996). The measured median NO values were 125 pptv and 75 pptv for the summer and winter flights, respectively, with

[1]June and November were analysed because measurements in the NAFC are available for these months (Schlager et al., 1996).

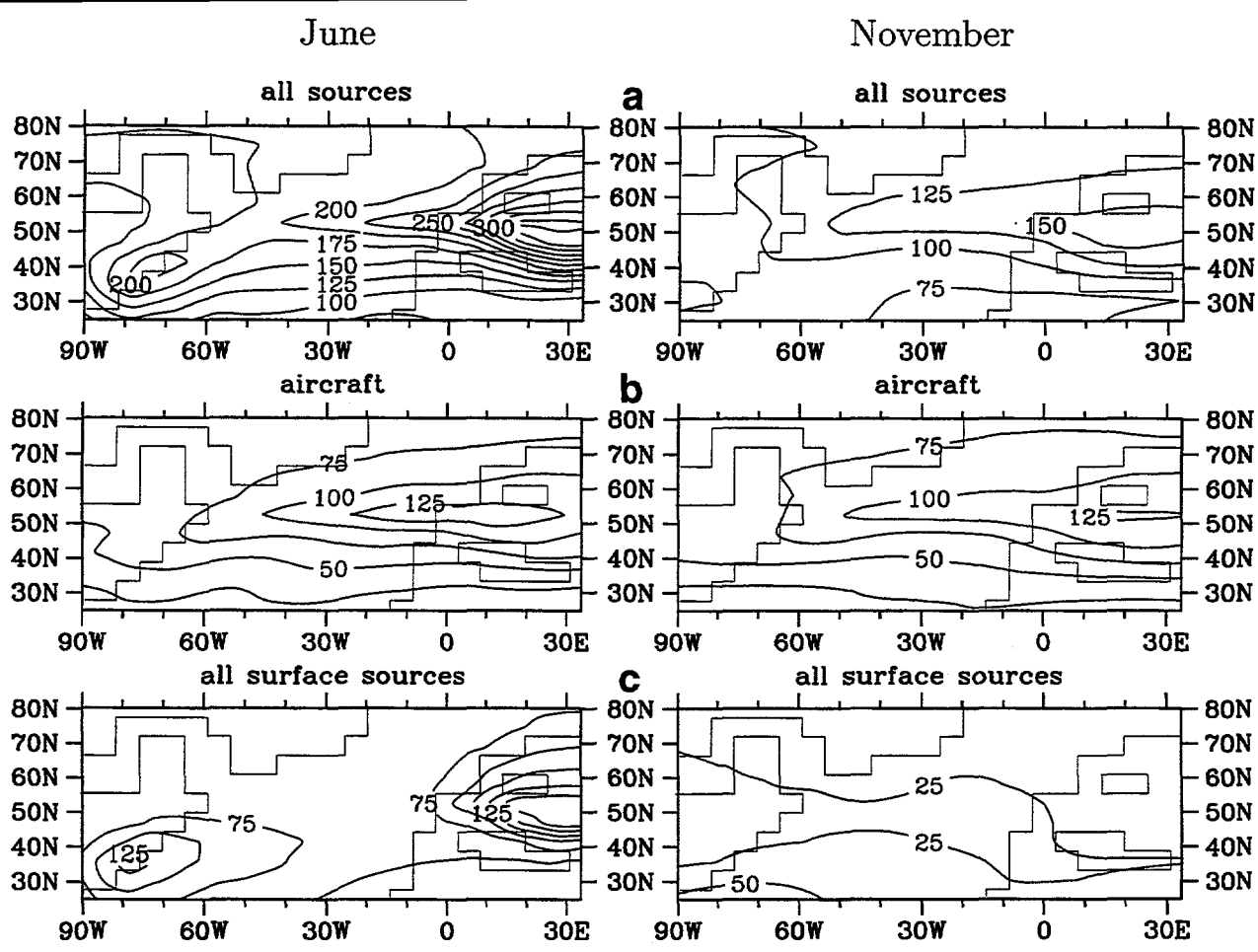

Fig. 1 - June (left) and November (right) mean NO_x volume mixing ratios at 200 hPa as calculated by ECHAM3 with all NO_x sources included (a), with aircraft emissions only (b), and with all surface emissions only (c). Convective tracer transport is switched on. Contour interval: 25 pptv. The land–sea–mask indicates the horizontal resolution of the model.

a standard deviation of ± 70 pptv. Using measured NO and O_3 mixing ratios, calculated photo dissociation coefficients of NO_2 and assuming a photochemical steady-state, the total observed mean NO_x concentration in this area is about 150 pptv in June/July and 100 pptv in November with an uncertainty of 20% to 30%.

The contribution of aircraft to the NO_x mixing ratio is shown in *Figure 1b* for June (left) and November (right). In both months the NO_x distribution due to aircraft emissions is not fundamentally different from each other.

Contrary to the aircraft emission results the June and November mean distributions of surface emissions are completely different (*Fig. 1c*). Not only that the NO_x values are much higher in June than in November (more than 175 pptv in June in contrast to 25 pptv in November) but also the horizontal pattern is different. In November the structure is almost zonal, but not in June. High NO_x mixing ratios can be locally found over Europe and North America.

The relative contributions of aircraft emissions and surface emissions to the total NO_x burden at 200 hPa (*Fig. 2*) are quite different for the two months: in November aircraft contribute more than 70% to the total NO_x burden in the NAFC and over Europe (*Fig. 2a right*). In June the respective numbers are lower: less than 60% in the NAFC and about 40% over

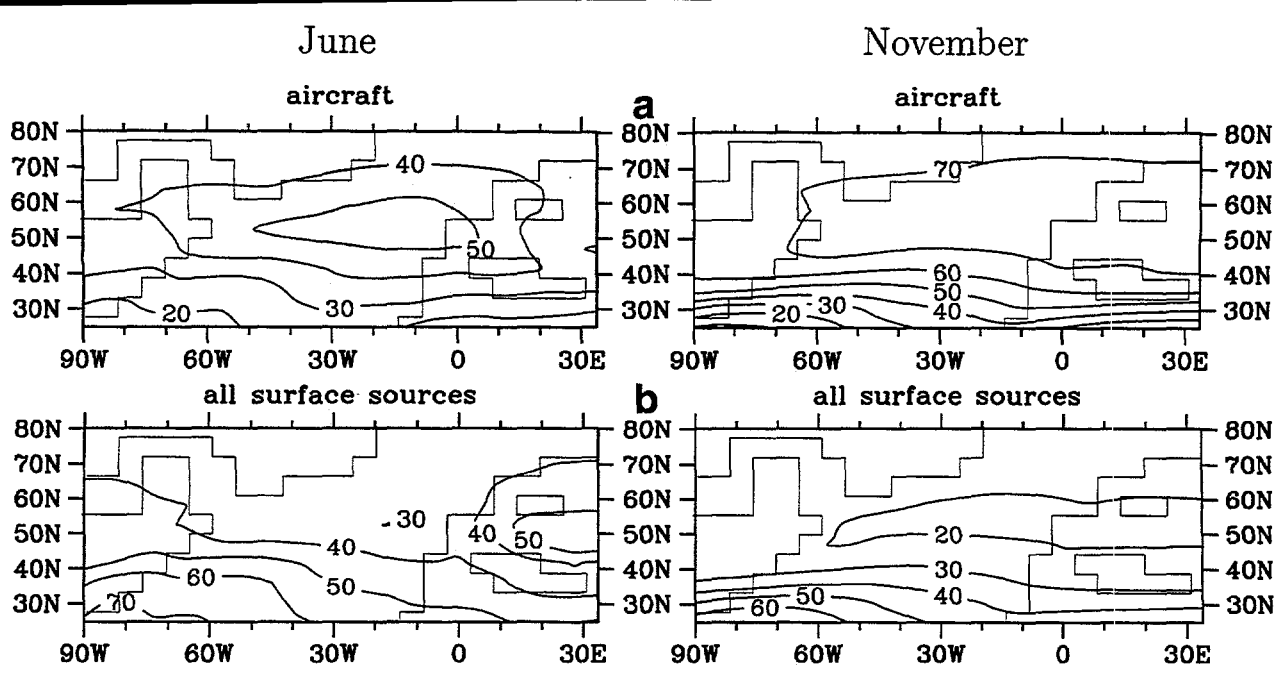

Fig. 2 - June (left) and November (right) mean relative contributions of aircraft emissions (a) and surface emissions (b) to the total concentration of NO_x at 200 hPa as calculated by ECHAM3. Convective tracer transport is switched on. Contours are drawn at intervals of 10%.

Europe. The relative contributions of the surface emissions are almost vice versa (*Fig. 2b*): lower in winter ($\approx$ 20%) and higher in summer ($\approx$ 35% in the NAFC and $\approx$ 50% over Europe).

3.2 Relative contributions of individual sources to the atmospheric NO_x burden in the North Atlantic flight corridor

The absolute and relative contributions of all (aircraft and non–aircraft) sources of nitrogen oxides to the total NO_x burden for June and November in the NAFC are summarized in *Table II*. The smallest relative contributions (< 7%) arise from the stratospheric input, from surface sources from Asia and from the southern hemisphere throughout the year. In winter the relative contribution by lightning is of similar magnitude, but in summer it is somewhat higher. The highest relative contribution of more than 60% is caused by aircraft emissions in winter. In summer it is less than 40%. Now the highest relative contribution is caused by surface sources (50%). In winter the absolute and relative contributions of surface sources are much smaller. Surface sources in the USA and Europe differently contribute to the NO_x background concentration in June (23% and 14%, respectively), but smaller and almost equally in November. The contribution of surface emissions from Europe is smaller than from USA, because the emissions in the upper troposphere are mainly transported eastward. The seasonal variation of the individual contributions primary originates from different convective tracer transport (see Section 3.3).

3.3 Impact of convective tracer transport

Figure 1 and *Table II* show that the total NO_x content in the NAFC is about a factor 1.5 higher in June than in November. Especially, the NO_x contributions due to the total surface emissions and the surface emissions from the USA, Europe, Asia and the southern hemisphere are up to 4 times higher in June than in November, despite the fact that the surface sources have no annual cycle. That indicates that due to stronger vertical tracer transport in June

Table II - Masses (absolute contributions) of individual NO_x sources as calculated by ECHAM3 in June and November (left) and relative contributions of individual NO_x sources to the total atmospheric burden of NO_x (right) in the region 28° N to 72° N, 82° W to 14° E, and 175 to 325 hPa. Convective tracer transport is switched on.

source	absolute contribution [10^6 kg (NO_2)]		relative contribution [%]	
	June	November	June	November
total	12.27	7.82	—	—
surface sources	6.12	2.33	49.9%	29.8%
aircraft	4.72	4.95	38.5%	63.3%
lightning	1.07	0.53	8.7%	6.8%
stratospheric input	0.35	0.00	2.9%	0.0%
surface USA	2.85	0.65	23.3%	8.3%
surface Europe	1.62	0.39	13.7%	5.0%
surface Asia	0.68	0.55	5.5%	7.0%
surface south. hem.	0.06	0.05	0.5%	0.7%

Table III - Masses of individual NO_x sources as calculated by ECHAM3 for June and November in the region 28° N to 72° N, 82° W to 14° E, and 175 to 325 hPa with and without convection. The last two columns show the differences in the masses from individual NO_x sources between the control run and the run without convective tracer transport.

		mean values [10^6 kg (NO_2)]		differences [10^6 kg (NO_2)] (with minus without convection)	
source	convection	June	November	June	November
total	yes	12.27	7.82	5.17	1.31
	no	7.10	6.51		
surface sources	yes	6.12	2.33	5.44	1.77
	no	0.68	0.56		
aircraft	yes	4.72	4.95	–0.14	–0.08
	no	4.86	5.03		
surface USA	yes	2.85	0.65	2.56	0.40
	no	0.29	0.25		
surface Europe	yes	1.68	0.39	1.63	0.33
	no	0.05	0.06		

much more surface emissions are transported in the upper troposphere. According to *Tables III and IV* the contributions of the surface sources to the NO_x content in the NAFC are strongly influenced by convective tracer transport. When convective tracer transport is switched off in the model simulation almost no surface emissions are transported in the NAFC, both in June and in November. The relevance of convective processes is more distinct in summer than in winter, e.g. about 90% of the NO_x content due to all surface sources is transported by convective tracer transport in the upper troposphere in June (*Tab. IV*), the corresponding value for November is about 75%. Remind that in November less convective events occur than in June.

The effect of convective tracer transport to the contribution of aircraft emissions is very small and negative (*Tabs. III* and *IV*). If convection is switched off less NO_x is removed from the upper atmospheric levels.

Table IV - Ratio [%] of the NO_x content in the region 28°N to 72°N, 82°W to 14°E and 175 to 325 hPa which is caused by convective tracer transport. Positive values indicate an increase of the NO_x content due to convection and negative values a decrease.

	June	November
all sources	42.1%	16.8%
surface sources	88.8%	76.0%
aircraft	–3.0%	–1.6%
surface sources USA	89.8%	61.5%
surface sources Europe	97.0%	84.6%

4. Conclusions

The role of convective tracer transport on the NO_x distribution in the North Atlantic flight corridor was quantified. The convective tracer transport is the main physical process which leads to transportation of surface NO_x emissions into the North Atlantic flight corridor. Since these emissions are responsible for 50% of the NO_x content in this region, tracer transport due to convection is necessary to simulate a realistic NO_x content. Only then the changes in the ozone production rate due to aircraft NO_x emissions can be quantified.

Acknowledgments. This study was supported by the Commission of the European Community through grant EV5V-CT93-0310 (POLINAT project). The authors are grateful to the participants of the SP 2 group of the POLINAT project for helpful discussions. We also would like to thank Dr. Hans Feichter and Dipl.-Met. Ulrich Schlese for their assistance in running the ECHAM model.

References

ANCAT, 1995: A global inventory of aircraft NO_x emissions – A first version (April 1994) prepared for the AERONOX research project. In U. Schumann (ed.): AERONOX – The Impact of NO_x Emissions from Aircraft upon the Atmosphere at Flight Altitudes 8–15 km. EC–DLR Publication on Research Related to Aeronautics and Environment, Oberpfaffenhofen, 129–194.

ARNOLD, F. et al., 1995: Upper Tropospheric SO_2–Pollution and Condensation Nuclei Formation: Evidence from Aircraft Measurements over the North Atlantic. Submitted to *Geophys. Res. Lett.*

EHHALT, D.H. et al., 1992. *J. Geophys. Res. 97*, 3725–3738.

KÖHLER, I. et al., 1996: Contributions of Aircraft Emissions to the Atmospheric NO_x Content. *Atmos. Environ.*, in press.

LEE, D.S. et al., 1996: Estimations of Global NO_x Emissions and Their Uncertainties. *Atmos. Environ.*, in press.

LOHMANN, U. and E. ROECKNER, 1995. *Geophys. Res. Lett. 100*, 16306–16323.

ROECKNER, E. et al., 1992: Simulation of the present–day climate with the ECHAM model: impact of model physics and resolution. Max–Planck–Institut für Meteorologie, Report No. 93, ISSN 0937–1060, 171 pp.

SCHLAGER, H. et al., 1996: Aircraft–borne Measurements of NO_x, O_3, and CO_2. Pollution from Aircraft Emissions in the North Atlantic Flight Corridor (POLINAT). Draft version to the Commission of the European Communities (CEC Contract EV5V-CT93-0310), 6–33. Available from DLR–Institut für Physik der Atmosphäre, Oberpfaffenhofen, D–82234 Weßling, Germany.

Implications of Imprecision in Kinetic Rate Data for Photochemical Model Calculations

Richard W. Stewart, Anne M. Thompson
NASA Goddard Space Flight Center
Greenbelt, MD USA 20771

Abstract. Evaluation of uncertainties in photochemical model calculations is of great importance to scientists performing assessment modeling. A major source of uncertainty is the measurement imprecision inherent in photochemical reaction rate data that modelers rely on. A rigorous method of evaluating the impact of data imprecision on computational uncertainty is the study of error propagation using Monte Carlo techniques. There are two problems with the current implementation of the Monte Carlo method. First, there is no satisfactory way of accounting for the variation of imprecision with temperature in 1, 2, or 3D models; second, due to its computational expense, it is impractical in 3D model studies. ~~This paper addresses~~ These difficulties, are discussed

1. Introduction. The reaction rate data available for use in modeling studies consists of rate components and their associated imprecisions. These are tabulated in references such as [1] which we will refer to in this paper as 'the standard compilation'. Formulae for the rates are constructed from these components. For bimolecular rates the components typically consist of an activation temperature, a rate value at 298K, an Arrhenius coefficient, and imprecisions in the first two of these. The Arrhenius coefficient is not an independent datum, but is given for convenience. In this paper we investigate some implications of treating the given rate components as random variables with statistical properties derived from the stated component values and their imprecisions. We assume that the activation temperature and rate at 298K are, respectively, normally and lognormally distributed random variables. This leads to the conclusion that the reaction rate is a lognormally distributed random variable. We derive analytic expressions for the mean and median rates and show that the value used in modeling calculations is the median. The mean rate differs from the median through the explicit incorporation of component imprecisions in its analytic expression.

We have two goals in this paper. First, we seek a simple method of accounting for the change of rate imprecision with temperature in Monte Carlo studies of error propagation. We expect this to be of use in 1D and 2D model studies. Second, since Monte Carlo studies are impractical with 3D photochemical models, we develop a method which we suggest may be of use in estimating the effects of error propagation in such models.

Our first objective in attaining these goals will be to relate the data given for reaction rate components in the standard compilation to statistical properties of random variables. This will be the subject of section 2. Section 3 will then discuss the consequences of these relationships. We will deal only with bimolecular reaction rates. The results may be generalized, however, to termolecular and thermolysis rates [2].

2. A Reaction Rate Model for Uncertainty Estimation. To develop methods for establishing the relationship between imprecisions in kinetic rate data and species uncertainties in

photochemical model results we must make some initial assumptions about that data. We will make two qualitative and three quantitative assumptions,

Our first and most basic qualitative assumption is that we accept the stated rate values and imprecisions at face value. In effect, this means that although we realize that these data include a subjective component, we treat them as though they resulted from analysis of a body of measurements and as though these measurements were subject only to random and not systematic errors. Our second qualitative assumption is to interpret the rates and imprecisions of the standard rate compilation as statistical properties of random variables. This assumption is not necessary to the use of the rate data for calculating concentrations in photochemical models, but it is essential to their use in the study of error propagation in such models.

Our second qualitative assumption leads us to the first two of the quantitative assumptions that form the basis of our analysis.

1) The activation temperature and its imprecision, θ, $\Delta\theta$, are assumed to be the mean and standard deviation of a normally distributed random variable. We will also refer to this variable, Θ, as activation temperature.

2) The rate at 298K , k_0, and its associated imprecision, f_0, are assumed to be statistical properties of a lognormally distributed random variable, K_0, the rate coefficient at 298K.

We introduce a random variable, $X(\Theta)$, which depends on the random variable representing activation temperature, Θ, and on two parameters: temperatures, T, and $T_0 = 298$K.

$$X(\Theta) = \exp\left[\Theta\left(\frac{1}{T_0} - \frac{1}{T}\right)\right] \tag{1}$$

The random variable representing the reaction rate, $K(K_0, \Theta)$, is now defined as

$$K(K_0, \Theta) = K_0 \cdot X(\Theta) \tag{2}$$

and this leads us to the statement of our third assumption.

3) K_0 and $X(\Theta)$ are independently distributed.

The assumption that Θ is normally distributed implies that $X(\Theta)$ is lognormally distributed. The assumptions that K_0 is lognormally distributed and that K_0 and X are independently distributed leads to the conclusion that the reaction rate, K, is a lognormally distributed random variable. Details of the derivation of the statistical properties of K in terms of those of K_0 and Θ are given in [2]. Here we summarize the results.

The Arrhenius coefficient is given by the usual expression,

$$A = k_0 \exp\left(\frac{\theta}{T_0}\right) \tag{3}$$

The median of the lognormal distribution representing the reaction rate, K, is

$$k(T) = A\exp\left(-\frac{\theta}{T}\right) \tag{4}$$

and the mean is

$$\kappa(T) = \sqrt{1 + (f_0 - 1)^2}\, k(T) \exp\left(\eta(T)/2\right) \tag{5}$$

where the temperature dependent argument in the exponential is

$$\eta(T) = \left[\frac{\Delta\theta}{T_0}\left(1 - \frac{T_0}{T}\right)\right]^2 \tag{6}$$

This completes our initial objective of formulating the statistical properties of bimolecular chemical reaction rates, viewed as random variables, in terms of the data given in the standard compilation. We see that it is the median rate that is universally used in computing temperature dependent rates in photochemical models. The mean rate differs from the median through its explicit incorporation of the imprecisions f_0 and $\Delta\theta$.

One additional consequence of our assumptions is that the temperature dependence of the rate imprecision differs from the expression given in [1]. Their heuristic expression is

$$f(T) = f_0 \exp\left(\frac{\Delta\theta}{T_0}\left|1 - \frac{T_0}{T}\right|\right) \tag{7}$$

while our derivation of eqs. (4) and (5) leads to

$$f(T) = 1 + \left\{\left[1 + (f_0 - 1)^2\right]\exp\left[\frac{\Delta\theta}{T_0}\left(1 - \frac{T_0}{T}\right)\right]^2 - 1\right\}^{\frac{1}{2}} \tag{8}$$

Note that both reduce to $f(T) = f_0$ when $T = T_0$. The expression for the temperature dependence of the imprecision which we have found, eq (8), generally leads to a smaller increase in rate imprecision with increasing temperature difference from T_0 than does the imprecision given by eq. (7). Additional discussion of the differences in these expressions is given in [2].

3. Results. In this section we present two results following from the assumptions and subsequent derivation given in section 2. The first of these results is a prescription for incorporating the temperature dependence of reaction rate imprecision in Monte Carlo models which sample rate values on a grid over which temperature varies. The second is a suggested method of estimating the relative magnitudes of species concentration uncertainties resulting from given imprecisions in reaction rate components.

The procedure we use in computing sample rates for a Monte Carlo calculation is based on our assumptions regarding the probability distributions for random variables representing activation temperature, θ, and the rate at 298K, k_0. There are three steps:

1) Select a random variable from a normal distribution representing activation temperature. There is a distribution for each temperature dependent rate with mean and standard deviation taken from the standard compilation. We designate the sample activation temperature by θ_r.
2) Select a random variable from the lognormal distribution representing the rate at 298K. The mean and standard deviation are related to the quantities k_0 and f_0 given in the standard compilation [2]. Designate this component as k_{0r}.
3) Compute each model rate for the current Monte Carlo run using equations 1) and 2)

$$k_r(T) = k_{0r}\exp\left[\theta_r\left(\frac{1}{T_0} - \frac{1}{T}\right)\right] \tag{9}$$

After a series of Monte Carlo runs it may be verified that the numerical means of the rates given by eq (9), at a specified temperature, agree with the analytic expression given by eq. (5) and that the temperature dependence of the imprecisions is given by eq. (8). Note that the numerically computed mean should be compared with the theoretical mean given by eq. (5) rather than the

theoretical median given by eq. (4). Mean values are larger than the medians for a lognormal distribution.

Our second result is more in the nature of a conjecture than a proof. Our assertion is that if we make two model runs using median rates in one and mean rates in the other, then the differences in species concentrations in these two runs will order themselves in approximately the same way, largest to smallest, as would the concentration uncertainties computed from a series of Monte Carlo runs. We reason as follows. Although modeled species will depend to some degree on a large number of reaction rates, they typically will depend sensitively on only a few. A quantitative expression of this fact may be found in rate-species correlations computed with a Monte Carlo model [3]. If one or more rates to which a species is sensitive have large mean-median differences there will be correspondingly large concentration difference when these alternate rate formulations are used in model runs. Large mean-median differences are a consequence of large imprecisions, however, and such rates therefore have major impact on concentration uncertainties in Monte Carlo calculations.

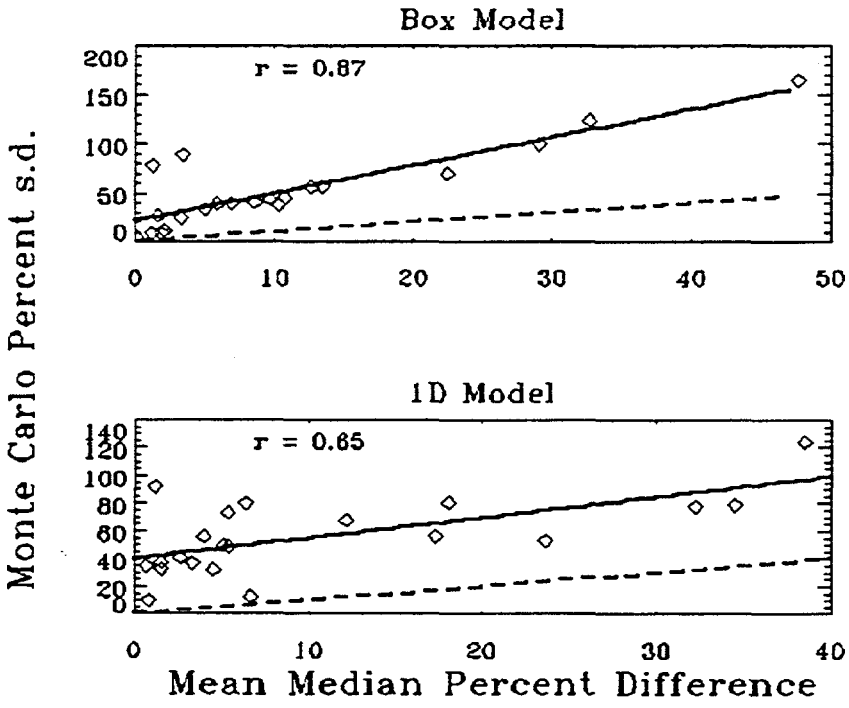

Fig. 1 Comparison of concentration differences using median and mean rates with uncertainties obtained from Monte Carlo calculations. The abscissas are absolute values of the difference expressed as a percentage of the value obtained with median rates. The ordinates are standard deviations expressed as a percentage of the mean.

We have tested its validity of this conjecture using two independently developed models. One of these is the 1D model used in the Monte Carlo study of [3] updated with rate values from [1] and with the algorithm given in eq. (9). The second is the box model described in [4] with modifications necessary for the Monte Carlo mode. The results shown for the 1D model are taken from the 10 km. altitude level. The temperature and pressure assumed for the box model calculations are also characteristic of 10 km. This is the altitude of interest for study of the impact of subsonic aircraft emissions on the atmosphere. A fuller description of these models is given in [2]. Each model was used to compare concentration differences resulting from the selection of median rates in one case and mean rates in a second, then used in a full Monte Carlo calculation of concentration uncertainties. *Fig. 1* shows a comparison of the Monte Carlo uncertainties with the absolute value of the mean median difference for the box model (upper panel) and 1D model

(lower panel). The abscissas are the absolute values of the percent differences in species concentrations using mean rates and median rates with the median case taken as the standard. The ordinates are the Monte Carlo uncertainties, or standard deviations, expressed as a percentage of the means. The solid lines are least squares linear fits to each case. The dashed lines are lines of unit slope. The correlation coefficients are 0.87 for the box model and 0.65 for the 1D model. The coefficients of the lines (a + bx) are (a,b) = (21.1,2.85) and (40.0, 1.49) for box and 1D models. This figure demonstrates the relationship hypothesized above between species differences based on use of mean vs. median rates and species uncertainties computed from a Monte Carlo analysis. The 1D model results are based on a set of 1500 runs while 6100 runs were performed with the box model. The greater scatter in the 1D model results may result from the smaller number of runs in this case. The lack of a zero intercept and the obvious increased scatter at low values indicates that the relationship we hypothesize is better for the more uncertain species in the model. These are, of course, the cases of greatest interest. *Fig. 1* implies that the uncertainty/difference relationship may be model dependent and thus not quantitatively applicable to other models. However, the fact that all points are above the lines of unit slope in both cases suggests that the differences may be used as lower bounds on model uncertainties computed with the Monte Carlo method.

4. Summary

We have assumed that reaction rate components given in standard references may be interpreted as statistical properties of random variables. Based on further assumptions of the probability distributions for these variables we have arrived at two results. First, we developed a simple algorithm for taking into account the temperature dependence of rate imprecisions in error propagation studies (eq. 9). Second, we used the difference in median and mean formulations of reaction rates to suggest that concentration differences obtained using median rates in one computer simulation and mean rates in another may be used to estimate the uncertainty that would result from a Monte Carlo analysis of the effect of rate imprecisions on species uncertainties. We suggest that the concentration differences are a lower bound on the concentration uncertainties.

References

[1] DeMore, W. B., S. P. Sander, D. M. Golden, R. F. Hampson, M. J. Kurylo, C. J. Howard, A. R. Ravishankara, C. E. Kolb, and M. J. Molina, Chemical kinetics and photochemical data for use in stratospheric modeling, *JPL publication 94-26*, 1994.

[2] Stewart, R. W., and A. M. Thompson, Kinetic data imprecisions in photochemical rate calculations: Means, medians, and temperature dependence, *J. Geophys. Res.*, in press, 1996.

[3] Thompson, A. M., and R. W. Stewart, Effect of Chemical Kinetics Uncertainties on Calculated Constituents in a Tropospheric Photochemical Model, *J. Geophys. Res.*, *96*, 13089-13108, 1991.

[4] Stewart, R. W., Dynamics of the low to high NO_x transition in a simplified tropospheric photochemical model, *J. Geophys. Res., 100,* 8929-8943, 1995.

A new 2D Climate Model with Chemistry and Selfconsistent Eddy-Parameterization: The Impact of Airplane NO_x on the Chemistry of the Atmosphere

R. Geprägs, G. Schmitz and D. Peters (Institut für Atmosphärenphysik, Schloßstr. 4-6, 18225 Kühlungsborn, Germany)

A 2D version of the ECHAM T21 climate model (~~DKRZ, Hamburg~~) has been developed. The new model includes an efficient spectral transport scheme with implicit diffusion. Furthermore, photodissociation and chemistry of the NCAR 2D model (~~Brasseur et al., 1995, private communication~~) have been incorporated. A selfconsistent parameterization scheme is used for eddy heat- and momentum flux in the troposphere. It is based on the heat flux parameterization of Branscome (~~1983~~) and mixing-length formulation for quasi-geostrophic vorticity. Above 150 hPa the mixing-coefficient K_{yy} is prescribed. Some of the model results are discussed, concerning especially the impact of aircraft NO_x emission on the model chemistry.

1. Description of the 2D Model

The 2D model is based on the 3D GCM ECHAM 3.2 of the DKRZ-Hamburg. The aim is to develop a selfconsistent 2D model for the lower stratosphere and the troposphere with realistic parameterizations of wave fluxes, radiation, condensation and convection. Chemical processes are included.

Characteristics:

- 19 Levels (top level 10 mb), T21-Resolution (32 meridional gridpoints),
  Aqua-planet. Parameterizations of radiation, boundary-layer and water-cycle have been adopted from the 3D model.

- Parameterization of cumulus convection with a vertical adjustment scheme (Alexeev et al., 1995).

- Selfconsistent parametererization of horizontal heat flux, vertical heat flux and horizontal momentum flux in the troposphere. This scheme is based on a heat flux parameterization of Branscome (1983) and the mixing length assumption for quasigeostrophic vorticity.

- Above 200 mb we use prescribed mixing coefficients for the quasigeostrophic vorticity.

- Residual circulation for the whole model.

- Spectral transport-scheme for tracers with an Eulerian timestep and implicit diffusion terms.

- Chemistry of the NCAR 2D model (Brasseur et al., 1995).

- Calculation of the photodissoziation with the radiation code of the NCAR 2D model (Brasseur et al., 1995).

2. Eddy Parameterizations

The method is based on a formula of Branscome (1983) for the mean heat flux. The main dependence of the flux upon the mean potential temperature field θ is given by

$$[v^*\theta^*] = -K_{yy}\frac{\partial\theta}{\partial y} \sim \left(\frac{\partial\theta}{\partial y}\right)^2 e^{-z/D} \tag{1}$$

$$[w^*\theta^*] = -\left(\frac{z}{D} - \left(1-\frac{z}{D}\right)^2\right)\frac{\partial\theta/\partial y}{\partial\theta/\partial p}[v^*\theta^*] \tag{2}$$

with a vertical scale $D \approx 7.5$ km. K_{yy} is the mixing coefficient. The flux grows quadratically with the meridional temperature gradient. In consequence there is a strong transport of heat from the tropics to higher latitudes.
K_{yy} is used in a mixing-length estimation for the meridional flux of the quasigeostrophic potential vorticity Q :

$$[v^*Q^*] = -K_{yy}\frac{\partial Q}{\partial y} \tag{3}$$

In quasigeostrophic approximation this flux is given by the divergence of the Eliassen Palm flux.

$$[v^*Q^*] = \left(-\frac{1}{\cos^2\varphi}\frac{\partial}{\partial y}\left(\cos^2\varphi\,[u^*v^*]\right) + f\frac{\partial}{\partial p}\left(\frac{[v^*\theta^*]}{\frac{\partial\theta}{\partial p}}\right)\right) \tag{4}$$

Therefore [u*v*] is determined.

We add [v*Q*] to the tendency of the zonal wind. This procedure leads to meridional and vertical wind fields (residual circulation) which give an appropriate description of two dimensional transport.

3. Results

The residual circulation is shown in *fig. 1*.

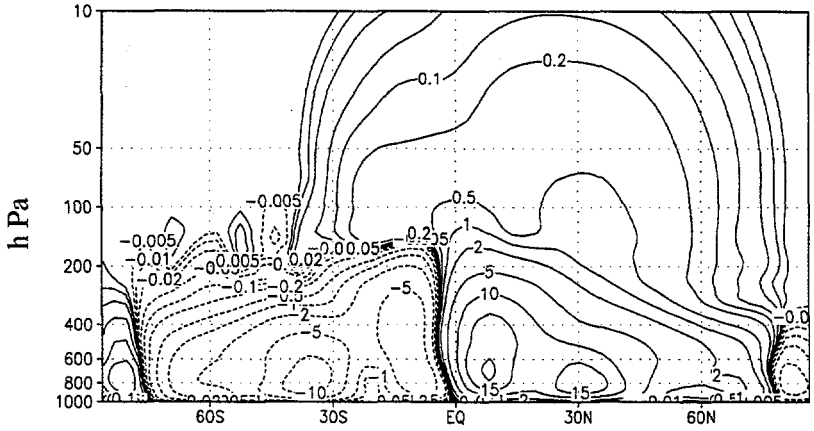

Fig. 1 - January mass-streamfunction of the residual circulation in 1.0^{10}kg/s.

It has the typical structure of the diabatic circulation, with an upward motion in the Tropics up to stratospheric heights and downward motion in subtropics and in polar regions. The mean circulation depends sensitively on the eddy-flux parameterizations and describes observational results qualitatively. In *fig. 2* the result for the parametrized Eliassen-Palm-flux-divergence is shown, with the contribution of vertical momentum flux being neglected.

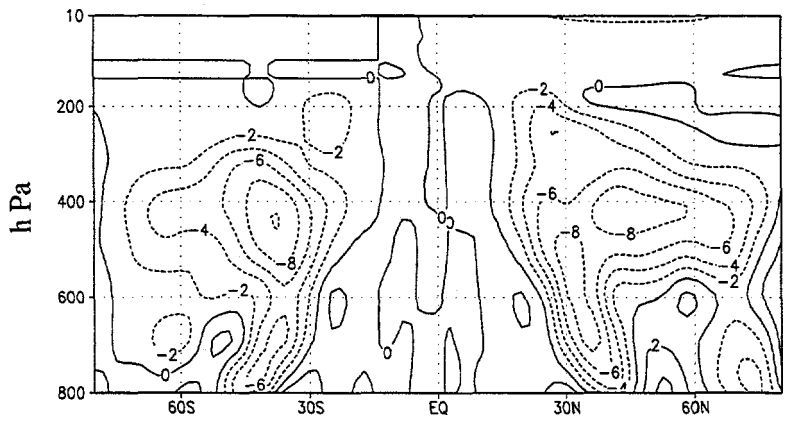

Fig. 2 - Eliassen-Palm-flux-divergence in [m/s/day]; January.

The EPF-divergence and the residual circulation yield a subtropical jet at 35°N (33 m/s) and a zonal wind maximum of 50 m/s at 30 mb level.
The mean ozone distribution has been calculated with an eddy-parameterization given by Branscome (1983) and is shown in *fig. 3*.

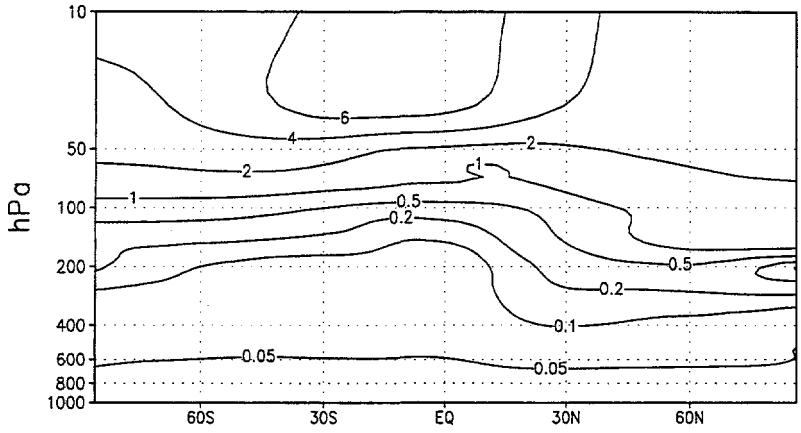

Fig. 3 - January O_3 - concentrations in ppbv.

The stratospheric ozone maximum is too weak. It seems that this a consequence of the description of photodissoziation above 10 hPa in the model. The tropospheric ozone concentration is comparable with other 2D-model results but stronger than in 3D-model-calculations (AERONOX, 1995).

The N_2O concentration is shown in *fig. 4.* It is characterized by an asymmetric distribution between the northern and southern hemisphere resulting from winter hemispheric „planetary wave" forcing due to the residual circulation. This model result is in a good agreement with observations.

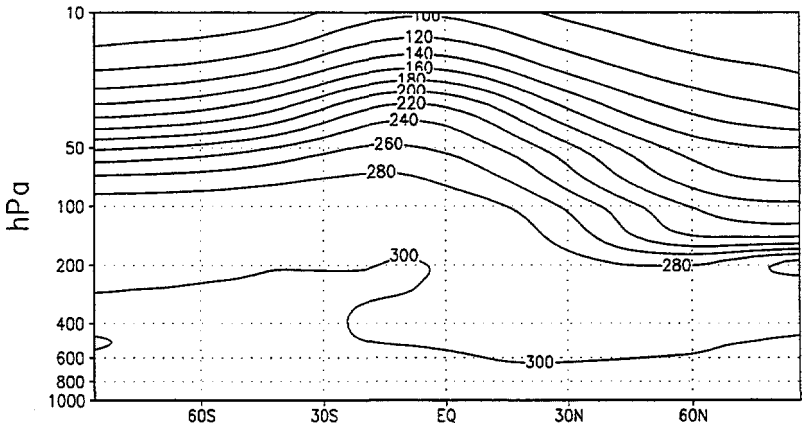

Fig. 4 - N_2O - concentrations in ppbv, January.

The change of NO_x concentration due to aircraft emission of NO_x (McInnes, Walker, 1992) is depicted in *fig. 5.*

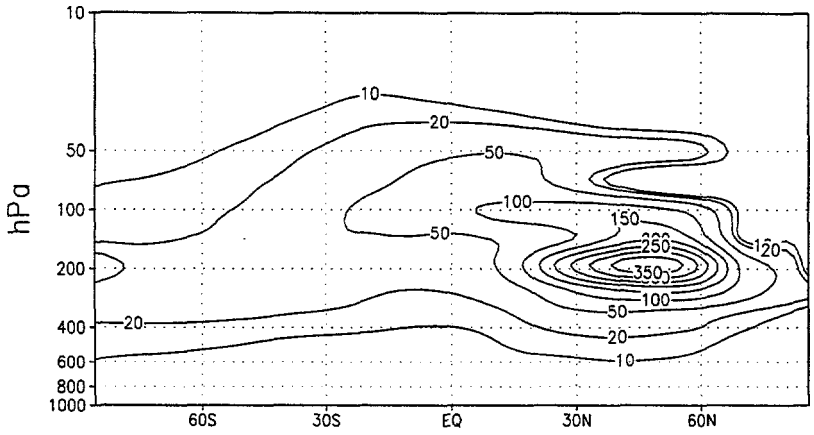

Fig. 5 - Changes of NO_x [pptv] concentrations due to aircraft NO_x emissions for January.

The maximum change is stronger than in other computations (AERONOX 1995). It seems that the large NO_x concentrations result from large NO_x chemical life times in the troposphere, so we need additional NO_x sinks in our model. The model describes well the chemical conversion between NO_x and O_3.

Literature:

[1] AERONOX 1995, The Impact of NO_x Emissions from Aircraft Upon the Atmosphere at Flight Altitudes 8-15 km. Editor U, Schumann., EC-DLR Publication.

[2] Alexeev, V.A. et al., 1994, A Description of a Global Atmospheric Circulation Model of the Institute of Numerical Mathematics of 1993 year. VINITI, 20.04.94, No. 983-B94.

[3] Branscome, L.E., 1983, A Parameterization of Transient Eddy Heat Flux on a Beta-Plane. J.A.S., Vol. 40, pp. 2508-2521.

[4] Brasseur, G. et al., 1990, An Interactive Chemical Dynamical Radiative Two-Dimensional Model of the Middle Atmosphere. J.G.R., Vol. 95, No D5, pp. 5639-5655.

[5] Brasseur, G. et al., 1995, Private Communication.

[6] McInnes, G. and C.T. Walker, 1992, The global distribution of aircraft air polution emissions. Warren Spring Lab., Report No. LR 872 (AD).

ON THE CLIMATIC IMPACT OF CONTRAILS

Bernhard Strauss, Ralf Meerkötter, Bruno Wissinger, and Peter Wendling

Deutsche Forschungsanstalt für Luft- und Raumfahrt
Institut für Physik der Atmosphäre
Oberpfaffenhofen, D-82234 Wessling, F.R. Germany

The impact of contrail induced cirrus clouds on regional climate is estimated for atmospheric conditions of Southern Germany that are typical for the months of July and October. This is done by the use of a regionalized one-dimensional radiative convective model (RCM). The influence of an increased ice cloud cover is studied by comparing RCM results using averaged climatological values of cloudiness with those of a case with modified cloudiness. It turns out that a 10 % increase in ice cloud cover leads to a surface temperature increase of 1.4 K and 1.2 K for the months of July and October, respectively.

1. INTRODUCTION

Air traffic influences the atmosphere by emission of various gases and particles. Among these, water vapour and aerosol particles acting as cloud nuclei are of special interest because they support cloud formation thus, modifying an important climate factor. In view of the strongly growing worldwide aircraft traffic the impact of contrail clouds is discussed recently again within the scope of airtraffic and climate in general (Schumann, 1994). The global influence of contrails on climate was studied by Liou et al. (1990) using a two dimensional energy balance model. As result, an increase in surface temperature of 1 K in the case of an increase of cloud cover of 5 % between 20° and 70° N was obtained. Ponater et al. (1995) studied the influence of an increase in water vapour and in cirrus cloud cover induced by airtraffic using a three-dimensional climate model. They show that a significant climate effect is more likely to occur on the basis of an additional contrail cloud cover rather than on the basis of an additional water vapour amount due to air traffic. For a contrail induced cloud cover of 5 % the lower troposphere is warming by about 1 K at 50° N.

However, one may expect that contrails have a stronger impact on a regional scale than on a global. To estimate this, a case study was carried out for an area of increased air traffic in Southern Germany. This was done by use of a one-dimensional radiative convective model (RCM), originally developed by Liou and Ou (1983) and modified within the present study to allow modelling of regional climate by taking into account advection as an additional energy source besides radiation and convection. The effects of an increased cirrus cloud cover on the equilibrium temperature of a July and October atmosphere were calculated and the results are presented in the following.

2. MODIFICATION OF THE RADIATIVE CONVECTIVE MODEL

2.1. Parameterization of advection

Radiative convective models are based on the assumption of a balance between the radiative and turbulent heat exchange in each atmospheric layer of a single column that represents globally averaged atmospheric conditions. They are widely used to determine the

vertical temperature profile as a global mean considering various forcing and feedback mechanisms. The model of Liou and Ou (1983) that is used within this study divides the atmosphere into 22 layers containing three cloud layers with a fixed cloud cover. To allow for a calculation of the temperature profile on a regional scale and for limited time periods, advection of energy has to be taken into account. For this purpose an 'atmospheric box' with vertical boundaries surrounding the region of Southern Germany was defined and the net energy flux of heat due to advective processes through the lateral faces of the box was determined by use of radiosonde data from the nearly station of Munich that were averaged for the years 1981 to 1985. The vertical profile of advected heat energy was set proportional to the wind profile. The absolute value of the advected energy was chosen such that the net radiative energy loss or gain at the top of the atmosphere is equal to the value determined by measurements of the ERBE-satellite experiment. These fluxes are - 59 W m^{-2} and 97 W m^{-2} for the months of July and October respectively, the minus sign indicating an energy gain for the box. The satellite data were taken for the area from 47.5° to 50° N and 10° to 12.5° E and cover quite accurately the area of Bavaria in Southern Germany. For July, a five years average of monthly averaged net fluxes is used (years 1985 to 1989). For October, corresponding data were available only for two years, 1985 and 1986 respectively.

2.2. Microphysical and radiative properties of cirrus clouds

Special emphasis is given to the parameterization of the radiative properties of ice clouds. In the original version of the RCM high level ice clouds consist of cylindrically shaped monodisperse ice particles with a mean length of 200 µm, a mean radius of 30 µm and a mean concentration of 0.05 cm^{-3}. However, recent research results enforce these assumptions to be modified. Models tend to underestimate the solar albedo of ice clouds when compared to measurements (Stackhouse and Stephens, 1991), whereby measurements indicate (Ström, 1993; Forkert et al., 1994) that a significant amount of ice particles with sizes smaller than 50 µm exists in ice clouds. These particles will have an appreciable influence on the radiative characteristics of ice clouds by enlarging the number of backscattered photons and herewith increasing cloud albedo. Therefore, the original parameterization of ice clouds in the RCM model was modified by assuming ice clouds to consist of a particle size distribution based on measurements of small ice particles down to 2 µm particle size (Forkert et al., 1994) and for particles larger than about 20 µm on the parameterization of Heymsfield and Platt (1984) which is a function of temperature. The measurements of Forkert et al. (1994) were carried out with an airborne Formvar ice particle replicator (Hallett, 1976) in a cirrus layer approximately at an altitude between 9.5 and 11 km in the area north of the Alps.

The shape of the particles was assumed to be that of hexagonal columns, the ratio of length to diameter following the measurements of Ono (1969) and the calculations of Hess and Wiegner (1994). *Table 1* shows the discretized ice particle size distribution as derived from the two separate data sources. The given size represents crystal length.

Table 1 Size distribution of ice cloud particles; particles in classes I and II are referred as 'small' particles in the text

size class	size range µm	particle number m^{-3}
I	2 - 6	$1.69 \cdot 10^5$
II	6 - 20	$3.87 \cdot 10^5$
III	20 - 40	$6.58 \cdot 10^3$
IV	40 - 90	$1.44 \cdot 10^3$
V	90 - 200	$2.36 \cdot 10^2$
VI	200 - 400	$3.70 \cdot 10^1$
VII	400 - 900	$8.25 \cdot 10^0$
VIII	900 - 2000	$1.32 \cdot 10^0$

In order to show the effect of neglecting the small particles with sizes lower than 20 µm calculations of the radiative properties of ice clouds are carried out in the following for two ice particle size distributions, with and without small particles. For the two cases, the total particle concentration is $5.64 \cdot 10^{-1}$ cm^{-3} and $8.33 \cdot 10^{-3}$ cm^{-3} respectively, meaning that 98.5 % of all particles are within the two classes I and II. Additional measurements in contrails near the Alps (Forkert et al., 1994) showed that within the particle size range from 2 to about 100 µm the measured size distribution for aged contrails (age larger than about 0.5 hour) lies within the variability of the one measured in natural cirrus. Therefore, for the following calculations with the RCM the radiative properties of natural and contrail induced high clouds have been assumed to be the same.

The applied radiative convective model (Liou and Ou, 1983) uses a parameterization of broadband infrared and solar radiative transfer and needs for this purpose the flux reflection, absorption/emission and transmission properties of separate distinct scattering layers (clouds) embedded in the atmosphere. These have been calculated by use of a radiative transfer model (RTM) based on the Matrix-Operator-Theory (Plass et al., 1973). This RTM accounts for processes of multiple scattering, absorption and thermal emission. The vertical profiles of temperature, pressure, air density and aerosol and gaseous absorbers were specified according to mean July and October conditions for the considered region of southern Germany.

In the visible part of the spectrum the optical properties of high ice clouds are approximated by the assumption of hexagonal crystal shapes and geometrical optics. The sharp forward peak of the phase function is truncated in the visible by applying the delta function approximation. In the terrestrical spectral range, a Hennyey-Greenstein approximation of the phase function is adapted which depends only on the asymmetry factor. Since the approximation of geometrical optics is no more valid in this spectral range ice particles were assumed as spheres with the same volume as those given in *Table 1* and Mie calculations were carried out to determine the optical properties. *Tables 2* and *3* list the resulting broadband radiative properties of high level ice clouds finally used interactively in the RCM. The radiative properties of middle and low level clouds were taken as those from the original RCM corresponding to the midlatitude case of Liou and Ou (1983). According to the results of *Table 2* the solar reflection of high ice clouds is strongly dominated by the amount of particles with sizes smaller than 20 µm. *Table 3* lists the corresponding properties for the broadband infrared cloud properties.

Table 2 Solar radiative properties of the cirrus layer as derived from RTM calculations

case	solar zenith angle	transmittance	reflectance
Jw	58.71°	0.961	0.031
JO	58.71°	0.980	0.012
OW	69.78°	0.936	0.054
OO	69.78°	0.970	0.021

JW : July, cloud with small particles
JO : July, cloud without small particles
OW : October, cloud with small particles
OO : October, cloud without small particles

Table 3 Derived ice cloud radiative properties in the terrestrial spectral range

case	emittance	transmittance	reflectance
JW	0.381	0.695	0.024
JO	0.319	0.784	0.011
OW	0.315	0.733	0.024
OO	0.248	0.751	0.010

3. MODEL RESULTS

Figure 1 shows results for the reference case, i.e. the case with climatological values of cloud cover in October. Cloud cover values are taken from Warren et al. (1988) and are based on ground observation averages for the years 1971 to 1981. Two resulting temperature profiles are shown, the one results from including advection as outlined above, whereas the other results from neglecting it. For comparison, the climatological October values of temperature as derived from radiosonde data of the Munich station are shown.

Remarkable is the great influence of advection inducing a temperature difference of up to 25 K throughout the troposphere. It is important to note that the uncertainty of the satellite data is in the order of 10 W/m^2 corresponding to an uncertainty in the temperature profile of about 3 K.

The impact of additional high cloudiness induced by air traffic is estimated by comparing the RCM results for an increased cloud cover with the ones for reference cases in July and October. It is assumed that the additional high cloudiness adds to the natural cloudiness at the expense of the uncovered area. The obtained results are depicted in *Figure 2*. As can be seen, an additional increase in high cloudiness of 10 % causes surface temperature increases of 1.4 K and 1.2 K, respectively. A linear relation between cloud cover and surface temperature is obtained, because the RCM weights fluxes linearly with cloud cover. Assuming the high clouds to be composed only of larger particles leads to corresponding increases in surface temperature of 1.5 K and 1.3 K for July and October conditions, respectively. This indicates that with inclusion of small ice particles the effect of the solar albedo increase exceeds the corresponding effect of the increase in terrestrial emission of radiation. The current cloud cover which is due to aircraft induced contrail cloudiness is estimated to be in the order of 0.5 % over Europe (Bakan et al., 1994). In this case the increases in surface temperature are 0.07 and 0.06 K in July and October, respectively.

Fig. 1 Modelled temperature profiles for October with (solid) and without (dashed) advection compared to radiosonde measurements (triangles)

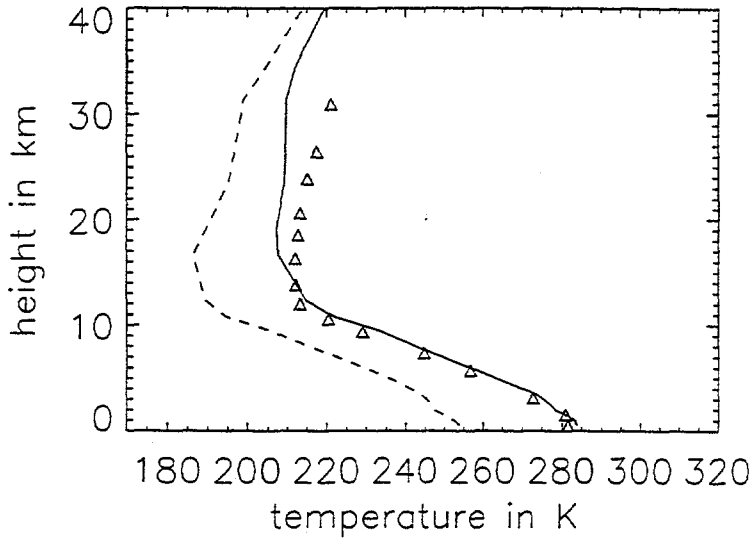

Fig. 2 Increase in surface temperature ΔT_{surf} as function of the additional cirrus cloud cover due to contrails η in the case of July (solid) and October (dashed over Southern Germany

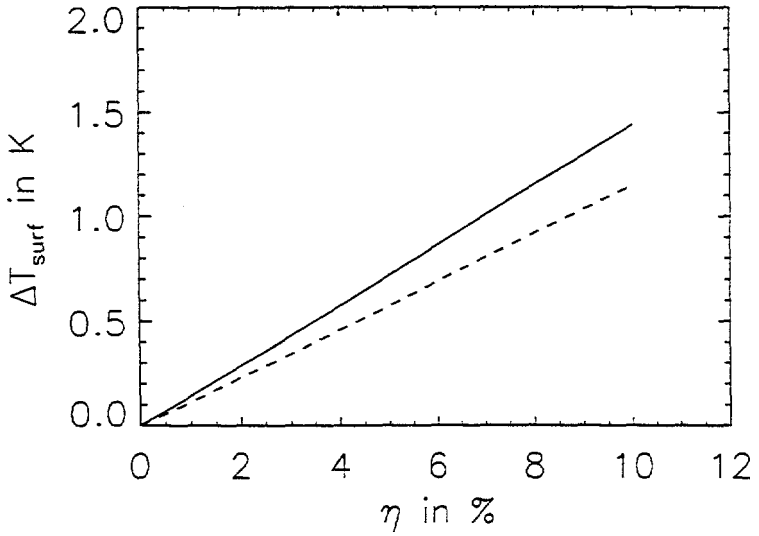

4. REFERENCES

[1] Bakan, S., M. Betancor, V. Gayler, H. Grassl, 1994: Contrail frequence over Europe from NOAA-Satellite images. Ann. Geophysicae., 12, 962-968

[2] Forkert, T., B. Strauss, P. Wendling, 1994: On the climatic impact of contrails. In: U. Schumann and D. Wurzel (Eds.): 'Impacts of Emissions from Aircraft and Spacecraft Upon the Atmosphere', Proceedings of an International Scientific Colloquium Köln, Germany, 18-20 April 1994, DLR-Mitteilung 94-06

[3] Hallett, J., 1976: Measurements of size, concentration and structure of atmospheric particulates by the airborne continuous replicator. Final report: Cloud particle replicator for use on a pressurized aircraft, 92 pp. I, II Supplementary Final Report, 1511 pp. Contract FGL-TR-76-0149, Air Force Geophys. Lab

[4] Hess, M., and M. Wiegner, 1994: COP: Data Library of Optical Properties of Hexagonal Ice Crystals. Appl. Opt., 33, 7740-7746

[5] Heymsfield, A.J., and C.M.R. Platt, 1984: A parameterization of the particle size spectrum of ice clouds in terms of the ambient temperature and the ice water content. J. Atmos. Sci., 41, 846-855

[6] Liou, K.N , and S.C. Ou, 1983: Theory of equilibrium temperatures in radiative-turbulent atmospheres. J. Atmos. Sci., 40, 214-229

[7] Liou, K.N., S.C. Ou, and G. Koenig, 1990: An investigation on the climatic effect of contrail cirrus. In: U. Schumann (Ed.): 'Air Traffic and the Environment - Background, Tendencies and Potential Global Atmospheric Effects'. Proceedings of a DLR International Colloquium, Bonn, Germany, 15-16 November 1990, Springer Verlag

[8] Ono, A., 1969: The shape and riming properties of ice crystals in natural clouds. J. Atmos. Sci., 26, 138-147

[9] Plass, G.N., G.W. Kattawar, and F.E. Catchings, 1973: Matrix operator theory of radiative transfer. I: Rayleigh scattering. Appl. Opt., 12, 314-323

[10] Ponater, M., S. Brinkop, R. Sausen, and U. Schumann, 1995: Simulating the global atmospheric response to aircraft water vapour emsissions and contrails. Submitted to: Ann. Geophysicae

[11] Schumann, U, 1994: On the effect of emissions from aircraft engines on the state of the atmosphere. Ann. Geophysicae., 12, 365-384

[12] Stackhouse, P.W., and G.L. Stephens, 1991: A theoretical and observational study of the radiative properties of cirrus: Results from FIRE 1986, J. Atmos. Sci., 48, 2044-2059

[13] Ström, J., 1993: Numerical and airborne experimental studies of aerosol and cloud properties in the troposphere. Dissertation, Department of Meteorology, Stockholm University, ISBN 91-7173-168-8

[14] Warren, S.G., C.J. Hahn, J. London, R.M. Chervin, R.L. Jenne, 1988: Global distribution of total cloud cover and cloud type amounts over land. NCAR Technical Notes

Observational Evidence for the Impact of Jet Condensation Trails Upon The Earths Radiation Budget

Dieter Meinert
Institut für Atmosphärenphysik
GKSS Forschungszentrum, P.O.–Box 1160
D–21494 Geesthacht, Germany

20th September 1996

Abstract

Jet condensation trails have been classified in AVHRR images from a couple of month. It was tried to estimate their impact upon the radiation budget from the observed radiances. This has been performed by direct comparison of contrail image points to neighboring image points, assuming a slowly varying background. The classification method, basing on an artificial neural network for pattern recognition is explained in this paper. The details of the estimation of the net impact of contrails upon the radiation budget are shown by one example.

1 Introduction

During the last years the impact of air traffic upon the earth's atmosphere is heavily discussed. Besides the input of Carbon Dioxide affecting the greenhouse effect and pollutants probably damaging the ozone layer one obvious impact has only recently become subject to discussions: The condensation trails of jet aircraft (Wendling 1990, Graßl 1990, Roll 1990, Betancor et al. 1994). Due to their optical similarity to cirrus clouds (both consist of tiny ice particles) contrails are suspected to affect the greenhouse effect in some unknown way. This Poster deals with an idea to measure the impact of contrails directly and simply from AVHRR Satellite images.

2 Neural networks to detect contrails in satellite images

In order to quickly identify contrails at GKSS in near real time we installed two kinds of backpropagation neural networks. Originally realized using the *Stuttgart Neural Network Simulator* (Zell et al. 1993),the network was trained to identify one image pixel as contrail or not depending on the pixels neighbourhood. Training of this network was performed using handpicked data samples. With this approch we were able to identify about 90% of the contrails present in an image, while the misclassification of background is strongly suppressed. The problem was that this network still needed several hours to work through one image when we get a satellite image every two hours.

Figure 1: *Design of the Mark II neural network to identify all contrail pixels inside an image area.*

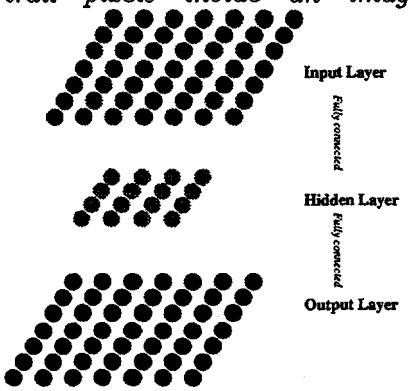

Figure 2: *Observational geometry of a polar orbiting satellite at noon*

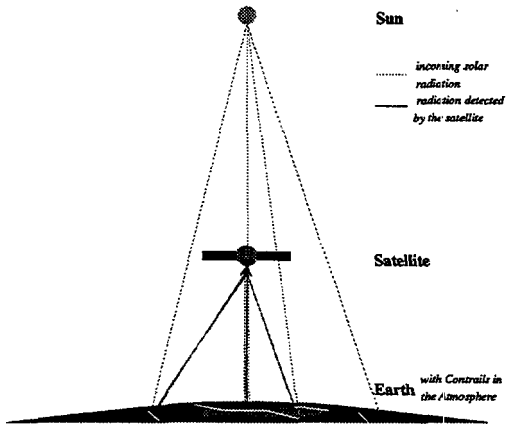

Currently we are using our Mark II network, realized in c++ code, trained by using results from the first. This network shall identify all contrail pixels in the area at the same time, thus increasing the computing time by a factor corresponding to the size of its output layer (Fig.2). Since our old network sometimes leaves a contrail pixel unidentified we have to check and correct each training pattern by hand.

3 A simple scheme for preliminary estimation of the impact of contrails from satellite images

To get some preliminary results from Satellite images without consuming too much computing time it seems appropriate to find a phenomenological way estimating the impact of contrails upon the radiation budget.
The resolution of the NOAA–N series satellites in the SubSatellitePoint (SSP) is 1.1 km. Assuming that the state of the atmosphere is changing on a larger scale than this, say, about 6 km, one may, at a first glance, say that the additional effect of jet condensation trails may be found by subtracting the radiance of the background from that of the contrail. For a noon overpass of a satellite the observational geometry is nearly as shown in Fig.2.

- *Is the contrail visible in all five AVHRR channels ?*
- *How large are the errors introduced by this approach ?*
- *Where are we most error prone ?*
- *How may we compensate for the errors thus introduced ?*

Errors may be introduced by neglecting bi–directional reflectance, by different background structure, due to variations in calibration.

4 Procedure

To get an impression of an answer to these questions we selected a set of contrails from a satellite image following very restrictive guidelines:

- *The contrail must extend along the scan direction to avoid confusion by a variation in the calibration*

- *The contrail must cross the SSP to simplify observational geometry*
- *The satellite must be on a noon overpass, s.o.*
- *The background to the contrail must be very homogeneous*

We are, for practical purposes, not considering solar zenith angle here.
Along the contrail we estimated the radiance detected by the satellite for every tenth pixel, if that was clearly discernible in the split window. Also, for each selected contrail pixel we estimated the background radiance by taking that of a pixel detected within 5 pixels of the contrail, across–scan. The difference of the detected radiances ($\Delta R = R_{contrail} - R_{background}$) for the contrails and each AVHRR channel is plotted in Fig.3 versus the position of the observed pixel along the scan (for display purposes normalized to the maximum value found for ΔR in each channel).

5 Observations and Results

Figure 3: *Difference of the Radiances detected from a contrail pixel and that from a corresponding background pixel for every tenth pixel of the contrails, plotted against the position of the pixel along scan direction. Data have been normalized to their maximum value for each channel.*

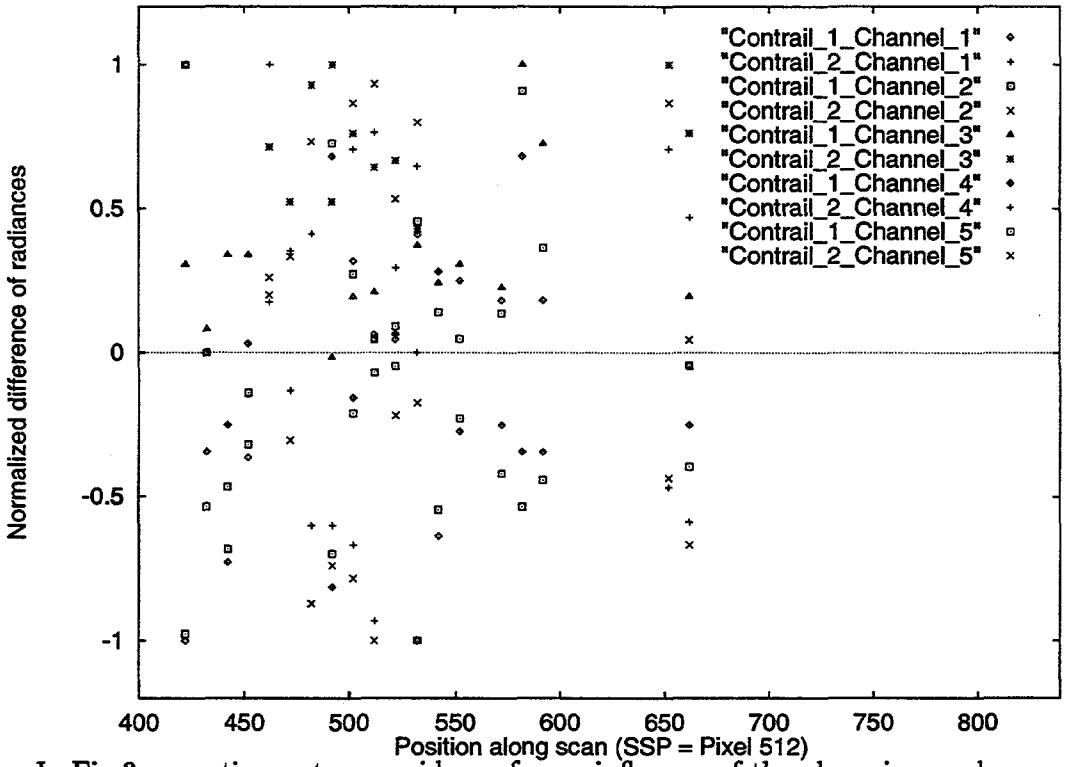

In Fig.3 we notice a strong evidence for an influence of the observing angle on our results for both solar channels 1 and 2, while for the terrestrial channels there seems to be no evidence. Furthermore the impact of the observing angle depends on the background of the contrail, it seems strongest for clear but negligible for low clouds. The effect of bi–directional reflectance already appears for small angles (see Contrail 2 in Fig.3) in the observation geometry as shown in Fig.2.

On the other hand the method investigated here seems fit to quickly estimate the impact of contrails upon the terrestrial radiation, where no directional bias appears.

6 Summary

A simple idea to estimate the additional impact of jet condensation trails upon the Earths Radiation budget on a phenomenological basis has been testet on a sample of contrails selected from NOAA–AVHRR images.
It was found that observations in the Infrared bands are quite simple to interpret, while in the visible bands even for such a simple approach diverse influences have to be considered, like the background and the observational geometry to a very high degree ! Though impacts from observation geometry may be overcome by rather simple regression calculations, we first have to classify the background to our observed object.

7 Open Questions:

- *How to classify the background in a fast way ?*
- *How reliable is our estimation for the infrared channels of the AVHRR ?*
- *How may we integrate our measurements to estimate the broad–band effect of a contrail from our five narrow–band measurements ?*

Acknowledgements

This work has been supported by the German Ministery for Education, Science and Technology under Grant 01LL9505/9.
I want to thank Drs. Rolf Stuhlmann (GKSS) and Franz Berger (TU Dresden) for their very useful comments on atmospheric radiation and the influence of the low atmosphere on the detected radiation.

References

BETANCOR, M., BAKAN, S., GAYLER, V., GRASSL, H. (1994) Contrail Frequency over Europe from NOAA–Satellite Images; Proceedings of an international scientific colloquium on "Impact of Emissions From Aircraft and Spacecraft Upon the Atmosphere", Cologne, 18. – 21. April 1994, DLR Mitteilungen 94–06, eds.: U.Schumann, D.Wurzel, pp389

GRASSL, H. (1990) Possible Climatic Effects of Contrails and Additional Water Vapor; DGLR/AAAF/RAes European Propulsion Forum. Future Civil Engines and the Protection of the Atmosphere. Cologne- Porz, April 3-5,1990

ROLL, ORTRUN: Kondensstreifen im Satellitenbild; Diploma Thesis, University of Cologne, 1990

WENDLING, PETER: Wirkung von Kondenstreifen auf Strahlungshaushalt und Klima; in: Luftverkehr und Umwelt, ein Querschnittsprojekt der DLR, 40-43 1990

ZELL, A., MACHE, N., HÜBNER, R., MAMIER, G., VOGT, M., HERRMANN, K.–U., SCHMALZL, M., SOMMER, T., HATZIGEORGIOU, A., DÖRING, S., POSSELT, D.: SNNS Stuttgart Neural Network Simulator User Manual, Version 3.1; Report No. 3/93, University of Stuttgart, Institute for Parallel and Distributed High Performance Systems, 1993

Author's email: dieter.meinert@gkss.de, Homepage: http://w3.gkss.de/~dieter/

The Model Evaluation of Subsonic Aircraft Effect on the Ozone and Radiative Forcing

E. Rozanov, V. Zubov, T. Egorova, Y. Ozolin
Main Geophysical Observatory, St. Petersburg, Russia

Abstract. Two dimensional transient zonally averaged model was used for the evaluation of the effect of subsonic aircraft exhausts upon the ozone, trace gases and radiation in the troposphere and lower stratosphere. The mesoscale transformation of gas composition was included on the base of the box model simulations. It has been found that the transformation of the exhausted gases in subgrid scale is able to influence the results of the modeling. The radiative forcing caused by gas, sulfate aerosol, soot and contrails changes was estimated as big as 0.12-0.15 W/m^2 (0.08 W/m^2 globally and annually averaged).

1. Introduction

The exhausts from aircraft engines may substantially influence tropospheric nitrogen budget and, therefore, ozone and radiation fields in the troposphere [1,2]. One of the main factor of uncertainty is the initial composition of the exhausted products to be introduced in the global model as an initial perturbation.. Two dimensional transient zonally averaged model of radiation, dynamics and photochemistry in the atmosphere has been used for the study of the model sensitivity to the composition of initial perturbation caused by present day emissions of subsonic fleet. The changes of gas species have been calculated for the cases with pure NO_x release and with the initial gas perturbations based on the results of mesoscale box model reported in [3].The radiation forcing from such perturbation as well as from the changes of stratospheric sulfate aerosol, soot and contrails formation have been also estimated with model simulations.

2. Description of the model

2-D transient zonally averaged model describes the radiation, dynamics, photochemistry processes in the atmosphere and their interactions. The prognostic variables in the model are temperature, zonal and meridional wind components, K_{yy} , concentrations of chemical species and radiative net heating rates in the atmosphere. The model domain extends from 90°S to 90°N with 10° latitude step and from surface to 66 km altitude with 2km vertical step. The time step is 2 hours for photochemical and gas transport calculations, one day for the integration of the model dynamics equations. The diurnal course of photolysis rates is recalculated every 7th model day.

The equations governing the dynamics of the model atmosphere express the principles of conservation of mass, momentum, energy and also the ideal gas law. They have been used in a spherical, log-pressure coordinate system according to quasi-geostrophic and hydrostatic approximations. The system of equations is integrated in the stratosphere by the method used in [4]. The stratospheric temperature is obtained by the numerical solution of the thermodynamic prognostic equation. Zonal winds are derived from the thermal wind relation. Residual mean meridional circulation is computed as a solution of an elliptic partial differential diagnostic equation. The relation for a wave driving is based on the gravity wave dissipation treatment by Rayleigh friction and Rossby wave absorption parameterization by [5]. The contribution of the convergence of the eddy heat fluxes is parameterized in the terms of the gradient potential temperature and the mixing coefficients K_{zz} and K_{yy}. In the troposphere the temperature, humidity, wind components distributions, cloud optical properties and surface albedo are prescribed on the base of observed data.

The background values of K_{yy} and K_{zz} are also prescribed in the whole atmosphere. In this study we have used the well known temperature climatology [6]. The water vapor mixing ratio is also specified in the troposphere.

The annual course of the vertical velocity component is specified at the atmospheric level 16 km and the meridional tropospheric circulation has been obtained by linear interpolation from this level to the ground. The values of vertical velocity at 16 km were taken from [7] with some modifications. The zonal mean circulation in the troposphere was prescribed as in [7].

The heat transport equation is solved according to Prather's scheme [8] for the zonal mean advection and to forward time central differencing scheme for the small and large-scale diffusion. The elliptic equation for the components of the mean meridional circulation is solved by the alternative direction method.

The chemical scheme of the model includes 37 gas species of oxygen, nitrogen, chlorine, hydrogen and carbon groups as well as the products of methane oxidation. About 100 gas phase and 5 heterogeneous reaction on PSC's and sulfate particles were taken into account. The numerical scheme is based on the implicit Newton-Raphson scheme. Kinetic rates were taken mainly from JPL-94 publication.

In the radiation code the calculations of heating and cooling rates are carried out separately for three spectral regions: UV and visible (0.17-0.75 μm) , near infrared (0.75 - 4 μm) and infrared (> 4 μm). In the short-wave interval the Delta-Eddington approximation is used in 26 spectral subintervals. Absorption and scattering of solar radiation by O_3, H_2O, CH_4, N_2O, NO_2, aerosol, clouds as well as reflection by the surface are included in the radiation code. In the infrared region, which has been divided into 17 spectral subintervals, the absorption of radiation by O_3, CO_2, H_2O, CH_4, N_2O, NO_2, CF_2Cl_2, $CFCl_3$, by aerosol and clouds are accounted for. The Goody's type statistical band model was used for the parameterization of gas transmission function in the infrared and near infrared spectral areas.

The model performance is illustrated by the results of numerical simulations for the 1990 year boundary conditions. The calculated total ozone distribution is presented in *Fig.1*, and it gives the most important information on model performance because the total ozone time-latitude distribution

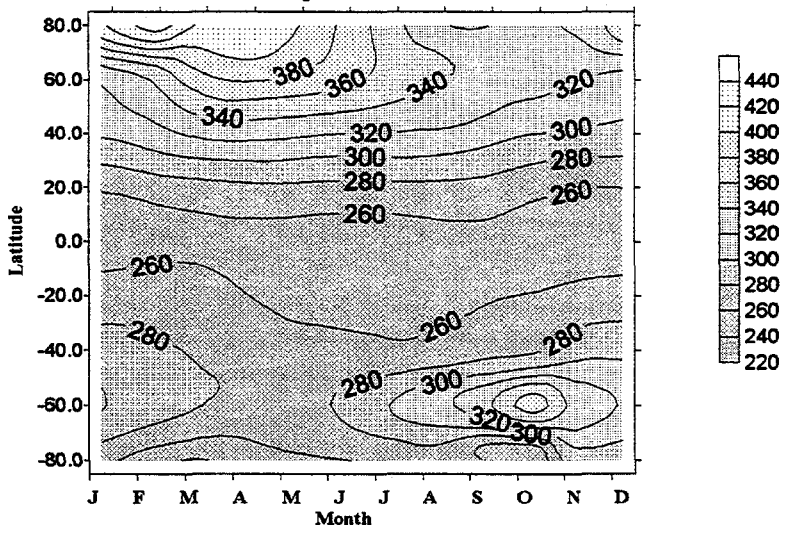

Fig.1 Simulated total ozone (D.U.) latitude - time cross section for 1990 year condition.

depends on almost all processes included in the model. It follows from the comparison, that the model reproduces the location of main utmost points in space and time. The lowest total ozone

values (less than 260 D.U.) take place in tropics and over the South Pole in October whereas the maximum values (about 460 D.U.) occur over the North Pole in February/March and over the subpolar of the Southern hemisphere in September/October (about 380 D.U.).

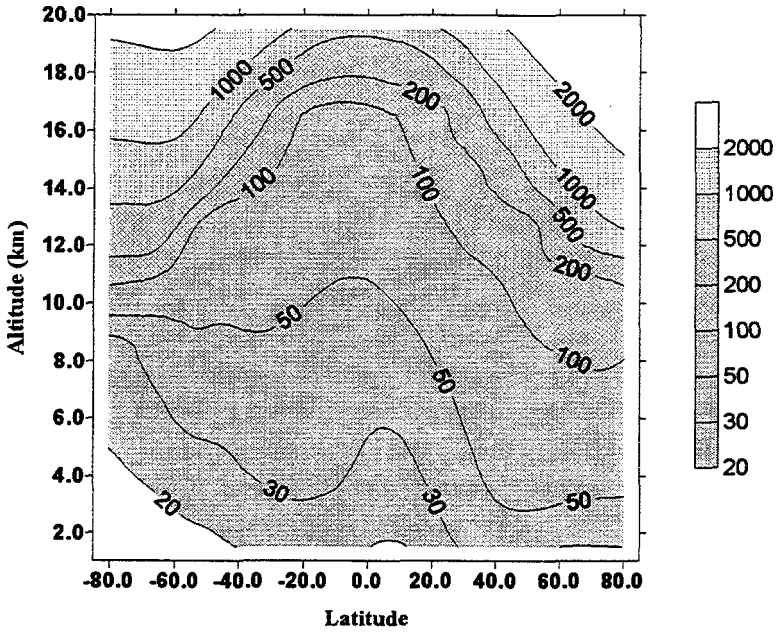

Fig.2 Simulated total ozone (ppbv) latitude - altitude cross section for June.

Two local minima (in March over the South Pole and in September over the North Pole) are also in agreement with observations. However,. the intensity (about 220 D.U.) and duration of ozone hole event are different from the observation data. It can be explained by poor model description of PSC formation and early breaking of polar vortex in the model. The shape of the total ozone distribution from February up to May over the North Hemisphere is also different from observational data. Probably, it can be connected with highly parameterized representation of planetary wave breaking processes, which play a significant role in the ozone transport from tropics to poleward direction during winter and spring time.

It should be noted that the above model faults are typical for 2-D models and can be substantially improved only in frame of 3-D models. The latitude - altitude cross sections of ozone and NO_x ($NO+NO_2$) presented in *Fig.2,3* for June are in a relatively good agreement with observation data and other model simulations.

3. Numerical simulations

To estimate the sensitivity of the model to the changes of the composition of initial gas perturbation three model runs have been carried out. Control model run without aircraft emission was described in previous section. Two steady-state 10 years simulations have been performed with aircraft emission included according to NASA database. For the first run the emission consists of 90% NO and 10% NO_2 according to the data published in [9,10]. For the second run the following scenario have been adopted according to the mesoscale box-model calculations reported in [3]: NO - 20%; NO_2 - 25%; HNO_3 - 40%; HO_2NO_2 - 15%. The last scenario reflects a fast transformation of initial gas exhaust during the firs day after the emission. For the last simulations the changes in sulfates aerosol, soot and contrails formation were taken into account according to the estimation reported in [10]. These perturbations are listed in *Tabl.1*.

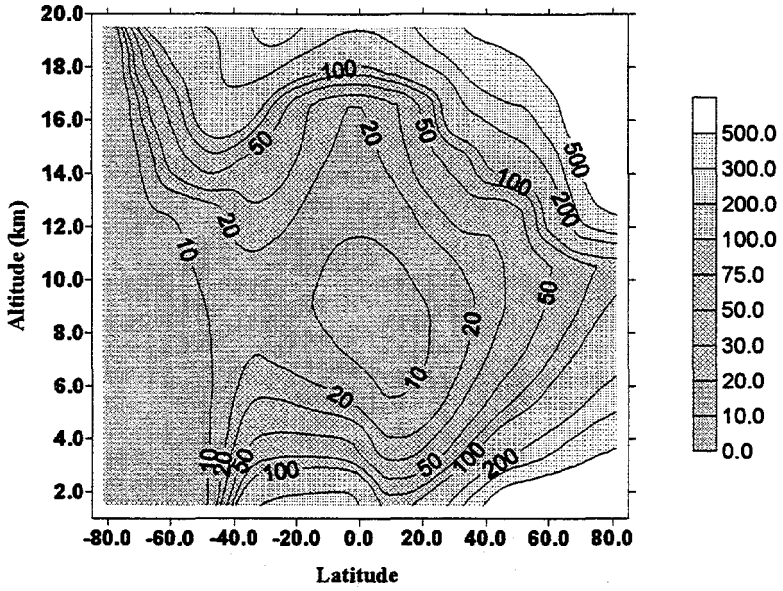

Fig.3 Simulated total NO_X (pptv) latitude - altitude cross section for June.

The simulated changes of ozone are presented in the *Fig.4, 5*. In case of pure NO_x emissions (*Fig.4)* the ozone changes are located mainly in Northern Hemisphere(NH) with maximum values around 7% in the upper troposphere (8-10 km) in narrow latitude belt 20° - 40° north. In the Southern Hemisphere (SH) the ozone changes does not exceed 2%. The obtained results are in a good agreement with the model estimations published in [1,2,9]. In the case with transformed emission (*Fig.5)* the magnitude of the ozone changes decreases in the NH (up to 30%) and increases in the SH up to 50%. It can be explained by enhanced transport of more conservative species toward SH. The HNO_3 increase over the southern high latitudes leads to the enhancement of PSC formation there and to the small decrease of ozone. Thus, as a result of the initial gas input changes the sensitivity of the model decrease in the Northern hemisphere, but the effect become more extended in space. The changes of NO_x distribution (not shown here) reveal same features. The obtained NO_x changes in the NH decrease up to 30% but become large in SH with almost the same magnitude.

Calculated latitude - time cross section of tropopause radiative forcing (RF) caused by gas and aerosol perturbation is presented in *Fig.6* for the pure NO_x emissions. According to ozone changes the maximum values of RF (0.12-0.14 W/m^2) are located in the northern mid-latitude during the summer. The globally and annually averaged value of RF is found to be equal 0.08 W/m^2.The magnitude of RF is at least two time larger than reported in [2]. Because of the similar changes of ozone presented here and published in [2] such substantial disagreement can be explained by additional perturbation of CO_2 and aerosol adopted in our model.

Table. 1 The perturbation caused by subsonic fleet emissions introduced in the model

Variable	Factor of changes
CO2	+0.5%
Sulfate aerosol (SA)	+10%
Contrails	+0.4% of cirrus clouds
Soot	1% of background SA optical thickness

4. Conclusions

Two dimensional transient zonally averaged model was used for the evaluation of subsonic aircraft emission impact upon the ozone, trace gases and radiation in the troposphere and lower stratosphere. The performance of the proposed model is demonstrated by the successful comparison with observed

distribution of species. The sensitivity of the model to the composition of initial gas perturbation was studied. The results of simulations revealed that if the fast mesoscale transformation of the gas emission is accounted for the sensitivity of the model decrease in the Northern Hemisphere up to 30% with almost the same increase in the Southern Hemisphere.

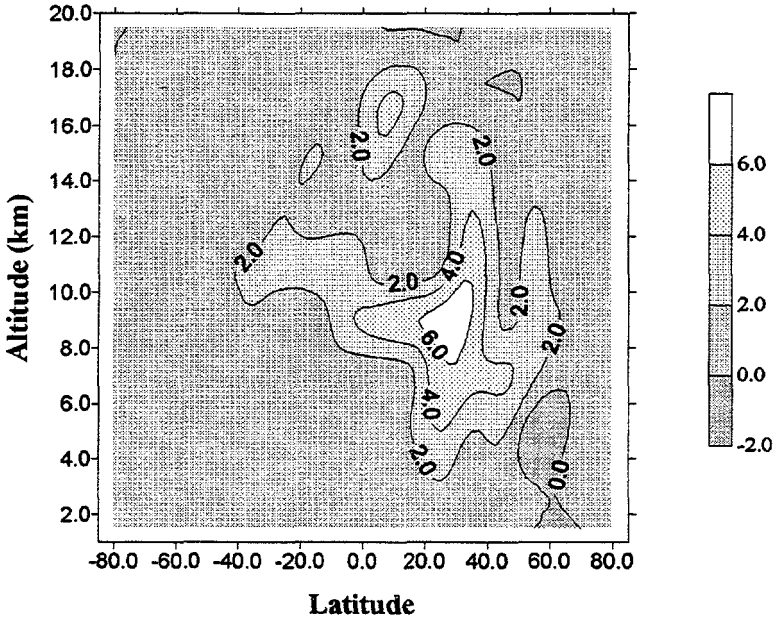

Fig.4 Simulated latitude - altitude cross section of ozone changes (%) for June in case of pure NO_X perturbation.

Thus, the effect of aircraft emission becomes less but more extended in space and it should be accounted in the global model. The radiative forcing caused by gas and aerosol perturbation was estimated as big as 0.12 - 0.14 W/m^2 in the summer of the Northern Hemisphere while its globally and annually averaged value is equals to 0.08 W/m^2.

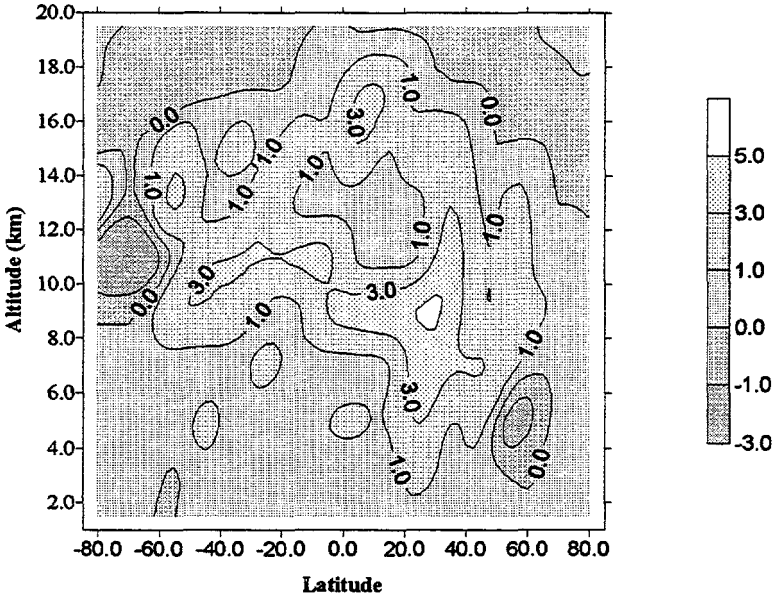

Fig.5 Simulated latitude - altitude cross section of ozone changes (%) for June when the mesoscale transformation of initial perturbation were taken into account.

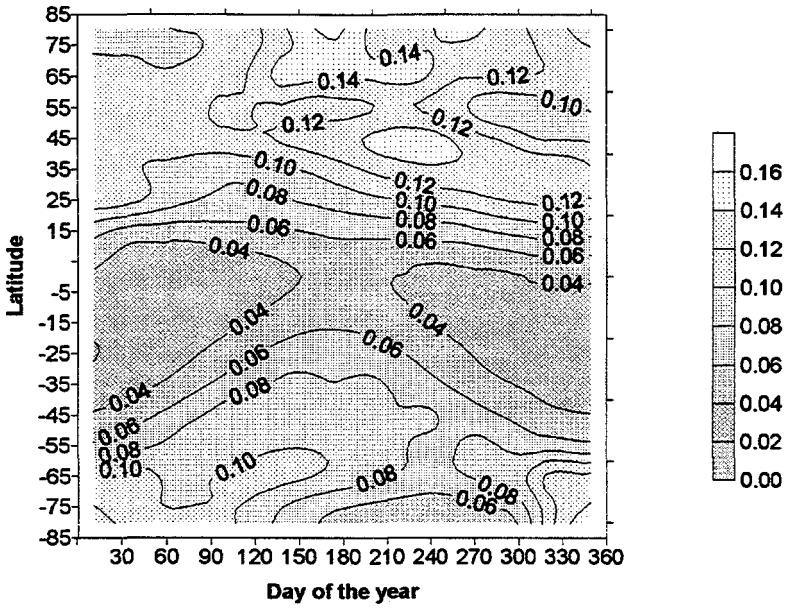

Fig.6 Simulated latitude - time cross section of radiation forcing caused by the aircraft emissions.

References

1. Jones, A.E., K.S. Law and J.A. Pyle, 1996: Subsonic Aircraft and Ozone Trends, *J. of Atm. Chem.*, **23**, 89-105.

2. Hauglustaine, D.A., C.Granier, G.P.Brasseur, and G. .Mégie, 1994: Impact of present aircraft emission of nitrogen oxides on tropospheric ozone and climate forcing, *Geoph. Res. Lett.*, **21**, 2031-2034.

3. Karol, I.L., Y. Ozolin, and E.Rozanov, 1994: Modeling Mesoscale Gas-Phase and Heterogeneous Photochemistry in the Aircraft Engine Exhaust Plume Interacting with the Ambient Atmosphere, - in: "Impact of Emissions from Aircraft and Spacecraft Upon the Atmosphere, U.Schumann and D.Wurzel (eds.) DLR-Mitteilung 94-06, 342-347.

4. Garcia,R.R, and S. Solomon, 1983:A numerical model of the zonally averaged dynamical and chemical structure of the middle atmosphere, *J.Geophys.Res.*, **88**, 1379-1400

5. Hitchman, M.H., and G.Brasseur, 1988: Rossby wave activity in a two -dimensional model: closure for wave driving and meridional eddy diffusivity, *J.Geophys.Res.*, **93**, 9405-9417

6. Barnett, J.J. and M.Corney, 1985: Middle atmosphere reference model derived from satellite data, *Handbook for MAP*, **16**, 47-85

7. Brasseur,G., M.H.Hitchman, S.Walters, M.Dymek, E.Falise and M.Pirre, 1990: An interactive chemical dynamical radiative two-dimensional model of the middle atmosphere. *J.Geophys.Res.*, **95**, 5639-5655

8. Prather, M.J., Numerical advection by conservation of second-order moments, 1986: *J.Geophys.Res.*, **91**, 6671-6681

9. The impact of NO_x Emissions from Aircraft Upon the Atmosphere at Flight Altitudes 8-15 km (AERONOX), U.Schumann (ed.), ISBN-92-826-8281-1, 1995, 471 pages.

10.WMO, 1995: Scientific Assessment of Ozone Depletion: 1994, World Meteorological Organization, Report No. **37**, Geneva

Hybrid Advection Scheme for 3-Dimensional Atmospheric Models: Testing and Application for a Study of NO_x Transport

Vladimir A. Zubov*, Eugene V. Rozanov*,
Michael E. Schlesinger**, Natalia G. Andronova**
* Main Geophysical Observatory, St. Petersburg, Russia
** Department of Atmospheric Sciences,
University of Illinois at Urbana-Champaign

Abstract. ~~We have developed~~ A hybrid transport scheme, consisting of the semi-Lagrangian scheme for horizontal advection and the Prather scheme for vertical transport, which ~~we~~ have used ~~in the University of Illinois at Urbana-Champaign (UIUC) 3-D~~ Atmospheric Chemical Transport ~~(ACT)~~ model to calculate the distributions of different chemical species. The performance of the new hybrid scheme has been evaluated in comparison with other transport schemes on the basis of specially designed tests. The seasonal cycle of the distribution of N_2O simulated by the ~~ACT~~ model, as well as the dispersion of NO_x exhausted from subsonic aircraft, are in a good agreement with published data.

1. Introduction

The problems of ozone depletion, climate change and atmospheric pollution strongly depend on the processes of production, destruction and transport of chemical species. Of fundamental importance in understand these problems via computer simulations by mathematical models is the accurate calculation of the 3-dimensional advective transport of the chemical species over the globe. Here we present a hybrid transport scheme that is not only highly accurate, but is also computationally efficient.

2. Description of the Hybrid Scheme

The hybrid scheme is a combination of the Prather scheme [1], which is used in the vertical direction, and a semi-Lagrangian (SL) scheme, which is used for horizontal advection on a sphere [2]. Both the Prather and SL schemes have properties that are desirable for numerical transport of chemical species. The SL scheme is monotonic, has small numerical diffusion and small phase error, is able to calculate the transport of species having large spatial gradients, and guarantees the stability and accuracy for time steps larger than the CFL limit [3]. In contrast, the Prather scheme is strictly conservative, but guarantees stability only for time steps smaller than the CFL limit.

The maximum stable time step (Δt) in a quasi-hydrostatic model using spherical coordinates is generally determined by the minimum east-west grid distance nearest the poles. Accordingly, it is generally possible to use a larger time step in the vertical direction than in the horizontal direction. For example, in the UIUC atmospheric general circulation model having a 4°x5° latitude-longitude resolution and a vertical resolution of about 2 km, the Δt for vertical transport can exceed 10 times the Δt for horizontal transport. Accordingly, in the hybrid scheme we use the Prather scheme for vertical transport and the SL scheme for horizontal transport. The use of the SL scheme for the horizontal transport allows a significantly larger time step, and smaller dependence on any increase of horizontal resolution, than would use of the Prather scheme. Furthermore, use of the Prather scheme for transport in only a single direction (vertical) instead of three reduces from 10 to 3 the number of moments that define the distribution of species in each model box. Moreover, combination of the SL scheme with the Prather scheme yields a significant economy in the transport calculation compared to using the Prather scheme alone, but attains an accuracy higher than that of the semi-Lagrangian method scheme alone.

It is difficult to combine the Prather and SL schemes because of their inherent differences. The SL scheme describes the transport of particles, hence it is used for the numerical solution of the species continuity equation in advective form,

$$\frac{\partial \mu}{\partial t} + U\frac{\partial \mu}{a\cos\theta \partial \lambda} + V\frac{\partial \mu}{a\partial \theta} + W\frac{\partial \mu}{\partial z} = P_{AD} - L\mu \quad , \tag{1}$$

where μ is the species mixing ratio, $\lambda \in (0, 2\pi)$ is longitude; $\theta \in (-\pi/2, \pi/2)$ is latitude; $z = H\log(P_0 / P)$ is altitude, with H the scale height, P the pressure and $P_0 = 1013$ mb; a is the radius of the earth; P_{AD} is the species source for the equation in advective form; L is a parameter of the species sink; and U, V and W are the velocity components in the λ, θ and z directions, respectively. In contrast, the Prather scheme is essentially an Euler scheme which is applied to the species continuity equation in flux form,

$$\frac{\partial(\mu\rho)}{\partial t} + \frac{1}{a\cos\theta}\frac{\partial}{\partial \lambda}(U\mu\rho) + \frac{1}{a\cos\theta}\frac{\partial}{\partial \theta}(V\mu\rho\cos\theta) + \frac{\partial}{\partial z}(W\mu\rho) = P_{DI} - L\mu\rho \quad , \tag{2}$$

where $\rho = \rho_0 \exp(-z/H)$ is density, with ρ_0 a reference density at P_0, and P_{DI} is the species source for the equation of flux (divergent) form.

Of course, both forms of the species continuity equation, Eqs. (1) and (2), are equivalent when the law of mass conservation for the atmosphere is valid,

$$\frac{1}{a\cdot\cos\theta}\cdot\frac{\partial}{\partial \lambda}(U\rho) + \frac{1}{a\cos\theta}\frac{\partial}{\partial \theta}(V\rho\cos\theta) + \frac{\partial}{\partial z}(W\rho) = 0 \quad . \tag{3}$$

Accordingly, to use the Prather scheme in the vertical direction and the SL scheme in the horizontal direction we transform the last term on the left-hand side of Eq. (1) to flux form by adding to it the divergence of vertical atmospheric mass flux,

$$W\frac{\partial \mu}{\partial z} = \frac{1}{\rho}\frac{\partial}{\partial z}(W\mu\rho) - \frac{\mu}{\rho}\frac{\partial W\rho}{\partial z} \quad , \tag{4}$$

to obtain the form of the species continuity equation for the hybrid scheme,

$$\frac{\partial \mu}{\partial t} + U\frac{\partial \mu}{a\cos\theta \partial \lambda} + V\frac{\partial \mu}{a\partial \theta} + \frac{1}{\rho}\frac{\partial}{\partial z}(W\mu\rho) - \frac{\mu}{\rho}\frac{\partial W\rho}{\partial z} = P - L\mu \quad . \tag{5}$$

The hybrid scheme uses the splitting method [4] in three steps. First, the vertical transport by the Prather scheme – the third term on the right-hand side of Eq. (5) – is calculated. Second, the vertical divergence of the atmospheric mass flux – the last term on the right-hand side of Eq. (5) – is evaluated by an implicit scheme. Third, the horizontal transport is calculated by the SL scheme [2]. In this SL method we use Hermit's cubic interpolation, with estimation of derivatives by the Hyman method.

The general stability analysis of the splitting method shows that it is stable if its individual steps are stable [4]. Thus the hybrid scheme is conditionally stable. The stability condition is that required by the Prather scheme to satisfy the CFL condition, $W\Delta t < \Delta z$, where Δz is the vertical resolution of the model. The order of accuracy for the hybrid scheme can be evaluated from the orders of accuracy of its component schemes. The Prather scheme has third-order accuracy in space and first-order accuracy in time [1]. According to [3], the SL scheme with cubic-spline interpolation also has third-order accuracy in space (estimation made for the 1-D transport with constant speed) and first-order accuracy in time. Thus, the accuracy of hybrid scheme can be estimated as $O(\Delta x^3)$ in space and $O(\Delta t)$ in time.

3. Comparison of the Prather, SL and Hybrid schemes.

Rather than test the hybrid scheme in comparison with the Prather and SL schemes for an idealized flow such as 2-D solid-body rotation on either a plane or sphere [2], we have developed a new testing procedure and have applied it to the realistic problem of the 3-D steady-state global distribution for a species having a tropospheric source. The new testing procedure consists of four steps: (1) prescription of analytical expressions for the 3-D distributions of the wind field and the concentration and sink of a chemical species; (2) determination of the consistent analytical expression for the 3-D distribution of the source of the species from the species continuity equation and the prescribed analytical expressions; (3) numerical simulation of the species distribution for any particular transport scheme using the analytical expressions for the wind and chemical sink and source; and (4) analysis of the accuracy and performance of the numerical transport scheme, determined by comparing its numerical solution for the species distribution with the analytical distribution.

The results of numerical simulation for the Prather scheme show that its error relative to the analytical solution is less than 1% almost everywhere in the model atmosphere.

Figure 1(a-c) presents the ratio of the absolute value of the error, relative to the analytical solution, of the numerical solutions for the SL and hybrid schemes to the corresponding error for the Prather scheme. It is evident that, for the same timestep, the hybrid scheme is everywhere more accurate than the SL scheme. The maximum ratio for the hybrid scheme is 3-4 in comparison to 20-30 for the SL scheme. Furthermore, it is seen that the hybrid scheme is superior to the SL scheme even when it has a threefold larger timestep.

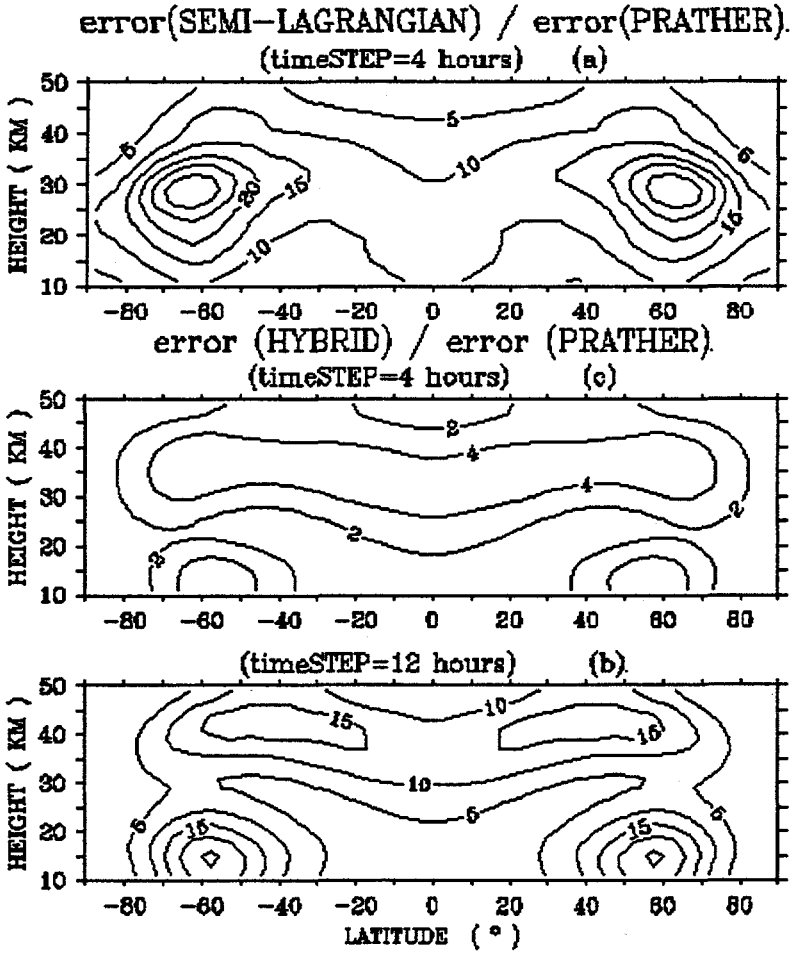

Fig. 1. – Ratio of the absolute value of the error of the numerical solution relative to the analytical solution: (a) SL scheme to Prather scheme, timestep = 4 hours; (c) hybrid scheme to Prather scheme, timestep = 4 hours; (b) hybrid scheme to Prather scheme, timestep = 12 hours.

Table 1 presents the accuracy of the Prather, SL and hybrid schemes relative to the analytical solution in terms of their maximum positive error, maximum negative error, mean absolute error, and total mass conservation error over the model atmosphere. Also presented for each scheme are its timestep, the CPU time required on a DEC AXP 3000/600 (175 MHz) computer to calculate the transport of 20 species for a day, and the operational memory (RAM) requires for the 20 model species. It is evident from *Table 1* that the Prather scheme has the highest accuracy and that the accuracy of the hybrid scheme is superior to that of the LS scheme and is close to that of the Prather scheme. Although the hybrid scheme requires 3 times more memory than the SL scheme, this does not appear to be a serious constraint for contemporary computers. Furthermore, although none of the schemes exactly conserve species mass, the hybrid scheme performs nearly as well as the Prather scheme in mass conservation.

4. Model simulation of NO_x and N_2O distributions

Of great interest is how well the hybrid transport scheme is able to reproduce the distribution of different species under realistic atmospheric conditions. Accordingly, we have implemented the hybrid scheme in the UIUC 3-D Atmospheric Chemical Transport (ACT) Model. The ACT model has 4° x5° latitude-longitude resolution, 24-vertical layers from the surface to 1 mb, and uses the daily-mean wind fields from the 24-layer UIUC 3-D atmospheric general circulation model. To evaluate the performance of the hybrid transport scheme, the ACT model was used without its chemical package.

Table 1. *Comparison of the Prather, SL and hybrid transport schemes.*

Quantity/Scheme	Prather	SL	Hybrid
Maximum positive error (%)	1.68	6.53	1.52
Maximum negative error (%)	0.41	0.27	2.51
Mean absolute error (%)	0.18	3.96	0.48
Total mass conservation error (%)	–0.01	1.72	0.09
Timestep (hr)	~ 1	~ 4	~ 4
RAM for 20 species (Mb)*	40	4	12
CPU Time for 20 species for 1 day (s)*	770	84	84

* Estimated for the AXP 3000/600, 175 MHz computer

For the simulation of the N_2O distribution, the mixing ratio of N_2O was prescribed from the surface to 2 km height. The stratospheric chemical sink was parameterized by the very simple formulae proposed for the comparison of 2-D and 3-D transport models [5]. The ACT model was run for 3 years and the distribution of N_2O for the last year was analyzed.

Figure 2 displays the simulated zonally averaged monthly mean N_2O mixing ratio for March and September, and *Fig. 3* shows the latitude-longitude cross section at 4 mb for March. These results show that the hybrid scheme reproduces the principal features of the observed N_2O distribution reasonably well, including the displacement of the concentration peak toward the summer hemisphere, the polar minimum connected with the downward motion in the high latitudes, and some of the flattening of the zonal-mean distribution in the northern hemisphere reported in [6]. The mixing zone in the tropical upper stratosphere reported in [7] is also clearly seen in *Fig. 3* between the equator and 30-35°S.

For the simulation of the dispersion of NO_x, the ACT model was run for three years with the emissions of NO_x by subsonic-aircraft prescribed on the basis of the NASA database. The chemical sink of NO_x was calculated according to the simple parameterization proposed in Schumann [8] for the comparison of transport schemes for 3-D models, with the NO_x half-life taken as 10 days.

The January latitude-longitude cross section of NO_x mixing ratio at 200 mb is shown in *Fig. 4*. The results of this simulation can be compared with those for other 3-D ACT models published by Schumann [8]. The location of the maximum NO_x mixing ratio simulated by our model is in a good agreement with that simulated by all the other models because the NO_x distribution is mainly determined by the location of its source – the exhaust from aircraft in the Atlantic flight corridor between 30°N and 60°N. The maximum mixing ratio simulated by our model is about 70 pptv, which is slightly less than the mean value published by Schumann [8]. This occurs because the intensity of the NO_x emission according to the NASA data is less than

that of the emission used by Schumann [8]. The location, shape and length of the region wherein the NO_x mixing ratio exceeds 40 pptv is comparable with these features simulated by most of the other models. This agreement is the result of having the correct intensity of meridional circulation in our atmospheric general circulation model and the correct treatment of advection by the hybrid scheme.

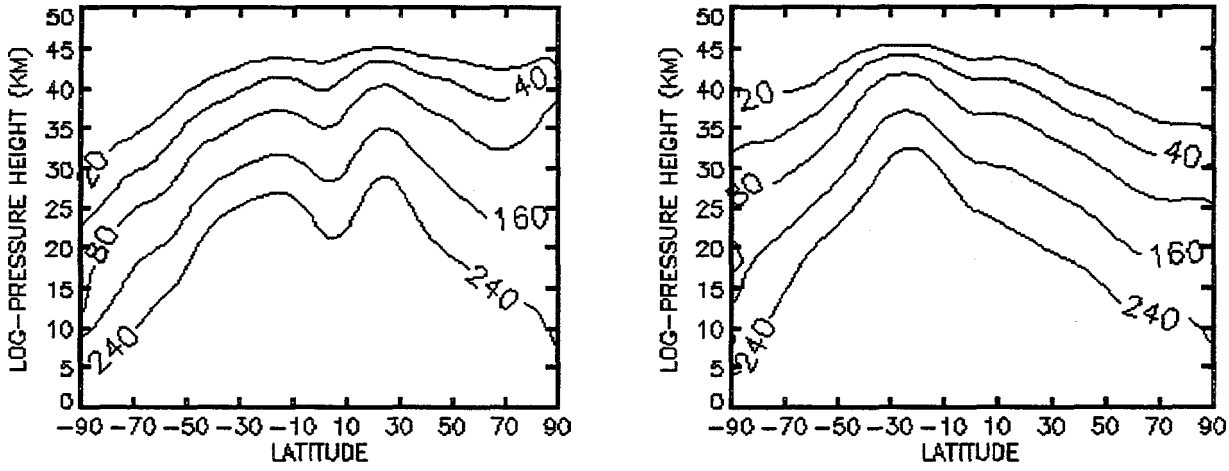

Fig. 2. – Simulated latitude-altitude cross section of N_2O mixing ratio (ppbv) for March (right panel) and September (left panel).

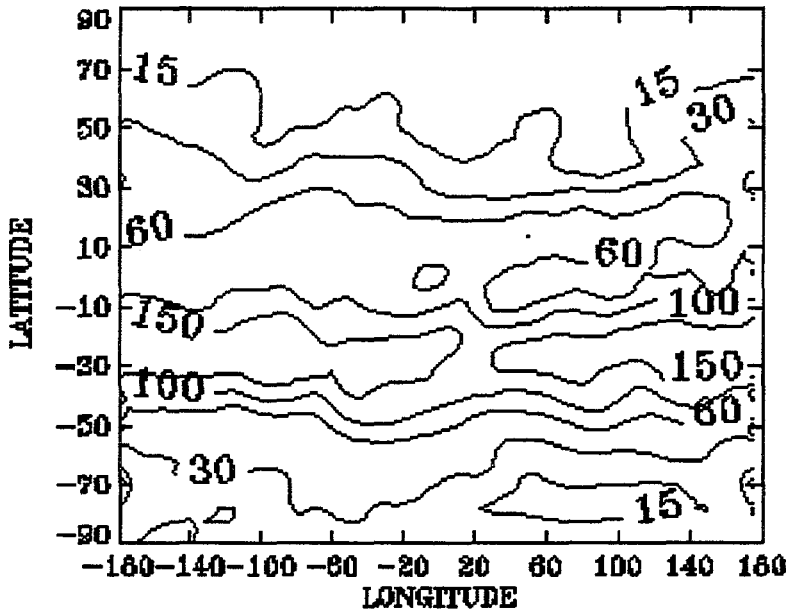

Fig. 3. – Simulated latitude-longitude cross section of N_2O mixing ratio (ppbv) at 4 mb for March.

5. Conclusion

In this study we have presented a hybrid numerical scheme for the 3-D global advective transport of chemical species. The hybrid scheme uses the Prather algorithm [1] for vertical transport and the semi-Lagrangian method [2] for horizontal transport. With the help of a specially developed test, a comparison is made among the hybrid, Prather and semi-Lagrangian

schemes. This test uses analytic solutions, is easy to perform, and gives a more complete evaluation of a numerical transport scheme for realistic atmospheric conditions, including large spatial gradients developed by the sources of advective transport, than does a test based on simulating solid-body fluid rotation.

According to this test, the accuracy of the hybrid scheme exceeds that of the semi-Lagrangian scheme by a factor of 4-5 (*Fig. 1, Table 1*). Also, the hybrid scheme is closer in accuracy to the Prather scheme than is the semi-Lagrangian scheme, but requires 9 times less computer time (*Table 1*) than the Prather scheme. Comparison with observational data and other models of the seasonal variation of N_2O mixing ratio and the dispersion of aircraft NO_x emission simulated by the UIUC 3-D ACT model demonstrates the reliability and performance of the hybrid scheme. Accordingly, we conclude that the hybrid scheme is a suitable method to simulate the 3-D global transport of non-conservative chemical species.

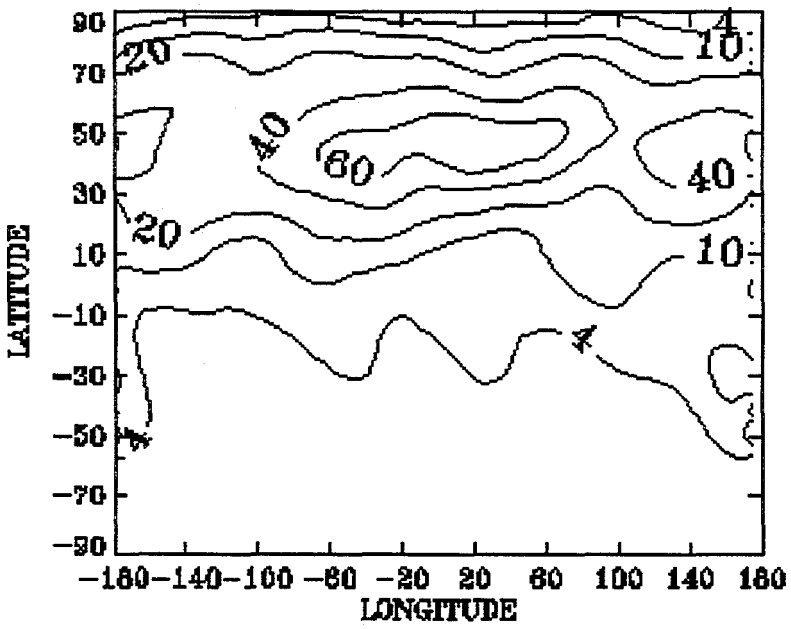

Fig. 4. – Simulated latitude-longitude cross section of NO_x mixing ratio (pptv) at 200 mb for January.

References

1. Prather, 1986: Numerical advection by conservation of second-order moments, J. Geophys., Res., **91**, 6671-6681.

2. Williamson, D.L., and P.J. Rasch, 1989: Two-dimensional semi-Lagrangian transport with sharp-preserving interpolation, Mon. Wea. Rev., **117**, 102-129.

3. Staniforth, A., and J. Cote, 1991: Semi-Lagrangian integration schemes for atmospheric models – A review, Mon. Wea. Rev., **119**, 2209-2223.

4. Mesinger, F., and A. Arakawa, 1976: Numerical methods used in atmospheric models, , World Meteorological Organization: Geneva. pp. 64.

5. Hall, T.M., and M.J. Prather, 1995: Seasonal evolution of N_2O, O_3 and CO_2: Three dimensional simulations of stratospheric correlations, J. Geophys. Res., **100**, 16,699-16,720.

6. Rasch, P.J., B.A. Boville, and G.P. Brasseur, 1995: A three-dimensional general circulation model with coupled chemistry for the middle atmosphere, J. Geophys. Res., **100**, 9041-9071.

7. Dunkerton, T.J., and D.J. O'Sullivan, 1996: Mixing zone in the tropical stratosphere above 10 mb, Geophys. Res. Lettr., **23**, 2497-2500.

8. Schumann, U. (ed.), 1995: The impact of NOX emissions from aircraft upon the atmosphere at flight altitudes 8-15 km (AERONOX), EUR 16209 EN, European Commission, Brussels.

Impact of Air Traffic on the Climate

Giselle Stief, Università degli Studi di Firenze, Ist. di Agrometeorologia
Piazzale delle Cascine, I - 50144 Firenze, Italy

Abstract

Though emission from world-wide air traffic may seem to be relatively small in comparison to that from all other anthropogenic sources, the deleterious effect on the climate of the gases and particles emitted by planes is disproportionately large. It is thought that air traffic, working together with pollutants that have already accumulated at critical heights, and depending on humidity and temperature, plays a decisive role in helping to cause the changes, presented below, in global radiation, sunshine duration, rainfall and maximum and minimum temperatures which are taking place.

1. Introduction

Climatic factors are growing more and more important, in a negative sense, where the national economy is concerned. It is not only scientists who are observing, with continually growing concern, the disappearance of the classical four seasons that are typical for our latitudes. The normal progress of the seasons is being more and more disturbed by periods of unnatural heat or cold that occur with great abruptness. The situation is being aggravated by a shifting of the rainy seasons, changes in the amounts of daily rainfall, serious changes in the global radiation budget and fewer hours of sunshine. All this is even more injurious because it is usually linked with the presence of harmful substances in the air, the concentration of which is often above tolerable levels. The events listed are, in their effect as a whole, the more damaging the more quickly they follow one another . While anomalies or extremes of climate were at one time the exception, it has become steadily clearer in recent years that the irregularities of climate which are so extraordinarily unfavourable for vegetation - and in particular for agriculture (failed harvests) - and for the health of human beings, are seeming to become the norm.

2. Base material

The "SIC" programme (an information system concerning climatic development) is a research project sponsored by the Italian Ministry for Agriculture and Forests. It is PC-compatible and enables the user to trace climatic events and their irregularity and to produce graphic images on the monitor screen. Climatic data has been gathered from 27 Italian weather stations over the period from 1951 to 1991 and evaluated. The decisive factor in the selection of the weather stations was that those chosen had available large amounts of data concerned with global radiation.

The Italian results are to a great extent also valid for central Europe and possibly for the whole of the northern hemisphere that lies between 30° and 65° north and below heavily-used flight corridors.

3. Problems

The debate about the climate is concerned in particular with the question as to whether air pollution is leading to a global increase in temperature. Research results have proved that, above all, CO_2 emission, ozone and water vapour lead to an increase in temperatures. Looking at the

question of temperature increase as a whole, however, takes insufficient account of the fact that, apart from the question of a global increase in temperature, short or long phases of zonal temperature decrease are suddenly occurring with increasing frequency. [Stief]

An initial evaluation of the data bank is shown in the appended tables. The individual climate parameters in many cases reveal trends that seem to be contradictory. There are strong grounds for concluding that the meteorological phenomena, which seem to be of a completely different nature, have a common cause, namely, the enrichment of the troposphere, the tropopause zone and the lower stratosphere with gases and particles and with H_20, the significance of which becomes increasingly greater above the upper troposphere. Responsible for this are the very varied sources of emission near the ground; in the upper troposphere and beyond, however, and, above all, at the altitudes of air traffic, it is the exhaust gases of aircraft that are responsible. Air traffic has a very special significance since it is the only source of pollution that continuously covers large areas of the upper troposphere, the tropopause and the lower stratosphere. These zones react very sensitively to "injections" of gases, particles and water vapour. This is further aggravated by the fact that every aeroplane at a high level acts as a "catalyst".

Particles of anthropogenic origin, which can carry condensation nuclei leading to cloud formation, are either directly emitted or are formed, in the course of complicated physical-chemical processes, from nitric acid ($HN0_3$), sulphuric acid (H_2S0_4), water (H_20) and soot, etc. They increase the number and change the size of natural ice kernels and condensation nuclei [Fabian, Schumann]. They are not only able to change the character of natural clouds (amounts and duration of rainfall, radiation charac-teristics) but they also lead with increasing frequency to additional pollutant-affected cloud formation which are not easy to classify according to meteorological criteria hitherto used.These additional clouds can often be visually recognised because of their different colouring and their greater, optical density. It would be valuable to take air samples from those additional clouds that are clearly recognisable as clouds formed by harmful substances.

Contrails are visible plumes of aircraft exhaust fumes. On some days in the year, a dense network of contrails remains clearly visible in the sky for protracted periods. Satellite pictures taken on these days assist in becoming aware of the extent to which the whole of the air space over Europe (and over other regions of the Earth where there is heavy air traffic) is adversely affected "hazed" by aircraft emission every day.

The exhaust fumes emitted by aircraft do not, however, always manifest themselves as visible contrails. The widespread "blanket" of harmful substances is renewed *every day*. The emitted substances accumulate, particularly in the tropopause, where there is a kind of permanent inversion, and above; under certain conditions in the upper troposphere, too (e.g. in high pressure zones and where there are stagnating masses of air; also in "mixed" situations). Even when this emission, usually in the early stages, is not easy to see, it has a clearly recognisable influence on all meteorological processes. When the sun is shining, concentrated layers of photo-chemical smog with a high proportion of soot form at the various levels of the flight corridors.

This can lead, among other things, to an increase in the temperature of the emission-loaded layers. For this reason alone, a very critical view should already be taken of air traffic in the lower strato-sphere. It would be irresponsible to increase its occurrence there since an increase in temperature and cloud formation in these layers could lead to a lowering of temperature at ground level. In addition to this, the condensation nuclei potential of these layers (e.g. when thunderstorms occur) is "available" for cloud formation, i.e. it is carried to and becomes involved in the meteorological events taking place in the troposphere. This happens when heavily polluted, relatively humid air above heated surfaces rises to great heights and is added to the layer of harmful substances

emitted by aircraft which has already accumulated there. This can spark off spontaneous saturation processes, with the formation of large ice particles. This could be one of the causes of the ever more frequent hailstorms and cloudbursts (up to 600 mm per day). It would become dangerous if the humidity in the normally very dry layers were to increase (e.g. as the result of a big volcanic eruption). This could set off a spontaneous condensation process covering a large area and the enlarged layers of stratospheric cloud could lead to a long-term, drastic cooling of the ground underneath. This would be comparable to the "nuclear winter" effect.

On over 60% of all the days on which visible contrails form, clouds are formed below their level during the course of the day. *For the additional cloud formation caused by air traffic, however, it is not important whether visible contrails are formed by the emission of aircraft exhaust fumes.* By far the largest part of the additional cloud caused by air traffic in conjunction with other pollutants already in the atmosphere is formed without this initial phase that the layman can easily recognise. What is decisive is that CO_2, NOx, H_2O, CO, SO_2, HC and soot particles, etc. in damaging quantities are released into the critical layers referred to. Strong winds in the upper troposphere can thin out these layers or carry them away and this can lead to a temporary improvement of the situation. Where there is a high concentration of these pollutants this leads, depending on the meteorological situation in each case, on the surrounding temperature and relative humidity and on the height of the sun above the horizon, to very differing phenomena:

- flat, dense layers of photo-chemical or condensed smog
- additional cirrus, cirro-cumulus and cirrostratus clouds
- additional altocumulus and altostratus clouds
- additional nimbostratus clouds
- "islands" of clouds of harmful substances, flat, from grey-brown to anthracite in colour, transparent or opaque, mostly without sharp contours.

The once so typical, stable, good weather associated with high pressure situations is seriously affected by these phenomena with increasing frequency. Because of the absence of air movement, which encourages the accumulation of harmful substances, many periods of high pressure are spoilt by grey skies, untypically low temperatures and even "artificial" rain. At holiday times, when the number of week-end flights drastically increases, such conditions have become the norm, as if the air masses have been given such a dosage of condensation nuclei that spontaneous rainfall occurs.

The cloud formations, in part "artificial" caused by air pollution, change the meteorological parameters decisively. Their varying forms, however, are determined by the particular meteorological conditions in each case. In order to calculate the amount of additional cloud caused by air traffic it is insufficient, for the reasons given above, to estimate only the amount of cloud caused by visible contrails.

4. Results

That air pollution already has a very marked effect on meteorological events can be confirmed by the analysis of climate data.The SIC programme (Sistema Informativo sull'andamento del Clima) was developed at the request of the Italian Ministry of Agriculture and Forestry. The first version of this programme, which can be run on any PC, enables the user to call up climate data for 27 Italian weather stations, in the form of diagrams and graphs, covering the period 1951 to 1991 . With this programme, the user can trace and graphically represent climatic events and their irregularities in a variety of ways.
A first evaluation of the data bank led to the results shown in the tables to the side. The individual climate parameters indicate trends that often seem to be conflicting. The supposition immediately presents itself that meteorological phenomena which seem to be of a completely

different nature have a common cause: the enrichment of the lower and upper atmosphere with condensation nuclei, ice kernels and ice particles, principally from aircraft and cars.
Unusual climatic events usually have a negative effect on vegetation as a whole and, as a consequence, affect economic equilibrium adversely. This applies to the abrupt onset of unusually high or low temperatures (heat or cold "shocks"), persisting periods of untypically low temperatures, long hot spells, rainfall that continues for too long, heavy rainfall or long periods of aridity that are untypical for a particular time of year. All these events are even more harmful because they are usually coupled with the presence of pollutants in the atmosphere, the concentration of which often exceeds tolerable levels. The combined effect of all the events listed is all the more harmful in proportion to the rapidity with which the separate events follow one another. The damage to the economy where agriculture, forestry, tourism, health care, the building trade, transport, the preservation of monuments are concerned and the damage caused by natural catastrophes have now passed beyond the limit of what the economy can bear. It is urgently necessary that everything possible is done to change this situation.

4.1 Hours of sunshine

Of the 22 weather stations the data from which has been evaluated, 18 reveal a reduction - 11, in fact, a significant reduction - in the amount of sunshine. As one can see from the tables, the greatest reduction is to be seen in the period May to September, months which are decisive where plant growth is concerned.
The greatest reduction, 7% per decade, has been measured in Bolzano. If this trend continues unchanged. by 2000, Bolzano will have about 610 hours less sunshine than in 1961, amounting to about 1.7 hours less sunshine per day. The figures for sunshine duration alone, however, tells us nothing about the intensity of the sunshine which reaches the Earth's surface. Even if the sun shines for a comparable length of time, air pollution has the effect of worsening the quality of the sunshine. Reductions of the order of 12% in 30 years can have a negative effect on all photosynthetic processes and on health.
A study by G.R. Weber of the duration of sunshine in the FRG indicates the same trend. Weber established that there was a reduction in the annual duration of sunshine between 1951 and 1987 at all 54 weather stations that were included in the study. At some stations, the recorded loss was more than 300 hours (18%).

4.2 Global solar radiation

Of the 27 stations, 21 indicate a downward trend. The reduction is significant in 7 cases. This alarming drop is found at all latitudes throughout Italy. The greatest reduction radiation, as with the duration of sunshine, is to be seen in the period May to September, months which are decisive where plant growth and ripening is concerned.
The supposition that a reduction in global radiation is always coupled with a reduction in the duration of sunshine cannot be confirmed without reservation. While it applies to most stations, the Milan and Crotone stations report a reduction in global radiation despite a slight increase in the duration of sunshine.
The greatest reduction (25% in 27 years) has been measured in Venice. Thus, Venice showed, at the end of the data list made available, the same level of radiation for 1987 as the Hohenpeissenberg (Bavaria) station. In 1959, the values for Venice were far in excess of those for Hohenpeissenberg:

	Venice	Hohenpeissenberg	
1959	538 000 J/cm^2	454 000 J/cm^2	1959
1987	414 000 J/cm^2	414 000 J/cm^2	1987

Here are some fundamental reflections that these figures provoke:
Fluctuations in atmospheric micro-contaminants such as gases, aerosol and particles, which are carried into the atmosphere by volcanic eruptions and/or, directly or indirectly, as a result of human activity, can influence the processes by which the penetration of global radiation through the atmosphere is regulated. Changes in the energy budget of our planet and the chemical composition of its atmosphere can very quickly lead to changes in the delicate balance of the climatic system and to far-reaching changes in the basic preconditions for all vital processes.

4.3 Precipitation

There has been no significant change in the total yearly amount of precipitation registered at most of the stations. On the other hand, there has been considerable change in the distribution of periods of rainfall throughout the year and an increase in bursts of heavy rainfall. It is almost always the latter which determine the trend.
The tables showing precipitation of over 100 mm/d enables us to recognise that these violent events, as recorded at many stations, have taken place during the last 30 years with continually increasing frequency and increasing intensity. A large part of the rainfall also occurs outside the classic rainy seasons. The concentration of rainfall is provoking ever more frequent floods throughout Europe and, absurd though it seems, is increasing the problem of soil aridity, particularly in the Mediterranean area. Whereas water has time to seep through to the deeper earth layers when rainfall is "normal" and evenly distributed, with periods of heavy rain it flows away on the surface and quickly reaches the sea.
One cause of the ever more frequent bursts of heavy rain and the shifting of the rainy seasons could be the enrichment of the upper air with aerosols, ice kernels, ice particles and water vapour. A warming of the air between about 4 and 13 km high, which is caused by air pollution, can, over a longer period of time, hinder a condensation process and thus prevent the formation of clouds - despite an excess of condensation kernels. When a state of super-saturation is reached and cold moist is drawn to the area in question, unusually heavy rainfall or some other violent climatic event is the result.

4.4Temperatures

The data show that the theory of global temperature increase is not reconcilable with "Italian reality".

Maximum temperatures

The records of the majority of mainland stations show a marked fall in temperatures for the months of April, May, June and November. The last column of each table of temperature trends shows the mean values for the period April till June and not, as is the case with global radiation, from March to October. The almost continuously high temperatures in July and August would distort the trend figures and would lead to a failure to recognise the reality of the situation in spring, a situation that is now critical for agriculture. Depending on the height of the sun (i.e. the time of year) and also on the varying meteorological conditions, the air pollution that is found in the various atmospheric layers has very conflicting effects: at certain times of the year it leads to abnormal cooling and at others to an unnatural increase in temperature. The drop in temperature that has been recorded for the months of April, May, June and November has already led to heavy losses in agriculture in recent years (field crops, citrus fruit, wine, olives). Cold has also damaged agriculture in countries outside Europe, for example in Brazil, where twice in the last three years a large part of the Brazilian coffee harvest has been destroyed by cold.

Minimum temperatures

Almost exactly the same applies to minimum temperatures: a drop in temperature during the months of April, May, June and November recorded at almost all mainland stations, as well as at Alghero and Cagliari; temperature increases have been recorded at almost all stations, above all in the months of July and August.

Bibliography

Fabian P. : Atmosphäre und Umwelt, Springer Verlag, Berlin, 1994

Pfeiffer,M., Fischer,M.: Unheil über unseren Köpfen, Quell Verlag Stuttgart, 1989

Schumann U. : Emissionen des Luftverkehrs im Reiseflug und dadurch bedingte Änderungen in der Atmosphäre, "Luftreinhaltung im Flugverkehr", die Umweltakademie, Weßling, 1996

Schumann U. : On Conditions for Contrail Formation from Aircraft Exhausts, Meteorolog. Z., N.F. 5, 1996

Schumann U. : Determination of Contrails from Satellite Data and Observational Results, lecture notes in Engrg., Vol. 60, Springer Verlag, Berlin, 1990

Stief G. : Pianeta Azzuro - Pianeta Grigio, Collana Verde del Ministero dell'Agricoltura e delle Foreste, 90/1992, Roma

Stief, G. : The Atmospheric Pollution Effect on Climate and on Radiation Budget in Italy, Annales Geophysicae, Suppl.3,Vol.13, 1995

LONGWAVE ATMOSPHERIC RADIATION AS A POSSIBLE INDICATOR OF THE AVIATION IMPACT

N.A.Zaitseva, Central Aerological Observatory of the Russian Federal Service for Hydrometeorology and Environmental Monitoring, Dolgoprudny of Moscow Region, 141700, Russia

Radiative regime plays a very important role in the formation of the thermal regime in the free atmosphere where aircraft routes go. As far as aircraft emissions obviously change composition of the atmospheric air they should be sensed by radiation parameters, such as downward (in first turn) and upward long-wave fluxes. Basing on the well-known fact that the long-wave (LW) radiation fluxes form the atmosphere temperatures, it might be supposed that the accurate measurements of the fluxes in regions of crowded aircraft routes and at the same time outside these regions, could detect the influence.

Studies of the atmosphere radiative regime usually attracts large attention of specialists in different fields because the energetics of the atmosphere is one of major meteorological problems. Statistical data on the radiative fluxes in the atmosphere and their parameterized relations are widely used in the cloud physics, theory of the weather modification, numerical modelling of the atmospheric circulation and global climate as well as in hydrology, meteorology, building problems and other branches of the human activity. The most complicated problem of numerical modelling is account of the non-adiabacy of the atmospheric processes, and successful solution of this problem is retarded by the extreme complication of the processes of radiation transfer in the free atmosphere and its interaction with clouds, aerosol and other atmospheric substances.

While the main part of the short-wave radiation coming from the Sun is transformed at the dividing boundaries of the environment (atmosphere-underlying surface, cloud boundaries), main transformation of the long-wave radiation (LWR) proceeds in the troposphere which both, absorbes and irradiates the LWR. This is the most powerful factor of the heat loss by the system "Earth-Atmosphere" as well as one of most important one of the energy re-distribution in the atmosphere and precisely the LWR transfer is the major reason of the atmospheric processes non-adiabacy. So far, calculations of the LWR fluxes are rather satisfactory only for cloudsless conditions or for cases with very extended Stratus clouds. In this connection, the empirical data of different measurements obtained under different weather conditions prctically all over the globe are of great interest [1]. We should add to the above that "in situ" measurements of the LWR fluxes in the upper atmospheric levels could be detector of the long-term changes of the atmospheric air composition.

Absence of simplified methods of calculations and strong need to have observational data stimulated researchers to develop different instruments to measure the LWR fluxes. To lift LWR sensors in te atmosphere actually all available platforms may be used: manned and automatical balloons , aircrafts and radiosondes. But, while designing an instrument it should be taken into careful consideration that measuring of the heat radiation is very complicated task, first of all, due to the "noise" irradiance from all around (sensor carrier different parts), then it is rather difficult to consider and calculate the heat exchange inside a sensor, practically impossible to measure correctly LWR on the background of the short-wave radiation fluxes during a day time, etc. [2, 3, 4]. Manned balloon, in principle, alloz using on its board the standard ground instruments, such as pyrgeometer and balancemeter. The seria of the unique observations from board of a manned balloons in the troposphere was conducted at the middle Russia by specialists of the Central Aerological Observatory after the Second World War [5]. The moving air

transformation was studied in these flights and first strict indications on the significant role of the LWR fluxes was emphasized. Wide balloon observations at night time were made in 1952-1954 by V.I.Shlyakhov [2] aime at study of vertical LWR fluxes and net radiation regulariries. Role of the dust in free atmosphere was first time shown. Flights of manned balloons are limited by heights of 7-8 km and so do not allow to reach higher levels in the atmosphere. The same difficulty is met when aircraft platform is used for similar measurements. Efforts to install complicated spectral radiation equipment on board of automatical high-level balloon were undertaken [6, 7], but they are also rather complicated and expensive therefore can not be used for monitoring purposes probes it

(3) The only mass method of the LWR measurements in the free atmosphere became the radiometersonde one [4, 8, 9]. In the former USSR, the radiometersonde was succesfully developed in 1961 [4], and already since 1963 the special radiometersounding network started to make regular observations over the USSR territory [10]. It should be emphasized that the mass radiometersonde observations were made only in this country although similar observations were made occasionally in the USA, Germany, Japan and India. In some years the USSR network consisted of 15 stations, the observations were also made from boards of many research ships over oceans (Pacific, Atlantic, Indian) and in the Antarctic. These observations were conducted only at night time because all sensors of the above mentioned radiometersondes could measure LWR fluxes only under full absence of the solar radiation.

Analysis of climatic characteristics of the LWR radiation fluxes had been done in the Central Aerological Observatory and the results were reported and published so we do not describe them here. But the fact of rather small spatial variations of the downward LWR (DLWR) flux was observed at the analysis and it indicates on rather high homogeneity of the (4) atmosphere composition on the high levels over diffrerent regions. At the same time, analysis of the seasonal variations of the downward LWR has revealed that over some stations it has the opposite course of changes from summer to winter and it is mainly observed at rather high levels (50-30 hPa). In the stratosphere over such stations summer values of the DLWR are less than winter ones that means there are negative diffreneces "summer minus winter". Analysis has shown that it was caused by that the optical ozone mass in summer over many regions of the Northern hemisphere is less than in winter due to atmospheric circulation (for example, the well-known fact for Russian Far-East regions). We believe that if the radiometersonde method is able to sense and detect diffirences caused by the ozone variations, it could be possible also to detect by means of regular accurate measurements of the LW fluxes in the high levels possible trends due to influence of the aircraft emissions. The method accuracy was proved by the radiometersonde intercomparison [9] as well as by comparison with other data, and with satellites also.

At this time radiometesounding is not carried out any more but if a necessity to organize rather simple system of a regular monitoring of the LW radiation variations over the most intensive aircraft routes and at the same time over territories which are outside the last ones it could be good tool to reveal a global influence of the aviation impact upon the atmosphere. There is considerable internationa activity in the development of numerical models for different purposes to detect the climate changes due to different resons but we strongly believe that direct "in situ" measurements by rather simple and cheap method also could play important role in the long-term monitoring of the atmosphere state.

References:

1. Feigelson E.M. (Editor), 1981: Radiation in the cloudy atmosphere. L,.Gidrometeoizdat, 280 p.

2. Shlyakhov V.I., 1956: Study of the long-wave radiation balance in the troposphere. L., Gidrometeoizdat, 83 p.

3. Businger I.A., Kuhn P.M., 1960: On the observation of total and net radiation. Journ. of Met., v.10, N 14, pp. 951-964.
4. Kostyanoy G.N., 1963: Actinometric radiosonde ARZ-CAO. Meteorology and Hydrology, N 7, pp. 33-43.
5. Gaigerov S.S. and Kastrov V.G., 1954: Some summaries regarding thermal air transformation based on data of the balloon flights. Trudy CAO, iss. 13, pp. 3-17.
6. Kondratiev K.Ya., Gaevskaya G.N., Nikolsky G.A., 1963: Vertical profile of the radiation balance of the system "Earth`s surface - Atmosphere". Space Researches, v. 1, N 3, pp. 56-59.
7. Kondratiev K.Ya., Gaevskaya G.N., Nikolsky G.A., 1963: Balloon studies of the radiation balance of the system "Earth`s surface - Atmosphere". Space Researches, v. 1, N 3, pp. 60-65.
8. Suomi V.E. and Kuhn P.M., 1958: An economic net radiometer. Tellus, v. 10, pp. 57-63.
9. Kostyanoy G.N., Shlyakhov V.I., 1967: International radiometersonde intecomparison. Meteorology and Hydrology, N 5, pp. 12-17.
10. Zaitseva N.A., Kostyanoy G.N., Shlyakhov V.I., 1971: Mean climatic characteristics of the LWR fields in the free atmosphere. Meteorology and Hydrology, N 7, pp. 43-56.

Model estimate of NO_x production during the cooling of a lightning flash

R. Berton

ONERA, 8 rue des Vertugadins, F-92190 Meudon

Abstract

Since discrepancies of two orders of magnitude are detected in current estimations, the question of NO_x production by lightning has been addressed, and a new theoretical estimate is proposed. The new model deals with a unit length of an evanescent cooling branch of lightning supposed to be cylindrical and axisymmetrical, 1 mm in radius. The kinetics of five chemical species (N, O, N_2, O_2, NO) has been coupled to the full set of hydrodynamic equations expressing the conservation of momentum and energy together with an equation of state. This highly non-linear system is completed by suitable boundary conditions in subsonic regime and then time-integrated by finite differences. It appears that the amount of NO produced in a cross section of channel reaches a maximum at $4{,}6.10^{-7}$ mol/m after 50 µs cooling. At that moment the average temperature is about 3000 K, at which NO is most easily formed. The net yield of NO is found to be 10^{16} molecules per Joule, which is one order of magnitude smaller than other theoretical results.

1. State of the problem

The equivalent amount of NO_x produced by airplanes every year may reach between 0.4 and 0.9 Mt N (subsonic) and 0.1 Mt N (supersonic), while between 1 and 300 Mt N/year are possibly formed in storms by lightning (Liaw, Sisterson & Miller, 1992). Thus the airplane yield is known to within ***a factor two***, whereas the production by lightning (either observational or theoretical) shows discrepancies of ***two orders of magnitude***, which is hardly reliable. The shock wave of the return stroke, which delivers much energy, is often thought of as the main responsible, though it keeps a very high temperature throughout (Chameides, 1979 ; Goldenbaum & Dickerson, 1993). That is why we address the question again, by focussing on the cooling phase of one among many of the evanescent branches.

2. Model

Our model deals with a unit length of a cylindrical channel assumed axisymmetrical, 1 mm in radius. Five chemical species (N, O, N_2, O_2, NO) have been considered to react with each other according to 16 chemical reactions. Their kinetics is coupled to the full set of hydrodynamic equations expressing the conservation of momentum and energy together with an equation of state. This highly non linear system is completed by suitable boundary conditions in subsonic regime and then time-integrated by finite differences with Euler explicit schemes for the dynamical part and Gear's method for the chemical part. The initial temperature is gaussian with a maximum (10000K) on the symmetry axis, the initial pressure is uniform (1 atm) and the chemical concentrations have been taken to be the equilibrium values at the corresponding local temperature.

3. Results

It appears that the instantaneous amount of NO produced ***in a cross section of channel*** reaches a maximum at $4{,}6.10^{-7}$ mol/m after 50 µs cooling. At that time the average temperature is about 3000 K, at which NO is most easily formed. This cooling timescale is quite consistent with the theoretical value obtained from the ratio of the characteristic diameter squared to the thermal diffusivity. The evolution of radial profiles, not displayed here (Berton, 1996) show that a plateau in the pression profile develops with a sharp front at the characteristic radius of the channel (1 mm) and that NO is produced with a maximum at the same place. ***The net yield of NO is found to be 10^{16} molecules per Joule***, which is one order of magnitude smaller than other theoretical results, because of the difference in diameter (two orders of magnitude). In any case, the NO produced in the channel at some time dissappears later simply because the local temperature goes down back to the ambient conditions, in which ***the proportion of NO at equilibrium is negligible***.

4. Conclusion and extensions

Nevertheless, it must be kept in mind that the total production due to one lightning flash depends on the channel length, which may be larger than that of the main stroke linking cloud to ground. More generally, even if our estimate is lower than others (Goldenbaum & Dickerson, 1993), it should be emphasized that the net quantity of NO produced by soft mechanisms may be larger than that produced by more drastic processes such as shock waves ***in the case the former take place in a bigger volume than the latter***.

The effect of radiative transfer has been shown to speed up the cooling and consequently to make the formation of NO quicker, with a slight decrease of the produced amount, but this does not affect significantly our conclusion.

There remains other relevant effects to be included in the model, either physical : turbulent transport, differential velocities, or chemical : others species, electrons, ions, heterogeneous reactions, photodissociations. Of course, the decrease of NO amount when the situation goes back to the ambient should be circumvented by taking into account transport mechanisms (convection, scavenging) that could remove NO before it dissociates.

5. References

Berton, R. : 1996, Model of NO production in the cooling channel of a leader discharge, Geophys. Res. Lett., to be submitted

Chameides, W.L. : 1979, *The implications of CO production in electrical discharges*, Geophys. Res. Lett., **6**, 287-290

Goldenbaum, G.C. & Dickerson, R.R. : 1993, *Nitric oxide production by lightning discharges*, J. Geophys. Res., **98**(D10), 18333-18338

Liaw, Y.P., Sisterson, D.L. & Miller, N.L. : 1992, *Comparison of field, laboratory and theoretical estimates of global nitrogen fixation by lightning*, J. Geophys. Res., **95**(D13), 22489-22494

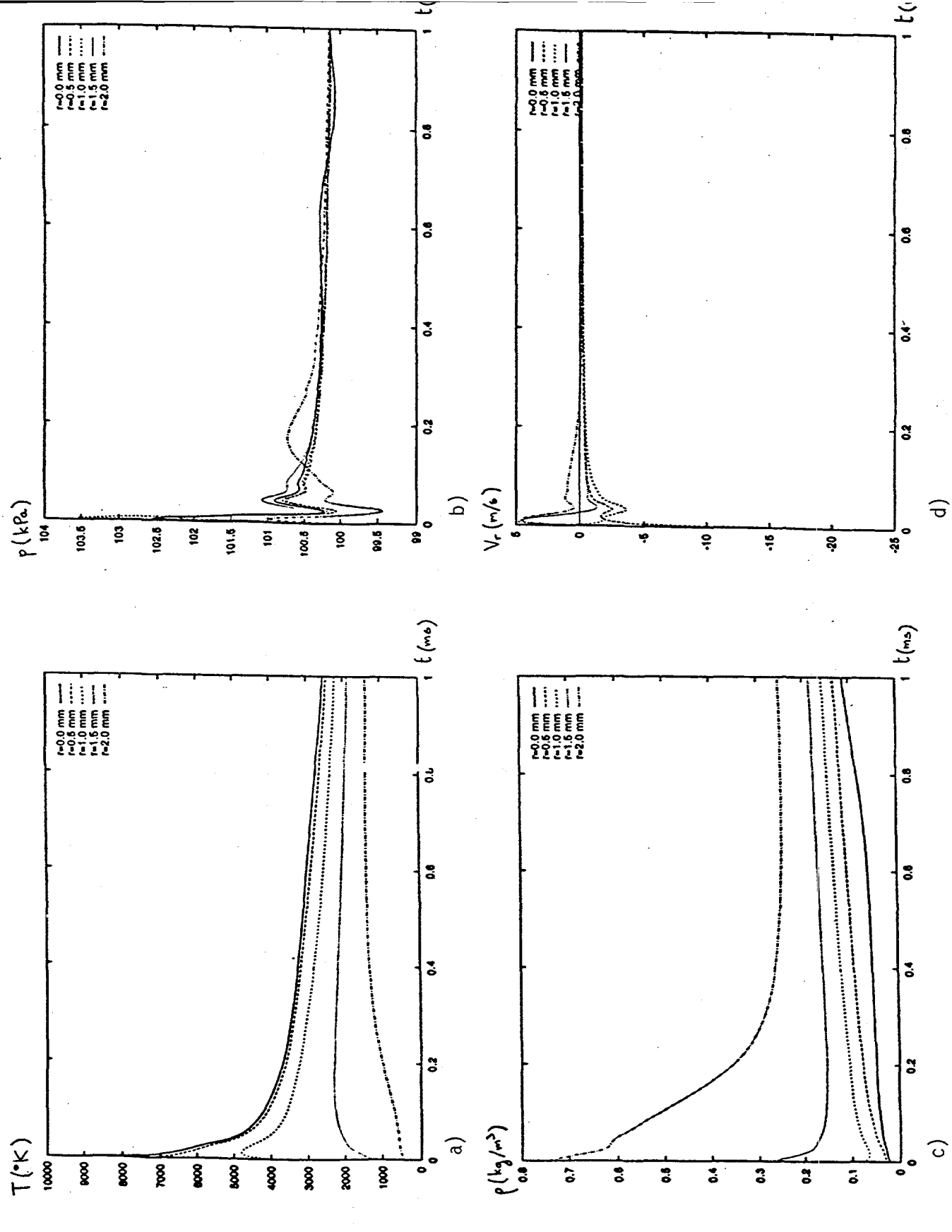

Figure 1 Time evolution of physical parameters : temperature (a), total pressure (b), density (c), radial velocity (d)

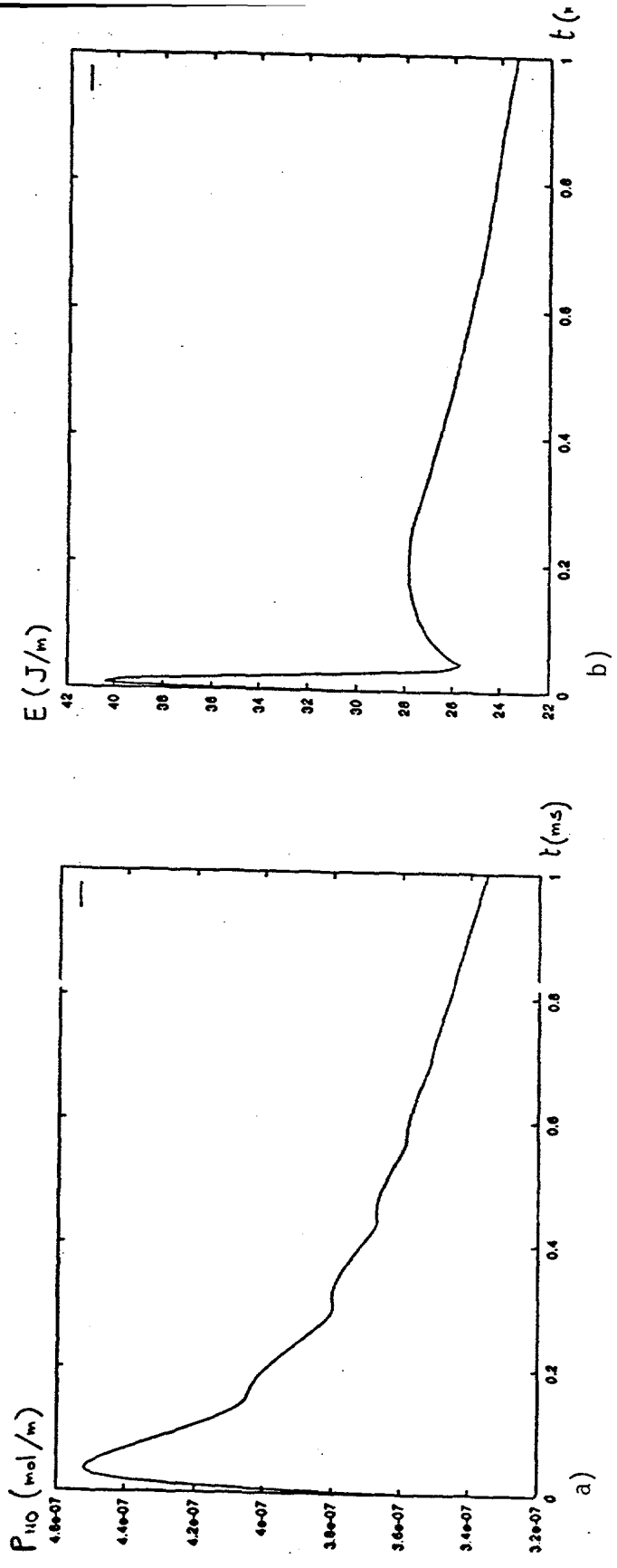

Figure 2 Time evolution of NO amount (a) and thermal energy consumption (b) in a cylinder of unit length